Reaction cascades coupled to surface-chemical nanoscale patterns

Figueiredo da Silva, J.

DOI
10.4233/uuid:a477b7fa-0b2d-44e9-8fbd-68d2320f66c6

Publication date
2025

Document Version
Final published version

Citation (APA)
Figueiredo da Silva, J. (2025). *Reaction cascades coupled to surface-chemical nanoscale patterns*. [Dissertation (TU Delft), Delft University of Technology]. https://doi.org/10.4233/uuid:a477b7fa-0b2d-44e9-8fbd-68d2320f66c6

REACTION CASCADES COUPLED TO SURFACE-CHEMICAL NANOSCALE PATTERNS

JACQUELINE FIGUEIREDO DA SILVA

Reaction cascades coupled to surface-chemical nanoscale patterns.

Dissertation
for the purpose of obtaining the degree of doctor
at Delft University of Technology
by the authority of the Rector Magnificus, Prof.dr.ir. T.H.J.J. van der Hagen,
chair of the Board of Doctorates
to be defended publicly on
Wednesday 15 October 2025 at 10 o'clock

by

Jacqueline FIGUEIREDO DA SILVA
Master of Science in Chemistry,
Jagiellonian University, Poland and Université de Lille, France.

Born in Belém, Brazil.

This dissertation has been approved by the promotors.

Composition of the doctoral committee:

Rector Magnificus	Chairperson
Prof. dr. J.H.van Esch	Delft University of Technology, promotor
Dr. E. Mendes	Delft University of Technology, promotor
Dr. H. Wolf	IBM Research Europe – Zurich, external advisor

Independent members:

Prof. dr. S.J. Picken	Delft University of Technology
Dr. A. Accardo	Delft University of Technology
Prof.dr. J.J.L.M. Cornelissen	University of Twente
Prof. dr. V. Garbin	Delft University of Technology
Prof. dr. R. Eelkema	Delft University of Technology, reserve member

The work described in this dissertation was conducted in IBM Research Europe- Zurich, Switzerland and in the Advanced Soft Matter (ASM) group, Department of Chemical Engineering, Faculty of Applied Sciences, Delft University of Technology, Netherlands. The research was funded by the European Innovative Training Network (ITN) entitled "Chemical Reaction Networks: Signal amplification, spatiotemporal control, and materials" (CReaNet), IBM Research Europe - Zurich and TU Delft.

Table of Contents

Chapter 1

Introduction

1.1 Background

The varied manifestations of life encompass elements such as clocks, [1,2] switches, [3] computation, [4–7] autonomous oscillators, [8–10] and components associated with dynamic behavior. Such manifestations include the computational capacities of neuron synapses [11] and other 'magic' biological systems, [12] which can be understood and modeled through chemical reaction networks (CRNs). [13] In response to the ongoing need for innovative materials to enhance the well-being of society, researchers have taken on the challenge of replicating the remarkable efficiency observed in natural systems. [14–19] Scientists have been designing and investigating artificial CRNs, with focus on the control, prediction, and optimization of chemical processes. [20] These networks can be programmed to perform specific tasks, [21] respond to external stimuli, [22–25] or exhibit dynamic behaviors. [26] The main objective is to comprehend, manipulate, and harness CRNs to create functional and programmable systems. [27,28]

The exploration of spatial and temporal control over CRNs is essential for utilizing them to regulate other spatially confined processes.[24] For instance, this control can ensure the accurate transport of molecules to predetermined locations within a complex environment. [29,30] Approaches to spatiotemporal control of CRNs can be categorized as passive or active. [31] The passive method depends on the natural properties of the chosen chemical system to determine the location and timing of the reaction. In contrast, the active approach depends on external actions that remotely control the CRN onset.

1.2 Passive spatiotemporal control of CRNs

Passive techniques offer the means to control the initiation of a CRN without external stimulus. [31] The term 'passive' indicates the self-regulating nature of the system, as the periodic behavior emerges inherently from the interplay of reaction kinetics and initial conditions without the need for external triggers. [32–36] The passive system utilizes the intrinsic properties of the selected chemical system to anticipate the location and timing of the reaction. [37,38] The initial chemical composition of a system dictates temporal parameters such as the lifetime of a pH transient state. [39] The spatial control of passive CRNs can be achieved by patterning the surface beforehand with an essential chemical in a given system. [40–42] Numerous chemical oscillators have been documented, spanning various fields, including DNA, [43–45] small organic molecule oscillators, [27] and inorganic

redox oscillators. [34] These equilibrium systems demonstrate a self-regulating autonomous behavior, which is a characteristic widespread in living systems. [24]

1.3 Active spatiotemporal control of CRNs

Unlike passive methods, active approaches necessitate an external trigger to start a chemical process. [48] They facilitate the activation and deactivation of a CRN at specific times through a trigger, thereby exerting control over the location and/or timing of the reaction. For instance, light is a well-established trigger to remotely activating or controlling a CRN. [46]

Efforts to achieve spatial control also involve the confinement and controlled delivery of chemical reactants. [47] Researchers developed metallic containers with volumes ranging from picoliters to nanoliters, incorporating modulated pores for the controlled release of specific guests. Temporal control depends on pore size and solvent conditions, while magnetic fields enable remote guidance for spatial control. [48] Furthermore, chemical release is affected by the gel or polymer used for immobilization. [49–53]

1.4 Research goals

To advance the spatiotemporal control of CRNs at the nanoscale, it is vital not only to explore the fabrication of suitable materials and development of micro/nanoscale sensors but also to investigate methods for chemical confinement and transportation. [24] Beyond proof-of-concept, it is important to analyze practical applications by fully expanding and investigating the scope of CRNs in various technologies, to thoroughly realize the potential of these autonomous material systems.

In this context, there has been extensive exploration of systems responsive to pH, with the goal of creating innovative materials [54] and developing applications in biomedicine, such as in drug delivery. [55] This intense research is attributed to the fact that the impacts caused by pH changes act as triggers for numerous artificial and natural CRNs. [24,56] The use of pH as a trigger enables the production of switchable rheology modifiers [24,57,58] and development toward molecular computing. [59]

Studies conducted at TU Delft have reported the use of proton-catalyzed supramolecular gel [60] on catalytic surfaces of micropatterned proton sites through microprinting, [61] micro localized polymer brushes, [62] and nanoparticles. [63] The structures primarily grew in areas where the catalyst was present. Gelator precursors interacted with catalytic sites to create building blocks that self-assemble into nanofibers. Building blocks were incorporated into the fibers within a confined space at the solid-liquid interface. At the IBM Research Europe-Zurich, a device capable of actively controlling a proton-catalyzed CRN through an external trigger was developed. [64] This device demonstrated nanoscale-controlled deposition of bacteriorhodopsin (bR), a light-driven proton gradient.

Within the scope of this thesis, we used microfabrication processes to design devices that enable the spatiotemporal control of established artificial CRNs. Our first approach aimed to couple purple membranes (PM) containing bR with a proton-catalyzed CRN on a substrate. The main goal of this study was to actively control a CRN spatiotemporally at the micro/nanoscale using light-driven proton pumps that deliver CRN fuel. We developed strategies to externally trigger the CRN via (1) spatiotemporal control of catalyst gradient and (2) catalyst transport at the nanoscale. These strategies aimed to spatiotemporally control the construction of synthetic self- assembled systems.

As another application, we explored an autocatalytic CRN that oscillates over time, called the Belousov–Zhabotinsky (BZ) reaction. [65] The passive spatiotemporal control of the BZ reaction at the microscale enables its application on the development of unconventional systems, such as chemical computers. [66] Current computers based on micro-electronic chips struggle with the demand for energy-efficient processing of continuously increasing amounts of data. A silicon-based CRN-driven system represents a potential solution to these issues.

1.5 Thesis outline

This thesis reports “Reaction cascades coupled to surface-chemical nanoscale patterns.” The six chapters of this thesis show the steps conducted to achieve the aim of our research based on different subgoals. This introduction chapter (Chapter 1) briefly overviews the research theme. Chapter 2 presents the microengineering fabrication techniques used in this study, and it describes the investigated CRNs and analytical methods used to characterize the fabricated materials.

Chapters 3, 4, and 5 provide new strategies for the spatiotemporal control of an externally triggered catalyzed CRN, which was expected to promote the development of functional soft materials. More specifically, Chapter 3 reports the development of a microscale pH sensor based on a maskless chemical lift-off method. The chapter aims to measure the pH gradient of a light-driven proton pump PM-containing bR. In Chapter 4, we present a system that incorporates our proton-catalyzed CRN to PM patches. [67] These patches act as a catalyst source when exposed to light. The in-situ formation of the gel was monitored using liquid atomic force microscopy and confocal laser scanning microscopy. In Chapter 5, we describe the fabrication of a nanochannel network in a silicon-based substrate, [68] which was developed aiming to control the transport of a proton gradient from the PM to the other side of the material surface. The goal was to deliver CRN catalyst to different locations.

Chapter 6 reports the development of an unconventional device driven by a self- catalyzed oscillatory CRN. The goal was to establish a chemical computer vision with specific characteristics, including self-powering capability, low energy consumption, highly parallel systems, and complex systems. For that, we developed a microscale diffusion-driven network toward information processing. A summary of this scientific journey is provided

at the end of this thesis.

1.6 References

(1) Tyson, J. J.; Chen, K. C.; Novak, B. Sniffers, Buzzers, Toggles and Blinkers: Dynamics of Regulatory and Signaling Pathways in the Cell. *Current opinion in cell biology* **2003**, *15* (2), 221–231.

(2) Tyson, J. J.; Albert, R.; Goldbeter, A.; Ruoff, P.; Sible, J. Biological Switches and Clocks. *Journal of The Royal Society Interface* **2008**, 5 (suppl_1), S1–S8.

(3) Tyson, J. J. Modeling the Cell Division Cycle: Cdc2 and Cyclin Interactions. *Proceedings of the National Academy of Sciences* **1991**, *88* (16), 7328–7332.

(4) Moore, C.; Mertens, S. *The Nature of Computation*; OUP Oxford, 2011.

(5) Zenil, H. *A Computable Universe: Understanding and Exploring Nature as Computation*; World Scientific, 2013.

(6) Regev, A.; Shapiro, E. Cellular Abstractions: Cells as Computation. *Nature* **2002**, 419 (6905), 343–343.

(7) de Castro, L. N. Fundamentals of Natural Computing: An Overview. Physics of Life Reviews 2007, 4 (1), 1–36.

(8) Ferrell, J. E.; Tsai, T. Y.-C.; Yang, Q. Modeling the Cell Cycle: Why Do Certain Circuits Oscillate? *Cell* **2011**, 144 (6), 874–885.

(9) Qiao, L.; Nachbar, R. B.; Kevrekidis, I. G.; Shvartsman, S. Y. Bistability and Oscillations in the Huang-Ferrell Model of MAPK Signaling. *PLoS computational biology* **2007**, 3 (9), e184.

(10) Nakajima, M.; Imai, K.; Ito, H.; Nishiwaki, T.; Murayama, Y.; Iwasaki, H.; Oyama, T.; Kondo, T. Reconstitution of Circadian Oscillation of Cyanobacterial KaiC Phosphorylation in Vitro. *Science* **2005**, 308 (5720), 414–415.

(11) Abbott, L. F.; Regehr, W. G. Synaptic Computation. *Nature* **2004**, 431 (7010), 796–803.

(12) Novichkov, A. I.; Hanopolskyi, A. I.; Miao, X.; Shimon, L. J.; Diskin-Posner, Y.; Semenov, S. N. Autocatalytic and Oscillatory Reaction Networks That Form Guanidines and Products of Their Cyclization. *Nature communications* **2021**, 12 (1), 2994.

(13) Feinberg, M. Foundations of Chemical Reaction Network Theory. **2019**.

(14) Pecqueur, S.; Mastropasqua Talamo, M.; Guérin, D.; Blanchard, P.; Roncali, J.; Vuillaume, D.; Alibart, F. Neuromorphic Time-dependent Pattern Classification with Organic Electrochemical Transistor Arrays. *Advanced Electronic Materials* **2018**, 4 (9), 1800166.

(15) Adamatzky, A. *Advances in Unconventional Computing: Volume 1*: Theory; Springer, **2016**; Vol. 22.

(16) Adamatzky, A. *Reaction-Diffusion Automata: Phenomenology, Localisations, Computation*; Springer Science & Business Media, **2012**; Vol. 1.

(17) Cucchi, M.; Kleemann, H.; Tseng, H.; Ciccone, G.; Lee, A.; Pohl, D.; Leo, K. Directed Growth of Dendritic Polymer Networks for Organic Electrochemical Transistors and Artificial Synapses. *Advanced Electronic Materials* **2021**, 7 (10), 2100586.

(18) Usami, Y.; van de Ven, B.; Mathew, D. G.; Chen, T.; Kotooka, T.; Kawashima, Y.; Tanaka, Y.; Otsuka, Y.; Ohoyama, H.; Tamukoh, H. In-materio Reservoir Computing in a Sulfonated Polyaniline Network. *Advanced Materials* **2021**, 33 (48), 2102688.

(19) van Duppen, P.; Robinson, W.; Daines, E.; Huck, W. Trajectory-Dependent Compositional Outcomes in a Prebiotic Reaction Network. **2022**.

(20) Sharko, A.; Spitzbarth, B.; Hermans, T. M.; Eelkema, R. Redox-Controlled Shunts in a Synthetic Chemical Reaction Cycle. *J. Am. Chem. Soc.* **2023**, 145 (17), 9672–9678. https://doi.org/10.1021/jacs.3c00985.

(21) Ivanov, N. M.; Baltussen, M. G.; Regueiro, C. L. F.; Derks, M. T. G. M.; Huck, W. T. S. Computing Arithmetic Functions Using Immobilised Enzymatic Reaction Networks. *Angewandte Chemie* **2023**, 135 (7), e202215759. https://doi.org/10.1002/ange.202215759.

(22) Singh, N.; Lopez-Acosta, A.; Formon, G. J. M.; Hermans, T. M. Chemically Fueled Self-Sorted Hydrogels. *J. Am. Chem. Soc.* **2022**, 144 (1), 410–415. https://doi.org/10.1021/jacs.1c10282.

(23) Sharko, A.; Livitz, D.; De Piccoli, S.; Bishop, K. J. M.; Hermans, T. M. Insights into Chemically Fueled Supramolecular Polymers. *Chem. Rev.* **2022**, 122 (13), 11759–11777. https://doi.org/10.1021/acs.chemrev.1c00958.

(24) Sharma, C.; Maity, I.; Walther, A. pH-Feedback Systems to Program Autonomous Self-Assembly and

Material Lifecycles. *Chem. Commun.* **2023**, 59 (9), 1125–1144. https://doi.org/10.1039/D2CC06402B.
(25) Maity, I.; Wagner, N.; Mukherjee, R.; Dev, D.; Peacock-Lopez, E.; Cohen-Luria, R.; Ashkenasy, G. A Chemically Fueled Non-Enzymatic Bistable Network. *Nature Communications* **2019**, 10 (1), 4636.
(26) Leira-Iglesias, J.; Tassoni, A.; Adachi, T.; Stich, M.; Hermans, T. M. Oscillations, Travelling Fronts and Patterns in a Supramolecular System. *Nature Nanotech* **2018**, 13 (11), 1021–1027. https://doi.org/10.1038/s41565-018-0270-4.
(27) Ter Harmsel, M.; Maguire, O. R.; Runikhina, S. A.; Wong, A. S.; Huck, W. T.; Harutyunyan, S. R. A Catalytically Active Oscillator Made from Small Organic Molecules. *Nature* **2023**, 621 (7977), 87–93.
(28) Wang, Q.; Qi, Z.; Chen, M.; Qu, D.-H. Out-of-equilibrium Supramolecular Self-assembling Systems Driven by Chemical Fuel. *Aggregate* **2021**, 2 (5), e110.
(29) Wang, F.; Zhang, X.; Liu, X.; Fan, C.; Li, Q. Programming Motions of DNA Origami Nanomachines.*Small* **2019**, 15 (26), 1900013. https://doi.org/10.1002/smll.201900013.
(30) Desrosiers, A.; Derbali, R. M.; Hassine, S.; Berdugo, J.; Long, V.; Lauzon, D.; De Guire, V.; Fiset, C.; DesGroseillers, L.; Leblond Chain, J.; Vallée-Bélisle, A. Programmable Self-Regulated Molecular Buffers for Precise Sustained Drug Delivery. *Nat Commun* **2022**, 13 (1), 6504. https://doi.org/10.1038/s41467-022-33491-7.
(31) Aubert, S.; Bezagu, M.; Spivey, A. C.; Arseniyadis, S. Spatial and Temporal Control of Chemical Processes. *Nat Rev Chem* **2019**, 3 (12), 706–722. https://doi.org/10.1038/s41570-019-0139-6.
(32) Mai, A. Q.; Bánsági Jr, T.; Taylor, A. F.; Pojman Sr, J. A. Reaction-Diffusion Hydrogels from Urease Enzyme Particles for Patterned Coatings. *Communications Chemistry* **2021**, 4 (1), 101.
(33) Xie, X.-Q.; Zhang, Y.; Liang, Y.; Wang, M.; Cui, Y.; Li, J.; Liu, C.-S. Programmable Transient Supramolecular Chiral G-quadruplex Hydrogels by a Chemically Fueled Non-equilibrium Self-Assembly Strategy. *Angewandte Chemie* **2022**, 134 (9), e202114471.
(34) Shandilya, E.; Brar, S. K.; Mahato, R. R.; Maiti, S. Spatiotemporal Dynamics of Self-Assembled Structures in Enzymatically Induced Agonistic and Antagonistic Conditions. *Chemical Science* **2022**, 13 (1), 274–282.
(35) Paikar, A.; Novichkov, A. I.; Hanopolskyi, A. I.; Smaliak, V. A.; Sui, X.; Kampf, N.; Skorb, E. V.; Semenov, S. N. Spatiotemporal Regulation of Hydrogel Actuators by Autocatalytic Reaction Networks. *Advanced Materials* **2022**, 34 (13), 2106816. https://doi.org/10.1002/adma.202106816.
(36) Orbán, M.; Kurin-Csörgei, K.; Epstein, I. R. pH-Regulated Chemical Oscillators. *Accounts of Chemical Research* **2015**, 48 (3), 593–601.
(37) Ashkenasy, G.; Hermans, T. M.; Otto, S.; Taylor, A. F. Systems Chemistry. *Chem. Soc. Rev.* **2017**, 46 (9), 2543–2554. https://doi.org/10.1039/C7CS00117G.
(38) Wagner, N.; Hochberg, D.; Peacock-Lopez, E.; Maity, I.; Ashkenasy, G. Open Prebiotic Environments Drive Emergent Phenomena and Complex Behavior. *Life* **2019**, 9 (2), 45.
(39) Tóth-Szeles, E.; Horváth, J.; Holló, G.; Szűcs, R.; Nakanishi, H.; Lagzi, I. Chemically Coded Time-Programmed Self-Assembly. *Molecular Systems Design & Engineering* **2017**, 2 (3), 274–282.
(40) Durie, K.; Yatvin, J.; McNitt, C. D.; Reese, R. A.; Jung, C.; Popik, V. V.; Locklin, J. Multifunctional Surface Manipulation Using Orthogonal Click Chemistry. *Langmuir* **2016**, 32 (26), 6600–6605.
(41) Arnold, R. M.; Patton, D. L.; Popik, V. V.; Locklin, J. A Dynamic Duo: Pairing Click Chemistry and Postpolymerization Modification to Design Complex Surfaces. *Accounts of chemical research* **2014**, 47 (10), 2999–3008.
(42) Arnold, R. M.; McNitt, C. D.; Popik, V. V.; Locklin, J. Direct Grafting of Poly (Pentafluorophenyl Acrylate) onto Oxides: Versatile Substrates for Reactive Microcapillary Printing and Self-Sorting Modification. *Chemical Communications* **2014**, 50 (40), 5307–5309.
(43) Franco, E.; Friedrichs, E.; Kim, J.; Jungmann, R.; Murray, R.; Winfree, E.; Simmel, F. C. Timing Molecular Motion and Production with a Synthetic Transcriptional Clock. *Proceedings of the National Academy of Sciences* **2011**, 108 (40), E784–E793. https://doi.org/10.1073/pnas.1100060108.
(44) Padirac, A.; Fujii, T.; Estévez-Torres, A.; Rondelez, Y. Spatial Waves in Synthetic Biochemical Networks. *J. Am. Chem. Soc.* **2013**, 135 (39), 14586–14592. https://doi.org/10.1021/ja403584p.
(45) Tayar, A. M.; Karzbrun, E.; Noireaux, V.; Bar-Ziv, R. H. Synchrony and Pattern Formation of Coupled Genetic Oscillators on a Chip of Artificial Cells. *Proceedings of the National Academy of Sciences* **2017,** 114 (44), 11609–11614.
(46) Kalayci, K.; Frisch, H.; Truong, V. X.; Barner-Kowollik, C. Green Light Triggered [2+ 2] Cycloaddition of Halochromic Styrylquinoxaline—Controlling Photoreactivity by pH. *Nature Communications* **2020**, 11

(1), 4193.
(47) Kalinin, Y. V.; Murali, A.; Gracias, D. H. Chemistry with Spatial Control Using Particles and Streams. *RSC advances* **2012**, 2 (26), 9707–9726.
(48) Leong, T.; Gu, Z.; Koh, T.; Gracias, D. H. Spatially Controlled Chemistry Using Remotely Guided Nanoliter Scale Containers. *Journal of the American Chemical Society* **2006,** 128 (35), 11336–11337.
(49) Monks, P.; Wychowaniec, J. K.; McKiernan, E.; Clerkin, S.; Crean, J.; Rodriguez, B. J.; Reynaud, E. G.; Heise, A.; Brougham, D. F. Spatiotemporally Resolved Heat Dissipation in 3D Patterned Magnetically Responsive Hydrogels. *Small* **2021**, 17 (5), 2004452.
(50) Hobich, J.; Blasco, E.; Wegener, M.; Mutlu, H.; Barner-Kowollik, C. Synergistic, Orthogonal, and Antagonistic Photochemistry for Light-Induced 3D Printing. *Macromolecular Chemistry and Physics* **2023**, 224 (1), 2200318.
(51) Gregor, A.; Filová, E.; Novák, M.; Kronek, J.; Chlup, H.; Buzgo, M.; Blahnová, V.; Lukášová, V.; Bartoš, M.; Nečas, A. Designing of PLA Scaffolds for Bone Tissue Replacement Fabricated by Ordinary Commercial 3D Printer. *Journal of biological engineering* **2017**, 11 (1), 1–21.
(52) Hippler, M.; Lemma, E. D.; Bertels, S.; Blasco, E.; Barner-Kowollik, C.; Wegener, M.; Bastmeyer, M. 3D Scaffolds to Study Basic Cell Biology. *Advanced Materials* **2019**, 31 (26), 1808110.
(53) Barner-Kowollik, C.; Bastmeyer, M.; Blasco, E.; Delaittre, G.; Müller, P.; Richter, B.; Wegener, M. 3D Laser Micro-and Nanoprinting: Challenges for Chemistry. *Angewandte Chemie International Edition* **2017,** 56 (50), 15828–15845.
(54) Wang, G.; Liu, Y.; Liu, Y.; Xia, N.; Zhou, W.; Gao, Q.; Liu, S. The Non-Equilibrium Self-Assembly of Amphiphilic Block Copolymers Driven by a pH Oscillator. *Colloids and Surfaces A: Physicochemical and Engineering Aspects* **2017**, 529, 808–814. https://doi.org/10.1016/j.colsurfa.2017.06.078.
(55) Sonawane, S. J.; Kalhapure, R. S.; Govender, T. Hydrazone Linkages in pH Responsive Drug Delivery Systems. *European Journal of Pharmaceutical Sciences* **2017**, 99, 45–65. https://doi.org/10.1016/j.ejps.2016.12.011.
(56) Wang, X.; Moreno, S.; Boye, S.; Wen, P.; Zhang, K.; Formanek, P.; Lederer, A.; Voit, B.; Appelhans, D. Feedback-Induced and Oscillating pH Regulation of a Binary Enzyme–Polymersomes System. *Chem. Mater.* **2021,** 33 (17), 6692–6700. https://doi.org/10.1021/acs.chemmater.1c00897.
(57) Go, D.; Rommel, D.; Chen, L.; Shi, F.; Sprakel, J.; Kuehne, A. J. Programmable Phase Transitions in a Photonic Microgel System: Linking Soft Interactions to a Temporal pH Gradient. *Langmuir* **2017**, 33 (8), 2011–2016.
(58) Boekhoven, J.; Hendriksen, W. E.; Koper, G. J. M.; Eelkema, R.; Van Esch, J. H. Transient Assembly of Active Materials Fueled by a Chemical Reaction. *Science* **2015**, 349 (6252), 1075–1079. https://doi.org/10.1126/science.aac6103.
(59) Draper, T. C.; Poros-Tarcali, E.; Pérez-Mercader, J. pH Oscillating System for Molecular Computation as a Chemical Turing Machine. *ACS Omega* **2022**, 7 (7), 6099–6103. https://doi.org/10.1021/acsomega.1c06505.
(60) Boekhoven, J.; Poolman, J. M.; Maity, C.; Li, F.; Van Der Mee, L.; Minkenberg, C. B.; Mendes, E.; Van Esch, J. H.; Eelkema, R. Catalytic Control over Supramolecular Gel Formation. *Nature Chem* **2013**, 5 (5), 433–437. https://doi.org/10.1038/nchem.1617.
(61) Olive, A. G.; Abdullah, N. H.; Ziemecka, I.; Mendes, E.; Eelkema, R.; Van Esch, J. H. Spatial and Directional Control over Self-Assembly Using Catalytic Micropatterned Surfaces. *Angewandte Chemie International Edition* **2014**, 53 (16), 4132–4136.
(62) Wang, Y.; Oldenhof, S.; Versluis, F.; Shah, M.; Zhang, K.; Van Steijn, V.; Guo, X.; Eelkema, R.; Van Esch, J. H. Controlled Fabrication of Micropatterned Supramolecular Gels by Directed Self-Assembly of Small Molecular Gelators. *Small* **2019**, 15 (8), 1804154. https://doi.org/10.1002/smll.201804154.
(63) Wang, Y.; Versluis, F.; Oldenhof, S.; Lakshminarayanan, V.; Zhang, K.; Wang, Y.; Wang, J.; Eelkema, R.; Guo, X.; Van Esch, J. H. Directed Nanoscale Self-Assembly of Low Molecular Weight Hydrogelators Using Catalytic Nanoparticles. *Advanced Materials* **2018**, 30 (21), 1707408. https://doi.org/10.1002/adma.201707408.
(64) Ruggeri, F.; Schwemmer, C.; Stauffer, M.; Nicollier, P. M.; Figueiredo da Silva, J.; Bosshart, P. D.; Kochems, K.; Fotiadis, D.; Knoll, A.; Wolf, H. Placement of Biological Membrane Patches in a Nanofluidic Gap With Control Over Position and Orientation. *Advanced materials interfaces* **2022,** 9 (23), 2200941.
(65) Field, R. J.; Noyes, R. M. Oscillations in Chemical Systems. IV. Limit Cycle Behavior in a Model of a Real Chemical Reaction. The Journal of Chemical Physics 1974, 60 (5), 1877–1884.

https://doi.org/10.1063/1.1681288.

(66) Dueñas-Díez, M.; Pérez-Mercader, J. How Chemistry Computes: Language Recognition by Non-Biochemical Chemical Automata. From Finite Automata to Turing Machines. *iScience* **2019**, 19, 514–526. https://doi.org/10.1016/j.isci.2019.08.007.

(67) Figueiredo da Silva, J.; Roshanasan, A.; Bus, M.; Fotiadis, D.; Knoll, A. W.; van Esch, J. H.; Wolf, H. Control of a Gel-Forming Chemical Reaction Network Using Light-Triggered Proton Pumps. *Langmuir* **2025**.

(68) Figueiredo Da Silva, J.; Bacheva, V.; Drechsler, U.; Nicollier, P.; Reidt, S.; Fotiadis, D.; Knoll, A.; Wolf, H. Fabrication of a Hybrid Device for the Integration of Light-Triggered Proton Pumps. *Micro and Nano Engineering* **2024**, 23, 100250. https://doi.org/10.1016/j.mne.2024.100250.

Chapter 2

Nanofabrication and microfabrication: techniques and materials

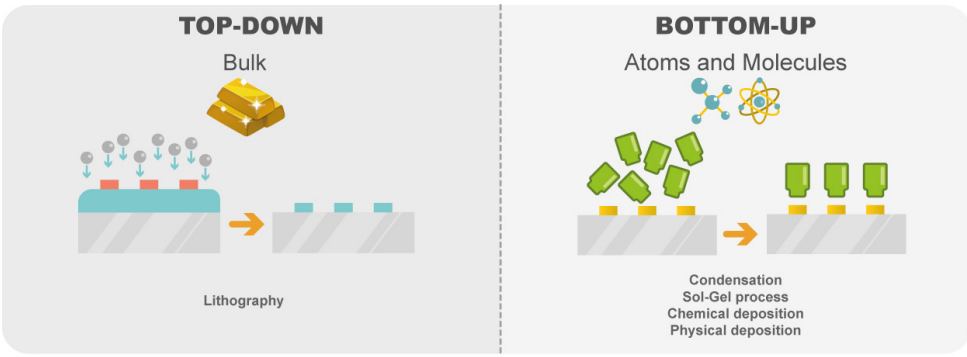

Abstract: This chapter covers the top-down and bottom-up fabrication techniques employed in the fabrication of the devices presented in the thesis. Additionally, an introduction to purple membranes—a light-driven proton pump explored in chapters 3, 4, and 5—and chemical reaction networks utilized in the thesis is provided. Lastly, a brief overview of the analytical techniques employed to study our system is presented.

2.1 Introduction

Research on materials development has been conducted worldwide to address current and future societal needs. [1] Specifically, the study of polymers and surface chemistry has attracted increasing interest owing to their large utilization scope, from the development of household items to biomedical applications. These fields of study are the background for the development of nanomaterials. The manipulation of micro/nano-objects is essential for the development of novel lab-on-chip devices to diagnose and fabricate next-generation nanoscale electronic devices. [2] Nano and microscale materials can be synthesized via top-down or bottom-up methods. These methods are complementary to each other, so nanotechnology-based products must converge these approaches to enable large-scale fabrication. [3]

2.2 Top-down fabrication

The top-down approach comprises a controlled and repeatable method for the nanofabrication of surface patterns and devices. Lithography is an example of a top-down method, and it is used to introduce patterns to materials. We used three types of lithography techniques: thermal scanning probe lithography (t-SPL), photolithography, and direct laser writing (DLW). The patterns transferred by lithography are commonly transferred to a functional layer via etching.

2.2.1 Thermal scanning probe lithography

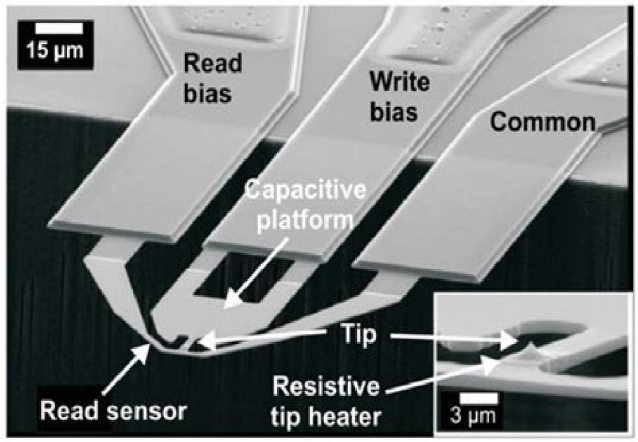

Figure 2.1. Cantilever of t-SPL with two resistive heaters, one under the tip (inset), and the other acting as a read sensor. [4]

The t-SPL developed by IBM, [5] is a cutting-edge direct-write scanning probe lithographic technique utilizing heated tips to generate various nanostructures. This method can write high-resolution nanoscale patterns with structures as small as 10 nm, even under

atmospheric conditions. It employs a heated nanoscale tip to directly write patterns onto a surface by locally removing or modifying material. [5] When the hot cantilever tip is pushed into contact with a heat-labile resist placed on the substrate surface, the resist is removed, forming a topographical pattern (Figure 2.1). [4] The tool contains a read sensor that can produce high-resolution topographic images based on the heat flow from the sensor to the surface through the air.

The t-SPL is mostly operated for material removal by using the heated tip to modify the surface topography. In this context, polyphthalaldehyde (PPA) is an excellent resist material that can be used to transfer a pattern to the deposited substrate for the manufacture of topographical nanostructures using t-SPL. [6,7] That is, PPA behaves as a self-amplifying resist material. PPA is a metastable compound with low ceiling temperature (−43 °C), [8] and it readily depolymerizes upon cleavage of a single bond of the main chain, even at room temperature (Figure 2.2). For t-SPL patterning using PPA, the hot tip induces bond breakage. It simultaneously promotes patterning and polymer removal, thereby superseding the wet development of PPA. The resist depolymerizes completely into phthalaldehyde monomer units at temperatures above 150 °C.

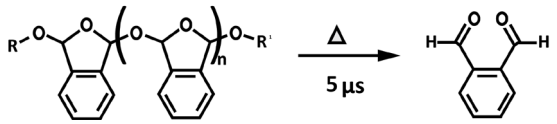

Figure 2.2. Depolymerization of polyphthalaldehyde after heating. [6]

The advantages of t-SPL include the absence of charging during material modification, a robust and compact setup compatible with ambient conditions, in-situ Atomic Force Microscopy (AFM) imaging, closed-loop lithography, and maskless overlay and stitching. [9] Owing to its precise control of actuation force and the duration of the tip– sample contact, the t-SPL technique can also be used to perform 3D patterning. This differs from mask-dependent approaches because the latter are limited to the fabrication of 2D structures. T-SPL is explored in Chapter 3 concerning localized surface functionalization and in Chapter 5 regarding the overlay of nanoscale and microscale patterning.

2.2.2 Photolithography

Photolithography [10,11] is widely utilized in the production of semiconductor devices, advanced electronic components, displays, and other related objects. Photolithography, in contrast to t-SPL, is suitable for batch fabrication. Its main advantage is the efficient and reliable transfer of high-fidelity, accurate replicas of the desired device structures onto silicon. It does so at a cost-effective rate while ensuring high wafer throughput. This technique operates by using optical wavelength radiation to imprint patterns onto the substrate surface. A photosensitive layer is coated onto the substrate, which is then irradiated with optical radiation in a controlled manner to transfer the design. In traditional

photolithography, a photomask is created, serving as a template, the desired design is transferred onto a resist-covered wafer. A mask aligner is then used to transfer the pattern.

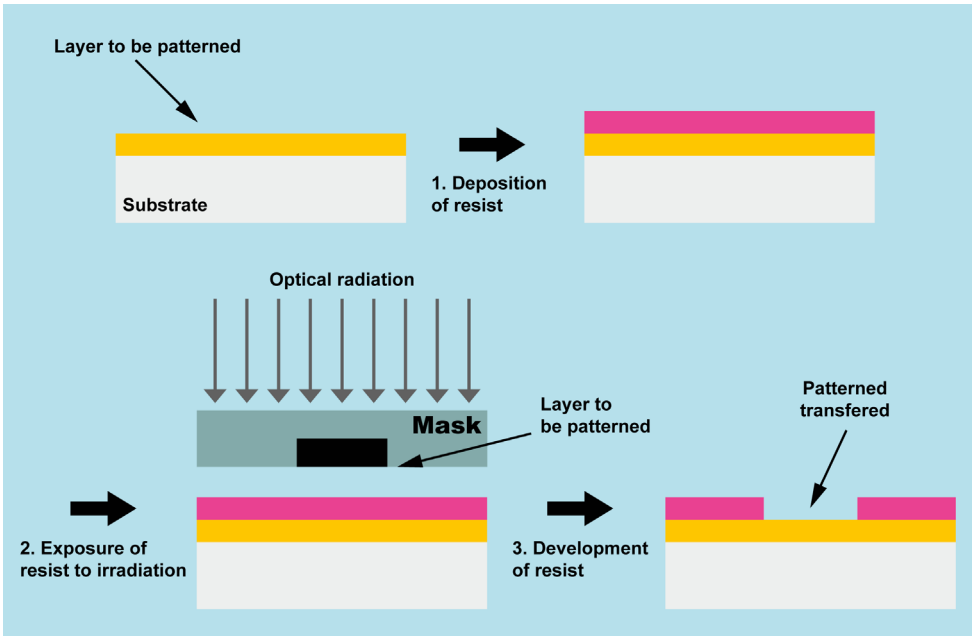

Figure 2.3. Common steps in pattern transfer through photolithography. Step 1: deposition of photosensitive resist. Step 2: exposure of sample to irradiation in localized areas defined by a photomask. Step 3: transfer of pattern from mask to photoresist on the substrate surface after resist development.

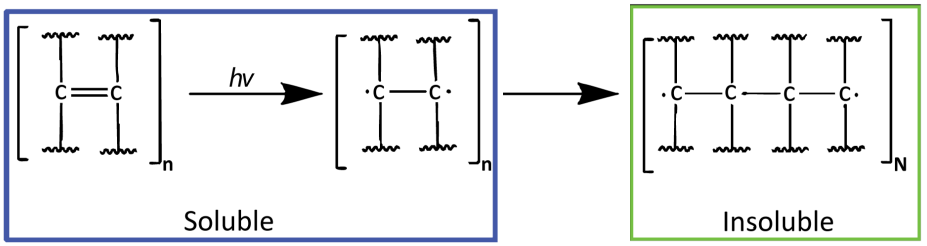

Figure 2.4. General mechanism of negative photoresists. The mechanism involves the creation of unstable free radicals by ultraviolet energy, which break a double bond. These radicals then bond head-to-tail, forming cross-linked polymers or long chains.

As shown in Figure 2.3, photolithography involves several stages, including substrate surface preparation, resist application, heating of the resist (to remove excess solvents), resist development, and inspection to verify accurate pattern transfer and alignment. The

employed photoresist can be either positive or negative. In positive resist, the exact mask design is replicated onto the photoresist, whereas a negative resist creates an inverted pattern. Following exposure, the photosensitive layer is treated with a developer solution, dissolving the resist in unwanted areas. After patterning the resist, the design is transferred onto the substrate's surface, typically via etching.

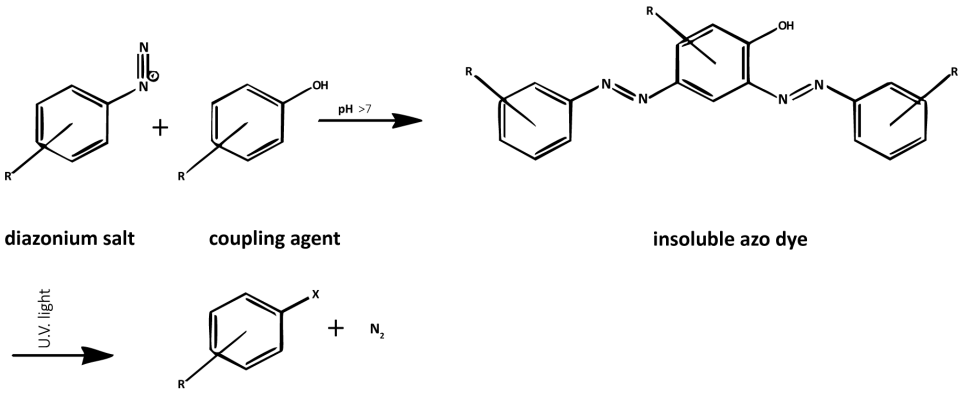

Figure 2.5. Example of reactions involved in positive photoresists.

Negative photoresists typically consist of compounds with double or ethylenic bonds that, when exposed to UV light (Figure 2.4), break into diradicals. These free radicals rapidly form head-to-tail bonds, leading to the formation of cross-linked or long-chain polymers. As a result, exposed regions have low solubility and increased chemical resistance, while unexposed areas remain soluble and are removed during development, leaving a patterned structure.

Photolithography with positive photoresists relies on reactions, such as those shown in Figure 2.5, where diazonium salts or diazides react with phenolic compounds in alkaline conditions to form insoluble azo dyes. Upon exposure to UV light, the diazo group in these compounds decomposes, releasing nitrogen and preventing further dye formation. As a result, the exposed regions become soluble and are dissolved by the developer, while the unexposed areas remain intact. The developer provides the necessary alkalinity to facilitate this coupling reaction, ensuring precise pattern formation. Photolithography was employed in Chapters 5 and 6 for the design of microfluidic and nanofluidic channels.

2.2.3 Direct laser writing

DLW is used to fabricate features at sub-micron dimensions. [12] This is achieved by utilizing spatial light modulator micro-arrays to directly project the pattern onto the substrate.[13] In our experiments, the patterns were transferred onto a photoresist placed on a transparent substrate fully covered by a layer of chromium on one side. Next, a wet chemical etching process was performed to transfer the patterns from the resist onto a silicon wafer. [14] Depending on the photoresist type, either the exposed areas (in positive resist) or the

unexposed areas (in negative resist) can be removed. DLW was employed in Chapters 5 and 6 for the design of photolithography masks.

2.2.4 Etching of material

Material removal in semiconductor device fabrication is carried out through a chemical process known as etching. [15] In this process, the samples are exposed to chemicals, such as acids or halogen compounds (Br, Cl, F), which react with the exposed surfaces for a controllable material loss. Certain parts of the device can be coated with etch-resistant materials, as resists, to obtain different device geometries. The specific patterns are defined by masks on the material surface. Etching methods can be classified as (1) wet etching, which is based on liquids; and (2) dry etching, which is based on gas- or vapor-phase chemistry. Usually, wet etching can define an undercut beneath a masked feature. (isotropic etch), whereas dry etching acts vertically (anisotropic etch) (Figure 2.6).

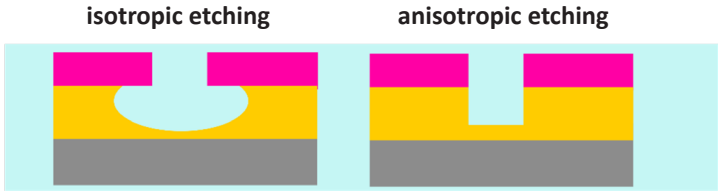

Figure 2.6. Etch profiles obtained from isotropic and anisotropic etching. The pink and yellow areas represent the resist and etched material, respectively.

Wet etching [11,15] uses liquid chemicals and chemical solutions to remove materials from a dipped substrate. Wet chemical etching comprises three key mechanisms: (1) diffusion of reactants to the surface, (2) chemical reaction at the substrate, and (3) removal of by-products via diffusion and evacuation. The etch rate, which indicates how much material is removed per unit of time, is controlled by the temperature of the solution, the concentration of the etchant, and the agitation of the liquid. Since the process relies on chemical reactions, high selectivity can be achieved between the etch rates of different materials. Other advantages of wet etching include comparatively flat etching profile, high consistency, and adjustable etching rate. However, wet etching often results in the isotropic removal of etchable materials, which leads to the undercutting of masking materials. This can decrease the resolution of the etched pattern. In this study, we used Cr wet etching to fabricate photolithography masks. Other etching processes were performed under dry conditions.

In dry etching, [11,15] plasmas or etchant gases or plasmas are utilized to remove material from the substrate. This process can be classified into physical, chemical, or physicochemical etching methods. Physical dry etching relies on the kinetic energy of photon beams, electrons or ions to strike the substrate surface. These high-energy particles dislodge atoms, causing the material to evaporate as it leaves the surface. Given that no chemical reaction happens, this technique can etch a broad range of materials. However, its main drawbacks

include a slow etch rate, reduced selectivity and trenching effects from reflected ions.

In contrast, chemical dry etching depends on the chemical interaction among different etchant gases and the substrate material. The reaction produces gaseous by-products that are crucial because solid product deposition would block the etching process by protecting the surface. This method offers relatively high selectivity, and it is usually isotropic. Chemical dry etching is commonly used for wafer cleaning, where oxygen plasma, by way of example, can remove photoresists and other organic films.

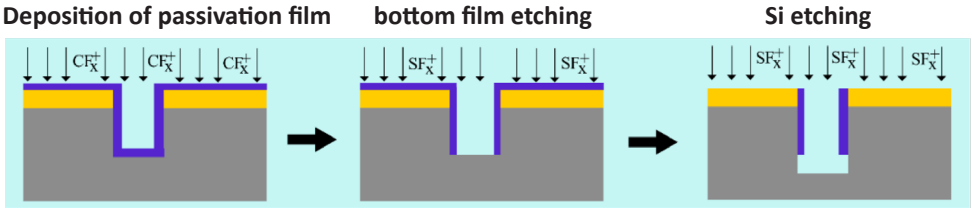

Figure 2.7. Representation of the Bosch process cycle: (1) deposition of passivation films by the C_4F_8 reaction, which forms CFx radicals; (2) bottom film etching by SF_6 gas, which forms fluorine radicals and ions; and (3) Si etch, which forms fluorine radicals.

Reactive Ion Etching (RIE) operates based on the principles of physical-chemical etching. The etch rates fall within a range that is intermediate between those of purely physical and purely chemical etching processes. Ions are directed almost perpendicularly to the substrate under strong electric field and low pressure. However, the high aspect-ratio of dry etch is less desirable than that of wet etch. A technique called deep RIE (DRIE), or Bosch process, can be used to fabricate a high aspect-ratio structure (Figure 2.7). The DRIE process is independent of the crystal orientation of the wafers. The etch cycle consists of two phases: etching and deposition. During the etching phase, silicon is removed using SF_6, and the etch front advances by 0.5 to 1.5 µm over 5 to 15 seconds. During the passivation phase, the gas supply is changed to C_4F_8, forming a 10 nm fluorocarbon polymer film on the trench wall. In the subsequent cycle, ion bombardment removes the polymer film from the bottom surface, while the film on the sidewalls remains intact, protecting them from etching.

A variant of RIE is the dual power inductively coupled plasma reaction RIE (ICP-RIE), [16] generates a high-density plasma at low pressure. In ICP-RIE, the ICP power and substrate bias can be adjusted independently to control both plasma density and ion energy. The low-pressure environment improves anisotropy and etch rate by enhancing ion flux directionality, even at low bias voltages. Consequently, it enables the full spectrum of physical to chemical processes and possible combinations. Table 2.1. lists the etch recipes used in this thesis.

Table 2.1. Recipe of etchants used in this thesis.

Etched material	Etching technique	Type of etch	Chemical components
Si	RIE	Isotropic	SF_6/Ar
Si	DRIE	Anisotropic	C_4F_8/ SF_6
Si	ICP-RIE	Anisotropic	HBr
SiO_2	RIE	Anisotropic	CHF_3/Ar
Al_2O_3	ICP-RIE	Anisotropic	BCl_3/Ar
Cr	Wet	Isotropic	$(NH_4)_2[Ce(NO_3)_6]$

2.3 Bottom-up fabrication

In bottom-up methods, simple building blocks come together in a coordinated manner to form larger and more complex supramolecular assemblies. [17] The building blocks are formed by atoms, molecules, and particles that self-stack onto the substrate to form macro- to nanoscale structures. This method demands a strong comprehension of each molecular structure involved in the system, the respective assembling manner, and the dynamic components. The material growth promoted by deposition leads to a high level of control over the material composition, and significant advantages include the size precision and control of the physical properties of the developed material. In this study, the bottom-up methods used for the deposition of materials included thermal oxidation (TO), plasma-enhanced chemical vapor deposition (PECVD), atomic layer deposition (ALD), anodic bonding, molecular self-assembly (MSA), and tunable nanofluidic confinement (TNCA).

2.3.1 Thermal oxidation

TO is employed to generate a thin oxide layer on the material surface. [15,18] This technique compels the oxidant to spread through the material at elevated temperatures, where it reacts with the material. When silicon is exposed to an oxygen-rich environment, it reacts to form a silicon dioxide layer

$$Si_{(solid)} + O_{2\,(gas)} \rightarrow SiO_{2\,(solid)}$$

As the reaction progresses, the oxidation rate slows as oxygen diffuses through the SiO_2 layer to the silicon surface, where the reaction continues, forming more oxide. The typical layer thickness obtained by TO ranges from 6 to 1000 nm. [19] In Chapter 3 and 5, TO-SiO_2 layers were used on silicon surfaces in the devices presented.

2.3.2 Plasma-enhanced chemical vapor deposition

As an alternative to TO, SiO_2 layers can be deposited on silicon from the gas phase via PECVD. In PECVD, the plasma is made up of neutral species, ions and electrons in both their ground and excited states. [20] Plasma is generated and sustained by applying high-frequency voltage to a low-pressure gas, where electron-gas collisions produce reactive

species like free radicals, ions, and electrons. When transport gases interact with the wafer, a chemical reaction takes place on its surface, leading to the deposition of new material. The electrons gain adequate energy from the applied electric field to generate highly reactive species. PECVD utilizes these reactive species to deposit thin films, which enables the use of lower temperatures, typically from 100 to 300 °C. The species present in the gases facilitate the deposition of thin semiconductor layers, such as silicon layers with controlled dopant concentrations or insulators like SiO_2. The benefits of SiO_2 PECVD over thermal SiO_2 include (1) rapid growth of thick layers compared to TO, (2) the unbiased composition of the SiO_2 layer in relation to the substrate, and (3) the capability to process a larger number of wafers simultaneously. Furthermore, the PECVD SiO_2 is more amorphous, and its etch rate is higher. PECVD SiO_2 layers were used in chapter 4, and 5.

2.3.3 Atomic layer deposition

ALD [15,21] is a thin film deposition method that can produce conformal layers with thickness ranging from angstrom to nanometers. Its distinct self-limiting growth mechanism ensures a film maintaining conformality and consistent thickness, including intricate 3D structures. While like CVD, this process depends on an alternating sequence of self-limiting chemical reactions on the wafer surface. During each cycle, the wafer is subjected to gaseous precursors, facilitating surface reactions that continue until the complete formation of a single atomic layer is attained. The new surface is then exposed to a second set of self-limiting precursors to produce a new nuclear layer on the first layer; the material is purged with inert gas between each pulse. The deposition of ALD Al_2O_3 and SiO_2 was extensively explored in Chapter 5.

2.3.4 Anodic bonding

Anodic bonding is an electrochemical process that produces a sealing effect between silicon or metal and glass. [11] We applied this technique by setting a glass wafer and a silicon wafer. Bonding takes place when the wafers are positioned within the chuck, and the temperature is raised to a level just below the glass transition temperature (approximately 400 °C), followed by the application of an electric potential of approximately 1 kV. When a specific temperature is reached, the oxides dissociate, and under the influence of an electric field, alkali ions are transported into the glass, leading to the formation of an oxygen-enriched layer at the wafer interface. In this electrochemical process, silicon serves as the anode, connected to the positive electrode, while the glass functions as the cathode. The anodic bonding process results in a significant temperature variation within the glass/silicon stack. The coefficient of thermal expansion of the processed glass should closely match that of silicon.

Because glass is optically transparent, this bonding technique is ideal for the fabrication of microfluidic networks that require optical access for the control and analysis of the fluid. Anodic bonding was utilized for the fabrication of microfluidic networks in Chapters 5 and 6.

2.3.5 Molecular self-assembly

Self-assembly is the natural grouping of individual components into ordered patterns. [22] MSA is based on the recognition of relatively simple building blocks by themselves or with a substrate (self-assembled monolayer), which generates ordered structures at the micro- to nanoscale. [17] The order and specific recognition of the building blocks are based on the combination of various non-covalent interactions. [23]

Nanoscale MSA is based on the interplay between different forces in the self-assembly that are often related because of the combined effect of long-range repulsive forces and short-range attractive forces. [24] Assemblies can also be related to long-range attractive forces, such as negatively charged nanoparticles assembled on positively charged lines. In this case, the particles are attracted by the long-range electrostatic energy of the positive potential of the lines, and they are guided into the lines by their repulsive force. Their line density is also governed by the repulsion among them. [25]

MSA can be classified as static or dynamic. In a system, static self-assemblies are governed by the reduction of free energy, which represents the moment when the system approaches equilibrium. Dynamic self-assembly occurs when the system dissipates energy, thereby forming an out-of-equilibrium system in which the competition between kinetic and thermodynamic forces of a chemical reaction occurs. [26] Usually, considering the same thermodynamic conditions, the solid phase displays less entropy on a macro scale than the liquid and gas phases. However, this can change at the nanoscale. An increase in entropy might drive nanoscale objects to form organized patterns in a controllable manner. [27] This phenomenon is common in biological systems, in which the self-assembly of multiple building blocks includes more ordered structures under the total or partial influence of an energy source. [28]

In this thesis, a dynamic proton-catalyzed chemical reaction network (CRN) is directly explored in Chapter 4. Chapter 5 discusses the application of such CRN in a fabricated device.

2.3.6 Tunable nanofluidic confinement

The simultaneous deposition of nanomaterials in specific positions on a substrate demands their attraction to the desired positions, short-range alignment, and stable long-range means of transport. TNCA enables the accurate deposition of nanoparticles by confining colloids and molecules in a nanoscale slit between a topographically patterned substrate and a movable cover.

TNCA manipulates particles via geometry-induced energy landscapes in a nanofluidic gap (Figure 2.8). Trapping relies on the repulsive force between like-charged particles and a patterned surface. The particles are transported and immobilized on a specific spot designed by lithography. [29] As the nanofluidic gap closes, Van der Waals forces surpass

hydration and electrostatic repulsion, permanently depositing trapped particles (Figure 2.9). [30] After this contact, the particles become adsorbed onto the surface. In this case, the topographical nanostructures on the substrates were patterned in the PPA using t-SPL.

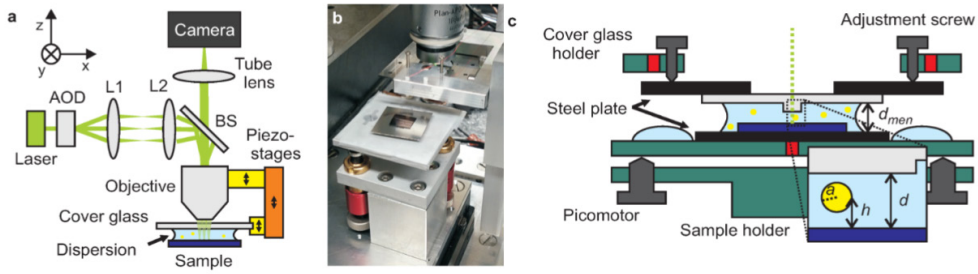

Figure 2.8. a) Optical configuration of TNCA for the deposition of gold particles. One coarse positioning stage (orange) and two linear piezo stages (yellow) provide independent adjustments for focus and confinement, in addition to offering access to a broad range of gap distances. **b)** Image of the nanofluidic confinement setup. **c)** Illustration of the system's vertical profile; the inset highlights the nanofluidic slit with gap distance d, where a particle of radius a is confined at height h. [29]

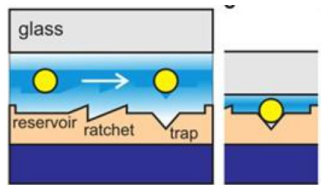

Figure 2.9. A schematic illustration of the nanoparticle assembly process flow through nanofluidic confinement, where t-SPL is employed to pattern the PPA (beige) and create reservoirs, ratchets, and traps. [30]

In Chapters 3 and 5 of this PhD thesis, TNCA was utilized to confine bacteriorhodopsin (bR) between two parallel, tunable surfaces. Additionally, Section 2.4.1 includes a summary of a publication [31] in which the thesis author contributed, presenting the first study that employed TNCA for the deposition of bR.

2.4 Purple membranes

The bR is an integral protein with a supramolecular structure, and it can be found in 5- nm purple membranes (PMs) of Halobacterium salinarum (Figure 2.10). [32] The bR acts as a light-driven cross-membrane proton pump. It actively transports hydrogen ions across the cell membrane, and the established hydrogen gradient facilitates the synthesis of adenosine triphosphate (ATP) from adenosine diphosphate (ADP) within the cells. [33] Moreover, bR has directionality in pumping and an orientation in the membrane. The pumping occurs from the cytoplasmatic side (C-terminus), inside the cell, to the extracellular side (N-terminus),

outside the cell. As shown in Figure 2.10, the retinal molecule undergoes isomerization from trans to cis upon absorbing a photon. Although the oriented deposition of PM patches has been achieved in previous work, [34] the simultaneous control of orientation and position has not been reported. The control of membrane orientation is essential to realize a high photoelectric conversion efficiency.

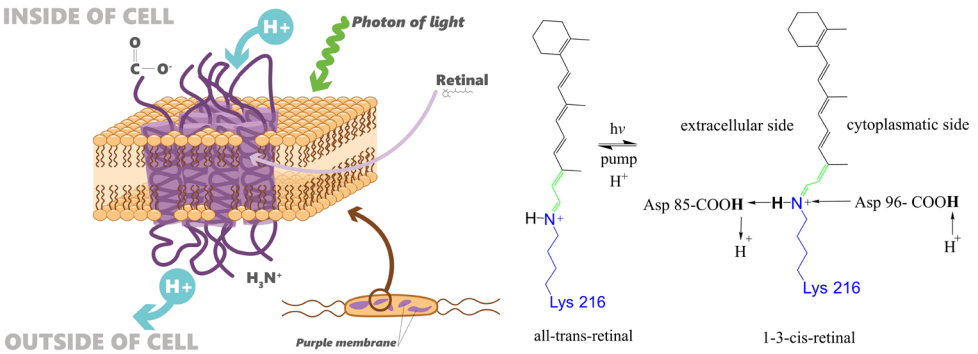

Figure 2.10. Schematic of bacteriorhodopsin pumping and its reaction mechanism. The conformational changes upon light exposure altered the pKa values of amino acids Asp85 (cytoplasmic side) and Asp96 (extracellular side).

CRNs can be controlled by a local proton gradient as catalysts. Therefore, in this thesis, we aimed to couple similar CRNs with light-driven bR proton pumps to form a localized CRN that can be switched on and off by an optical trigger. Moreover, we investigated spectroscopic techniques to quantify the bR pumping [35] to enable the use of PMs in hybrid devices. A study documented the controlled localization and orientation of PM deposition. [31] The main results of this publication are described in the following paragraphs.

2.4.1 Placement of biological membrane patches in nanofluidic gap with control over position and orientation

We aimed to supply protons as catalysts for CRNs by positioning proton pumps in a small compartment of a planar surface. To modulate membrane patch orientation during deposition, we used PM patches containing bR with a deca-histidine (His_{10}-tag) attached to either the C-terminus (C-His) or N-terminus (N-His) of the bR (Figure 2.11). The positive charge of His_{10}-tag increased the charge asymmetry of the membrane surface. Fluorescently labeled antibodies targeting the His_{10}-tag were employed to detect the presence of the His_{10}-tag upon membrane deposition, specifically when it was oriented toward the surface.

TNCA was used to deposit bR-containing membrane patches that were deposited onto a patterned substrate to control their orientation. Trapping sites with negatively (Figure 2.12a) or positively (Figure 2.12b) charged interfaces were prepared using t-SPL. Figures

2.13a and 2.13b display scanning electronic microscopy (SEM) and AFM images of C-His_{10}-tag PM patches in Al_2O_3 traps, confirming successful membrane deposition. Figure 2.13c shows fluorescence microscopy (FM), where membranes with the His_{10}-tag facing up exhibit green fluorescence, indicating antibody recognition. In contrast, membranes on SiO_2 (His_{10}-tag down) showed no fluorescence. Figure 2.13d illustrates the ratio of fluorescent to non-fluorescent membranes on positively and negatively charged interfaces, with each bar representing data from at least seven trap arrays and a minimum of two deposition experiments. These results confirm that PM orientation can be controlled by the presence of a His_{10}-tag on either the C- or N-terminal side of bR.

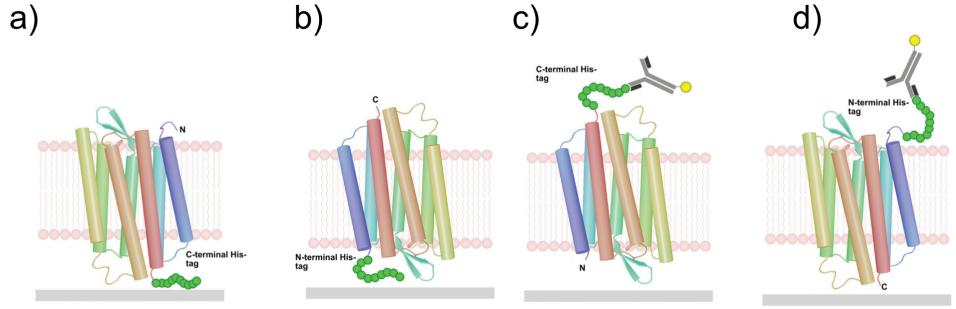

Figure 2.11. Scheme of orientation control upon attachment of His_{10}-tag on the C- terminus (a) and c)) or N-terminus (b) and d)). The antibody binds to the His_{10}-tag mostly when His_{10}-tag is facing up (c and d). [31]

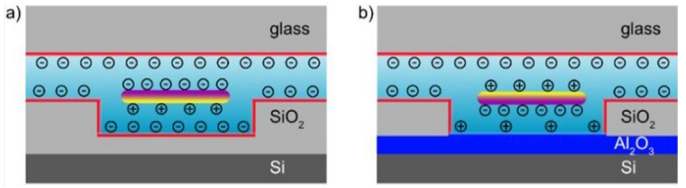

Figure 2.12. Asymmetrical charged membrane in nanofluidic confinement with orientation dependent on the trap surface charge: **a)** negative and **b)** positive. [31]

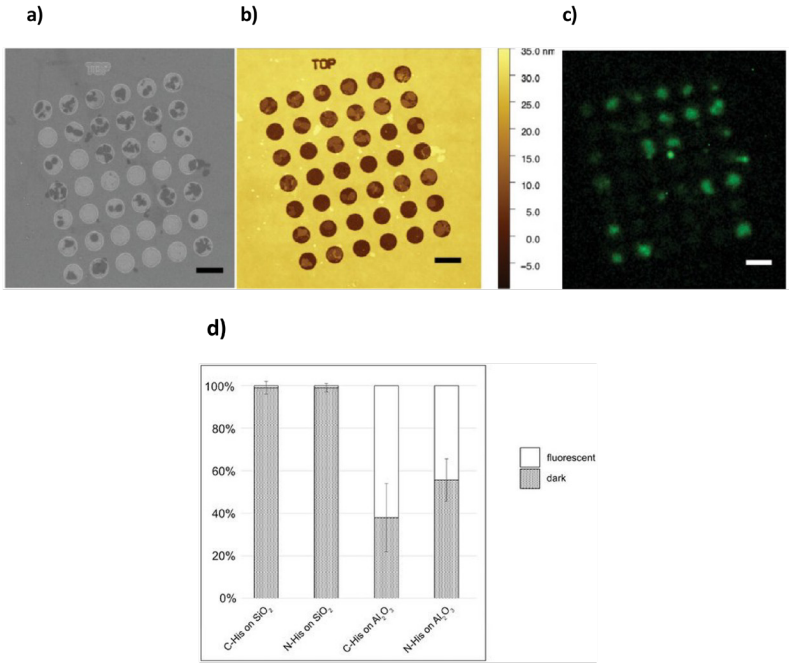

Figure 2.13. a) SEM image of a circular Al_2O_3 trap array with deposited C-His_{10}-tag PM patches. **b)** AFM image of the array shown in (a). **c)** Fluorescence microscopy image of the array shown in a), presenting green fluorescence from membranes with the His_{10}-tag facing up. **d)** Graph showing the distribution of PM orientations in different trap types, illustrating the ratio of dark (non- fluorescent) to fluorescent membranes. Scale bars: 2 µm. [31]

2.5 Chemical reaction networks

A chemical reaction involves substances transforming into others through atomic bond breakage and formation. Chemical kinetics studies the speed of reactions and the mechanisms behind them, explaining why reactions occur under specific conditions. A CRN is a set of coupled reaction steps, represented by elementary reactions that describe systems like enzymatic cycles or self-assembly networks. [36] In this thesis, we used two CRNs: a proton-catalyzed hydrogel self-assembly and a self-catalyzed chemical reaction oscillatory network.

2.5.1 Dissipative chemical reaction network - Hydrogel self-assembly

Dissipative self-assembly refers to a system that remains dynamically stable in a far-from-equilibrium state through continuous chemical fuel consumption. Supramolecular structure formation can be precisely controlled in space and time by modulating the molecular self-assembly rate, often using external stimuli like light or pH, controlling their properties. In nature, feedback-driven catalysis regulates the turnover of self-assembled

structures, shaping soft materials' distribution and properties.

In an in-situ study, Boekloven et al. [37] observed that catalyzed gelator molecule formation accelerated supramolecular hydrogel creation. Supramolecular gels, often metastable, are influenced by kinetic factors. With external catalysts, supramolecular hydrogels can form in minutes under ambient conditions, using simple soluble building blocks, and offer tunable gel strength. Catalysis-driven gelator formation alters gelation speed and morphology, yielding metastable gels with enhanced strength and appearance despite identical compositions. Such a CRN will be spatiotemporally controlled by the presence of PMs and light, as shown in Chapter 4.

2.5.2 Oscillatory chemical reaction network - Belousov–Zhabotinsky reaction

Chemical reactions far from equilibrium can display oscillations under certain conditions, such as chemical concentrations, incident light color, pH, temperature, and electrode potential. The Belousov-Zhabotinsky (BZ) reaction is an example of this. It is based on the oxidation of an organic compound by bromic acid ($HBrO_3$) mediated by a transition-metal catalyst in an acidic aqueous solution. [38] Although other BZ recipes can be used, we selected a standard formula using tris(bipyridine)ruthenium (II) chloride ($Ru(bpy)_3]Cl_2$) as the catalyst, and sodium bromate ($NaBrO_3$) and malonic acid (MA; $C_3H_4O_4$) as oxidizing and reducing reactants, in that order. The reaction is conducted in an acidic environment obtained by using sulfuric acid (H_2SO_3). During the oscillations, the catalyst switches between two oxidation states.

This BZ reaction is given by:

$$3BrO^- + 3CH_2(COOH)_2 + 2\ H^+ \rightarrow 2BrCH\ (COOH)_2 + 3CO_2 + 4H_2O$$

While the mechanism is complex, it can be effectively simulated using simple three-variable kinetic reactions to model the overall behavior. In the first process, bromide is consumed in two fast reactions, and $HBrO_2$ is produced and consumed:

$$BrO_3^- + Br^- + 2H^+ \rightarrow HBrO_2 + HOBr$$

$$HBrO_2 + Br^- + H^+ \rightarrow 2HOBr$$

Second, when the bromide concentration becomes low enough, bromous acid ($HBrO_2$) is autocatalytically produced, and the metal ion catalyst is oxidized by supplying electrons for the process.

$$BrO^- + HBrO_2 + 2Ru^{2+} + 3H^+ \rightarrow 2HBrO_2 + 2Ru^{3+} + H_2O$$

The third process involves the reduction of the oxidized metal catalyst and the production of bromide:

$$BrMA + MA + 2Ru^{3+} \rightarrow Br^{-} + 2Ru^{2+} + CO_2 + H^{+}$$

Recently, a new field of study has aimed to use oscillatory CRNs for information processing, [39] and BZ CRN is gaining importance. One of the approaches utilizing the BZ reaction towards the development of a chemical computer is presented in Chapter 6.

2.6 Analytical techniques

The development and manufacture of microsystems require several metrology techniques and instruments. In manufacturing, metrology plays a crucial role in measuring key process outcomes and ensuring the quality of microsystems. It also enables the monitoring of processing equipment during production. Furthermore, these techniques are used to accurately identify and diagnose issues in design and fabrication. In this study, we used five types of analytical techniques, namely AFM, FM, SEM, focused ion beam (FIB), and spectroscopy ellipsometry (SE).

2.6.1 Atomic force microscopy

AFM [40] is a microscopy technique that employs a mechanical sampling method, wherein an atomically sharp tip is scanned across the sample surface under controlled conditions to capture high-resolution images of material surfaces at the nanoscale. AFM is commonly utilized at various stages of semiconductor manufacturing to inspect and evaluate fabrication processes.

The AFM principle is shown in Figure 2.14. In AFM, piezoelectric actuators enable precise positioning and scanning of the tip. Cantilever deflection is detected by reflecting a laser off its backside onto a four-quadrant photodiode. Tip-sample interactions during raster scanning cause cantilever deflections. These deflections are recorded through the movement of the laser beam reflection, with the data being measured by the photodiode output. The tip provides topographic information (z) of the sample as a function of x-y coordinates.

Although the instrumentation is relatively elementary, several conditions must be met to ensure the accuracy of AFM measurements. First, an appropriate probe should be selected for the specific type of measurement and substrate. Second, the feedback mode should be selected, and the parameters should be optimized. Third, the detection of possible measurement-related artifacts should be avoided. These artifacts can originate from an error in choosing the appropriate analysis conditions or specific sample properties, such as high adhesion from blunt tips or hydrophilicity.

Regardless of the application and information to be sensed, there are three potential modes of AFM operation: contact, non-contact, and intermittent. These methods use different approaches to probe the surface morphology, as shown in Figure 2.15. In contact

mode, the cantilever's static deflection is measured when it makes physical contact with the surface. In non-contact mode, the cantilever oscillates dynamically with small vibrations, and the tip does not physically touch the surface. In intermittent mode, the tip apex remains in partial contact with the surface while the cantilever vibrates with larger amplitudes.

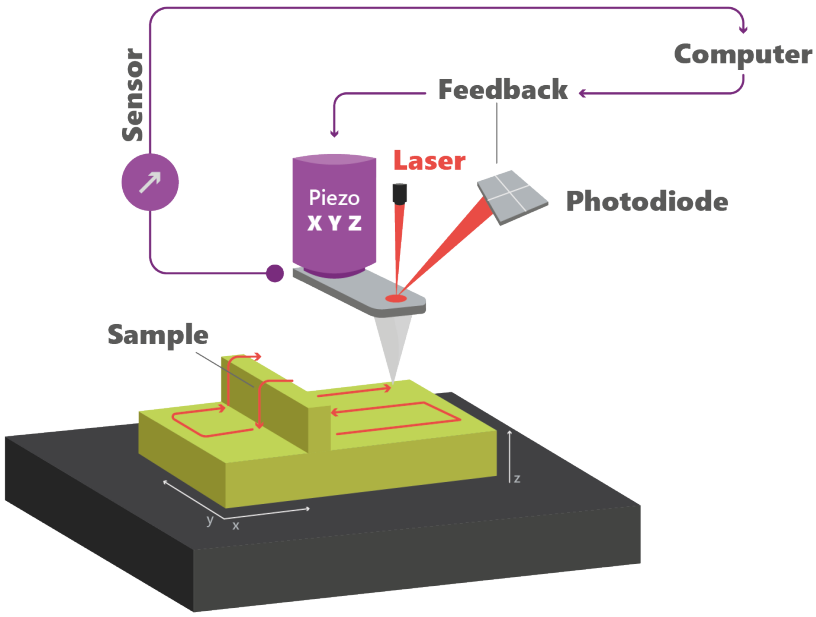

Figure 2.14. A typical AFM setup involves fixing the sample in place while the probe moves in the x, y, and z directions.

The contact approach can be intuitively interpreted as the tip engaging with the sample surface through a normal reaction force. In contrast, the other two techniques involve the cantilever vibrating at or close to its natural resonance frequency, with an amplitude like the mean tip–sample distance. The interactions between tip and surface (van der Waals and contact forces) lead to a shift in resonance frequency and phase. The feedback maintains one of the two constants while recording the topography. Recently, a hybrid method named peak force-mapping was implemented in commercial tools. In this method, the tip oscillates at lower frequencies than its natural resonance. In each oscillation, the tip touches the surface. With an operating frequency of 1–10 kHz, this technique enables high-bandwidth force sensors to trail individual tip oscillations upon each surface contact during imaging. Recording the force at every tap allows for the acquisition of thousands of unique force curves as adjacent pixels are scanned, providing a notable benefit. Since these force curves provide insight into local mechanical properties, this method allows for nanoscale mapping of adhesion, modulus, dissipation, and deformation. Furthermore,

this capability opens new pathways for reliably detect weak tip–sample interactions. Consequently, operation is simple, parameters can be optimized by the software, and operation on difficult surfaces is possible.

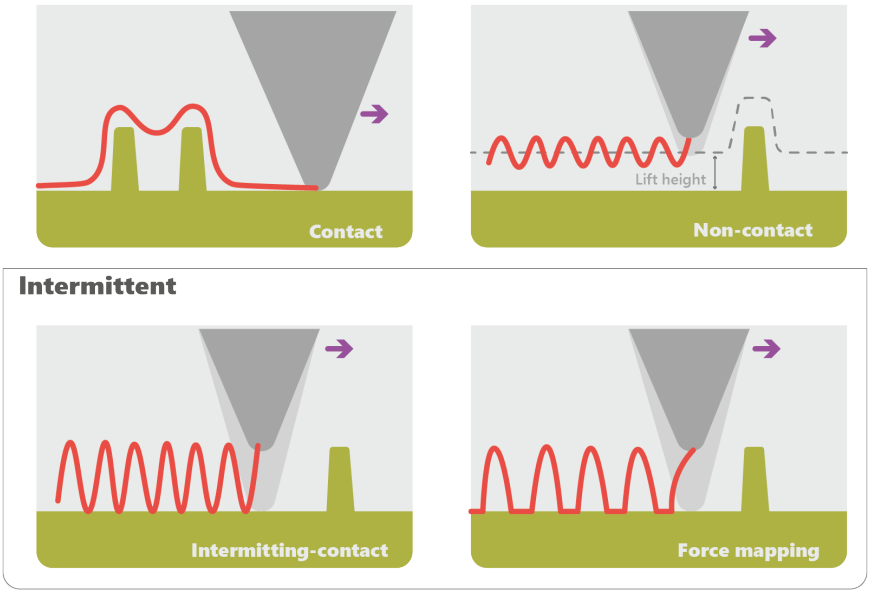

Figure 2.15. Different AFM modes employing various types of tip–sample interactions.

AFMs are capable of functioning in a wide range of environments, including liquid solutions. [41] However, acquiring an AFM image of immersed liquid surfaces is challenging owing to several physical characteristics, such as the viscosity of the liquid, which can cause issues when the AFM probe moves across sample surface. [42] Moreover, objects deposited on a surface are often only weakly bound, depending on the conditions of the liquid. Such objects might move by themselves or may be triggered by interactions with the scanning tip, often at a shorter period than the one needed to acquire a single AFM image. To minimize these effects, PeakForce Tapping mode [43] can be used. In this mode, tip–sample interactions are precisely regulated at ultralow forces, while lateral forces are significantly reduced, creating an optimal imaging condition for delicate samples.

AFM in liquid environments necessitates specific adaptations, including a specialized liquid cell. This component ensures that the laser beam can travel unimpeded through the liquid, striking the cantilever and reflecting back without significant scattering. At nearly all air–liquid boundaries, minor mechanical disturbances give rise to surface waves, which, in turn, scatter laser light. When operating in dynamic modes—where the cantilever must vibrate close to its natural resonance frequency, these effects become particularly relevant, increasing the need for a more sophisticated liquid cell design. The low frequencies of operation in PeakForce Tapping simplify this challenge considerably.

Liquid AFM in PeakForce Tapping mode was used for an in-situ study of proton-catalysed molecular self-assembly under spatiotemporal control presented in Chapter 4.

2.6.2 Fluorescence microscopy

A fluorescence microscope typically consists of an adapted optical microscope system designed to illuminate a sample using both visible and ultraviolet light. [10] The FM [44] model is utilized for analyzing the characteristics of organic and inorganic materials by detecting fluorescence and phosphorescence phenomena. In this type of microscopy, the enlarged image is generated by the longer-wavelength light emitted from fluorescent molecules. The term Stokes shift describes the variation between the wavelengths of emitted fluorescence and the absorbed (excitation) light. When this difference is significant, filters can be utilized to isolate the exciting and fluorescence signals, ensuring that only the fluorescence light reaches the detector. A fluorescence microscope generally includes essential components like the light source, excitation filter, dichromatic mirror, and emission filter. These filters and mirrors are selected based on the specific excitation and emission wavelengths of the fluorophores being studied FM was used in Chapters 3, 5 and 6 of this thesis.

2.6.3 Scanning electron microscopy

The SEM [10] is an imaging system that uses a focused electron beam to capture detailed images of a sample. Due to the shorter wavelengths of electrons compared to optical photons, SEM microscopes offer higher resolution than optical microscopes. Additionally, SEM significantly improves depth of focus, enabling the visualization of features at varying depths without the need to refocus. The precision of dimensional measurements in SEM are greater at higher magnifications than at lower ones. A standard multipurpose SEM allows for the adjustment of various parameters, such as viewing angle, accelerating voltage, and magnification. All of these factors can impact the precision of dimensional measurements. SEM was used in Chapters 3 and 5 to inspect fabricated devices.

2.6.4 Focused ion beam

The FIB technology [10] can be used to cross-section and image sections of the device structures which could otherwise remain unseen owing to their coverage by thin films or other material coatings. FIB is used to perform nanometer dimensional-scale machining. Conventional FIB machining requires an ion source, usually gallium ions. Gallium interacts with a heated needle, where its electrical potential causes ionization and field emission of ions, which are accelerated to 5–50 keV and focused into a small spot by electrostatic lenses. Upon striking the sample surface, the focused Ga^+ ion beam causes sputtering of the surface material. The ejected material then exits the surface as neutral atoms or secondary ions. Additionally, secondary electrons are generated in the process. By collecting these sputtered ions and secondary electrons, a high-resolution surface image can be produced, similar to the imaging technique used in SEM. Cross-sectional images of the devices were obtained using FIB technology in Chapter 5.

2.6.5 Spectroscopy ellipsometry

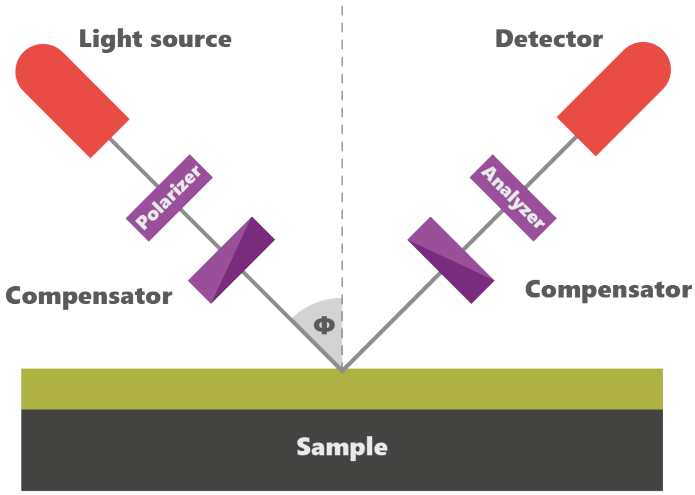

Figure 2.16. Scheme of ellipsometer components: polarizer, compensator (retarder or photoelastic modulator), analyzer, and detector and a white light source. [46]

SE is a non-destructive, contactless optical technique for characterizing bulk materials and thin films, including dielectrics, semiconductors, and metals, with thicknesses down to a few tens of nanometers. [45,46] SE works by examining alterations in the polarization state of a polarized light beam after it reflects off a surface or interface, as illustrated in Figure 2.16. This method allows for accurate determination of optical properties, composition and layer thickness. Unlike absolute light intensity measurements, SE is unaffected by scattering and fluctuations and does not require a standard sample or reference beam. A broad spectral range—from UV to mid-IR— enhances analysis precision and depth. Far-UV detects subtle variations in ultrathin layers and low-contrast interfaces, while near-IR determines thickness in materials with strong visible absorption.

2.7 References

(1) Roco, M. C.; Mirkin, C. A.; Hersam, M. C. Nanotechnology Research Directions for Societal Needs in 2020: Summary of International Study. *Journal of nanoparticle research* **2011**, 13, 897–919.

(2) Elnaggar, A.; Kang, S.; Tian, M.; Han, B.; Keshavarz, M. State of the Art in Actuation of Micro/Nanoro bots for Biomedical Applications. *Small Science* **2024**, 4 (3), 2300211.

(3) Mijatovic, D.; Eijkel, J. C.; Van den Berg, A. Technologies for Nanofluidic Systems: Top-down vs. Bottom-up—a Review. *Lab on a Chip* **2005**, 5 (5), 492–500.

(4) Paul, P. C.; Knoll, A. W.; Holzner, F.; Despont, M.; Duerig, U. Rapid Turnaround Scanning Probe Nanolithography. *Nanotechnology* **2011**, 22 (27), 275306.

(5) Vettiger, P.; Despont, M.; Drechsler, U.; Durig, U.; Haberle, W.; Lutwyche, M. I.; Rothuizen, H. E.; Stutz, R.; Widmer, R.; Binnig, G. K. The "Millipede"—More than Thousand Tips for Future AFM Storage. *IBM Journal of Research and Development* **2000**, 44 (3), 323–340.

(6) Coulembier, O.; Knoll, A.; Pires, D.; Gotsmann, B.; Duerig, U.; Frommer, J.; Miller, R. D.; Dubois, P.; Hedrick, J. L. Probe-Based Nanolithography: Self-Amplified Depolymerization Media for Dry Lithography. *Macromolecules* **2010**, 43 (1), 572–574.

(7) Knoll, A. W.; Pires, D.; Coulembier, O.; Dubois, P.; Hedrick, J. L.; Frommer, J.; Duerig, U. Probe-based 3-D Nanolithography Using Self-amplified Depolymerization Polymers. *Advanced Materials* **2010**, 22 (31), 3361–3365.

(8) Aso, C.; Tagami, S. Polymerization of Aromatic Aldehydes. III. the Cyclopolymerization of Phthaldehyde and the Structure of the Polymer. *Macromolecules* **1969**, 2 (4), 414–419.

(9) Howell, S. T.; Grushina, A.; Holzner, F.; Brugger, J. Thermal Scanning Probe Lithography—a Review. *Microsyst Nanoeng* **2020**, 6 (1), 21. https://doi.org/10.1038/s41378-019-0124-8.

(10) Huff, M. Microsystems Manufacturing Methods: Integrated Circuit Processing Steps. *Process Variations in Microsystems Manufacturing*, **2020**, 45–97. https://doi.org/10.1007/978-3-030-40560- 1_3.

(11) Nguyen, N.-T. Micromixers: Fundamentals, *Design and Fabrication*; William Andrew, **2011**.

(12) Franssila, S. *Introduction to Microfabrication*; John Wiley & Sons, **2010**.

(13) Jung, I. W.; Wang, J.-S.; Solgaard, O. Spatial Light Modulators for Maskless Lithography. In IEEE/LEOS *International Conference on Optical MEMS and Their Applications Conference*, **2006**.; IEEE, 2006; pp 150–151.

(14) Kunwar, P.; Soman, P. Direct Laser Writing of Fluorescent Silver Nanoclusters: A Review of Methods and Applications. *ACS applied nano materials* **2020**, 3 (8), 7325–7342.

(15) Lilak, A. D.; Keys, P. H. CMOS Manufacturing Processes. In Springer Handbook of Semiconductor Devices; *Springer*, **2022**; pp 3–36.

(16) Pinto, R. M. R.; Gund, V.; Calaza, C.; Nagaraja, K. K.; Vinayakumar, K. B. Piezoelectric Aluminum Nitride Thin-Films: A Review of Wet and Dry Etching Techniques. *Microelectronic Engineering* **2022**, 257, 111753. https://doi.org/10.1016/j.mee.2022.111753.

(17) Gazit, E. Self-Assembled Peptide Nanostructures: The Design of Molecular Building Blocks and Their Technological Utilization. *Chemical Society Reviews* **2007**, 36 (8), 1263–1269.

(18) Sadhukhan, S.; Acharya, S.; Panda, T.; Mandal, N. C.; Bose, S.; Nandi, A.; Das, G.; Maity, S.; Chakraborty, S.; Chaudhuri, P.; Saha, H. Chapter 4 - Evolution of High Efficiency Passivated Emitter and Rear Contact (PERC) Solar Cells. In Sustainable Developments by Artificial Intelligence and *Machine Learning for Renewable Energies*; Kumar, K., Rao, R. S., Kaiwartya, O., Kaiser, M. S., Padmanaban, S., Eds.; Elsevier, 2022; pp 63–129. https://doi.org/10.1016/B978-0-323-91228- 0.00007-0.

(19) *Thermal Oxidation.* https://eesemi.com/oxidation.htm (accessed 2023-07-18).

(20) Warner, J. H.; Schäffel, F.; Bachmatiuk, A.; Rümmeli, M. H. Chapter 4 - Methods for Obtaining Graphene. *In Graphene*; Warner, J. H., Schäffel, F., Bachmatiuk, A., Rümmeli, M. H., Eds.; Elsevier, **2013**; pp 129–228. https://doi.org/10.1016/B978-0-12-394593-8.00004-7.

(21) Leskelä, M.; Niinistö, J.; Ritala, M. 4.05 - Atomic Layer Deposition. I*n Comprehensive Materials Processing*; Hashmi, S., Batalha, G. F., Van Tyne, C. J., Yilbas, B., Eds.; Elsevier: Oxford, 2014; pp 101–123. https://doi.org/10.1016/B978-0-08-096532-1.00401-5.

(22) Black, C. T.; Ruiz, R.; Breyta, G.; Cheng, J. Y.; Colburn, M. E.; Guarini, K. W.; Kim, H.-C.; Zhang, Y. Polymer Self Assembly in Semiconductor Microelectronics. *IBM Journal of Research and Development* **2007**, 51 (5), 605–633.

(23) Kraus, T.; Wolf, H. Templated Self-Assembly of Particles. *Springer handbook of nanotechnology* **2010**, 187–210.

(24) Lowack, K.; Helm, C. A. Molecular Mechanisms Controlling the Self-Assembly Process of Polyelectrolyte Multilayers. *Macromolecules* **1998**, 31 (3), 823–833.

(25) Carroll, K. M.; Wolf, H.; Knoll, A.; Curtis, J. E.; Zhang, Y.; Marder, S. R.; Riedo, E.; Duerig, U. Understanding How Charged Nanoparticles Electrostatically Assemble and Distribute in 1-D. *Langmuir* **2016**, 32 (51), 13600–13610.

(26) Barth, J. V.; Costantini, G.; Kern, K. Engineering Atomic and Molecular Nanostructures at Surfaces. *Nature* **2005**, 437 (7059), 671–679.

(27) Geng, Y.; van Anders, G.; Dodd, P. M.; Dshemuchadse, J.; Glotzer, S. C. Engineering Entropy for the Inverse Design of Colloidal Crystals from Hard Shapes. *Science advances* **2019**, 5 (7), eaaw0514.

(28) Boekhoven, J.; Brizard, A. M.; Kowlgi, K. N.; Koper, G. J.; Eelkema, R.; van Esch, J. H. Dissipative Self-assembly of a Molecular Gelator by Using a Chemical Fuel. *Angewandte Chemie* **2010**, 122 (28), 4935–4938.

(29) Fringes, S.; Holzner, F.; Knoll, A. W. The Nanofluidic Confinement Apparatus: Studying Confinement-Dependent Nanoparticle Behavior and Diffusion. *Beilstein Journal of Nanotechnology* **2018**, 9 (1), 301–310.

(30) Fringes, S.; Schwemmer, C.; Rawlings, C. D.; Knoll, A. W. Deterministic Deposition of Nanoparticles with Sub-10 Nm Resolution. *Nano Letters* **2019**, 19 (12), 8855–8861.

(31) Ruggeri, F.; Schwemmer, C.; Stauffer, M.; Nicollier, P. M.; Figueiredo da Silva, J.; Bosshart, P. D.; Kochems, K.; Fotiadis, D.; Knoll, A.; Wolf, H. Placement of Biological Membrane Patches in a Nanofluidic Gap With Control Over Position and Orientation. *Advanced materials interfaces* **2022**, 9 (23), 2200941.

(32) Stoeckenius, W.; Lozier, R. H.; Bogomolni, R. A. Bacteriorhodopsin and the Purple Membrane of Halobacteria. Biochimica et Biophysica Acta (BBA) - *Reviews on Bioenergetics* **1979**, 505 (3–4), 215–278. https://doi.org/10.1016/0304-4173(79)90006-5.

(33) Al-Aribe, K. M.; Knopf, G. K.; Bassi, A. S. Fabrication of an Optically Driven pH Gradient Generator Based on Self-Assembled Proton Pumps. *Microfluidics and nanofluidics* **2012**, 12 (1), 325–335.

(34) Fisher, K.; Yanagimoto, K.; Stoeckenius, W. Oriented Adsorption of Purple Membrane to Cationic Surfaces. *The Journal of cell biology* **1978**, 77 (2), 611–621. https://doi.org/10.1083/jcb.77.2.611.

(35) Mahyad, B.; Janfaza, S.; Hosseini, E. S. Bio-Nano Hybrid Materials Based on Bacteriorhodopsin: Potential Applications and Future Strategies. *Advances in Colloid and Interface Science* **2015**, 225, 194–202. https://doi.org/10.1016/j.cis.2015.09.006.

(36) Soranzo, N.; Altafini, C. ERNEST: A Toolbox for Chemical Reaction Network Theory. *Bioinformatics* **2009**, 25 (21), 2853–2854.

(37) Boekhoven, J.; Poolman, J. M.; Maity, C.; Li, F.; Van Der Mee, L.; Minkenberg, C. B.; Mendes, E.; Van Esch, J. H.; Eelkema, R. Catalytic Control over Supramolecular Gel Formation. *Nature Chem* **2013,** 5 (5), 433–437. https://doi.org/10.1038/nchem.1617.

(38) Field, R. J.; Noyes, R. M. Oscillations in Chemical Systems. IV. Limit Cycle Behavior in a Model of a Real Chemical Reaction. *The Journal of Chemical Physics* **1974**, 60 (5), 1877–1884. https://doi.org/10.1063/1.1681288.

(39) Dueñas-Díez, M.; Pérez-Mercader, J. How Chemistry Computes: Language Recognition by Non-Biochemical Chemical Automata. From Finite Automata to Turing Machines. *iScience* **2019**, 19, 514–526. https://doi.org/10.1016/j.isci.2019.08.007.

(40) Celano, U. The Atomic Force Microscopy for Nanoelectronics. *Electrical Atomic Force Microscopy for Nanoelectronics* **2019**, 1–28.

(41) Reifenberger, R. G.; Baró, A. M. *Atomic Force Microscopy in Liquid: Biological Applications*; John Wiley & Sons, **2012**.

(42) Costa, L.; Li-Destri, G.; Pontoni, D.; Konovalov, O.; Thomson, N. H. Liquid–Liquid Interfacial Imaging Using Atomic Force Microscopy. *Adv Materials Inter* **2017**, 4 (16), 1700203. https://doi.org/10.1002/admi.201700203.

(43) Kaemmer, S. B. Introduction to Bruker's Scanasyst and Peakforce Tapping Afm Technology. Bruker application note. *Bruker Nano Inc.*, Santa Barbara, CA **2011**.

(44) Badilescu, S.; Packirisamy, M. BioMEMS: *Science and Engineering Perspectives*; CRC Press, **2016**.

(45) Wasserman, S. R.; Whitesides, G. M.; Tidswell, I. M.; Ocko, B. M.; Pershan, P. S.; Axe, J. D. The Structure of Self-Assembled Monolayers of Alkylsiloxanes on Silicon: A Comparison of Results from Ellipsometry and Low-Angle x-Ray Reflectivity. *J. Am. Chem. Soc.* **1989,** 111 (15), 5852–5861. https://doi.org/10.1021/ja00197a054.

(46) Losurdo, M.; Bergmair, M.; Bruno, G.; Cattelan, D.; Cobet, C.; De Martino, A.; Fleischer, K.; Dohcevic Mitrovic, Z.; Esser, N.; Galliet, M. Spectroscopic Ellipsometry and Polarimetry for Materials and Systems Analysis at the Nanometer Scale: State-of-the-Art, Potential, and Perspectives. *Journal of Nanoparticle Research* **2009**, 11, 1521–1554.

Chapter 3

Quantification of proton pumping in biological membrane patches

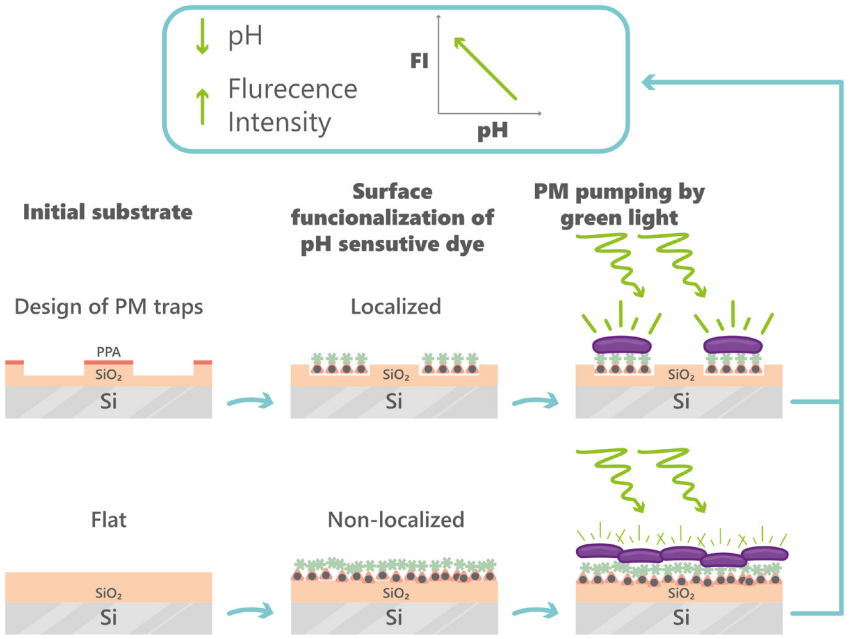

Abstract: Bacteriorhodopsin (bR) in purple membranes (PM) of Halobacterium salinarum acts as a light-driven cross-membrane proton pump. Isolated PM patches can be transported and positioned with orientation control at predefined locations by a tunable nanofluidic confinement apparatus. However, there is still a need for a method to measure the proton pumping in a device that enables precise PM orientation and localization. We functionalized a SiO_2 surface with a pH-sensitive dye for the measurement of proton pumping. To achieve a measurement of proton pumping with controlled orientation and localization, we introduced a maskless chemical lift-off method. This strategy uses thermal scanning probe lithography to locally bind a pH-sensitive dye onto the SiO_2 substrate. In both cases, fluorescence microscopy was employed to investigate protein functionality within the experimental setup by documenting proton pumping across the PM. Issues concerning reproducibility of surface functionalization were found.

3.1 Introduction

The synthesis of functional materials is essential for the development of novel highly functional devices. Accordingly, controlling the design and structures of materials at the nanometer scale is crucial to producing unique material properties for application in many fields, from informatics to biomedical engineering. [1] In biological systems, the dynamic self-assembly of molecules, such as the aggregation and folding of proteins, can be totally or partially influenced by energy sources. [2] In supramolecular materials operating out-of-equilibrium, the self-assembly of reagents can be driven by a chemical reaction network (CRN) that consumes a chemical fuel. [3]

A local proton gradient can be used as a bottom-up strategy to catalyze spatially controlled self-assemblies. [4–6] Local control of proton gradients can be observed in nature, for instance, in purple membranes (PM) of Halobacterium salinarum, mainly consisting of bacteriorhodopsin (bR). [7] The bR acts as a light-driven cross-membrane proton pump that transports protons across the cell membrane. The absorption spectrum of bR molecules reveals heightened efficiency within the 550 nm wavelength range due to their characteristic purple coloration. [8] Consequently, this spectral preference enables the activation and precise control of proton pumping through the utilization of green light. Over the past decades, researchers have explored the use of bR proton pumps to modulate the pH of target solutions. A wild- type (WT) bR proton pump typically operates at approximately 20 cycles per second. [9] Under light-saturating conditions, its performance can increase to up to 100 cycles per second. [10] The distribution and geometry of bR molecules within PM fragments confer chemical and thermal stability to bR. Upon exposure to visible light, each bR protein facilitates proton translocation into the extracellular medium through photoinduced structural and spectral modifications. [10]

Integrating PMs onto a surface enables the production of a localized light-triggered proton gradient. This system holds potential for diverse applications, including the precise spatiotemporal control of proton-catalyzed CRNs. [11] However, bR exhibits inherent directionality in proton pumping and a specific orientation within the membrane, with protons being transported from the cytoplasmic side (C-terminus) to the extracellular side (N-terminus). [7] Therefore, precise control over the orientation of membrane patches is essential for optimizing photoelectric conversion efficiency. [12]

Ruggeri et al. [13] demonstrated that isolated PM patches can be precisely transported and oriented at designated locations. by a tunable nanofluidic confinement apparatus (TNCA). To control the orientation of PMs, their charge asymmetry was increased by attaching a deca-histidine (His_{10})-tag to either their cytoplasmatic side (C-His_{10}-tag PMs) or extracellular side (N-His_{10}-tag PMs). [14] During the deposition stage on a negatively charged interface (SiO_2), the PMs were assembled with the His_{10}-tag down. Contrarily, when the traps presented a positively charged interface (Al_2O_3), the membranes were deposited preferentially with the His_{10}-tag up. [13]

After establishing a method to control PM orientation on a surface, the available methods for localized pH measurement on substrates remain limited. They usually require sophisticated techniques such as voltammetric nanosensor measurements, [15] scanning electrochemical microscopy, [16] or scanning ion conductance microscopy. [17] Gaitzsch et al. [18] reported the insertion of a proton pump with orientational control into an artificial asymmetric membrane. However, the experiment was executed in vesicles, which do not provide control over the localization of pumping activity on a planar substrate. Biologically self-powered steady-state ionic current nanopore sensing enables the investigation of bR proton pumping activity at the single-molecule level within a nanofluidic system, providing insights into its response to light. [19] The green light irradiation of this device resulted in a charge density generated by each bR monomer that was 580x higher than the previously reported value. [20] Although the results are very encouraging, such an approach requires a complex setup.

Fluorescence microscopy (FM) is a versatile optical technique that can be used to control and measure bR pumping using light. [21] Lee et al. [22] demonstrated the controlled orientation of bR in thin films of an ABA block copolymer. They used pyranine, a pH-sensitive dye, to provide a visual clue for pH changes. Pyranine is highly sensitive to pH changes at pH values near 7.2 [21] and its concentration controls the saturation of the observed color. Therefore, the adjustment of dye concentration produces variations of the same hue. [22] Gonçalves et al. [23] used pyranine to investigate the occurrence of proton pumping by bR in closed chambers according to membrane orientation. They combined atomic force microscopy (AFM) and FM to demonstrate the functionality of PMs in the setup. [23] However, the challenges associated with covalently attaching pyranine to surfaces such as SiO_2 [24] pose significant limitations, primarily due to its propensity to leach from sensor surfaces. [25] Therefore, achieving controlled localization and orientation when using pyranine to measure PM pumping becomes particularly difficult.

Considering these challenges, this study aims to utilize FM to measure proton pumping of PM patches. For that, we have functionalized an amino-functionalized SiO_2 surface with pHrodo, a pH-sensitive dye. pHrodo increases its fluorescence intensity (FI) as the medium becomes more acidic. Given its amino-reactive nature, pHrodo can covalently attach to surfaces containing amino groups, facilitating its covalent bonding to surfaces. This dye has been utilized, for example, in the functionalization of amino-functionalized beads, [26] nanoprobes, [27] and cells [28,29] to facilitate the detection of pH within these environments.

After depositing PM on the pHrodo-SiO_2 surface, we obtained an optically triggered device to assess PM pumping activity in situ. We measured the intensity of the pH-sensitive dye on the SiO_2 substrate to evaluate localized photo-induced proton pump activity. The PM embedded in the substrate generated ion flow, facilitating the measurement of the active surface based on light intensity. Additionally, we developed a maskless lift-off (MLO) method to locally couple a pH-sensitive dye on a SiO_2 substrate, aiming to assess single PM pumping activity in situ. However, reproducibility remained an issue, indicating that further optimization for the pHrodo functionalization protocol on a SiO_2 surface is required.

3.2 Results and discussion

We developed two protocols to covalently link a pH-sensitive dye (pHrodo) to a SiO_2 surface via aminosilanization followed by PM deposition, to study their activity in situ. In the first protocol, PM pumping was detected on a flat substrate through pHrodo bonded to the surface, onto which PMs were deposited. In the second protocol, we designed a device to detect single-patch PM proton pumping based on patch localization and position. This was achieved by combining aminosilanization with thermal scanning probe lithography (t-SPL) to functionalize a micro-area of the substrate with pHrodo. PMs were then deposited on this substrate using TNCA.

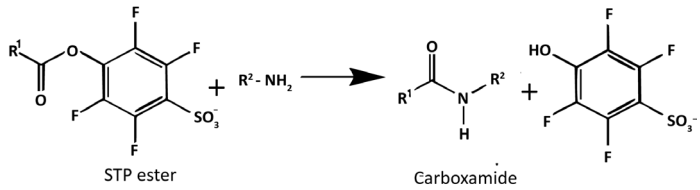

Figure 3.1. Reaction of primary amine with 1, 4-sulfo-2,3,5,6-tetra fluorophenyl (STP) ester.

The presence of PMs on the pH sensor dye eliminates the need for advanced instrumentation or external hardware to electronically or optically amplify the fluorescence signal. To use FM as an optical trigger for the proton gradient, a dye excited at a wavelength different than that of bR is needed to measure the local proton concentration. For that, we selected the amino-reactive pHrodo™ green STP ester (pHrodo) as a pH-sensitive fluorescent dye. This dye is excited at 488 nm (blue light) and emits green light at 530 nm. [30] Its main characteristic is the substantial increase in fluorescence signal as the pH of its surroundings becomes more acidic. [31] Amino silanes were used as coupling agents because of their reaction with the SiO_2 surface and the possibility of the attachment of an amino-reactive molecule in the second step. [32]

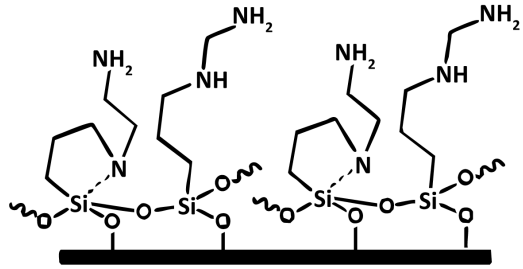

Figure 3.2. Steric hindrance from N-(2-aminoethyl)-3-aminopropyltrimethoxysilane (AEAPTMS).

As shown in Figure 3.1, 4-sulfo-2,3,5,6-tetrafluorophenyl (STP) esters readily react with primary amines to produce acylation products. [33] We selected N-(2-aminoethyl)-3-aminopropyltrimethoxysilane (AEAPTMDS) to functionalize the SiO_2 surface because it

produces a relatively stable and reproducible monolayer (Figure 3.2). AEAPTMS exhibits catalytic activity in siloxane bond formation. However, steric hindrance obstructs the intramolecular catalysis of bond detachment, which enables the reactivity of amino-reactive molecules in the silane layer. [32]

3.2.1 Functionalization of pHrodo on a flat unpatterned substrate

As a first step, the functionalization of the pHrodo on a Si/SiO_2 substrate was optimized on a flat substrate to implement the obtained system for PM pumping measurement. The process began by covalently bonding AEAPTMS to the SiO_2 surface. Subsequently, pHrodo functionalization was conducted at the amino group presented by the AEAPTMS.

Table 3.1. Ellipsometer data of pHrodo thickness throughout the functionalization steps on the SiO_2 substrate. Refractive index (n) SiO_2 = 1.46; n_{silane} = 1.48; [32] n_{pHrodo} = unknown; n values obtained at wavelength = 633 nm.

Sample	Thickness (nm)	Experimental *n* at 633 nm
Thermal oxide (SiO_2)	57.7 ± 0.1	-
Silane	0.5 ±0.0	1.47
Silane + pHrodo	9.3 ±0.1	1.52

We utilized ellipsometry to confirm the presence of an AEAPTMS layer on the silane-functionalized SiO_2 substrate and to detect pHrodo on the same substrate, as shown in Table 3.1. We estimated an increase of 0.5 nm in substrate thickness attributed to the AEAPTMS functionalization. Subsequently, an additional increase of approximately 8.8 nm indicated the successful functionalization of pHrodo on the substrate surface. The progressive increase in thickness from one step to the next provides compelling evidence for the successful functionalization of AEAPTMS, followed by the subsequent pHrodo functionalization.

Following the functionalization of pHrodo on the silane-SiO_2 substrates, the resulting SiO_2-silane-pHrodo surfaces were coated with a dispersion of PM containing WT, C- His_{10}-tag, or N-His_{10}-tag PMs. One sample was coated with a mixture of N- and C-His_{10}-tag PMs. As a control, we used a PM-free substrate ('pHrodo only'). A second control sample, a pHrodo-free substrate ('PM only'), was used to investigate the intrinsic signal originating from PM patches alone. All these substrates were exposed to fluorescence measurements for 100.0 s in a non-buffered aqueous media. First, proton pumping was activated by 1.0 s exposure to green light using TRITC (tetramethylrhodamine Isothiocyanate) filter. Then, fluorescence was measured by 500 ms excitation of blue light using FITC (fluorescein isothiocyanate) filter. Figure 3.3 displays the temporal evolution of FI for these substrates. Figure 3.4 shows six fluorescence images captured at 8 and 100 s on three substrates of this same experiment. Two substrates contained a mixture of N- and C-His_{10}-tag PMs, with ('PM+pHrodo') and without pHrodo ('PM only') at the surface. The remaining substrate

contained pHrodo at the surface without PMs (`pHrodo only´).

When PMs are exposed to green light, protons were pumped from the C-terminal to the N-terminal side. This proton transport leads to a progressive increase in fluorescence over time on substrates with PMs deposited on a pHrodo-functionalized surface. Observations showed that for all types of PMs, FI increased on PM-pHrodo- silane-SiO_2 substrates under green light, while no such increase was noted for pHrodo- silane-SiO_2 substrates alone (see Figures 3.3 and 3.4). This suggests that the system can detect PM proton pumping activity. However, Figure 3.4 indicates that individual PM patches on the pHrodo surface were not distinguishable, due to the limited resolution of the microscope. Only an overall increase in FI across the entire area was observed.

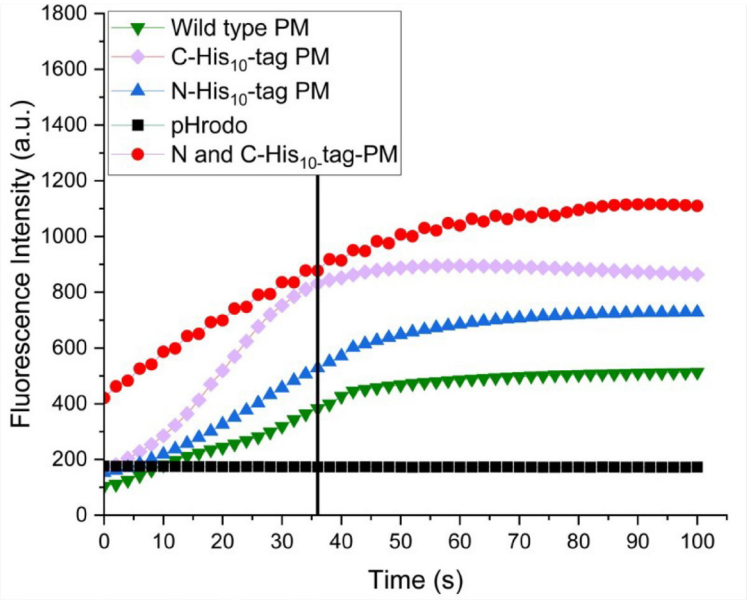

Figure 3.3. Fluorescence response of pHrodo to PM pumping over time. Experiments were performed in Milli-Q water. Images were captured with 500 ms exposure time using 40x objective lens. Green light (TRITC filter) activated the pumping, and pHrodo fluorescence intensity was measured using blue light (FITC filter). The signal of 'PM only' was approximately 0 counts (not shown). Green: wild-type PM. Violet: C-His_{10}-tag PM. Blue: N-His_{10}-tag PM. Black: pHrodo (control). Red: mixture of N- and C-His_{10}-tag PM.

To correlate FI with pH, we formulated Equation (1) considering that the pHrodo intensity exhibited a linear increase for pH values from 8.0 to 4.0 [31]

$$(1)\quad \frac{I_{PMpHrodo}}{IpHrodo} = -3.65 \times pH_{PMpHrodo} \pm 0.40 + 25.95 \pm 2.23$$

where I_{pHrodo} is the FI of the substrate at a specific pH (represented by pH_{pHrodo}) in the

absence of PMs; $I_{PMpHrodo}$ is the pHrodo intensity at a particular time in the presence of PMs; and $pH_{PMpHrodo}$ is the pH value at a specific time in the presence of PMs. The formulation of this formula through linear regression is based on data from Dolman et al. [34] Figure S3.1, in the supplementary information (SI) shows the graphical representation of the plot of this equation.

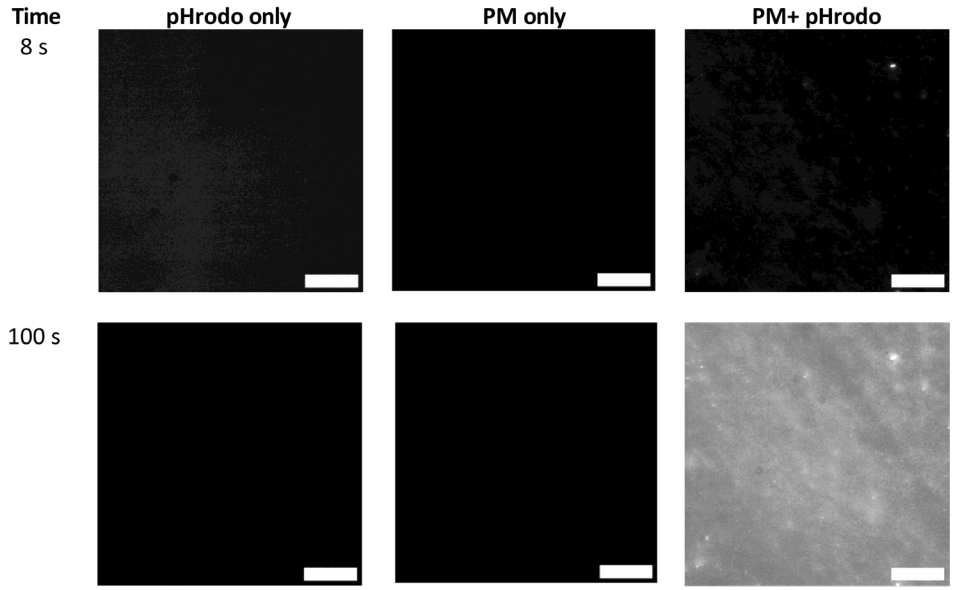

Figure 3.4. Fluorescence images of pHrodo response under three conditions: in the absence of PMs ('pHrodo only'), in the presence of PM pumping for a mixture of N- and C-His_{10}-tag PM ('PM+pHrodo') and in the absence of pHrodo ('PM only'). Images were acquired using 500 ms exposure time and 40x objective lens. The pumping was activated using green light (TRITC filter), whereas pHrodo fluorescence intensity was measured under blue light (FITC filter). The scale bar corresponds to 20 µm.

Table 3.2 displays the results of the linear regression for 'PM+pHrodo' substrates, extracted from a subset of data shown in Figure 3.3. For the linear regression, we considered the interval from t = 0.0 to t = 36.0 s, which presented almost linear behavior of all substrates containing 'PMs+pHrodo` (coefficient of determination (COD) around 1.0). Based on the FI values from Figure 3.3 and Equation (1), we calculated the initial (t = 0 s) and final (t = 100 s) pH values, as shown in Table 3.2. A pH decrease (ΔpH) of approximately 1.08 was observed for the C and N-His_{10}-tag PMs mixture and for C- His_{10}-tag PMs, 0.89 for N-His_{10}-tag PMs, and 0.64 for WT PMs. The calculated pH values closely match those documented in the literature, with a ΔpH of approximately 0.5–2.0.[7,35]

In Figure 3.3, the fluorescence signal of all PM types, except for C-His_{10}-tag PM, increased over time until the end of the measurements. This provides evidence of a decrease in pH

overtime. However, the FI rate of increase decelerated over time. In the case of C-His_{10}-tag PM, its FI increased until reaching a maximum and then began to decrease. This phenomenon may be associated with the saturation of pumping activity or dye bleaching. Interestingly, we did not observe a fluorescence decrease in the other PM types. Therefore, we assumed that the pumping activity of this PM type reached a saturation point. A more extended exposure time to green light could validate this assumption. This is further analyzed in Figure 3.6.

Table 3.2. Linear regression analysis of fluorescence intensity over time, measured from timelapse experiments on a flat substrate coated with different types of PMs: C-His_{10}-tag PMs, N- His_{10}-tag PMs, wild-type PMs, and a mixture of N and C-His_{10}-tag PMs. The table includes the calculated ratios of $I_{PMpHrodo}$ to I_{pHrodo} fluorescence intensities, as well as the initial and final pH values derived from these intensities using Equation (1). COD= The coefficient of determination.

Sample	Linear regression values			$\frac{I_{PMpHrodo}}{I_{pHrodo}}$		Calculated pH	
	Intercept	Slope	COD	Initial	Final	Initial	Final
Mixture C and N-His_{10}-tag PM	444.6 ± 6.2	12.7 ± 0.3	0.99	2.39	6.41	6.50	5.42
C-His_{10}-tag PM	112.1 ± 12.2	20.6 ± 0.6	0.99	0.97	4.99	6.88	5.80
N-His_{10}-tag PM	120.0 ± 6.4	11.0 ± 0.3	0.99	0.86	4.20	6.90	6.01
Wild-type PM	99.4 ± 3.4	7.5 ± 0.2	0.99	0.59	2.96	6.98	6.34

Figure 3.3 demonstrates that C-His_{10}-tag PM exhibited the steepest slope in proton pumping activity, followed by the mixture of C- and N-His_{10}-tag PM, N-His_{10}-tag PM, and WT PM. The mixture of C- and N-His_{10}-tag PM also exhibited a higher initial FI relative to the other PM types. These findings suggest that all PM types contribute to proton pumping toward pHrodo to some extent. The differences in FI values between PM types may be attributed to the lower surface density of WT and N-His_{10}-tag PMs on the coated substrate (see Figure S3.2, SI).

To investigate proton diffusion, we used SiO_2-silane-pHrodo substrates with adsorbed PM membranes (WT PM, C-His_{10}-tag PM, N-His_{10}-tag PM, or a mixture of C and N-His_{10}-tag PM). The light exposure sequence is shown in Figure 3.5. After adding water to the substrate, proton pumping was activated with 1.0 s of green light exposure (TRITC filter). Fluorescence was measured with 500 ms excitation under blue light (FITC filter). The sample was then kept in the dark for 21.0 s, followed by another fluorescence measurement with 500 ms excitation (FITC filter). Following a 1.0 s exposure to the TRITC filter, fluorescence was re-measured with 500 ms excitation (FITC filter). The dark-light cycle was repeated for 456.0 s. The sample then underwent several sequences of 1.0 s exposures to green light, with fluorescence measured using 500 ms blue light exposure to assess the linearity of pHrodo intensity response to green light. The fluorescence of pHrodo-silane-SiO_2 substrate ('pHrodo') and PMs on SiO_2 ('PM only') were measured under the same conditions for

reference.

Figure 3.6a presents the timelapse sequence of FI shown in Figure 3.5. Accordingly, with prolonged exposure to green light, the FI of all PM-pHrodo-silane-SiO_2 substrates increased. After 456.0 s from the beginning of the experiment, the slope of the intensity values increased even further. This indicated that an increasing exposure to green light over time accelerated the fluorescence signal slope, which corresponded to a faster decrease in pH. Furthermore, except for WT PM, the FI of PMs presented a linear increase until they reached a maximum and then started to decrease. This is likely related to the saturation of pumping activity or dye bleaching. We did not observe bleaching in WT PM and control samples. So, we conclude that the genetically modified PMs reached their saturation faster than WT PM. The pH of WT PM continued to decrease until the end of the measurement, but at a lower rate.

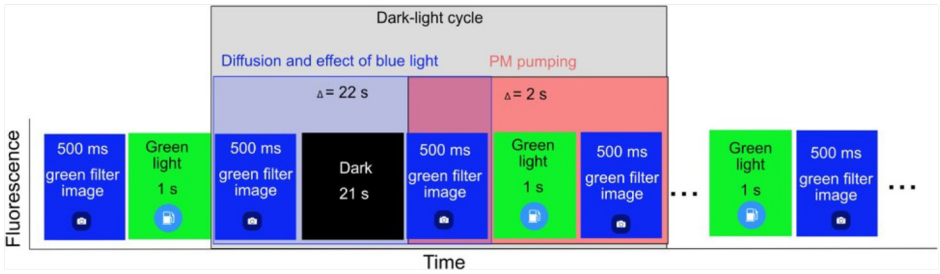

Figure 3.5. Schematic diagram of a sequence of FM images obtained to study the proton diffusion of PM on a pHrodo-functionalized surface. Blue light (FITC filter) was used for imaging, and green light (TRITC filter) was used for PM pumping.

Figure 3.6a also shows that, except for C-His_{10}-tag PM, the initial fluorescence of 'PM+pHrodo' substrates started at approximately 100 counts (cps), similarly to the results shown in Figure 3.3. However, the 'pHrodo only' substrate signal shown in Figure 3.6 exhibited a substantially lower signal than that shown in Figure 3.3 (190 to 110 cps). This variation might be related to surface contamination by unbound pHrodo, which could not be prevented. Consequently, the results should not be considered quantitative due to the significant deviation from earlier measurements presented in Table 3.2. Nonetheless, qualitative interpretation remains feasible under these conditions, as fluorescence intensity increases over time.

Figure 3.6b and c shows, respectively, the difference in fluorescence signal after exposure to green light, which was responsible for the pumping (red-transparent area, Figure 3.5) and after 21.0 s in the dark (blue-transparent area, Figure 3.5). We observed that for all samples, diffusion did not substantially influence the PM proton pumping as the FI did not decrease after 21.0 s in the dark. We assumed that the blue light affected the PM pumping to some extent. Owing to its broad excitation spectrum (detection wavelength between 700–800 nm), bR exerts considerable pumping for excitation wavelengths between 470

nm (blue light) and 650 nm (red light).[8] Compared to our results, a previous study showed that the suspension of PM cells in response to a short light pulse led to pH changes only under minor or medium acidification, which reversed in the dark.[7] We concluded that our result was different because of the exposure of our sample to blue light.

In summary, pHrodo-functionalized surfaces effectively detect proton pumping from PMs by monitoring FI. Green light stimulation induced stepwise increases in FI (Figure 3.6), demonstrating its efficacy. All PM types exhibit proton pumping activity, and the pHrodo-functionalized surface does not appear to influence PM orientation; observed differences are likely due to variations in PM density. However, several factors may affect the reproducibility of quantification, including PM density after deposition and the quality of the pHrodo layer, which depends on the efficiency of surface functionalization. Image resolution for visualizing single patches was a challenge, underscoring the need for a more controllable method to spatially regulate PM deposition. Consequently, the locally controlled deposition of single PM patches in traps functionalized with a pH-sensitive dye was investigated, as discussed in Section 3.2.2.

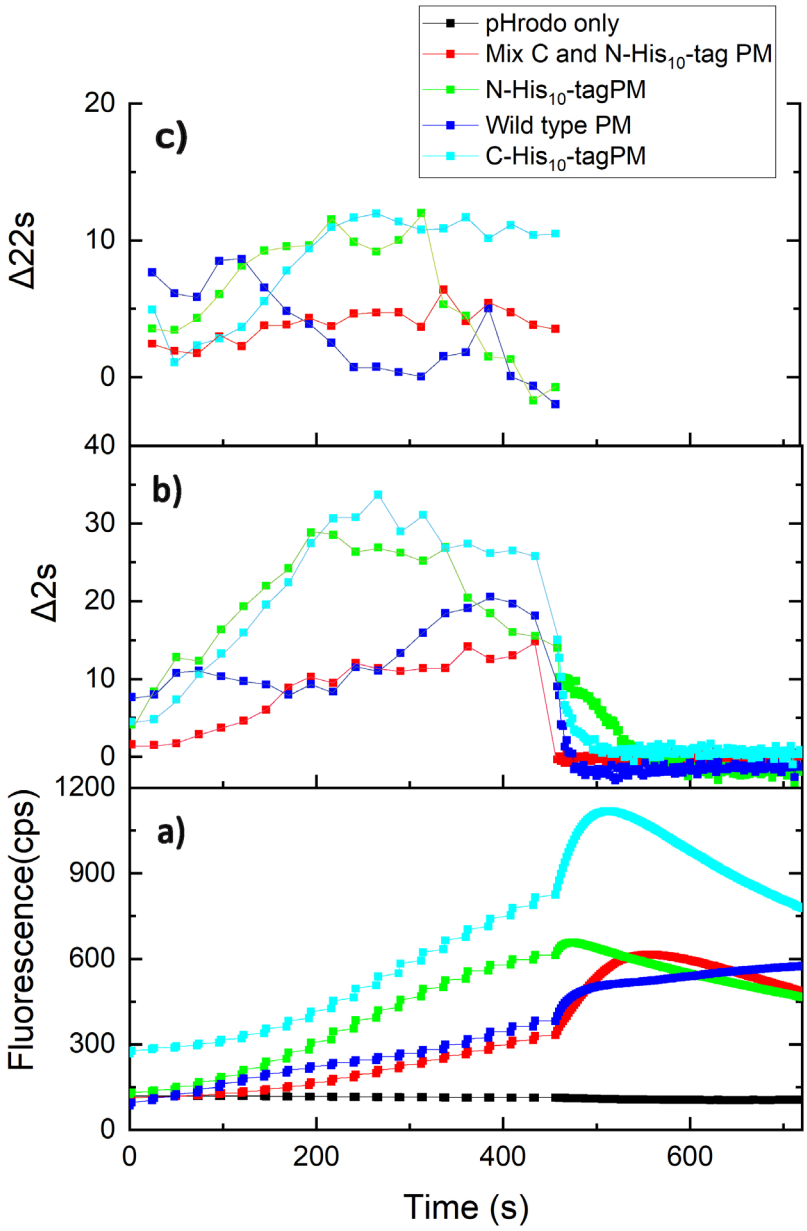

Figure 3.6. a) Fluorescence response of pHrodo to PM pumping used to investigate the diffusion of protons over time. Experiments were performed in Milli-Q water. Images were captured under 500 ms exposure time using 60x objective lens. Green light (TRITC filter) activated the pumping, and pHrodo fluorescence intensity was measured using blue light (FITC filter). The signal of 'PM only' was approximately 0 cps (not shown). **b)** Difference in fluorescence intensity (obtained from Figure 3.6a) between b) 21.0 s in the dark (Δ 22.0 s) and **c)** 1.0 s under green light (Δ2s) by pHrodo response.

3.2.2 Nanofunctionalization of proton gradient from Bacteriorhodopsin

The microlocalized measurement of PM pumping is crucial for the spatiotemporal examination of the pumping activity of a single patch of PM. For localized silanization of a surface, current micro chemical functionalization techniques, such as nano printing and chemical lift-off, require sophisticated preparation steps. [36,37] Moreover, these methods are incompatible with the device developed in this study because a 3D pattern is necessary to trap PMs. [13]

T-SPL is well-suited for designing 3D patterns, and polyphthalaldehyde (PPA) is an excellent polymer for creating topographical nanostructures using this method. [38] PPA does not require resist development and is resistant to ethanol or methanol, solvents commonly used for aminosilanization. [39] Thus, it serves both as a t-SPL resist and a mask to protect non-patterned areas. PPA shields these areas from silanization and can be removed afterward with solvents like tetrahydrofuran (THF) and isopropanol, [40] so the resist can be removed after the silanization and/or dye functionalization.

The approach used in this study to measure a localized single-patch PM pumping is shown in Figure 3.7. The fabrication steps for the device included the deposition of PPA resist, lithographic writing of PM traps in the resist, etching of traps on the SiO_2 substrate, silanization of the PPA and SiO_2 area, removal of the resist by THF and, finally, the localized functionalization of pHrodo in the traps. We used t-SPL to design 1.2 µm diameter traps, reactive ion etching (RIE) to transfer the traps into the SiO_2 layer and PPA, and a PPA as a mask to prevent non-patterned areas from being silanized. The designed traps were functionalized with AEAPTMS and pHrodo green STP ester. After the microlocalized pHrodo functionalization (step 7, Figure 3.7), we applied a drop of WT PM to the chip's surface and conducted PM deposition specifically in the designated traps using TNCA [13] (step 8, Figure 3.7).

Figure 3.8. shows images of pHrodo localized functionalization (step 7 in Figure 3.7). Figure 3.8a presents a bright-field image of a field designed using t-SPL. Figures 3.8b and 3.8c display fluorescent images of a dry sample and a sample immersed in pH 4.0 buffer, respectively. The fluorescent images show brighter spots only in areas written by t-SPL, which highlights the contrast between the functionalized traps and the surrounding regions. This demonstrates the success of the t-SPL chemical lift-off process. The fluorescent intensity contrast ($FI_{contrast}$), defined by Equation (2), is the ratio between I_{pHrodo} (FI in the pHrodo-functionalized area) and $I_{background}$ (FI in the non- functionalized area).

$$(2)\ FI_{contrast} = \frac{I_{pHrodo}}{I_{background}}$$

In Figures 3.8b and 3.8c, $FI_{contrast}$ was 74% and approximately 50%, respectively. In conclusion, our MLO method effectively achieved microlocalized functionalization of PM traps with pHrodo.

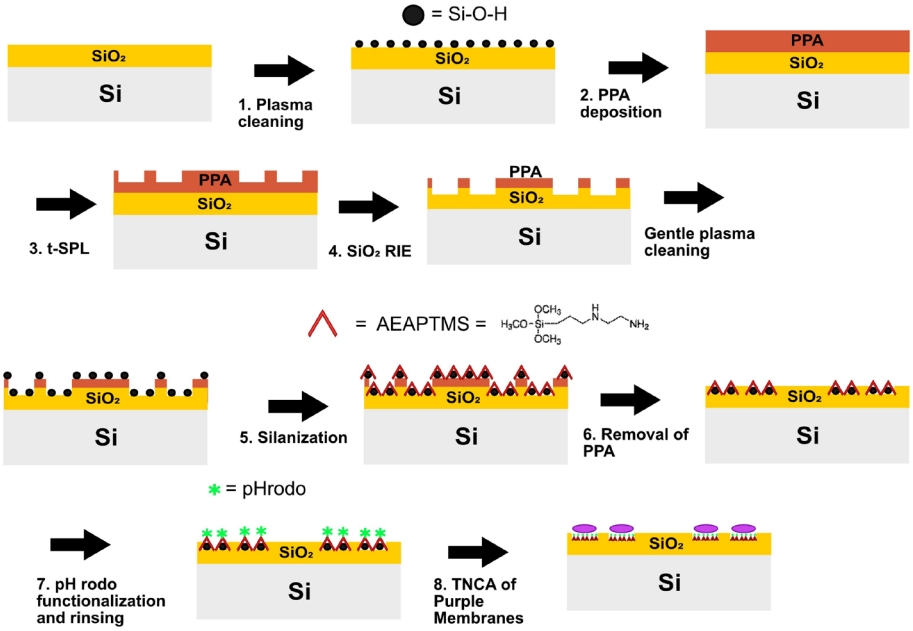

Figure 3.7. Substrate used for single-patch PM proton pumping measurements: 1. Plasma cleaning. 2. PPA spin-coating. 3. t-SPL writing. 4. SiO_2 RIE. 5. Substrate silanization. 6. PPA removal. 7. Functionalization of pHrodo. 8. Deposition of PM by TNCA. PPA = polyphthalaldehyde; t-SPL = thermal scanning probe lithography; RIE = reactive ion etching; TNCA = tunable nanofluidic confinement apparatus.

a)	b)	c)
Bright-field image	Fluorescence image (FITC filter)	
Dry sample		pH 4 buffer

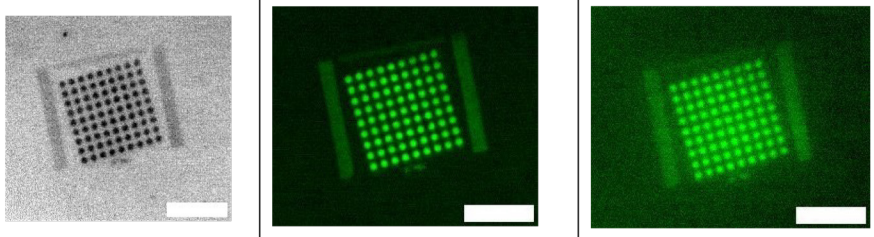

Figure 3.8. a) Image of a dry sample of localized pHrodo-silane-SiO_2 substrate (step 7, Figure 3.7) in a bright-field. FITC filter fluorescent image of **b)** dry sample and **c)** sample immersed in buffer 4 solution. The scale bar represents 10 µm.

a)	b)	c)
Localized silanization	Localized deposition of wild-type PM	Non-localized deposition of wild-type PM
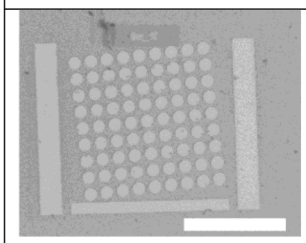	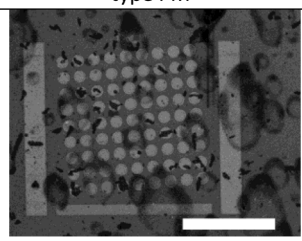	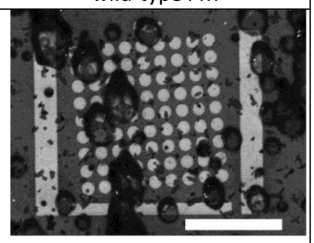

Figure 3.9. SEM images of PM deposition field at different steps: **a)** Localized silane-SiO_2 substrate after PPA removal by THF (step 6, Figure 3.7), **b)** localized pHrodo-silane-SiO_2 substrate after wild-type PM deposition (step 8, Figure 3.7), and **c)** non-localized pHrodo-silane-SiO_2 substrate after wild-type PM deposition (step 8, Figure 3.7). The scale bar represents 10 µm.

SEM images of the device fabrication at different stages are presented in Figure 3.9. Figure 3.9a shows the substrate after localized silanization and subsequent removal of PPA. The contrast between the traps and the surrounding area suggests that the silanization was effective, as indicated by the difference in material inside and outside the traps. The SEM image shown in Figure 3.9b, representing the substrate after step 8 in Figure 3.7 (following the deposition of PMs by TNCA), reveals the presence of darker spots with an ellipsoidal shape, each with an approximate size of 500 nm. These dimensions correspond to the average size of a PM patch. This image provides evidence of the possibility of localized deposition of PMs on this device. Figure 3.9c presents a field of the same device as shown in Figure 3.9b, where TNCA was not performed. Although PMs are visible, they were not solely deposited in the traps. Instead, they were also randomly spread at the designated area. Figure 3.9c underscores the significance of the TNCA in achieving a more controlled deposition of PMs within the traps.

The fluorescence signal of the localized-pHrodo-silane-SiO_2 substrates, shown in Figure 3.9b, could not be measured. A substantial amount of dirt was visible on the substrate surface after PM deposition, as represented by the large black circles. We assumed that the unbound pHrodo prevented the device from obtaining localized fluorescence signals in the PM traps area. To overcome that, the MLO method should be better controlled to prevent unbound pHrodo in areas outside the PM traps.

The MLO method was thoroughly investigated, with each step analyzed via ellipsometry to achieve reproducibility, as detailed in the SI. However, through our studies, reproducibility remained an issue. We propose that factors such as surface contamination from solvents used in rinsing steps and gases from RIE can impede silanization and lead to uneven coverage. Additionally, moisture sensitivity of amino silanes in humid environments may reduce reactivity, while inadequate reaction conditions can result in incomplete silanization.

Achieving precise control over the silane layer thickness presents further challenges, and environmental variability may contribute to inconsistent results. Moreover, amino groups may lose functionality under harsh conditions. Despite these challenges, the MLO method shows promise for the microscale functionalization of small molecules. Optimizing these parameters could enable a simple, maskless lift-off protocol for localized functionalization.

3.3 Conclusion and outlook

We developed a method that can be used to measure the proton gradient of PMs per unit of time. For the localized and oriented controlled measurement of PM pumping, we developed a chemical lift-off method that locally functionalizes amino-reactive pHrodo dye. However, we faced issues concerning reproducibility, and the main challenges were the presence of unlocalized pHrodo dye and agglomerates at the SiO_2 surface. Future studies should further implement the t-SPL chemical lift-off method using other dyes and amino-reactive molecules to expand the applications of this new silanization method.

3.4 References

(1) Nande, A.; Kalyani, N. T.; Tiwari, A.; Dhoble, S. J. 1 - Exploring the World of Functional Materials. In Functional Materials from Carbon, Inorganic, and Organic Sources; Dhoble, S. J., Nande, A., Kalyani, N. T., Tiwari, A., Arof, A. K., Eds.; Woodhead Publishing Series in Electronic and Optical Materials; *Woodhead Publishing*, **2023;** pp 1–19. https://doi.org/10.1016/B978-0-323-85788-8.00014-8.

(2) Das, K.; Gabrielli, L.; Prins, L. J. Chemically Fueled Self-assembly in Biology and Chemistry. *Angewandte Chemie International Edition* **2021**, 60 (37), 20120–20143.

(3) Boekhoven, J.; Brizard, A. M.; Kowlgi, K. N.; Koper, G. J.; Eelkema, R.; van Esch, J. H. Dissipative Self-assembly of a Molecular Gelator by Using a Chemical Fuel. *Angewandte Chemie* **2010**, 122 (28), 4935–4938.

(4) Wang, Y.; Oldenhof, S.; Versluis, F.; Shah, M.; Zhang, K.; van Steijn, V.; Guo, X.; Eelkema, R.; van Esch, J. H. Controlled Fabrication of Micropatterned Supramolecular Gels by Directed Self-Assembly of Small Molecular Gelators. *Small* **2019**, 15 (8), 1804154.

(5) Wang, Y.; Versluis, F.; Oldenhof, S.; Lakshminarayanan, V.; Zhang, K.; Wang, Y.; Wang, J.; Eelkema, R.; Guo, X.; van Esch, J. H. Directed Nanoscale Self-Assembly of Low Molecular Weight Hydrogelators Using Catalytic Nanoparticles. *Advanced Materials* **2018**, 30 (21), 1707408.

(6) Olive, A. G.; Abdullah, N. H.; Ziemecka, I.; Mendes, E.; Eelkema, R.; Van Esch, J. H. Spatial and Directional Control over Self-Assembly Using Catalytic Micropatterned Surfaces. *Angewandte Chemie International Edition* **2014**, 53 (16), 4132–4136.

(7) Stoeckenius, W.; Lozier, R. H.; Bogomolni, R. A. Bacteriorhodopsin and the Purple Membrane of Halobacteria. *Biochimica et Biophysica Acta (BBA)-Reviews on Bioenergetics* **1979**, 505 (3–4), 215–278.

(8) Schenkl, S.; Zgrablić, G.; Portuondo-Campa, E.; Haacke, S.; Chergui, M. On the Excitation Wavelength Dependence of the Fluorescence of Bacteriorhodopsin. *Chemical physics letters* **2007,** 441 (4–6), 322–326.

(9) Perrino, A. P.; Miyagi, A.; Scheuring, S. Single Molecule Kinetics of Bacteriorhodopsin by HS-AFM. *Nature Communications* **2021**, 12 (1), 7225.

(10) Hampp, N. Bacteriorhodopsin as a Photochromic Retinal Protein for Optical Memories. *Chemical Reviews* **2000**, 100 (5), 1755–1776.

(11) Boekhoven, J.; Poolman, J. M.; Maity, C.; Li, F.; Van Der Mee, L.; Minkenberg, C. B.; Mendes, E.; Van Esch, J. H.; Eelkema, R. Catalytic Control over Supramolecular Gel Formation. *Nature chemistry* **2013**, 5 (5), 433–437.

(12) Lozier, R. H.; Bogomolni, R. A.; Stoeckenius, W. Bacteriorhodopsin: A Light-Driven Proton Pump in Halobacterium Halobium. *Biophysical journal* **1975**, 15 (9), 955.

(13) Ruggeri, F.; Schwemmer, C.; Stauffer, M.; Nicollier, P. M.; Figueiredo da Silva, J.; Bosshart, P. D.; Kochems, K.; Fotiadis, D.; Knoll, A.; Wolf, H. Placement of Biological Membrane Patches in a Nanofluidic Gap With Control Over Position and Orientation. *Advanced materials interfaces* **2022**, 9 (23), 2200941.

(14) Stauffer, M.; Hirschi, S.; Ucurum, Z.; Harder, D.; Schlesinger, R.; Fotiadis, D. Engineering and Production of the Light-Driven Proton Pump Bacteriorhodopsin in 2D Crystals for Basic Research and Applied Technologies. *Methods and protocols* **2020**, 3 (3), 51.

(15) Michalak, M.; Kurel, M.; Jedraszko, J.; Toczydlowska, D.; Wittstock, G.; Opallo, M.; Nogala, W. Voltammetric pH Nanosensor. *Analytical chemistry* **2015**, 87 (23), 11641–11645.

(16) Al-Jeda, M.; Mena-Morcillo, E.; Chen, A. Micro-Sized pH Sensors Based on Scanning Electrochemical Probe Microscopy. *Micromachines* **2022**, 13 (12), 2143.

(17) Nadappuram, B. P.; McKelvey, K.; Al Botros, R.; Colburn, A. W.; Unwin, P. R. Fabrication and Characterization of Dual Function Nanoscale pH-Scanning Ion Conductance Microscopy (SICM) Probes for High Resolution pH Mapping. *Analytical chemistry* **2013**, 85 (17), 8070–8074.

(18) Gaitzsch, J.; Hirschi, S.; Freimann, S.; Fotiadis, D.; Meier, W. Directed Insertion of Light-Activated Proteorhodopsin into Asymmetric Polymersomes from an ABC Block Copolymer. *Nano letters* **2019**, 19 (4), 2503–2508.

(19) Wang, D.; Wang, Y.; Li, H.; Han, Y.; Hu, P.; Ma, K.; Sheves, M.; Jin, Y. Photoactivated Bacteriorhodopsin/SiN x Nanopore-Based Biological Nanofluidic Generator with Single-Protein Sensitivity. *ACS nano* **2022**, 16 (1), 1589–1599.

(20) Bamberg, E.; Apell, H.-J.; Dencher, N. A.; Sperling, W.; Stieve, H.; Läuger, P. Photocurrents Generated by Bacteriorhodopsin on Planar Bilayer Membranes. *Biophysics of structure and mechanism* **1979**, 5, 277–292.

(21) Seigneuret, M.; Rigaud, J.-L. Use of the Fluorescent pH Probe Pyranine to Detect Heterogeneous Directions of Proton Movement in Bacteriorhodopsin Reconstituted Large Liposomes. *FEBS letters* **1985**, 188 (1), 101–106.

(22) Lee, H.; Ho, D.; Kuo, K.; Montemagno, C. D. Vectorial Insertion of Bacteriorhodopsin for Directed Orientation Assays in Various Polymeric Biomembranes. *Polymer* **2006**, 47 (9), 2935–2941. https://doi.org/10.1016/j.polymer.2006.02.082.

(23) Gonçalves, R. P.; Agnus, G.; Sens, P.; Houssin, C.; Bartenlian, B.; Scheuring, S. Two-Chamber AFM: Probing Membrane Proteins Separating Two Aqueous Compartments. *Nature methods* **2006**, 3 (12), 1007–1012.

(24) Chandra, A.; Prasad, S.; Iuele, H.; Colella, F.; Rizzo, R.; D'Amone, E.; Gigli, G.; Del Mercato, L. L. Highly Sensitive Fluorescent pH Microsensors Based on the Ratiometric Dye Pyranine Immobilized on Silica Microparticles. *Chemistry–A European Journal* **2021**, 27 (53), 13318–13324.

(25) Ulrich, S.; Osypova, A.; Panzarasa, G.; Rossi, R. M.; Bruns, N.; Boesel, L. F. Pyranine-modified Amphiphilic Polymer Conetworks as Fluorescent Ratiometric pH Sensors. *Macromolecular rapid communications* **2019**, 40 (21), 1900360.

(26) Hirose, H.; Maekawa, M.; Ida, H.; Kuriyama, M.; Takahashi, Y.; Futaki, S. A Noncanonical Endocytic Pathway Is Involved in the Internalization of 3 Mm Polystyrene Beads into HeLa Cells. *Biomaterials Science* **2022**, 10 (24), 7093–7102.

(27) Arppe, R.; Näreoja, T.; Nylund, S.; Mattsson, L.; Koho, S.; Rosenholm, J. M.; Soukka, T.; Schäferling, M. Photon Upconversion Sensitized Nanoprobes for Sensing and Imaging of pH. *Nanoscale* **2014**, 6 (12), 6837–6843.

(28) Lindner, B.; Burkard, T.; Schuler, M. Phagocytosis Assays with Different pH-Sensitive Fluorescent Particles and Various Readouts. *Biotechniques* **2020**, 68 (5), 245–250.

(29) von Kaeppler, E. P.; Wang, Q.; Raghu, H.; Bloom, M. S.; Wong, H.; Robinson, W. H. Interleukin 4 Promotes Anti-Inflammatory Macrophages That Clear Cartilage Debris and Inhibits Osteoclast Development to Protect against Osteoarthritis. *Clinical Immunology* **2021**, 229, 108784.

(30) Miller, A.; Fantone, K. M.; Tucker, S. L.; Gokanapudi, N.; Goldberg, J. B.; Rada, B. Short Chain Fatty Acids Reduce the Respiratory Burst of Human Neutrophils in Response to Cystic Fibrosis Isolates of Staphylococcus Aureus. *Journal of Cystic Fibrosis* **2023**. https://doi.org/10.1016/j.jcf.2023.04.022.

(31) *pHrodo*™ Dyes for Amine Labeling. https://www.thermofisher.com/order/catalog/product/br/en/P36010 (accessed 2023-01-06).

(32) Zhu, M.; Lerum, M. Z.; Chen, W. How to Prepare Reproducible, Homogeneous, and Hydrolytically Stable Aminosilane-Derived Layers on Silica. **Langmuir 2012**, 28 (1), 416–423.

(33) Gee, K. R.; Archer, E. A.; Kang, H. C. 4-Sulfotetrafluorophenyl (STP) Esters: New Water-Soluble Amine-Reactive Reagents for Labeling Biomolecules. *Tetrahedron Letters* **1999,** 40 (8), 1471–1474.
(34) Dolman, N. J.; Kilgore, J. A.; Davidson, M. W. A Review of Reagents for Fluorescence Microscopy of Cellular Compartments and Structures, Part I: BacMam Labeling and Reagents for Vesicular Structures. *Current protocols in cytometry* **2013**, 65 (1), 12.30. 1-12.30. 27.
(35) Renthal, R.; Lanyi, J. K. Light-Induced Membrane Potential and pH Gradient in Halobacterium Halobium Envelope Vesicles. *Biochemistry* **1976**, 15 (10), 2136–2143. https://doi.org/10.1021/bi00655a017.
(36) Chen, C.-Y.; Wang, C.-M.; Liao, W.-S. A Special Connection between Nanofabrication and Analytical Devices: Chemical Lift-off Lithography. B*ulletin of the Chemical Society of Japan* **2019**, 92 (3), 600– 607.
(37) Elbersen, R.; Vijselaar, W.; Tiggelaar, R. M.; Gardeniers, H.; Huskens, J. Fabrication and Doping Methods for Silicon Nano-and Micropillar Arrays for Solar-cell Applications: A Review. *Advanced materials* **2015**, 27 (43), 6781–6796.
(38) Coulembier, O.; Knoll, A.; Pires, D.; Gotsmann, B.; Duerig, U.; Frommer, J.; Miller, R. D.; Dubois, P.; Hedrick, J. L. Probe-Based Nanolithography: Self-Amplified Depolymerization Media for Dry Lithography. *Macromolecules* **2010**, 43 (1), 572–574.
(39) Miranda, A.; Martínez, L.; De Beule, P. A. Facile Synthesis of an Aminopropylsilane Layer on Si/SiO2 Substrates Using Ethanol as APTES Solvent. *MethodsX* **2020**, 7, 100931.
(40) Howell, S. T.; Grushina, A.; Holzner, F.; Brugger, J. Thermal Scanning Probe Lithography—A Review *Microsystems & nanoengineering* **2020,** 6 (1), 1–24.

3.5 Supplementary information

This section describes the materials and methods used in this chapter. Unless otherwise stated, all chemicals and solvents were purchased from Sigma-Aldrich.

3.5.1 Fabrication of device

Covalent functionalization of pHrodo on a Si/SiO_2 substrate

The chips were produced using a highly doped silicon wafer, diced to 8 mm × 8 mm. The samples were thermally oxidized to a SiO_2 thickness of 60 nm. Before the experiments, the substrates were dried and treated with oxygen plasma (Tepla AG) for 10 min to provide O-H groups to the SiO_2 surface. The substrate was then functionalized with N-(2-aminoethyl)-3-aminopropyltrimethoxysilane (AEAPTMS) for 6h. The 0.5 mM AEAPTMS solution was prepared in anhydrous ethanol. The substrate was rinsed sequentially with anhydrous ethanol, methanol, 1.0 mM acetic acid solution (AcOH), and Milli-Q water. The pHrodo™ green STP ester (pHrodo) stock solution (5 µL of 10 mM pHrodo diluted in dimethyl sulfoxide) was diluted in 163 µL of 1 mM sodium bicarbonate solution (pH 8.3) for a final concentration of 0.3 mM. Subsequently, 25 µl of 0.3 mM pHrodo solution was added to the sample, which was incubated for 40 min in the dark, and then sequentially rinsed with anhydrous methanol, 1 mM acetic acid, and Milli-Q water.

The biological engineering of the membrane patches is described elsewhere. [1] In addition to the genetically modified C-His_{10}-tag and N-His_{10}-tag PMs, wild-type PMs were also investigated. For all PM types, PM was deposited on a flat substrate by dispersing 50 µL of 10^{-2} mg·mL^{-1} PM in water, which was added to the pHrodo- functionalized substrates. The samples were then dried in air, rinsed with Milli-Q water, and dried with nitrogen gas.

Ultimately, the samples were inserted in an upright fluorescence microscope while being immersed in Milli-Q water, with a thin layer (170 µm) of glass slide placed on top of the chip.

Maskless chemical lift-off on Si/SiO_2 surface by thermal scanning probe lithography (t-SPL)

We designed a pH-sensitive fluorescence microcompartment to measure the nanolocalized proton gradient of the PM patches. The samples in our experiments were thermally oxidized and treated similarly to the unpatterned flat substrates. Subsequently, 25 µm of 5 wt% polyphthalaldehyde (PPA) (Allresist) solution dissolved in anisole was spun at 2900 rpm for 1.5 min by spin-coating. The substrate was then annealed at 110 °C for 1 min, which resulted in an 89 nm PPA layer, as confirmed by atomic force microscopy (AFM) and ellipsometry.

We used thermal scanning probe lithography (t-SPL) to write the desired patterns. The trap locations were defined via t-SPL using a custom-built instrument. [2] The PPA was patterned using a heated tip (at 1000 °C) capacitively pulled into contact with the substrate. The PPA underwent local decomposition, forming cylindrical indentations throughout the polymer. Each device contained a 9 × 9 array of cavities, each 1.2 µm in diameter and spaced 2.0 µm apart. After oxygen descum, the pattern was etched into a silica layer to a depth of 20 nm using RIE. For the RIE, we used a mixture of CHF_3, argon, and oxygen (12, 38, and 1 sscm, respectively) at 100 W and 30 mbar chamber pressure. After etching, the samples were treated with 200 W oxygen plasma for 30 s (Tepla AG). The silanization conditions were the same as those described for unpatterned flat substrates. The rinsing steps were also the same, except for a step after silanization, during which tetrahydrofuran (THF) was used to remove PPA after the methanol rinse. The samples were then cleaned with 1.0 mM acetic acid and Milli- Q water. The procedure for dye functionalization was the same as that for unpatterned substrates. Ultimately, the samples were inserted in a fluorescence microscope while being immersed in Milli-Q water, with a thin layer (170 µm) of glass slide placed on top of the chip. For the precise positioning and deposition of individual PM patches, TCNA was performed on the functionalized substrate. Details of the membrane deposition procedure are provided in a separate publication. [3]

3.5.2 Spectroscopic measurements

We utilized spectroscopic ellipsometry (Woollam VASE) to examine the functionalization of pHrodo on the silanized SiO_2 substrate.

Proton pumping was measured using upright fluorescence microscopy (Nikon Eclipse 90i microscope with 40× or 60× Plan Apo objective lens, NA = 0.45). Fluorescence images were captured with a Nikon DS-1QM/H CCD camera and analyzed using ImageJ. FITC (fluorescein isothiocyanate) was employed for imaging with an excitation wavelength of 490 nm and a 500 ms exposure time, while the TRITC filter, with an excitation wavelength

of 550 nm and 1.0 s exposure time, was used for green light exposure. To assess the effect of green light exposure on proton pumping, samples were alternately exposed to blue light for imaging and then to green light a 100.0 s period. To investigate proton diffusion in the medium, samples were exposed to green light, followed by image acquisition using an FITC filter. The sample was then kept in darkness for 21.0 s before fluorescence was measured again using the FITC filter. This cycle was repeated for a total duration of 456.0 s. Subsequently, the sample underwent several sequences of 1.0 s exposure to green light, with fluorescence measured using blue light. Fluorescence values were calculated by averaging the fluorescence signal of the image and subtracting the background signal.

Scanning electron microscopy (SEM) images were acquired with a Leo 1550 (Zeiss) with a material contrast mode.

Linear regression for pHrodo green

A method for analyzing fluorescence intensity changes across different pH levels is outlined, involving normalization of the data to pH 7.0 and assessment of model accuracy through regression analysis. With the dataset provided by Dolman et al. [4] for pHrodo green, the relative fluorescence intensity for each pH (I_{pHrodo}) was calculated by dividing each value by the intensity at pH 7.0 ($I_{pHrodopH7}$). The regression analysis produced a coefficient of determination (COD) of 0.98.

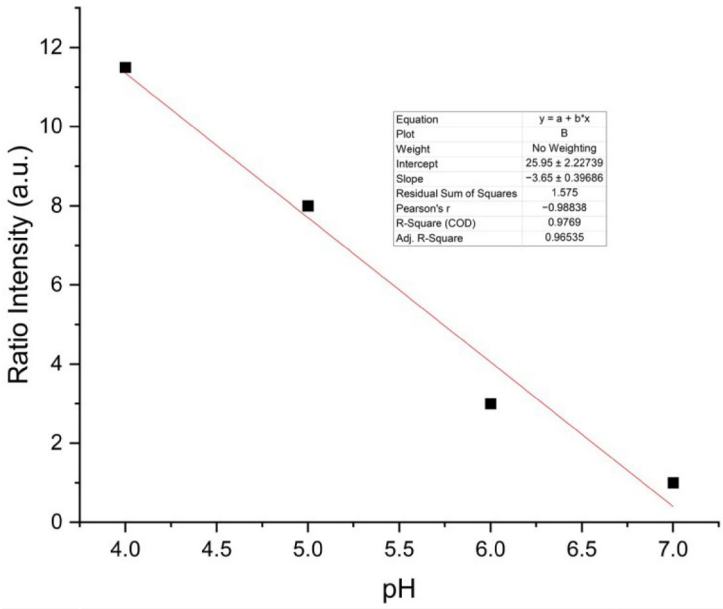

Figure S3.1. Linear regression calculated from data presented by Dolman et al. [4]

3.5.3 Experimental data

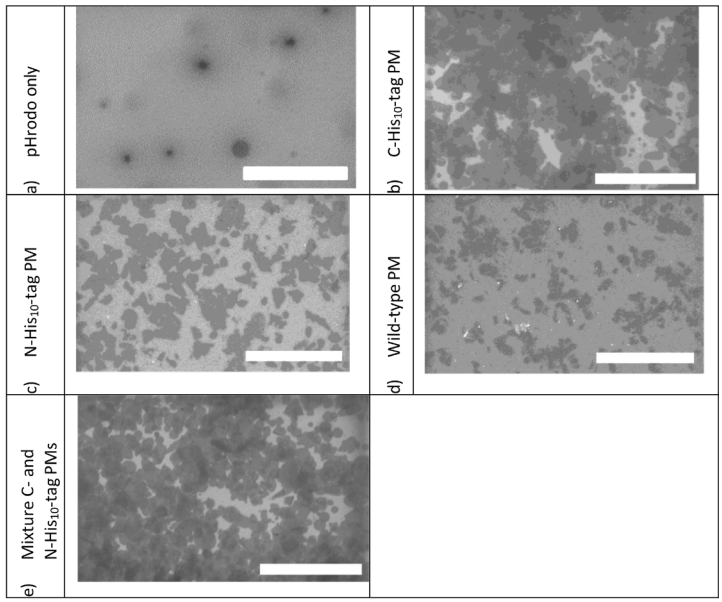

Figure S3.2. SEM images of deposited PMs-pHrodo-silane and pHrodo-silane substrate in SiO_2/Si surface: **a)** pHrodo substrate, **b)** N-His_{10}-tag PM, **c)** C-His_{10}-tag PM, **d)** wild-type PM, **e)** mixture of N- and C-His_{10}-tag PM.

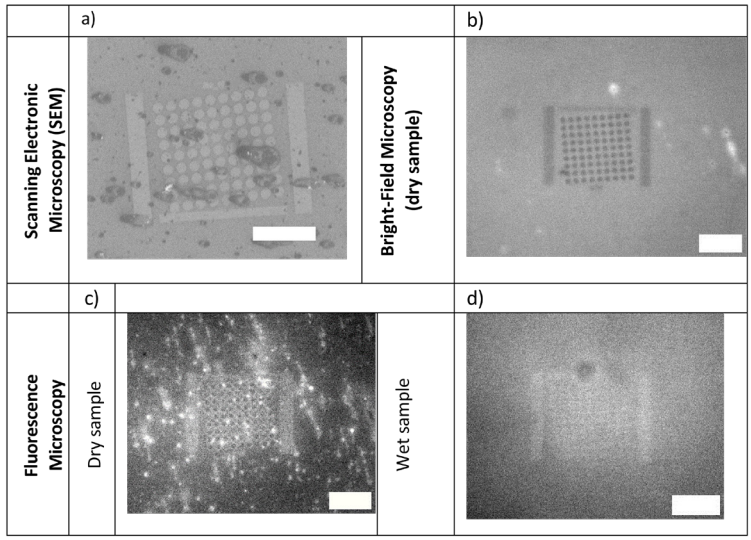

Figure S3.3. Failed localized pHrodo-silane-SiO_2 substrate (step 7, Figure 3.7): **a)** SEM image, **b)** bright-field microscopy image. Fluorescence microscopy image of **c)** dry and **d)** wet sample. The scale bar represents 10 μm.

Ellipsometry analysis of PPA removal

Table S3.1, Table S3.2, Table S3.3 and Table S3.4 present the results of the PPA removal study performed to identify the optimal conditions for the maskless lift-off (MLO) method. The mean squared error (MSE) quantifies the difference between the calculated and measured reflectance values and it is unitless. [5] An MSE value between 2 and 10 signifies an improved fit of the model to the data, implying that the model's predictions closely match the observed values.

Table S3.1. Ellipsometer data used to identify the optimal t-SPL chemical lift-off protocol. Plasma conditions: 200 W and 30 s. Refractive index (n) SiO_2 = 1.48; [6] n_{PPA} = 1.57; [7] n values obtained at wavelength = 633 nm.

Sample	Thickness PPA (nm)	Uncertainty (nm)	MSE
Thermal oxide (SiO_2)	0.0	0.0	67.49
PPA	96.6	0.6	22.05
PPA and THF	0.0	0.3	56.47
PPA and RIE	11.9	0.2	9.15
PPA, RIE, and plasma	3.1	0.9	19.95
PPA, RIE, plasma, and THF	0.0	0.0	66.52

Table S3.2. Ellipsometer data of different methods for PPA removal after RIE on silicon substrates with thermal oxide SiO_2 on top. Refractive index (n) SiO_2 = 1.48, n_{PPA} = 1.57, n values obtained at wavelength = 633 nm.

Sample	Thickness PPA (nm)	Uncertainty (nm)	MSE
7 min 600 W plasma	0.0	0.0	66.52
Acetone	10.9	0.1	53.69
THF	7.0	0.1	13.65
15 s plasma + THF	2.5	1.1	11.92
30 s plasma + THF	0.0	0.0	179.90

Table S3.1 reports the thickness of the SiO_2 and PPA layers individually, followed by the thickness of the PPA layer under various conditions, including exposure to THF, plasma treatment, and RIE etching. We observed that when the PPA was not etched, it could be removed with THF. However, when the PPA was etched, THF alone was insufficient for its removal. In such cases, a 30.0 s plasma treatment prior to THF rinsing was employed to ensure complete resist removal. This can be attributed to the presence of small amounts of moisture and sputtered contamination from fluorinated RIE recipes, which formed microscopic "masks" scattered across the substrate. During anisotropic etching, these micro-masked areas were shielded from etchant species, resulting in random raised features resembling grass. The plasma treatment effectively removed these fluorinated

ions from the remaining resist, allowing for complete removal of the PPA after THF immersion.

The MSE was higher when the PPA thickness was near zero. This was attributed to the absence of material. We observed this evidence in different experiments in which the PPA thickness was approximately 0.

Table S3.3. Ellipsometer data of silicon substrates with thermal oxide SiO_2 on top after PPA spin-coating, RIE, plasma cleaning, silanization, and rinsing with ethanol, methanol, THF, AcOH, and Milli-Q water at different plasma times. Refractive index (n) SiO_2 = 1.48, n_{PPA} = 1.57, n values obtained at wavelength = 633 nm.

Plasma time	Thickness PPA (nm)	Uncertainty (nm)	MSE
15 s	1.6	0.2	10.13
30 s	0.0	0.1	30.92
45 s	1.5	0.1	9.843
60 s	1.9	0.2	9.785

Table S3.2 presents different strategies for the complete removal of PPA after RIE. Both acetone and THF alone proved insufficient for the complete PPA removal. Consistent with the findings in Table S3.1, a 30 s plasma treatment followed by THF was effective in removing PPA. A 7 min plasma treatment with high power was also successful for this purpose. Table S3.3 shows the influence of plasma cleaning time before silanization on PPA removal. The results indicate that if an excessive amount of plasma is applied to the surface, fluorinated residuals from the resist can remain in the substrate surface.

Table S3.4 illustrates the influence of silanization time on PPA removal. A silanization time of 6 hours was found to be optimal for producing a monolayer of AEAPTMS [8] and ensuring effective PPA removal.

Table S3.4. Ellipsometer data of silicon substrates with thermal oxide SiO_2 on top after PPA spin-coating, RIE, plasma cleaning, silanization, and rinsing with ethanol, methanol, THF, AcOH, and Milli-Q water at different silanization times. Refractive index (n) SiO_2 = 1.46, n_{PPA} = 1.57, $n_{AEAPTMS}$ = 1.48, [8] n values obtained at wavelength = 633 nm. Plasma conditions: 30 s, 200 W.

Silanization time	Thickness AEAPTMS (nm)	Uncertainty (nm)	MSE
1 h	0.0	0.6	10.48
3 h	1.6	0.5	9.89
6 h	0.5	0.5	10.20
12 h	3.8	0.3	13.51

3.5.4 References

(1) Stauffer, M.; Hirschi, S.; Ucurum, Z.; Harder, D.; Schlesinger, R.; Fotiadis, D. Engineering and Production of the Light-Driven Proton Pump Bacteriorhodopsin in 2D Crystals for Basic Research and Applied Technologies. *MPs* **2020**, 3 (3), 51. https://doi.org/10.3390/mps3030051.

(2) Paul, P. C.; Knoll, A. W.; Holzner, F.; Despont, M.; Duerig, U. Rapid Turnaround Scanning Probe Nanolithography. *Nanotechnology* **2011**, 22 (27), 275306.
(3) Ruggeri, F.; Schwemmer, C.; Stauffer, M.; Nicollier, P. M.; Figueiredo da Silva, J.; Bosshart, P. D.; Kochems, K.; Fotiadis, D.; Knoll, A.; Wolf, H. Placement of Biological Membrane Patches in a Nanofluidic Gap With Control Over Position and Orientation. *Advanced materials interfaces* **2022**, 9 (23), 2200941.
(4) Dolman, N. J.; Kilgore, J. A.; Davidson, M. W. A Review of Reagents for Fluorescence Microscopy of Cellular Compartments and Structures, Part I: BacMam Labeling and Reagents for Vesicular Structures. *Current protocols in cytometry* **2013**, 65 (1), 12.30. 1-12.30. 27.
(5) Jellison, G. E. Data Analysis for Spectroscopic Ellipsometry. *In Handbook of Ellipsometry; Springer*, **2005**; pp 237–296.
(6) Awazu, K.; Onuki, H. Photo-Induced Synthesis of Amorphous SiO2 Film from Tetramethoxy-Silane on Polymethylmethacrylate at Room Temperature. *Journal of non-crystalline solids* **1997**, 215 (2–3),176–181.
(7) Howell, S. T.; Grushina, A.; Holzner, F.; Brugger, J. Thermal Scanning Probe Lithography—A Review. *Microsystems & nanoengineering* **2020**, 6 (1), 1–24.
(8) Zhu, M.; Lerum, M. Z.; Chen, W. How To Prepare Reproducible, Homogeneous, and Hydrolytically Stable Aminosilane-Derived Layers on Silica. *Langmuir* **2012**, 28 (1), 416–423. https://doi.org/10.1021/la203638g.

Chapter 4

Control of a gel-forming chemical reaction network using light-triggered proton pumps[1,2]

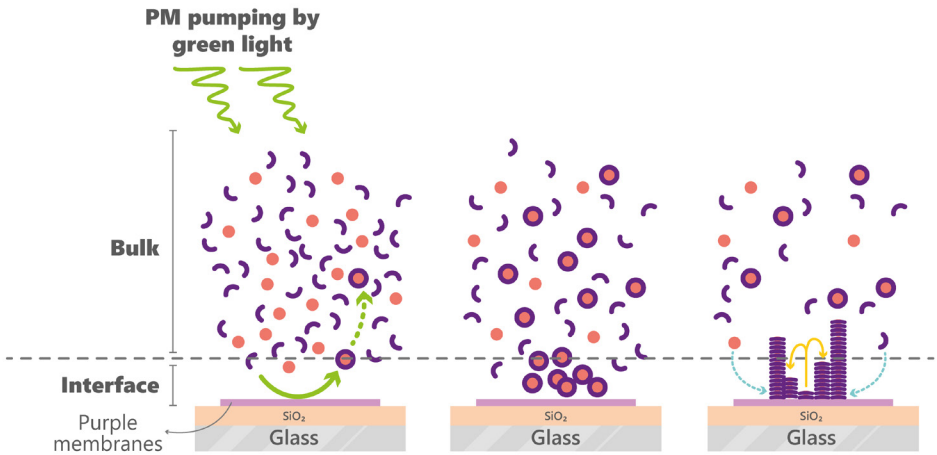

Abstract: Numerous metabolic processes in nature are governed by extrinsic stimuli such as light and pH variations, which afford opportunities for synthetic and biological applications. In developing a multi-sensor apparatus, we have integrated sub-micrometer purple membrane patches, each harboring bacteriorhodopsin, onto a surface. Bacteriorhodopsin is a light-driven proton pump. We conducted monitoring of the interactions between this system and a pH-responsive supramolecular hydrogel to evaluate fibrous matrix growth. Initial photostimulation induced localized reductions in pH at the membrane surface, thereby catalyzing fibrogenesis within the hydrogel. Utilizing liquid atomic force microscopy alongside confocal laser scanning microscopy, we observed the hydrogel's morphogenesis and structural adaptations in real time. The system adeptly modulated microscale pH environments, fostering targeted fibrous development within the hydrogel matrix. This elucidates the potential for engineering responsive materials that emulate natural bioprocesses.

[1] Chapter shared with Ardeshir Roshanasan (A.R.), TU Delft. Substrate fabrication and liquid atomic force microscopy was performed by J.F. da Silva. Synthesis of gel reagents and confocal laser scanning microscopy were performed by A.R.

[2] This chapter has been published: Figueiredo da Silva, J. et al. " Control of a gel-forming chemical reaction network using light-triggered proton pumps" Langmuir (2025).

4.1 Introduction

Eukaryotic cells have evolved distinct compartments to accommodate the unique environmental requirements of diverse metabolic activities and facilitate energy storage using electrochemical gradients. Metabolism of fuels or harvesting of light are used to generate pH gradients, [1] which are then exploited for a variety of key intracellular processes [2] e.g. to maintain intracellular organization, transport molecules, and facilitate ion exchange between cellular compartments and with the environment. [3] Hence, leveraging local pH variations as a stimulus for responsive systems has gained great interest for biomimetic applications and particularly in drug delivery systems. A similar prominence has been found in hydrogels [4] which are also designed to respond to external stimuli. [5–9] These hydrogels have been applied in controlled release applications; for example, they act as ionic networks for the oral delivery of proteins, [10] which is facilitated by the triggered collapse of the hydrogel. Alternatively, the hydrogel formation can be derived by a pH trigger. Although the formation of hydrogel by the means of a pH gradient has been demonstrated before, [11,12] achieving rigorous, microscale spatiotemporal control over this process remains a challenge. Accordingly, our objective is to attain microscale regulation of the hydrogel formation via exposure to light as an external trigger, aiming to expand the applications of this material across various domains.

In nature, a microscale externally triggered pH gradient source is found in purple membranes (PMs). Bacteriorhodopsin (bR) is the main component of 5-nm thick PMs of Halobacterium salinarum. [13] The bR acts as a light-driven proton pump, and the resulting pH gradient is used for energy storage within the cells. [14] Moreover, bR is a unique photochromic protein, and it has been successfully incorporated into various materials for the development of bio hybrid materials and nanostructured devices. [15,16] The advantages of bR include broad absorption range of visible light, high thermal and photochemical stability, resistance to environmental perturbations, environmental friendliness, and the availability of genetic variants with enhanced spectral properties for specific device applications. [15]

Previous studies [3,13] provide strong evidence that light irradiation directly drives a localized proton pump in PMs, mediated by the unique structural and functional properties of bR. When fabricating such hybrid devices, it should be noted that bR exhibits directionality in proton pumping and orientation within the membrane. The pumping occurs from the cytoplasmatic side (C-terminus) inside the cell to the extracellular side (N-terminus). [17] Therefore, it is crucial to control the orientation of the membrane patches during deposition to optimize the photoelectric conversion efficiency. Through genetic modification, we generate a charge asymmetry between the cytoplasmic and extracellular sides of the PMs, which we use to control their orientation. [18,19] Confocal laser scanning microscopy (CLSM), atomic force microscopy (AFM), and AFM-derived techniques such as single molecule force spectroscopy (SMFS) have been combined to unveil information on PMs structure, functionality, and dynamics. [20]

Boekhoven et al. [5] designed a chemical reaction network (CRN) driven by a synthetic

self-assembled system featuring a supramolecular hydrogelator. The CRN shows directed molecular self-assembly dynamics, where catalysis modulates reaction rates, impacting fiber morphology and promoting branching to form a dense gel network. The two-stage assembly—initial fiber formation followed by branching— yields gels with tailored mechanical properties. By encompassing kinetics-driven assembly, non-equilibrium states, and reversible hydrazone chemistry, the CRN demonstrates how catalysis governs material properties, transitioning from building blocks to functional hydrogels through a dynamic and tunable pathway. This hydrogelator not only regulates the self-assembly rate but also the properties of the resulting materials via bulk catalysis in aqueous medium, with a formation rate that can be tuned in situ by acidic catalysis. Examples of surface-confined catalysis that provide spatial control over the gelation process without external stimuli have been demonstrated, including micro-scaled surface-confined catalysis,[21] protonated polymer brushes,[22] and charged catalytic nanoparticles.[23] To introduce external control, a photoswitchable homogeneous catalyst for light-activated gelation process was investigated. [24] Building on these advancements, this study presents a novel approach that leverages light driven metabolic proton pumping to locally trigger gelation.

In this work, a bi-component system has been fabricated, comprising localized light responsive proton pumps coupled with a pH-responsive hydrogel-forming CRN. The transient local proton gradient, sustained by illumination, facilitates confined material formation. Specifically, we exploit PMs to produce local light-driven proton gradients via incorporating them into miniaturized systems, thus enabling the localized control of proton-catalyzed hydrogel formation. We detected a pH decrease in a microscale area indicated by an irreversible fiber growth locally accelerated by protons. The direct influence of PM pumping on the microscale hydrogel formation over time was demonstrated in situ by liquid AFM and CLSM. The approach can be used to characterize the formation of the hydrogel at the microscale under relevant conditions.

4.2 Results and discussion

The system developed in this work includes a substrate containing PM patches for generating a local pH gradient under light, and a pH-triggered hydrogel system for detecting this gradient. The hydrogel system consists of the acid-catalyzed reaction of cyclohexane-1,3,5-triscarbohydrazide **1** with three molecules of 3,4-bis[2-(2- methoxyethoxy)ethoxy] benzaldehyde **2** to form the actual hydrazone hydrogelator **3**, which subsequently self-assembles in water to form fibers. [5,25,26] Above a certain concentration threshold, these fibers form a network in the aqueous phase, thereby leading to the formation of hydrogels, Figure 4.1a. The PM part of the system is constructed from PMs that are deposited on SiO_2 substrates.

Previously, it was documented that PMs can adhere to SiO_2.[19] To control the orientation of PM adsorbed to SiO_2 substrates, we have used three types of PMs: WT PMs, and two genetically modified PMs, namely N-His_{10}-tag and C-His_{10}-tag PMs. As shown in Figure 4.1b, in aqueous media, SiO_2 layers present a negatively charged surface, whereas His_{10}-tag

peptide sequences impart a positive charge on the designated side of the PM (C-terminus or N-terminus).[18] Thus, given the asymmetric positive surface charge on the extracellular side of the membrane juxtaposed with the negative charge of SiO_2 layer in water, [27] the $NHis_{10}$-tag PMs are expected to preferentially pump protons from the PM-aqueous interface to the substrate–PM interface. Therefore, for N-His_{10}-tag PMs we anticipate a photo-induced proton gradient towards the SiO_2 substrate. The C-His_{10}-tag PMs, on the other hand, should preferentially pump protons from the substrate–PM interface across the PM membrane toward the PM-aqueous interface, thereby creating a proton gradient oriented predominantly away from the SiO_2 substrate. WT PMs have fragments with net negative charge on both sides of the membrane because of the amino-acid residues on the bR surface and the intrinsic acidity of PM lipids. However, at pH > 5 the PM surface charge density is more negative on the cytoplasmic side than on the extracellular side. [17] Consequently, the orientation of the WT PM fragments is expected to be akin to that of N-His_{10}-tag PMs.

The preparation of substrates for the experiments was carried out as described in the experimental section. Successful deposition of PMs across all types was confirmed by AFM imaging under ambient conditions, as shown in Figure S4.2, Supplementary Information (SI). Further detailed analysis revealed variations in the density of PMs on the SiO_2 substrate surface, with N-His_{10}-tag PMs exhibiting the highest density, followed by WT PMs, and finally C-His_{10}-tag PMs. These differences are attributable to the interplay between the surface charge properties of SiO_2 and those inherent to the PMs. [17]

We have used these PM-SiO_2 systems in combination with the hydrogel-forming CRN to investigate surface-confined hydrogel formation. Micro-localized light exposure and higher imaging resolution were utilized to understand the effect of proton pumping orientation on the catalytic process. Our study incorporates experiments using CLSM for microlocalized excitation and compares these findings with liquid AFM offering sub-micrometer resolution. This complementary methodology facilitates a thorough analysis of the mechanisms responsible for the in-situ formation of nanoscale hydrogels triggered by external stimuli.

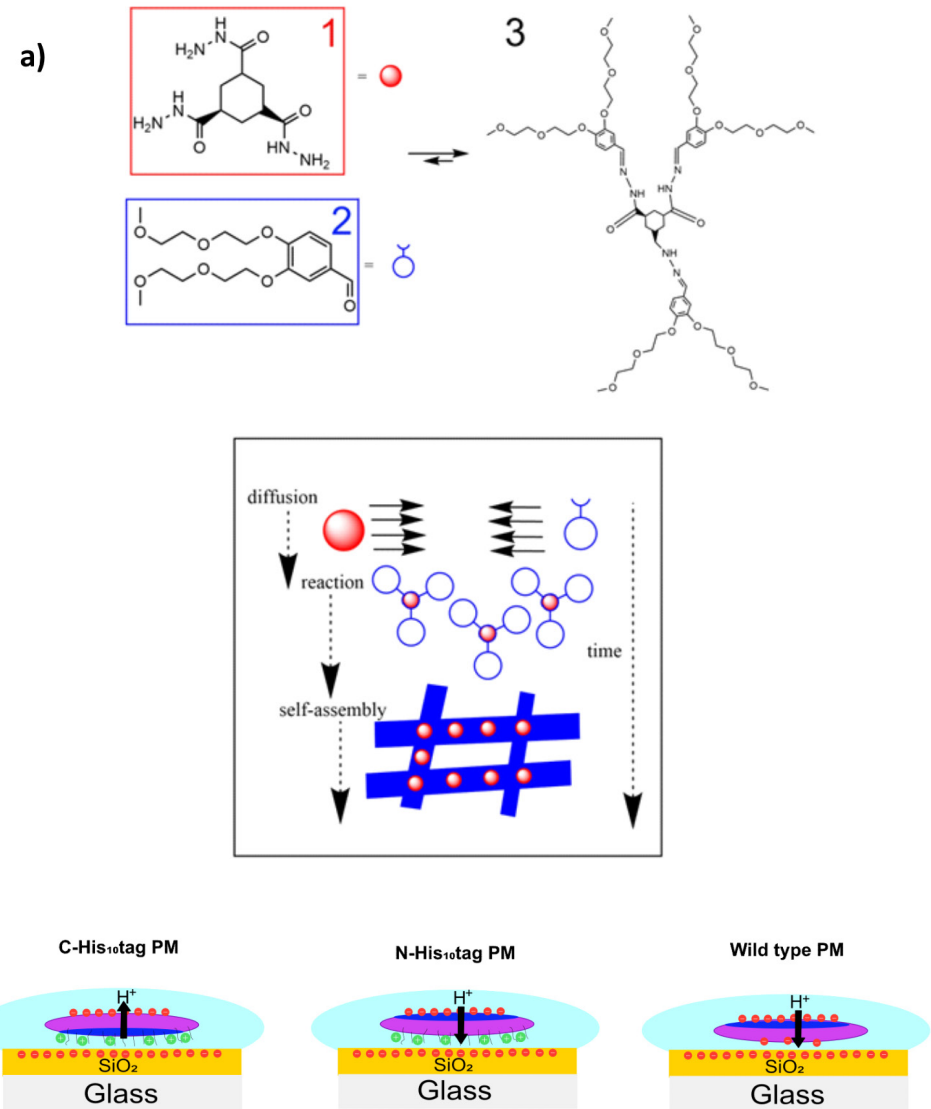

Figure 4.1. a) Catalytic formation of tris hydrazone hydrogelator **3** from soluble building blocks **1** and **2**, leading to fiber formation by self-assembly and, subsequently, to a network of fibers that trapped the surrounding solvent to form a gel network. **b)** Charge distribution between SiO_2 surface and PM in aqueous media for C-His_{10}-tag, N-His_{10}-tag, and wild-type PMs; and respective pump orientation of PMs. The purple, navy blue, light blue, red and green areas represent PMs, cytoplasmatic side of PMs, aqueous media, negative charge, and positive charge, respectively.

4.2.1 Spatiotemporal control of hydrogel formation at microscale via confocal laser scanning microscopy

In a demonstration for in-situ, externally triggered, microlocalized hydrogel formation, we explored whether a PM-coated surface could catalyze the formation of hydrogels confined to a surface. The preparation of the substrate involved covering a PM-coated glass surface with a solution containing hydrogel precursors in a buffered environment at pH 7.0. This minimizes the likelihood of premature gelation in the bulk. [25] A detailed observation of a selected area on the PM-functionalized glass substrate was conducted to examine the aggregate formation resulting from light exposure. In contact with solution, the area was exposed to cycles of monochromatic excitations, alternating between wavelengths of 488 and 543 nm, each for approximately 1 min. The former was used for image acquisition at 517 nm, and the latter was implemented to induce proton pumping. Aiming at scanning the sample prior to expected gelation, the aforementioned light exposure cycle commenced with image acquisition. A blank glass substrate that was not coated with PM served as a control and was subjected to the same experimental procedure, which granted access to a comparative analysis to distinguish the effects and changes attributable to the presence of PMs.

CLSM images in Figure 4.2 present the time progression of gel reactants, where different types of the PMs are present, in comparison to a blank sample in absence of PMs. We noted the onset of a novel phase characterized by globular cluster formation, that further coalesce to form larger domains. This phase does not form in the blank sample. Moreover, the gelation occurs in different timescales depending on the type of PMs; while the gel clusters start appearing for C-His_{10}-tag PM under 7 min and reach a steady state within 44 min they only start forming after 22 min and 55 min for WT PMs and N-His_{10}-tag, respectively. This earlier aggregation likely resulted from the formation of a favorably aligned local pH gradient at the substrate surface due to PM orientation. Previous work [5,25] using turbidity measurements demonstrated that gelation developed much faster in catalyzed samples than in uncatalyzed ones. The acid-catalyzed sample reached maximum absorbance within 60 minutes, while the uncatalyzed sample took approximately nine hours. These findings confirm that gelation is significantly slower in a pH 7.0 buffered medium without a catalyst, consistent with our results.

Interestingly, repeated experiments indicated that gel formation for the C-His_{10}-tag PM coated substrate can occur even prior to exposure to green light (543 nm) intended for pumping. It should be noted, however, that the samples already have been exposed to blue light (488 nm) to acquire the images at t=0 min. This suggests excitation of the PM by 488 nm already leads to proton pumping. Previous work on PMs [28] reported that electrical signals due to PM pumping peak at approximately 560 nm, but still have a significant response at 488 nm, which corroborates this lack of a selective pumping response. It is worth mentioning that the gelation was not observed in samples with N-His_{10}-tag and WT PMs in the initial images, but only at significant later stages.

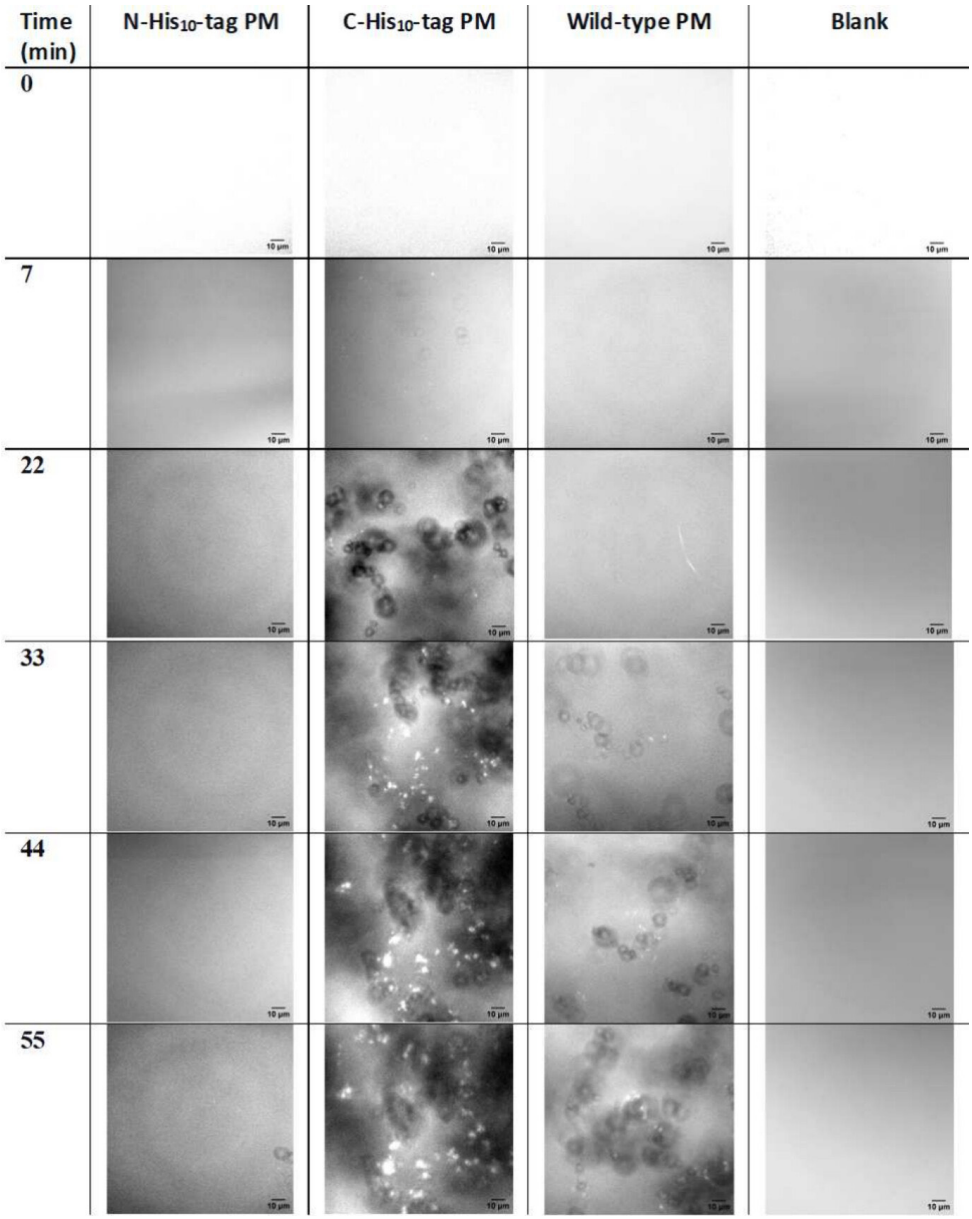

Figure 4.2. Confocal laser scanning microscopic images of the progression of hydrogel formation for different types of PMs and in the absence of PMs (blank). Snapshots were taken at 0, 7, 22, 33, 44, and 55 minutes at 63x magnification.

In summary, the presence and type of PMs significantly influenced the gelation rates. Specifically, C-His_{10}-tag PMs, that are expected to pump protons from the SiO_2 substrate–PM interface to the PM–aqueous interface, promote aggregates directly adjacent to the PM aqueous interface, presumably by creating a favorably aligned pH gradient. In contrast, for WT-PM patches and N-His_{10}-tag PMs, the gel formation is significantly slower. While the supposedly unfavorably aligned pH gradient generated by N-His_{10}-tag PMs exhibits the longest formation time, the unsystematically alignment in WT-PMs yields a much shorter formation time. The most likely explanation is that their relatively reversed orientation does not lead to the same pH decrease near the PM-aqueous interface upon pumping. The C-His_{10}-tag PM-induced pH gradients from the surface toward the bulk solution accelerate formation of the bi-component hydrazone gelator,[25] thereby increasing its local concentration and facilitating the gelation close to the surface. Therefore, the gelation rate is affected by the pH gradient generated by different PM types.

The developed system encouraged further analysis. Although the observations were aligned with our expectations, the limited wavelength selectivity of PM excitation and proton pumping during CLSM measurements asked for additional evidence. Therefore, another set of light-induced gel formation experiments were conducted, where in-situ liquid AFM for image acquisition in the dark in combination with excitation of the PM by an independently operated light source were utilized.

4.2.2 Atomic force microscopy for capturing temporal control over gel formation at nanoscale

Liquid AFM was used to investigate nanoscale hydrogel formation influenced by PM and light near PM-covered SiO_2 surfaces. The conditions for light exposure diverged from those utilized in CLSM as the setup enables image acquisition without irradiation, thereby counteracting the limited wavelength selectivity of CLSM in imaging and pumping. Thus, it was possible to separate pumping and imaging steps, while observing structure formation directly at the PM-aqueous interface for individual PM patches by employing multiple periods of green light exposure (543 nm) interspersed with dark periods.

Figure 4.3 shows the protocol of the AFM and irradiation experiments. Initially, the AFM scan was conducted in the absence of light on a surface coated with PM, which was covered with a buffer at pH 7.0 devoid of any gelator precursor molecules. After two scans, a solution of the gelator precursor molecules was added to the buffer. The final concentrations of gelator precursor reagents were half of those used in CLSM experiments. This reduction was crucial to prevent contamination of the AFM cantilever prior to scanning. Because of the change in liquid refractive index and temperature fluctuations due to addition of reagents, the photodiode signal was unstable for a few minutes (from 4 to 10 min). After the signal stabilized, the image acquisition-irradiation sequence was continued. For all PM types, the scan position remained nearly unchanged, except for C-His_{10}-tag PMs, which shifted to a different area. We scanned two images in the dark, after which we irradiated with green light using a light-emitting diode (LED) localized at

the back of the substrate (Figure S4.1b, SI) for 10 min while scanning. Next, the sample was scanned in the dark for 10 min, and again for another 10 min upon exposure to green light. Finally, the substrate was scanned repeatedly until 1 h after addition of the gelator precursor reagents. Subsequently, a larger scan of 5 x 5 µm² was performed to check for any influence of the tip scan on the structure formation at the surface. For C-His_{10}-tag PMs, this investigation was not possible because the gel had already formed around the entire substrate area before the end of the experiment, contaminating the AFM cantilever with fiber deposits and preventing any further scans.

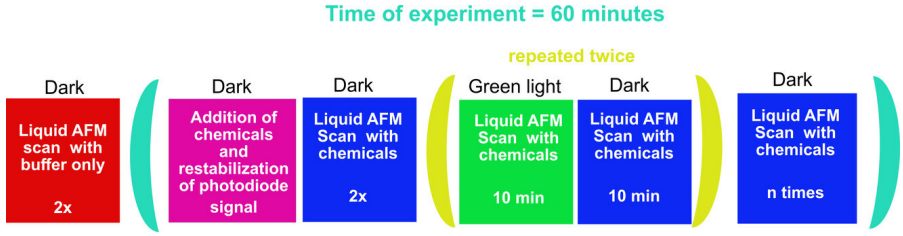

Figure 4.3. Diagram of the protocol of AFM experiments, including irradiation sequences and AFM image acquisition. Red: AFM scan without gel reagents; pink: procedure without scan; blue AFM scan of sample after addition of chemicals in the dark; green: AFM scan of sample after addition of chemicals and under green light.

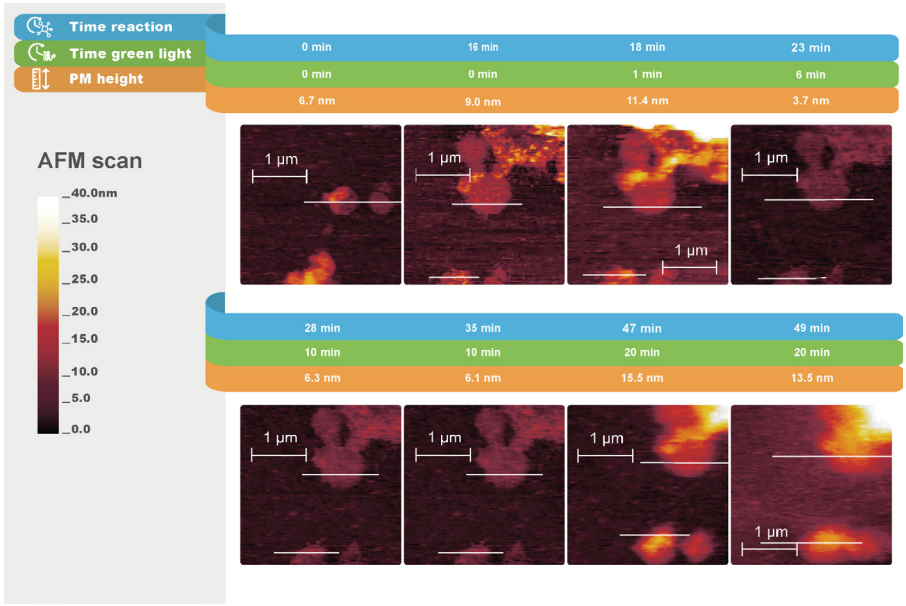

Figure 4.4. In-situ AFM Peakforce Tapping in fluid mode height images of hydrogel formation under the influence of PMs (C-His_{10}-tag PMs) and light at different time points. The lines highlighted in white indicate the cross sections of PMs. The scan direction is from right to left, with a 0◦ scan angle. Cross sectional values for these images are shown in Figure S4.5, SI.

First, a PM-free substrate (Figure S4.3, SI) was subjected to scanning as described in Figure 4.3 as a control experiment. As expected, the AFM scan of the PM-free substrate remained a flat homogeneous surface without any new objects appearing up to 1 h after the addition of gel reagents, even for a large scan area (Figure S4.4, SI). Therefore, we concluded that in the PM-free samples, fibers were not formed on the substrate surface in the dark, nor upon irradiation with green light.

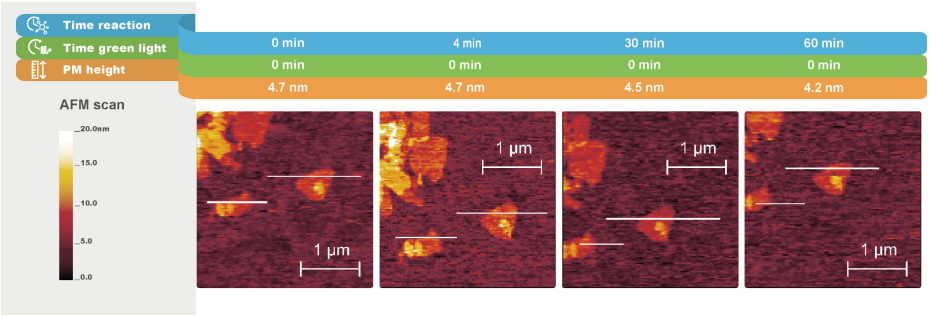

Figure 4.5. In-situ AFM Peakforce Tapping in fluid mode height images of a C-His_{10}-tag PM covered substrate kept in the dark at different time points. The lines highlighted in white indicate the cross sections of PMs. Cross sectional values for these images are shown in Figure S4.6, SI.

In a subsequent series of experiments, we studied the substrates covered with the different types of PM. For all PM types, the AFM scans before the addition of reagents showed ellipsoidal ~500 nm wide homogeneous patches with a height of approximately 5 to 8 nm on an otherwise flat surface (Figure 4.4, Figure 4.5, Figure 4.7 and Figure 4.8, Time reaction = 0 min) that we assigned to PMs adsorbed at the interface. The maximum force at which the AFM tip scanned the membrane was limited to ~ 100 pN to prevent mechanical deformation of bR,[29] and the parameters of the AFM feedback loop were optimized to reduce error signal. [30]

Given the CLSM results, we anticipated a rapid gel formation soon after the green light exposure in the AFM scan of C-His_{10}-tag PM, shown in Figure 4.4. At the onset of the experiment, a patch height difference of 2.3 nm was observed in the dark between AFM scans taken before and after the addition of reactants. This may be associated with variations in patch height. After a 1-minute exposure to green light, the relative height in the PM patches area increased from 9.0 nm to 11.4 nm, along with a general change in the scan image height. Subsequently, while still under light, the relative height in the PM patches area decreased to 3.7 nm. During the time in the dark (reaction times = 28 and 35 minutes), no change in the patch height was observed. From 10 to 20 min of exposure to green light, the height increased again to 15.5 nm. It is hypothesized that fiber networks initially form locally on the patches. The initial increase in the height of the patches of approximately 2.5 nm under illumination is consistent with the height of fibers reported in previous studies. [21]

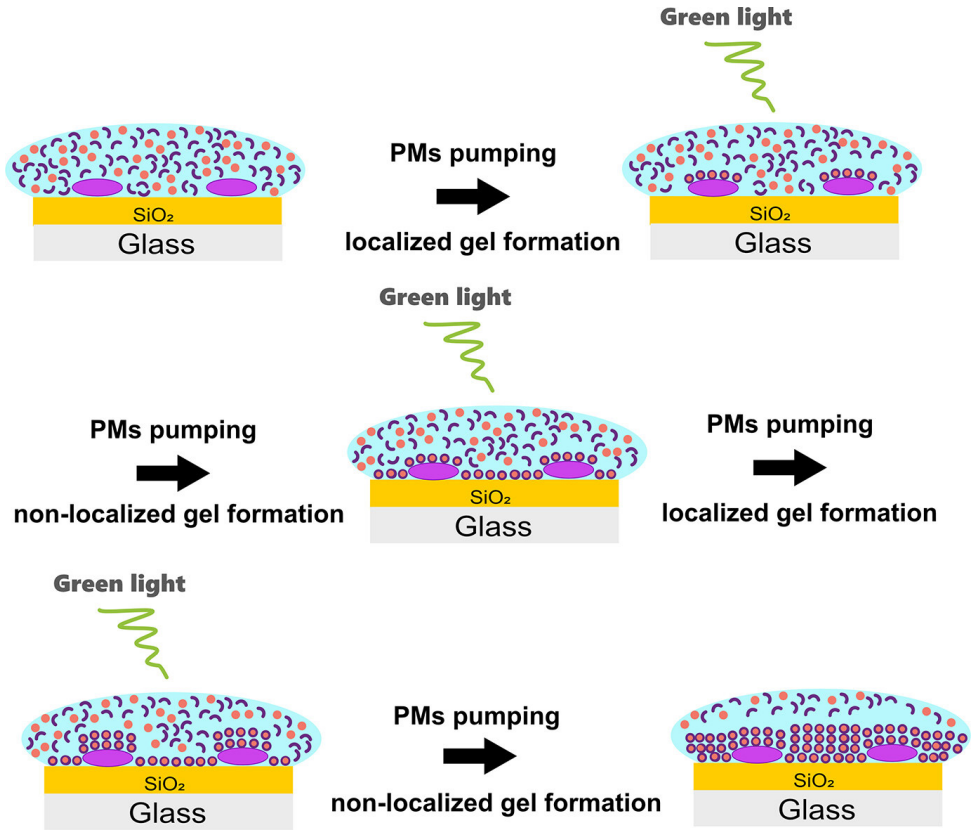

Figure 4.6. Time-lapse illustration of hydrogel formation after contact with C-His_{10}-tag PM and green light observed by liquid AFM. The purple, light blue, dark blue, and red areas represent PMs, aqueous media, hydrazine molecules, and benzaldehyde molecules, respectively. The fiber is formed when three hydrazine molecules react with benzaldehyde.

Subsequently, a reduction in the relative height of the patches is noted. Localized gel formation is observed when the sample is subjected to green light once more, with the patch height increasing from 6.1 nm (Figure 4.4, Time reaction = 35 min) to 15.5 nm (Figure 4.4, Time reaction = 47 min). Ultimately, the hydrogel domains start to coalesce, and fiber formation is observed throughout the scanned area. The results suggest that initially the fibers grew preferentially on the PMs when exposed to light; subsequently, owing to proton diffusion, growth occurred in other areas as well. This indicates the light-triggering influence within the system. To demonstrate this assumption, we compared these results with a C-His_{10}-tag PM-coated substrate scanned by AFM for 1 h in presence of gel reactants in the dark (Figure 4.5). For this sample, the formation of fibrillar structures of gel patches was not observed. Therefore, we concluded that gel fiber formation is driven by the presence of both, C-His_{10}-tag PMs and light.

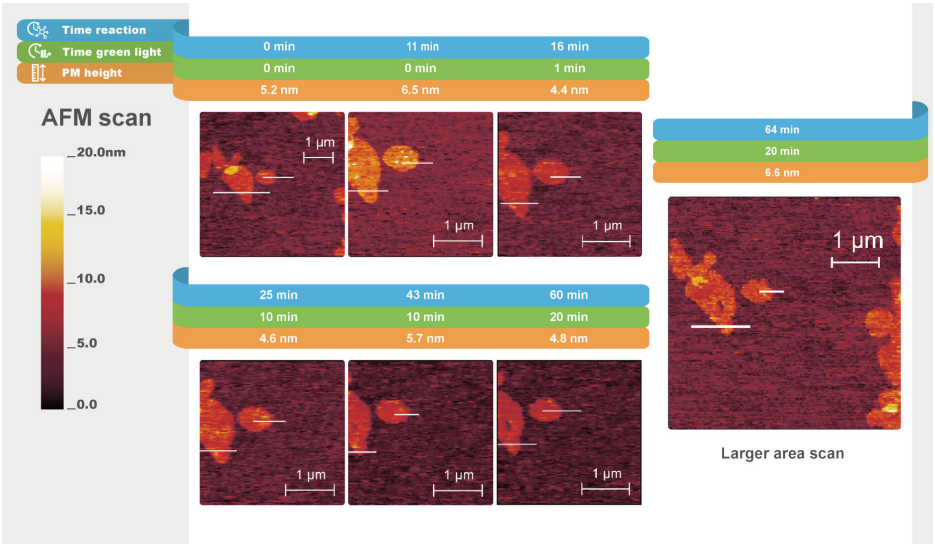

Figure 4.7. In-situ AFM Peakforce Tapping in fluid mode height images of hydrogel formation under the influence of PM (wild-type PM) and light at different time points. The lines highlighted in white indicate the cross sections of PMs. The scan direction is from right to left, with a 0◦ scan angle. Cross sectional values for these images are shown in Figure S4.7, SI.

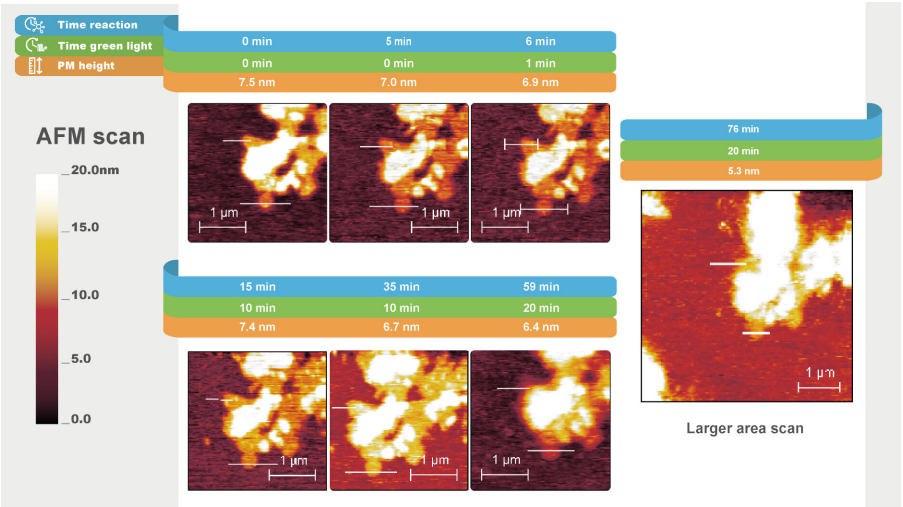

Figure 4.8. In-situ AFM Peakforce Tapping in fluid mode height images of hydrogel formation under the influence of PM (N-His_{10}-tag PM) at different time points. The lines highlighted in white indicate the cross sections of PMs. The scan direction is from right to left, with a 0◦ scan angle. Cross sectional values for these images are shown in Figure S4.8, SI.

Figure 4.6 illustrates the mechanism of gel formation under the influence of PMs and light, specifically observed for C-His_{10}-tag PM. This process initiates with the acid-catalyzed transformation of precursor molecules into the active gelator. Then, when the local concentration of gelator molecules exceeds the critical gelation concentration, gel fibers start to form. During this process, protons diffuse into the bulk, resulting in acidification and the formation of fiber networks across the substrate. This leads to the formation of gelator molecules and eventually to the formation of fibers and gels. However, a localized gel formation then reoccurs. Finally, a fibrous network is observed throughout the substrate owing to the proton diffusion.

Given the behavior of the WT and N-His_{10}-tag PM in comparison to that of C-His_{10}-tag PM in CLSM, the detection of fiber networks near the PM area during the liquid AFM scan was expected to be more challenging. The CLSM results indicate that gel formation rate for the C-His_{10}-tag PM was at least 40 and 80 times faster than that for WT and N-His_{10}-tag PMs, respectively (Figure 4.2). Indeed, the AFM scan of WT PMs (Figure 4.7) after the addition of reagents showed homogeneous PM patches before and after exposure to green light. Changes in relative height were observed over time. The most substantial change occurred when green light was applied to the sample after the addition of chemicals, resulting in a 1.9 nm decrease in patch height. However, over time, no changes in the shape or size of the PM patches were observed, and no new interfacial objects appeared (Figure S4.7, SI). The roughness of the AFM scan was approximately 0.5 nm, and the height difference ranged from approximately 0.2 to 1.1 nm in other cases after the addition of chemicals. The results strongly suggest that fiber growth at or near the WT-PM-aqueous interface did not take place upon exposure to light.

The AFM scan of N-His_{10}-tag PMs (Figure 4.8) showed similar behavior to that of WT PMs. Following the addition of reagents, initially, homogeneous patches approximately 7.0 nm in height were observed before green light exposure. During all irradiation cycles and until the end of the experiment, the relative height of the N-His_{10}-tag PMs did not vary by more than 0.9 nm which we consider insignificant in respect of fiber growth (Figure 4.8). Like with the WT PM, no changes to the shape and size of the PM patches were observed over time and no other interfacial objects appeared (Figure S4.8, SI). Therefore, we concluded that fiber growth near the N-His_{10}-tag PM aqueous interface did not occur upon exposure to light.

4.3 Conclusions

This work demonstrates the possibility of using PM patches to spatiotemporally control the growth pattern of oriented self-assembled gel agglomerates. We expect that the formation of these structures can be used to detect the local formation of pH gradients, which in turn are controlled by the localization and orientation of PM patches and the presence of light. The results show that light-driven catalysts can be confined to produce patterned out-of-equilibrium gel materials. The experiments underscore the feasibility of employing an external stimulus, such as light, to direct self-assembly in synthetic systems through the

spatial confinement of catalytic activity.

The results indicate that the presence and type of PMs significantly influence gelation rates. Depositing PMs on a negatively charged surface, CLSM showed faster in-situ gel formation for C-His_{10}-tag PMs, likely due to a favorably aligned pH gradient. AFM revealed that for C-His_{10}-tag PMs, gels initially formed on PMs, and as protons spread, fibers grew around the PM area. The liquid AFM results were consistent with those obtained from CLSM, and both methodologies provided valuable insights into the effects of PM and light on our system. Specifically, CLSM effectively showed the sensitivity of our system to light, whereas liquid AFM illustrated the process of fiber formation in the vicinity of the PM area. The combination of CLSM and AFM introduced here provides a multifunctional toolbox for the optical imaging and characterization of spatiotemporal control of CRNs, which can be used to examine surface structures of fibers with high-resolution. It may be used to identify and further characterize other CRNs and clarify the manner through which they dynamically assemble into functional domains. However, the identification of different fibers with higher resolution and scan rates remains a challenge. Moreover, for other CRNs, a more complex environment, such as apolar CRN products, can substantially increase the challenges of the experiment.

The strength of the formed hydrogel is a critical factor for its potential applications, particularly in biomaterials science. This study indicates that the components exhibit fast gelation under proton catalysis and stability of the hydrogel under physiological conditions. These properties make this platform highly promising for various biomedical applications, including tissue engineering and drug delivery. Furthermore, the ability to tune the hydrogels strength [31] offers significant potential for biomaterials scientists exploring new materials for these fields. We anticipate that this study can underscore the potential for integrating synthetic self-assembly systems with living metabolic processes, opening avenues for innovative applications to enhance existing biological functions or develop entirely new ones.

Future studies should quantitatively measure the proton gradient based on the amount of light. This would enable the development of intelligent hydrogel networks at the nanoscale for application in sensing pH gradients.

4.4 References

(1) Casey, J. R.; Grinstein, S.; Orlowski, J. Sensors and Regulators of Intracellular pH. *Nat Rev Mol Cell Biol* **2010**, 11 (1), 50–61. https://doi.org/10.1038/nrm2820.

(2) Asokan, A.; Cho, M. J. Exploitation of Intracellular pH Gradients in the Cellular Delivery of Macromolecules. *Journal of pharmaceutical sciences* **2002**, 91 (4), 903–913.

(3) Al-Aribe, K. M.; Knopf, G. K.; Bassi, A. S. Fabrication of an Optically Driven pH Gradient Generator Based on Self-Assembled Proton Pumps. *Microfluidics and nanofluidics* **2012**, 12 (1), 325–335.

(4) Hoffman, A. S. Hydrogels for Biomedical Applications. *Advanced drug delivery reviews* **2012**, 64, 18– 23.

(5) Boekhoven, J.; Poolman, J. M.; Maity, C.; Li, F.; Van Der Mee, L.; Minkenberg, C. B.; Mendes, E.; Van Esch, J. H.; Eelkema, R. Catalytic Control over Supramolecular Gel Formation. *Nature Chem* **2013**, 5 (5), 433–437. https://doi.org/10.1038/nchem.1617.

(6) Aktaş, D. K.; Öztekin, F. pH-Sensitive Poly (Acrylic Acid-Co-Acrylamide) Anionic Hydrogels for Jejunum Targeted Drug Delivery Systems. *Polymer Bulletin* **2023**, 80 (3), 2801–2813.
(7) Syed Azhar, S. N.; Ashari, S. E.; Zainuddin, N.; Hassan, M. Nanostructured Lipid Carriers-Hydrogels System for Drug Delivery: Nanohybrid Technology Perspective. *Molecules* **2022**, 27 (1). https://doi.org/10.3390/molecules27010289.
(8) Zhao, Y.-L.; Stoddart, J. F. Azobenzene-Based Light-Responsive Hydrogel System. *Langmuir* **2009**, 25 (15), 8442–8446.
(9) Gupta, P.; Vermani, K.; Garg, S. Hydrogels: From Controlled Release to pH-Responsive Drug Delivery. *Drug discovery today* **2002**, 7 (10), 569–579.
(10) Ward, J. H.; Bashir, R.; Peppas, N. A. Micropatterning of Biomedical Polymer Surfaces by Novel UV Polymerization Techniques. Journal of Biomedical Materials Research: A*n Official Journal of The Society for Biomaterials, The Japanese Society for Biomaterials, and The Australian Society for Biomaterials and the Korean Society for Biomaterials* **2001**, 56 (3), 351–360.
(11) Ziemecka, I.; Koper, G. J.; Olive, A. G.; van Esch, J. H. Chemical-Gradient Directed Self-Assembly of Hydrogel Fibers. *Soft Matter* **2013**, 9 (5), 1556–1561.
(12) Vigier-Carrière, C.; Boulmedais, F.; Schaaf, P.; Jierry, L. Surface-Assisted Self-Assembly Strategies Leading to Supramolecular Hydrogels. *Angewandte Chemie International Edition* **2018**, 57 (6), 1448–1456.
(13) Stoeckenius, W.; Lozier, R. H.; Bogomolni, R. A. Bacteriorhodopsin and the Purple Membrane of Halobacteria. *Biochimica et Biophysica Acta (BBA) - Reviews on Bioenergetics* **1979**, 505 (3–4), 215–278. https://doi.org/10.1016/0304-4173(79)90006-5.
(14) Oesterhelt, D. Bacteriorhodopsin as an Example of a Light-driven Proton Pump. *Angewandte Chemie International Edition in English* **1976**, 15 (1), 17–24.
(15) Mahyad, B.; Janfaza, S.; Hosseini, E. S. Bio-Nano Hybrid Materials Based on Bacteriorhodopsin: Potential Applications and Future Strategies. *Advances in Colloid and Interface Science* **2015**, 225, 194–202. https://doi.org/10.1016/j.cis.2015.09.006.
(16) Figueiredo Da Silva, J.; Bacheva, V.; Drechsler, U.; Nicollier, P.; Reidt, S.; Fotiadis, D.; Knoll, A.; Wolf, H. Fabrication of a Hybrid Device for the Integration of Light-Triggered Proton Pumps. *Micro and Nano Engineering* **2024**, 23, 100250. https://doi.org/10.1016/j.mne.2024.100250.
(17) Fisher, K.; Yanagimoto, K.; Stoeckenius, W. Oriented Adsorption of Purple Membrane to Cationic Surfaces. *The Journal of cell biology* **1978**, 77 (2), 611–621. https://doi.org/10.1083/jcb.77.2.611.
(18) Stauffer, M.; Hirschi, S.; Ucurum, Z.; Harder, D.; Schlesinger, R.; Fotiadis, D. Engineering and Production of the Light-Driven Proton Pump Bacteriorhodopsin in 2D Crystals for Basic Research and Applied Technologies. *MPs* **2020**, 3 (3), 51. https://doi.org/10.3390/mps3030051.
(19) Ruggeri, F.; Schwemmer, C.; Stauffer, M.; Nicollier, P. M.; Figueiredo da Silva, J.; Bosshart, P. D.; Kochems, K.; Fotiadis, D.; Knoll, A.; Wolf, H. Placement of Biological Membrane Patches in a Nanofluidic Gap With Control Over Position and Orientation. *Advanced materials interfaces* **2022,** 9 (23), 2200941.
(20) Laskowski, P. R.; Pfreundschuh, M.; Stauffer, M.; Ucurum, Z.; Fotiadis, D.; Müller, D. J. High- Resolution Imaging and Multiparametric Characterization of Native Membranes by Combining Confocal Microscopy and an Atomic Force Microscopy-Based Toolbox. *ACS Nano* **2017**, 11 (8), 8292– 8301. https://doi.org/10.1021/acsnano.7b03456.
(21) Olive, A. G.; Abdullah, N. H.; Ziemecka, I.; Mendes, E.; Eelkema, R.; Van Esch, J. H. Spatial and Directional Control over Self-Assembly Using Catalytic Micropatterned Surfaces. *Angewandte Chemie International Edition* **2014**, 53 (16), 4132–4136.
(22) Wang, Y.; Oldenhof, S.; Versluis, F.; Shah, M.; Zhang, K.; Van Steijn, V.; Guo, X.; Eelkema, R.; Van Esch, J. H. Controlled Fabrication of Micropatterned Supramolecular Gels by Directed Self-Assembly of Small Molecular Gelators. *Small* **2019**, 15 (8), 1804154. https://doi.org/10.1002/smll.201804154.
(23) Wang, Y.; Versluis, F.; Oldenhof, S.; Lakshminarayanan, V.; Zhang, K.; Wang, Y.; Wang, J.; Eelkema, R.; Guo, X.; Van Esch, J. H. Directed Nanoscale Self-Assembly of Low Molecular Weight Hydrogelators Using Catalytic Nanoparticles. *Advanced Materials* **2018**, 30 (21), 1707408. https://doi.org/10.1002/adma.201707408.
(24) Maity, C.; Hendriksen, W. E.; van Esch, J. H.; Eelkema, R. Spatial Structuring of a Supramolecular Hydrogel by Using a Visible-light Triggered Catalyst. *Angewandte Chemie International Edition* **2015**, 54 (3), 998–1001.
(25) Poolman, J. M.; Boekhoven, J.; Besselink, A.; Olive, A. G. L.; Van Esch, J. H.; Eelkema, R. Variable Gelation

Time and Stiffness of Low-Molecular-Weight Hydrogels through Catalytic Control over Self- Assembly. *Nat Protoc* **2014**, 9 (4), 977–988. https://doi.org/10.1038/nprot.2014.055.

(26) Boekhoven, J.; Brizard, A. M.; Kowlgi, K. N.; Koper, G. J.; Eelkema, R.; van Esch, J. H. Dissipative Self-assembly of a Molecular Gelator by Using a Chemical Fuel. *Angewandte Chemie* **2010**, 122 (28), 4935–4938.

(27) Carroll, K. M.; Wolf, H.; Knoll, A.; Curtis, J. E.; Zhang, Y.; Marder, S. R.; Riedo, E.; Duerig, U. Understanding How Charged Nanoparticles Electrostatically Assemble and Distribute in 1-D. *Langmuir* **2016**, 32 (51), 13600–13610.

(28) Bamberg, E.; Apell, H.-J.; Dencher, N. A.; Sperling, W.; Stieve, H.; Läuger, P. Photocurrents Generated by Bacteriorhodopsin on Planar Bilayer Membranes. Biophys. *Struct. Mechanism* **1979,** 5 (4), 277–292. https://doi.org/10.1007/BF02426663.

(29) Medalsy, I.; Hensen, U.; Muller, D. J. Imaging and Quantifying Chemical and Physical Properties of Native Proteins at Molecular Resolution by Force–Volume AFM. *Angewandte Chemie International Edition* **2011,** 50 (50), 12103–12108.

(30) Pfreundschuh, M.; Martinez-Martin, D.; Mulvihill, E.; Wegmann, S.; Muller, D. J. Multiparametric High-Resolution Imaging of Native Proteins by Force-Distance Curve–Based AFM. *Nature Protocols* **2014**, 9 (5), 1113–1130. https://doi.org/10.1038/nprot.2014.070.

(31) Abdullah, N. H.; Bakar, W. A. W. A.; Hussain, R.; Bakar, M. B.; van Esch, J. H. Effect of Homogeneous Acidic Catalyst on Mechanical Strength of Trishydrazone Hydrogels: Characterization and Optimization Studies. *Arabian journal of chemistry* **2018**, 11 (5), 635–644.

4.5 Supplementary information

4.5.1 Experimental details

General remarks

All reagents were purchased from commercial sources and were used as provided unless otherwise stated. Tri-acyl hydrazide cyclohexane and benzaldehyde were prepared according to published procedures. Liquid atomic force microscopy (AFM) imaging, data visualization, and data analysis were conducted using Gwyddion. [1] Confocal laser scanning microscopy (CLSM) data were processed using ZEN 2011 (Carl Zeiss) and ImageJ. [2] All imaging was performed at room temperature.

Preparation of glass substrates for spatiotemporal control of gel formation

Before use, glass substrates (24 × 24 mm^2) were treated with acetone and isopropanol, and the samples were cleaned with plasma under a nitrogen stream. The thickness of the glass chips was 170 µm for CLSM and liquid AFM. SiO_2 was deposited (100 nm) on top of the glass chips via plasma-enhanced chemical vapor deposition (PECVD). In the dark, 12.5 µmL of dispersed PM (wild-type (WT), or the genetically modified C-His_{10}-tag or N-His_{10}-tag PMs) was added to the substrates in water at a concentration of 10^{-2} mg·mL^{-1}. The deca-histidine His_{10}-tag attachment to either the cytoplasmatic side (C-His_{10}-tag) or extracellular side (N-His_{10}-tag) of the PM was used to increase a charge asymmetry. [3,4] The engineering of the biological membrane patches is described elsewhere. [3] The samples were dried in the dark under ambient air, rinsed with Milli-Q water, and then dried under a nitrogen stream.

Confocal laser scanning microscopy

In the CLSM experiments, a PM-coated glass was carefully placed on a polydimethylsiloxane (PDMS) cuvette (12 mm x 12 mm x 3 mm) containing gelator precursors in a phosphatebuffered saline (PBS) at pH 7.0. [5] The PMs were facing the solution. The two elements were then flipped and placed on the microscope. A fluorescein-based aldehyde-labeled probe [6] was used at 0.01 molar percentage.

Samples were monitored using a Zeiss LSM 980 equipped with a Zeiss Axio Observer inverted microscope, and Plan-Apochromat 63x oil immersion objective lens (NA 1.4). Incident wavelengths of 488 and 543 nm were used to visualize the gel formation and PM pumping, respectively; and emission at 517 nm was recorded. A z-step size of 48 µm was used to optically section the samples to seven planes. Snapshots of z-stacks were acquired every 67 s using a 488 nm laser, after which the sample was exposed to a 543 nm for PM pumping with the same time exposure. The 8-bit images of the middle plane were used for analysis.

Liquid Atomic force microscopy

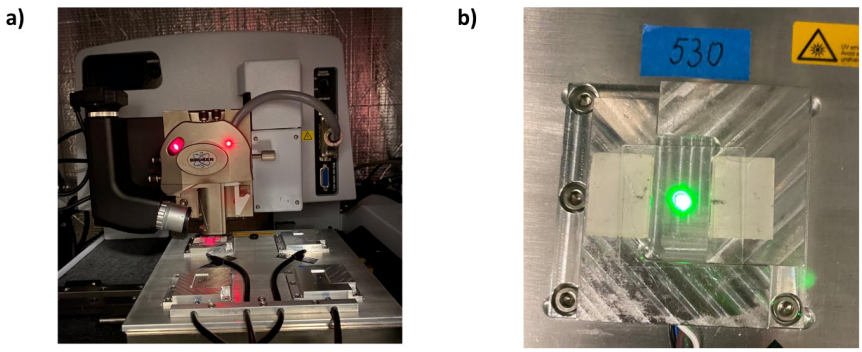

Figure S4.1. a) Liquid AFM setup during a substrate scan. **b)** 24 × 24 mm^2 glass sample exposed to green light by LED.

We operated a commercial Dimension-Icon AFM (Bruker)(Figure S4.1a) equipped with triangular oxide-sharpened silicon nitride (Si_3N_4) cantilevers (length: 70 mm; ScanAssist Fluid$^+$) in PeakAssist Tapping in fluid mode. Images were obtained from cantilevers under 2 kHz oscillation frequency, 3 Hz scanning rate, and 150 nm amplitude. An area of 3 × 3 μm^2 was scanned at 128 × 128 samples/line. After the photodiode signal was stabilized, we began scanning the area again at a rate of 1 scan/min for 1 h. For all samples, we immersed the glass substrate in 140 µl of PBS buffer (100 mM, pH 7.0), and then imaged an area containing at least one PM patch. Subsequently, we injected 140 µl of gelator precursor solution onto the substrate at pH 7.0, at a concentration presented elsewhere. [6] The experiment time is initiated from this point. One hour after the addition of gel chemicals,

an area of 5 × 5 µm² was scanned at 256 × 256 samples/line to check for any tip-induced desorption of gel agglomerates. For illuminating the scanning substrate with green light, we utilized a customized stage comprising a chip holder and a light-emitting diode (LED) green light source (530 nm) with variable intensities positioned beneath the chip holder, as depicted in Figure S4.1b. The intervals and duration of illumination were manually controlled using the T-Cube™ LED Driver (ThorLabs). All experiments were performed with the same light power.

To measure AFM heights, we analysed at least two PM patches and calculated the average intensity within a 10-pixel region around the height line. The average height was then determined from these two areas.

4.5.2 Supplementary results

Air atomic force microscopy

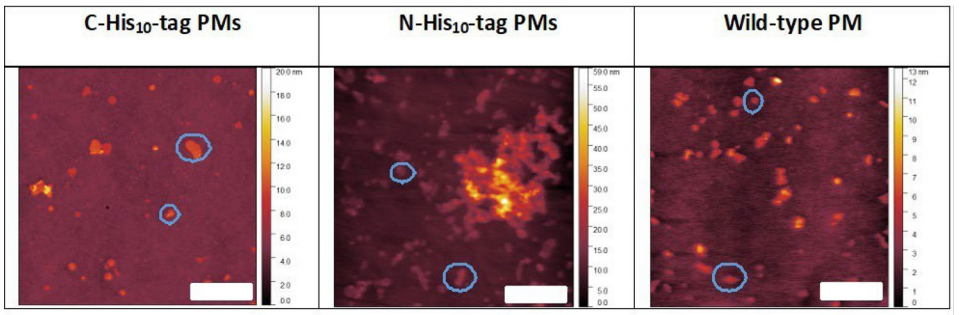

Figure S4.2. Topographical air-AFM image of deposited PMs (wild-type, C-His_{10}-tag, and N-His_{10}- tag PMs on the surface). Blue circles represent examples of single PM patches. Scale bar represents 5 µm.

Figure S4.2 shows a 400 µm² air-AFM scan (Park Systems - NX20, contact mode tetrahedral cantilever) of different PM types. The blue circles indicate an example of single PM patches found under this technique. In air-AFM, a single PM patch presented a height of 5 nm. A height higher than 10 nm indicates a PM agglomeration in the target area. Therefore, the quantitative analysis of Figure S4.2 reveals that N-His_{10}-tag PMs presented the highest density of PM patches, covering 53.5 % of the area scanned. This is followed by WT PMs, with a coverage of 6.4 %, and then C-His_{10}-tag PMs, with a coverage of 4.5%.

Liquid Atomic Force Microscopy

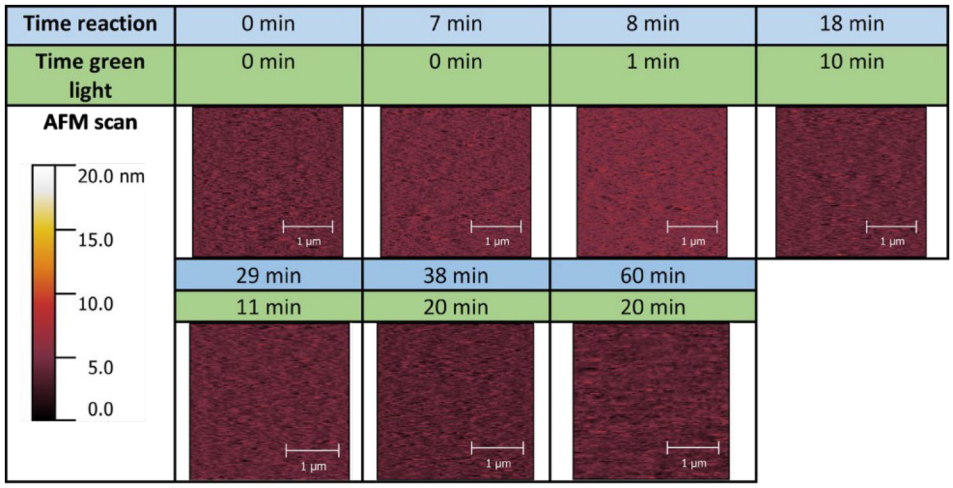

Figure S4.3. In-situ AFM Peakforce Tapping in fluid mode height images of a SiO_2 substrate embedded with hydrogel reagents but without PM patches, under exposure to green light at various time intervals. The scan direction is from right to left, with a 0° scan angle.

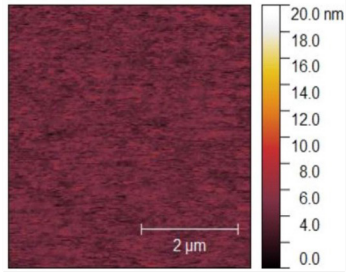

Figure S4.4. In-situ AFM Peakforce Tapping in fluid mode height image of a SiO_2 substrate embedded with hydrogel reagents, but devoid of PM patches, exposed to green light at the conclusion of the experiment. The scan was conducted over a 5 × 5 μm^2 area, with the scanning direction oriented from right to left and at a 0 ° scan angle.

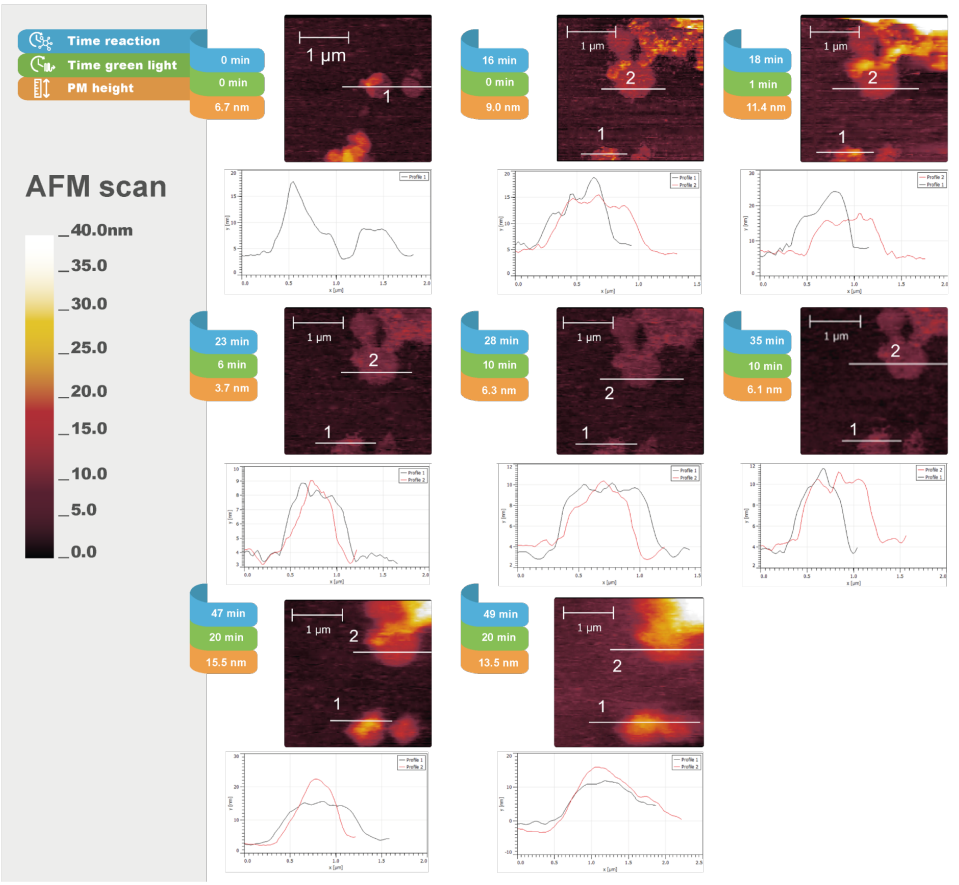

Figure S4.5. In-situ AFM Peakforce Tapping in fluid mode height cross sections of hydrogel formation under the influence of PMs (C-His_{10}-tag PMs) and light at different time points, presented in Figure 4.4 (main text).

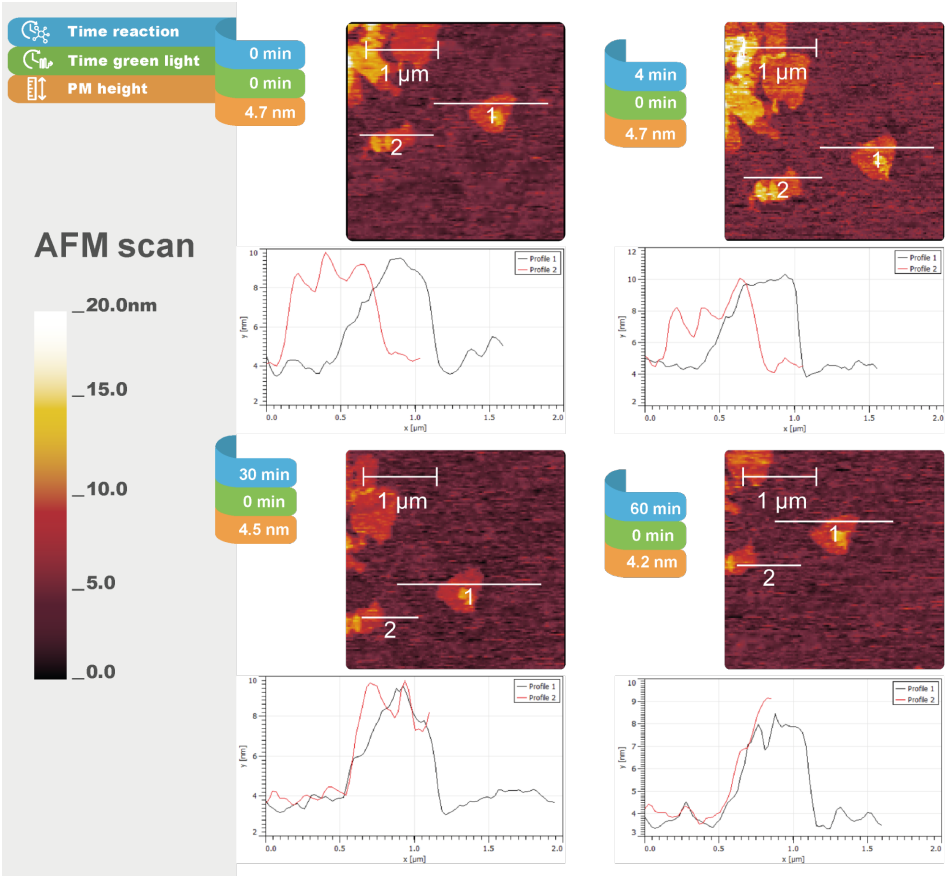

Figure S4.6. In-situ AFM Peakforce Tapping in fluid mode height cross sections of hydrogel formation under the influence of PMs (C-His_{10}-tag PMs) in the dark at different time points, presented in Figure 4.5 (main text).

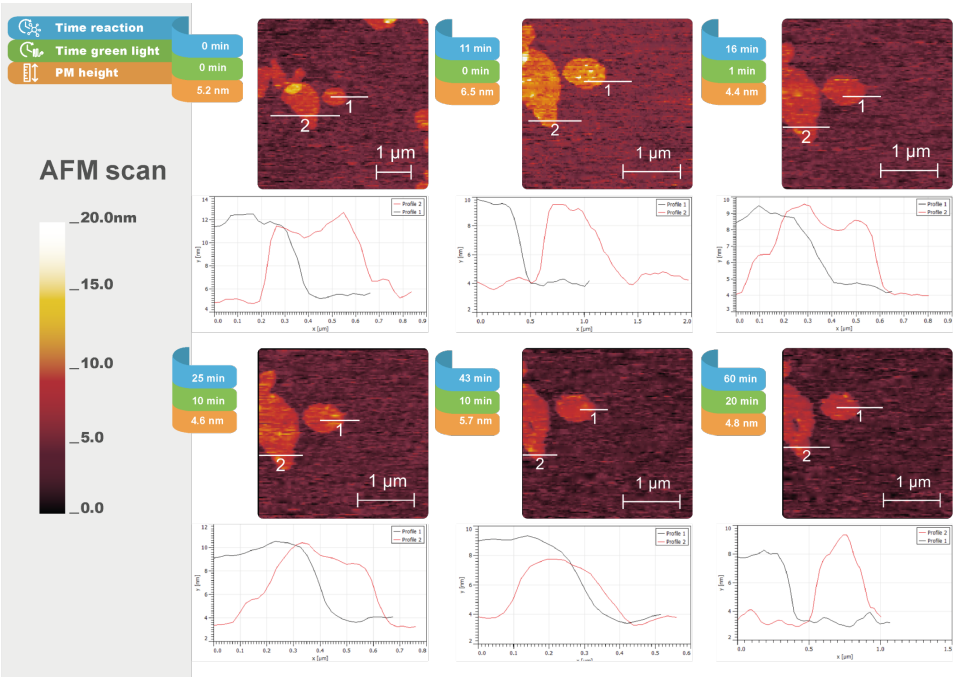

Figure S4.7. In-situ AFM Peakforce Tapping in fluid mode height cross sections of hydrogel formation under the influence of PMs (wild-type PMs) and light at different time points, presented in Figure 4.7 (main text).

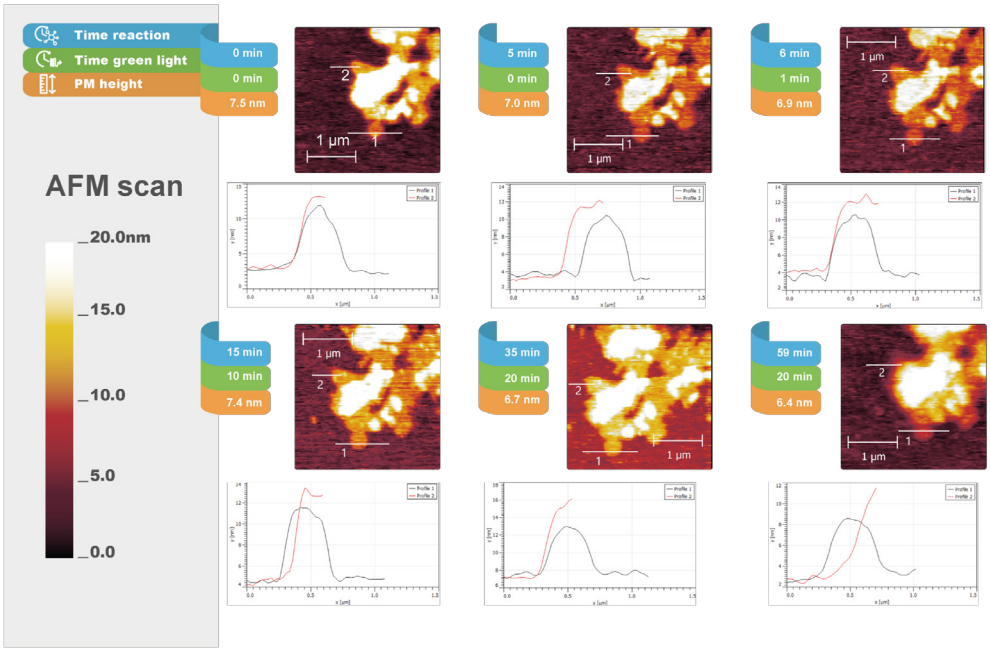

Figure S4.8. In-situ AFM Peakforce Tapping in fluid mode height cross sections of hydrogel formation under the influence of PMs (N-His_{10}-tag PMs) and light at different time points, presented in Figure 4.8 (main text).

4.5.3 References

(1) Nečas, D.; Klapetek, P. Gwyddion: An Open-Source Software for SPM Data Analysis. *Open Phys*. **2012**, 10 (1), 181–188.

(2) Schneider, C. A.; Rasband, W. S.; Eliceiri, K. W. NIH Image to ImageJ: 25 Years of Image Analysis. Nat. *Methods* **2012**, 9 (7), 671–675.

(3) Stauffer, M.; Hirschi, S.; Ucurum, Z.; Harder, D.; Schlesinger, R.; Fotiadis, D. Engineering and Production of the Light-Driven Proton Pump Bacteriorhodopsin in 2D Crystals for Basic Research and Applied Technologies. *Methods Protoc.* **2020**, 3 (3), 51. https://doi.org/10.3390/mps3030051.

(4) Ruggeri, F.; Schwemmer, C.; Stauffer, M.; Nicollier, P. M.; Figueiredo da Silva, J.; Bosshart, P. D.; Kochems, K.; Fotiadis, D.; Knoll, A.; Wolf, H. Placement of Biological Membrane Patches in a Nanofluidic Gap With Control Over Position and Orientation. *Adv. Mater. Interfaces* **2022**, 9 (23), 2200941.

(5) Olive, A. G.; Abdullah, N. H.; Ziemecka, I.; Mendes, E.; Eelkema, R.; Van Esch, J. H. Spatial and Directional Control over Self-Assembly Using Catalytic Micropatterned Surfaces. *Angew. Chem. Int. Ed.* **2014**, 53 (16), 4132–4136.

(6) Boekhoven, J.; Poolman, J. M.; Maity, C.; Li, F.; Van Der Mee, L.; Minkenberg, C. B.; Mendes, E.; Van Esch, J. H.; Eelkema, R. Catalytic Control over Supramolecular Gel Formation. *Nat. Chem.* **2013**, 5 (5), 433–437. https://doi.org/10.1038/nchem.1617.

Chapter 5

Network of light-triggered proton pumps[‡]

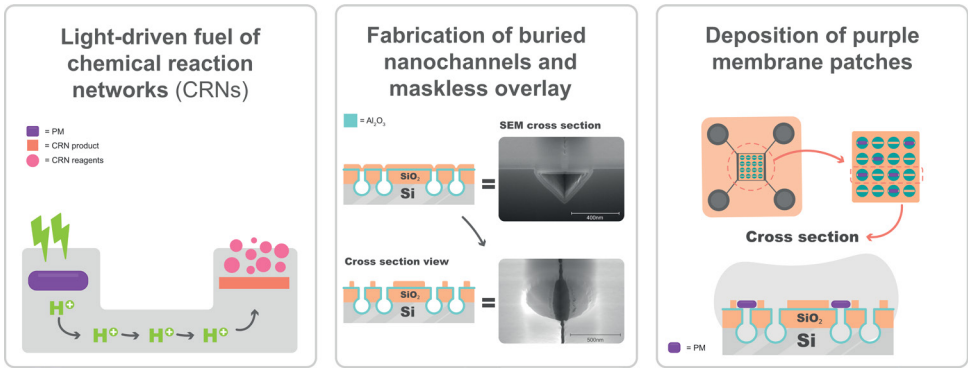

Abstract: Biological ion pumps, such as bacteriorhodopsin (bR), utilize photons to move ions against concentration gradients, offering energy harvesting and spatiotemporal control of chemical gradients. This capability goes far beyond the capabilities of today's synthetic devices, suggesting a hybrid approach to embed bRs in synthetic devices in order to direct the proton flow towards useful system applications. In this study, a hybrid silicon-based nanochannel network with integrated purple membranes (PM) containing bR was fabricated. The fabrication method combines thermal scanning probe lithography, etching techniques, atomic layer deposition, plasma-enhanced chemical vapor deposition, and photolithography to create devices with buried nanochannels on silicon substrates. PM patches were deposited onto specified sites by a tunable nanofluidic confinement apparatus. The resulting device holds the potential for locally controlling directed ion transport in micrometer scale devices, a first step towards applications, such as locally affected proton-catalyzed chemical reaction networks. Furthermore, this fabrication strategy, employing a maskless overlay, is a tool for constructing intricate nanofluidic network designs which are mechanically robust and straightforward to fabricate.

[‡] Part of this chapter has been published: Figueiredo da Silva, J. et al. "Fabrication of a hybrid device for the integration of light-triggered proton pumps." *Micro and Nano Engineering* 23 (2024): 100250.

5.1 Introduction

In biological organisms, efficient energy harvesting systems based on ion transport operate in nanofluidic entities, namely ion pumps and ion channels. [1] The energy conversion and storage systems of these biological networks are based on ion transport and energy storage in molecules. Two ion transport modes, namely passive and active ion transport, are widely used by these organisms. [1,2] An example of an energy harvesting biological ion pump is bacteriorhodopsin (bR), which is the main component of 5-nm thick and ~ 500-nm sized purple membranes (PM) of the archeon Halobacterium salinarum. Upon photon irradiation, bR pumps protons across the membrane, thereby creating an osmotic potential. [3]

Systems based on directed ion transport – also artificial ones – have advantages over electron transport systems, including the robustness against radiation and the inherent supply with energy through delivered ions. [2] However, for practical applications, these energy conversion systems and devices should be further investigated, optimized, and simplified. [4] A recent study reported an artificial proton pump inspired by bR in the development of a photovoltaic device based on a membrane of carbon nitride nanotubes. [5] The device can be reused in photoelectric energy conversion because it remains unchanged before and after illumination. Moreover, different electrolytes, including acid, saline, and alkali solutions, did not modify the energy conversion system. However, sophisticated micro and nanoscale networks cannot be designed in such approach.

Researchers have recently developed “on-chip” pH gradient generators for various applications, primarily for the study of biological phenomena related to pH change. [6] Despite these developments, high intensity illumination and external electric fields can negatively affect biological samples. To address these challenges, in-situ fabrication methods have been developed to create porous structures in microchannels. However, these techniques can leave residues that are toxic to biological processes. While there are improved systems described, [5] the most synthetic pumping systems are less effective in generating gradients from photons than biological ion pumps, [1] which can create membrane potentials even against steep gradients. Earlier work shows that PMs or bR can be positioned over sub-micron holes or nanopores separating aqueous compartments and thus create a proton gradient upon irradiation. [7,8] With a network of nanoscale channels, it will be possible to guide pumped protons towards desired locations by diffusive transport with high efficiency. Such hybrid devices with light- driven ion pumps that can deliver protons to dedicated locations would have many potential applications, e.g., for the local proton-catalyzed synthesis of materials [9] or for the local release of materials trapped in a polymer gel by a pH-driven phase change. [10] Nevertheless, their design remains a challenge. For example, it is crucial to control the orientation of PMs during deposition in hybrid devices [6] to reflect the directionality in bR pumping.

A low power optically driven pH gradient generator can provide an alternative noninvasive mechanism to modify the acidity of a target solution without inducing a strong electric

field near the solution or exposing the solution to high intensity illumination or heat. A previous work [11] showed that bR proton pumps can maintain their primary function when removed from a living organism. In another study, authors used an optically driven pH gradient generator to exploit the photon-activated molecular proton pumps found in PMs. [12] The authors identified several limitations attributed to the random orientation of the proton pumps. Therefore, directional orientation is critical to efficiently use biological materials to pump protons in microfluidic and nanofluidic channels.

The size of PM patches used as building blocks in hybrid devices requires fabrication methods in the size range of single digit micrometers and below. Fabricating fluidic channels traditionally involves standard photolithography followed by wet or dry substrate etching. For dimensions below 2 μm, alternatives such as electron beam lithography and focused ion beam (FIB) lithography are viable options. However, nanochannel fabrication typically demands intricate processes and expensive equipment, making the production of chips inaccessible to many researchers. To address this challenge, there is a need for a simpler fabrication approach that is maskless, highly efficient, and offers precise control of device design. [13]

To optimize the photo efficiency of PM pumps, we formerly developed a strategy to simultaneously control its orientation and position on a device. [14] For localization control, we used a tunable nanofluidic confinement apparatus (TNCA) to accurately deposit bR-containing membrane patches on a patterned substrate. The trapping sites for the membrane interface were prepared by thermal scanning probe lithography (t- SPL).

To fill the gap in the design of light-driven proton transport using PMs, we designed a nanochannel network containing PM patches. We used a combination of fabrication methods to create buried nanochannels [15] with a length of a few ten micrometers between dedicated areas (traps) for the placement and integration of biological building blocks. As a demonstrator of a biological building block, we selected wild-type (WT) PM patches. Furthermore, we initiated the development of a more direct method to identify PM orientation and presence during TNCA deposition. Our objective was to assess the efficiency of PM deposition on the device while maintaining pumping activity. The developed device is expected to provide a nanolocalized proton gradient and to enable the spatiotemporal control of a proton-catalyzed molecular self- assembly, [9] with an optical trigger that can be switched on and off.

5.2 Results and discussion

We used a combination of traditional and unconventional microfabrication methods to prepare the nanofluidic architectures of buried channels and deposition sites for biological membrane patches. As a demonstrator, WT PM patches were deposited at predefined positions of the hybrid device to install light-triggered proton pumps at defined openings of the nanochannels. Finally, we functionalized PM patches with a pH-sensitive dye for use as a pH sensor to identify PM localization and pumping activity in situ.

5.2.1 Device fabrication

In a first step, the pattern of nanochannels was defined by t-SPL. t-SPL is a versatile top-down technique based on heated tips. It can create different nanostructures and write patterns in an organic resist material under atmospheric conditions. Unlike electron beam lithographic tools, the t-SPL instrument is relatively simple and cost- effective. [16] Lines with a width of ~50 nm were patterned by t-SPL on a PPA/thermal oxide/Si substrate (Figure 5.1, step 2; Figure 5.2a). A first anisotropic etch into the SiO_2 was performed to expose the Si in the channels (Figure 5.1, step 3; Figure 5.2b). Subsequently, an isotropic reactive ion etch (RIE) of Si was conducted to form a cavity under the thermal oxide edges (Figure 5.1, step 4). The cavity was substantially wider than the line opened in the thermal oxide layer. As shown in the scanning electron microscope (SEM) images (Figure 5.2c,d), the fabricated channels were successfully patterned by t-SPL and etched via RIE. A cross-sectional SEM image was captured to identify a channel opening of 36 nm in the SiO_2 layer and a triangular-shaped nanochannel of approximately 360 nm × 300 nm (width × height) in the Si layer. Note that the upward bending in Figure 5.2c is likely caused by the stress arising from the Pt deposition. The effect is absent when the channel is closed in Figure 5.2d.

Using a single-layer of PPA patterned to a depth of 50 nm limits lateral resolution in t-SPL to roughly 50 nm due to the conical shape of the tip. Dimensions of <20 nm can be achieved by using a more elaborate three-layer transfer stack in so called high- resolution t-SPL patterning. [16,17] However, in the simple single-layer process used here the wider lines facilitate the isotropic etching of the underlying Si, and the wide opening can still be closed by sufficiently thick atomic layer deposition (ALD) layers. To examine the trench width resulting from our single-layer PPA resist in relation to the targeted line width of the t-SPL layout, we prepared four different trench structures with line widths of 2, 3, 4, and 5 pixels (corresponding to 23, 35, 46, and 58 nm, respectively). The CHF_3 and SF_6/Ar dry etching times were constant (10 and 2 min, respectively) for all samples. The line width in the patterns transferred to the SiO_2 layer varied from 35 to 71 nm (Figure 5.1, step 3). However, the variability of lines of the same pixel width was ±10 nm rather large. In extreme cases, we obtained SiO_2 channels with 117 nm width (Figure S5.1, Supplementary Information (SI)), which could be attributed to instabilities in the SiO_2 dry etching step and/or a blunt tip used for t-SPL patterning. The challenge of achieving exact sub-100 nm line dimensions by t- SPL in a single resist layer is the unknown tip-shape, which may vary due to tip contamination and tip wear. [16] Still, the line dimensions achieved with this standard t- SPL patterning were sufficient for the fabrication of buried nanochannels.

The top of the nanochannels was closed using ALD (Figure 5.1, steps 5,6). ALD is a thin film deposition technique based on the cyclic use of gas phase chemical processes. In each cycle a thin layer (~monolayer) of material is deposited on all accessible surfaces. Therefore, the deposition is very conformal, even in buried holes and channels, as long as there is access to the process gases. First, a 10 nm thin layer of Al_2O_3 was deposited on the substrate which later forms the bottom material for the PM deposition sites and supports the assembly of PMs in the correct orientation. [14] Afterwards, 30 nm of SiO_2 were deposited

by ALD to completely close the nanochannels. ALD has two unique advantages over other methods for nanochannel fabrication. First, the conformal film deposition during ALD allows the self-sealing of nanochannels if the film thickness can cover the entire top trench gap. Second, the nanochannels are also coated with the ALD material, which gives them well-defined surface properties and automatically provides them with a defined diameter once the channel top is sealed, regardless of the deposited ALD film thickness. [15] This self-limiting behavior is promising for the fabrication of highly controllable nanochannels with sublithographic dimensions. After the nanochannels were sealed by ALD, an additional SiO_2 layer of 100 nm was deposited on the substrate by plasma-enhanced chemical vapor deposition (PECVD) (Figure 5.1, step 7).

For the above-mentioned samples of varying line width in the t-SPL patterning step, the dimensions of the cavity in the Si were ranging from 360 to 453 nm in width and 259 to 300 nm in height. After ALD deposition, the buried channel dimensions were ranging from 294 to 362 nm in width and 221 to 290 nm in height (Figure 5.2d). For another set of samples, the duration of the isotropic silicon etch step (Figure 5.1, step 4) was reduced from 2 min to 1 min to achieve smaller channel dimensions. As expected, the channel dimensions were significantly reduced to 235 nm × 132 nm (width × height) before ALD and to 97 nm × 67 nm after ALD (Figure S5.2, SI). Also, we observed a more circular shape of the closed channels as compared to the triangular shape of the larger channels. Thus, sub-100-nm channel dimensions can be achieved by reducing the duration of the silicon etch step.

We performed a maskless t-SPL overlay patterning of 500-nm-diameter circular holes on the buried channels which were intended to act as traps for PM deposition (Figure 5.1, steps 8–10). The main challenges of maskless overlay patterning are the detection of the existing pattern and the accurate placement of the overlay pattern. The maskless process eliminates the need for dedicated alignment marks associated with difficulties in marker degradation and inconsistencies in the positioning of hardware used for reading and writing. [18] The t-SPL instrument can read topography with sub-nanometer sensitivity in the area of interest without causing any resist exposure and pattern nanometer-sized structures into the resist, which provides a unique method for nanometer-precise device fabrication. [17,18] The t-SPL maskless overlay process can be divided into three stages (Figure 5.3). First, the location and orientation of existing patterns were determined by topography measurements (Figure 5.3a). Second, this information was used to calculate the overlay pattern (Figure 5.3b). In this step, cross-correlation between the design file of the nano-channels (cyan lines in Figure 5.3b) and the measured topography is used to find the correct scaling and rotation of the sample and the precise location. Third, the trap pattern (blue in Figure 5.3b) was written on the sample surface aligned with the nanochannel pattern (Figure 5.3c).

Following the overlay process, the PPA underwent complete etching, removing ~70 nm of the >100 nm thick SiO_2 top layer, as illustrated in Figure 5.1, step 11. After completing this step, the nanochannels remained completely sealed, also in the PM trap patterns which formed as cylindrical depressions in the SiO_2 layer. This strategy was implemented

to avoid contamination within the nanochannel structures during subsequent fabrication stages. Subsequently, we utilized photolithography with a positive photoresist to define the microfluidic channels and filling pads, followed by three rounds of etching (SiO_2, Al_2O_3, and Si etch) within the designated photolithographic region (Figure 5.1, steps 12–18).

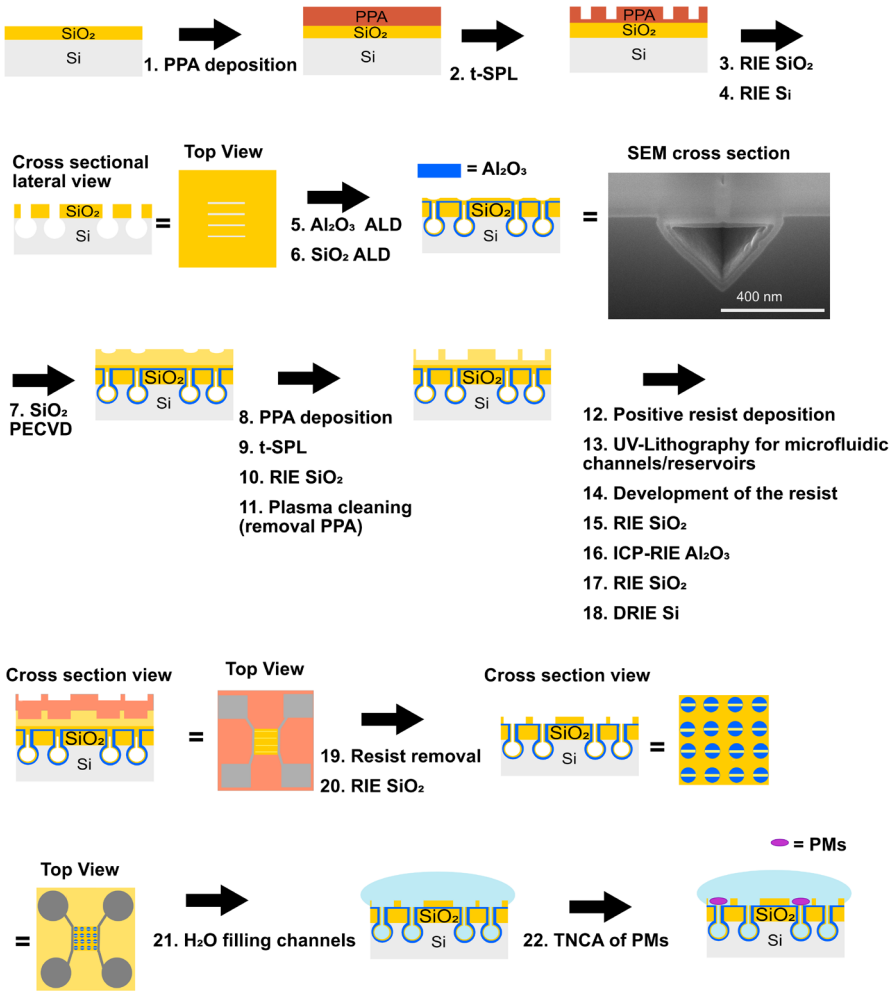

Figure 5.1. Summary of fabrication of bR-nanochannel device. Steps 1 to 4: fabrication of nanochannels by t-SPL. Steps 5 and 6: closure of t-SPL channels by ALD. [15] Steps 7 to 11: design of PM traps by t-SPL. Steps 12 to 18: fabrication of microchannels and macro reservoirs by photolithography. Steps 19 and 20: opening of nanochannels on PM traps. Step 21: filling of channels with water. Step 22: PM deposition. PPA = polyphthalaldehyde; t-SPL = thermal scanning probe lithography; RIE = reactive ion etching; ALD = atomic layer deposition; PECVD = plasma-enhanced chemical vapor deposition; SEM= scanning electron microscope; ICP-RIE = inductively coupled plasma – RIE; TNCA = tunable nanofluidic confinement apparatus; PM = purple membrane.

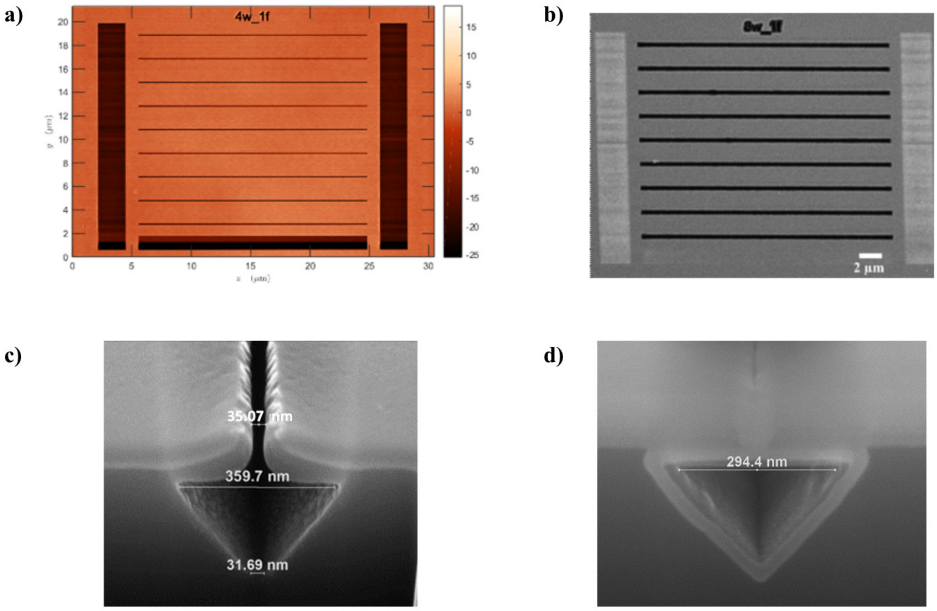

Figure 5.2 a) t-SPL image of 50-nm wide channels after t-SPL patterning in PPA resist (color gradient bar: Z-scale in nanometers). **b)** SEM top view image of channels after RIE, **c)** FIB cross sectional image of nanochannel before and **d)** after ALD.

After removing the photolithographic resist (Figure 5.1, step 19), we subjected the remaining SiO_2 layer to dry etching, as illustrated in Figure 5.1, step 20. This enabled precise control over the opening of nanochannels solely in the trap area. Moreover, it exposed the Al_2O_3 surface at the bottom of the trapping sites and provided finer control over the thickness of the remaining SiO_2 layer, which defines the depth of capture sites for the PMs. It is crucial for the PM layer deposition to achieve a trap depth of 15–20 nm, considering the PM thickness and their optimal deposition conditions. [14]

Figure 5.4 shows the successful photolithographic overlay of the nano and microchannels. Figure 5.4a is a top view of the buried nanochannels with the circular deposition sites for the PMs. On the right and left, the edge towards the much deeper microfluidic channel of the filling structure is visible. Figure 5.4b is a tilted view of the silicon ridge that contains the buried nanochannels which demonstrates the size proportion of the nano and microchannels. Microfluidic channels are approximately 23 µm deep. The horizontal structures on the side of the silicon ridge are due to the Bosch etching process. If needed, the cycle time of the Bosch process can be adjusted: short cycles yield smoother walls, and long cycles yield higher etch rates. [19] Figure 5.4c shows a tilted image of the opening of a buried nanochannel in the upper part of the silicon ridge. The nanochannels were open in the interception of nano and microchannels, which demonstrated the successful

and simple photolithographic overlay of a relatively small structure (20-µm-long channels). Moreover, there was no need for extra etching to open the nanochannel edges to remove dirt, contrary to the procedure reported by Nam et al. [15] The traps' depth, determined to be 20 nm, was measured using atomic force microscopy (AFM). This measurement accurately reflected the remaining SiO_2 layer after the various fabrication steps.

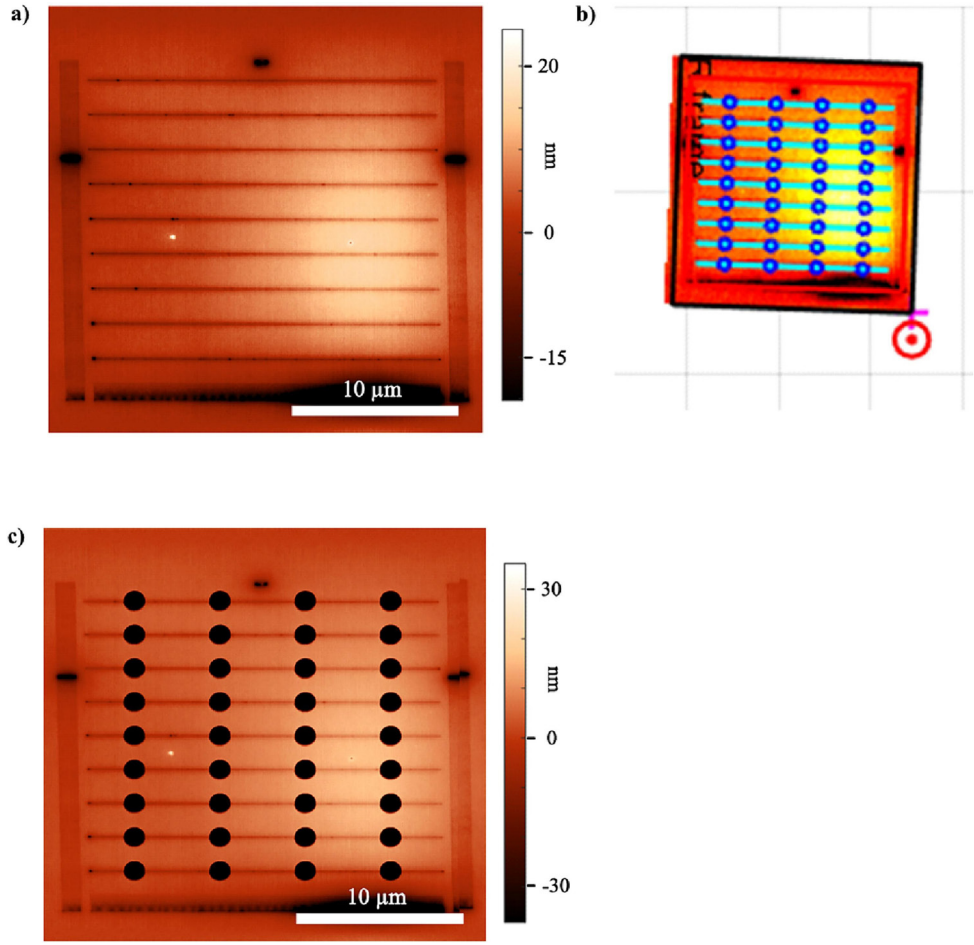

Figure 5.3. Overlay of circular traps on buried nanochannels. **a)** Topography image of buried nanochannels covered by 89 nm PPA resist. **b)** Image from panel a) in real space coordinates (slightly rotated sample). Overlayed are the gds-file layouts of the nanochannels (cyan) and the circular traps (blue). **c)** t-SPL topography image after patterning 1.2 µm diameter traps centered on the nanochannels.

Figure 5.5 presents a successful t-SPL overlay of 500 nm circles on the nanochannels. PECVD of SiO_2 achieved a faster deposition rate than ALD, and the additional material enabled us to design trap patterns on specific areas of the nanochannels, which were locally opened

towards the nanochannels, as shown in Figure 5.5a. The channels elsewhere in the overlay areas remained closed, as shown in Figure 5.5b and Figure 5.5c. The results show that we can locally control the material in a buried structure by combining bottom-up and top-down approaches. This provides us with freedom to design 3D structures for different applications.

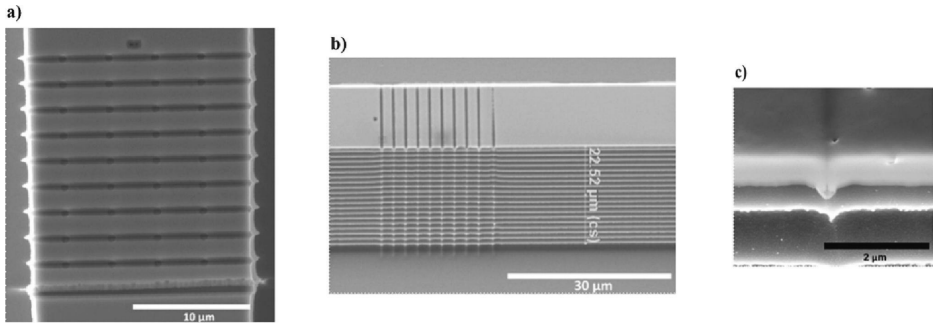

Figure 5.4. **a)** Planar top view and **b)** tilted SEM images of nanochannels and PM traps. **c)** End of open nanochannel after DRIE etch of inlet and outlet microfluidic channels.

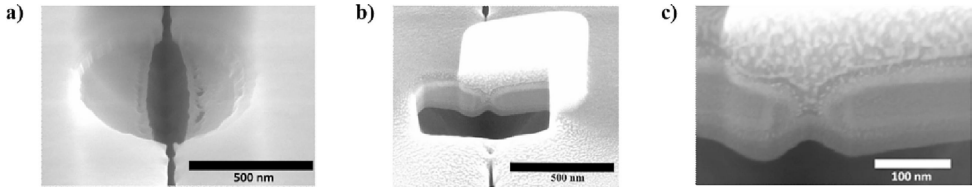

Figure 5.5. SEM-FIB images of **a)** PM trap (titled view); **b)** cross-section of buried part of nanochannel after step 20 (Figure 5.1) followed by platinum deposition, which was used to verify if the channel was open; and **c)** nanochannel closure (zoomed image of b).

5.2.2 PM deposition

The thus fabricated device can receive PM patches with controlled localization and orientation by TNCA. [14] PM deposition and proton pumping must be performed in a liquid environment. Therefore, channels must be prefilled before PM deposition and maintained filled throughout the experiments. Because PMs could only be deposited after the nanochannel filling and the TNCA deposition process requires top access to the PM traps, we could not close the device using a polydimethylsiloxane (PDMS) sheet or via anodic bonding of a cover glass. Thus, filling by pressure was not possible, and we aimed to fill the nanochannels by capillary action. However, surface tension hindered the filling of the device with an aqueous liquid. To decrease the surface tension, we used a 1:3 (V/V) ethanol/Milli-Q water mixture. Filling of nanochannels was observed using a fluorescent dye at micromolar concentrations (Figure S5.3, SI). Because ethanol can interfere with the

bR photocycle, [20] we immersed the substrate in Milli-Q water after filling the nanochannels to dilute the ethanol to negligible levels before the PM deposition. Moreover, TNCA requires reduced ion concentration and a PM density suitable for tracking. [21] Therefore, we did not use any buffered solution for the PM deposition.

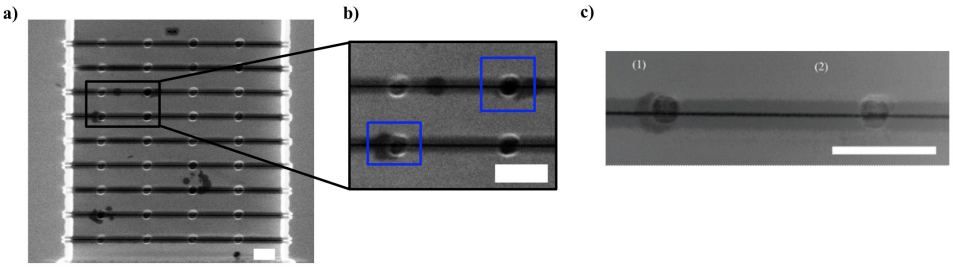

Figure 5.6. SEM images of **a)** device field after deposition of PMs; **b)** 500-nm PM traps, with deposited PMs (dark patches), indicated by blue rectangles; **c)** 500-nm traps from another field **c)-(1)** with deposited PM (dark patch) and **c)-(2)** without deposited PMs. Scale bar: 2 µm.

Finally, we deposited a drop of WT PM at the surface of the chip, and we performed the PM deposition by TNCA. The PM traps of our substrates have a layer of Al_2O_3 at the bottom because it controls the orientation of PM patches with its slightly positive charge in aqueous media. [14] From the SEM image displayed in Figure 5.6a, we identified the presence of darker gray, rounded material on the Al_2O_3 surface of the traps in 5 out of the 36 traps inspected. This observation leads us to infer that certain Al_2O_3 traps were coated with PMs (Figure 5.6b). The visualization of Al_2O_3 material in SEM presents challenges, including surface charging, which can result in distorted or blurry images. Consequently, our ability to visualize PM on such media is compromised. Figure 5.6c) displays two traps in a field following PM deposition: one featuring a PM patch (Figure 5.6c-(1)) and another without any such patch (Figure 5.6c-(2)). This observation highlights the presence of material concentrated in distinct traps. We conclude that we designed a device that can receive PM patches with controlled localization.

5.2.3 Deposition of functionalized PMs with dye (PM-pHrodo)

Our next step is to develop a strategy for measuring PM pumping within our nanochannel network. To achieve this, we aim to integrate a sensor into the system that preserves the integrity of the PMs. This advancement will enable precise control of nanoscale localized proton gradients using our device.

As an initial step in this study, we used fluorescence microscopy (FM) to detect the presence of PM and measure proton pumping in individual PM patches on a flat substrate. To achieve this, PMs were functionalized with pHrodo, a pH-sensitive dye that increases fluorescence intensity as the medium becomes more acidic.

We selected the pHrodo™ iFL STP red ester dye (pHrodo) as a pH-sensitive fluorescent dye for its specificity in detecting pH changes. The pHrodo derivative, containing an amino-reactive group, has a pKa of approximately 6.8. This amino-reactive group enables covalent attachment to surface with amino groups, facilitating stable surface bonding. [22,23] The rationale behind employing amino-reactive dyes lies in their reactivity with the side chains of some of the amino acids in the bR peptide chain. pHrodo has been utilized, for example, in the functionalization of amino-functionalized beads, [24] nanoprobes, [25] and cells [26,27] to facilitate the detection of pH within these environments. The intensity of pHrodo amplifies by 1000% as the pH decreases from 8.0 to 4.0, showcasing its effectiveness in acidic environments. [28,29] The operational characteristics of pHrodo include excitation and emission maxima at approximately 560 nm and 585 nm, respectively, allowing for detection using standard tetramethylrhodamine isothiocyanate (TRITC) filter. Optimal excitation for the pHrodo dye is achieved with green light, which aligns well with the preferred wavelength for PM pumping activity. [30]

The substrates employed in these experiments were prepared as follows: PM patches, dispersed in an aqueous medium, were incubated with the amino-reactive pHrodo derivative. Following incubation, these modified PMs were subsequently coated on an Al_2O_3 surface, as it is for our device traps. To check the functionalization of PMs with pHrodo and evaluate their pumping activity, a drop of Mili-Q water (pH 7.0) or a buffer solution at pH 4.0 (0.10 M acetic acid/0.02 M sodium acetate buffer) was added at the top of the substrates, and fluorescence measurements were undertaken.

Proof-of-concept functionalization of PMs with pHrodo

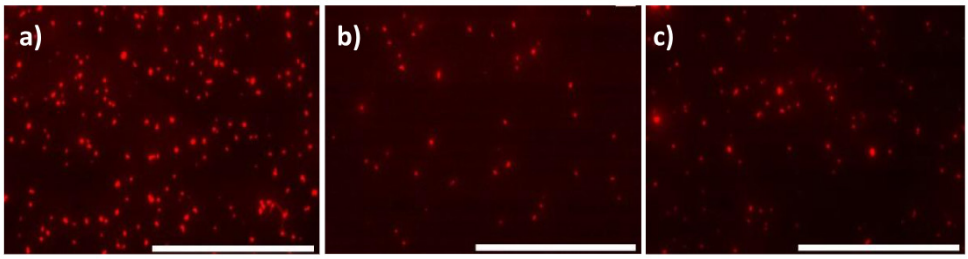

Figure 5.7. Fluorescence images (TRITC filter) of PMs functionalized with pHrodo deposited on an Al_2O_3 substrate with a drop of aqueous buffer at pH 4.0. **a)** Wild-type PM, **b)** C-His_{10}-tag PM, **c)** N-His_{10}-tag PM. Data were obtained from 500 ms exposure time images and 60x objective lens. The scale bar represents 100 µm.

Initially, we confirmed the successful functionalization of PMs with pHrodo, applying this process to WT PM (Figure 5.7a), as well as on two genetically modified variants: C- His_{10}-tag PM (Figure 5.7b) and N-His_{10}-tag PMs (Figure 5.7c). Any native fluorescence of PMs, if present, is not sufficient for imaging with standard fluorescence-based techniques. [3,14] As a result, we anticipate that dye-free PM patches will not exhibit fluorescence. As shown in Fig. 5.7, for all types of PM-pHrodo deposited on surfaces, we observed red

ellipsoids around 1 µm, indicating that these bright objects correspond to individual PMs functionalized with pHrodo. This result proves that all three PM types used in this study could be functionalized with the pHrodo dye.

Measuring PM pumping patch activity using FM

After functionalization, our next step was to determine whether we can study the proton activity of PMs while they are functionalized with pHrodo. For that, we tracked the background-corrected fluorescence intensity (BCFI) variation under different exposure conditions for all PM patch types, as illustrated in Figure 5.8 for neutral non-buffered medium and Figure 5.9 for acidic buffered medium. BCFI variation over time was determined by averaging signals from PM patches and subtracting background fluorescence values. Further details on data processing can be found in the SI.

The substrate underwent exposures to green light, with each exposure lasting 500 ms. The intervals between exposures were varied, set at 30, 20, 10, and 5 seconds. Each interval sequence was maintained for a duration of 10 minutes. We expected that the slope of the fluorescence signal would rise proportionally with shorter intervals between light exposure. This assumption is founded on the reasoning that shorter intervals result in more frequent exposure of the sample to light within a given time.

Measurement of PM patch pumping activity in neutral non-buffered media

The BCFI of all PM patch types in non-buffered neutral medium increased linearly over time, as depicted in Figure 5.8, indicating active pumping detected by the attached dye. Raw fluorescence signals and background details are provided in Figure S5.5, SI. Regression analysis in Table 5.1 examined light exposure intervals, showing increased slopes with shorter intervals from 20 to 5 s. The coefficient of determination (COD) for all PM types and intervals confirms a robust linear relationship between time and BCFI. We conclude that exposing PMs to 500 ms of light at intervals shorter than 20 seconds enhances the proton pumping rate. For the 30-second interval, we observed unstable initial values, and a lower COD compared to the other time intervals.

We aimed to convert fluorescence counts into pH values. Equation (1) was used to translate fluorescence values into pH at different time points

$$(-0.64 \pm 0.03) \times pH_{PMpHrodo} + 5.44 \pm 0.20 = \frac{I_{PMpHrodo}}{I_{pH7}} = \text{BCRFI} \quad (1)$$

where I_{pH7} is the BCFI of a target area at pH 7.0 and time = 0 s; $I_{PMpHrodo}$ is the BCFI intensity at a particular time; and $pH_{PMpHrodo}$ is the pH value at this specific time. The background-corrected ratio FI (BCRFI) is the ratio of $I_{PMpHrodo}$ to I_{pH7}, representing the mathematical relationship between FI and pH: a more pronounced BCRFI indicates a lower pH. The dataset for this Equation was taken from Dolman et al. [29] It assumes that the pHrodo intensity linearly

increased from basic to acidic media. The detailed linear regression used for finding this Equation is described in Figure S5.8, SI.

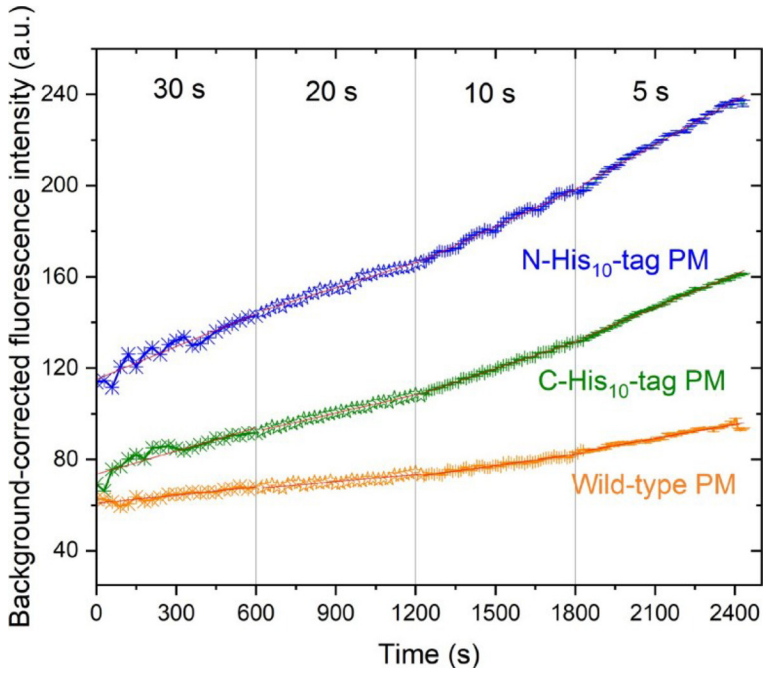

Figure 5.8. Background-corrected ratio fluorescence intensity of PM functionalized with pHrodo over time in Milli-Q water (pH 7.0). Data were obtained with 500 ms exposure time images using a TRITC filter and a 60x objective lens. Orange: wild-type PM. Green: C-His_{10}-tag- PM. Blue: N- His_{10}-tag-PM. The red lines represent linear fit for respective PM data.

Table 5.1. Linear regression of background-corrected fluorescence over time of time-lapse measurement of PM-pHrodo in Milli-Q water. COD = coefficient of determination.

	C-His_{10}-tag PMs		N-His_{10}-tag PMs		Wild-type PMs	
Time interval	**Slope**	**COD**	**Slope**	**COD**	**Slope**	**COD**
30 s	0.034 ± 0.003	0.83	0.048 ± 0.003	0.92	0.012 ± 0.001	0.84
20 s	0.027 ± 0.001	0.99	0.037 ± 0.001	0.99	0.010 ± 0.001	0.88
10 s	0.039 ± 0.000	0.99	0.054 ± 0.001	0.99	0.016 ± 0.000	0.95
5 s	0.048 ± 0.000	0.99	0.064 ± 0.001	0.99	0.020 ± 0.000	0.94

Table 5.2. Background-corrected fluorescence intensity (BCFI), background-corrected ratio fluorescence intensity (BCRFI) and calculated pH from time-lapse measurements of PM-pHrodo patches at MiliQ water (pH 7.0). The pH values were obtained from the fluorescent intensity applied to Equation (1).

	C-His_{10}-tag PMs			N-His_{10}-tag PMs			Wild-type PMs		
Time (s)	**BCFI**	**BCRFI**	**pH**	**BCFI**	**BCRFI**	**pH**	**BCFI**	**BCRFI**	**pH**
0	69.2	1.00	6.94	113.9	1.00	6.94	62.7	1.00	6.94
600	91.6	1.32	6.45	143.0	1.25	6.53	68.1	1.09	6.81
900	100.5	1.45	6.23	154.7	1.36	6.36	69.4	1.11	6.77
1200	108.7	1.57	6.06	165.7	1.46	6.20	74.5	1.19	6.64
1500	119.4	1.72	5.81	180.0	1.58	6.00	77.4	1.24	6.57
1800	131.3	1.89	5.54	197.1	1.73	5.75	83.2	1.33	6.43
2100	146.8	2.12	5.18	217.8	1.91	5.45	88.1	1.41	6.31
2400	159.6	2.30	4.90	237.5	2.09	5.17	98.0	1.56	6.06

Assuming the initial pH of the medium was approximately 7.0, equivalent to that of Mili-Q water, we calculated pH values for pHrodo-functionalized patches over time using Equation (1). The results, presented in Table 5.2, indicate initial differences in BCFI values among various PM types. Despite the initially higher value and more prominent slope of the linear regression of the N-His_{10}-tag PM data, the C-His_{10}-tag PM type presented the highest BCRFI over time (Figure S5.6, SI), corresponding to a greater pH decrease (ΔpH) of approximately 2.1 units. In comparison, the N-His_{10}-tag PM type showed a decrease of 1.8 units, and WT PMs decreased by approximately 0.9 units by the end of the experiments. These calculated pH values align closely with literature-reported values, typically ranging from ΔpH 0.5 to 2.0. [3,31] Furthermore, the findings suggest that attaching pHrodo to the PM surface may minimally affects the pumping behavior of PM patches.

Measurement of PM patch pumping activity in acidic buffered media

As shown in Figure 5.9, the BCFI of all PM patch types increased over time in a buffered acidic medium. Linear regression analysis (Table 5.3) revealed that genetically modified PMs exhibited non-linear pumping behavior, with poor COD for BCFI values, while WT PMs showed a linear BCFI increase across all light intervals. Interestingly, unlike the data in Table 5.1, Table 5.3 indicates that the slope for WT PMs decreases with shorter light exposure intervals, being highest at the 30-second interval and lowest at the 5-second interval. Raw fluorescence signals from the patches and background are shown in Figure S5.7, SI.

Our results indicate that, in an acidic buffer medium, the pumping activity of WT is enhanced compared to that in a non-buffered aqueous medium. This is demonstrated by the higher ΔBCFI = 2.9 (Table S1, SI) between the start and end of the experiment, relative to both other PM types in acidic medium and the ΔBCFI of WT in non-buffered conditions.

Equation (1) could not be used to measure pH over time for the WT PMs due to the lack of an initial pH reference at t=0. Correlating BCFI with actual pH values is of interest but challenging due to limited control experiments and references. A semi-quantitative approach for studying pH changes in an acidic buffered medium is suggested in the SI.

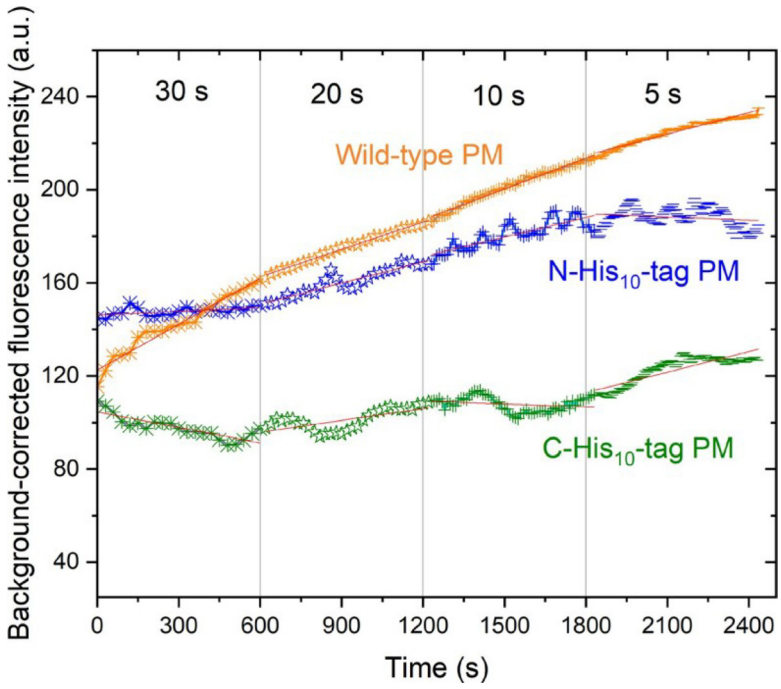

Figure 5.9. Background-corrected ratio fluorescence intensity (BCFI) of PM functionalized with pHrodo over time in buffered acidic medium (pH 4.0). Data were obtained with 500 ms exposure time images using a TRITC filter and a 60x objective lens. Orange: wild-type PM. Green: C-His_{10}- tag-PM. Blue: N-His_{10}-tag-PM. The red lines represent linear fit for respective PM data.

Table 5.3. Linear regression of background-corrected fluorescence intensity (BCFI) over time of time-lapse measurement of PM-pHrodo in buffered acidic media (pH 4). COD = coefficient of determination.

	C-His_{10}-tag PMs		N-His_{10}-tag PMs		Wild-type PMs	
Time interval	**Slope**	**COD**	**Slope**	**COD**	**Slope**	**COD**
30 s	-0.022 ± 0.003	0.72	0.006 ± 0.002	0.32	0.066 ± 0.003	0.96
20 s	0.017 ± 0.003	0.47	0.030 ± 0.002	0.87	0.039 ± 0.001	0.99
10 s	-0.004 ± 0.002	0.06	0.028 ± 0.002	0.71	0.044 ± 0.001	0.98
5 s	0.029 ± 0.002	0.75	-0.005 ± 0.002	0.35	0.030 ± 0.001	0.96

In this study, PM-pHrodo patches coated onto SiO_2 surfaces were excluded from examination due to an adherence failure, which precluded the generation of fluorescent signals from SiO_2-coated PM-pHrodo surfaces. Conversely, it was documented that PMs,

in the absence of pHrodo conjugation, exhibit the capacity to adhere to both SiO_2 and Al_2O_3 surfaces. [14] This observed divergence in adhesion properties between PM-pHrodo and non-functionalized PMs may be ascribed to the augmentation of negative charge on the PM surface following pHrodo conjugation.

Such an increase in surface charge is likely to induce repulsion from SiO_2 surfaces, which are recognized for exhibiting a negative surface charge within aqueous environments. [14] The use of PM-pHrodo in our nanochannel device is advantageous, as we expect PM deposition to occur exclusively in the Al_2O_3 traps, without unintended deposition elsewhere.

Initial Explanations of the results

The differences in pHrodo attachment to the PM surface and the variations in ΔpH across different PM types remain unclear. Additionally, the impact of charge distribution following functionalization with pHrodo has not been fully assessed. We hypothesize that the surface charge of the PMs remains unaffected by pHrodo functionalization, as previous studies suggest that pHrodo attachment does not alter the charge characteristics of amino-silanized surfaces. [24] The nature of the pHrodo functionalization—whether covalent or ionic—has yet to be determined.

Experimental observations revealed the following: (1) pHrodo attachment: pHrodo was detected on all PM types, with the strongest initial BCFI observed in the N-His_{10}-tag PM. The WT and C-His_{10}-tag PMs showed almost identical initial BCFI. (2) Pumping activity: differences in pumping activity between the PM types were minimal, with the C-His_{10}-tag PM exhibiting slightly more activity. The WT PM showed less pronounced pH changes over time compared to the genetically modified PMs. (3) Response in acidic buffer: in an acidic buffer (pH 4.0), genetically modified PMs displayed a non-linear response to green light, while WT PMs showed a significant pH increase under green light exposure.

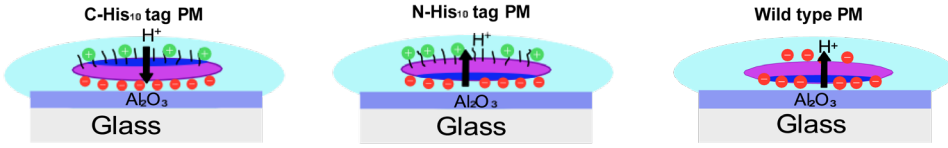

Figure 5.10. Illustration of charge distribution between Al_2O_3 surface and PM in aqueous media for C-His_{10}-tag, N-His_{10}-tag, and wild-type PMs. For each PM type, the pump orientation is demonstrated. Purple, navy blue, and light blue areas represent PMs, cytoplasmatic side of PMs, and aqueous media, respectively.

Before taking initial conclusions, it is important to consider the charge distribution of PM and their pumping orientation. Both are presented in Figure 5.10. Al_2O_3 imparts a mildly positive surface charge in an aqueous environment. [32,33] WT PMs possess fragments with a net negative charge on both sides of the membrane due to the amino acid residues on the bR surface and the PM lipid acidity, while His-tag_{10} peptide sequences confer a positive

charge on the designated side of the PM (C-terminus or N-terminus). [34] C-His_{10}-tag PMs pump protons preferentially from the substrate–PM interfacial layer across the membrane towards the PM-aqueous interfacial layer due to an asymmetric surface charge on the cytoplasmic side, resulting in a substrate- oriented proton gradient. In contrast, N-His_{10}-tag PMs exhibit an extracellular side asymmetric charge, creating a substrate-averse proton gradient. Above pH 5, WT PMs show a more negative surface charge density on the cytoplasmic side, [35] aligning their orientation with N-His_{10}-tag PMs.

The following conclusions can be drawn from these observations. **(1) Extracellular side charge and pHrodo attachment:** the extracellular side charge likely influences pHrodo attachment to the PMs. When the extracellular side charge is more positive, as with the N-His_{10}-tag PM, pHrodo attachment is more substantial. In contrast, both the C-His_{10}-tag and WT PMs exhibit similar fluorescence intensities due to their negatively charged extracellular side surfaces. **(2) Pumping activity and PM orientation:** in the C-His_{10}-tag PM, protons accumulated beneath the PMs, opposite to the orientation observed in the N-His_{10}-tag and WT PMs. This explains the slightly more substantial pumping activity (larger ΔpH) observed for this PM in a neutral pH medium. However, pumping activity was detected in all PM types, suggesting that pHrodo was attached to both sides of the PM, allowing for detection of pumping activity. As PM-pHrodo could not be attached to SiO_2 surfaces, conclusions regarding the efficiency of pumping activity in relation to surface charge and orientation cannot be drawn. **(3) Acidic conditions and histidine ionization:** the variability in pumping activity under acidic conditions can be attributed to the ionization of His_{10}-tag molecules, which is influenced by solution pH and the local pKa of histidine residues. [36] Factors such as burial depth and interactions with neighboring residues contribute to this variability, explaining the inconsistent pumping activity observed in genetically modified PMs under acidic buffered conditions.

In conclusion, the pHrodo sensor effectively detects pumping activity in all PM types, regardless of orientation. However, the relationship between pumping orientation, surface charge, and pumping efficiency remains inconclusive. Despite this limitation, PM-pHrodo represents a promising tool for detecting and studying PM pumping in aqueous, non-buffered media.

5.3 Conclusions

Hybrid devices prepared by micro- and nanofabrication with integrated biological building blocks are promising architectures for energy harvesting, spatiotemporal control of chemical gradients and thus for manipulating chemical reaction networks locally. We use a fabrication method based on a combination of t-SPL, etching methods, ALD and photolithography to prepare devices with buried nanochannels on silicon substrates. The maskless overlay capabilities of t-SPL facilitate the fabrication of deposition sites for functional membrane patches on local nanochannel openings. The combination of etch cycles and ALD offers the opportunity to control the dimensions of the buried nanochannels, whereas the materials used for ALD control the surface chemistry and surface potential of the channels and of

the deposition sites. Inlet and outlet ports integrated with the nanochannels were created using photolithography and DRIE, and the filling of nanochannels was demonstrated by fluorescence detection.

As a demonstrator for the integration of a biological building block, we used WT PM patches as light-triggered proton pumps. The PM patches were deposited onto the selected sites by nanofluidic confinement. The developed device can be potentially used to control the transport of protons and to study their role in nanoscale compartments, as well as in other practical applications that benefit from a mechanically robust and simple fabrication process. The strategies developed in our study represent important tools for fabricating 3D device systems, e. g., the fabrication of connected microreactors with multiple channels crossing in 3D.

Furthermore, we initiated the development of a simplified methodology using pHrodo dyes to quantify proton pumping within our device. Our findings show that PM patches functionalized with pHrodo active ester can carry an internal pH sensor. This sensor works effectively when PMs are in a neutral pH medium. Further progress is needed to refine this approach, including conducting control experiments with PMs and assessing the impact of buffers with varying pH levels on PM-pHrodo-coated substrates. Once these refinements are made, PM pumping can be measured using a straightforward setup and methodology.

Moving forward, the next step involves depositing PM-pHrodo patches using TNCA into our 3D fabricated device. We anticipate several advantages from employing PM-pHrodo patches for orientation-controlled PM deposition. These patches offer a direct means to detect PM presence on traps concurrently with TNCA deposition. Moreover, immediate analysis of proton pumping activity post-deposition allows us to assess deposition efficiency while maintaining functional pumping capability.

5.4 References

(1) Gadsby, D. C. Ion Channels versus Ion Pumps: The Principal Difference, in Principle. *Nature reviews Molecular cell biology* **2009**, 10 (5), 344–352.

(2) Xiao, K.; Schmidt, O. G. Light-Driven Ion Transport in Nanofluidic Devices: Photochemical, Photoelectric, and Photothermal Effects. *CCS Chem* **2022**, 4 (1), 54–65. https://doi.org/10.31635/ccschem.021.202101297.

(3) Stoeckenius, W.; Lozier, R. H.; Bogomolni, R. A. Bacteriorhodopsin and the Purple Membrane of Halobacteria. *Biochimica et Biophysica Acta (BBA) - Reviews on Bioenergetics* **1979**, 505 (3–4), 215–278. https://doi.org/10.1016/0304-4173(79)90006-5.

(4) Feng, Y.; Zhu, W.; Guo, W.; Jiang, L. Bioinspired Energy Conversion in Nanofluidics: A Paradigm of Material Evolution. *Advanced Materials* **2017**, 29 (45), 1702773. https://doi.org/10.1002/adma.201702773.

(5) Xiao, K.; Chen, L.; Chen, R.; Heil, T.; Lemus, S. D. C.; Fan, F.; Wen, L.; Jiang, L.; Antonietti, M. Artificial Light-Driven Ion Pump for Photoelectric Energy Conversion. *Nature communications* **2019**, 10 (1), 74.

(6) Al-Aribe, K. M.; Knopf, G. K.; Bassi, A. S. Fabrication of an Optically Driven pH Gradient Generator Based on Self-Assembled Proton Pumps. *Microfluidics and nanofluidics* **2012**, 12 (1), 325–335.

(7) Gonçalves, R. P.; Agnus, G.; Sens, P.; Houssin, C.; Bartenlian, B.; Scheuring, S. Two-Chamber AFM: Probing Membrane Proteins Separating Two Aqueous Compartments. *Nat Methods* **2006**, 3 (12), 1007–1012.

https://doi.org/10.1038/nmeth965.

(8) Wang, D.; Wang, Y.; Li, H.; Han, Y.; Hu, P.; Ma, K.; Sheves, M.; Jin, Y. Photoactivated Bacteriorhodopsin/SiN x Nanopore-Based Biological Nanofluidic Generator with Single-Protein Sensitivity. *ACS nano***2022**, 16 (1), 1589–1599.

(9) Boekhoven, J.; Poolman, J. M.; Maity, C.; Li, F.; Van Der Mee, L.; Minkenberg, C. B.; Mendes, E.; Van Esch, J. H.; Eelkema, R. Catalytic Control over Supramolecular Gel Formation. *Nature Chem* **2013**, 5 (5),433–437. https://doi.org/10.1038/nchem.1617.

(10) Gupta, P.; Vermani, K.; Garg, S. Hydrogels: From Controlled Release to pH-Responsive Drug Delivery. *Drug discovery today* **2002**, 7 (10), 569–579.

(11) Ort, D. R.; Parson, W. W. Flash-Induced Volume Changes of Bacteriorhodopsin-Containing Membrane Fragments and Their Relationship to Proton Movements and Absorbance Transients. *Journal of Biological Chemistry* **1978**, 253 (17), 6158–6164. https://doi.org/10.1016/S0021-9258(17)34593-3.

(12) Eroğlu, I.; Aydemir, A.; Türker, L.; Yücel, A. M. Photoresponse of Bacteriorhodopsin Immobilized i Polyacrylamide Gel Membranes. *Journal of membrane science* **1994**, 86 (1–2), 171–179.

(13) Wang, H.; Deng, C.; Xiao, C.; Liu, L.; Liu, J.; Peng, Y.; Yu, B.; Qian, L. Fast and Maskless Nanofabrication for High-Quality Nanochannels. *Sensors and Actuators B: Chemical* **2019**, 288, 383–391.

(14) Ruggeri, F.; Schwemmer, C.; Stauffer, M.; Nicollier, P. M.; Figueiredo da Silva, J.; Bosshart, P. D.; Kochems, K.; Fotiadis, D.; Knoll, A.; Wolf, H. Placement of Biological Membrane Patches in a Nanofluidic Gap With Control Over Position and Orientation. *Advanced materials interfaces* **2022**, 9 (23), 2200941.

(15) Nam, S.-W.; Lee, M.-H.; Lee, S.-H.; Lee, D.-J.; Rossnagel, S. M.; Kim, K.-B. Sub-10-Nm Nanochannels by Self-Sealing and Self-Limiting Atomic Layer Deposition. *Nano letters* **2010**, 10 (9), 3324–3329.

(16) Howell, S. T.; Grushina, A.; Holzner, F.; Brugger, J. Thermal Scanning Probe Lithography—A Review. *Microsystems & nanoengineering* **2020**, 6 (1), 1–24.

(17) Ryu Cho, Y. K.; Rawlings, C. D.; Wolf, H.; Spieser, M.; Bisig, S.; Reidt, S.; Sousa, M.; Khanal, S. R.; Jacobs,T. D. B.; Knoll, A. W. Sub-10 Nanometer Feature Size in Silicon Using Thermal Scanning Probe Lithography. *ACS Nano* **2017**, 11 (12), 11890–11897. https://doi.org/10.1021/acsnano.7b06307.

(18) Rawlings, C.; Duerig, U.; Hedrick, J.; Coady, D.; Knoll, A. Nanometer Control of the Markerless Overlay Process Using Thermal Scanning Probe Lithography. In 2014 *IEEE/ASME International Conference on Advanced Intelligent Mechatronics*; IEEE, **2014**; pp 1670–1675.

(19) Laermer, F.; Urban, A. MEMS at Bosch–Si Plasma Etch Success Story, History, Applications, and Products. *Plasma Processes and Polymers* **2019**, 16 (9), 1800207.

(20) Kikukawa, T.; Araiso, T.; Shimozawa, T.; Mukasa, K.; Kamo, N. Restricted Motion of Photoexcited Bacteriorhodopsin in Purple Membrane Containing Ethanol. *Biophysical journal* **1997**, 73 (1), 357–366.

(21) Fringes, S.; Holzner, F.; Knoll, A. W. The Nanofluidic Confinement Apparatus: Studying Confinement Dependent Nanoparticle Behavior and Diffusion. *Beilstein Journal of Nanotechnology* **2018**, 9 (1), 301–310.

(22) HECHT, K.; WiELAND, F.; JAENICKE, R. The Cell Surface Glycoprotein of Halobacterium Halobium. *Physico-Chemical Characterization in the Absence and Presence of Salt*. **1986**.

(23) Fisher, K. A.; Yanagimoto, K.; Stoeckenius, W. Oriented Adsorption of Purple Membrane to Cationic Surfaces. *Journal of Cell Biology*, 1978, 77, 611–621.

(24) Hirose, H.; Maekawa, M.; Ida, H.; Kuriyama, M.; Takahashi, Y.; Futaki, S. A Noncanonical Endocytic Pathway Is Involved in the Internalization of 3 Mm Polystyrene Beads into HeLa Cells. *BiomaterialsScience* **2022**, 10 (24), 7093–7102.

(25) Arppe, R.; Näreoja, T.; Nylund, S.; Mattsson, L.; Koho, S.; Rosenholm, J. M.; Soukka, T.; Schäferling, M.Photon Upconversion Sensitized Nanoprobes for Sensing and Imaging of pH. *Nanoscale* **2014**, 6 (12), 6837–6843.

(26) Lindner, B.; Burkard, T.; Schuler, M. Phagocytosis Assays with Different pH-Sensitive Fluorescent Particles and Various Readouts. *Biotechniques* **2020**, 68 (5), 245–250.

(27) von Kaeppler, E. P.; Wang, Q.; Raghu, H.; Bloom, M. S.; Wong, H.; Robinson, W. H. Interleukin 4Promotes Anti-Inflammatory Macrophages That Clear Cartilage Debris and Inhibits Osteoclast Development to Protect against Osteoarthritis. *Clinical Immunology* **2021**, 229, 108784.

(28) pHrodo™ Dyes for Amine Labeling. https://www.thermofisher.com/order/catalog/product/br/en/P36010 (accessed 2023-01-06).

(29) Dolman, N. J.; Kilgore, J. A.; Davidson, M. W. A Review of Reagents for Fluorescence Microscopy of Cellular Compartments and Structures, Part I: BacMam Labeling and Reagents for Vesicular Structures.

Current protocols in cytometry **2013**, 65 (1), 12.30. 1-12.30. 27.
(30) Schenkl, S.; Zgrablić, G.; Portuondo-Campa, E.; Haacke, S.; Chergui, M. On the Excitation Wavelength Dependence of the Fluorescence of Bacteriorhodopsin. *Chemical Physics Letters* **2007**, 441 (4–6), 322–326. https://doi.org/10.1016/j.cplett.2007.04.086.
(31) Renthal, R.; Lanyi, J. K. Light-Induced Membrane Potential and pH Gradient in Halobacterium Halobium Envelope Vesicles. *Biochemistry* **1976,** 15 (10), 2136–2143.
(32) Hinterdorfer, P.; Dufrêne, Y. F. Detection and Localization of Single Molecular Recognition Events Using Atomic Force Microscopy. *Nature methods* **2006**, 3 (5), 347–355.
(33) Ben Ismail, M.; Carreiras, F.; Agniel, R.; Mili, D.; Sboui, D.; Zanina, N.; Othmane, A. Application of APTES-Anti-E-Cadherin Film for Early Cancer Monitoring. *Colloids and Surfaces B: Biointerfaces* **2016**, 146, 550–557. https://doi.org/10.1016/j.colsurfb.2016.06.048.
(34) Stauffer, M.; Hirschi, S.; Ucurum, Z.; Harder, D.; Schlesinger, R.; Fotiadis, D. Engineering and Production of the Light-Driven Proton Pump Bacteriorhodopsin in 2D Crystals for Basic Research and Applied Technologies. *Methods and protocols* **2020**, 3 (3), 51.
(35) Fisher, K. A.; Yanagimoto, K.; Stoeckenius, W. Oriented Adsorption of Purple Membrane to Cationic Surfaces. *The Journal of cell biology* **1978**, 77 (2), 611–621.
(36) Chaudhury, S.; Ripoll, D. R.; Wallqvist, A. Structure-Based pKa Prediction Provides a Thermodynamic Basis for the Role of Histidines in pH-Induced Conformational Transitions in Dengue Virus. *Biochemistryand biophysics reports* **2015**, 4, 375–385.

5.5 Supplementary information

This section describes the methods used to produce and analyze the device reported in this Chapter. Unless otherwise stated, all chemicals and solvents were purchased from Sigma-Aldrich.

5.5.1 Device fabrication

Thermal scanning probe lithography (t-SPL) and reactive ion etching (RIE)

4-inches silicon wafers with 500 µm thickness were used to fabricate the nanochannels. A 50 nm thick silicon oxide layer was grown by thermal oxidation and characterized using ellipsometry. The wafer was diced into 8 mm × 8 mm-sized chips. For the t-SPL process, 55 nm thick polyphthalaldehyde (PPA) (Allresist) thermal resist was spun onto the chips from 5% anisole solution, and then soft baked at 110°C for 1 min. t-SPL was performed in our homemade system, which is described in detail elsewhere. [1] The t- SPL tool can locally remove the resist (PPA) using a tip that can be heated to several hundred degrees centigrade. The lines were written in the resist to a depth of 45 nm, a nominal width of 58 nm (5 pixels), and length of 20 µm (1700 pixels). No development was needed. The pattern was transferred from PPA into the SiO_2 layer on the substrate using RIE (Oxford Plasmalab 80). As etchant CHF_3 (20 sccm) plasma was used for 10 min, at 15 mTorr and 100 W radio frequency (RF) power. Subsequently, Si was etched isotropically to form the nanochannels. Here, a mixture of SF_6 (80 sccm) + Ar (80 sccm) plasma was used for 2 min, at 100 mTorr and 40 W RF power. Finally, O_2 plasma at 600 W for 7 min was used to remove the remaining PPA resist.

Atomic layer deposition (ALD) and plasma-enhanced chemical vapor deposition (PECVD)

To deposit conformal films of Al_2O_3 and SiO_2, a R-150 ALD (Picosun Sunale, Finland) and a FlexAL ALD (Oxford Instruments, United Kingdom) were used for deposition, respectively. In the Al_2O_3 deposition, we used trimethylaluminum, $Al_2(CH_3)_6$ (TMA), and H_2O as precursors, at a substrate temperature of 250°C. One cycle of Al_2O_3 ALD consisted of precursor pulsing (1 s), vacuum (3 s), Ar purging (3 s), vacuum (3 s), O_2 plasma (RF power 120 W, 7 s), and vacuum (3 s). For the ALD of SiO_2, the substrate temperature was 300°C. We used tris (dimethylamino)silane (3DMAS) and oxygen plasma as SiO_2 precursors. One cycle of SiO_2 ALD consisted of precursor pulsing (1 s), Ar pulsing (5 s), H_2O pulsing (1 s), and Ar purging (5 s). The first Al_2O_3 (10 nm) layer served as a promoting layer of ALD SiO_2 (30 nm). Following the Al_2O_3 deposition (which did not close the nanochannels) and SiO_2 deposition (which closed the nanochannels), we performed PECVD of SiO_2 (100 nm) to completely seal the seam over the nanochannels.

RIE and t-SPL maskless overlay

For the t-SPL maskless overlay, 5% PPA/anisole solution was spun on the substrate to a thickness of 89 nm, and the sample was then soft baked at 110oC for 1 min. The patterns were written into the resist to a depth of 55 nm. RIE was used to remove the PPA and SiO_2 using CHF_3 (12 sccm) + Ar (38 sccm), at 15 mTorr and 100 W RF power for ~6 min.

Photolithography, RIE and deep reactive ion etching (DRIE)

Photolithography was used to create microchannels, which provided a fluidic interface with the nanochannels. One chrome mask was fabricated using a Heidelberg DWL2000 laser writer. The device was first patterned via photolithography (Microchemicals AZ1512 resist and Süss Mask Aligner M6), and a 1.7 μm thick positive photoresist was used to design the inlet and outlet microfluidic channels of the substrate. Only the ends of the nanochannels were exposed to photolithography. After the resist development, multilayer material films under the designed pattern (SiO_2 (130 nm)/Al_2O_3 (10 nm)/SiO_2 (50 nm)/Si (~20 μm)) were etched to connect the microchannels to the end of the embedded nanochannels.

We conducted a four-step RIE process: (1) CHF_3-based RIE for SiO_2 removal using CHF_3 (12 sccm) + Ar (38 sccm), at 15 mTorr and 100 W RF for ~10 min; (2) inductively coupled plasma (ICP)-RIE for Al_2O_3 removal using BCl_3 (40 sccm) + Cl_2 (8 sccm) + Ar (2 sccm), at 6 Pa, 700 W ICP power, and 120 W RF power for ~40 s; (3) RIE using CHF_3 (12 sccm) + Ar (38 sccm), at 15 mTorr and 100 W RF power for ~4 min; and (4) DRIE for Si removal using C_4F_8 (500 sccm) + SF_6 (680 sccm), passivation layer 300 sccm for ~20 min. DRIE was used to fabricate the inlet and outlet ports of these nanochannels. [2]

Subsequently, the substrate was treated with O_2 plasma (600 W, 5 min), followed by acetone and isopropanol sonication, and again with O_2 plasma to remove the photoresist and clean the sample surface. During the device fabrication, the channel entrance was blocked a few times by the redeposition of etching by-products. Therefore, a piranha

solution (H_2SO_3:H_2O_2 3:1, at 25 ◦C) was used to remove by-products. To open the purple membrane (PM) traps, we removed the SiO_2 by CHF_3-based RIE for ~10 min. Finally, the substrate was treated again with O_2 plasma for 5 min.

Nanochannel imaging

The samples for cross sectional- scanning electron microscope (SEM) imaging were prepared on a focused ion beam (FIB)/SEM machine (Helios Nanolab 450S, FEI, Netherlands). We used the standard protocol of a FIB lift-out procedure to prepare the cross-section: the region of interest was locally covered with a protective layer of platinum and then extracted from the bulk using a micromanipulator.

Deposition of PMs

The genetic engineering of biological membrane patches is described elsewhere. [3] For a controlled positioning and deposition of individual PM patches, tunable nanofluidic confinement apparatus (TNCA) was used for the deposition of wild type (WT) PMs on the functionalized substrate. The membrane deposition is described elsewhere. [4]

Functionalization of PMs with pHrodo dye

The PM incubation (C-His_{10}-tag PM, N-His_{10}-tag PM or WT PMs) experiment with pHrodo™ iFL STP red ester dye (pHrodo, Thermo Fisher) was conducted by adding 75 µL of a 0.2 mg.mL^{-1} PM dispersion to a 1.5 mL Eppendorf tube. Subsequently, 167 µL of a 0.3 mM pHrodo solution was added. This solution comprised 5 µL of 10 mM of pHrodo dispersed in dimethyl sulfoxide (DMSO) dissolved in 163 µL of 1 mM of a $NaHCO_3$ buffer at a pH of 8.5. Finally, Milli-Q water was added to achieve a final volume of 300 µL. The material was incubated for 2 h in the dark. After the incubation, the PMs were separated by centrifugation (4000 rpm, 20 min) and washed twice with 0.1 M NaCl solution. Subsequently, PMs were centrifugated and washed ten times with Milli-Q water. The final sample volume was 50 µL, and the supernatant volume was approximately 3000 µL.

PMs were deposited on a 24 × 24 mm^2 diced glass chip with 10 nm of ALD Al_2O_3 on top using 12.5 µL of PM-pHrodo dispersion. Samples were air dried, and the substrates were then rinsed with Milli-Q water and dried with nitrogen gas.

To illustrate the functionalization of PM-pHrodo and its pumping mechanism, a droplet of Milli-Q water or a buffer solution adjusted to pH 4.0 (0.10 M acetic acid/0.02 M sodium acetate buffer) was added to the substrates. Subsequently, fluorescence measurements were conducted. PM patches functionalized with pHrodo were imaged on a Nikon Eclipse Ti inverted bright-field/fluorescence microscope CCD camera (Clara camera, ANDOR technology). TRITC (tetramethylrhodamine) filter images were captured every 30 s for 10 min, then every 20 s for 10 min, every 10 s for 10 min, and finally every 5 s for 10 min. Images were captured with an exposure time of 500 ms. During the remaining time, the chip was

in the dark. All images were taken using a 60x magnification lens. The measurement of fluorescence intensity over time for PM-pHrodo patches was conducted using ImageJ.

5.5.2 Fabrication challenges

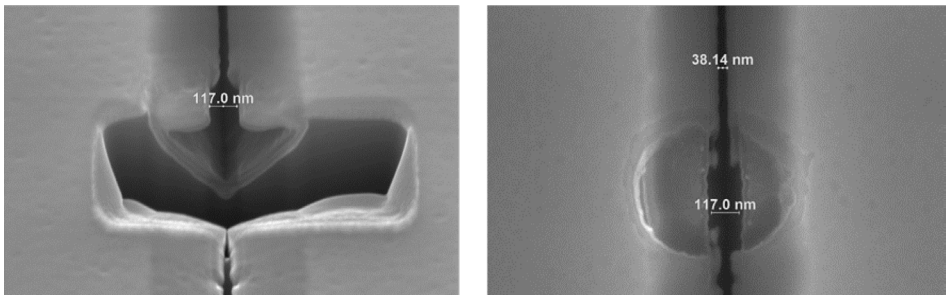

Figure S5.1. Failed sealing of nanochannels by ALD (SiO_2). The SEM tilted view image on the left shows a cross-section of the channel, and the one on the right shows the top view of the channel opening.

In our fabrication, for some devices, control over the t-SPL writing size of 50-nm lines was not always successful (step 2, Figure 5.1). An example is shown in Fig. S5.1. This device was imaged after step 20 (Figure 5.1). We observed the nanochannel being open towards the top both inside and outside the overlay area. Within the trap, the opening has a width of around 117 nm due to the thinner layer of PECVD-SiO_2 present in that area. The size of the nanochannel was self-limited by the Al_2O_3 layer, which does not etch in the presence of CHF_3, used for the SiO_2 etch. Outside the trap, the top opening has a width of around 38 nm.

Nam et al.[5] reported that the shape of channels generated by PECVD was less uniform and circular than those generated by ALD, hindering the production of sub-10-nm dimension nanochannels. When the open channel top was excessively wide after step 3 (Figure 5.1), it could still be sealed by a combination of ALD and PECVD with an adequate thickness. Therefore, the structure of buried nanochannels can be maintained by adopting a thick PECVD layer. Under these conditions, the overlay results were satisfactory.

The variations of the t-SPL writing on PPA can be attributed to the sharpness of t-SPL tips that can vary from one tip to another. Tip deterioration caused by friction and contamination during patterning and imaging depends on the tip and sample materials and affects the heat transfer from the tip to the sample. The attainable resolution generally reduces with tip use. [6]

Influence of duration of silicon etch

The influence of the duration of the silicon etch (Figure 5.1, step 4) was investigated. In Figure S5.2, SEM images showcase nanochannels fabricated with half the silicon etch

time compared to that presented in the main section (1 min etch instead of 2 min). We observed that the nanochannels obtained a circular shape (width: 235.3 nm; height: 132 nm) before ALD, with half the size achieved with a 2 min long etch (Figure 5.2). After ALD, they retained a circular shape (width: 97; height: 67 nm), equivalent to approximately 1/4 of the size achieved with a 2 min long etch (Figure 5.2). A smaller ratio between the SiO_2 opening and Si channel size can provide sub-100 nm buried nanochannels.

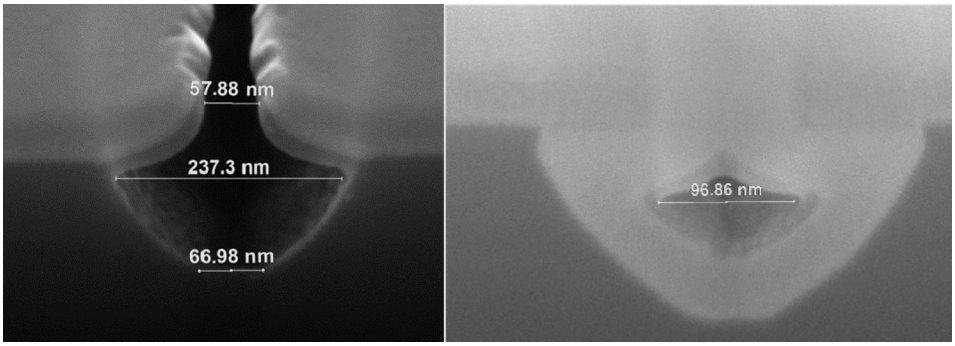

Figure S5.2. Influence of isotropic silicon etch duration on the final size of channels. The SEM image on the left shows the cross-section of the channel for 1 min Si etch time, and the image on the right shows the cross-section of the channel after ALD.

5.5.3 Proof-of-concept: filling of nanochannels

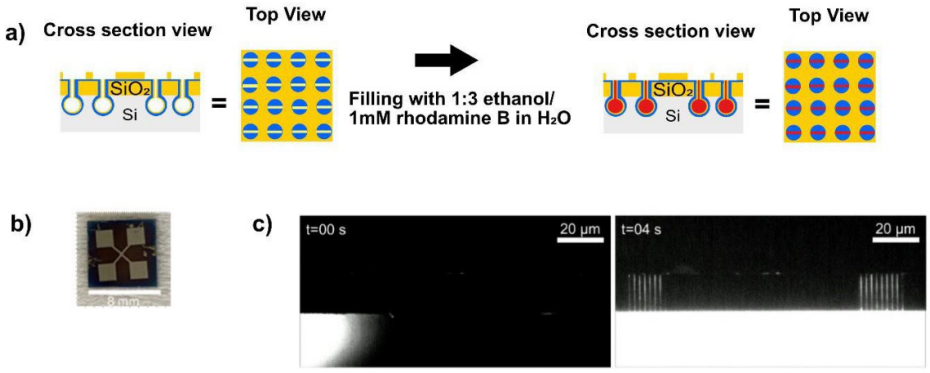

Figure S5.3. a) Scheme of experiment and device design, **b)** photo of device, **c)** fluorescence microscopic images of the device before and after channel filling. Nanochannel length: 20 µm.

We used fluorescence microscopy (FM) to prove the filling of buried nanochannels by capillary action. We observed the nanochannels from the top and filled them through inlet ports from the top to enable the upright microscope to achieve the optimal collection of fluorescent signals. Chips were cleaned by O_2 plasma to render their surface hydrophilic.

We then added a low-surface-tension liquid (ethanol) to a solution containing 1 mM of rhodamine B, a fluorescence dye. After 4.0 s, the nanochannels were filled, as shown by the fluorescence microscopy images in Figure S5.3. A TRITC filter cube was used for imaging, and images were exposed for 20 ms.

5.5.4 Deposition of functionalized PMs with dye (PM-pHrodo)

Data analysis and PM single-patch dye analysis

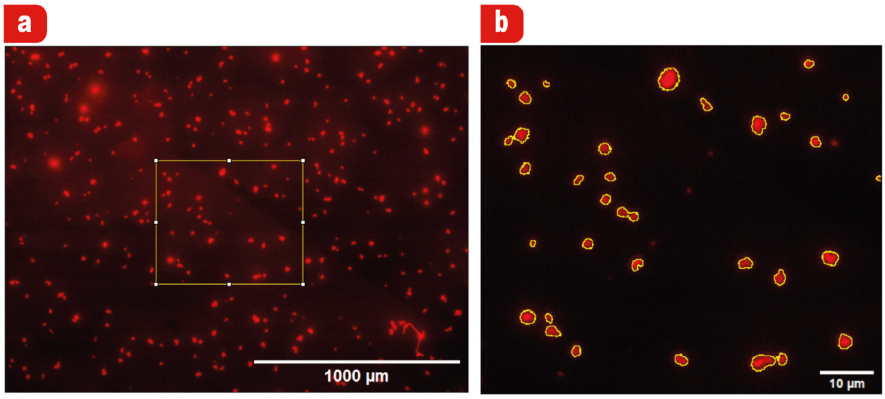

Figure S5.4. Fluorescence images showing **a)** total area of the image with the area of interest (yellow rectangle) and **b)** the cropped area of interest displayed on the right, analyzed using ImageJ.

To investigate the fluorescence intensity (FI) of PM patches functionalized with pHrodo™ iFL STP ester dye (pHrodo), we employed a macro script written in ImageJ for analyzing the FM images. The steps of this process are outlined below:

1. **Region of interest (ROI):** A specific area within an image was selected for analysis. This ROI contained between 20 to 30 PM-pHrodo patches, as exemplified in Figure S5.4.
2. **Threshold method and auto threshold function:** To analyze the images, a threshold method was chosen to distinguish PM-pHrodo patches from the background. The 'Auto Threshold' function was used to automatically set this threshold.
3. **Average signal calculation:** For each PM patch within the ROI, the FI was calculated. This step provided:
   Area count: The area (in arbitrary units (a.u.)) of patches identified.
   Average fluorescence signal (FS): The average brightness of the patches in a.u.
4. **Weighted average intensity (WAFS):** The weighted average FS (WAFS) was calculated by considering the proportion of the area of each patch relative to the total patch area. Larger patches had a greater influence on the average intensity value.
5. **Background subtraction:** To correct any background noise, the background signal was subtracted from the FI values over time.

In summary, the process involved selecting an area of interest in images, applying a

threshold to identify patches, calculating and weighting the fluorescence intensity of those patches, and then correcting the results by subtracting background noise. To calculate the background signal of the stack images, we selected 3 to 4 regions that were free of PMs. We then measured and averaged the intensity of these regions over time.

Figure S5.5 illustrates the variation in FI over time in the neutral non-buffered medium (MiliQ water, pH 7.0). Figure S5.6 represents the background-corrected ratio FI over time in the neutral non-buffered medium. Figure S5.7 illustrates variation in FI over time in the acidic buffered medium (pH 4.0). The shown data at Figure S5.5 and Figure S5.7 incorporates both the weighted average signal from PM patches and the value from areas without PMs (background).

For all PM types in all mediums, we observed lower FI signals from the background compared to the PM. We also observed background values decreased over time, indicating that pHrodo was exclusively attached to the PM surface. Furthermore, an increase in PM FI over time was noted, demonstrating detectable pumping activity under these conditions. Figure S5.6 shows that over time, C-His_{10}-tag PM exhibits the highest BCRFI values, closely followed by N-His_{10}-tag PM. Given the inverse relationship between BCRFI and pH, this suggests that C-His_{10}-tag PM corresponds to lower pH values.

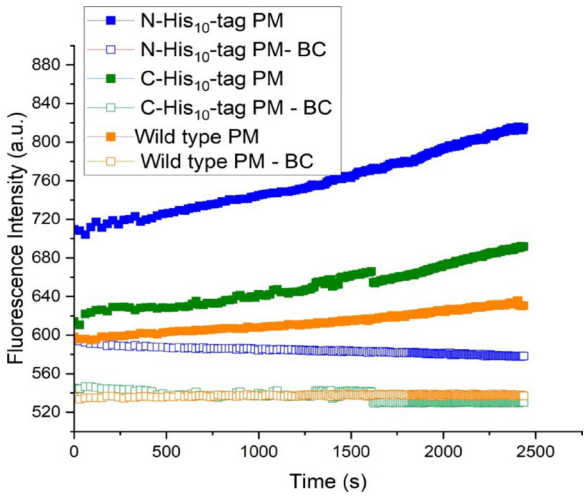

Figure S5.5. FI of PM functionalized with pHrodo over time in Milli-Q water (pH 7.0). Data were obtained with 500 ms exposure time images using a TRITC filter and a 60x objective lens. Orange: wild-type PM. Green: C-His_{10}-tag- PM. Blue: N-His_{10}-tag-PM. Square: FI of PM area. Empty square: background intensity.

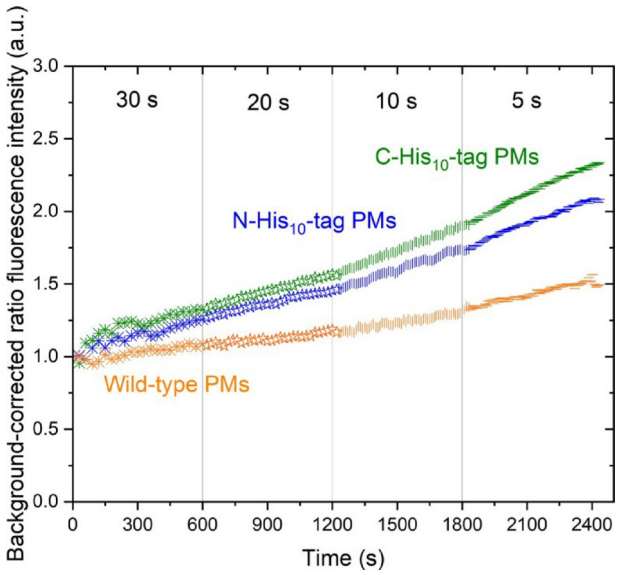

Figure S5.6. Background-corrected ratio Fluorescence intensity (BCRFI) of PM functionalized with pHrodo over time in Milli-Q water (pH 7.0). Data were obtained with 500 ms exposure time images using a TRITC filter and a 60x objective lens. Orange: wild-type PM. Green: C-His_{10}-tag- PM. Blue: N-His_{10}-tag-PM.

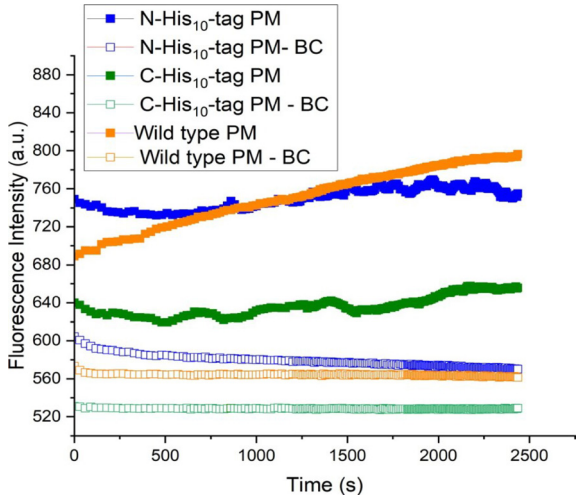

Figure S5.7. FI of PM functionalized with pHrodo over time in a pH 4 buffer. Data were obtained with 500 ms exposure time images using a TRITC filter and 60x objective lens. Orange: wild-type PM. Green: C-His_{10}-tag- PM. Blue: N-His_{10}-tag-PM. Square: FI of PM area. Empty square: background intensity.

pH measurement of PM-pHrodo patches in an acidic buffered medium

The study presented in Table S5.1 aimed to measure pH values for WT PMs in a buffered acidic medium using Equation (1) (main text). The results in Table S5.1 show variations

in background-corrected FI (BCFI) and BCRFI among different PM types and provide pH values. These measurements were based on a reference BCFI ($I_{pHrodo7}$ = 62.7 a.u.) obtained from neutral, non-buffered medium data (Figure 5.8 and Table 5.2). We can rely on this reference value because the PM patches, prior to pHrodo functionalization, were initially stored in non-buffered Milli-Q water, suggesting that the optimal PM-pHrodo reference value was established under these conditions. However, the results are preliminary due to uncertainty about whether the initial pH (t=0) for the buffered acidic medium data (Figure 5.9) was indeed around pH 4.0 or not. In our calculations, we did not account for the initial pH of the PM-pHrodo patches were 4.0.

The C-His_{10}-tag PM type reached a final pH value of approximately 5.6, while the N-His_{10}-tag PM type exhibited a final pH value of 5.8, both lower than those observed in neutral non-buffered medium. However, the final pH for WT PMs decreased by approximately 2.9 units to 2.7, significantly more acidic than at pH 7.0. This indicates that the pumping activity of WT PMs is more pronounced under acidic conditions, likely due to the surplus of protons in the medium.

Table S5.1. Background-corrected fluorescence intensity (BCFI), background-corrected ratio fluorescence intensity (BCRFI) and calculated pH from time-lapse measurements of PM-pHrodo patches at buffered acidic medium (pH 4.0). The pH values were obtained from the fluorescent intensity applied to Equation (1).

	C-His_{10}-tag PMs			N-His_{10}-tag PMs			Wild-type PMs		
Time (s)	**BCFI**	**BCRFI**	**pH**	**BCFI**	**BCRFI**	**pH**	**BCFI**	**BCRFI**	**pH**
0	109.0	1.57	6.06	144.9	1.39	6.32	115.4	1.84	5.63
600	97.3	1.41	6.30	150.3	1.44	6.24	160.8	2.57	4.50
900	95.1	1.37	6.35	158.6	1.52	6.11	175.2	2.80	4.13
1200	108.2	1.56	6.07	167.9	1.61	5.98	185.3	2.96	3.88
1500	105.6	1.53	6.14	184.5	1.77	5.73	201.0	3.2	3.49
1800	110.6	1.60	6.00	184.0	1.77	5.74	212.4	3.38	3.21
2100	126.2	1.82	5.65	192.8	1.86	5.60	225.8	3.60	2.88
2400	126.8	1.83	5.64	180.0	1.73	5.79	232.1	3.70	2.72

Linear regression of pHrodo™ iFL STP ester red dye

To derive a formula correlating pH with the FI from pHrodo, we utilized a dataset reported by Dolman et al. [7] and conducted a linear regression analysis, as depicted in Fig. S5.8. In this dataset, we calculated the relative intensities at each pH (RI_{pHrodo}) and normalized them by dividing them by the relative intensity at pH 7.0, $RI_{pHrodo7}$. The regression achieved a coefficient of determination of 0.99.

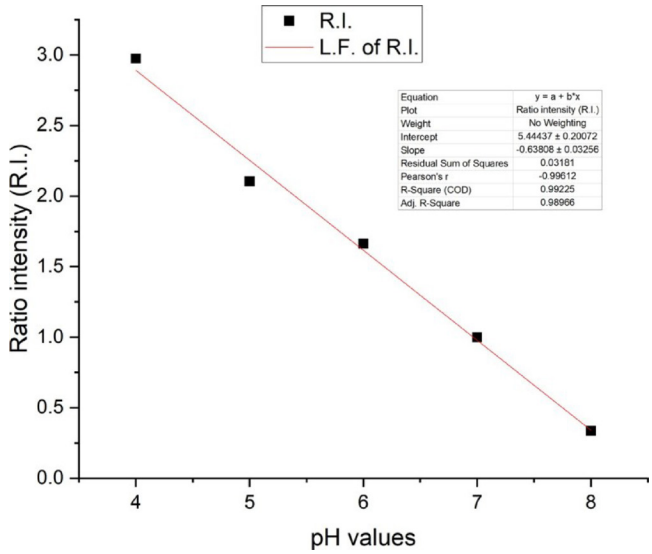

Figure S5.8. Linear regression (L.F.) of pHrodo iFL STP ester red, calculated from data presented at Dolman et al. [7]

5.5.5 Other device applications

We designed another device aiming to fabricate 25 µm deep microreservoir networks below photolithographic magnification with a precise overlay of microreservoirs. The fabrication strategy is shown in Figure S5.9. The length of the microreservoirs varied from 2 to 10 µm, and they were localized on the buried channels. Deep microreservoirs and inlet and outlet channels were etched simultaneously. The maskless overlay was achieved by t-SPL.

As shown in Figure S5.10, the fabrication process for the microreactor network device was inspired by that used for the PM trap device shown in Figure 5.1. In the microreactor network device, the SiO_2 PECVD layer served as a protective coating during the DRIE. The photolithography resist was removed before the DRIE step (step 16, Figure S5.9). Moreover, only ALD SiO_2 was used to close the nanochannels, with the intention of completely exposing the channel in the reactor area during subsequent fabrication stages (step 5, Figure S5.9). A thicker layer of PECVD SiO_2 was deposited on the device (step 6, Figure S5.9), and this layer subsequently functioned as a protective barrier for the buried channels during the DRIE etching. The results indicate that the fabrication approach involving buried nanochannels, elaborately described in Figure 5.1, can be extended to various systems and applications. Following fabrication, we introduced a 500 µm thick glass layer for anodic bonding (step 20, Figure S5.9) to fill the channels using vacuum. The channels were then filled with a 1 mM rhodamine B solution, as evidenced by fluorescence microscopy (Figure S5.11).

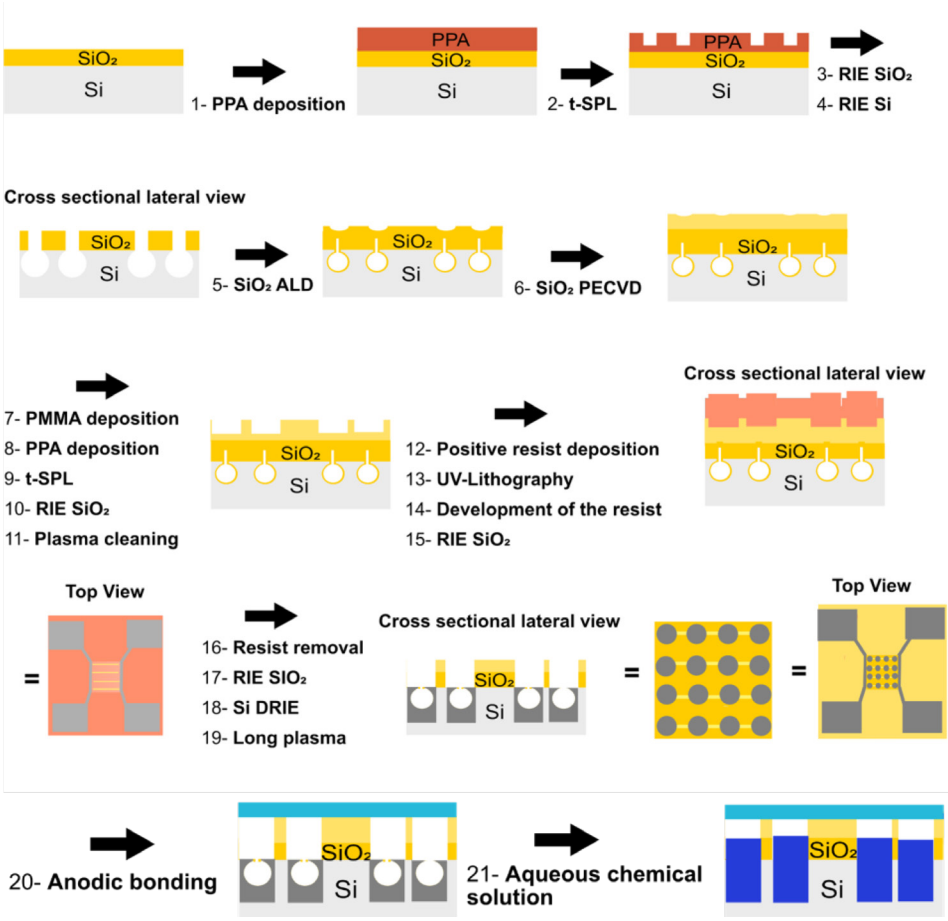

Figure S5.9. Fabrication of microreactor network device. Steps 1 to 4: Fabrication of nanochannels by t-SPL. Step 5: Closure of t-SPL channels by ALD. Steps 6 to 11: Design of microreservoirs by t-SPL. Steps 12 to 15: Fabrication of microchannels and macroreservoirs by photolithography. Steps 16 to 19: Opening of nanochannels on microreservoir area. Steps 20 and 21: Filling of channels with liquid. PPA = Polyphthalaldehyde; t-SPL = thermal scanning probe lithography; RIE = reactive ion etching; ALD = atomic layer deposition; PECVD = plasma- enhanced chemical vapor deposition.

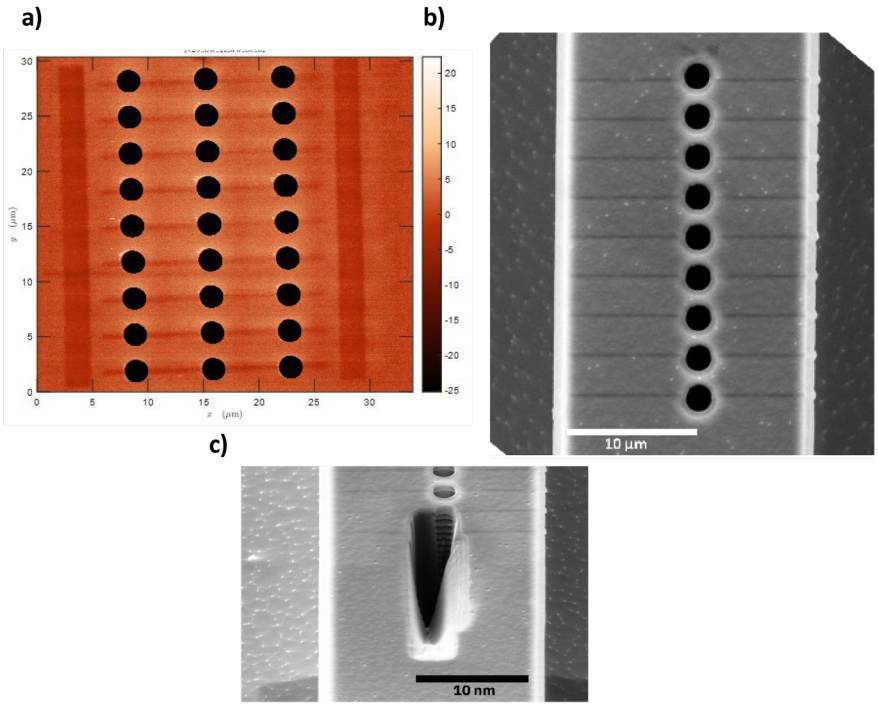

Figure S5.10. a) t-SPL image of maskless overlay pattern. Scale bars indicate writing depth in nanometers. SEM image of **b)** top view of final device, and **c)** FIB cross-section of overlay structure on nanochannels

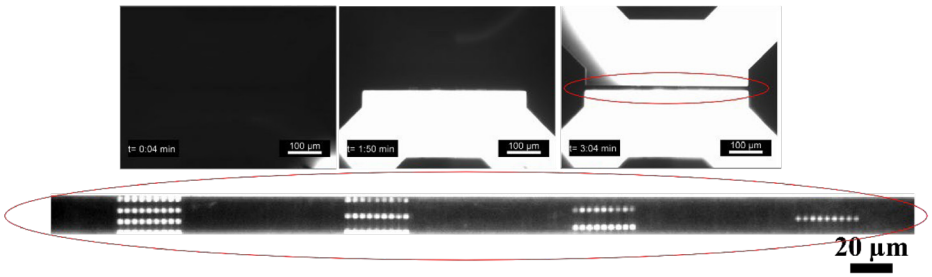

Figure S5.11. Sequence of fluorescence microscopic images of the device before and after channel filling. Nanochannel length: 20 µm. Reservoir depth: 20 µm.

5.5.6 References

(1) Paul, P. C.; Knoll, A. W.; Holzner, F.; Despont, M.; Duerig, U. Rapid Turnaround Scanning Probe Nanolithography. *Nanotechnology* **2011**, 2 2 (27), 275306.

(2) Wu, C.; Jin, Z.; Wang, H.; Ma, H.; Wang, Y. Design and Fabrication of a Nanofluidic Channel by

Selective Thermal Oxidation and Etching Back of Silicon Dioxide Made on a Silicon Substrate. J. *Micromechanics Microengineering* **2007**, 17 (12), 2393.

(3) Stauffer, M.; Hirschi, S.; Ucurum, Z.; Harder, D.; Schlesinger, R.; Fotiadis, D. Engineering and Production of the Light-Driven Proton Pump Bacteriorhodopsin in 2D Crystals for Basic Research and Applied Technologies. *Methods Protoc.* **2020**, 3 (3), 51.

(4) Ruggeri, F.; Schwemmer, C.; Stauffer, M.; Nicollier, P. M.; Figueiredo da Silva, J.; Bosshart, P. D.; Kochems, K.; Fotiadis, D.; Knoll, A.; Wolf, H. Placement of Biological Membrane Patches in a Nanofluidic Gap With Control Over Position and Orientation. Adv. Mater. *Interfaces* **2022**, 9 (23), 2200941.

(5) Nam, S.-W.; Lee, M.-H.; Lee, S.-H.; Lee, D.-J.; Rossnagel, S. M.; Kim, K.-B. Sub-10-Nm Nanochannels by Self-Sealing and Self-Limiting Atomic Layer Deposition. *Nano Lett.* **2010**, 10 (9), 3324–3329.

(6) Howell, S. T.; Grushina, A.; Holzner, F.; Brugger, J. Thermal Scanning Probe Lithography—A Review. Microsyst. *Nanoeng.* **2020**, 6 (1), 1–24.

(7) Dolman, N. J.; Kilgore, J. A.; Davidson, M. W. A Review of Reagents for Fluorescence Microscopy of Cellular Compartments and Structures, Part I: BacMam Labeling and Reagents for Vesicular Structures. *Curr. Protoc. Cytom.* **2013**, 65 (1), 12.30. 1-12.30. 27.

Chapter 6

Networks of microscale chemical oscillators - toward chemical computing

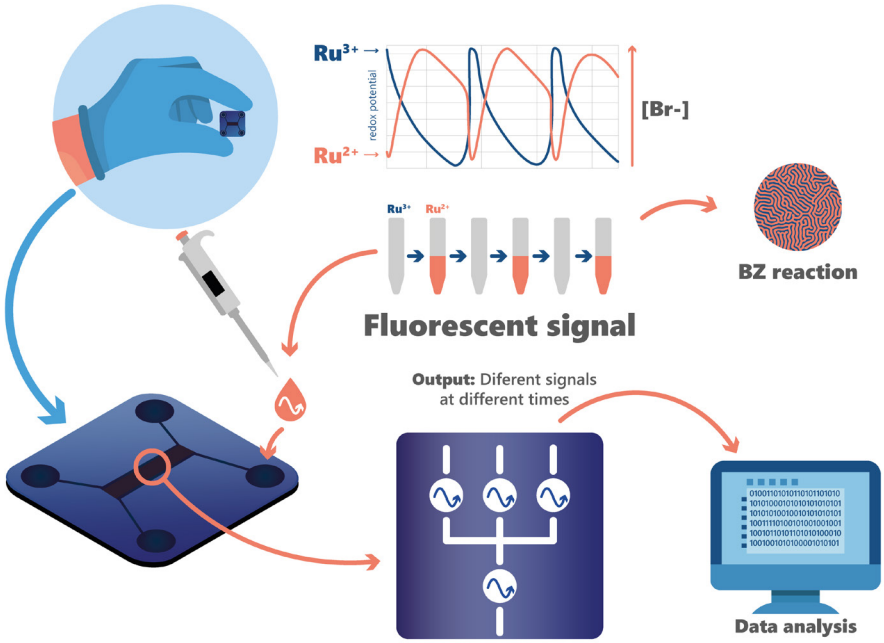

Abstract: This chapter explores the development of chemical computers (CCs) based on information processing by an oscillatory reaction in microscale compartments. We designed and fabricated a diffusion-driven network comprising several sub-100 µm silicon-based microchemical reactors (MCRs) connected by nanofluidic channels. We employed the Belousov–Zhabotinsky (BZ) reaction as oscillatory chemistry in the MCRs. The catalyst of the BZ reaction enabled the visualization of oscillations by fluorescence microscopy. We demonstrated the diffusion-related coupling and synchronization of MCRs. The connecting channels mediated the coupling between compartments, which led to synchronization, an important step in data processing. The results represent an important foundation for the development of scalable chemical computing architectures based on simple molecules.

6.1 Introduction

6.1.1 Unconventional computing

Digital computers execute programmed arithmetic and logical operations and consist of two main components: (1) hardware, the physical elements such as screens, keyboards, and printers that perform tasks as directed by software; and (2) software, the intangible programs and data that provide instructions to the hardware, written in languages like Python or C++ and stored digitally. [1]

As illustrated in Figure 6.1, a computer comprises five primary components: (1) input, where data is received; (2) processing, carried out by the central processing unit (CPU), which includes registers for temporary storage and combinational logic for operations; (3) storage (main memory), used to retain information; (4) the control unit, which manages resources and coordinates hardware and software activities; and (5) output, where results are communicated. These components function through algorithms and binary code (0 and 1), executed via electrical signals within the hardware. [1]

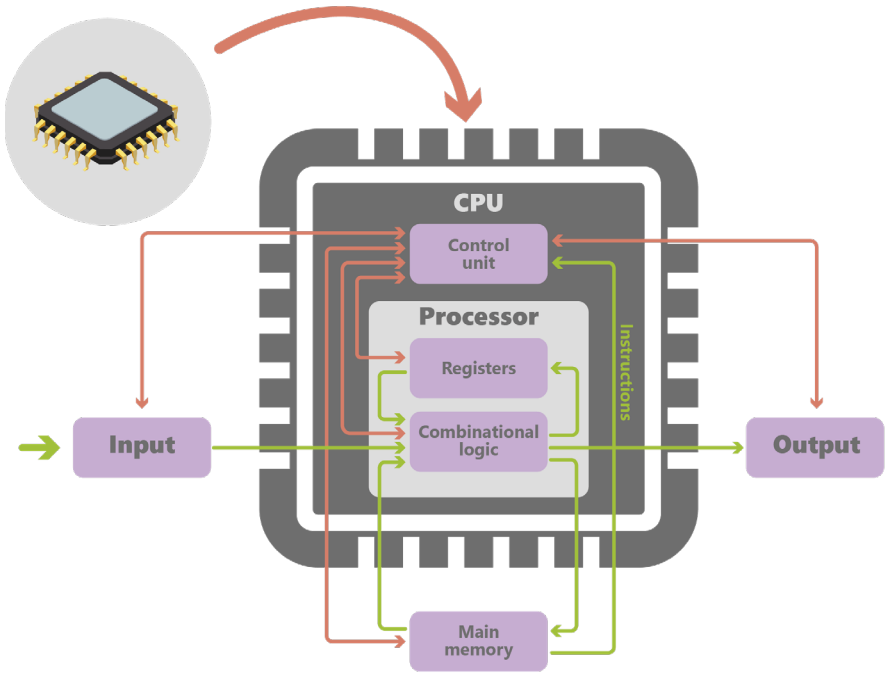

Figure 6.1. Block diagram of a basic computer with a uniprocessor central processing unit (CPU).

Semiconductor technology, primarily based on silicon devices, forms the backbone of modern electronics, including digital computers. [2] Its effectiveness in machine information

processing is primarily attributed to the creation of numerous highly reliable logic gates, which execute logical operations on binary inputs to generate an output. [3] These gates, operated by programmable software, offer extended error-free functionality and can be scaled down to the nanoscale. [2] When integrated into circuits, they enable more complex information processing functions.

Moore's law asserts that the complexity of circuits, and consequently their functionality, doubles in under two years.[2] Undoubtedly, the semiconductor industry has consistently pushed the boundaries to incorporate more transistors onto increasingly compact chips, a trend evident in the evolution of smartphones and microsensors. Additionally, multiprocessor computers have been available for several years, they have reached massive parallelism, which is supposed to solve complex problems. However, the sustained adherence to Moore's Law faces inevitable obstacles. These challenges arise from both physical constraints, such as quantum effects and heat dissipation, and the escalating costs associated with the continuous increase in transistor count on microchips. [2] Furthermore, both data generation and the demand for computing are growing exponentially over time, even more with the development of artificial intelligence (AI). To address the growing demands for computational power, there is a critical need to create new computing primitives, encompassing both hardware and algorithms.

The concept of AI stems from the notion that computers can replicate specific learning abilities akin to those of the human brain. [4] The brain outperforms standard computers in energy efficiency, adaptability, and pattern recognition. It uses minimal power, processes analog signals, [5] and adapts through plasticity. [2] Key features include neurons for signal transmission, synapses for chemical communication, and integrated computation that enables multitasking and collaboration across brain regions. [4] For instance, Microsoft has developed a device that operates according to the principles underlying networks of spiking neurons. The power consumption of this device was roughly four orders of magnitude lower than that of a conventional computer. [6] Therefore, there is high motivation for the development of alternative computing methods that can mimic the brain's functionality. [2]

Unconventional computation (UC) represents a specialized field within interdisciplinary science, and it blends elements of chemistry, physics, mathematics, computer science, nanotechnology, among others. The goal of UC is to reveal and leverage rules and methods that link functional properties with information processing across physical, chemical, and biological systems. This includes designing optimal architectures, developing efficient algorithms, and creating functional prototypes for future-proof computing devices. [7] In a UC, computation occurs when the system is stimulated with input signals, such as oscillations, grounded in coupled oscillator systems across different length scales. UC views the natural progression of time within a spatially distributed environment, the temporal evolution across all regions occurs concurrently, and the algorithms executed are typically characterized by high levels of parallelism. To improve computation through parallelism, a new computing device may incorporate millions or billions of oscillatory units, which must satisfy strict requirements, including low power consumption, high frequency,

programmability, and energy-efficient readout capabilities. Nevertheless, only a limited number of oscillators can meet these specified requirements. [2]

Reaction-diffusion computation based on chemistry-driven devices, also known as chemical computers (CCs), has the potential to fulfill some of these criteria. Chemical computing can be founded on information processing through nonlinear oscillatory chemical reaction networks (CRNs). Chemical substrates have proven effective in implementing computations, [8] making CCs an important category of unconventional computers.

6.1.2 Chemical computing

A chemical computer (CC) is a liquid-based device that executes logical operations through chemical reactions. In a CC, the computation state is defined by the 'collective state' of molecules, determined by their properties and interactions. [9] The key feature of a CC is the spontaneous motion of molecules. In principle, after a CC system is prepared, it does not require external power to operate, except for the thermodynamic necessity of functioning at a finite (room) temperature. This means the system evolves autonomously, without the need for an external influence or explicit wiring. [10]

"CCs" can be observed in nature, such as in the human neural network and in chemical communication, synchronization, and collective behavior among cell colonies. These processes occur through the emission, interdiffusion, and reception of specific messenger molecules, all with minimal energy consumption. [11,12] To emulate nature by developing an 'information processing' system that converts information encoded in reagent concentrations, one approach is to utilize a chemical medium exhibiting highly nonlinear oscillatory behavior, which can integrate incoming signals in a complex way. The next step is to identify non-equilibrium conditions that allow the medium to self-organize into a structure suitable for information processing, such as a product concentration that fluctuates over time. Lastly, factors that alter interactions within the medium, such as introducing additional chemicals or changing reagent concentrations, can be applied to facilitate the learning process, such as the addition of another chemical or the change of concentration of some reagent. In other words, the mechanism which molecular interactions encode and execute algorithms should be clarified. [13] The Belousov–Zhabotinsky (BZ) reaction can be used to match part of these requisites. [14]

6.1.3 Belousov–Zhabotinsky reaction

The BZ reaction is a well-established chemical oscillator, and its mechanism is governed by the interaction between activators and inhibitory feedback loops, and it can generate periodic chemical signals. The BZ reaction is based on the oxidation of an organic compound by bromic acid ($HBrO_3$) [15] mediated by a transition-metal catalyst in an acidic aqueous solution. [16] The BZ reaction consists of two stages: (1) a rapid autocatalytic oxidation of the catalyst by bromate (BrO^-), and (2) a slower reduction of the catalyst by an organic compound, usually malonic acid (MA). During oscillations, the catalyst switches between

two oxidation states that offer several readout possibilities, including color, fluorescence, and redox potential. Moreover, these oscillations can be detected by changes in bromide (Br^-) concentration and/or pH. [15] In the BZ reaction, the intermediate Br^- ion has a crucial function because the system state depends on its concentration. [17] If its concentration surpasses a critical concentration, the catalyst predominantly exists in its reduced state. Conversely, if the Br^- concentration falls below a critical level, an autocatalytic process initiates the production of the activator, $HBrO_2$, and the catalyst switches to its oxidized state. Biochemical oscillators model chemical information [18,19], but are hard to interpret due to complex dynamics. In contrast, the well-understood BZ reaction has documented rate constants.[20] Even though these oscillators have inherent oscillations, external stimuli can modify their phase [11] and amplitude. [21,22]

The oscillation period of a BZ system typically is several tens of seconds (s), [20] which is suboptimal for conventional computation, as the latter operates at significantly higher speeds. Accordingly, researchers have aimed to decrease the BZ oscillation period. A previous study reported that, under specific conditions, changes in temperature and concentration increased the frequency of BZ oscillations by 3–4 orders of magnitude. [23] The BZ reaction exhibited sinusoidal oscillations at elevated temperatures and high concentrations, at frequency of 10 Hz or greater. The study documented the system's complex temporal behavior and proposed pathways for achieving higher frequencies.[23] Another study showed that the frequency cannot increase exponentially, as oscillations eventually cease when the temperature reaches a critical value. [24]

Electrons are faster than ions, and electronic currents outpace chemical diffusion. Electrons are >100,000 times lighter than the atom nucleus, and they travel close to the speed of light. Diffusion is more substantial initially and decays over distance because of its stochastic nature. [25] Then, the potentially high oscillatory speed of BZ reaction is not the central stimulus for creating a BZ driven CC. Instead, the brain's primary functions can be chemically replicated using the BZ reaction with low energy consumption, including (1) nonlinear dynamics and oscillations that forms the basis for simulating processes such as pattern recognition, memory or even decision making; (2) self-organization into evolving dynamic structures or patterns; (3) parallel processing, as the BZ reaction can carry out multiple reactions at once without interference; and (4) information encoding, with the BZ reaction using oscillatory behaviour and chemical interactions to encode information. [26] The interaction between two chemical oscillators can occur through either diffusive coupling or long-range interactions. Long- range interactions, in particular, can be facilitated by mechanisms such as mass exchange regulated by peristaltic pumps, [21] or light pulses. [21,26]

The photosensitive BZ reaction, often catalyzed by $Ru(bpy)_3^{2+}$, is commonly employed to investigate the effects of external perturbations due to its unique photochemical and photophysical properties.[27,28] Variations in both oscillatory period and amplitude have been noted in relation to the applied light intensity. [20] Due to that, light can serve as an attractive alternative input to electricity in our system, as it enables selective and rapid modulation of reaction rates in the BZ reaction. However, an increase in light intensity causes a transition

from large-amplitude periodic oscillations to stable steady states, a phenomenon known as photoinhibition, which limits the use of light for extended durations and high intensities. [20]

Advances have been recently reported towards the use of BZ reaction in information processing [26,29] At the macro scale, researchers have reported a language-recognizing Turing machine based on the addition of aliquots of BZ reagents in a one-pot reactor. [29] Another example features a programmable BZ-based chemical processor in a fluidically-connected reaction array of cells. [30,31] In theoretical study, classification tasks were successfully performed with a reasonable degree of accuracy by training a network of interacting chemical oscillators. [32] However, large reaction volumes require external forces, such as stirring, as diffusion alone cannot ensure uniform molecular distribution. These volumes also demand greater quantities of reactants and result in longer diffusion times, leading to slower computation and reduced energy efficiency, as more chemicals are required per unit of ´processed information´. To address these challenges, the miniaturization of chemical systems has been proposed. [26,33] Microscale systems offer advantages such as faster diffusion, energy efficiency, parallel operations, and enhanced capabilities for complex communication.

6.1.4 Microfluidics for chemical communication

In chemical communication, microfluidic platforms are beneficial for the generation of diffusive-driven reproducible geometrically homogeneous systems and reactors with precisely chemical composition and determined dimensions, all of which can act as microchemical reactors (MCRs). A MCR network comprises microscale reactors (tens to hundreds of microns) housing oscillatory CRNs, such as the BZ reaction. These reactors can communicate by diffusing reaction intermediates, facilitating the spatiotemporal transmission of chemical "information." This process ultimately gives rise to collective behaviors, including coupling and synchronization, which hold potential for advancing complex communication networks. [20]

Studies have demonstrated that networks of chemical micro-oscillators can execute logical operations like AND and OR, [21,34] recognize patterns, make decisions, [35,36] and, in certain cases, exhibit adaptive behavior by responding to external signals. [21,37] Individual compartments can be designed with tailored properties, such as surfactants for emulsions micro-droplets [11] or tailored membranes for liposomes and microspheres. [21,38] However, their multidirectional diffusive interactions and inability to replenish reactants limit functionality. Additionally, in microspheres, ion-exchange resin may degrade under BZ conditions due to oxidation and polymer cross-link rupture.[21]

To enhance the robustness of MCR networks, channels precisely defining diffusive coupling pathways between individual compartments have been used to connect MCRs. Previous study achieved this by arranging MCRs through lithography. [39] Earlier research has demonstrated that wave interactions with complex boundaries support the implementation of path optimization at the microscopic scale. [40] Previous simulation

studies have similarly demonstrated that the geometry of the interconnecting channels between MCRs exerts a greater influence on wave speed and diffusion than the channels' material composition. [41] Further examples of BZ-based chemical micro-oscillators were discussed in a previous review. [21] However, high parallelism and complex synchronization continue to pose limitations. To advance BZ- MCR networks, improvements in the design of the reaction medium are needed. [16] Additionally, the exploration of MCR network architectures with directional diffusive coupling between MCRs is lacking. Difficulties include fabrication strategies, along with the visualization and control of input chemical signals in MCR networks.

To advance the development of a BZ-driven chemical computer, we employed silicon-based chips housing MCR networks with units ranging from tens of microns, containing up to 6000 MCR units. Oscillation visualization was performed with fluorescence microscopy (FM), and wave transmission occurred primarily through diffusion, without the need for electricity or fluidic flow. Our results demonstrate that BZ-MCRs enable high parallelism and complex communication at the microscale, while requiring a minimal amount of reactants. This approach could represent a step toward a BZ-MCR network into a miniature device powered entirely by chemical fuel for chemical computation.

6.2 Results and discussion

Fabricating a chemical medium for thousands of MCRs for long-term operation is complex. Practical CCs require MCR networks with well-defined initial conditions, reliable oscillatory states, and sustained dynamics. The network developed in this study consisted of MCRs connected by nanofluidic channels of varying interconnections and sizes, all containing the same concentration of BZ-CRN reactants. Long-range chemical communication occurred between MCRs over micrometer distances. The study of this phenomenon relies on three main features, namely (1) the use of microfluidics to compartmentalize 'chemical information', (2) stable emission of periodic chemical signals within compartments via the BZ reaction, and (3) appropriate spatiotemporal monitoring of the emitted chemical signals. [38] The input consisted of the initial concentration of BZ reactants and, in certain cases, wave propagation from the microfluidic channels. The output was determined by analyzing the period of oscillations observed in selected MCRs. The transmission of signals through the propagation of waves was propelled by the diffusion of Br_2 and autocatalytic species $HBrO_2$. [20,21] In Section 6.2.1, we discussed the photolithographic fabrication of the BZ-MCR network and how the experiment was executed.

6.2.1 Device fabrication

Silicon, widely used in the semiconductor industry, provides a stable and inert platform for supporting oscillatory BZ reaction. [42] Polydimethylsiloxane (PDMS)-based microfluidic devices, a widely used material in microfluidics, are unsuitable for this study because bromine produced by the BZ reaction is absorbed by PDMS, significantly disrupting oscillatory behavior. [39,41,42] We fabricated miniaturized BZ-MCR networks on silicon using a

two-step photolithography process, as shown in Figure 6.2. The first step was the definition of nanofluidic channels to connect MCRs designed via photolithography (1.5 µm width) and etched (500 nm deep) by inductively coupled plasma– reactive ion etching (ICP–RIE), which provide anisotropic Si etch with smooth walls. [43] The second step was the definition of microfluidic channels (inlet, outlet, and bypass channels) and MCRs (Figure 6.3), which have circular designs with diameters from 5 to 30 µm. MCRs and microfluidic channels were anisotropically etched to a 20 µm depth by deep RIE, which is known as the Bosch process. [44] The bypass channel was designed to extend the duration of oscillations and provide continuous chemical filling in the device. This approach allowed for the precise design of the geometry and size of the MCR networks, the integration of nanofluidic channels with the MCRs, and the creation of distinct feeding channels for fresh reactants and removal of reaction products. To enable the filling of the microfluidic chips by pressure after fabrication on a silicon wafer, we anodically bonded a 500 µm thick glass wafer containing 0.7 mm holes at specific positions. Finally, we diced individual microfluidic chips from the wafer. An image of the chip is shown in Figure 6.3.

The experiment was conducted as follows: first, we pre-filled the microfluidic system with CO_2 at high pressure to prevent air trapping. [45] The microfluidic chip was subsequently installed in the microscope. Following this, all BZ compounds were mixed, and once the first oscillation was observed, the chip was filled with BZ reaction under high pressure. This process enabled the rapid filling of a thousand MCRs and nanochannels, which was monitored in situ via FM. FM measurements were initiated once the filling process was complete. In the experiments conducted, we observed the MCR networks filled with BZ reactants by monitoring the propagation of waves through time-lapse fluorescence images. The process was operated in batch mode, with no continuous or additional input of chemicals after the initial filling of MCRs. For FM measurements, samples were exposed to short light pulses (400 ms) every 1 s. Until the end of this thesis, we could not explore the refilling of our device using bypass channel.

In our experiments, the catalyst of the BZ reaction was a ruthenium bipyridyl complex, $Ru(bpy)_3^{2+}$, which enabled the visualization of oscillations by FM. The Ru complex fluoresces only in the Ru^{2+} state, and it is dark in the Ru^{3+} state. The maximum $Ru(bpy)^{2+}$ absorption occurs at 480 nm. [26] The maximum emission of $Ru(bpy)^{2+}$ occurs at 675 nm. [27] Therefore, the BZ $Ru(bpy)^{2+}$-catalyzed solution periodically fluoresced bright orange when irradiated with blue light, with a high quantum yield and long lifetime. [27] Notably, an intensively illuminated BZ medium typically does not oscillate, as light inhibits oscillations. Under identical initial reagent concentrations, a medium that exhibits oscillatory behavior in darkness transitions to an excitable state under low light intensity and stabilizes into a steady state under strong illumination [27] For this reason, the sample was exposed to light in short pulses during measurement. The light intensity was sufficient to induce fluorescence in the illuminated MCRs while remaining weak enough to preserve periodic oscillations in the MCRs.

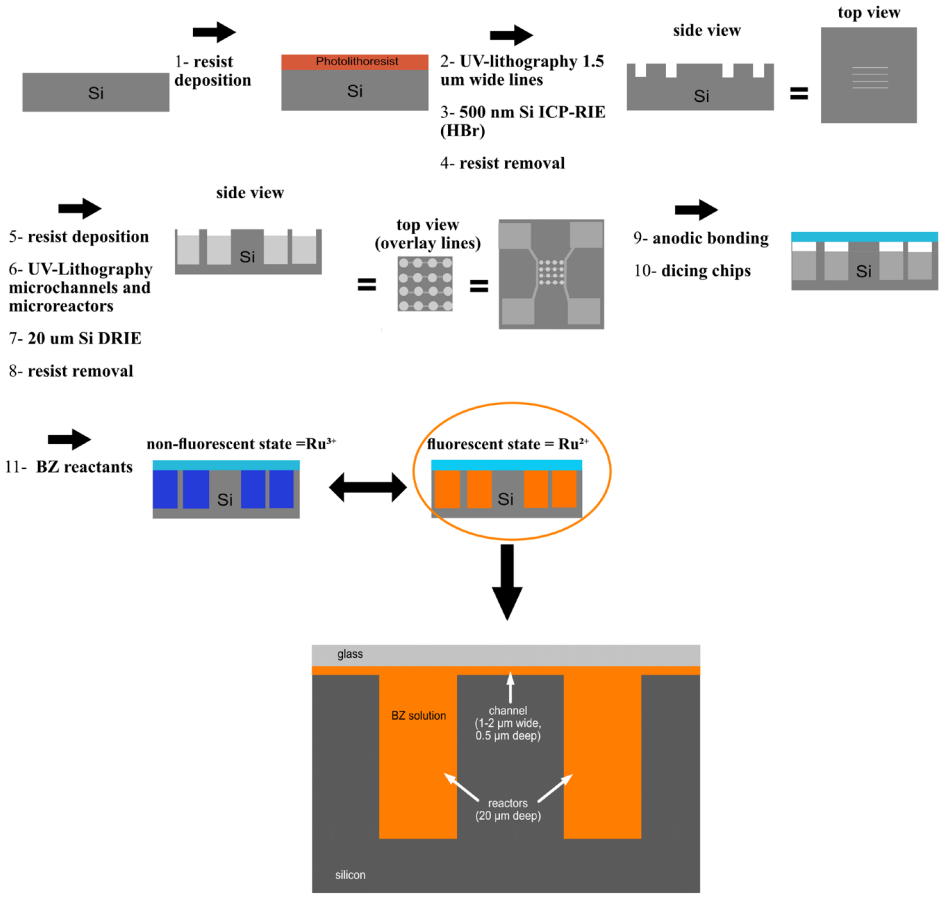

Figure 6.2. Steps for fabrication of BZ-MCR networks. Two photolithographic steps and anodic bonding were conducted at the wafer scale. In the first step, a network of nanochannels was formed. The microreactors, filling, and waste channels were prepared in the second step. RIE = reactive ion etching; ICP–RIE = inductively coupled plasma–RIE; DRIE = deep RIE.

Figure 6.4 illustrates that over 3000 MCRs with diameters ranging from 5 to 15 µm oscillated simultaneously, with the chip housing around 6000 MCRs in total. A mere 3 µL of low-cost reagents sustained the BZ-MCR network, demonstrating the device's reliability, parallelism, and low energy consumption. Fluorescence signals were detected only from MCRs and microfluidic channels, while nanochannels, with a 40-fold shallower depth, exhibited weak fluorescence and were used solely for chemical transport and MCR filling. The discrete nature of the wave's propagation between MCRs and channels was visualized. After the passage of a wavefront, the medium nearly returned to its original state. A trigger wave initiated from the inlet channel led to the formation of a wave along nanochannel-

connected MCRs. Signal offsets in neighboring MCRs reflected variations in oscillator rates and couplings, influenced by distance and size. The amplitude of oscillations slowly decreased over time, ceasing after approximately 50 minutes as the system reached equilibrium. Multiple inputs from waves in the microfluidic channels resulted in outputs—signals in the MCRs— dependent on the geometrical configuration and BZ concentration in each MCR over time. These findings underscore the challenge of optimizing parameters for such "computation" while highlighting the system's robustness in handling multiple wave transmissions simultaneously.

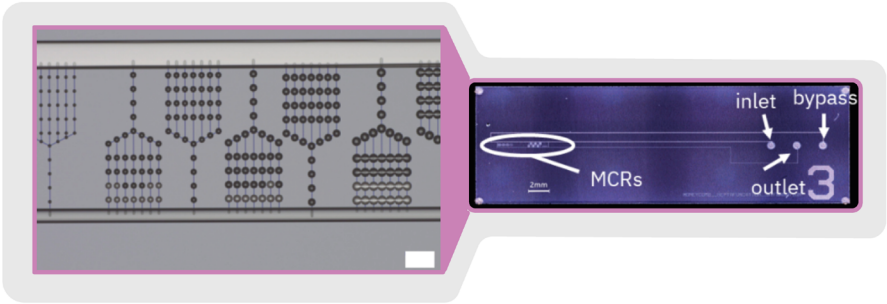

Figure 6.3. The bright-field image on the left shows part of the MCR network during the filling. The scale bar represents 100 µm. The bright-field image on the right shows a 36 × 12 mm chip after step 10 (Figure 6.2). The openings of inlet, outlet, and bypass channels are shown. The scale bar represents 2 mm.

We demonstrated that (1) FM can effectively visualize MCR networks in light-sensitive chemical excitable media; (2) our system enables the design of complex networks of interlinked oscillations with arbitrary arrangements; (3) the CRN operated on chemical waves as a small, chemically driven network without requiring electricity; (4) our BZ- MCR network exhibited significant complexity, enhanced by the increased number of MCRs; (5) the wave transmission time between MCRs on the same line did not affect the wave traveling time between MCRs on other lines, as all operations occurred in parallel. From these statements, we propose that complex information processing can be realized through relatively simple reaction kinetics, provided that the spatial arrangement of reactive regions is carefully designed.[12]

Spatial control over the origin of the wave was lacking in these experiments, with waves randomly initiating simultaneously in multiple MCRs. A more precise data analysis approach is needed to better understand communication between MCRs. For the following discussion, we selected a specific area from time-lapse images containing coupled MCRs with the desired geometry for a detailed study of their oscillatory behavior, although the presented studies remain primarily qualitative. Depending on the amount of air/CO_2 in the inlet and outlet microfluidic channels, it was difficult to control the amount of BZ reactants in these channels. In most situations, the MCRs responded to the trigger signal

when the inlet channel oscillated. When the inlet channel did not oscillate, the triggering of MCRs was determined by their communication with each other. Statistical analysis of the relationship between the size and frequency of MCRs can be done when input is more finely controlled. Moreover, a better time resolution would improve the visualization of oscillations. Regardless, meaningful insights about synchronization, communication, fan-out, and complex communication between MCRs were taken.

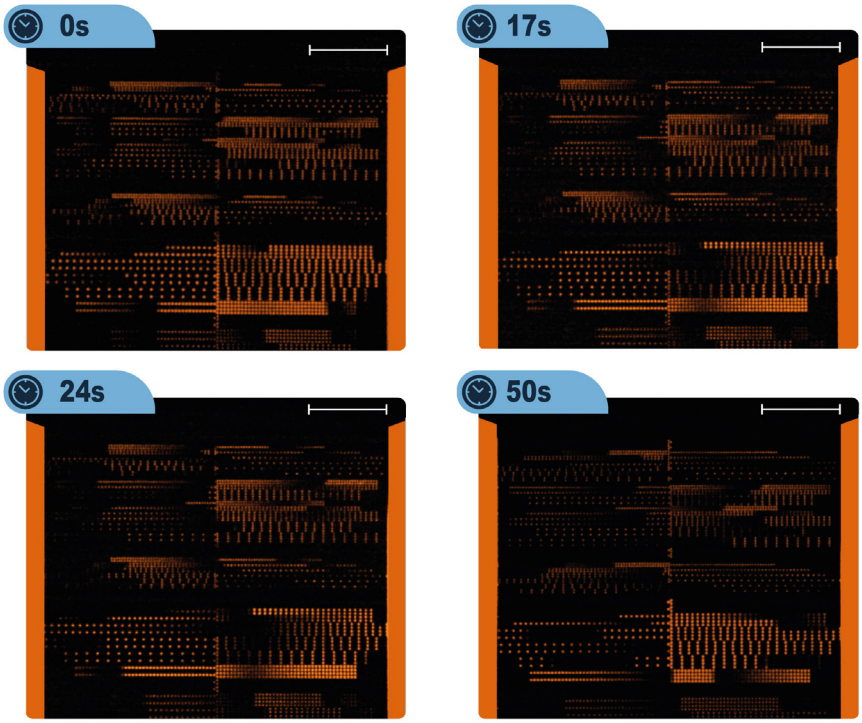

Figure 6.4. Sequence of fluorescence images of MCR networks filled with BZ reactants at different times. Scale bar = 200 µm. Bright orange: low redox potential state of BZ reaction (Ru^{2+}); dark color: high redox potential state of BZ (Ru^{3+}).

6.2.2 Proof-of-concept of MCR communication – MCRs with branching-reactors layout

To employ MCRs in chemical computation, unidirectional diffusive communication between reactors is preferred. Therefore, when analyzing a coupled MCR network, it is crucial to assess how waves are transmitted between MCRs and whether this transmission is influenced by their geometric arrangement. We hypothesized that the wavefront of the BZ reaction propagates between MCRs through diffusion, with the transmission dynamics influenced by their arrangement relative to other MCRs, and the distance from

the wave origin. To validate this, we analyzed the temporal and spatial dynamics of wave propagation within a branched MCR design, where a single nanochannel splits into two, and all channels contain evenly MCRs of identical size (22.5 µm diameter).

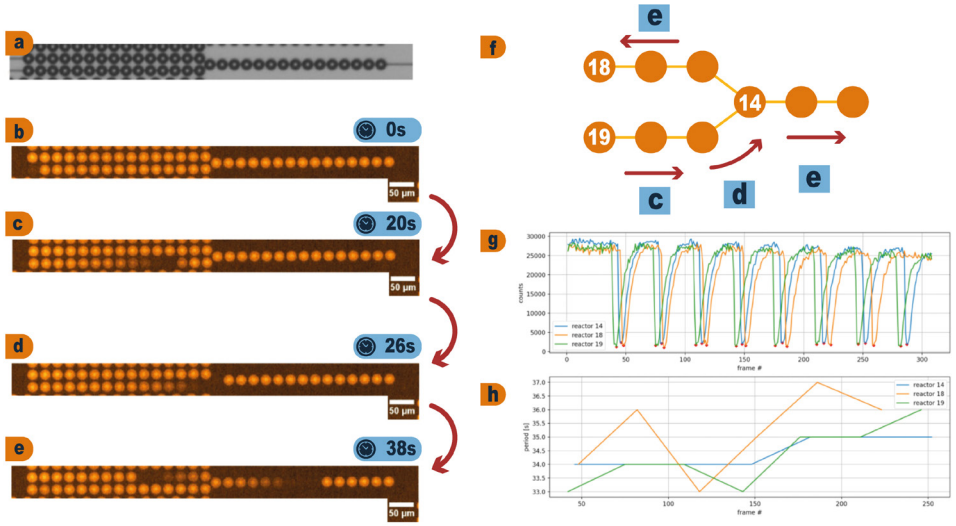

Figure 6.5. Proof-of-concept of communication in an MCR-BZ network. The set of images shows a couple of 22.5 µm diameter MCRs. **a)** Bright-field image of silicon device before filling. **b)** to **e)** Fluorescence images of MCRs at different times. Bright orange: low redox potential state of BZ reaction (Ru^{2+}); dark color: high redox potential state of BZ (Ru^{3+}). **f)** BZ wave direction of images **c)** to **e)**. Graphs illustrate the temporal evolution of **g)** amplitude and **h)** period of MCRs over time. One frame represents 1 s of the experiment.

Figures 6.5b to e show FM images illustrating communication within the MCR network, while Figures 6.5g and h present a semiquantitative study of the oscillatory period and amplitude of selected MCRs. Figure 6.5f illustrates the directionality of the BZ wave as observed in the FM images. As presented in Figure 6.5b, initially, the wave originated in one of the coupled MCR channels. As the wave reached the branching point (Figure 6.5d), it propagated into the two remaining channels (Figure 6.5e). This provided evidence of diffusion-driven wave transmission and directionality between MCRs. Additionally, MCRs '18' and '19' (Figure 6.5f), located at similar distances from the branching MCR (MCR '14'), both exhibited nearly identical oscillation periods of approximately 33-37 s (Figure 6.5h), despite the wave initially propagating through MCR '18'. This observation confirms that oscillation in the MCRs is influenced by their geometric arrangement.

In conclusion, we demonstrate that MCRs communicate via diffusion, with the geometric arrangement playing an important role in the directionality of the diffusion wave from the BZ reaction.

6.2.3 Influence of reactor size – anisometric-reactors layout MCRs

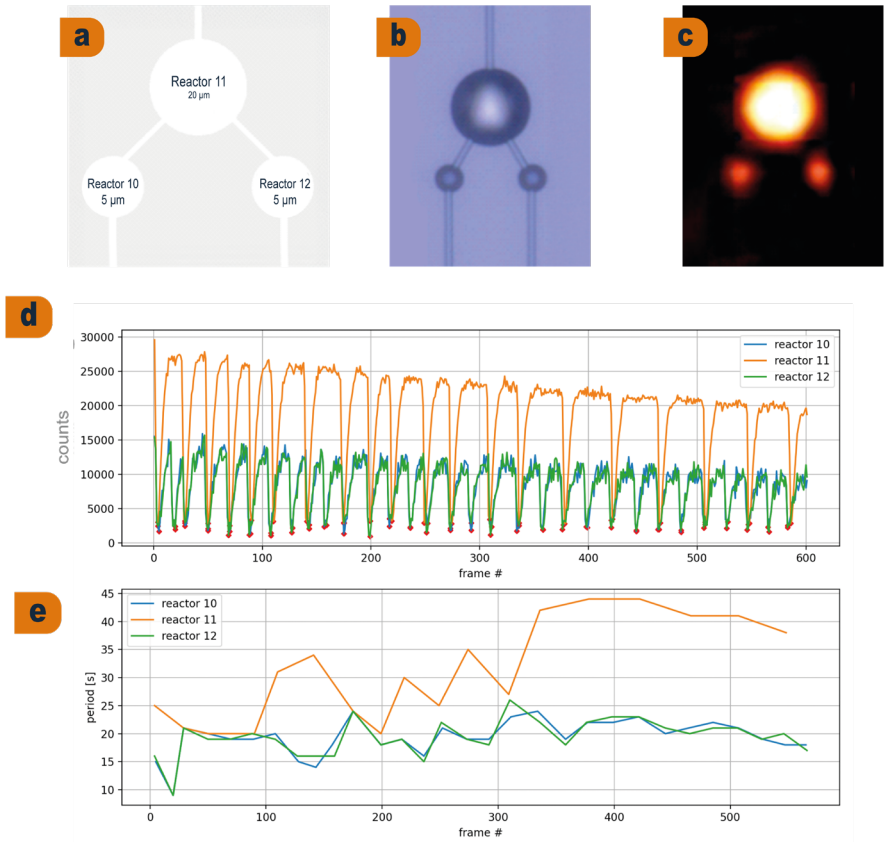

Figure 6.6. Effect of communication among MCRs-BZ network on the oscillation period of different MCR sizes. **a)** MCR design. **b)** Bright-field image of MCR network before channel filling. **c)** Fluorescence image of MCR bright state. Graphs illustrate the temporal evolution of **d)** amplitude and **e)** period of MCRs over time. The scale bar represents 20 µm. One frame represents 1 s of the experiment.

Achieving precise timing and coordination is essential for reliable operation and error correction. We aim to investigate whether synchronization occurs in MCR networks and how it correlates with the size of the MCRs. To this end, we present an anisometric-MCR layout, where a larger MCR is connected to two smaller MCRs. The oscillation period study for MCRs of different sizes is presented in Figure 6.6. We analyzed three MCRs: two with a 5 µm diameter (MCRs '10' and '12') connected to a 20 µm diameter MCR (MCR '11') (Figure 6.6a). Figures 6.6b and c show, respectively, the bright-field and FM images of the MCR network. Figures 6.6d and e present time-lapse data on the amplitude and period of the mentioned MCRs. Period analysis revealed a clear relationship between oscillation period and MCR diameter. After multiple cycles, the larger MCR ('11') oscillated at roughly half the frequency of the smaller MCRs ('10' and '12'). These results show that

the smaller MCRs synchronized to a common frequency, while the larger MCR exhibited a slower final frequency due to its size. This observation, despite identical initial BZ reactant concentrations, can be attributed to the slower diffusion that occurs when the distance over which the molecules must travel is greater, as is the case with larger volumes. Additionally, factors such as light exposure may also play a role, as the BZ reaction with Ruthenium as a catalyst is photoinhibited with increased light exposure. Since larger MCR areas result in greater light exposure per MCR, this may further influence the observed results.

These findings highlight the role of synchronization within the MCR network, which can occur not only among MCRs of the same size but also across MCRs of different sizes. This synchronization was detectable through their intrinsic frequencies, which were related to the diameter of each MCR. It suggests that a system composed of many interconnected units, like MCRs, can reliably synchronize their activities through diffusion. By altering the size and arrangement of the MCRs, their behavior can be controlled to produce specific oscillatory patterns. These oscillations can be influenced by the intrinsic properties of each MCR, such as its volume, as well as the connections between MCRs, including microfluidic channels and neighboring MCRs. Through the manipulation of these factors, the system can recognize or generate distinct patterns of activity within the network.

6.2.4 Parallel transmission of chemical waves - fan-out layout MCRs

Fan-out refers to the capacity of a single logic element to distribute its output signal to multiple subsequent components or devices without compromising functionality or stability. In semiconductor electronics, the number of devices that can be connected to an element is determined by its output current capacity and the input current requirements of the connected components. Each logic gate has a specific capacity for processing input signals and driving output signals. Exceeding this capacity can lead to problems such as signal degradation or improper functionality.

To address the limitations of semiconductor-based computation, which restrict the number of devices that can be connected simultaneously, we investigated a chemically driven fan-out signal by observing the propagation of a chemical wave between channels. We connected one line of MCRs to seven other MCR-containing lines (Figure 6.7a). All MCRs have the same size (25 µm diameter), and the heptafurcation lines contain an equal number of MCRs. Figures 6.7b to d present time-lapse FM images, while Figure 6.7e illustrates the wave propagation, using the FM images as a reference.

We anticipated that wave transmission would be influenced by the geometric arrangement, as well as the number and distance of MCRs from the wave source channel. Fluorescent images in Figures 6.7b to d demonstrate that the network of coupled, synchronizing MCR oscillators can propagate the signal across all seven lines. As expected, the wave propagation along the lines was influenced by the number of MCRs and their distance from the signal source. This is highlighted by the observation that signal from the lines equidistant from the wave source exhibit similar speed (Figure 6.7e). We conclude that the splitting of the

wave in the heptafurcation design of the BZ-MCR network can be successfully achieved, and wave propagation can be controlled by adjusting the distance from the wave source.

These results suggest that wave splitting can be effectively achieved across multiple channels with minimal interference. Therefore, we propose that 3D connectivity could improve the system's fan-out capability, facilitating more complex interconnections between MCRs. This approach allows each MCR to interact with multiple others, improving the network's capacity for complex information processing and synchronization. In Chapter 5 of this thesis, [46] a strategy was introduced for fabricating buried nanofluidic networks. This technique could be extended to the fabrication of 3D BZ-MCR networks. By employing this method, it becomes possible to integrate MCRs at different layers, forming a three-dimensional structure that can increase connectivity and support more complex chemical computation tasks.

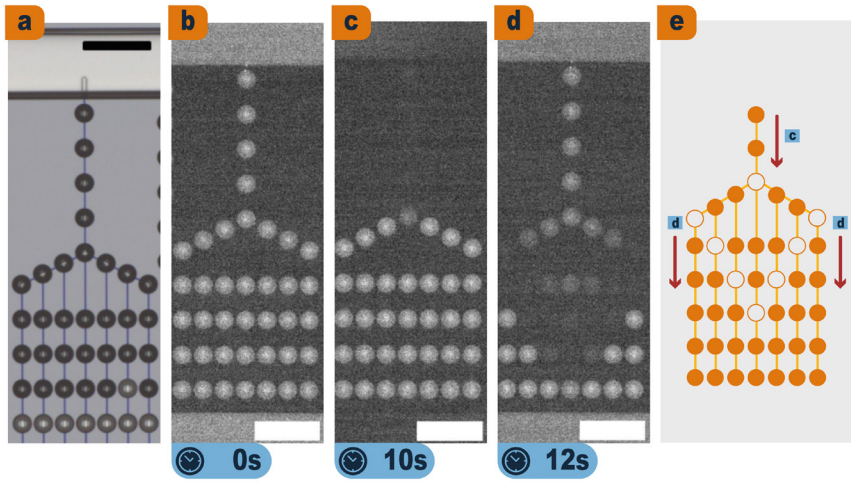

Figure 6.7. Images illustrating the fan-out in an MCR-BZ network with 25 µm diameter MCRs. **a)** Bright-field image of silicon device during filling. **b–d)** Fluorescence images of MCR-network at different times. **e)** Demonstration of BZ wave front of images c and d. Bright color: low redox potential state of BZ reaction (Ru^{2+}); dark areas: high redox potential state of BZ (Ru^{3+}). The scale bar represents 100 µm.

6.2.5 Behavior of complex MCR connections - honeycomb layout MCRs

Essential for applying MCRs to CC is a chemical medium that effectively integrates incoming signals in a non-trivial manner. A method for controlling the coupling strength of MCRs by altering their topographic connections was proposed. Apart from networks of two- and three-coupled active MCRs, the impact on the dynamic modes of a network comprising multiple wave-coupled MCRs in a honeycomb structure was investigated. In this case, the expected outcome remains uncertain; however, we anticipate observing more complex

behavior arising from the intricate geometric arrangements between MCRs.

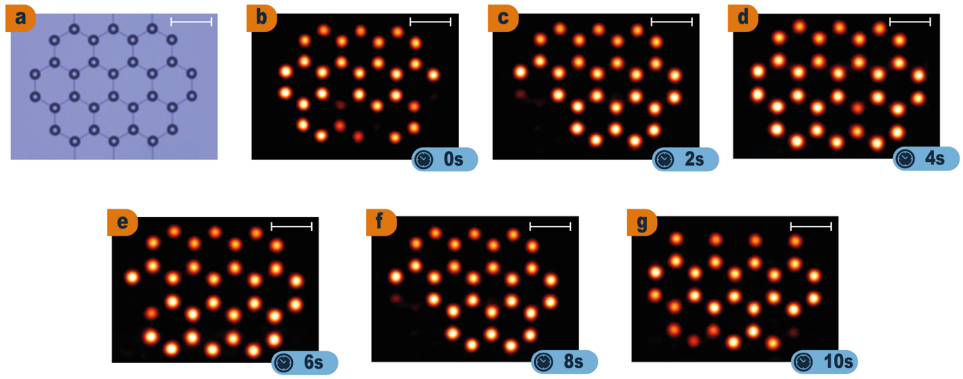

Figure 6.8. Images of a 20 µm honeycomb layout non-triggered MCRs. **a)** Bright-field image of MCRs prior to channel filling. **b)** to **g)** Time-lapse fluorescence images from 0 to 10 seconds. The white scale bar represents 100 µm.

Two types of results were obtained. In the 20 µm coupled MCRs (Figure 6.8), where the inlet channel did not oscillate, the adjustment of coupling strengths led to substantial spontaneous switching among network configurations. FM images in Figure 6.8b to g display six distinct spatial patterns from this design, representing only a subset of the patterns observed in the experiments. Based on this, we suggest that more complex architectures could provide a larger number of states, facilitating the ´processing´ of ´more information`. In the case of honeycomb MCRs triggered by oscillations from the inlet channel, as presented in Figure 6.9b to g, the 20 µm coupled MCRs exhibited uniform wave transmission. Consequently, the oscillations of the MCRs followed the wave originating from the inlet channel, transmitting signals from the MCRs closer to the inlet channels to those farther away. Over time, the MCRs maintained the same sequence of patterns.

Based on these results, we conclude that input signals play a crucial role in determining the oscillatory behavior of complex MCR connections. This highlights a key step toward developing CCs, as the same architecture can produce different outputs depending on the input. When the input is solely from BZ-MCR diffusion among MCRs, the oscillations exhibit a complex pattern, whereas an external diffusive wave source results in a comparatively simpler output.

Building on the outcomes of the previously mentioned studies, we are progressing along a pathway aimed at establishing fundamental and experimentally achievable design principles for the creation of "materials that compute". [47] In our experiments, the main challenges of using such device toward the development of a CC are the prediction and control of their computational behavior. We suggest that the primary challenge in the practical implementation of CC arises from the absence of an efficient signal coding

strategy tailored to this type of chemical network.

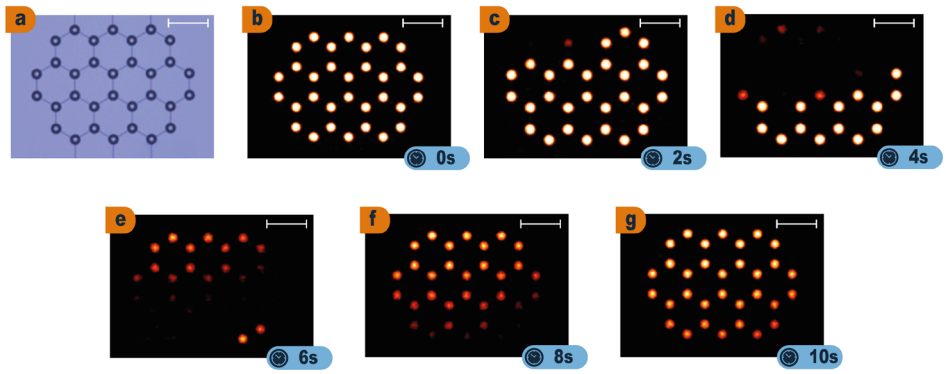

Figure 6.9. Images of a 20 µm honeycomb layout triggered MCRs. **a)** Bright-field image of MCRs prior to channel filling. **b)** to **g)** Time-lapse fluorescence images from 0 to 10 seconds. The white scale bar represents 100 µm.

A widely adopted approach to chemical computing seeks to replicate information processing mechanisms found in semiconductor devices. [29] Another type of readout can be provided by analog computation [48] or cellular automata (CA), which are alternative types of language approaches for computation. CA has been commonly used to investigate explore complex phenomena, such as chemical reaction-diffusion processes and excitation wave dynamics, in various physical, chemical, and biological systems, including models of BZ media. [49–51] Reservoir computation (RC) [52] can also be well applied to CC because due to its versality: only the connections between readout layer and output layer need to be trained. Examples concerning such approach for mimicking neural networks were presented by some groups [5,52–55].

6.2.6 Outlook

We developed a self-sustained device that operates without dependence on an external power supply, enabling sensing, actuation, and communication. Distinct MCR networks, each designed to perform a specific pattern function, were subjected to a series of input patterns. These input patterns corresponded to the initial phase of the oscillations imposed on the respective units. The technique developed in this work used the propagation of waves along defined channels based on the BZ reaction. The results obtained by the fabrication strategy and protocol used to visualize the oscillatory networks indicate that CCs can be successfully created soon. However, despite the observations and advances shown here, improvements are needed to enable the production of reliable CCs. In this regard, the drawbacks, and future perspectives to improving this system are presented.

(1) The time resolution needed for visualizing the oscillations remains limited. To address this issue, modifications to the oscillatory CRN are necessary. A

version of the BZ system that is less sensitive to light but still provides a fluorescence signal indicative of the oscillatory regime would be important. This improvement can also be achieved by employing another oscillatory CRN that enables continuous exposure to light, ensuring an adequate time-lapse signal and short image exposure time. The introduction of light would not interrupt the oscillators and could enhance the signal from the MCRs. Nanoreactors with diameters below 2 µm could be a solution to improve rate of diffusion because of larger surface/ratio area. Chapter 5 of this thesis presents a fabrication strategy using buried nanochannels that can be used to produce chemical networks of nanoreactors.

(2) Control over the input waves is lacking. MCR fabrication allows for the integration of electrical and optical components, such as electrodes. This integration can be achieved through lithographically defined metal patterns, like platinum thin films, which can be utilized for electro-osmotic flow, electrophoresis, and for amperometry and conductometry. [56] Additionally, introducing oxygen into the microfluidic channels to halt oscillations in the main channel can serve as a solution to this issue, as oxygen exerts an inhibitory effect in the BZ reaction. [57]

(3) Insufficient control over light exposure in the chip area is identified as a limitation in the current setup. Presently, a substantial chip area is subjected to blue light, leading to the influence of light on numerous MCRs. To address this, chip design should incorporate sections where microfluidic channels are shielded from light, thereby ensuring a more controllable input. Moreover, laser-based techniques, such as confocal microscopy, should be adopted to enable the exposition of only specific parts of the chip to light. For example, in a medium with a photosensitive BZ reaction, selective illumination of a spatially distributed system can generate excitable channels that facilitate signal propagation. By optimizing the geometric arrangement of excitable and non-excitable regions, excitation dynamics can be precisely controlled, enabling functionalities such as the development of a signal diode. [58] Light can also be used as an input signal for the system. [26] This illustrates that individual optical control of chemical activity in BZ reactors can generate the required input.

(4) Integrating MCRs with a continuous feeding operation in the BZ reaction offers significant potential for improving the stability and control of BZ-MCR systems for CC applications. Unlike batch operation, where the BZ reaction eventually reaches equilibrium and oscillations cease—disrupting radical species dynamics— the continuous inflow of reactants and outflow of products maintains a persistent out- of-equilibrium oscillatory state. This approach ensures well-defined, predictable oscillatory behavior and more consistent radical dynamics. [59]

6.3 Conclusions

In this chapter, we conducted an initial investigation into the behavior of a silicon-based device featuring extensive arrays of MCRs, capable of generating diverse spatiotemporal patterns driven by the BZ reaction. We presented time-lapse FM images of connecting channels mediating the coupling between compartments, which led to communication, synchronization, and fan-out. More complex communication can be developed using more intricate architectures, as demonstrated by the honeycomb MCRs design. These steps are critical first results for the development of scalable chemical computing architectures based on simple molecules.

We believe that the platform and experimental investigation presented in this work can offer a viable new perspective for advancing CC through the utilization of silicon-based devices. Despite their dynamics being constrained in speed by reaction and diffusion rates, silicon-based MCR networks provide opportunities for autonomy, rendering them suitable for targeted functionalities in liquid settings. Additionally, the system described here has the potential to inspire new algorithm designs that uniquely exploit the features of a CC. Such systems could exhibit a vast number of states with low power consumption. Based on our results, we propose that the design of unconventional computing devices should consider silicon-based architecture fabrication and machine-learning algorithms, with implements from by surface chemistry, molecular self-assembly systems, spectroscopic advancements, and new oscillatory artificial CRNs.

As presented by [26,30], we initially considered that chemical computation should be based on the development of experimental hybrid computer architectures, where certain components operate electronically while others function chemically. We then propose that these dependencies be gradually eliminated to facilitate a transition from hybrid CC to a fully autonomous system, in which only inputs and outputs are electronic, mediated by electrochemistry or light-derived mechanisms. We believe that, as a readout of the MCR network, the RC provides an opportunity to explore its maximum performance. We anticipate that, beyond their computational potential, the development of such networks could also provide profound insights into the functioning of the human brain. [21]

6.4 References

(1) Braun, E. L. Digital Computer Design: Logic, Circuitry, and Synthesis; *Academic Press,* **2014**.

(2) Waldrop, M. M. The Chips Are down for Moore's Law. *Nature News* **2016**, 530 (7589), 144.

(3) Moore, G. E. Cramming More Components onto Integrated Circuits. *Proceedings of the IEEE* **1998**, 86 (1), 82–85.

(4) Kendall, J. D.; Kumar, S. The Building Blocks of a Brain-Inspired Computer. *Applied Physics Reviews* **2020**, 7 (1), 011305. https://doi.org/10.1063/1.5129306.

(5) Cucchi, M.; Abreu, S.; Ciccone, G.; Brunner, D.; Kleemann, H. Hands-on Reservoir Computing: A Tutorial for Practical Implementation. *Neuromorphic Computing and Engineering* **2022**, 2 (3), 032002.

(6) Vanag, V. K. Networks of Spike Oscillators and Their Application for Creating Autonomous Intelligent Devices. *Phys. Usp* **2022**, 65, 440–452.

(7) Adamatzky, *A. Advances in Unconventional Computing: Volume 1: Theory*; Springer, **2016**; Vol. 22.

(8) Chatzinikolaou, T. P.; Fyrigos, I.-A.; Ntinas, V.; Kitsios, S.; Tsompanas, M.-A.; Bousoulas, P.; Tsoukalas, D.; Adamatzky, A.; Sirakoulis, G. C. Chemical Wave Computing from Labware to Electrical Systems. *Electronics* **2022**, 11 (11), 1683.

(9) *Advances in Unconventional Computing*; Adamatzky, A., Ed.; Emergence, Complexity and Computation; Springer International Publishing: Cham, **2017**; Vol. 22. https://doi.org/10.1007/978-3- 319-33924-5.

(10) Bergh, E.; Konkoli, Z. On Improving the Expressive Power of Chemical Computation. *Advances in Unconventional Computing: Volume 1*: Theory **2017**, 677–709.

(11) Torbensen, K.; Rossi, F.; Ristori, S.; Abou-Hassan, A. Chemical Communication and Dynamics of Droplet Emulsions in Networks of Belousov–Zhabotinsky Micro-Oscillators Produced by Microfluidics. *Lab ona Chip* **2017**, 17 (7), 1179–1189.

(12) Gorecki, J.; Gizynski, K.; Guzowski, J.; Gorecka, J. N.; Garstecki, P.; Gruenert, G.; Dittrich, P. Chemical Computing with Reaction–Diffusion Processes. *Philosophical Transactions of the Royal Society A: Mathematical, Physical and Engineering Sciences* **2015**, 373 (2046), 20140219.

(13) McAvoy, M. Pulse-Coupled Belousov-Zhabotinsky Oscillators with Activity Dependent Coupling, Brandeis University, Graduate School of Arts and Sciences, 2015.

(14) Kopets, E. E.; Karimov, A. I.; Khafizova, A. M.; Katser, E. A.; Shchetinina, T. G. Simulation of Chemical Oscillator Network. In 2022 *Conference of Russian Young Researchers in Electrical and Electronic Engineering (ElConRus); IEEE,* **2022**; pp 704–707.

(15) Field, R. J.; Koros, E.; Noyes, R. M. Oscillations in Chemical Systems. II. Thorough Analysis of Temporal Oscillation in the Bromate-Cerium-Malonic Acid System. *Journal of the American Chemical Society***1972**, 94 (25), 8649–8664.

(16) Masuda, T.; Akimoto, A. M.; Furusawa, M.; Tamate, R.; Nagase, K.; Okano, T.; Yoshida, R. Aspects of the Belousov–Zhabotinsky Reaction inside a Self-Oscillating Polymer Brush. *Langmuir* **2018**, 34 (4), 1673–1680.

(17) Ruoff, P.; Varga, M.; Koros, E. How Bromate Oscillators Are Controlled. *Accounts of Chemical Research* **1988**, 21 (9), 326–332.

(18) Semenov, S. N.; Wong, A. S.; Van Der Made, R. M.; Postma, S. G.; Groen, J.; Van Roekel, H. W.; De Greef, T. F.; Huck, W. T. Rational Design of Functional and Tunable Oscillating Enzymatic Networks. *Nature chemistry* **2015**, 7 (2), 160–165.

(19) Novák, B.; Tyson, J. J. Design Principles of Biochemical Oscillators. *Nature reviews Molecular cell biology* **2008**, 9 (12), 981–991.

(20) Taylor, A. F. Mechanism and Phenomenology of an Oscillating Chemical Reaction. *Progress in Reaction Kinetics and Mechanism* **2002**, 27 (4), 247–326.

(21) Mallphanov, I. L.; Vanag, V. K. Chemical Micro-Oscillators Based on the Belousov–ZhabotinskyReaction. *Russian Chemical Reviews* **2021**, 90 (10), 1263.

(22) Gáşpár, V.; Bazsa, G.; Beck, M. T. The Influence of Visible Light on the Beloasoy-Zhabotinskii Oscillating Reactions Applying Different Catalysts. *Zeitschrift für Physikalische Chemie* **1983**, 264 (1), 43–48.

(23) Bánsági Jr, T.; Leda, M.; Toiya, M.; Zhabotinsky, A. M.; Epstein, I. R. High-Frequency Oscillations in the Belousov– Zhabotinsky Reaction. *The Journal of Physical Chemistry A* **2009**, 113 (19), 5644–5648.

(24) Misra, G. P. Effect of Temperature and Associated Bifurcation in the Oscillatory Belousov— Zhabotinskii Reaction in a Flow Reactor. *Chemical physics letters* **1992**, 191 (5), 435–440.

(25) Elwood, J. ATOMIC AND NUCLEAR STRUCTURE. *Passing the State Science Proficiency Tests: Essential Content for Elementary and Middle School Teachers* **2013**, 51.

(26) Proskurkin, I. S.; Smelov, P. S.; Vanag, V. K. Experimental Verification of an Opto-Chemical "Neurocomputer." *Physical Chemistry Chemical Physics* **2020**, 22 (34), 19359–19367.

(27) Toth, R.; Taylor, A. F. The Tris (2, 2'-Bipyridyl) Ruthenium-Catalysed Belousov–Zhabotinsky Reaction. *Progress in Reaction Kinetics and Mechanism* **2006**, 31 (2), 59–115.

(28) Jinguji, M.; Ishihara, M.; Nakazawa, T. Primary Process of Illumination Effect on the Tris (Bipyridine) Ruthenium (2+)-Catalyzed Belousov-Zhabotinskii Reaction. *The Journal of Physical Chemistry* **1992**, 96 (11), 4279–4281.

(29) Dueñas-Díez, M.; Pérez-Mercader, J. How Chemistry Computes: Language Recognition by Non-Biochemical Chemical Automata. From Finite Automata to Turing Machines. *Iscience* **2019,** 19, 514–526.

(30) Parrilla-Gutierrez, J. M.; Sharma, A.; Tsuda, S.; Cooper, G. J.; Aragon-Camarasa, G.; Donkers, K.; Cronin, L. A Programmable Chemical Computer with Memory and Pattern Recognition. *Nature communications*

2020, 11 (1), 1442.
(31) Sharma, A.; Ng, M. T.-K.; Parrilla Gutierrez, J. M.; Jiang, Y.; Cronin, L. A Programmable Hybrid Digital Chemical Information Processor Based on the Belousov-Zhabotinsky Reaction. *Nat Commun* **2024**, 15 (1), 1984. https://doi.org/10.1038/s41467-024-45896-7.
(32) Konrad, G.; Jerzy, G. A Chemical System That Recognizes the Shape of a Sphere. *CMST* **2016**, 22 (4),167–177.
(33) Gruenert, G.; Gizynski, K.; Escuela, G.; Ibrahim, B.; Gorecki, J.; Dittrich, P. Understanding Networksof Computing Chemical Droplet Neurons Based on Information Flow. *Int. J. Neur. Syst.* **2015**, 25 (07), 450032. https://doi.org/10.1142/S0129065714500324.
(34) Adamatzky, A.; De Lacy Costello, B.; Dittrich, P.; Gorecki, J.; Zauner, K.-P. On Logical Universality of Belousov-Zhabotinsky Vesicles. *International Journal of General Systems* **2014**, 43 (7), 757–769.
(35) Gizynski, K.; Gorecki, J. Cancer Classification with a Network of Chemical Oscillators. *Phys. Chem.Chem. Phys.* **2017**, 19 (42), 28808–28819. https://doi.org/10.1039/C7CP05655A.
(36) Gizynski, K.; Gorecki, J. Chemical Memory with States Coded in Light Controlled Oscillations of Interacting Belousov–Zhabotinsky Droplets. *Phys. Chem. Chem. Phys.* **2017**, 19 (9), 6519–6531. https://doi.org/10.1039/C6CP07492H.
(37) Vanag, V. K. Plasticity in Networks of Active Chemical Cells with Pulse Coupling. Chaos: *An Interdisciplinary Journal of Nonlinear Science* **2022**, 32 (12).
(38) Tomasi, R.; Noël, J.-M.; Zenati, A.; Ristori, S.; Rossi, F.; Cabuil, V.; Kanoufi, F.; Abou-Hassan, A. Chemical Communication between Liposomes Encapsulating a Chemical Oscillatory Reaction. *Chemical Science* **2014**, 5 (5), 1854–1859.
(39) Sheehy, J.; Hunter, I.; Moustaka, M. E.; Aghvami, S. A.; Fahmy, Y.; Fraden, S. Impact of PDMS-Based Microfluidics on Belousov–Zhabotinsky Chemical Oscillators. *J. Phys. Chem. B* **2020**, 124 (51), 11690–11698. https://doi.org/10.1021/acs.jpcb.0c08422.
(40) Steinbock, O.; Tóth, Á.; Showalter, K. Navigating Complex Labyrinths: Optimal Paths from Chemical Waves. *Science* **1995**, 267 (5199), 868–871.
(41) Litschel, T.; Norton, M. M.; Tserunyan, V.; Fraden, S. Engineering Reaction–Diffusion Networks with Properties of Neural Tissue. *Lab on a Chip* **2018**, 18 (5), 714–722.
(42) Ginn, B. T.; Steinbock, B.; Kahveci, M.; Steinbock, O. Microfluidic Systems for the Belousov−Zhabotinsky Reaction. *The Journal of Physical Chemistry A* **2004**, 108 (8), 1325–1332.
(43) Fouchier, M.; Pargon, E. HBr/O2 Plasma Treatment Followed by a Bake for Photoresist Linewidth Roughness Smoothing. *Journal of Applied Physics* **2014**, 115 (7).
(44) Laermer, F.; Urban, A. MEMS at Bosch–Si Plasma Etch Success Story, History, Applications, and Products. *Plasma Processes and Polymers* **2019**, 16 (9), 1800207.
(45) Tamaki, E.; Hibara, A.; Kim, H.-B.; Tokeshi, M.; Ooi, T.; Nakao, M.; Kitamori, T. Liquid Filling Method for Nanofluidic Channels Utilizing the High Solubility of CO2. *Analytical sciences* **2006**, 22 (4), 529– 532.
(46) Figueiredo Da Silva, J.; Bacheva, V.; Drechsler, U.; Nicollier, P.; Reidt, S.; Fotiadis, D.; Knoll, A.; Wolf, H. Fabrication of a Hybrid Device for the Integration of Light-Triggered Proton Pumps. *Micro and Nano Engineering* **2024**, 23, 100250. https://doi.org/10.1016/j.mne.2024.100250.
(47) Fang, Y.; Yashin, V. V.; Levitan, S. P.; Balazs, A. C. Pattern Recognition with "Materials That Compute." *Science advances* **2016**, 2 (9), e1601114.
(48) MacLennan, B. J. Analog Computation. Encyclopedia of Complexity and Systems Science, 2009, 271–294. https://doi.org/10.1007/978-0-387-30440-3_19.
(49) Adamatzky, A.; Costello, B. D. L.; Asai, T. Reaction-Diffusion Computers; *Elsevier*, **2005**.
(50) Gerhardt, M.; Schuster, H.; Tyson, J. J. A Cellular Automaton Model of Excitable Media Including Curvature and Dispersion. *Science* **1990**, 247 (4950), 1563–1566.
(51) Markus, M.; Hess, B. Isotropic Cellular Automaton for Modelling Excitable Media. *Nature* **1990**, 347 (6288), 56–58.
(52) Baltussen, M. G.; De Jong, T. J.; Duez, Q.; Robinson, W. E.; Huck, W. T. S. Chemical Reservoir Computation in a Self-Organizing Reaction Network. *Nature* **2024**, 631 (8021), 549–555. https://doi.org/10.1038/s41586-024-07567-x.
(53) Pecqueur, S.; Mastropasqua Talamo, M.; Guérin, D.; Blanchard, P.; Roncali, J.; Vuillaume, D.; Alibart, F. Neuromorphic Time-dependent Pattern Classification with Organic Electrochemical Transistor Arrays. *Advanced Electronic Materials* **2018**, 4 (9), 1800166.
(54) Usami, Y.; van de Ven, B.; Mathew, D. G.; Chen, T.; Kotooka, T.; Kawashima, Y.; Tanaka, Y.; Otsuka, Y.;

Ohoyama, H.; Tamukoh, H. In-materio Reservoir Computing in a Sulfonated Polyaniline Network. *Advanced Materials* **2021**, 33 (48), 2102688.

(55) Cucchi, M.; Kleemann, H.; Tseng, H.; Ciccone, G.; Lee, A.; Pohl, D.; Leo, K. Directed Growth of Dendritic Polymer Networks for Organic Electrochemical Transistors and Artificial Synapses. *Advanced Electronic Materials* **2021**, 7 (10), 2100586.

(56) Gardeniers, H. J. Chemistry in Nanochannel Confinement. Analytical and bioanalytical chemistry2009, 394 (2), 385–397.

(57) Luengviriya, J.; Phantu, M.; Müller, S. C.; Luengviriya, C. Inhibitory Effect of Oxygen on Excitation Waves in the Belousov–Zhabotinsky Reaction with Different Excitability. *Chemical Physics Letters***2015**, 618, 6–10.

(58) Agladze, K.; Aliev, R. R.; Yamaguchi, T.; Yoshikawa, K. Chemical Diode. *The Journal of Physical Chemistry* **1996**, 100 (33), 13895–13897.

(59) Hou, L.; Dueñas-Díez, M.; Srivastava, R.; Pérez-Mercader, J. Flow Chemistry Controls Self-Assemblyand Cargo in Belousov-Zhabotinsky Driven Polymerization-Induced Self-Assembly. *Communications Chemistry* **2019**, 2 (1), 139.

6.5 Supplementary information

6.5.1 Materials and methods

6.5.1.1 Chemicals

Commercially available sodium bromate ($NaBrO_3$; Sigma-Aldrich), malonic acid (MA) ($CH_2(COOH)_2$; Sigma-Aldrich), tris(2,2'-bipyridyl) dichlororuthenium (II) hexahydrate ($Ru(bpy)_3Cl_2(6H_2O)$; Sigma-Aldrich), and sulfuric acid solution (H_2SO_4, 5 M; Merck) were used without further purification. Millipore water (18.2 Megaohm) was used to prepare the following stock solutions: 1 M H_2SO_4, 2 M $NaBrO_3$, 3.5 M $CH_2(COOH)_2$, and 0.0125 M $Ru(bpy)_3Cl_2(6H_2O)$.

6.5.1.2 Device fabrication

Silicon wafers with 100 mm diameter and 500 µm thickness were obtained from the University Wafer. Borofloat glass wafers (100 mm) with 500 µm thickness were obtained from PlanOptik AG. Patterns of 0.7 mm holes were drilled through the glass for the fluidic connections. Two chrome masks designed for the device layer structures were fabricated using a Heidelberg DWL2000 laser writer. The silicon wafer was first patterned via photolithography (Microchemicals AZ4533 resist and Süss Mask Aligner M6) and then etched via inductively coupled plasma reactive ion etching (ICP-RIE) using an Oxford Instruments Plasmalab 100. In this fabrication step, the small channels with 1.5 µm width and 500 nm depth were obtained. Subsequently, another photoresist layer (Microchemicals AZ4512) was spin-coated on top of the sample, thereby covering all structures on the device layer. In this step, we patterned the larger microfluidic channels and circular microreactors (diameter: 5 to 30 µm). Their depth of 20 µm was obtained using a deep reactive ion etching (DRIE) tool (Alcatel AMS 200SE I-Speeder). Finally, the channels were sealed by anodic bonding of the drilled cover glass to the wafer at 485 °C and 1.3 kV for ~1 h using a homemade substrate bonder. The glass-covered wafer was diced via ADT ProVectus LA 7100 into twelve 36x12 mm chips. To prevent the channels from being filled with cooling

water during the dicing process, the holes were pre-covered with foil.

Microfluidic setup

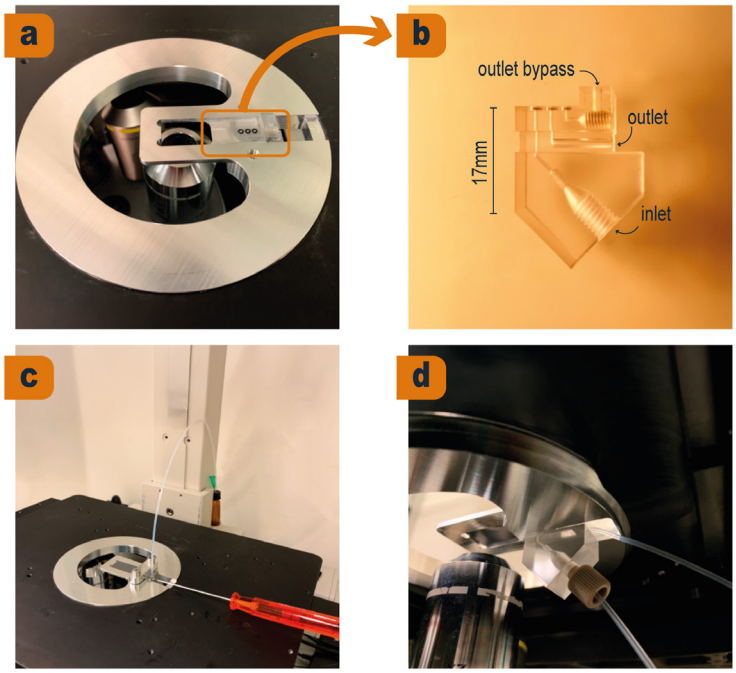

Figure S6.1. Microfluidic design setup used on a Nikon inverted microscope: **a)** chip holder with PMMA fluid interface, **b)** details of fluidic interface, with 0.5 mm O-rings, inlet, outlet, and bypass fluid connections. Setup with the inserted chip: **c)** top view, and **d)** bottom view. The setup was designed by Dr. Robert Lovchik (IBM Research Europe - Zurich, Switzerland).

The microfluidic interface was designed using CATIA V5R20. The aluminum parts of the assembly were machined using a computer numerical control (CNC) tool. The fluidic interface was fabricated by micro milling in poly(methyl methacrylate) (PMMA). The design comprises an inlet, an outlet, and a bypass aperture with a diameter of 0.5 mm. The interface presented ports compatible with 10-32 coned microfluidic fittings (Idex). The fluidic connections to the chips were sealed using Markez FFKM O-rings. The microfluidic setup with the chip was mounted on the stage of an inverted microscope for experiments. Figure S6.1 shows photos of this setup. We used a Nikon Eclipse Ti inverted bright-field/fluorescence microscope with a CCD camera (Clara camera, ANDOR technology) with 10x magnification lens. A customized filter set was used because of the peculiar Ruthenium emissions and excitation wavelengths: excitation filter = FITC filter = 475 nm (blue); emission filter = mCherry filter = 641 nm (orange); dichroic filter = GFP filter = 505–800 nm.

Belousov–Zhabotinsky (BZ) reaction in a microfluidic setup

To fill the nanochannels, we inserted CO_2 gas in the microfluidic tube connected to the inlet channel under pressure for 5 min. During that time, two solutions were prepared in separate Eppendorfs: solution 1 was composed of 1000 µL H_2SO_4 (1 M), 40 µL $Ru(bpy)_3Cl_2(6H_2O)$ (0.0125 M), and 200 µl of $NaBrO_3$ (2 M); whereas solution 2 was composed of 1000 µL H_2SO_4 (1 M), 40 µL Ru(bpy)3Cl2(6H2O) (0.0125 M), and 50 µL MA (3.5 M). Recipe was adapted from [1]. Equal amounts of solutions 1 and 2 were mixed in another Eppendorf. As soon as oscillations could be visually observed, we used a 250 µl syringe to inject the BZ solution under high pressure in the tube connected to the inlet microfluidic channel. The nanochannel filling was observed by fluorescence microscopy. Fluorescence images were obtained at 400 ms exposure time. One picture was taken every second for 10 min.

6.5.2 Data analysis

We employed a macro script scripted in ImageJ to examine the oscillatory signal of MCRs over time and employed a Python script to extract the oscillation periods and generate corresponding plots. Within ImageJ, the initial step included the opening of the image stack from time-lapse experiments. Subsequently, the "Threshold" option was applied to generate an image encapsulating the average signal emanating from the MCRs. This image served as the mask delineating the spatial locations of MCRs. The subsequent operation involved converting the mask into a binary format.

During the "Analyze Particles" step, the "Add to Manager" option was selected. This resulted in the presentation of all positions detected by the binary mask within the region of interest (ROI). The program provided the average intensity of the MCRs area. In the ROI manager, the "measure" option was executed, facilitating the measurement of MCR intensity over time for all components identified by the "analyze particles" function. Consequently, the localized intensity values of MCRs per image were obtained. Each detected area is assigned a numerical identifier.

ImageJ code was as follows:

```
waitForUser("Open", "Welcome to the BZ-micro-reactor analysis. Please choose your BZ-IS image sequence!");
run("Open...");
waitForUser("Z Project", "Please choose the interval of images to be used for averaging!"); run("Z Project...");
waitForUser("Subtract Background", "Please choose the background subtraction parameters for the averaged image!");
run("Subtract Background..."); run("Gaussian Blur...", "sigma=1 stack"); run("Enhance Contrast...", "saturated=0.35");
waitForUser("Threshold", "Please choose the threshold for the averaged image! (Will be used as mask for the location of bz reactors.)");
run("Threshold...");
waitForUser("Click OK when you are done!");
saveAs("tif"); showMessage("Results saved.");
run("Set Measurements...", "mean display redirect=None decimal=3"); run("Analyze Particles...", " show=Outlines display exclude summarize add"); close(); close();
```

```
waitForUser("Subtract Background", "Please choose background subtraction parameters!"); run("Subtract Background...");
// waitForUser("Click OK when you are done!"); run("Gaussian Blur...", "sigma=1 stack");
run("Enhance Contrast...", "saturated=0.35");
run("Set Measurements...", "mean display redirect=None decimal=3"); roiManager("multi-measure measure_all one append");
orgName = getTitle();
output_path = getDirectory("Choose output folder!"); roiManager("save", output_path + orgName + ".zip") showMessage("ROI Extraction saved."); selectWindow("Results");
saveAs("results", output_path + orgName + ".csv"); showMessage("Results saved.");
close();
name = output_path + "AVG_" + orgName open(name);
roiManager("show all with labels"); run("Flatten");
name = getTitle();
name = replace(name, "-1.tif", "_ann.png"); fpath = output_path + name
saveAs("png", fpath); showMessage("Saved annotated image."); roiManager("reset");
close("*");
selectWindow("Results");
run("Close"); selectWindow("Threshold"); run("Close"); selectWindow("Summary"); run("Close"); selectWindow("ROI Manager"); run("Close");
exit;
```

The examination of the oscillations of the MCRs was conducted using a Python script. Upon opening the csv script file that contained the mean intensity of each MCR over time, we identified the MCRs based on their enumeration determined by ImageJ program. Subsequently, the plot of the oscillations and periods over time was generated. The Python script was written by Dr. Heiko Wolf, IBM Research Laboratory – Zurich.

6.5.3 Photolithographic masks in K-layout software design

We employed K-layout software to create photolithographic masks. Figure S6.2a illustrates the mask designed by K-layout for the nanochannels (pink) and another mask designed for the MCRs and microfluidic channels (violet). Figure S6.2b shows the positions of the 0.7 mm holes in the glass with a 100 nm size wafer. The holes precisely corresponded to the features specified in the mask designed by photolithography.

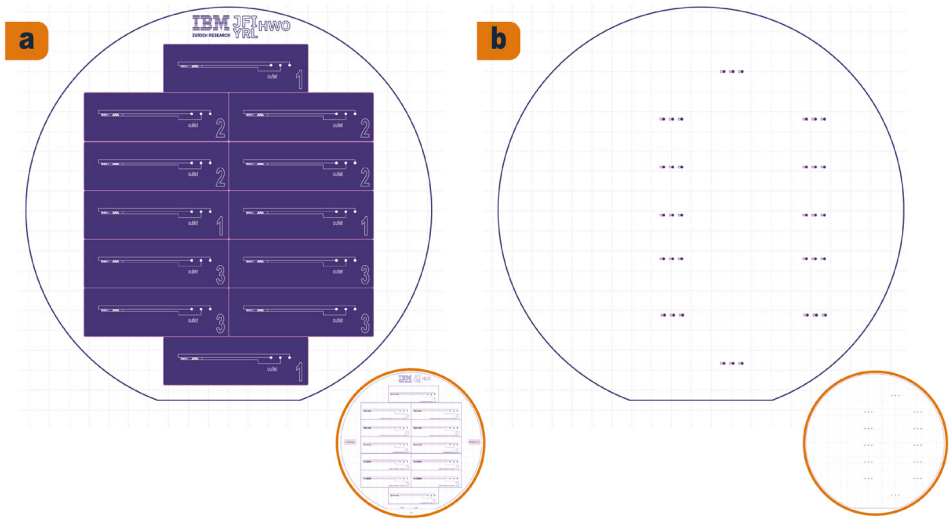

Figure S6.2. K-layout drawings of **a)** photolithographic masks used to fabricate silicon chips (presented in Figure 6.3), and **b)** 0.7 mm holes designed in the glass by drilling, which were anodically bonded to the silicon wafer.

6.5.4 First device generation

In the initial part of this project, we designed a microfluidic device that allowed us to fill the channels at a high pressure (Figure S6.3a). However, we were unable to visualize the in-situ MCR filling using the fluorescent microscope. As shown in Figure S6.3a, the adapter used to connect the tubing to the chips was made from PMMA and aluminum.

Additionally, we used a polydimethylsiloxane (PDMS) gasket to ensure a leak-free connection between the adapter and the chips. This setup was able to withstand the high pressures (> 20 Bar) when we filled the channels (Figure S6.3b). As the sample chips comprised two openings for the inlet, one of them was closed by the PMDS gasket and the side in which the liquid was inserted was held open. The outlet channel was always open.

The chip was fabricated using the procedure described in Chapter 6, except for the absence of a bypass channel and the chip size, which was 12 x 12 mm, as shown in Figure S6.3c. Figure S6.4a shows the K-layout drawing of photolithographic masks of the wafer used to fabricate the chips. Figure S6.4b shows the K-layout drawing for 2 mm holes in the glass.

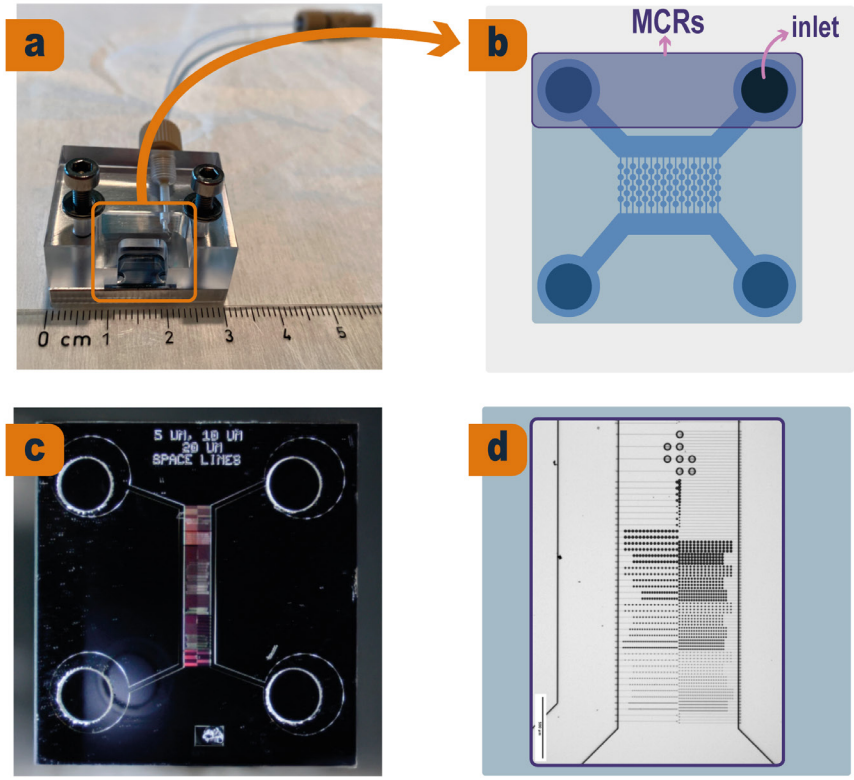

Figure S6.3. Microfluidic design setup using high pressure filling: **a)** chip setup; **b)** PDMS interface, which comprises one hole on one side of the inlet channel; **c)** bright-field image of 12x12 mm chip; **d)** part of MCR network before filling; scale bar = 500 µm.

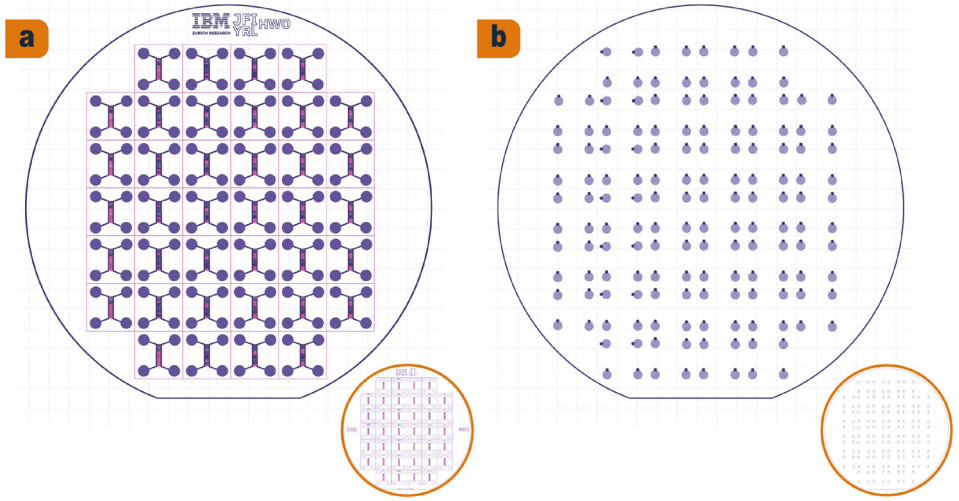

Figure S6.4. K-layout drawings of **a)** photolithographic masks used to fabricate silicon chips (presented in Figure S6.3-c), and **b)** 2 mm holes designed in the glass by sandblasting which were anodically bonded to the silicon wafer.

6.5.5 References

(1) Dueñas-Díez, M.; Pérez-Mercader, J. How Chemistry Computes: Language Recognition by Non-Biochemical Chemical Automata. From Finite Automata to Turing Machines. *Iscience* **2019**, 19, 514–526.

Summary

This PhD thesis, titled **"Reaction Cascades Coupled to Surface-Chemical Nanoscale Patterns,"** aims to develop strategies for spatiotemporal control of chemical reaction networks (CRNs) at the micro- and nanoscale. By controlling the size and shape of nanostructures, the research facilitates the creation of unique material properties and applications. The study integrates micro/nanoscale lithography with two types of CRNs: the first, driven by a synthetic self-assembled system featuring a supramolecular hydrogelator catalyzed by protons, and the second, the Belousov-Zhabotinsky (BZ) reaction, a non-linear chemical oscillatory CRN. Both approaches seek to control local and transient CRNs using micro/nanoscale patterns.

Chapter 1 provides an overview of current methods for spatiotemporal CRN control. **Chapter 2** details the top-down and bottom-up fabrication techniques and outlines the CRN and analytical methods used in the thesis.

Chapter 3, titled **"Quantification of Proton Pumping in Biological Membrane Patches,"** focuses on measuring localized proton gradients from Purple Membranes (PMs), a light-driven proton pump. It describes the design and fabrication of an optically triggered device and uses fluorescence microscopy to document and control proton pumping. Potential applications include managing fuel density and production rates in proton-catalyzed CRNs.

Chapter 4, titled "**Control of a Gel-Forming Chemical Reaction Network Using Light-Triggered Proton Pumps,**" combines an acid catalyst-assisted self-assembly CRN with PMs. It aims to create a localized CRN that can be switched on and off with an optical trigger. The chapter details a system for measuring pH increases through irreversible fiber growth accelerated by protons and demonstrates the influence of PM pumping on microscale hydrogel formation using liquid atomic force microscopy and confocal laser scanning microscopy. The system is designed to develop a pH-responsive hydrogel that responds to external stimuli.

Chapter 5, titled **"Network of Light-Triggered Proton Pumps,"** explores manipulating proton flux for spatiotemporal control of CRNs. It involves fabricating a device that combines nanochannels with locally controlled PM deposition for nanoscale fuel transport. The chapter covers the fabrication of nanochannels on a $Si/SiO_2/Al_2O_3$ substrate using thermal scanning probe lithography (t-SPL), atomic layer deposition, plasma-enhanced chemical vapor deposition, and photolithography. It also discusses localized PM deposition in the Tunable Nanofluidic Confinement Apparatus (TNCA) and the development of a pH sensor using a pH-sensitive dye.

Chapter 6, titled **"Networks of Microscale Chemical Oscillators: Toward Chemical Computing,"** aims to miniaturize and couple microscale chemical reactors (MCRs) to create a network of communicating chemical oscillators. The chapter demonstrates chemical

communication (coupling and synchronization) within complex MCR networks driven by the BZ reaction, aiming to mimic signaling and regulate BZ reactions at specific locations and times. The study proposes new methods for diversifying and optimizing information processing.

Overall, this thesis presents the development and study of CRN-driven devices for spatiotemporal control, advancing applications in sensing, material property studies, and computation. The research is expected to enhance emerging technologies and deepen the understanding of chemistry in relation to biology, materials science, physics, and computing.

Samenvatting

Dit proefschrift, getiteld " **Reaction Cascades Coupled to Surface-Chemical Nanoscale Patterns**," heeft als doel het ontwikkelen van strategieën voor spatiotemporale controle van chemische reactienetwerken (CRN's) op micro- en nanoschaal. Door de grootte en vorm van nanostructuren te beheersen, bevordert dit onderzoek de ontwikkeling van unieke materiaaleigenschappen en toepassingen. De studie integreert micro/nanoschaal lithografie met twee soorten CRN's: de eerste, aangedreven door een synthetisch zelfgeassembleerd systeem met een supramoleculaire hydrogelator die door protonen wordt gecatalyseerd, en de tweede, de Belousov-Zhabotinsky (BZ) reactie, een niet-lineaire chemische oscillatoire CRN. Beide benaderingen beogen het beheersen van lokale en tijdelijke CRN's door middel van micro/nanoschaalpatronen.

Hoofdstuk 1 biedt een overzicht van de huidige methoden voor spatiotemporale controle van CRN's. **Hoofdstuk 2** beschrijft de top-down en bottom-up fabricagetechnieken en schetst de CRN- en analysemethoden die in het proefschrift worden toegepast.

Hoofdstuk 3, getiteld " **Quantification of Proton Pumping in Biological Membrane Patches**," richt zich op het meten van gelokaliseerde protongradiënten van Paarse Membranen (PM's), een lichtgestuurde protonpomp. Dit hoofdstuk beschrijft het ontwerp en de fabricage van een optisch getriggerd apparaat en maakt gebruik van fluorescentiemicroscopie om protonpompen te beschrijven en te controleren. Mogelijke toepassingen omvatten het reguleren van brandstofdichtheid en productiesnelheid in proton-gecatalyseerde CRN's.

Hoofdstuk 4, getiteld " **Control of a Gel-Forming Chemical Reaction Network Using Light-Triggered Proton Pumps**," combineert een door een zuur-catalysator ondersteunde zelfassemblage CRN met PM's. Het doel is het creëren van een gelokaliseerd CRN dat kan worden in- en uitgeschakeld met een optische trigger. Dit hoofdstuk behandelt een systeem voor het meten van pH-verhogingen door middel van onomkeerbare vezelgroei versneld door protonen, en demonstreert de invloed van PM-pompen op de vorming van nanoschaal hydrogel met behulp van liquid atomic force microscopy en confocale laser scanningmicroscopie. Het systeem is ontworpen om een pH-responsieve hydrogel te ontwikkelen reageert op externe stimuli.

Hoofdstuk 5, getiteld " **Network of Light-Triggered Proton Pumps**," onderzoekt de manipulatie van protonflux voor spatiotemporale controle van CRN's. We fabriceren een apparaat dat nanochannels combineert met lokaal gecontroleerde PM-depositie voor nanoschaal brandstoftransport. Dit hoofdstuk behandelt de fabricage van nanochannels op een $Si/SiO_2/Al_2O_3$-substraat met behulp van thermische scanning probe lithografie (t-SPL), atomaire laagafzetting, thermal scanning probe lithography (t-SPL), atomic layer

deposition, plasma-enhanced chemical vapor deposition, en photolithography. Daarnaast wordt lokale PM-depositie in de Tunable Nanofluidic Confinement Apparatus (TNCA) besproken, evenals de ontwikkeling van een pH-sensor met een pH-gevoelige kleurstof.

Hoofdstuk 6, getiteld "**Networks of Microscale Chemical Oscillators: Toward Chemical Computing**," heeft als doel het miniaturiseren en koppelen van microschaal chemische reactors (MCR's) om een netwerk van communicerende chemische oscillatoren te creëren. Dit hoofdstuk demonstreert chemische communicatie (koppeling en synchronisatie) binnen complexe MCR-netwerken die worden aangedreven door de BZ-reactie, met als doel het nabootsen van signalering en het reguleren van BZ- reacties op specifieke locaties en tijdstippen. De studie stelt nieuwe methoden voor om informatieverwerking te diversifiëren en te optimaliseren.

Al met al presenteert dit proefschrift de ontwikkeling en bestudering van CRN- gestuurde apparaten voor spatiotemporale controle, met vooruitgang in toepassingen op het gebied van sensing, materiaaleigenschappen en computationele studies.

Dit onderzoek verbeterd de toepassingen van opkomende technologieën en verdiept de kennis van chemie in relatie tot biologie, materiaalkunde, fysica en computationele wetenschappen.

Acknowledgement

This Ph.D. represents the realization of a long-standing aspiration. Before starting, I was somewhat aware of the challenges involved, but I now fully appreciate how demanding this journey is. Throughout this time, I have grown in many ways, guided by the goal of completing this endeavor to the best of my ability.

Pursuing my Ph.D. at TU Delft, in collaboration with IBM Research – Zurich (IBM ZRL), has been an opportunity beyond my expectations. Living in Switzerland had been a personal goal since my first visit, and beginning my academic work in the Netherlands was an entirely new and rewarding experience. It is an honor to conduct research in both institutions. The combination of academic and industrial environments was essential for broadening my experience. Furthermore, being part of the ITN project was especially valuable, as it enabled me to strengthen both my academic and transferable skills.

I would like to thank my supervisor, **Heiko**, for guiding me throughout my research, supporting the development of my ideas, and providing patient corrections whenever necessary. I also appreciate your collegial support. I thank my promotor, **Jan**, for your constructive and kind feedback on my progress, and for your insights and support in our joint project. I am also grateful to my promotor **Eduardo** for his guidance at the conclusion of this work, and for his motivating and insightful perspectives. I thank **Armin** for his patience, his willingness to share expertise, and his valuable questions and suggestions. **Rolf**, my first manager at IBM ZRL, thank you for your encouragement and supportive leadership, which were vital at an early stage. **Bernd**, my second manager at IBM ZRL, thank you for your support and commitment to the team. I am also grateful to **Heike**, head of the department, for her support.

I thank **Dimitri** (University of Bern) for providing PM patches and for our helpful discussions. I also thank **Juan** (Harvard University) for the opportunity to work in his lab.

This Ph.D. was possible thanks to substantial technical support. I am grateful to the Cleanroom Operations Team at the Binnig and Rohrer Nanotechnology Center (BRNC) and the model shot at IBM-ZRL. In particular, I thank **Ute** for her remarkable teaching and support in the cleanroom, from whom I learned much of what I know about cleanroom facilities. I am also grateful to **Steffen** for his assistance with the FIB-SEM tool at a critical stage of this work, and for his continued support. I also thank **Robi** for his essential contribution to the microfluidics work, and for his clear guidance. At TU Delft, I thank **Marcel** for his exceptional support, patience, and instruction with liquid AFM, from which I learned extensively. From Heidelberg Instruments Nano, I thank **Jana** for her assistance with t-SPL and her collegiality, as well as **Nick**, **Emine**, and **Samuel** for sharing their expertise with the tool and for being excellent officemates.

At IBM, I would like to thank my colleague and friend **Vesna** for her support in the

cleanroom, her scientific contributions, and her friendship. I am also grateful to **Chloe** and **Philippe** for their scientific discussions and contributions, **Silvia** for her assistance with translations and practical matters in Switzerland, **Daniel** for his support and conversations, and **Jilly** for her kind help with technical issues and our discussions.

At TU Delft, I thank **Ardeshir** for his collaboration on one of the projects of this thesis. I also thank **Benni** and **Elmira** for their support, conversations, and moments together. **Suellen**, thank you for your assistance regarding the university and for speaking Portuguese with me in Delft. **Veby**, thank you for your support and kindness.

From ITN CreaNet, I would like to thank all my colleagues, as well as the researchers, for sharing valuable experiences. Although the pandemic limited our interactions, we made every effort to remain connected. From Harvard, I thank **Alberto**, **Jennifer**, and **Chenyu** for their support during my stay, as well as my friend **Jaqueline**, whose companionship was important during the winter in Cambridge. Thanks to **Artur** for his support before and during my stay in USA.

From UniMainz, I thank **Andreas** for the opportunity to work with him and his team. I am grateful to **Oliver** for introducing me to the new world of soft robots, **Piet** for his help in translating my summary into Dutch and for his support, and to colleagues **Kohei**, **Brigitta**, **Yuheng**, and **Diego** for their support and friendship. I also thank **Daniel**, **Maria**, **Lorena**, **Soumya**, **Manju**, **Lydia**, **Nikta**, **Ali**, **Miao**, **Doruk**, **Ricarda**, as well as the many other colleagues in the laboratory.

I also wish to thank female colleagues and mentors in science who supported me. My bachelor's supervisor, **Maria Aparecida**, has been an ongoing source of encouragement and guidance, for which I am sincerely grateful. **Camila**, thank you for your kindness and support during my earlier academic years. **Min**, thank you for motivating my frequent visits to Italy and for your example as a researcher and colleague. **Cuifeng**, thank you for your support in pursuing a Ph.D. and for your inspiring example.

For my friends in Mainz, I would like to thank **Yueh-Jen** for making my move to Mainz happier. Also, **Helena** for being a support and grateful company in Germany. **Raimunda** and **Tatá** for making me feel part of your familiar cycle. I also thank my flatmates, **Sara** and **Blerta**, for their support and friendship.

During my years in Zurich, I was fortunate to have friends who provided invaluable companionship: **Antonia** and **Neide**, for being my family in Switzerland; **Patricia**, forcing me to not forget my French and my love for Paris; **Nalva**, for her kindness; **Clara** and **Silvan**, for her presence and art, and for taking the nice profile picture of me presented at this thesis; **Leticia**, for her steadfast friendship; **Lorena**, for her continued company over the phone; **Luci**, for being an inspiration as a strong woman; **Christine** and her family, for supporting me in my move to Switzerland; and **Doris**, for her guidance and support during the process of this thesis.

I also thank my friends in Brasília. **Lais**, for your friendship since the day we met; **Heloísa**, for your integrity, authenticity, and support, as well as for designing the cover and making this thesis book looks so nice; **Aline**, for your strength and inspiration; **Natan**, for your long-standing friendship; **Agni**, for your trust and friendship; **Xani** and **Rodrigo**, for our mutual support and shared experiences; and **Victor**, for being the first friend I made in Brasília and for introducing me to many others. **Jean**, for your companionship; **Manuela**, my partner in crime through long library hours.

From Belém, my hometown, I thank **Andreiza** and **José Adailton** for their long time friendship and their support during my master's and Ph.D. studies with the grammar and illustrations. I also thank **Dilermando** for our reciprocal visits and shared experiences in Europe, **Raimunda** for her understanding and encouragement, **Ana Raquel** for her continuous support, **Matheus** for his life-long friendship, **Laercio** for his inspiring example, **Débora** for her kind messages and sensibility, **Davi** and **Lucas** for staying in touch, **Rodrigo** for his insights about the propositions of this thesis and **Eliana** for her spiritual support.

Finally, I thank my family. My grandmother **Ana**, my godmother that always by my side. My uncles and aunts — especially **Maria do Socorro** — for their care and support during my childhood. My brother **Jhoseffer** for supporting my parents while I have been abroad, and my nephew **Francisco** for the joy he brings. I thank my father **José** for fostering my interest in literature and cinema and for supporting my choices, and my mother **Ana Lúcia** for encouraging my education and respecting my decisions from the beginning.

To anyone not explicitly mentioned but who contributed to this journey, please accept my sincere gratitude.

About the author

Jacqueline Figueiredo da Silva was born on 17 October 1991 in Belém do Pará, in the Amazon region of Brazil. She obtained a bachelor's degree in Chemistry and Industrial Chemistry from the Universidade de Brasília, Brazil, in 2016. As part of her undergraduate studies, she spent one year (2014) as an exchange student at the Université de Savoie, France, supported by *Ciências sem Fronteiras* scholarship, and completed a four-month research internship (2015) at the Université de Montréal, Canada, funded by *ELAP* scholarship.

In 2019, she completed the Erasmus Mundus Joint Master's Degree in Advanced Spectroscopy in Chemistry from the Université de Lille, France, and the Jagiellonian University, Poland, supported by *Erasmus+* scholarship. During her master's studies, she also conducted a summer research internship (2018) at the Adolphe Merkle Institute, Switzerland.

Following the completion of her master's degree, she commenced an industrial doctoral project within the CReaNeT network under an ITN–Marie Skłodowska-Curie Action at IBM Research – Europe, Switzerland, under the supervision of Dr. Heiko Wolf. Her doctoral degree was pursued at TU Delft, the Netherlands, in the Advanced Soft Matter group under the supervision of Prof. Dr. Jan van Esch. In 2023–2024, she also undertook a five-month research internship at Harvard University, United States of America. Her doctoral research focused on the design and fabrication of nanoscale surface-chemical patterns to control the spatial distribution and local concentration of chemical reaction network components, as detailed in this thesis.

Since 2024, she has held a postdoctoral research position at the University of Mainz, Germany, in the laboratory of Prof. Dr. Andreas Walther, where her work is directed toward the development of autonomous soft robotic engines.

List of publications

1. Related to this thesis

- **Publications**

- **Figueiredo da Silva, J.**, Roshanasan, A., Bus, M., Fotiadis, D., Knoll, A. W., van Esch, J. H., & Wolf, H. (2025). Control of a Gel-Forming Chemical Reaction Network Using Light-Triggered Proton Pumps. *Langmuir*, 41(12), 8071-8080.

- **Figueiredo da Silva, J.**, Bacheva, V., Drechsler, U., Nicollier, P., Reidt, S., Fotiadis, D., ... & Wolf, H. (2024). Fabrication of a hybrid device for the integration of light-triggered proton pumps. *Micro and Nano Engineering*, 23, 100250.

- Ruggeri, F., Schwemmer, C., Stauffer, M., Nicollier, P. M., **Figueiredo da Silva, J.**, Bosshart, P. D., ... & Wolf, H. (2022). Placement of Biological Membrane Patches in a Nanofluidic Gap With Control Over Position and Orientation. *Advanced Materials Interfaces*, 9(23), 2200941.

- **Patent**

- Knoll, A., Wolf, H., Nicollier, P. M., Widmer, D., & **da Silva, J. F.** (2024). U.S. Patent Application No. 18/052,989.

2. Not related to the thesis

- **Master thesis**

- **Figueiredo da Silva, J.** (2020). Functionalization of SERS substrates for ex vivo detection of inflammatory state [Master's thesis, Jagiellonian University in Krakow].

- **Publications**

- Skarsetz, O., Swinkels, P. J., **Figueiredo da Silva, J.**, Vozzolo, G., Masukawa, M., Fusi, G., ... & Walther, A. (2025). Soft Robotic Engines with Non-Reciprocal Motion by Physical Intelligence. *Advanced Materials*, e11630.

- De Vreede, L. J., Ying, C., Houghtaling, J., **Da Silva, J. F.**, Hall, A. R., Lovera, A., & Mayer, M. (2019). Wafer-scale fabrication of fused silica chips for low-noise recording of resistive pulses through nanopores. *Nanotechnology*, 30(26), 265301.


TU Delft
Delft
University of
Technology

Reaction cascades coupled to surface-chemical nanoscale patterns

Figueiredo da Silva, J.

DOI
10.4233/uuid:a477b7fa-0b2d-44e9-8fbd-68d2320f66c6

Publication date
2025

Document Version
Final published version

Citation (APA)
Figueiredo da Silva, J. (2025). *Reaction cascades coupled to surface-chemical nanoscale patterns*. [Dissertation (TU Delft), Delft University of Technology]. https://doi.org/10.4233/uuid:a477b7fa-0b2d-44e9-8fbd-68d2320f66c6

REACTION CASCADES COUPLED TO SURFACE-CHEMICAL NANOSCALE PATTERNS

JACQUELINE FIGUEIREDO DA SILVA

Reaction cascades coupled to surface-chemical nanoscale patterns.

Dissertation
for the purpose of obtaining the degree of doctor
at Delft University of Technology
by the authority of the Rector Magnificus, Prof.dr.ir. T.H.J.J. van der Hagen,
chair of the Board of Doctorates
to be defended publicly on
Wednesday 15 October 2025 at 10 o'clock

by

Jacqueline FIGUEIREDO DA SILVA
Master of Science in Chemistry,
Jagiellonian University, Poland and Université de Lille, France.

Born in Belém, Brazil.

This dissertation has been approved by the promotors.

Composition of the doctoral committee:

Rector Magnificus	Chairperson
Prof. dr. J.H.van Esch	Delft University of Technology, promotor
Dr. E. Mendes	Delft University of Technology, promotor
Dr. H. Wolf	IBM Research Europe – Zurich, external advisor

Independent members:

Prof. dr. S.J. Picken	Delft University of Technology
Dr. A. Accardo	Delft University of Technology
Prof.dr. J.J.L.M. Cornelissen	University of Twente
Prof. dr. V. Garbin	Delft University of Technology
Prof. dr. R. Eelkema	Delft University of Technology, reserve member

The work described in this dissertation was conducted in IBM Research Europe- Zurich, Switzerland and in the Advanced Soft Matter (ASM) group, Department of Chemical Engineering, Faculty of Applied Sciences, Delft University of Technology, Netherlands. The research was funded by the European Innovative Training Network (ITN) entitled "Chemical Reaction Networks: Signal amplification, spatiotemporal control, and materials" (CReaNet), IBM Research Europe - Zurich and TU Delft.

Table of Contents

Chapter 1

Introduction

1.1 Background

The varied manifestations of life encompass elements such as clocks, [1,2] switches, [3] computation, [4–7] autonomous oscillators, [8–10] and components associated with dynamic behavior. Such manifestations include the computational capacities of neuron synapses [11] and other 'magic' biological systems, [12] which can be understood and modeled through chemical reaction networks (CRNs). [13] In response to the ongoing need for innovative materials to enhance the well-being of society, researchers have taken on the challenge of replicating the remarkable efficiency observed in natural systems. [14–19] Scientists have been designing and investigating artificial CRNs, with focus on the control, prediction, and optimization of chemical processes. [20] These networks can be programmed to perform specific tasks, [21] respond to external stimuli, [22–25] or exhibit dynamic behaviors. [26] The main objective is to comprehend, manipulate, and harness CRNs to create functional and programmable systems. [27,28]

The exploration of spatial and temporal control over CRNs is essential for utilizing them to regulate other spatially confined processes.[24] For instance, this control can ensure the accurate transport of molecules to predetermined locations within a complex environment. [29,30] Approaches to spatiotemporal control of CRNs can be categorized as passive or active. [31] The passive method depends on the natural properties of the chosen chemical system to determine the location and timing of the reaction. In contrast, the active approach depends on external actions that remotely control the CRN onset.

1.2 Passive spatiotemporal control of CRNs

Passive techniques offer the means to control the initiation of a CRN without external stimulus. [31] The term 'passive' indicates the self-regulating nature of the system, as the periodic behavior emerges inherently from the interplay of reaction kinetics and initial conditions without the need for external triggers. [32–36] The passive system utilizes the intrinsic properties of the selected chemical system to anticipate the location and timing of the reaction. [37,38] The initial chemical composition of a system dictates temporal parameters such as the lifetime of a pH transient state. [39] The spatial control of passive CRNs can be achieved by patterning the surface beforehand with an essential chemical in a given system. [40–42] Numerous chemical oscillators have been documented, spanning various fields, including DNA, [43–45] small organic molecule oscillators, [27] and inorganic

redox oscillators. [34] These equilibrium systems demonstrate a self-regulating autonomous behavior, which is a characteristic widespread in living systems. [24]

1.3 Active spatiotemporal control of CRNs

Unlike passive methods, active approaches necessitate an external trigger to start a chemical process. [48] They facilitate the activation and deactivation of a CRN at specific times through a trigger, thereby exerting control over the location and/or timing of the reaction. For instance, light is a well-established trigger to remotely activating or controlling a CRN. [46]

Efforts to achieve spatial control also involve the confinement and controlled delivery of chemical reactants. [47] Researchers developed metallic containers with volumes ranging from picoliters to nanoliters, incorporating modulated pores for the controlled release of specific guests. Temporal control depends on pore size and solvent conditions, while magnetic fields enable remote guidance for spatial control. [48] Furthermore, chemical release is affected by the gel or polymer used for immobilization. [49–53]

1.4 Research goals

To advance the spatiotemporal control of CRNs at the nanoscale, it is vital not only to explore the fabrication of suitable materials and development of micro/nanoscale sensors but also to investigate methods for chemical confinement and transportation. [24] Beyond proof-of-concept, it is important to analyze practical applications by fully expanding and investigating the scope of CRNs in various technologies, to thoroughly realize the potential of these autonomous material systems.

In this context, there has been extensive exploration of systems responsive to pH, with the goal of creating innovative materials [54] and developing applications in biomedicine, such as in drug delivery. [55] This intense research is attributed to the fact that the impacts caused by pH changes act as triggers for numerous artificial and natural CRNs. [24,56] The use of pH as a trigger enables the production of switchable rheology modifiers [24,57,58] and development toward molecular computing. [59]

Studies conducted at TU Delft have reported the use of proton-catalyzed supramolecular gel [60] on catalytic surfaces of micropatterned proton sites through microprinting, [61] micro localized polymer brushes, [62] and nanoparticles. [63] The structures primarily grew in areas where the catalyst was present. Gelator precursors interacted with catalytic sites to create building blocks that self-assemble into nanofibers. Building blocks were incorporated into the fibers within a confined space at the solid-liquid interface. At the IBM Research Europe-Zurich, a device capable of actively controlling a proton-catalyzed CRN through an external trigger was developed. [64] This device demonstrated nanoscale-controlled deposition of bacteriorhodopsin (bR), a light-driven proton gradient.

Within the scope of this thesis, we used microfabrication processes to design devices that enable the spatiotemporal control of established artificial CRNs. Our first approach aimed to couple purple membranes (PM) containing bR with a proton-catalyzed CRN on a substrate. The main goal of this study was to actively control a CRN spatiotemporally at the micro/nanoscale using light-driven proton pumps that deliver CRN fuel. We developed strategies to externally trigger the CRN via (1) spatiotemporal control of catalyst gradient and (2) catalyst transport at the nanoscale. These strategies aimed to spatiotemporally control the construction of synthetic self- assembled systems.

As another application, we explored an autocatalytic CRN that oscillates over time, called the Belousov–Zhabotinsky (BZ) reaction. [65] The passive spatiotemporal control of the BZ reaction at the microscale enables its application on the development of unconventional systems, such as chemical computers. [66] Current computers based on micro-electronic chips struggle with the demand for energy-efficient processing of continuously increasing amounts of data. A silicon-based CRN-driven system represents a potential solution to these issues.

1.5 Thesis outline

This thesis reports “Reaction cascades coupled to surface-chemical nanoscale patterns.” The six chapters of this thesis show the steps conducted to achieve the aim of our research based on different subgoals. This introduction chapter (Chapter 1) briefly overviews the research theme. Chapter 2 presents the microengineering fabrication techniques used in this study, and it describes the investigated CRNs and analytical methods used to characterize the fabricated materials.

Chapters 3, 4, and 5 provide new strategies for the spatiotemporal control of an externally triggered catalyzed CRN, which was expected to promote the development of functional soft materials. More specifically, Chapter 3 reports the development of a microscale pH sensor based on a maskless chemical lift-off method. The chapter aims to measure the pH gradient of a light-driven proton pump PM-containing bR. In Chapter 4, we present a system that incorporates our proton-catalyzed CRN to PM patches. [67] These patches act as a catalyst source when exposed to light. The in-situ formation of the gel was monitored using liquid atomic force microscopy and confocal laser scanning microscopy. In Chapter 5, we describe the fabrication of a nanochannel network in a silicon-based substrate, [68] which was developed aiming to control the transport of a proton gradient from the PM to the other side of the material surface. The goal was to deliver CRN catalyst to different locations.

Chapter 6 reports the development of an unconventional device driven by a self- catalyzed oscillatory CRN. The goal was to establish a chemical computer vision with specific characteristics, including self-powering capability, low energy consumption, highly parallel systems, and complex systems. For that, we developed a microscale diffusion-driven network toward information processing. A summary of this scientific journey is provided

at the end of this thesis.

1.6 References

(1) Tyson, J. J.; Chen, K. C.; Novak, B. Sniffers, Buzzers, Toggles and Blinkers: Dynamics of Regulatory and Signaling Pathways in the Cell. *Current opinion in cell biology* **2003**, *15* (2), 221–231.

(2) Tyson, J. J.; Albert, R.; Goldbeter, A.; Ruoff, P.; Sible, J. Biological Switches and Clocks. *Journal of The Royal Society Interface* **2008**, 5 (suppl_1), S1–S8.

(3) Tyson, J. J. Modeling the Cell Division Cycle: Cdc2 and Cyclin Interactions. *Proceedings of the National Academy of Sciences* **1991**, *88* (16), 7328–7332.

(4) Moore, C.; Mertens, S. *The Nature of Computation*; OUP Oxford, 2011.

(5) Zenil, H. *A Computable Universe: Understanding and Exploring Nature as Computation*; World Scientific, 2013.

(6) Regev, A.; Shapiro, E. Cellular Abstractions: Cells as Computation. *Nature* **2002**, 419 (6905), 343–343.

(7) de Castro, L. N. Fundamentals of Natural Computing: An Overview. Physics of Life Reviews 2007, 4 (1), 1–36.

(8) Ferrell, J. E.; Tsai, T. Y.-C.; Yang, Q. Modeling the Cell Cycle: Why Do Certain Circuits Oscillate? *Cell* **2011**, 144 (6), 874–885.

(9) Qiao, L.; Nachbar, R. B.; Kevrekidis, I. G.; Shvartsman, S. Y. Bistability and Oscillations in the Huang-Ferrell Model of MAPK Signaling. *PLoS computational biology* **2007**, 3 (9), e184.

(10) Nakajima, M.; Imai, K.; Ito, H.; Nishiwaki, T.; Murayama, Y.; Iwasaki, H.; Oyama, T.; Kondo, T. Reconstitution of Circadian Oscillation of Cyanobacterial KaiC Phosphorylation in Vitro. *Science* **2005**, 308 (5720), 414–415.

(11) Abbott, L. F.; Regehr, W. G. Synaptic Computation. *Nature* **2004**, 431 (7010), 796–803.

(12) Novichkov, A. I.; Hanopolskyi, A. I.; Miao, X.; Shimon, L. J.; Diskin-Posner, Y.; Semenov, S. N. Autocatalytic and Oscillatory Reaction Networks That Form Guanidines and Products of Their Cyclization. *Nature communications* **2021**, 12 (1), 2994.

(13) Feinberg, M. Foundations of Chemical Reaction Network Theory. **2019**.

(14) Pecqueur, S.; Mastropasqua Talamo, M.; Guérin, D.; Blanchard, P.; Roncali, J.; Vuillaume, D.; Alibart, F. Neuromorphic Time-dependent Pattern Classification with Organic Electrochemical Transistor Arrays. *Advanced Electronic Materials* **2018**, 4 (9), 1800166.

(15) Adamatzky, A. *Advances in Unconventional Computing: Volume 1*: Theory; Springer, **2016**; Vol. 22.

(16) Adamatzky, A. *Reaction-Diffusion Automata: Phenomenology, Localisations, Computation*; Springer Science & Business Media, **2012**; Vol. 1.

(17) Cucchi, M.; Kleemann, H.; Tseng, H.; Ciccone, G.; Lee, A.; Pohl, D.; Leo, K. Directed Growth of Dendritic Polymer Networks for Organic Electrochemical Transistors and Artificial Synapses. *Advanced Electronic Materials* **2021**, 7 (10), 2100586.

(18) Usami, Y.; van de Ven, B.; Mathew, D. G.; Chen, T.; Kotooka, T.; Kawashima, Y.; Tanaka, Y.; Otsuka, Y.; Ohoyama, H.; Tamukoh, H. In-materio Reservoir Computing in a Sulfonated Polyaniline Network. *Advanced Materials* **2021**, 33 (48), 2102688.

(19) van Duppen, P.; Robinson, W.; Daines, E.; Huck, W. Trajectory-Dependent Compositional Outcomes in a Prebiotic Reaction Network. **2022**.

(20) Sharko, A.; Spitzbarth, B.; Hermans, T. M.; Eelkema, R. Redox-Controlled Shunts in a Synthetic Chemical Reaction Cycle. *J. Am. Chem. Soc.* **2023**, 145 (17), 9672–9678. https://doi.org/10.1021/jacs.3c00985.

(21) Ivanov, N. M.; Baltussen, M. G.; Regueiro, C. L. F.; Derks, M. T. G. M.; Huck, W. T. S. Computing Arithmetic Functions Using Immobilised Enzymatic Reaction Networks. *Angewandte Chemie* **2023**, 135 (7), e202215759. https://doi.org/10.1002/ange.202215759.

(22) Singh, N.; Lopez-Acosta, A.; Formon, G. J. M.; Hermans, T. M. Chemically Fueled Self-Sorted Hydrogels. *J. Am. Chem. Soc.* **2022**, 144 (1), 410–415. https://doi.org/10.1021/jacs.1c10282.

(23) Sharko, A.; Livitz, D.; De Piccoli, S.; Bishop, K. J. M.; Hermans, T. M. Insights into Chemically Fueled Supramolecular Polymers. *Chem. Rev.* **2022**, 122 (13), 11759–11777. https://doi.org/10.1021/acs.chemrev.1c00958.

(24) Sharma, C.; Maity, I.; Walther, A. pH-Feedback Systems to Program Autonomous Self-Assembly and

Material Lifecycles. *Chem. Commun.* **2023**, 59 (9), 1125–1144. https://doi.org/10.1039/D2CC06402B.
(25) Maity, I.; Wagner, N.; Mukherjee, R.; Dev, D.; Peacock-Lopez, E.; Cohen-Luria, R.; Ashkenasy, G. A Chemically Fueled Non-Enzymatic Bistable Network. *Nature Communications* **2019**, 10 (1), 4636.
(26) Leira-Iglesias, J.; Tassoni, A.; Adachi, T.; Stich, M.; Hermans, T. M. Oscillations, Travelling Fronts and Patterns in a Supramolecular System. *Nature Nanotech* **2018**, 13 (11), 1021–1027. https://doi.org/10.1038/s41565-018-0270-4.
(27) Ter Harmsel, M.; Maguire, O. R.; Runikhina, S. A.; Wong, A. S.; Huck, W. T.; Harutyunyan, S. R. A Catalytically Active Oscillator Made from Small Organic Molecules. *Nature* **2023**, 621 (7977), 87–93.
(28) Wang, Q.; Qi, Z.; Chen, M.; Qu, D.-H. Out-of-equilibrium Supramolecular Self-assembling Systems Driven by Chemical Fuel. *Aggregate* **2021**, 2 (5), e110.
(29) Wang, F.; Zhang, X.; Liu, X.; Fan, C.; Li, Q. Programming Motions of DNA Origami Nanomachines.*Small* **2019**, 15 (26), 1900013. https://doi.org/10.1002/smll.201900013.
(30) Desrosiers, A.; Derbali, R. M.; Hassine, S.; Berdugo, J.; Long, V.; Lauzon, D.; De Guire, V.; Fiset, C.; DesGroseillers, L.; Leblond Chain, J.; Vallée-Bélisle, A. Programmable Self-Regulated Molecular Buffers for Precise Sustained Drug Delivery. *Nat Commun* **2022**, 13 (1), 6504. https://doi.org/10.1038/s41467-022-33491-7.
(31) Aubert, S.; Bezagu, M.; Spivey, A. C.; Arseniyadis, S. Spatial and Temporal Control of Chemical Processes. *Nat Rev Chem* **2019**, 3 (12), 706–722. https://doi.org/10.1038/s41570-019-0139-6.
(32) Mai, A. Q.; Bánsági Jr, T.; Taylor, A. F.; Pojman Sr, J. A. Reaction-Diffusion Hydrogels from Urease Enzyme Particles for Patterned Coatings. *Communications Chemistry* **2021**, 4 (1), 101.
(33) Xie, X.-Q.; Zhang, Y.; Liang, Y.; Wang, M.; Cui, Y.; Li, J.; Liu, C.-S. Programmable Transient Supramolecular Chiral G-quadruplex Hydrogels by a Chemically Fueled Non-equilibrium Self-Assembly Strategy. *Angewandte Chemie* **2022**, 134 (9), e202114471.
(34) Shandilya, E.; Brar, S. K.; Mahato, R. R.; Maiti, S. Spatiotemporal Dynamics of Self-Assembled Structures in Enzymatically Induced Agonistic and Antagonistic Conditions. *Chemical Science* **2022**, 13 (1), 274–282.
(35) Paikar, A.; Novichkov, A. I.; Hanopolskyi, A. I.; Smaliak, V. A.; Sui, X.; Kampf, N.; Skorb, E. V.; Semenov, S. N. Spatiotemporal Regulation of Hydrogel Actuators by Autocatalytic Reaction Networks. *Advanced Materials* **2022**, 34 (13), 2106816. https://doi.org/10.1002/adma.202106816.
(36) Orbán, M.; Kurin-Csörgei, K.; Epstein, I. R. pH-Regulated Chemical Oscillators. *Accounts of Chemical Research* **2015**, 48 (3), 593–601.
(37) Ashkenasy, G.; Hermans, T. M.; Otto, S.; Taylor, A. F. Systems Chemistry. *Chem. Soc. Rev.* **2017**, 46 (9), 2543–2554. https://doi.org/10.1039/C7CS00117G.
(38) Wagner, N.; Hochberg, D.; Peacock-Lopez, E.; Maity, I.; Ashkenasy, G. Open Prebiotic Environments Drive Emergent Phenomena and Complex Behavior. *Life* **2019**, 9 (2), 45.
(39) Tóth-Szeles, E.; Horváth, J.; Holló, G.; Szűcs, R.; Nakanishi, H.; Lagzi, I. Chemically Coded Time-Programmed Self-Assembly. *Molecular Systems Design & Engineering* **2017**, 2 (3), 274–282.
(40) Durie, K.; Yatvin, J.; McNitt, C. D.; Reese, R. A.; Jung, C.; Popik, V. V.; Locklin, J. Multifunctional Surface Manipulation Using Orthogonal Click Chemistry. *Langmuir* **2016**, 32 (26), 6600–6605.
(41) Arnold, R. M.; Patton, D. L.; Popik, V. V.; Locklin, J. A Dynamic Duo: Pairing Click Chemistry and Postpolymerization Modification to Design Complex Surfaces. *Accounts of chemical research* **2014**, 47 (10), 2999–3008.
(42) Arnold, R. M.; McNitt, C. D.; Popik, V. V.; Locklin, J. Direct Grafting of Poly (Pentafluorophenyl Acrylate) onto Oxides: Versatile Substrates for Reactive Microcapillary Printing and Self-Sorting Modification. *Chemical Communications* **2014**, 50 (40), 5307–5309.
(43) Franco, E.; Friedrichs, E.; Kim, J.; Jungmann, R.; Murray, R.; Winfree, E.; Simmel, F. C. Timing Molecular Motion and Production with a Synthetic Transcriptional Clock. *Proceedings of the National Academy of Sciences* **2011**, 108 (40), E784–E793. https://doi.org/10.1073/pnas.1100060108.
(44) Padirac, A.; Fujii, T.; Estévez-Torres, A.; Rondelez, Y. Spatial Waves in Synthetic Biochemical Networks. *J. Am. Chem. Soc.* **2013**, 135 (39), 14586–14592. https://doi.org/10.1021/ja403584p.
(45) Tayar, A. M.; Karzbrun, E.; Noireaux, V.; Bar-Ziv, R. H. Synchrony and Pattern Formation of Coupled Genetic Oscillators on a Chip of Artificial Cells. *Proceedings of the National Academy of Sciences* **2017,** 114 (44), 11609–11614.
(46) Kalayci, K.; Frisch, H.; Truong, V. X.; Barner-Kowollik, C. Green Light Triggered [2+ 2] Cycloaddition of Halochromic Styrylquinoxaline—Controlling Photoreactivity by pH. *Nature Communications* **2020**, 11

(1), 4193.
(47) Kalinin, Y. V.; Murali, A.; Gracias, D. H. Chemistry with Spatial Control Using Particles and Streams. *RSC advances* **2012**, 2 (26), 9707–9726.
(48) Leong, T.; Gu, Z.; Koh, T.; Gracias, D. H. Spatially Controlled Chemistry Using Remotely Guided Nanoliter Scale Containers. *Journal of the American Chemical Society* **2006,** 128 (35), 11336–11337.
(49) Monks, P.; Wychowaniec, J. K.; McKiernan, E.; Clerkin, S.; Crean, J.; Rodriguez, B. J.; Reynaud, E. G.; Heise, A.; Brougham, D. F. Spatiotemporally Resolved Heat Dissipation in 3D Patterned Magnetically Responsive Hydrogels. *Small* **2021**, 17 (5), 2004452.
(50) Hobich, J.; Blasco, E.; Wegener, M.; Mutlu, H.; Barner-Kowollik, C. Synergistic, Orthogonal, and Antagonistic Photochemistry for Light-Induced 3D Printing. *Macromolecular Chemistry and Physics* **2023**, 224 (1), 2200318.
(51) Gregor, A.; Filová, E.; Novák, M.; Kronek, J.; Chlup, H.; Buzgo, M.; Blahnová, V.; Lukášová, V.; Bartoš, M.; Nečas, A. Designing of PLA Scaffolds for Bone Tissue Replacement Fabricated by Ordinary Commercial 3D Printer. *Journal of biological engineering* **2017**, 11 (1), 1–21.
(52) Hippler, M.; Lemma, E. D.; Bertels, S.; Blasco, E.; Barner-Kowollik, C.; Wegener, M.; Bastmeyer, M. 3D Scaffolds to Study Basic Cell Biology. *Advanced Materials* **2019**, 31 (26), 1808110.
(53) Barner-Kowollik, C.; Bastmeyer, M.; Blasco, E.; Delaittre, G.; Müller, P.; Richter, B.; Wegener, M. 3D Laser Micro-and Nanoprinting: Challenges for Chemistry. *Angewandte Chemie International Edition* **2017,** 56 (50), 15828–15845.
(54) Wang, G.; Liu, Y.; Liu, Y.; Xia, N.; Zhou, W.; Gao, Q.; Liu, S. The Non-Equilibrium Self-Assembly of Amphiphilic Block Copolymers Driven by a pH Oscillator. *Colloids and Surfaces A: Physicochemical and Engineering Aspects* **2017**, 529, 808–814. https://doi.org/10.1016/j.colsurfa.2017.06.078.
(55) Sonawane, S. J.; Kalhapure, R. S.; Govender, T. Hydrazone Linkages in pH Responsive Drug Delivery Systems. *European Journal of Pharmaceutical Sciences* **2017**, 99, 45–65. https://doi.org/10.1016/j.ejps.2016.12.011.
(56) Wang, X.; Moreno, S.; Boye, S.; Wen, P.; Zhang, K.; Formanek, P.; Lederer, A.; Voit, B.; Appelhans, D. Feedback-Induced and Oscillating pH Regulation of a Binary Enzyme–Polymersomes System. *Chem. Mater.* **2021,** 33 (17), 6692–6700. https://doi.org/10.1021/acs.chemmater.1c00897.
(57) Go, D.; Rommel, D.; Chen, L.; Shi, F.; Sprakel, J.; Kuehne, A. J. Programmable Phase Transitions in a Photonic Microgel System: Linking Soft Interactions to a Temporal pH Gradient. *Langmuir* **2017**, 33 (8), 2011–2016.
(58) Boekhoven, J.; Hendriksen, W. E.; Koper, G. J. M.; Eelkema, R.; Van Esch, J. H. Transient Assembly of Active Materials Fueled by a Chemical Reaction. *Science* **2015**, 349 (6252), 1075–1079. https://doi.org/10.1126/science.aac6103.
(59) Draper, T. C.; Poros-Tarcali, E.; Pérez-Mercader, J. pH Oscillating System for Molecular Computation as a Chemical Turing Machine. *ACS Omega* **2022**, 7 (7), 6099–6103. https://doi.org/10.1021/acsomega.1c06505.
(60) Boekhoven, J.; Poolman, J. M.; Maity, C.; Li, F.; Van Der Mee, L.; Minkenberg, C. B.; Mendes, E.; Van Esch, J. H.; Eelkema, R. Catalytic Control over Supramolecular Gel Formation. *Nature Chem* **2013**, 5 (5), 433–437. https://doi.org/10.1038/nchem.1617.
(61) Olive, A. G.; Abdullah, N. H.; Ziemecka, I.; Mendes, E.; Eelkema, R.; Van Esch, J. H. Spatial and Directional Control over Self-Assembly Using Catalytic Micropatterned Surfaces. *Angewandte Chemie International Edition* **2014**, 53 (16), 4132–4136.
(62) Wang, Y.; Oldenhof, S.; Versluis, F.; Shah, M.; Zhang, K.; Van Steijn, V.; Guo, X.; Eelkema, R.; Van Esch, J. H. Controlled Fabrication of Micropatterned Supramolecular Gels by Directed Self-Assembly of Small Molecular Gelators. *Small* **2019**, 15 (8), 1804154. https://doi.org/10.1002/smll.201804154.
(63) Wang, Y.; Versluis, F.; Oldenhof, S.; Lakshminarayanan, V.; Zhang, K.; Wang, Y.; Wang, J.; Eelkema, R.; Guo, X.; Van Esch, J. H. Directed Nanoscale Self-Assembly of Low Molecular Weight Hydrogelators Using Catalytic Nanoparticles. *Advanced Materials* **2018**, 30 (21), 1707408. https://doi.org/10.1002/adma.201707408.
(64) Ruggeri, F.; Schwemmer, C.; Stauffer, M.; Nicollier, P. M.; Figueiredo da Silva, J.; Bosshart, P. D.; Kochems, K.; Fotiadis, D.; Knoll, A.; Wolf, H. Placement of Biological Membrane Patches in a Nanofluidic Gap With Control Over Position and Orientation. *Advanced materials interfaces* **2022,** 9 (23), 2200941.
(65) Field, R. J.; Noyes, R. M. Oscillations in Chemical Systems. IV. Limit Cycle Behavior in a Model of a Real Chemical Reaction. The Journal of Chemical Physics 1974, 60 (5), 1877–1884.

https://doi.org/10.1063/1.1681288.

(66) Dueñas-Díez, M.; Pérez-Mercader, J. How Chemistry Computes: Language Recognition by Non-Biochemical Chemical Automata. From Finite Automata to Turing Machines. *iScience* **2019**, 19, 514–526. https://doi.org/10.1016/j.isci.2019.08.007.

(67) Figueiredo da Silva, J.; Roshanasan, A.; Bus, M.; Fotiadis, D.; Knoll, A. W.; van Esch, J. H.; Wolf, H. Control of a Gel-Forming Chemical Reaction Network Using Light-Triggered Proton Pumps. *Langmuir* **2025**.

(68) Figueiredo Da Silva, J.; Bacheva, V.; Drechsler, U.; Nicollier, P.; Reidt, S.; Fotiadis, D.; Knoll, A.; Wolf, H. Fabrication of a Hybrid Device for the Integration of Light-Triggered Proton Pumps. *Micro and Nano Engineering* **2024**, 23, 100250. https://doi.org/10.1016/j.mne.2024.100250.

Chapter 2

Nanofabrication and microfabrication: techniques and materials

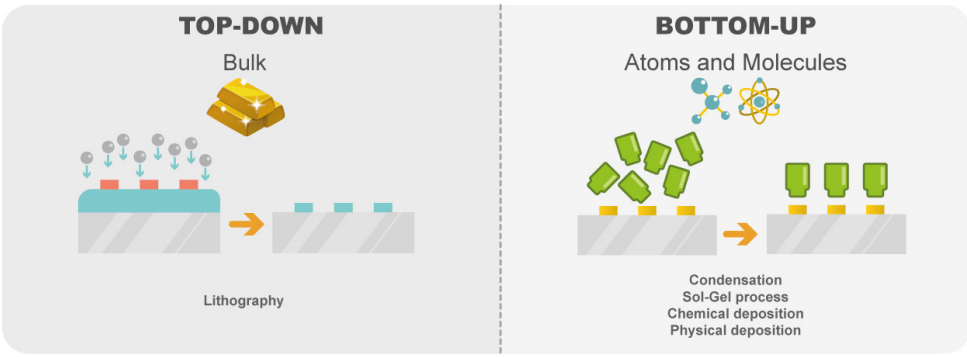

Abstract: This chapter covers the top-down and bottom-up fabrication techniques employed in the fabrication of the devices presented in the thesis. Additionally, an introduction to purple membranes—a light-driven proton pump explored in chapters 3, 4, and 5—and chemical reaction networks utilized in the thesis is provided. Lastly, a brief overview of the analytical techniques employed to study our system is presented.

2.1 Introduction

Research on materials development has been conducted worldwide to address current and future societal needs. [1] Specifically, the study of polymers and surface chemistry has attracted increasing interest owing to their large utilization scope, from the development of household items to biomedical applications. These fields of study are the background for the development of nanomaterials. The manipulation of micro/nano-objects is essential for the development of novel lab-on-chip devices to diagnose and fabricate next-generation nanoscale electronic devices. [2] Nano and microscale materials can be synthesized via top-down or bottom-up methods. These methods are complementary to each other, so nanotechnology-based products must converge these approaches to enable large-scale fabrication. [3]

2.2 Top-down fabrication

The top-down approach comprises a controlled and repeatable method for the nanofabrication of surface patterns and devices. Lithography is an example of a top-down method, and it is used to introduce patterns to materials. We used three types of lithography techniques: thermal scanning probe lithography (t-SPL), photolithography, and direct laser writing (DLW). The patterns transferred by lithography are commonly transferred to a functional layer via etching.

2.2.1 Thermal scanning probe lithography

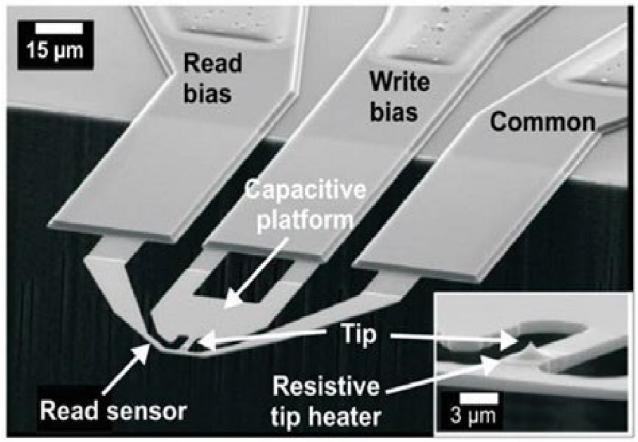

Figure 2.1. Cantilever of t-SPL with two resistive heaters, one under the tip (inset), and the other acting as a read sensor. [4]

The t-SPL developed by IBM, [5] is a cutting-edge direct-write scanning probe lithographic technique utilizing heated tips to generate various nanostructures. This method can write high-resolution nanoscale patterns with structures as small as 10 nm, even under

atmospheric conditions. It employs a heated nanoscale tip to directly write patterns onto a surface by locally removing or modifying material. [5] When the hot cantilever tip is pushed into contact with a heat-labile resist placed on the substrate surface, the resist is removed, forming a topographical pattern (Figure 2.1). [4] The tool contains a read sensor that can produce high-resolution topographic images based on the heat flow from the sensor to the surface through the air.

The t-SPL is mostly operated for material removal by using the heated tip to modify the surface topography. In this context, polyphthalaldehyde (PPA) is an excellent resist material that can be used to transfer a pattern to the deposited substrate for the manufacture of topographical nanostructures using t-SPL. [6,7] That is, PPA behaves as a self-amplifying resist material. PPA is a metastable compound with low ceiling temperature (−43 °C), [8] and it readily depolymerizes upon cleavage of a single bond of the main chain, even at room temperature (Figure 2.2). For t-SPL patterning using PPA, the hot tip induces bond breakage. It simultaneously promotes patterning and polymer removal, thereby superseding the wet development of PPA. The resist depolymerizes completely into phthalaldehyde monomer units at temperatures above 150 °C.

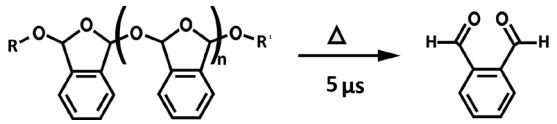

Figure 2.2. Depolymerization of polyphthalaldehyde after heating. [6]

The advantages of t-SPL include the absence of charging during material modification, a robust and compact setup compatible with ambient conditions, in-situ Atomic Force Microscopy (AFM) imaging, closed-loop lithography, and maskless overlay and stitching. [9] Owing to its precise control of actuation force and the duration of the tip– sample contact, the t-SPL technique can also be used to perform 3D patterning. This differs from mask-dependent approaches because the latter are limited to the fabrication of 2D structures. T-SPL is explored in Chapter 3 concerning localized surface functionalization and in Chapter 5 regarding the overlay of nanoscale and microscale patterning.

2.2.2 Photolithography

Photolithography [10,11] is widely utilized in the production of semiconductor devices, advanced electronic components, displays, and other related objects. Photolithography, in contrast to t-SPL, is suitable for batch fabrication. Its main advantage is the efficient and reliable transfer of high-fidelity, accurate replicas of the desired device structures onto silicon. It does so at a cost-effective rate while ensuring high wafer throughput. This technique operates by using optical wavelength radiation to imprint patterns onto the substrate surface. A photosensitive layer is coated onto the substrate, which is then irradiated with optical radiation in a controlled manner to transfer the design. In traditional

photolithography, a photomask is created, serving as a template, the desired design is transferred onto a resist-covered wafer. A mask aligner is then used to transfer the pattern.

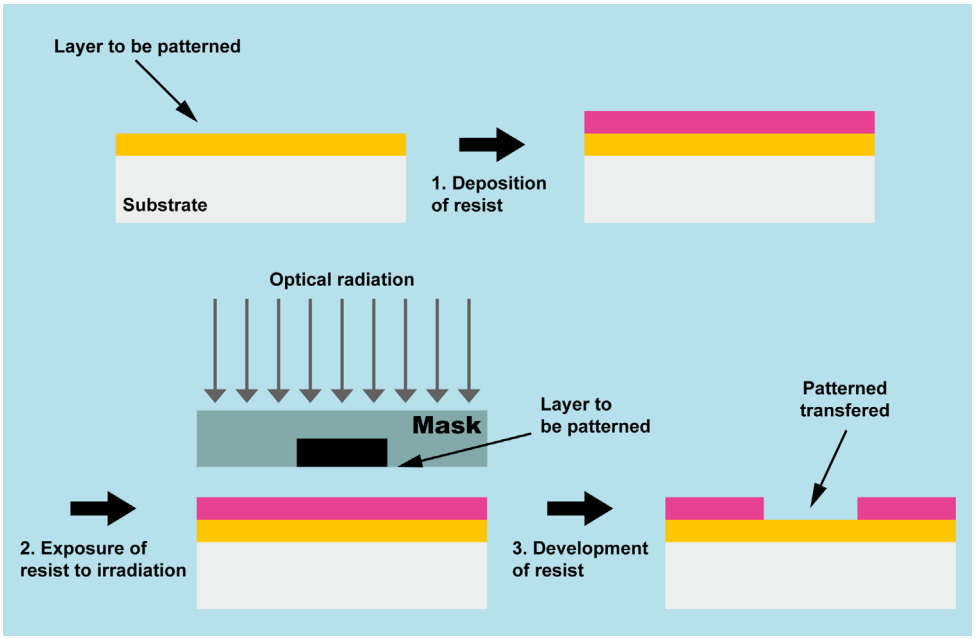

Figure 2.3. Common steps in pattern transfer through photolithography. Step 1: deposition of photosensitive resist. Step 2: exposure of sample to irradiation in localized areas defined by a photomask. Step 3: transfer of pattern from mask to photoresist on the substrate surface after resist development.

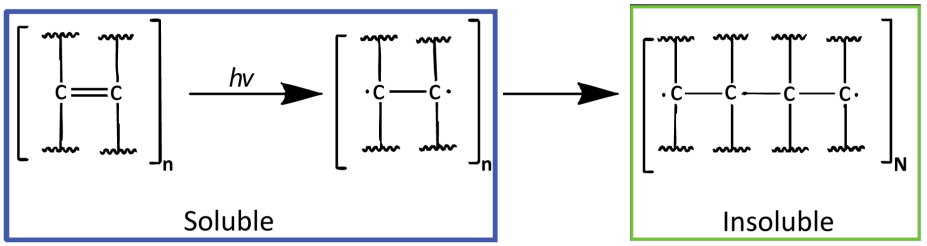

Figure 2.4. General mechanism of negative photoresists. The mechanism involves the creation of unstable free radicals by ultraviolet energy, which break a double bond. These radicals then bond head-to-tail, forming cross-linked polymers or long chains.

As shown in Figure 2.3, photolithography involves several stages, including substrate surface preparation, resist application, heating of the resist (to remove excess solvents), resist development, and inspection to verify accurate pattern transfer and alignment. The

employed photoresist can be either positive or negative. In positive resist, the exact mask design is replicated onto the photoresist, whereas a negative resist creates an inverted pattern. Following exposure, the photosensitive layer is treated with a developer solution, dissolving the resist in unwanted areas. After patterning the resist, the design is transferred onto the substrate's surface, typically via etching.

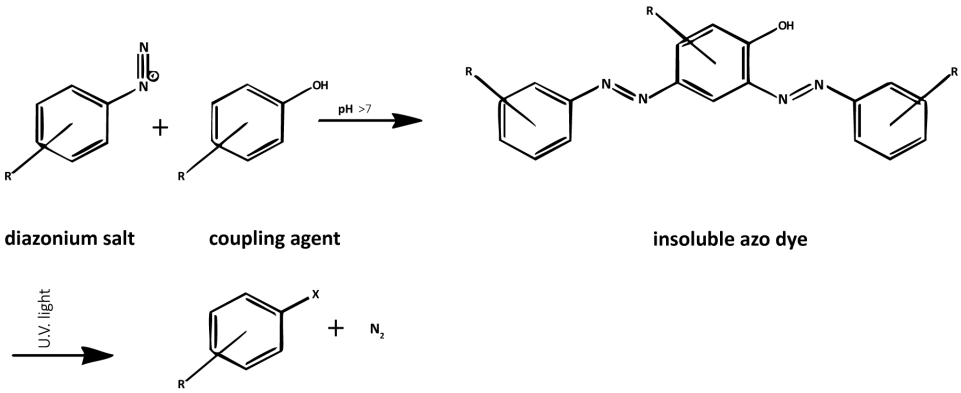

Figure 2.5. Example of reactions involved in positive photoresists.

Negative photoresists typically consist of compounds with double or ethylenic bonds that, when exposed to UV light (Figure 2.4), break into diradicals. These free radicals rapidly form head-to-tail bonds, leading to the formation of cross-linked or long-chain polymers. As a result, exposed regions have low solubility and increased chemical resistance, while unexposed areas remain soluble and are removed during development, leaving a patterned structure.

Photolithography with positive photoresists relies on reactions, such as those shown in Figure 2.5, where diazonium salts or diazides react with phenolic compounds in alkaline conditions to form insoluble azo dyes. Upon exposure to UV light, the diazo group in these compounds decomposes, releasing nitrogen and preventing further dye formation. As a result, the exposed regions become soluble and are dissolved by the developer, while the unexposed areas remain intact. The developer provides the necessary alkalinity to facilitate this coupling reaction, ensuring precise pattern formation. Photolithography was employed in Chapters 5 and 6 for the design of microfluidic and nanofluidic channels.

2.2.3 Direct laser writing

DLW is used to fabricate features at sub-micron dimensions. [12] This is achieved by utilizing spatial light modulator micro-arrays to directly project the pattern onto the substrate.[13] In our experiments, the patterns were transferred onto a photoresist placed on a transparent substrate fully covered by a layer of chromium on one side. Next, a wet chemical etching process was performed to transfer the patterns from the resist onto a silicon wafer. [14] Depending on the photoresist type, either the exposed areas (in positive resist) or the

unexposed areas (in negative resist) can be removed. DLW was employed in Chapters 5 and 6 for the design of photolithography masks.

2.2.4 Etching of material

Material removal in semiconductor device fabrication is carried out through a chemical process known as etching. [15] In this process, the samples are exposed to chemicals, such as acids or halogen compounds (Br, Cl, F), which react with the exposed surfaces for a controllable material loss. Certain parts of the device can be coated with etch-resistant materials, as resists, to obtain different device geometries. The specific patterns are defined by masks on the material surface. Etching methods can be classified as (1) wet etching, which is based on liquids; and (2) dry etching, which is based on gas- or vapor-phase chemistry. Usually, wet etching can define an undercut beneath a masked feature. (isotropic etch), whereas dry etching acts vertically (anisotropic etch) (Figure 2.6).

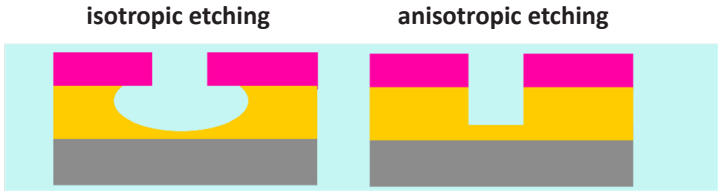

Figure 2.6. Etch profiles obtained from isotropic and anisotropic etching. The pink and yellow areas represent the resist and etched material, respectively.

Wet etching [11,15] uses liquid chemicals and chemical solutions to remove materials from a dipped substrate. Wet chemical etching comprises three key mechanisms: (1) diffusion of reactants to the surface, (2) chemical reaction at the substrate, and (3) removal of by-products via diffusion and evacuation. The etch rate, which indicates how much material is removed per unit of time, is controlled by the temperature of the solution, the concentration of the etchant, and the agitation of the liquid. Since the process relies on chemical reactions, high selectivity can be achieved between the etch rates of different materials. Other advantages of wet etching include comparatively flat etching profile, high consistency, and adjustable etching rate. However, wet etching often results in the isotropic removal of etchable materials, which leads to the undercutting of masking materials. This can decrease the resolution of the etched pattern. In this study, we used Cr wet etching to fabricate photolithography masks. Other etching processes were performed under dry conditions.

In dry etching, [11,15] plasmas or etchant gases or plasmas are utilized to remove material from the substrate. This process can be classified into physical, chemical, or physicochemical etching methods. Physical dry etching relies on the kinetic energy of photon beams, electrons or ions to strike the substrate surface. These high-energy particles dislodge atoms, causing the material to evaporate as it leaves the surface. Given that no chemical reaction happens, this technique can etch a broad range of materials. However, its main drawbacks

include a slow etch rate, reduced selectivity and trenching effects from reflected ions.

In contrast, chemical dry etching depends on the chemical interaction among different etchant gases and the substrate material. The reaction produces gaseous by-products that are crucial because solid product deposition would block the etching process by protecting the surface. This method offers relatively high selectivity, and it is usually isotropic. Chemical dry etching is commonly used for wafer cleaning, where oxygen plasma, by way of example, can remove photoresists and other organic films.

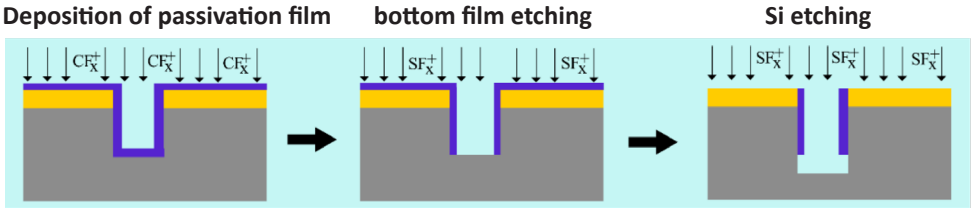

Figure 2.7. Representation of the Bosch process cycle: (1) deposition of passivation films by the C_4F_8 reaction, which forms CFx radicals; (2) bottom film etching by SF_6 gas, which forms fluorine radicals and ions; and (3) Si etch, which forms fluorine radicals.

Reactive Ion Etching (RIE) operates based on the principles of physical-chemical etching. The etch rates fall within a range that is intermediate between those of purely physical and purely chemical etching processes. Ions are directed almost perpendicularly to the substrate under strong electric field and low pressure. However, the high aspect-ratio of dry etch is less desirable than that of wet etch. A technique called deep RIE (DRIE), or Bosch process, can be used to fabricate a high aspect-ratio structure (Figure 2.7). The DRIE process is independent of the crystal orientation of the wafers. The etch cycle consists of two phases: etching and deposition. During the etching phase, silicon is removed using SF_6, and the etch front advances by 0.5 to 1.5 µm over 5 to 15 seconds. During the passivation phase, the gas supply is changed to C_4F_8, forming a 10 nm fluorocarbon polymer film on the trench wall. In the subsequent cycle, ion bombardment removes the polymer film from the bottom surface, while the film on the sidewalls remains intact, protecting them from etching.

A variant of RIE is the dual power inductively coupled plasma reaction RIE (ICP-RIE), [16] generates a high-density plasma at low pressure. In ICP-RIE, the ICP power and substrate bias can be adjusted independently to control both plasma density and ion energy. The low-pressure environment improves anisotropy and etch rate by enhancing ion flux directionality, even at low bias voltages. Consequently, it enables the full spectrum of physical to chemical processes and possible combinations. Table 2.1. lists the etch recipes used in this thesis.

Table 2.1. Recipe of etchants used in this thesis.

Etched material	Etching technique	Type of etch	Chemical components
Si	RIE	Isotropic	SF_6/Ar
Si	DRIE	Anisotropic	C_4F_8/ SF_6
Si	ICP-RIE	Anisotropic	HBr
SiO_2	RIE	Anisotropic	CHF_3/Ar
Al_2O_3	ICP-RIE	Anisotropic	BCl_3/Ar
Cr	Wet	Isotropic	$(NH_4)_2[Ce(NO_3)_6]$

2.3 Bottom-up fabrication

In bottom-up methods, simple building blocks come together in a coordinated manner to form larger and more complex supramolecular assemblies. [17] The building blocks are formed by atoms, molecules, and particles that self-stack onto the substrate to form macro- to nanoscale structures. This method demands a strong comprehension of each molecular structure involved in the system, the respective assembling manner, and the dynamic components. The material growth promoted by deposition leads to a high level of control over the material composition, and significant advantages include the size precision and control of the physical properties of the developed material. In this study, the bottom-up methods used for the deposition of materials included thermal oxidation (TO), plasma-enhanced chemical vapor deposition (PECVD), atomic layer deposition (ALD), anodic bonding, molecular self-assembly (MSA), and tunable nanofluidic confinement (TNCA).

2.3.1 Thermal oxidation

TO is employed to generate a thin oxide layer on the material surface. [15,18] This technique compels the oxidant to spread through the material at elevated temperatures, where it reacts with the material. When silicon is exposed to an oxygen-rich environment, it reacts to form a silicon dioxide layer

$$Si_{(solid)} + O_{2\,(gas)} \rightarrow SiO_{2\,(solid)}$$

As the reaction progresses, the oxidation rate slows as oxygen diffuses through the SiO_2 layer to the silicon surface, where the reaction continues, forming more oxide. The typical layer thickness obtained by TO ranges from 6 to 1000 nm. [19] In Chapter 3 and 5, TO-SiO_2 layers were used on silicon surfaces in the devices presented.

2.3.2 Plasma-enhanced chemical vapor deposition

As an alternative to TO, SiO_2 layers can be deposited on silicon from the gas phase via PECVD. In PECVD, the plasma is made up of neutral species, ions and electrons in both their ground and excited states. [20] Plasma is generated and sustained by applying high-frequency voltage to a low-pressure gas, where electron-gas collisions produce reactive

species like free radicals, ions, and electrons. When transport gases interact with the wafer, a chemical reaction takes place on its surface, leading to the deposition of new material. The electrons gain adequate energy from the applied electric field to generate highly reactive species. PECVD utilizes these reactive species to deposit thin films, which enables the use of lower temperatures, typically from 100 to 300 °C. The species present in the gases facilitate the deposition of thin semiconductor layers, such as silicon layers with controlled dopant concentrations or insulators like SiO_2. The benefits of SiO_2 PECVD over thermal SiO_2 include (1) rapid growth of thick layers compared to TO, (2) the unbiased composition of the SiO_2 layer in relation to the substrate, and (3) the capability to process a larger number of wafers simultaneously. Furthermore, the PECVD SiO_2 is more amorphous, and its etch rate is higher. PECVD SiO_2 layers were used in chapter 4, and 5.

2.3.3 Atomic layer deposition

ALD [15,21] is a thin film deposition method that can produce conformal layers with thickness ranging from angstrom to nanometers. Its distinct self-limiting growth mechanism ensures a film maintaining conformality and consistent thickness, including intricate 3D structures. While like CVD, this process depends on an alternating sequence of self-limiting chemical reactions on the wafer surface. During each cycle, the wafer is subjected to gaseous precursors, facilitating surface reactions that continue until the complete formation of a single atomic layer is attained. The new surface is then exposed to a second set of self-limiting precursors to produce a new nuclear layer on the first layer; the material is purged with inert gas between each pulse. The deposition of ALD Al_2O_3 and SiO_2 was extensively explored in Chapter 5.

2.3.4 Anodic bonding

Anodic bonding is an electrochemical process that produces a sealing effect between silicon or metal and glass. [11] We applied this technique by setting a glass wafer and a silicon wafer. Bonding takes place when the wafers are positioned within the chuck, and the temperature is raised to a level just below the glass transition temperature (approximately 400 °C), followed by the application of an electric potential of approximately 1 kV. When a specific temperature is reached, the oxides dissociate, and under the influence of an electric field, alkali ions are transported into the glass, leading to the formation of an oxygen-enriched layer at the wafer interface. In this electrochemical process, silicon serves as the anode, connected to the positive electrode, while the glass functions as the cathode. The anodic bonding process results in a significant temperature variation within the glass/silicon stack. The coefficient of thermal expansion of the processed glass should closely match that of silicon.

Because glass is optically transparent, this bonding technique is ideal for the fabrication of microfluidic networks that require optical access for the control and analysis of the fluid. Anodic bonding was utilized for the fabrication of microfluidic networks in Chapters 5 and 6.

2.3.5 Molecular self-assembly

Self-assembly is the natural grouping of individual components into ordered patterns. [22] MSA is based on the recognition of relatively simple building blocks by themselves or with a substrate (self-assembled monolayer), which generates ordered structures at the micro- to nanoscale. [17] The order and specific recognition of the building blocks are based on the combination of various non-covalent interactions. [23]

Nanoscale MSA is based on the interplay between different forces in the self-assembly that are often related because of the combined effect of long-range repulsive forces and short-range attractive forces. [24] Assemblies can also be related to long-range attractive forces, such as negatively charged nanoparticles assembled on positively charged lines. In this case, the particles are attracted by the long-range electrostatic energy of the positive potential of the lines, and they are guided into the lines by their repulsive force. Their line density is also governed by the repulsion among them. [25]

MSA can be classified as static or dynamic. In a system, static self-assemblies are governed by the reduction of free energy, which represents the moment when the system approaches equilibrium. Dynamic self-assembly occurs when the system dissipates energy, thereby forming an out-of-equilibrium system in which the competition between kinetic and thermodynamic forces of a chemical reaction occurs. [26] Usually, considering the same thermodynamic conditions, the solid phase displays less entropy on a macro scale than the liquid and gas phases. However, this can change at the nanoscale. An increase in entropy might drive nanoscale objects to form organized patterns in a controllable manner. [27] This phenomenon is common in biological systems, in which the self-assembly of multiple building blocks includes more ordered structures under the total or partial influence of an energy source. [28]

In this thesis, a dynamic proton-catalyzed chemical reaction network (CRN) is directly explored in Chapter 4. Chapter 5 discusses the application of such CRN in a fabricated device.

2.3.6 Tunable nanofluidic confinement

The simultaneous deposition of nanomaterials in specific positions on a substrate demands their attraction to the desired positions, short-range alignment, and stable long-range means of transport. TNCA enables the accurate deposition of nanoparticles by confining colloids and molecules in a nanoscale slit between a topographically patterned substrate and a movable cover.

TNCA manipulates particles via geometry-induced energy landscapes in a nanofluidic gap (Figure 2.8). Trapping relies on the repulsive force between like-charged particles and a patterned surface. The particles are transported and immobilized on a specific spot designed by lithography. [29] As the nanofluidic gap closes, Van der Waals forces surpass

hydration and electrostatic repulsion, permanently depositing trapped particles (Figure 2.9). [30] After this contact, the particles become adsorbed onto the surface. In this case, the topographical nanostructures on the substrates were patterned in the PPA using t-SPL.

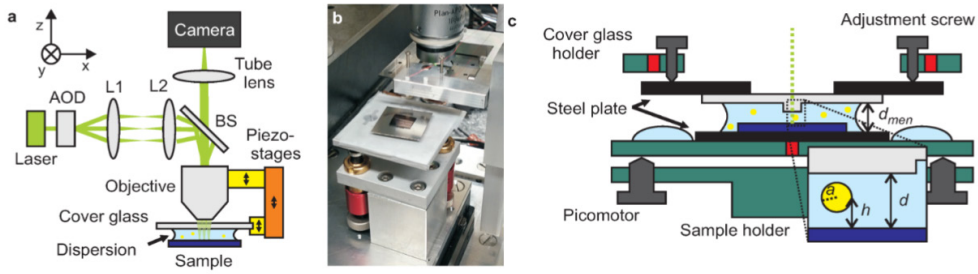

Figure 2.8. a) Optical configuration of TNCA for the deposition of gold particles. One coarse positioning stage (orange) and two linear piezo stages (yellow) provide independent adjustments for focus and confinement, in addition to offering access to a broad range of gap distances. **b)** Image of the nanofluidic confinement setup. **c)** Illustration of the system's vertical profile; the inset highlights the nanofluidic slit with gap distance d, where a particle of radius a is confined at height h. [29]

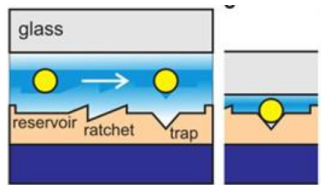

Figure 2.9. A schematic illustration of the nanoparticle assembly process flow through nanofluidic confinement, where t-SPL is employed to pattern the PPA (beige) and create reservoirs, ratchets, and traps. [30]

In Chapters 3 and 5 of this PhD thesis, TNCA was utilized to confine bacteriorhodopsin (bR) between two parallel, tunable surfaces. Additionally, Section 2.4.1 includes a summary of a publication [31] in which the thesis author contributed, presenting the first study that employed TNCA for the deposition of bR.

2.4 Purple membranes

The bR is an integral protein with a supramolecular structure, and it can be found in 5- nm purple membranes (PMs) of Halobacterium salinarum (Figure 2.10). [32] The bR acts as a light-driven cross-membrane proton pump. It actively transports hydrogen ions across the cell membrane, and the established hydrogen gradient facilitates the synthesis of adenosine triphosphate (ATP) from adenosine diphosphate (ADP) within the cells. [33] Moreover, bR has directionality in pumping and an orientation in the membrane. The pumping occurs from the cytoplasmatic side (C-terminus), inside the cell, to the extracellular side (N-terminus),

outside the cell. As shown in Figure 2.10, the retinal molecule undergoes isomerization from trans to cis upon absorbing a photon. Although the oriented deposition of PM patches has been achieved in previous work, [34] the simultaneous control of orientation and position has not been reported. The control of membrane orientation is essential to realize a high photoelectric conversion efficiency.

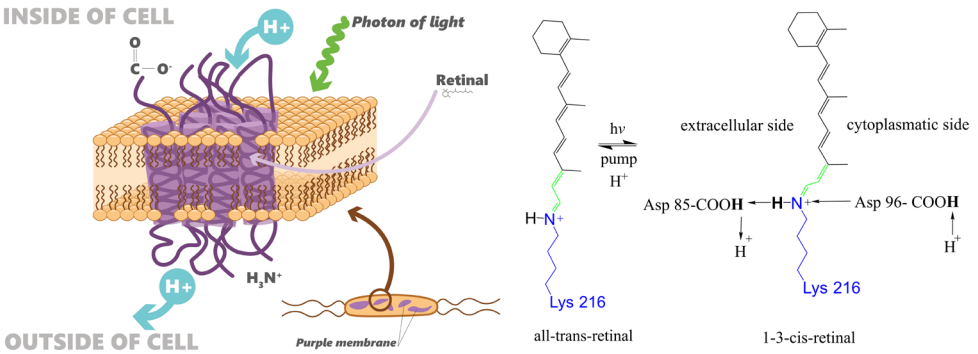

Figure 2.10. Schematic of bacteriorhodopsin pumping and its reaction mechanism. The conformational changes upon light exposure altered the pKa values of amino acids Asp85 (cytoplasmic side) and Asp96 (extracellular side).

CRNs can be controlled by a local proton gradient as catalysts. Therefore, in this thesis, we aimed to couple similar CRNs with light-driven bR proton pumps to form a localized CRN that can be switched on and off by an optical trigger. Moreover, we investigated spectroscopic techniques to quantify the bR pumping [35] to enable the use of PMs in hybrid devices. A study documented the controlled localization and orientation of PM deposition. [31] The main results of this publication are described in the following paragraphs.

2.4.1 Placement of biological membrane patches in nanofluidic gap with control over position and orientation

We aimed to supply protons as catalysts for CRNs by positioning proton pumps in a small compartment of a planar surface. To modulate membrane patch orientation during deposition, we used PM patches containing bR with a deca-histidine (His_{10}-tag) attached to either the C-terminus (C-His) or N-terminus (N-His) of the bR (Figure 2.11). The positive charge of His_{10}-tag increased the charge asymmetry of the membrane surface. Fluorescently labeled antibodies targeting the His_{10}-tag were employed to detect the presence of the His_{10}-tag upon membrane deposition, specifically when it was oriented toward the surface.

TNCA was used to deposit bR-containing membrane patches that were deposited onto a patterned substrate to control their orientation. Trapping sites with negatively (Figure 2.12a) or positively (Figure 2.12b) charged interfaces were prepared using t-SPL. Figures

2.13a and 2.13b display scanning electronic microscopy (SEM) and AFM images of C-His_{10}-tag PM patches in Al_2O_3 traps, confirming successful membrane deposition. Figure 2.13c shows fluorescence microscopy (FM), where membranes with the His_{10}-tag facing up exhibit green fluorescence, indicating antibody recognition. In contrast, membranes on SiO_2 (His_{10}-tag down) showed no fluorescence. Figure 2.13d illustrates the ratio of fluorescent to non-fluorescent membranes on positively and negatively charged interfaces, with each bar representing data from at least seven trap arrays and a minimum of two deposition experiments. These results confirm that PM orientation can be controlled by the presence of a His_{10}-tag on either the C- or N-terminal side of bR.

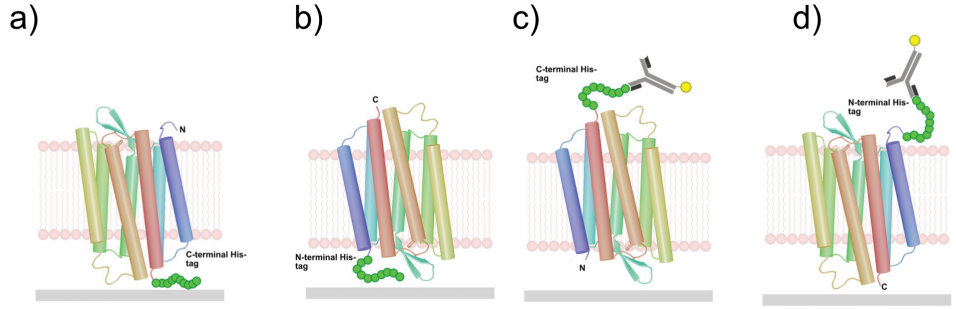

Figure 2.11. Scheme of orientation control upon attachment of His_{10}-tag on the C- terminus (a) and c)) or N-terminus (b) and d)). The antibody binds to the His_{10}-tag mostly when His_{10}-tag is facing up (c and d). [31]

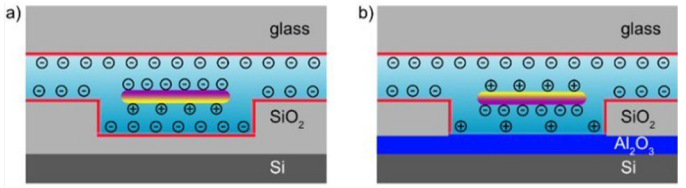

Figure 2.12. Asymmetrical charged membrane in nanofluidic confinement with orientation dependent on the trap surface charge: **a)** negative and **b)** positive. [31]

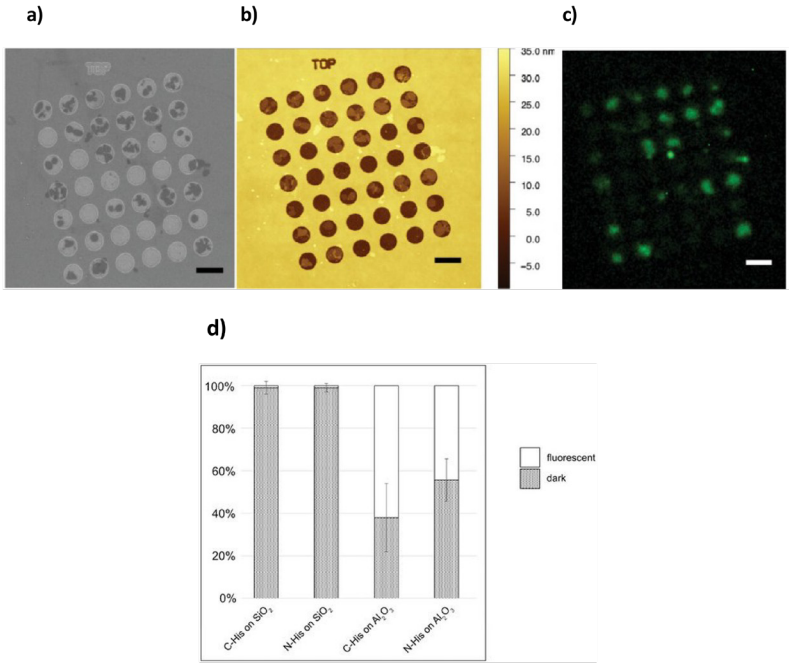

Figure 2.13. a) SEM image of a circular Al_2O_3 trap array with deposited C-His_{10}-tag PM patches. **b)** AFM image of the array shown in (a). **c)** Fluorescence microscopy image of the array shown in a), presenting green fluorescence from membranes with the His_{10}-tag facing up. **d)** Graph showing the distribution of PM orientations in different trap types, illustrating the ratio of dark (non- fluorescent) to fluorescent membranes. Scale bars: 2 µm. [31]

2.5 Chemical reaction networks

A chemical reaction involves substances transforming into others through atomic bond breakage and formation. Chemical kinetics studies the speed of reactions and the mechanisms behind them, explaining why reactions occur under specific conditions. A CRN is a set of coupled reaction steps, represented by elementary reactions that describe systems like enzymatic cycles or self-assembly networks. [36] In this thesis, we used two CRNs: a proton-catalyzed hydrogel self-assembly and a self-catalyzed chemical reaction oscillatory network.

2.5.1 Dissipative chemical reaction network - Hydrogel self-assembly

Dissipative self-assembly refers to a system that remains dynamically stable in a far-from-equilibrium state through continuous chemical fuel consumption. Supramolecular structure formation can be precisely controlled in space and time by modulating the molecular self-assembly rate, often using external stimuli like light or pH, controlling their properties. In nature, feedback-driven catalysis regulates the turnover of self-assembled

structures, shaping soft materials' distribution and properties.

In an in-situ study, Boekloven et al. [37] observed that catalyzed gelator molecule formation accelerated supramolecular hydrogel creation. Supramolecular gels, often metastable, are influenced by kinetic factors. With external catalysts, supramolecular hydrogels can form in minutes under ambient conditions, using simple soluble building blocks, and offer tunable gel strength. Catalysis-driven gelator formation alters gelation speed and morphology, yielding metastable gels with enhanced strength and appearance despite identical compositions. Such a CRN will be spatiotemporally controlled by the presence of PMs and light, as shown in Chapter 4.

2.5.2 Oscillatory chemical reaction network - Belousov–Zhabotinsky reaction

Chemical reactions far from equilibrium can display oscillations under certain conditions, such as chemical concentrations, incident light color, pH, temperature, and electrode potential. The Belousov-Zhabotinsky (BZ) reaction is an example of this. It is based on the oxidation of an organic compound by bromic acid ($HBrO_3$) mediated by a transition-metal catalyst in an acidic aqueous solution. [38] Although other BZ recipes can be used, we selected a standard formula using tris(bipyridine)ruthenium (II) chloride ($Ru(bpy)_3]Cl_2$) as the catalyst, and sodium bromate ($NaBrO_3$) and malonic acid (MA; $C_3H_4O_4$) as oxidizing and reducing reactants, in that order. The reaction is conducted in an acidic environment obtained by using sulfuric acid (H_2SO_3). During the oscillations, the catalyst switches between two oxidation states.

This BZ reaction is given by:

$$3BrO^- + 3CH_2(COOH)_2 + 2\ H^+ \rightarrow 2BrCH\ (COOH)_2 + 3CO_2 + 4H_2O$$

While the mechanism is complex, it can be effectively simulated using simple three-variable kinetic reactions to model the overall behavior. In the first process, bromide is consumed in two fast reactions, and $HBrO_2$ is produced and consumed:

$$BrO_3^- + Br^- + 2H^+ \rightarrow HBrO_2 + HOBr$$

$$HBrO_2 + Br^- + H^+ \rightarrow 2HOBr$$

Second, when the bromide concentration becomes low enough, bromous acid ($HBrO_2$) is autocatalytically produced, and the metal ion catalyst is oxidized by supplying electrons for the process.

$$BrO^- + HBrO_2 + 2Ru^{2+} + 3H^+ \rightarrow 2HBrO_2 + 2Ru^{3+} + H_2O$$

The third process involves the reduction of the oxidized metal catalyst and the production of bromide:

$$BrMA + MA + 2Ru^{3+} \rightarrow Br^{-} + 2Ru^{2+} + CO_2 + H^{+}$$

Recently, a new field of study has aimed to use oscillatory CRNs for information processing, [39] and BZ CRN is gaining importance. One of the approaches utilizing the BZ reaction towards the development of a chemical computer is presented in Chapter 6.

2.6 Analytical techniques

The development and manufacture of microsystems require several metrology techniques and instruments. In manufacturing, metrology plays a crucial role in measuring key process outcomes and ensuring the quality of microsystems. It also enables the monitoring of processing equipment during production. Furthermore, these techniques are used to accurately identify and diagnose issues in design and fabrication. In this study, we used five types of analytical techniques, namely AFM, FM, SEM, focused ion beam (FIB), and spectroscopy ellipsometry (SE).

2.6.1 Atomic force microscopy

AFM [40] is a microscopy technique that employs a mechanical sampling method, wherein an atomically sharp tip is scanned across the sample surface under controlled conditions to capture high-resolution images of material surfaces at the nanoscale. AFM is commonly utilized at various stages of semiconductor manufacturing to inspect and evaluate fabrication processes.

The AFM principle is shown in Figure 2.14. In AFM, piezoelectric actuators enable precise positioning and scanning of the tip. Cantilever deflection is detected by reflecting a laser off its backside onto a four-quadrant photodiode. Tip-sample interactions during raster scanning cause cantilever deflections. These deflections are recorded through the movement of the laser beam reflection, with the data being measured by the photodiode output. The tip provides topographic information (z) of the sample as a function of x-y coordinates.

Although the instrumentation is relatively elementary, several conditions must be met to ensure the accuracy of AFM measurements. First, an appropriate probe should be selected for the specific type of measurement and substrate. Second, the feedback mode should be selected, and the parameters should be optimized. Third, the detection of possible measurement-related artifacts should be avoided. These artifacts can originate from an error in choosing the appropriate analysis conditions or specific sample properties, such as high adhesion from blunt tips or hydrophilicity.

Regardless of the application and information to be sensed, there are three potential modes of AFM operation: contact, non-contact, and intermittent. These methods use different approaches to probe the surface morphology, as shown in Figure 2.15. In contact

mode, the cantilever's static deflection is measured when it makes physical contact with the surface. In non-contact mode, the cantilever oscillates dynamically with small vibrations, and the tip does not physically touch the surface. In intermittent mode, the tip apex remains in partial contact with the surface while the cantilever vibrates with larger amplitudes.

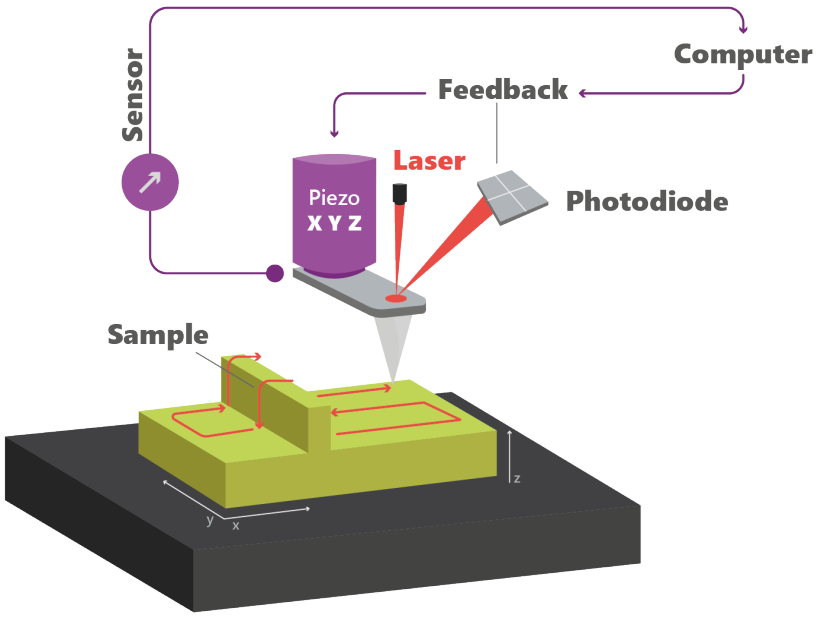

Figure 2.14. A typical AFM setup involves fixing the sample in place while the probe moves in the x, y, and z directions.

The contact approach can be intuitively interpreted as the tip engaging with the sample surface through a normal reaction force. In contrast, the other two techniques involve the cantilever vibrating at or close to its natural resonance frequency, with an amplitude like the mean tip–sample distance. The interactions between tip and surface (van der Waals and contact forces) lead to a shift in resonance frequency and phase. The feedback maintains one of the two constants while recording the topography. Recently, a hybrid method named peak force-mapping was implemented in commercial tools. In this method, the tip oscillates at lower frequencies than its natural resonance. In each oscillation, the tip touches the surface. With an operating frequency of 1–10 kHz, this technique enables high-bandwidth force sensors to trail individual tip oscillations upon each surface contact during imaging. Recording the force at every tap allows for the acquisition of thousands of unique force curves as adjacent pixels are scanned, providing a notable benefit. Since these force curves provide insight into local mechanical properties, this method allows for nanoscale mapping of adhesion, modulus, dissipation, and deformation. Furthermore,

this capability opens new pathways for reliably detect weak tip–sample interactions. Consequently, operation is simple, parameters can be optimized by the software, and operation on difficult surfaces is possible.

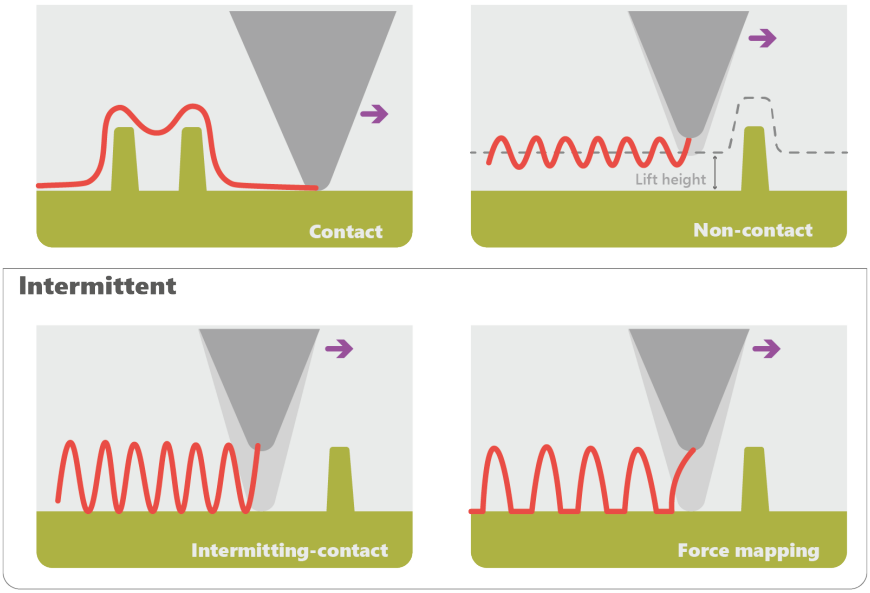

Figure 2.15. Different AFM modes employing various types of tip–sample interactions.

AFMs are capable of functioning in a wide range of environments, including liquid solutions. [41] However, acquiring an AFM image of immersed liquid surfaces is challenging owing to several physical characteristics, such as the viscosity of the liquid, which can cause issues when the AFM probe moves across sample surface. [42] Moreover, objects deposited on a surface are often only weakly bound, depending on the conditions of the liquid. Such objects might move by themselves or may be triggered by interactions with the scanning tip, often at a shorter period than the one needed to acquire a single AFM image. To minimize these effects, PeakForce Tapping mode [43] can be used. In this mode, tip–sample interactions are precisely regulated at ultralow forces, while lateral forces are significantly reduced, creating an optimal imaging condition for delicate samples.

AFM in liquid environments necessitates specific adaptations, including a specialized liquid cell. This component ensures that the laser beam can travel unimpeded through the liquid, striking the cantilever and reflecting back without significant scattering. At nearly all air–liquid boundaries, minor mechanical disturbances give rise to surface waves, which, in turn, scatter laser light. When operating in dynamic modes—where the cantilever must vibrate close to its natural resonance frequency, these effects become particularly relevant, increasing the need for a more sophisticated liquid cell design. The low frequencies of operation in PeakForce Tapping simplify this challenge considerably.

Liquid AFM in PeakForce Tapping mode was used for an in-situ study of proton-catalysed molecular self-assembly under spatiotemporal control presented in Chapter 4.

2.6.2 Fluorescence microscopy

A fluorescence microscope typically consists of an adapted optical microscope system designed to illuminate a sample using both visible and ultraviolet light. [10] The FM [44] model is utilized for analyzing the characteristics of organic and inorganic materials by detecting fluorescence and phosphorescence phenomena. In this type of microscopy, the enlarged image is generated by the longer-wavelength light emitted from fluorescent molecules. The term Stokes shift describes the variation between the wavelengths of emitted fluorescence and the absorbed (excitation) light. When this difference is significant, filters can be utilized to isolate the exciting and fluorescence signals, ensuring that only the fluorescence light reaches the detector. A fluorescence microscope generally includes essential components like the light source, excitation filter, dichromatic mirror, and emission filter. These filters and mirrors are selected based on the specific excitation and emission wavelengths of the fluorophores being studied FM was used in Chapters 3, 5 and 6 of this thesis.

2.6.3 Scanning electron microscopy

The SEM [10] is an imaging system that uses a focused electron beam to capture detailed images of a sample. Due to the shorter wavelengths of electrons compared to optical photons, SEM microscopes offer higher resolution than optical microscopes. Additionally, SEM significantly improves depth of focus, enabling the visualization of features at varying depths without the need to refocus. The precision of dimensional measurements in SEM are greater at higher magnifications than at lower ones. A standard multipurpose SEM allows for the adjustment of various parameters, such as viewing angle, accelerating voltage, and magnification. All of these factors can impact the precision of dimensional measurements. SEM was used in Chapters 3 and 5 to inspect fabricated devices.

2.6.4 Focused ion beam

The FIB technology [10] can be used to cross-section and image sections of the device structures which could otherwise remain unseen owing to their coverage by thin films or other material coatings. FIB is used to perform nanometer dimensional-scale machining. Conventional FIB machining requires an ion source, usually gallium ions. Gallium interacts with a heated needle, where its electrical potential causes ionization and field emission of ions, which are accelerated to 5–50 keV and focused into a small spot by electrostatic lenses. Upon striking the sample surface, the focused Ga^+ ion beam causes sputtering of the surface material. The ejected material then exits the surface as neutral atoms or secondary ions. Additionally, secondary electrons are generated in the process. By collecting these sputtered ions and secondary electrons, a high-resolution surface image can be produced, similar to the imaging technique used in SEM. Cross-sectional images of the devices were obtained using FIB technology in Chapter 5.

2.6.5 Spectroscopy ellipsometry

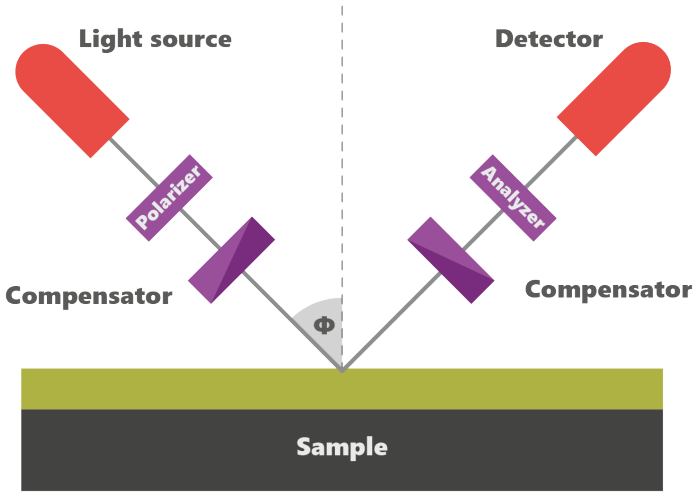

Figure 2.16. Scheme of ellipsometer components: polarizer, compensator (retarder or photoelastic modulator), analyzer, and detector and a white light source. [46]

SE is a non-destructive, contactless optical technique for characterizing bulk materials and thin films, including dielectrics, semiconductors, and metals, with thicknesses down to a few tens of nanometers. [45,46] SE works by examining alterations in the polarization state of a polarized light beam after it reflects off a surface or interface, as illustrated in Figure 2.16. This method allows for accurate determination of optical properties, composition and layer thickness. Unlike absolute light intensity measurements, SE is unaffected by scattering and fluctuations and does not require a standard sample or reference beam. A broad spectral range—from UV to mid-IR— enhances analysis precision and depth. Far-UV detects subtle variations in ultrathin layers and low-contrast interfaces, while near-IR determines thickness in materials with strong visible absorption.

2.7 References

(1) Roco, M. C.; Mirkin, C. A.; Hersam, M. C. Nanotechnology Research Directions for Societal Needs in 2020: Summary of International Study. *Journal of nanoparticle research* **2011**, 13, 897–919.

(2) Elnaggar, A.; Kang, S.; Tian, M.; Han, B.; Keshavarz, M. State of the Art in Actuation of Micro/Nanoro bots for Biomedical Applications. *Small Science* **2024**, 4 (3), 2300211.

(3) Mijatovic, D.; Eijkel, J. C.; Van den Berg, A. Technologies for Nanofluidic Systems: Top-down vs. Bottom-up—a Review. *Lab on a Chip* **2005**, 5 (5), 492–500.

(4) Paul, P. C.; Knoll, A. W.; Holzner, F.; Despont, M.; Duerig, U. Rapid Turnaround Scanning Probe Nanolithography. *Nanotechnology* **2011**, 22 (27), 275306.

(5) Vettiger, P.; Despont, M.; Drechsler, U.; Durig, U.; Haberle, W.; Lutwyche, M. I.; Rothuizen, H. E.; Stutz, R.; Widmer, R.; Binnig, G. K. The "Millipede"—More than Thousand Tips for Future AFM Storage. *IBM Journal of Research and Development* **2000**, 44 (3), 323–340.

(6) Coulembier, O.; Knoll, A.; Pires, D.; Gotsmann, B.; Duerig, U.; Frommer, J.; Miller, R. D.; Dubois, P.; Hedrick, J. L. Probe-Based Nanolithography: Self-Amplified Depolymerization Media for Dry Lithography. *Macromolecules* **2010**, 43 (1), 572–574.

(7) Knoll, A. W.; Pires, D.; Coulembier, O.; Dubois, P.; Hedrick, J. L.; Frommer, J.; Duerig, U. Probe-based 3-D Nanolithography Using Self-amplified Depolymerization Polymers. *Advanced Materials* **2010**, 22 (31), 3361–3365.

(8) Aso, C.; Tagami, S. Polymerization of Aromatic Aldehydes. III. the Cyclopolymerization of Phthaldehyde and the Structure of the Polymer. *Macromolecules* **1969**, 2 (4), 414–419.

(9) Howell, S. T.; Grushina, A.; Holzner, F.; Brugger, J. Thermal Scanning Probe Lithography—a Review. *Microsyst Nanoeng* **2020**, 6 (1), 21. https://doi.org/10.1038/s41378-019-0124-8.

(10) Huff, M. Microsystems Manufacturing Methods: Integrated Circuit Processing Steps. *Process Variations in Microsystems Manufacturing*, **2020**, 45–97. https://doi.org/10.1007/978-3-030-40560- 1_3.

(11) Nguyen, N.-T. Micromixers: Fundamentals, *Design and Fabrication*; William Andrew, **2011**.

(12) Franssila, S. *Introduction to Microfabrication*; John Wiley & Sons, **2010**.

(13) Jung, I. W.; Wang, J.-S.; Solgaard, O. Spatial Light Modulators for Maskless Lithography. In IEEE/LEOS *International Conference on Optical MEMS and Their Applications Conference*, **2006**.; IEEE, 2006; pp 150–151.

(14) Kunwar, P.; Soman, P. Direct Laser Writing of Fluorescent Silver Nanoclusters: A Review of Methods and Applications. *ACS applied nano materials* **2020**, 3 (8), 7325–7342.

(15) Lilak, A. D.; Keys, P. H. CMOS Manufacturing Processes. In Springer Handbook of Semiconductor Devices; *Springer*, **2022**; pp 3–36.

(16) Pinto, R. M. R.; Gund, V.; Calaza, C.; Nagaraja, K. K.; Vinayakumar, K. B. Piezoelectric Aluminum Nitride Thin-Films: A Review of Wet and Dry Etching Techniques. *Microelectronic Engineering* **2022**, 257, 111753. https://doi.org/10.1016/j.mee.2022.111753.

(17) Gazit, E. Self-Assembled Peptide Nanostructures: The Design of Molecular Building Blocks and Their Technological Utilization. *Chemical Society Reviews* **2007**, 36 (8), 1263–1269.

(18) Sadhukhan, S.; Acharya, S.; Panda, T.; Mandal, N. C.; Bose, S.; Nandi, A.; Das, G.; Maity, S.; Chakraborty, S.; Chaudhuri, P.; Saha, H. Chapter 4 - Evolution of High Efficiency Passivated Emitter and Rear Contact (PERC) Solar Cells. In Sustainable Developments by Artificial Intelligence and *Machine Learning for Renewable Energies*; Kumar, K., Rao, R. S., Kaiwartya, O., Kaiser, M. S., Padmanaban, S., Eds.; Elsevier, 2022; pp 63–129. https://doi.org/10.1016/B978-0-323-91228- 0.00007-0.

(19) *Thermal Oxidation.* https://eesemi.com/oxidation.htm (accessed 2023-07-18).

(20) Warner, J. H.; Schäffel, F.; Bachmatiuk, A.; Rümmeli, M. H. Chapter 4 - Methods for Obtaining Graphene. *In Graphene*; Warner, J. H., Schäffel, F., Bachmatiuk, A., Rümmeli, M. H., Eds.; Elsevier, **2013**; pp 129–228. https://doi.org/10.1016/B978-0-12-394593-8.00004-7.

(21) Leskelä, M.; Niinistö, J.; Ritala, M. 4.05 - Atomic Layer Deposition. I*n Comprehensive Materials Processing*; Hashmi, S., Batalha, G. F., Van Tyne, C. J., Yilbas, B., Eds.; Elsevier: Oxford, 2014; pp 101–123. https://doi.org/10.1016/B978-0-08-096532-1.00401-5.

(22) Black, C. T.; Ruiz, R.; Breyta, G.; Cheng, J. Y.; Colburn, M. E.; Guarini, K. W.; Kim, H.-C.; Zhang, Y. Polymer Self Assembly in Semiconductor Microelectronics. *IBM Journal of Research and Development* **2007**, 51 (5), 605–633.

(23) Kraus, T.; Wolf, H. Templated Self-Assembly of Particles. *Springer handbook of nanotechnology* **2010**, 187–210.

(24) Lowack, K.; Helm, C. A. Molecular Mechanisms Controlling the Self-Assembly Process of Polyelectrolyte Multilayers. *Macromolecules* **1998**, 31 (3), 823–833.

(25) Carroll, K. M.; Wolf, H.; Knoll, A.; Curtis, J. E.; Zhang, Y.; Marder, S. R.; Riedo, E.; Duerig, U. Understanding How Charged Nanoparticles Electrostatically Assemble and Distribute in 1-D. *Langmuir* **2016**, 32 (51), 13600–13610.

(26) Barth, J. V.; Costantini, G.; Kern, K. Engineering Atomic and Molecular Nanostructures at Surfaces. *Nature* **2005**, 437 (7059), 671–679.

(27) Geng, Y.; van Anders, G.; Dodd, P. M.; Dshemuchadse, J.; Glotzer, S. C. Engineering Entropy for the Inverse Design of Colloidal Crystals from Hard Shapes. *Science advances* **2019**, 5 (7), eaaw0514.

(28) Boekhoven, J.; Brizard, A. M.; Kowlgi, K. N.; Koper, G. J.; Eelkema, R.; van Esch, J. H. Dissipative Self-assembly of a Molecular Gelator by Using a Chemical Fuel. *Angewandte Chemie* **2010**, 122 (28), 4935–4938.

(29) Fringes, S.; Holzner, F.; Knoll, A. W. The Nanofluidic Confinement Apparatus: Studying Confinement-Dependent Nanoparticle Behavior and Diffusion. *Beilstein Journal of Nanotechnology* **2018**, 9 (1), 301–310.

(30) Fringes, S.; Schwemmer, C.; Rawlings, C. D.; Knoll, A. W. Deterministic Deposition of Nanoparticles with Sub-10 Nm Resolution. *Nano Letters* **2019**, 19 (12), 8855–8861.

(31) Ruggeri, F.; Schwemmer, C.; Stauffer, M.; Nicollier, P. M.; Figueiredo da Silva, J.; Bosshart, P. D.; Kochems, K.; Fotiadis, D.; Knoll, A.; Wolf, H. Placement of Biological Membrane Patches in a Nanofluidic Gap With Control Over Position and Orientation. *Advanced materials interfaces* **2022**, 9 (23), 2200941.

(32) Stoeckenius, W.; Lozier, R. H.; Bogomolni, R. A. Bacteriorhodopsin and the Purple Membrane of Halobacteria. Biochimica et Biophysica Acta (BBA) - *Reviews on Bioenergetics* **1979**, 505 (3–4), 215–278. https://doi.org/10.1016/0304-4173(79)90006-5.

(33) Al-Aribe, K. M.; Knopf, G. K.; Bassi, A. S. Fabrication of an Optically Driven pH Gradient Generator Based on Self-Assembled Proton Pumps. *Microfluidics and nanofluidics* **2012**, 12 (1), 325–335.

(34) Fisher, K.; Yanagimoto, K.; Stoeckenius, W. Oriented Adsorption of Purple Membrane to Cationic Surfaces. *The Journal of cell biology* **1978**, 77 (2), 611–621. https://doi.org/10.1083/jcb.77.2.611.

(35) Mahyad, B.; Janfaza, S.; Hosseini, E. S. Bio-Nano Hybrid Materials Based on Bacteriorhodopsin: Potential Applications and Future Strategies. *Advances in Colloid and Interface Science* **2015**, 225, 194–202. https://doi.org/10.1016/j.cis.2015.09.006.

(36) Soranzo, N.; Altafini, C. ERNEST: A Toolbox for Chemical Reaction Network Theory. *Bioinformatics* **2009**, 25 (21), 2853–2854.

(37) Boekhoven, J.; Poolman, J. M.; Maity, C.; Li, F.; Van Der Mee, L.; Minkenberg, C. B.; Mendes, E.; Van Esch, J. H.; Eelkema, R. Catalytic Control over Supramolecular Gel Formation. *Nature Chem* **2013,** 5 (5), 433–437. https://doi.org/10.1038/nchem.1617.

(38) Field, R. J.; Noyes, R. M. Oscillations in Chemical Systems. IV. Limit Cycle Behavior in a Model of a Real Chemical Reaction. *The Journal of Chemical Physics* **1974**, 60 (5), 1877–1884. https://doi.org/10.1063/1.1681288.

(39) Dueñas-Díez, M.; Pérez-Mercader, J. How Chemistry Computes: Language Recognition by Non-Biochemical Chemical Automata. From Finite Automata to Turing Machines. *iScience* **2019**, 19, 514–526. https://doi.org/10.1016/j.isci.2019.08.007.

(40) Celano, U. The Atomic Force Microscopy for Nanoelectronics. *Electrical Atomic Force Microscopy for Nanoelectronics* **2019**, 1–28.

(41) Reifenberger, R. G.; Baró, A. M. *Atomic Force Microscopy in Liquid: Biological Applications*; John Wiley & Sons, **2012**.

(42) Costa, L.; Li-Destri, G.; Pontoni, D.; Konovalov, O.; Thomson, N. H. Liquid–Liquid Interfacial Imaging Using Atomic Force Microscopy. *Adv Materials Inter* **2017**, 4 (16), 1700203. https://doi.org/10.1002/admi.201700203.

(43) Kaemmer, S. B. Introduction to Bruker's Scanasyst and Peakforce Tapping Afm Technology. Bruker application note. *Bruker Nano Inc.*, Santa Barbara, CA **2011**.

(44) Badilescu, S.; Packirisamy, M. BioMEMS: *Science and Engineering Perspectives*; CRC Press, **2016**.

(45) Wasserman, S. R.; Whitesides, G. M.; Tidswell, I. M.; Ocko, B. M.; Pershan, P. S.; Axe, J. D. The Structure of Self-Assembled Monolayers of Alkylsiloxanes on Silicon: A Comparison of Results from Ellipsometry and Low-Angle x-Ray Reflectivity. *J. Am. Chem. Soc.* **1989,** 111 (15), 5852–5861. https://doi.org/10.1021/ja00197a054.

(46) Losurdo, M.; Bergmair, M.; Bruno, G.; Cattelan, D.; Cobet, C.; De Martino, A.; Fleischer, K.; Dohcevic Mitrovic, Z.; Esser, N.; Galliet, M. Spectroscopic Ellipsometry and Polarimetry for Materials and Systems Analysis at the Nanometer Scale: State-of-the-Art, Potential, and Perspectives. *Journal of Nanoparticle Research* **2009**, 11, 1521–1554.

Chapter 3

Quantification of proton pumping in biological membrane patches

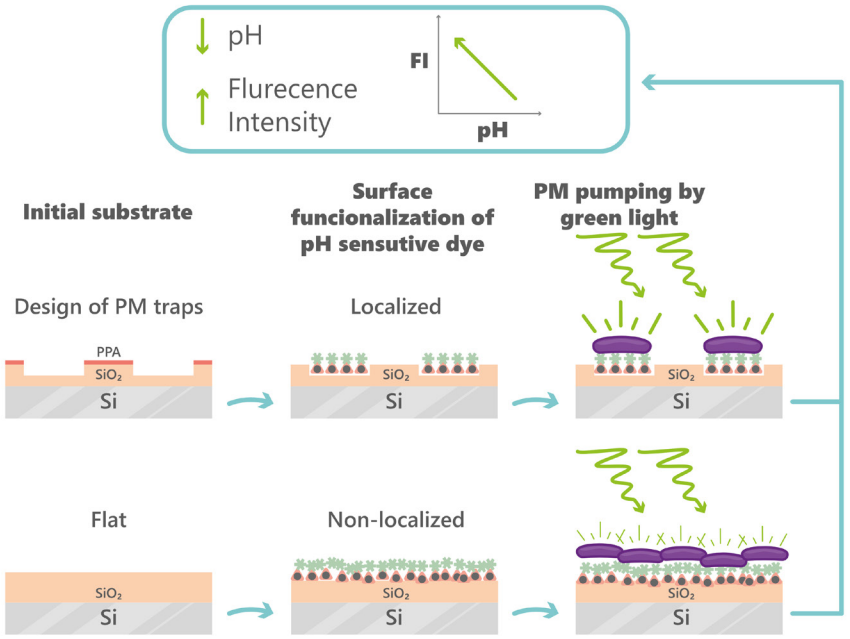

Abstract: Bacteriorhodopsin (bR) in purple membranes (PM) of Halobacterium salinarum acts as a light-driven cross-membrane proton pump. Isolated PM patches can be transported and positioned with orientation control at predefined locations by a tunable nanofluidic confinement apparatus. However, there is still a need for a method to measure the proton pumping in a device that enables precise PM orientation and localization. We functionalized a SiO_2 surface with a pH-sensitive dye for the measurement of proton pumping. To achieve a measurement of proton pumping with controlled orientation and localization, we introduced a maskless chemical lift-off method. This strategy uses thermal scanning probe lithography to locally bind a pH-sensitive dye onto the SiO_2 substrate. In both cases, fluorescence microscopy was employed to investigate protein functionality within the experimental setup by documenting proton pumping across the PM. Issues concerning reproducibility of surface functionalization were found.

3.1 Introduction

The synthesis of functional materials is essential for the development of novel highly functional devices. Accordingly, controlling the design and structures of materials at the nanometer scale is crucial to producing unique material properties for application in many fields, from informatics to biomedical engineering. [1] In biological systems, the dynamic self-assembly of molecules, such as the aggregation and folding of proteins, can be totally or partially influenced by energy sources. [2] In supramolecular materials operating out-of-equilibrium, the self-assembly of reagents can be driven by a chemical reaction network (CRN) that consumes a chemical fuel. [3]

A local proton gradient can be used as a bottom-up strategy to catalyze spatially controlled self-assemblies. [4–6] Local control of proton gradients can be observed in nature, for instance, in purple membranes (PM) of Halobacterium salinarum, mainly consisting of bacteriorhodopsin (bR). [7] The bR acts as a light-driven cross-membrane proton pump that transports protons across the cell membrane. The absorption spectrum of bR molecules reveals heightened efficiency within the 550 nm wavelength range due to their characteristic purple coloration. [8] Consequently, this spectral preference enables the activation and precise control of proton pumping through the utilization of green light. Over the past decades, researchers have explored the use of bR proton pumps to modulate the pH of target solutions. A wild- type (WT) bR proton pump typically operates at approximately 20 cycles per second. [9] Under light-saturating conditions, its performance can increase to up to 100 cycles per second. [10] The distribution and geometry of bR molecules within PM fragments confer chemical and thermal stability to bR. Upon exposure to visible light, each bR protein facilitates proton translocation into the extracellular medium through photoinduced structural and spectral modifications. [10]

Integrating PMs onto a surface enables the production of a localized light-triggered proton gradient. This system holds potential for diverse applications, including the precise spatiotemporal control of proton-catalyzed CRNs. [11] However, bR exhibits inherent directionality in proton pumping and a specific orientation within the membrane, with protons being transported from the cytoplasmic side (C-terminus) to the extracellular side (N-terminus). [7] Therefore, precise control over the orientation of membrane patches is essential for optimizing photoelectric conversion efficiency. [12]

Ruggeri et al. [13] demonstrated that isolated PM patches can be precisely transported and oriented at designated locations. by a tunable nanofluidic confinement apparatus (TNCA). To control the orientation of PMs, their charge asymmetry was increased by attaching a deca-histidine (His_{10})-tag to either their cytoplasmatic side (C-His_{10}-tag PMs) or extracellular side (N-His_{10}-tag PMs). [14] During the deposition stage on a negatively charged interface (SiO_2), the PMs were assembled with the His_{10}-tag down. Contrarily, when the traps presented a positively charged interface (Al_2O_3), the membranes were deposited preferentially with the His_{10}-tag up. [13]

After establishing a method to control PM orientation on a surface, the available methods for localized pH measurement on substrates remain limited. They usually require sophisticated techniques such as voltammetric nanosensor measurements, [15] scanning electrochemical microscopy, [16] or scanning ion conductance microscopy. [17] Gaitzsch et al. [18] reported the insertion of a proton pump with orientational control into an artificial asymmetric membrane. However, the experiment was executed in vesicles, which do not provide control over the localization of pumping activity on a planar substrate. Biologically self-powered steady-state ionic current nanopore sensing enables the investigation of bR proton pumping activity at the single-molecule level within a nanofluidic system, providing insights into its response to light. [19] The green light irradiation of this device resulted in a charge density generated by each bR monomer that was 580x higher than the previously reported value. [20] Although the results are very encouraging, such an approach requires a complex setup.

Fluorescence microscopy (FM) is a versatile optical technique that can be used to control and measure bR pumping using light. [21] Lee et al. [22] demonstrated the controlled orientation of bR in thin films of an ABA block copolymer. They used pyranine, a pH-sensitive dye, to provide a visual clue for pH changes. Pyranine is highly sensitive to pH changes at pH values near 7.2 [21] and its concentration controls the saturation of the observed color. Therefore, the adjustment of dye concentration produces variations of the same hue. [22] Gonçalves et al. [23] used pyranine to investigate the occurrence of proton pumping by bR in closed chambers according to membrane orientation. They combined atomic force microscopy (AFM) and FM to demonstrate the functionality of PMs in the setup. [23] However, the challenges associated with covalently attaching pyranine to surfaces such as SiO_2 [24] pose significant limitations, primarily due to its propensity to leach from sensor surfaces. [25] Therefore, achieving controlled localization and orientation when using pyranine to measure PM pumping becomes particularly difficult.

Considering these challenges, this study aims to utilize FM to measure proton pumping of PM patches. For that, we have functionalized an amino-functionalized SiO_2 surface with pHrodo, a pH-sensitive dye. pHrodo increases its fluorescence intensity (FI) as the medium becomes more acidic. Given its amino-reactive nature, pHrodo can covalently attach to surfaces containing amino groups, facilitating its covalent bonding to surfaces. This dye has been utilized, for example, in the functionalization of amino-functionalized beads, [26] nanoprobes, [27] and cells [28,29] to facilitate the detection of pH within these environments.

After depositing PM on the pHrodo-SiO_2 surface, we obtained an optically triggered device to assess PM pumping activity in situ. We measured the intensity of the pH-sensitive dye on the SiO_2 substrate to evaluate localized photo-induced proton pump activity. The PM embedded in the substrate generated ion flow, facilitating the measurement of the active surface based on light intensity. Additionally, we developed a maskless lift-off (MLO) method to locally couple a pH-sensitive dye on a SiO_2 substrate, aiming to assess single PM pumping activity in situ. However, reproducibility remained an issue, indicating that further optimization for the pHrodo functionalization protocol on a SiO_2 surface is required.

3.2 Results and discussion

We developed two protocols to covalently link a pH-sensitive dye (pHrodo) to a SiO_2 surface via aminosilanization followed by PM deposition, to study their activity in situ. In the first protocol, PM pumping was detected on a flat substrate through pHrodo bonded to the surface, onto which PMs were deposited. In the second protocol, we designed a device to detect single-patch PM proton pumping based on patch localization and position. This was achieved by combining aminosilanization with thermal scanning probe lithography (t-SPL) to functionalize a micro-area of the substrate with pHrodo. PMs were then deposited on this substrate using TNCA.

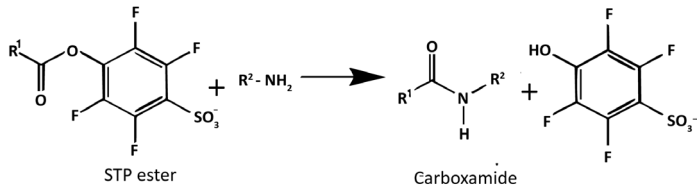

Figure 3.1. Reaction of primary amine with 1, 4-sulfo-2,3,5,6-tetra fluorophenyl (STP) ester.

The presence of PMs on the pH sensor dye eliminates the need for advanced instrumentation or external hardware to electronically or optically amplify the fluorescence signal. To use FM as an optical trigger for the proton gradient, a dye excited at a wavelength different than that of bR is needed to measure the local proton concentration. For that, we selected the amino-reactive pHrodo™ green STP ester (pHrodo) as a pH-sensitive fluorescent dye. This dye is excited at 488 nm (blue light) and emits green light at 530 nm. [30] Its main characteristic is the substantial increase in fluorescence signal as the pH of its surroundings becomes more acidic. [31] Amino silanes were used as coupling agents because of their reaction with the SiO_2 surface and the possibility of the attachment of an amino-reactive molecule in the second step. [32]

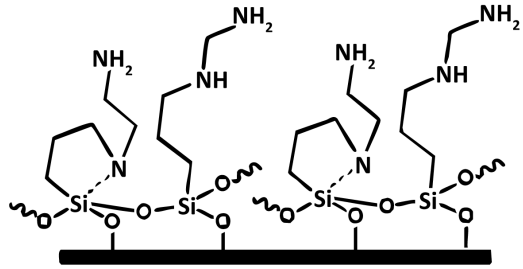

Figure 3.2. Steric hindrance from N-(2-aminoethyl)-3-aminopropyltrimethoxysilane (AEAPTMS).

As shown in Figure 3.1, 4-sulfo-2,3,5,6-tetrafluorophenyl (STP) esters readily react with primary amines to produce acylation products. [33] We selected N-(2-aminoethyl)-3-aminopropyltrimethoxysilane (AEAPTMDS) to functionalize the SiO_2 surface because it

produces a relatively stable and reproducible monolayer (Figure 3.2). AEAPTMS exhibits catalytic activity in siloxane bond formation. However, steric hindrance obstructs the intramolecular catalysis of bond detachment, which enables the reactivity of amino-reactive molecules in the silane layer. [32]

3.2.1 Functionalization of pHrodo on a flat unpatterned substrate

As a first step, the functionalization of the pHrodo on a Si/SiO_2 substrate was optimized on a flat substrate to implement the obtained system for PM pumping measurement. The process began by covalently bonding AEAPTMS to the SiO_2 surface. Subsequently, pHrodo functionalization was conducted at the amino group presented by the AEAPTMS.

Table 3.1. Ellipsometer data of pHrodo thickness throughout the functionalization steps on the SiO_2 substrate. Refractive index (n) SiO_2 = 1.46; n_{silane} = 1.48; [32] n_{pHrodo} = unknown; n values obtained at wavelength = 633 nm.

Sample	Thickness (nm)	Experimental *n* at 633 nm
Thermal oxide (SiO_2)	57.7 ± 0.1	-
Silane	0.5 ±0.0	1.47
Silane + pHrodo	9.3 ±0.1	1.52

We utilized ellipsometry to confirm the presence of an AEAPTMS layer on the silane-functionalized SiO_2 substrate and to detect pHrodo on the same substrate, as shown in Table 3.1. We estimated an increase of 0.5 nm in substrate thickness attributed to the AEAPTMS functionalization. Subsequently, an additional increase of approximately 8.8 nm indicated the successful functionalization of pHrodo on the substrate surface. The progressive increase in thickness from one step to the next provides compelling evidence for the successful functionalization of AEAPTMS, followed by the subsequent pHrodo functionalization.

Following the functionalization of pHrodo on the silane-SiO_2 substrates, the resulting SiO_2-silane-pHrodo surfaces were coated with a dispersion of PM containing WT, C- His_{10}-tag, or N-His_{10}-tag PMs. One sample was coated with a mixture of N- and C-His_{10}-tag PMs. As a control, we used a PM-free substrate ('pHrodo only'). A second control sample, a pHrodo-free substrate ('PM only'), was used to investigate the intrinsic signal originating from PM patches alone. All these substrates were exposed to fluorescence measurements for 100.0 s in a non-buffered aqueous media. First, proton pumping was activated by 1.0 s exposure to green light using TRITC (tetramethylrhodamine Isothiocyanate) filter. Then, fluorescence was measured by 500 ms excitation of blue light using FITC (fluorescein isothiocyanate) filter. Figure 3.3 displays the temporal evolution of FI for these substrates. Figure 3.4 shows six fluorescence images captured at 8 and 100 s on three substrates of this same experiment. Two substrates contained a mixture of N- and C-His_{10}-tag PMs, with ('PM+pHrodo') and without pHrodo ('PM only') at the surface. The remaining substrate

contained pHrodo at the surface without PMs (`pHrodo only´).

When PMs are exposed to green light, protons were pumped from the C-terminal to the N-terminal side. This proton transport leads to a progressive increase in fluorescence over time on substrates with PMs deposited on a pHrodo-functionalized surface. Observations showed that for all types of PMs, FI increased on PM-pHrodo- silane-SiO_2 substrates under green light, while no such increase was noted for pHrodo- silane-SiO_2 substrates alone (see Figures 3.3 and 3.4). This suggests that the system can detect PM proton pumping activity. However, Figure 3.4 indicates that individual PM patches on the pHrodo surface were not distinguishable, due to the limited resolution of the microscope. Only an overall increase in FI across the entire area was observed.

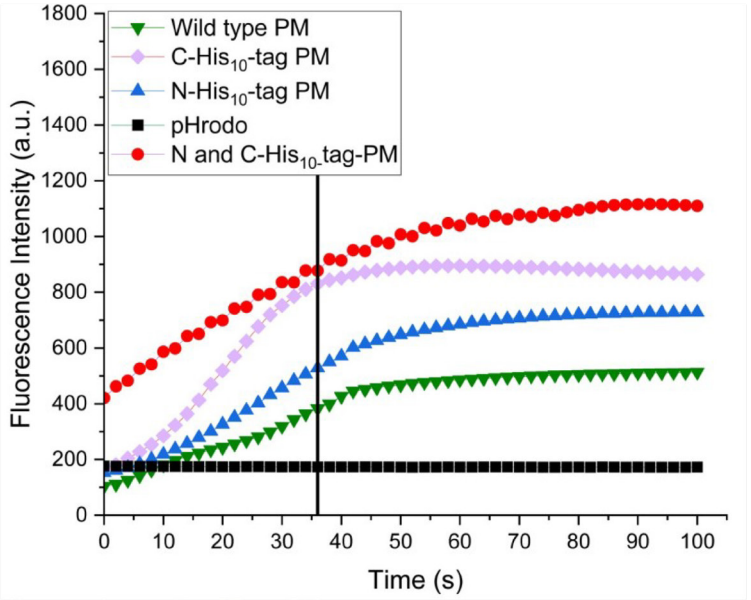

Figure 3.3. Fluorescence response of pHrodo to PM pumping over time. Experiments were performed in Milli-Q water. Images were captured with 500 ms exposure time using 40x objective lens. Green light (TRITC filter) activated the pumping, and pHrodo fluorescence intensity was measured using blue light (FITC filter). The signal of 'PM only' was approximately 0 counts (not shown). Green: wild-type PM. Violet: C-His_{10}-tag PM. Blue: N-His_{10}-tag PM. Black: pHrodo (control). Red: mixture of N- and C-His_{10}-tag PM.

To correlate FI with pH, we formulated Equation (1) considering that the pHrodo intensity exhibited a linear increase for pH values from 8.0 to 4.0 [31]

$$(1)\quad \frac{I_{PMpHrodo}}{IpHrodo} = -3.65 \times pH_{PMpHrodo} \pm 0.40 + 25.95 \pm 2.23$$

where I_{pHrodo} is the FI of the substrate at a specific pH (represented by pH_{pHrodo}) in the

absence of PMs; $I_{PMpHrodo}$ is the pHrodo intensity at a particular time in the presence of PMs; and $pH_{PMpHrodo}$ is the pH value at a specific time in the presence of PMs. The formulation of this formula through linear regression is based on data from Dolman et al. [34] Figure S3.1, in the supplementary information (SI) shows the graphical representation of the plot of this equation.

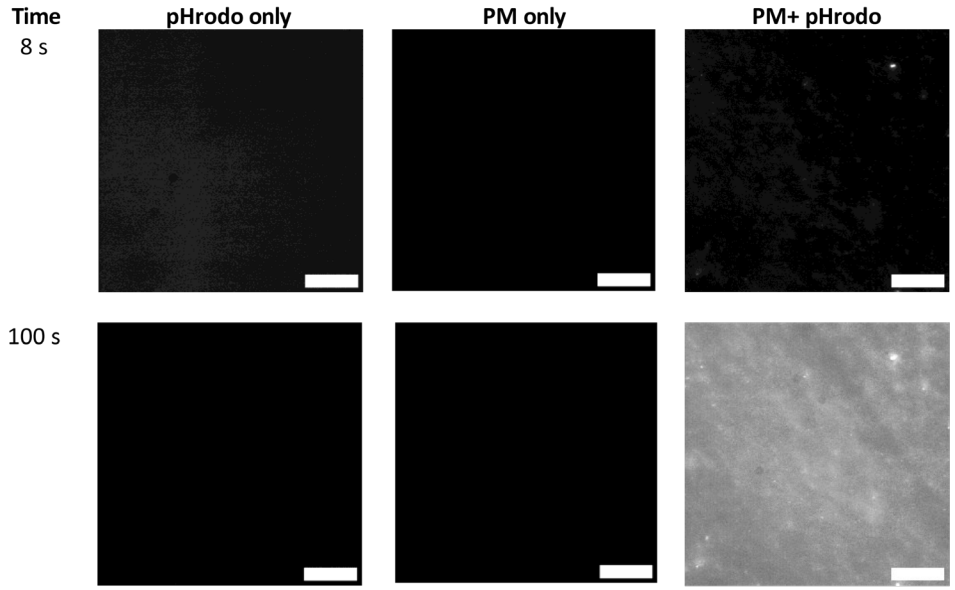

Figure 3.4. Fluorescence images of pHrodo response under three conditions: in the absence of PMs ('pHrodo only'), in the presence of PM pumping for a mixture of N- and C-His_{10}-tag PM ('PM+pHrodo') and in the absence of pHrodo ('PM only'). Images were acquired using 500 ms exposure time and 40x objective lens. The pumping was activated using green light (TRITC filter), whereas pHrodo fluorescence intensity was measured under blue light (FITC filter). The scale bar corresponds to 20 µm.

Table 3.2 displays the results of the linear regression for 'PM+pHrodo' substrates, extracted from a subset of data shown in Figure 3.3. For the linear regression, we considered the interval from t = 0.0 to t = 36.0 s, which presented almost linear behavior of all substrates containing 'PMs+pHrodo` (coefficient of determination (COD) around 1.0). Based on the FI values from Figure 3.3 and Equation (1), we calculated the initial (t = 0 s) and final (t = 100 s) pH values, as shown in Table 3.2. A pH decrease (ΔpH) of approximately 1.08 was observed for the C and N-His_{10}-tag PMs mixture and for C- His_{10}-tag PMs, 0.89 for N-His_{10}-tag PMs, and 0.64 for WT PMs. The calculated pH values closely match those documented in the literature, with a ΔpH of approximately 0.5–2.0.[7,35]

In Figure 3.3, the fluorescence signal of all PM types, except for C-His_{10}-tag PM, increased over time until the end of the measurements. This provides evidence of a decrease in pH

overtime. However, the FI rate of increase decelerated over time. In the case of C-His_{10}-tag PM, its FI increased until reaching a maximum and then began to decrease. This phenomenon may be associated with the saturation of pumping activity or dye bleaching. Interestingly, we did not observe a fluorescence decrease in the other PM types. Therefore, we assumed that the pumping activity of this PM type reached a saturation point. A more extended exposure time to green light could validate this assumption. This is further analyzed in Figure 3.6.

Table 3.2. Linear regression analysis of fluorescence intensity over time, measured from timelapse experiments on a flat substrate coated with different types of PMs: C-His_{10}-tag PMs, N- His_{10}-tag PMs, wild-type PMs, and a mixture of N and C-His_{10}-tag PMs. The table includes the calculated ratios of $I_{PMpHrodo}$ to I_{pHrodo} fluorescence intensities, as well as the initial and final pH values derived from these intensities using Equation (1). COD= The coefficient of determination.

Sample	Linear regression values			$\frac{I_{PMpHrodo}}{I_{pHrodo}}$		Calculated pH	
	Intercept	Slope	COD	Initial	Final	Initial	Final
Mixture C and N-His_{10}-tag PM	444.6 ± 6.2	12.7 ± 0.3	0.99	2.39	6.41	6.50	5.42
C-His_{10}-tag PM	112.1 ± 12.2	20.6 ± 0.6	0.99	0.97	4.99	6.88	5.80
N-His_{10}-tag PM	120.0 ± 6.4	11.0 ± 0.3	0.99	0.86	4.20	6.90	6.01
Wild-type PM	99.4 ± 3.4	7.5 ± 0.2	0.99	0.59	2.96	6.98	6.34

Figure 3.3 demonstrates that C-His_{10}-tag PM exhibited the steepest slope in proton pumping activity, followed by the mixture of C- and N-His_{10}-tag PM, N-His_{10}-tag PM, and WT PM. The mixture of C- and N-His_{10}-tag PM also exhibited a higher initial FI relative to the other PM types. These findings suggest that all PM types contribute to proton pumping toward pHrodo to some extent. The differences in FI values between PM types may be attributed to the lower surface density of WT and N-His_{10}-tag PMs on the coated substrate (see Figure S3.2, SI).

To investigate proton diffusion, we used SiO_2-silane-pHrodo substrates with adsorbed PM membranes (WT PM, C-His_{10}-tag PM, N-His_{10}-tag PM, or a mixture of C and N-His_{10}-tag PM). The light exposure sequence is shown in Figure 3.5. After adding water to the substrate, proton pumping was activated with 1.0 s of green light exposure (TRITC filter). Fluorescence was measured with 500 ms excitation under blue light (FITC filter). The sample was then kept in the dark for 21.0 s, followed by another fluorescence measurement with 500 ms excitation (FITC filter). Following a 1.0 s exposure to the TRITC filter, fluorescence was re-measured with 500 ms excitation (FITC filter). The dark-light cycle was repeated for 456.0 s. The sample then underwent several sequences of 1.0 s exposures to green light, with fluorescence measured using 500 ms blue light exposure to assess the linearity of pHrodo intensity response to green light. The fluorescence of pHrodo-silane-SiO_2 substrate ('pHrodo') and PMs on SiO_2 ('PM only') were measured under the same conditions for

reference.

Figure 3.6a presents the timelapse sequence of FI shown in Figure 3.5. Accordingly, with prolonged exposure to green light, the FI of all PM-pHrodo-silane-SiO_2 substrates increased. After 456.0 s from the beginning of the experiment, the slope of the intensity values increased even further. This indicated that an increasing exposure to green light over time accelerated the fluorescence signal slope, which corresponded to a faster decrease in pH. Furthermore, except for WT PM, the FI of PMs presented a linear increase until they reached a maximum and then started to decrease. This is likely related to the saturation of pumping activity or dye bleaching. We did not observe bleaching in WT PM and control samples. So, we conclude that the genetically modified PMs reached their saturation faster than WT PM. The pH of WT PM continued to decrease until the end of the measurement, but at a lower rate.

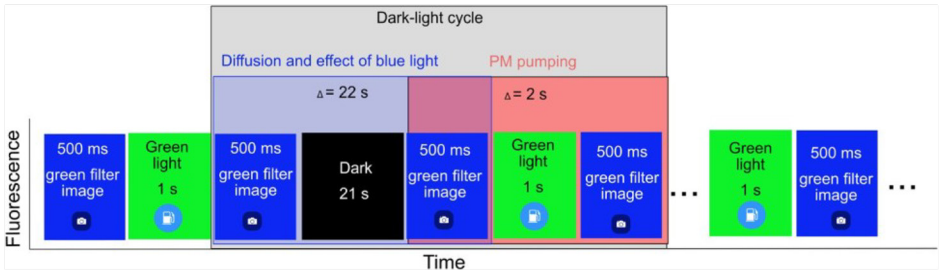

Figure 3.5. Schematic diagram of a sequence of FM images obtained to study the proton diffusion of PM on a pHrodo-functionalized surface. Blue light (FITC filter) was used for imaging, and green light (TRITC filter) was used for PM pumping.

Figure 3.6a also shows that, except for C-His_{10}-tag PM, the initial fluorescence of 'PM+pHrodo' substrates started at approximately 100 counts (cps), similarly to the results shown in Figure 3.3. However, the 'pHrodo only' substrate signal shown in Figure 3.6 exhibited a substantially lower signal than that shown in Figure 3.3 (190 to 110 cps). This variation might be related to surface contamination by unbound pHrodo, which could not be prevented. Consequently, the results should not be considered quantitative due to the significant deviation from earlier measurements presented in Table 3.2. Nonetheless, qualitative interpretation remains feasible under these conditions, as fluorescence intensity increases over time.

Figure 3.6b and c shows, respectively, the difference in fluorescence signal after exposure to green light, which was responsible for the pumping (red-transparent area, Figure 3.5) and after 21.0 s in the dark (blue-transparent area, Figure 3.5). We observed that for all samples, diffusion did not substantially influence the PM proton pumping as the FI did not decrease after 21.0 s in the dark. We assumed that the blue light affected the PM pumping to some extent. Owing to its broad excitation spectrum (detection wavelength between 700–800 nm), bR exerts considerable pumping for excitation wavelengths between 470

nm (blue light) and 650 nm (red light).[8] Compared to our results, a previous study showed that the suspension of PM cells in response to a short light pulse led to pH changes only under minor or medium acidification, which reversed in the dark.[7] We concluded that our result was different because of the exposure of our sample to blue light.

In summary, pHrodo-functionalized surfaces effectively detect proton pumping from PMs by monitoring FI. Green light stimulation induced stepwise increases in FI (Figure 3.6), demonstrating its efficacy. All PM types exhibit proton pumping activity, and the pHrodo-functionalized surface does not appear to influence PM orientation; observed differences are likely due to variations in PM density. However, several factors may affect the reproducibility of quantification, including PM density after deposition and the quality of the pHrodo layer, which depends on the efficiency of surface functionalization. Image resolution for visualizing single patches was a challenge, underscoring the need for a more controllable method to spatially regulate PM deposition. Consequently, the locally controlled deposition of single PM patches in traps functionalized with a pH-sensitive dye was investigated, as discussed in Section 3.2.2.

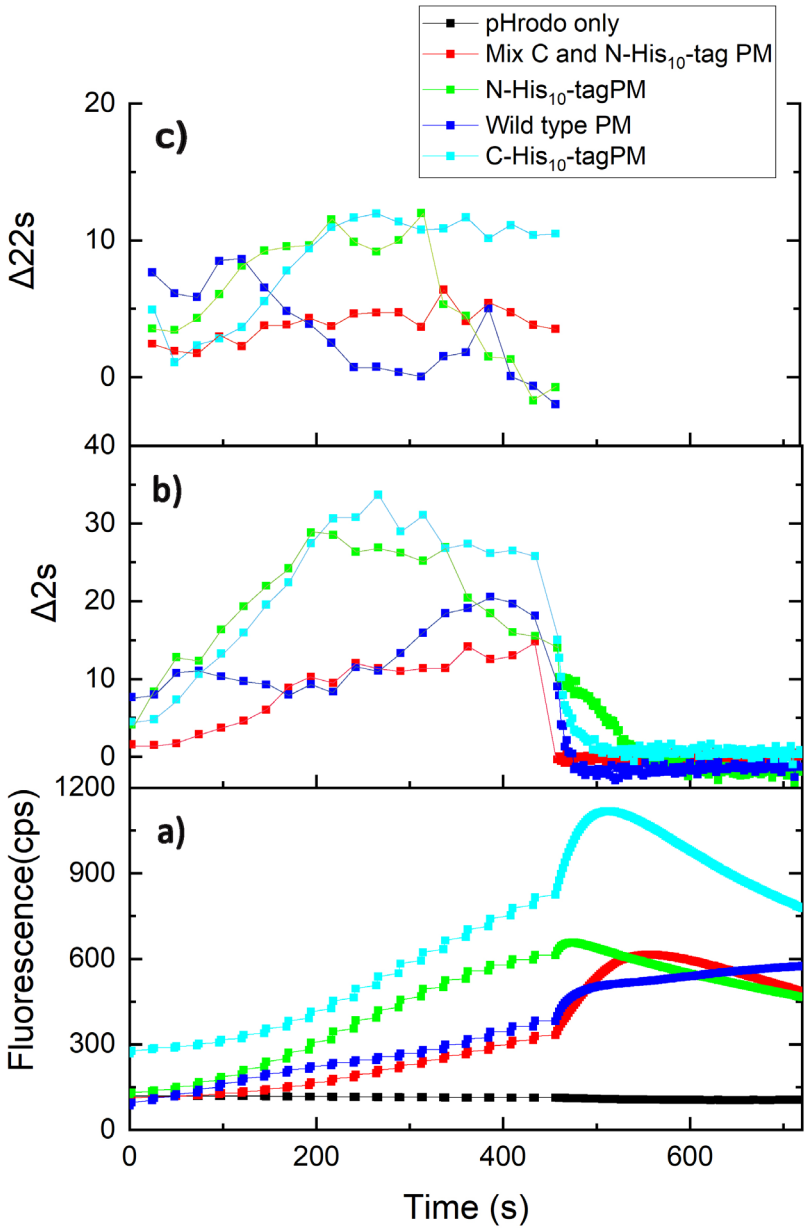

Figure 3.6. a) Fluorescence response of pHrodo to PM pumping used to investigate the diffusion of protons over time. Experiments were performed in Milli-Q water. Images were captured under 500 ms exposure time using 60x objective lens. Green light (TRITC filter) activated the pumping, and pHrodo fluorescence intensity was measured using blue light (FITC filter). The signal of 'PM only' was approximately 0 cps (not shown). **b)** Difference in fluorescence intensity (obtained from Figure 3.6a) between b) 21.0 s in the dark (Δ 22.0 s) and **c)** 1.0 s under green light (Δ2s) by pHrodo response.

3.2.2 Nanofunctionalization of proton gradient from Bacteriorhodopsin

The microlocalized measurement of PM pumping is crucial for the spatiotemporal examination of the pumping activity of a single patch of PM. For localized silanization of a surface, current micro chemical functionalization techniques, such as nano printing and chemical lift-off, require sophisticated preparation steps. [36,37] Moreover, these methods are incompatible with the device developed in this study because a 3D pattern is necessary to trap PMs. [13]

T-SPL is well-suited for designing 3D patterns, and polyphthalaldehyde (PPA) is an excellent polymer for creating topographical nanostructures using this method. [38] PPA does not require resist development and is resistant to ethanol or methanol, solvents commonly used for aminosilanization. [39] Thus, it serves both as a t-SPL resist and a mask to protect non-patterned areas. PPA shields these areas from silanization and can be removed afterward with solvents like tetrahydrofuran (THF) and isopropanol, [40] so the resist can be removed after the silanization and/or dye functionalization.

The approach used in this study to measure a localized single-patch PM pumping is shown in Figure 3.7. The fabrication steps for the device included the deposition of PPA resist, lithographic writing of PM traps in the resist, etching of traps on the SiO_2 substrate, silanization of the PPA and SiO_2 area, removal of the resist by THF and, finally, the localized functionalization of pHrodo in the traps. We used t-SPL to design 1.2 µm diameter traps, reactive ion etching (RIE) to transfer the traps into the SiO_2 layer and PPA, and a PPA as a mask to prevent non-patterned areas from being silanized. The designed traps were functionalized with AEAPTMS and pHrodo green STP ester. After the microlocalized pHrodo functionalization (step 7, Figure 3.7), we applied a drop of WT PM to the chip's surface and conducted PM deposition specifically in the designated traps using TNCA [13] (step 8, Figure 3.7).

Figure 3.8. shows images of pHrodo localized functionalization (step 7 in Figure 3.7). Figure 3.8a presents a bright-field image of a field designed using t-SPL. Figures 3.8b and 3.8c display fluorescent images of a dry sample and a sample immersed in pH 4.0 buffer, respectively. The fluorescent images show brighter spots only in areas written by t-SPL, which highlights the contrast between the functionalized traps and the surrounding regions. This demonstrates the success of the t-SPL chemical lift-off process. The fluorescent intensity contrast ($FI_{contrast}$), defined by Equation (2), is the ratio between I_{pHrodo} (FI in the pHrodo-functionalized area) and $I_{background}$ (FI in the non- functionalized area).

$$(2)\ FI_{contrast} = \frac{I_{pHrodo}}{I_{background}}$$

In Figures 3.8b and 3.8c, $FI_{contrast}$ was 74% and approximately 50%, respectively. In conclusion, our MLO method effectively achieved microlocalized functionalization of PM traps with pHrodo.

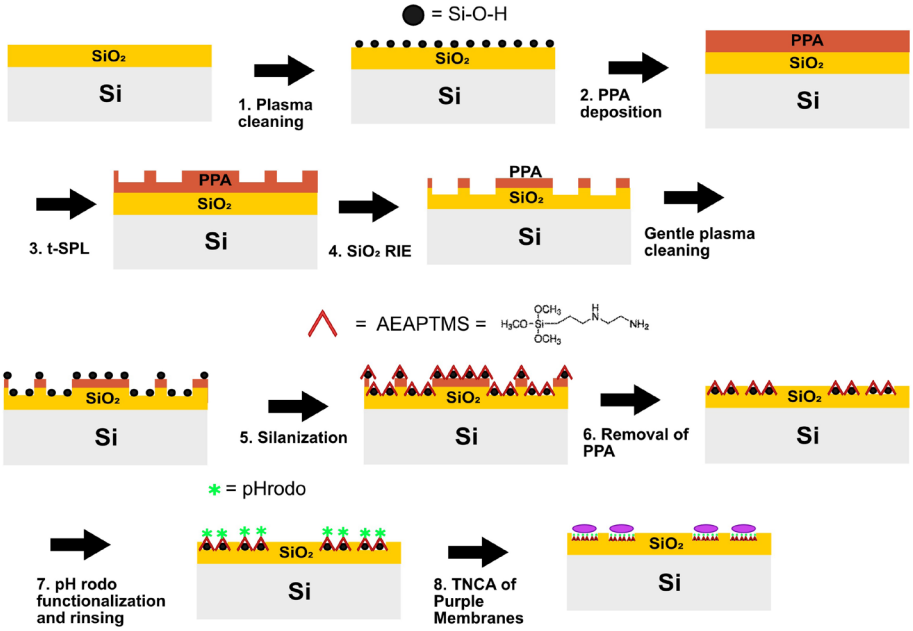

Figure 3.7. Substrate used for single-patch PM proton pumping measurements: 1. Plasma cleaning. 2. PPA spin-coating. 3. t-SPL writing. 4. SiO_2 RIE. 5. Substrate silanization. 6. PPA removal. 7. Functionalization of pHrodo. 8. Deposition of PM by TNCA. PPA = polyphthalaldehyde; t-SPL = thermal scanning probe lithography; RIE = reactive ion etching; TNCA = tunable nanofluidic confinement apparatus.

a)	b)	c)
Bright-field image	Fluorescence image (FITC filter)	
Dry sample		pH 4 buffer

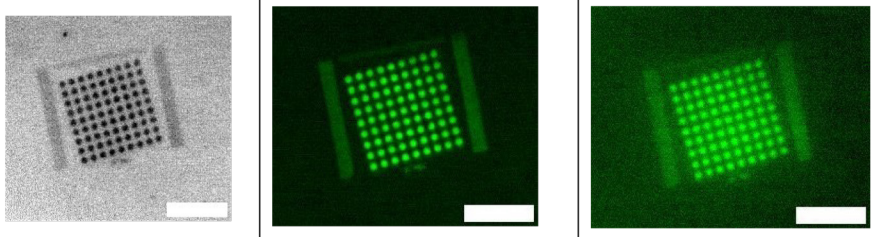

Figure 3.8. a) Image of a dry sample of localized pHrodo-silane-SiO_2 substrate (step 7, Figure 3.7) in a bright-field. FITC filter fluorescent image of **b)** dry sample and **c)** sample immersed in buffer 4 solution. The scale bar represents 10 µm.

a)	b)	c)
Localized silanization	Localized deposition of wild-type PM	Non-localized deposition of wild-type PM
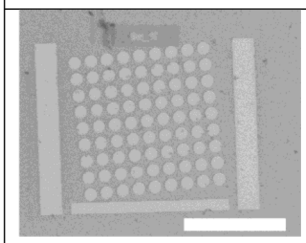	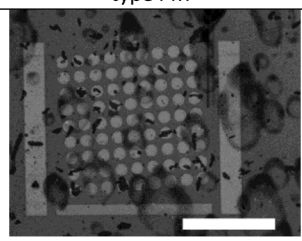	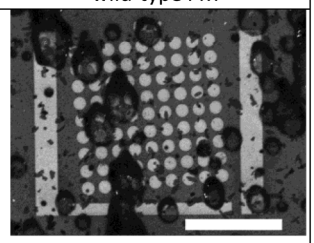

Figure 3.9. SEM images of PM deposition field at different steps: **a)** Localized silane-SiO_2 substrate after PPA removal by THF (step 6, Figure 3.7), **b)** localized pHrodo-silane-SiO_2 substrate after wild-type PM deposition (step 8, Figure 3.7), and **c)** non-localized pHrodo-silane-SiO_2 substrate after wild-type PM deposition (step 8, Figure 3.7). The scale bar represents 10 µm.

SEM images of the device fabrication at different stages are presented in Figure 3.9. Figure 3.9a shows the substrate after localized silanization and subsequent removal of PPA. The contrast between the traps and the surrounding area suggests that the silanization was effective, as indicated by the difference in material inside and outside the traps. The SEM image shown in Figure 3.9b, representing the substrate after step 8 in Figure 3.7 (following the deposition of PMs by TNCA), reveals the presence of darker spots with an ellipsoidal shape, each with an approximate size of 500 nm. These dimensions correspond to the average size of a PM patch. This image provides evidence of the possibility of localized deposition of PMs on this device. Figure 3.9c presents a field of the same device as shown in Figure 3.9b, where TNCA was not performed. Although PMs are visible, they were not solely deposited in the traps. Instead, they were also randomly spread at the designated area. Figure 3.9c underscores the significance of the TNCA in achieving a more controlled deposition of PMs within the traps.

The fluorescence signal of the localized-pHrodo-silane-SiO_2 substrates, shown in Figure 3.9b, could not be measured. A substantial amount of dirt was visible on the substrate surface after PM deposition, as represented by the large black circles. We assumed that the unbound pHrodo prevented the device from obtaining localized fluorescence signals in the PM traps area. To overcome that, the MLO method should be better controlled to prevent unbound pHrodo in areas outside the PM traps.

The MLO method was thoroughly investigated, with each step analyzed via ellipsometry to achieve reproducibility, as detailed in the SI. However, through our studies, reproducibility remained an issue. We propose that factors such as surface contamination from solvents used in rinsing steps and gases from RIE can impede silanization and lead to uneven coverage. Additionally, moisture sensitivity of amino silanes in humid environments may reduce reactivity, while inadequate reaction conditions can result in incomplete silanization.

Achieving precise control over the silane layer thickness presents further challenges, and environmental variability may contribute to inconsistent results. Moreover, amino groups may lose functionality under harsh conditions. Despite these challenges, the MLO method shows promise for the microscale functionalization of small molecules. Optimizing these parameters could enable a simple, maskless lift-off protocol for localized functionalization.

3.3 Conclusion and outlook

We developed a method that can be used to measure the proton gradient of PMs per unit of time. For the localized and oriented controlled measurement of PM pumping, we developed a chemical lift-off method that locally functionalizes amino-reactive pHrodo dye. However, we faced issues concerning reproducibility, and the main challenges were the presence of unlocalized pHrodo dye and agglomerates at the SiO_2 surface. Future studies should further implement the t-SPL chemical lift-off method using other dyes and amino-reactive molecules to expand the applications of this new silanization method.

3.4 References

(1) Nande, A.; Kalyani, N. T.; Tiwari, A.; Dhoble, S. J. 1 - Exploring the World of Functional Materials. In Functional Materials from Carbon, Inorganic, and Organic Sources; Dhoble, S. J., Nande, A., Kalyani, N. T., Tiwari, A., Arof, A. K., Eds.; Woodhead Publishing Series in Electronic and Optical Materials; *Woodhead Publishing*, **2023;** pp 1–19. https://doi.org/10.1016/B978-0-323-85788-8.00014-8.

(2) Das, K.; Gabrielli, L.; Prins, L. J. Chemically Fueled Self-assembly in Biology and Chemistry. *Angewandte Chemie International Edition* **2021**, 60 (37), 20120–20143.

(3) Boekhoven, J.; Brizard, A. M.; Kowlgi, K. N.; Koper, G. J.; Eelkema, R.; van Esch, J. H. Dissipative Self-assembly of a Molecular Gelator by Using a Chemical Fuel. *Angewandte Chemie* **2010**, 122 (28), 4935–4938.

(4) Wang, Y.; Oldenhof, S.; Versluis, F.; Shah, M.; Zhang, K.; van Steijn, V.; Guo, X.; Eelkema, R.; van Esch, J. H. Controlled Fabrication of Micropatterned Supramolecular Gels by Directed Self-Assembly of Small Molecular Gelators. *Small* **2019**, 15 (8), 1804154.

(5) Wang, Y.; Versluis, F.; Oldenhof, S.; Lakshminarayanan, V.; Zhang, K.; Wang, Y.; Wang, J.; Eelkema, R.; Guo, X.; van Esch, J. H. Directed Nanoscale Self-Assembly of Low Molecular Weight Hydrogelators Using Catalytic Nanoparticles. *Advanced Materials* **2018**, 30 (21), 1707408.

(6) Olive, A. G.; Abdullah, N. H.; Ziemecka, I.; Mendes, E.; Eelkema, R.; Van Esch, J. H. Spatial and Directional Control over Self-Assembly Using Catalytic Micropatterned Surfaces. *Angewandte Chemie International Edition* **2014**, 53 (16), 4132–4136.

(7) Stoeckenius, W.; Lozier, R. H.; Bogomolni, R. A. Bacteriorhodopsin and the Purple Membrane of Halobacteria. *Biochimica et Biophysica Acta (BBA)-Reviews on Bioenergetics* **1979**, 505 (3–4), 215–278.

(8) Schenkl, S.; Zgrablić, G.; Portuondo-Campa, E.; Haacke, S.; Chergui, M. On the Excitation Wavelength Dependence of the Fluorescence of Bacteriorhodopsin. *Chemical physics letters* **2007,** 441 (4–6), 322–326.

(9) Perrino, A. P.; Miyagi, A.; Scheuring, S. Single Molecule Kinetics of Bacteriorhodopsin by HS-AFM. *Nature Communications* **2021**, 12 (1), 7225.

(10) Hampp, N. Bacteriorhodopsin as a Photochromic Retinal Protein for Optical Memories. *Chemical Reviews* **2000**, 100 (5), 1755–1776.

(11) Boekhoven, J.; Poolman, J. M.; Maity, C.; Li, F.; Van Der Mee, L.; Minkenberg, C. B.; Mendes, E.; Van Esch, J. H.; Eelkema, R. Catalytic Control over Supramolecular Gel Formation. *Nature chemistry* **2013**, 5 (5), 433–437.

(12) Lozier, R. H.; Bogomolni, R. A.; Stoeckenius, W. Bacteriorhodopsin: A Light-Driven Proton Pump in Halobacterium Halobium. *Biophysical journal* **1975**, 15 (9), 955.

(13) Ruggeri, F.; Schwemmer, C.; Stauffer, M.; Nicollier, P. M.; Figueiredo da Silva, J.; Bosshart, P. D.; Kochems, K.; Fotiadis, D.; Knoll, A.; Wolf, H. Placement of Biological Membrane Patches in a Nanofluidic Gap With Control Over Position and Orientation. *Advanced materials interfaces* **2022**, 9 (23), 2200941.

(14) Stauffer, M.; Hirschi, S.; Ucurum, Z.; Harder, D.; Schlesinger, R.; Fotiadis, D. Engineering and Production of the Light-Driven Proton Pump Bacteriorhodopsin in 2D Crystals for Basic Research and Applied Technologies. *Methods and protocols* **2020**, 3 (3), 51.

(15) Michalak, M.; Kurel, M.; Jedraszko, J.; Toczydlowska, D.; Wittstock, G.; Opallo, M.; Nogala, W. Voltammetric pH Nanosensor. *Analytical chemistry* **2015**, 87 (23), 11641–11645.

(16) Al-Jeda, M.; Mena-Morcillo, E.; Chen, A. Micro-Sized pH Sensors Based on Scanning Electrochemical Probe Microscopy. *Micromachines* **2022**, 13 (12), 2143.

(17) Nadappuram, B. P.; McKelvey, K.; Al Botros, R.; Colburn, A. W.; Unwin, P. R. Fabrication and Characterization of Dual Function Nanoscale pH-Scanning Ion Conductance Microscopy (SICM) Probes for High Resolution pH Mapping. *Analytical chemistry* **2013**, 85 (17), 8070–8074.

(18) Gaitzsch, J.; Hirschi, S.; Freimann, S.; Fotiadis, D.; Meier, W. Directed Insertion of Light-Activated Proteorhodopsin into Asymmetric Polymersomes from an ABC Block Copolymer. *Nano letters* **2019**, 19 (4), 2503–2508.

(19) Wang, D.; Wang, Y.; Li, H.; Han, Y.; Hu, P.; Ma, K.; Sheves, M.; Jin, Y. Photoactivated Bacteriorhodopsin/SiN x Nanopore-Based Biological Nanofluidic Generator with Single-Protein Sensitivity. *ACS nano* **2022**, 16 (1), 1589–1599.

(20) Bamberg, E.; Apell, H.-J.; Dencher, N. A.; Sperling, W.; Stieve, H.; Läuger, P. Photocurrents Generated by Bacteriorhodopsin on Planar Bilayer Membranes. *Biophysics of structure and mechanism* **1979**, 5, 277–292.

(21) Seigneuret, M.; Rigaud, J.-L. Use of the Fluorescent pH Probe Pyranine to Detect Heterogeneous Directions of Proton Movement in Bacteriorhodopsin Reconstituted Large Liposomes. *FEBS letters* **1985**, 188 (1), 101–106.

(22) Lee, H.; Ho, D.; Kuo, K.; Montemagno, C. D. Vectorial Insertion of Bacteriorhodopsin for Directed Orientation Assays in Various Polymeric Biomembranes. *Polymer* **2006**, 47 (9), 2935–2941. https://doi.org/10.1016/j.polymer.2006.02.082.

(23) Gonçalves, R. P.; Agnus, G.; Sens, P.; Houssin, C.; Bartenlian, B.; Scheuring, S. Two-Chamber AFM: Probing Membrane Proteins Separating Two Aqueous Compartments. *Nature methods* **2006**, 3 (12), 1007–1012.

(24) Chandra, A.; Prasad, S.; Iuele, H.; Colella, F.; Rizzo, R.; D'Amone, E.; Gigli, G.; Del Mercato, L. L. Highly Sensitive Fluorescent pH Microsensors Based on the Ratiometric Dye Pyranine Immobilized on Silica Microparticles. *Chemistry–A European Journal* **2021**, 27 (53), 13318–13324.

(25) Ulrich, S.; Osypova, A.; Panzarasa, G.; Rossi, R. M.; Bruns, N.; Boesel, L. F. Pyranine-modified Amphiphilic Polymer Conetworks as Fluorescent Ratiometric pH Sensors. *Macromolecular rapid communications* **2019**, 40 (21), 1900360.

(26) Hirose, H.; Maekawa, M.; Ida, H.; Kuriyama, M.; Takahashi, Y.; Futaki, S. A Noncanonical Endocytic Pathway Is Involved in the Internalization of 3 Mm Polystyrene Beads into HeLa Cells. *Biomaterials Science* **2022**, 10 (24), 7093–7102.

(27) Arppe, R.; Näreoja, T.; Nylund, S.; Mattsson, L.; Koho, S.; Rosenholm, J. M.; Soukka, T.; Schäferling, M. Photon Upconversion Sensitized Nanoprobes for Sensing and Imaging of pH. *Nanoscale* **2014**, 6 (12), 6837–6843.

(28) Lindner, B.; Burkard, T.; Schuler, M. Phagocytosis Assays with Different pH-Sensitive Fluorescent Particles and Various Readouts. *Biotechniques* **2020**, 68 (5), 245–250.

(29) von Kaeppler, E. P.; Wang, Q.; Raghu, H.; Bloom, M. S.; Wong, H.; Robinson, W. H. Interleukin 4 Promotes Anti-Inflammatory Macrophages That Clear Cartilage Debris and Inhibits Osteoclast Development to Protect against Osteoarthritis. *Clinical Immunology* **2021**, 229, 108784.

(30) Miller, A.; Fantone, K. M.; Tucker, S. L.; Gokanapudi, N.; Goldberg, J. B.; Rada, B. Short Chain Fatty Acids Reduce the Respiratory Burst of Human Neutrophils in Response to Cystic Fibrosis Isolates of Staphylococcus Aureus. *Journal of Cystic Fibrosis* **2023**. https://doi.org/10.1016/j.jcf.2023.04.022.

(31) *pHrodo*™ Dyes for Amine Labeling. https://www.thermofisher.com/order/catalog/product/br/en/P36010 (accessed 2023-01-06).

(32) Zhu, M.; Lerum, M. Z.; Chen, W. How to Prepare Reproducible, Homogeneous, and Hydrolytically Stable Aminosilane-Derived Layers on Silica. **Langmuir 2012**, 28 (1), 416–423.

(33) Gee, K. R.; Archer, E. A.; Kang, H. C. 4-Sulfotetrafluorophenyl (STP) Esters: New Water-Soluble Amine-Reactive Reagents for Labeling Biomolecules. *Tetrahedron Letters* **1999,** 40 (8), 1471–1474.
(34) Dolman, N. J.; Kilgore, J. A.; Davidson, M. W. A Review of Reagents for Fluorescence Microscopy of Cellular Compartments and Structures, Part I: BacMam Labeling and Reagents for Vesicular Structures. *Current protocols in cytometry* **2013**, 65 (1), 12.30. 1-12.30. 27.
(35) Renthal, R.; Lanyi, J. K. Light-Induced Membrane Potential and pH Gradient in Halobacterium Halobium Envelope Vesicles. *Biochemistry* **1976**, 15 (10), 2136–2143. https://doi.org/10.1021/bi00655a017.
(36) Chen, C.-Y.; Wang, C.-M.; Liao, W.-S. A Special Connection between Nanofabrication and Analytical Devices: Chemical Lift-off Lithography. B*ulletin of the Chemical Society of Japan* **2019**, 92 (3), 600– 607.
(37) Elbersen, R.; Vijselaar, W.; Tiggelaar, R. M.; Gardeniers, H.; Huskens, J. Fabrication and Doping Methods for Silicon Nano-and Micropillar Arrays for Solar-cell Applications: A Review. *Advanced materials* **2015**, 27 (43), 6781–6796.
(38) Coulembier, O.; Knoll, A.; Pires, D.; Gotsmann, B.; Duerig, U.; Frommer, J.; Miller, R. D.; Dubois, P.; Hedrick, J. L. Probe-Based Nanolithography: Self-Amplified Depolymerization Media for Dry Lithography. *Macromolecules* **2010**, 43 (1), 572–574.
(39) Miranda, A.; Martínez, L.; De Beule, P. A. Facile Synthesis of an Aminopropylsilane Layer on Si/SiO2 Substrates Using Ethanol as APTES Solvent. *MethodsX* **2020**, 7, 100931.
(40) Howell, S. T.; Grushina, A.; Holzner, F.; Brugger, J. Thermal Scanning Probe Lithography—A Review *Microsystems & nanoengineering* **2020,** 6 (1), 1–24.

3.5 Supplementary information

This section describes the materials and methods used in this chapter. Unless otherwise stated, all chemicals and solvents were purchased from Sigma-Aldrich.

3.5.1 Fabrication of device

Covalent functionalization of pHrodo on a Si/SiO_2 substrate

The chips were produced using a highly doped silicon wafer, diced to 8 mm × 8 mm. The samples were thermally oxidized to a SiO_2 thickness of 60 nm. Before the experiments, the substrates were dried and treated with oxygen plasma (Tepla AG) for 10 min to provide O-H groups to the SiO_2 surface. The substrate was then functionalized with N-(2-aminoethyl)-3-aminopropyltrimethoxysilane (AEAPTMS) for 6h. The 0.5 mM AEAPTMS solution was prepared in anhydrous ethanol. The substrate was rinsed sequentially with anhydrous ethanol, methanol, 1.0 mM acetic acid solution (AcOH), and Milli-Q water. The pHrodo™ green STP ester (pHrodo) stock solution (5 µL of 10 mM pHrodo diluted in dimethyl sulfoxide) was diluted in 163 µL of 1 mM sodium bicarbonate solution (pH 8.3) for a final concentration of 0.3 mM. Subsequently, 25 µl of 0.3 mM pHrodo solution was added to the sample, which was incubated for 40 min in the dark, and then sequentially rinsed with anhydrous methanol, 1 mM acetic acid, and Milli-Q water.

The biological engineering of the membrane patches is described elsewhere. [1] In addition to the genetically modified C-His_{10}-tag and N-His_{10}-tag PMs, wild-type PMs were also investigated. For all PM types, PM was deposited on a flat substrate by dispersing 50 µL of 10^{-2} mg·mL^{-1} PM in water, which was added to the pHrodo- functionalized substrates. The samples were then dried in air, rinsed with Milli-Q water, and dried with nitrogen gas.

Ultimately, the samples were inserted in an upright fluorescence microscope while being immersed in Milli-Q water, with a thin layer (170 µm) of glass slide placed on top of the chip.

Maskless chemical lift-off on Si/SiO_2 surface by thermal scanning probe lithography (t-SPL)

We designed a pH-sensitive fluorescence microcompartment to measure the nanolocalized proton gradient of the PM patches. The samples in our experiments were thermally oxidized and treated similarly to the unpatterned flat substrates. Subsequently, 25 µm of 5 wt% polyphthalaldehyde (PPA) (Allresist) solution dissolved in anisole was spun at 2900 rpm for 1.5 min by spin-coating. The substrate was then annealed at 110 °C for 1 min, which resulted in an 89 nm PPA layer, as confirmed by atomic force microscopy (AFM) and ellipsometry.

We used thermal scanning probe lithography (t-SPL) to write the desired patterns. The trap locations were defined via t-SPL using a custom-built instrument. [2] The PPA was patterned using a heated tip (at 1000 °C) capacitively pulled into contact with the substrate. The PPA underwent local decomposition, forming cylindrical indentations throughout the polymer. Each device contained a 9 × 9 array of cavities, each 1.2 µm in diameter and spaced 2.0 µm apart. After oxygen descum, the pattern was etched into a silica layer to a depth of 20 nm using RIE. For the RIE, we used a mixture of CHF_3, argon, and oxygen (12, 38, and 1 sscm, respectively) at 100 W and 30 mbar chamber pressure. After etching, the samples were treated with 200 W oxygen plasma for 30 s (Tepla AG). The silanization conditions were the same as those described for unpatterned flat substrates. The rinsing steps were also the same, except for a step after silanization, during which tetrahydrofuran (THF) was used to remove PPA after the methanol rinse. The samples were then cleaned with 1.0 mM acetic acid and Milli- Q water. The procedure for dye functionalization was the same as that for unpatterned substrates. Ultimately, the samples were inserted in a fluorescence microscope while being immersed in Milli-Q water, with a thin layer (170 µm) of glass slide placed on top of the chip. For the precise positioning and deposition of individual PM patches, TCNA was performed on the functionalized substrate. Details of the membrane deposition procedure are provided in a separate publication. [3]

3.5.2 Spectroscopic measurements

We utilized spectroscopic ellipsometry (Woollam VASE) to examine the functionalization of pHrodo on the silanized SiO_2 substrate.

Proton pumping was measured using upright fluorescence microscopy (Nikon Eclipse 90i microscope with 40× or 60× Plan Apo objective lens, NA = 0.45). Fluorescence images were captured with a Nikon DS-1QM/H CCD camera and analyzed using ImageJ. FITC (fluorescein isothiocyanate) was employed for imaging with an excitation wavelength of 490 nm and a 500 ms exposure time, while the TRITC filter, with an excitation wavelength

of 550 nm and 1.0 s exposure time, was used for green light exposure. To assess the effect of green light exposure on proton pumping, samples were alternately exposed to blue light for imaging and then to green light a 100.0 s period. To investigate proton diffusion in the medium, samples were exposed to green light, followed by image acquisition using an FITC filter. The sample was then kept in darkness for 21.0 s before fluorescence was measured again using the FITC filter. This cycle was repeated for a total duration of 456.0 s. Subsequently, the sample underwent several sequences of 1.0 s exposure to green light, with fluorescence measured using blue light. Fluorescence values were calculated by averaging the fluorescence signal of the image and subtracting the background signal.

Scanning electron microscopy (SEM) images were acquired with a Leo 1550 (Zeiss) with a material contrast mode.

Linear regression for pHrodo green

A method for analyzing fluorescence intensity changes across different pH levels is outlined, involving normalization of the data to pH 7.0 and assessment of model accuracy through regression analysis. With the dataset provided by Dolman et al. [4] for pHrodo green, the relative fluorescence intensity for each pH (I_{pHrodo}) was calculated by dividing each value by the intensity at pH 7.0 ($I_{pHrodopH7}$). The regression analysis produced a coefficient of determination (COD) of 0.98.

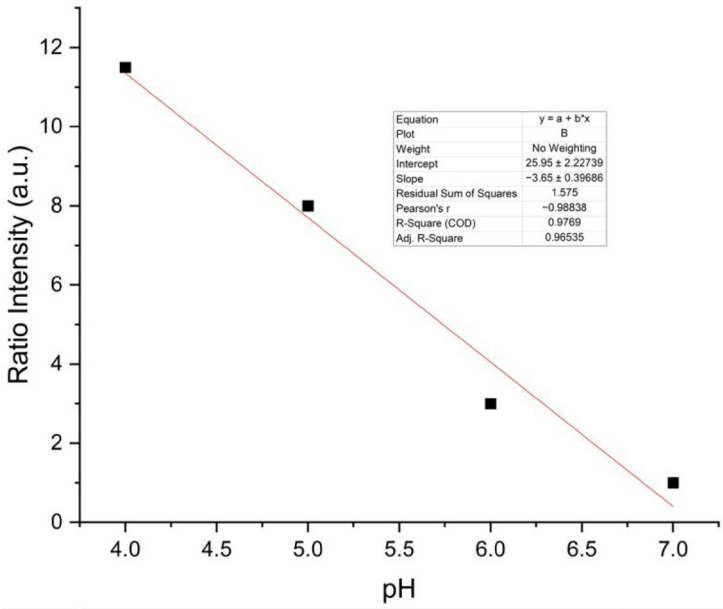

Figure S3.1. Linear regression calculated from data presented by Dolman et al. [4]

3.5.3 Experimental data

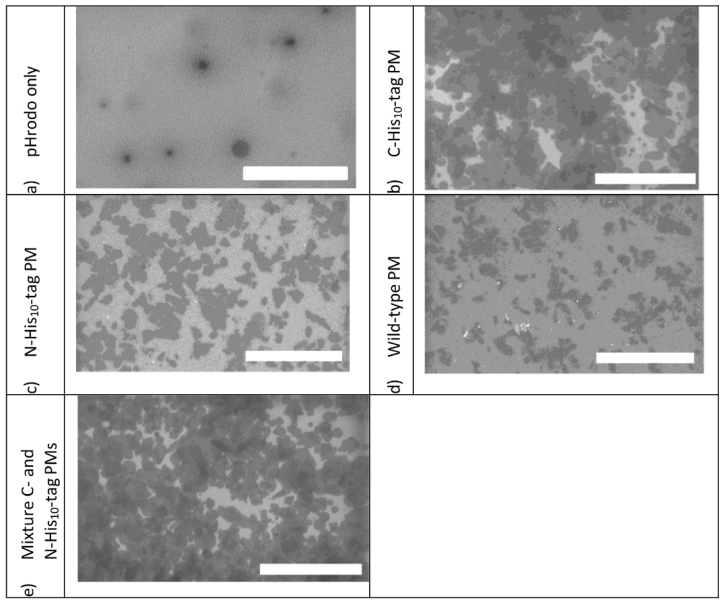

Figure S3.2. SEM images of deposited PMs-pHrodo-silane and pHrodo-silane substrate in SiO_2/Si surface: **a)** pHrodo substrate, **b)** N-His_{10}-tag PM, **c)** C-His_{10}-tag PM, **d)** wild-type PM, **e)** mixture of N- and C-His_{10}-tag PM.

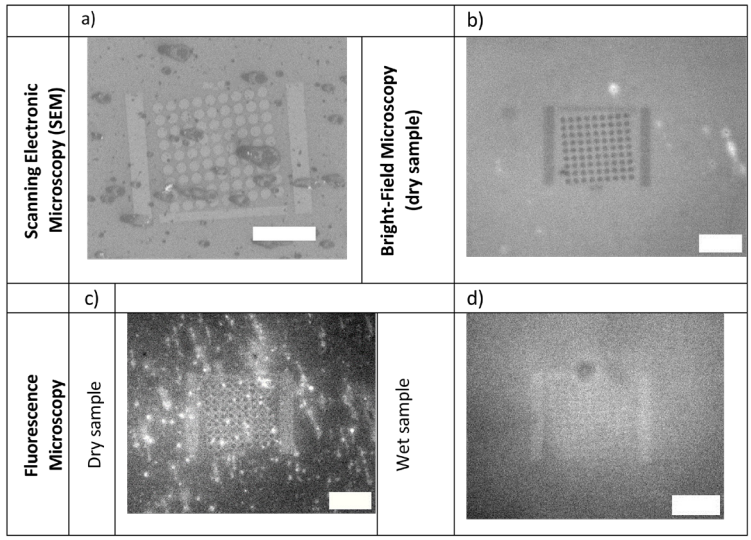

Figure S3.3. Failed localized pHrodo-silane-SiO_2 substrate (step 7, Figure 3.7): **a)** SEM image, **b)** bright-field microscopy image. Fluorescence microscopy image of **c)** dry and **d)** wet sample. The scale bar represents 10 μm.

Ellipsometry analysis of PPA removal

Table S3.1, Table S3.2, Table S3.3 and Table S3.4 present the results of the PPA removal study performed to identify the optimal conditions for the maskless lift-off (MLO) method. The mean squared error (MSE) quantifies the difference between the calculated and measured reflectance values and it is unitless. [5] An MSE value between 2 and 10 signifies an improved fit of the model to the data, implying that the model's predictions closely match the observed values.

Table S3.1. Ellipsometer data used to identify the optimal t-SPL chemical lift-off protocol. Plasma conditions: 200 W and 30 s. Refractive index (n) SiO_2 = 1.48; [6] n_{PPA} = 1.57; [7] n values obtained at wavelength = 633 nm.

Sample	Thickness PPA (nm)	Uncertainty (nm)	MSE
Thermal oxide (SiO_2)	0.0	0.0	67.49
PPA	96.6	0.6	22.05
PPA and THF	0.0	0.3	56.47
PPA and RIE	11.9	0.2	9.15
PPA, RIE, and plasma	3.1	0.9	19.95
PPA, RIE, plasma, and THF	0.0	0.0	66.52

Table S3.2. Ellipsometer data of different methods for PPA removal after RIE on silicon substrates with thermal oxide SiO_2 on top. Refractive index (n) SiO_2 = 1.48, n_{PPA} = 1.57, n values obtained at wavelength = 633 nm.

Sample	Thickness PPA (nm)	Uncertainty (nm)	MSE
7 min 600 W plasma	0.0	0.0	66.52
Acetone	10.9	0.1	53.69
THF	7.0	0.1	13.65
15 s plasma + THF	2.5	1.1	11.92
30 s plasma + THF	0.0	0.0	179.90

Table S3.1 reports the thickness of the SiO_2 and PPA layers individually, followed by the thickness of the PPA layer under various conditions, including exposure to THF, plasma treatment, and RIE etching. We observed that when the PPA was not etched, it could be removed with THF. However, when the PPA was etched, THF alone was insufficient for its removal. In such cases, a 30.0 s plasma treatment prior to THF rinsing was employed to ensure complete resist removal. This can be attributed to the presence of small amounts of moisture and sputtered contamination from fluorinated RIE recipes, which formed microscopic "masks" scattered across the substrate. During anisotropic etching, these micro-masked areas were shielded from etchant species, resulting in random raised features resembling grass. The plasma treatment effectively removed these fluorinated

ions from the remaining resist, allowing for complete removal of the PPA after THF immersion.

The MSE was higher when the PPA thickness was near zero. This was attributed to the absence of material. We observed this evidence in different experiments in which the PPA thickness was approximately 0.

Table S3.3. Ellipsometer data of silicon substrates with thermal oxide SiO_2 on top after PPA spin-coating, RIE, plasma cleaning, silanization, and rinsing with ethanol, methanol, THF, AcOH, and Milli-Q water at different plasma times. Refractive index (n) SiO_2 = 1.48, n_{PPA} = 1.57, n values obtained at wavelength = 633 nm.

Plasma time	Thickness PPA (nm)	Uncertainty (nm)	MSE
15 s	1.6	0.2	10.13
30 s	0.0	0.1	30.92
45 s	1.5	0.1	9.843
60 s	1.9	0.2	9.785

Table S3.2 presents different strategies for the complete removal of PPA after RIE. Both acetone and THF alone proved insufficient for the complete PPA removal. Consistent with the findings in Table S3.1, a 30 s plasma treatment followed by THF was effective in removing PPA. A 7 min plasma treatment with high power was also successful for this purpose. Table S3.3 shows the influence of plasma cleaning time before silanization on PPA removal. The results indicate that if an excessive amount of plasma is applied to the surface, fluorinated residuals from the resist can remain in the substrate surface.

Table S3.4 illustrates the influence of silanization time on PPA removal. A silanization time of 6 hours was found to be optimal for producing a monolayer of AEAPTMS [8] and ensuring effective PPA removal.

Table S3.4. Ellipsometer data of silicon substrates with thermal oxide SiO_2 on top after PPA spin-coating, RIE, plasma cleaning, silanization, and rinsing with ethanol, methanol, THF, AcOH, and Milli-Q water at different silanization times. Refractive index (n) SiO_2 = 1.46, n_{PPA} = 1.57, $n_{AEAPTMS}$ = 1.48, [8] n values obtained at wavelength = 633 nm. Plasma conditions: 30 s, 200 W.

Silanization time	Thickness AEAPTMS (nm)	Uncertainty (nm)	MSE
1 h	0.0	0.6	10.48
3 h	1.6	0.5	9.89
6 h	0.5	0.5	10.20
12 h	3.8	0.3	13.51

3.5.4 References

(1) Stauffer, M.; Hirschi, S.; Ucurum, Z.; Harder, D.; Schlesinger, R.; Fotiadis, D. Engineering and Production of the Light-Driven Proton Pump Bacteriorhodopsin in 2D Crystals for Basic Research and Applied Technologies. *MPs* **2020**, 3 (3), 51. https://doi.org/10.3390/mps3030051.

(2) Paul, P. C.; Knoll, A. W.; Holzner, F.; Despont, M.; Duerig, U. Rapid Turnaround Scanning Probe Nanolithography. *Nanotechnology* **2011**, 22 (27), 275306.
(3) Ruggeri, F.; Schwemmer, C.; Stauffer, M.; Nicollier, P. M.; Figueiredo da Silva, J.; Bosshart, P. D.; Kochems, K.; Fotiadis, D.; Knoll, A.; Wolf, H. Placement of Biological Membrane Patches in a Nanofluidic Gap With Control Over Position and Orientation. *Advanced materials interfaces* **2022**, 9 (23), 2200941.
(4) Dolman, N. J.; Kilgore, J. A.; Davidson, M. W. A Review of Reagents for Fluorescence Microscopy of Cellular Compartments and Structures, Part I: BacMam Labeling and Reagents for Vesicular Structures. *Current protocols in cytometry* **2013**, 65 (1), 12.30. 1-12.30. 27.
(5) Jellison, G. E. Data Analysis for Spectroscopic Ellipsometry. *In Handbook of Ellipsometry; Springer*, **2005**; pp 237–296.
(6) Awazu, K.; Onuki, H. Photo-Induced Synthesis of Amorphous SiO2 Film from Tetramethoxy-Silane on Polymethylmethacrylate at Room Temperature. *Journal of non-crystalline solids* **1997**, 215 (2–3),176–181.
(7) Howell, S. T.; Grushina, A.; Holzner, F.; Brugger, J. Thermal Scanning Probe Lithography—A Review. *Microsystems & nanoengineering* **2020**, 6 (1), 1–24.
(8) Zhu, M.; Lerum, M. Z.; Chen, W. How To Prepare Reproducible, Homogeneous, and Hydrolytically Stable Aminosilane-Derived Layers on Silica. *Langmuir* **2012**, 28 (1), 416–423. https://doi.org/10.1021/la203638g.

Chapter 4

Control of a gel-forming chemical reaction network using light-triggered proton pumps[1,2]

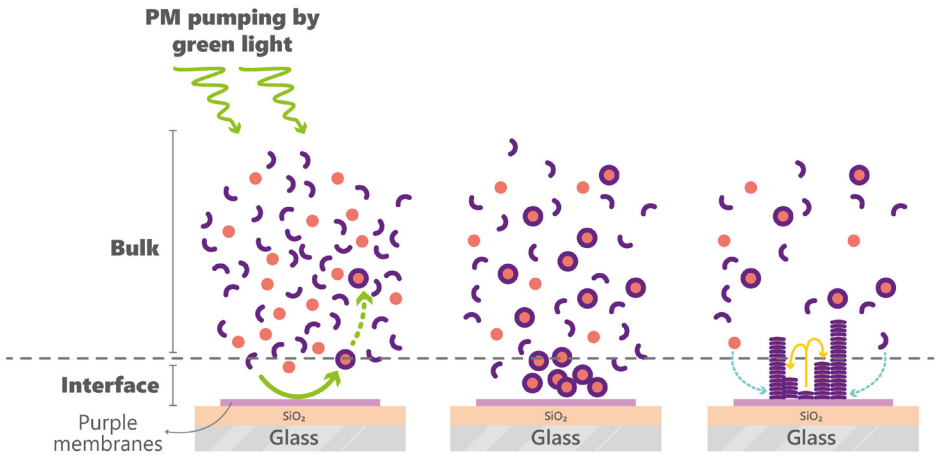

Abstract: Numerous metabolic processes in nature are governed by extrinsic stimuli such as light and pH variations, which afford opportunities for synthetic and biological applications. In developing a multi-sensor apparatus, we have integrated sub-micrometer purple membrane patches, each harboring bacteriorhodopsin, onto a surface. Bacteriorhodopsin is a light-driven proton pump. We conducted monitoring of the interactions between this system and a pH-responsive supramolecular hydrogel to evaluate fibrous matrix growth. Initial photostimulation induced localized reductions in pH at the membrane surface, thereby catalyzing fibrogenesis within the hydrogel. Utilizing liquid atomic force microscopy alongside confocal laser scanning microscopy, we observed the hydrogel's morphogenesis and structural adaptations in real time. The system adeptly modulated microscale pH environments, fostering targeted fibrous development within the hydrogel matrix. This elucidates the potential for engineering responsive materials that emulate natural bioprocesses.

[1] Chapter shared with Ardeshir Roshanasan (A.R.), TU Delft. Substrate fabrication and liquid atomic force microscopy was performed by J.F. da Silva. Synthesis of gel reagents and confocal laser scanning microscopy were performed by A.R.

[2] This chapter has been published: Figueiredo da Silva, J. et al. " Control of a gel-forming chemical reaction network using light-triggered proton pumps" Langmuir (2025).

4.1 Introduction

Eukaryotic cells have evolved distinct compartments to accommodate the unique environmental requirements of diverse metabolic activities and facilitate energy storage using electrochemical gradients. Metabolism of fuels or harvesting of light are used to generate pH gradients, [1] which are then exploited for a variety of key intracellular processes [2] e.g. to maintain intracellular organization, transport molecules, and facilitate ion exchange between cellular compartments and with the environment. [3] Hence, leveraging local pH variations as a stimulus for responsive systems has gained great interest for biomimetic applications and particularly in drug delivery systems. A similar prominence has been found in hydrogels [4] which are also designed to respond to external stimuli. [5–9] These hydrogels have been applied in controlled release applications; for example, they act as ionic networks for the oral delivery of proteins, [10] which is facilitated by the triggered collapse of the hydrogel. Alternatively, the hydrogel formation can be derived by a pH trigger. Although the formation of hydrogel by the means of a pH gradient has been demonstrated before, [11,12] achieving rigorous, microscale spatiotemporal control over this process remains a challenge. Accordingly, our objective is to attain microscale regulation of the hydrogel formation via exposure to light as an external trigger, aiming to expand the applications of this material across various domains.

In nature, a microscale externally triggered pH gradient source is found in purple membranes (PMs). Bacteriorhodopsin (bR) is the main component of 5-nm thick PMs of Halobacterium salinarum. [13] The bR acts as a light-driven proton pump, and the resulting pH gradient is used for energy storage within the cells. [14] Moreover, bR is a unique photochromic protein, and it has been successfully incorporated into various materials for the development of bio hybrid materials and nanostructured devices. [15,16] The advantages of bR include broad absorption range of visible light, high thermal and photochemical stability, resistance to environmental perturbations, environmental friendliness, and the availability of genetic variants with enhanced spectral properties for specific device applications. [15]

Previous studies [3,13] provide strong evidence that light irradiation directly drives a localized proton pump in PMs, mediated by the unique structural and functional properties of bR. When fabricating such hybrid devices, it should be noted that bR exhibits directionality in proton pumping and orientation within the membrane. The pumping occurs from the cytoplasmatic side (C-terminus) inside the cell to the extracellular side (N-terminus). [17] Therefore, it is crucial to control the orientation of the membrane patches during deposition to optimize the photoelectric conversion efficiency. Through genetic modification, we generate a charge asymmetry between the cytoplasmic and extracellular sides of the PMs, which we use to control their orientation. [18,19] Confocal laser scanning microscopy (CLSM), atomic force microscopy (AFM), and AFM-derived techniques such as single molecule force spectroscopy (SMFS) have been combined to unveil information on PMs structure, functionality, and dynamics. [20]

Boekhoven et al. [5] designed a chemical reaction network (CRN) driven by a synthetic

self-assembled system featuring a supramolecular hydrogelator. The CRN shows directed molecular self-assembly dynamics, where catalysis modulates reaction rates, impacting fiber morphology and promoting branching to form a dense gel network. The two-stage assembly—initial fiber formation followed by branching— yields gels with tailored mechanical properties. By encompassing kinetics-driven assembly, non-equilibrium states, and reversible hydrazone chemistry, the CRN demonstrates how catalysis governs material properties, transitioning from building blocks to functional hydrogels through a dynamic and tunable pathway. This hydrogelator not only regulates the self-assembly rate but also the properties of the resulting materials via bulk catalysis in aqueous medium, with a formation rate that can be tuned in situ by acidic catalysis. Examples of surface-confined catalysis that provide spatial control over the gelation process without external stimuli have been demonstrated, including micro-scaled surface-confined catalysis,[21] protonated polymer brushes,[22] and charged catalytic nanoparticles.[23] To introduce external control, a photoswitchable homogeneous catalyst for light-activated gelation process was investigated. [24] Building on these advancements, this study presents a novel approach that leverages light driven metabolic proton pumping to locally trigger gelation.

In this work, a bi-component system has been fabricated, comprising localized light responsive proton pumps coupled with a pH-responsive hydrogel-forming CRN. The transient local proton gradient, sustained by illumination, facilitates confined material formation. Specifically, we exploit PMs to produce local light-driven proton gradients via incorporating them into miniaturized systems, thus enabling the localized control of proton-catalyzed hydrogel formation. We detected a pH decrease in a microscale area indicated by an irreversible fiber growth locally accelerated by protons. The direct influence of PM pumping on the microscale hydrogel formation over time was demonstrated in situ by liquid AFM and CLSM. The approach can be used to characterize the formation of the hydrogel at the microscale under relevant conditions.

4.2 Results and discussion

The system developed in this work includes a substrate containing PM patches for generating a local pH gradient under light, and a pH-triggered hydrogel system for detecting this gradient. The hydrogel system consists of the acid-catalyzed reaction of cyclohexane-1,3,5-triscarbohydrazide **1** with three molecules of 3,4-bis[2-(2- methoxyethoxy)ethoxy] benzaldehyde **2** to form the actual hydrazone hydrogelator **3**, which subsequently self-assembles in water to form fibers. [5,25,26] Above a certain concentration threshold, these fibers form a network in the aqueous phase, thereby leading to the formation of hydrogels, Figure 4.1a. The PM part of the system is constructed from PMs that are deposited on SiO_2 substrates.

Previously, it was documented that PMs can adhere to SiO_2.[19] To control the orientation of PM adsorbed to SiO_2 substrates, we have used three types of PMs: WT PMs, and two genetically modified PMs, namely N-His_{10}-tag and C-His_{10}-tag PMs. As shown in Figure 4.1b, in aqueous media, SiO_2 layers present a negatively charged surface, whereas His_{10}-tag

peptide sequences impart a positive charge on the designated side of the PM (C-terminus or N-terminus).[18] Thus, given the asymmetric positive surface charge on the extracellular side of the membrane juxtaposed with the negative charge of SiO_2 layer in water, [27] the $NHis_{10}$-tag PMs are expected to preferentially pump protons from the PM-aqueous interface to the substrate–PM interface. Therefore, for N-His_{10}-tag PMs we anticipate a photo-induced proton gradient towards the SiO_2 substrate. The C-His_{10}-tag PMs, on the other hand, should preferentially pump protons from the substrate–PM interface across the PM membrane toward the PM-aqueous interface, thereby creating a proton gradient oriented predominantly away from the SiO_2 substrate. WT PMs have fragments with net negative charge on both sides of the membrane because of the amino-acid residues on the bR surface and the intrinsic acidity of PM lipids. However, at pH > 5 the PM surface charge density is more negative on the cytoplasmic side than on the extracellular side. [17] Consequently, the orientation of the WT PM fragments is expected to be akin to that of N-His_{10}-tag PMs.

The preparation of substrates for the experiments was carried out as described in the experimental section. Successful deposition of PMs across all types was confirmed by AFM imaging under ambient conditions, as shown in Figure S4.2, Supplementary Information (SI). Further detailed analysis revealed variations in the density of PMs on the SiO_2 substrate surface, with N-His_{10}-tag PMs exhibiting the highest density, followed by WT PMs, and finally C-His_{10}-tag PMs. These differences are attributable to the interplay between the surface charge properties of SiO_2 and those inherent to the PMs. [17]

We have used these PM-SiO_2 systems in combination with the hydrogel-forming CRN to investigate surface-confined hydrogel formation. Micro-localized light exposure and higher imaging resolution were utilized to understand the effect of proton pumping orientation on the catalytic process. Our study incorporates experiments using CLSM for microlocalized excitation and compares these findings with liquid AFM offering sub-micrometer resolution. This complementary methodology facilitates a thorough analysis of the mechanisms responsible for the in-situ formation of nanoscale hydrogels triggered by external stimuli.

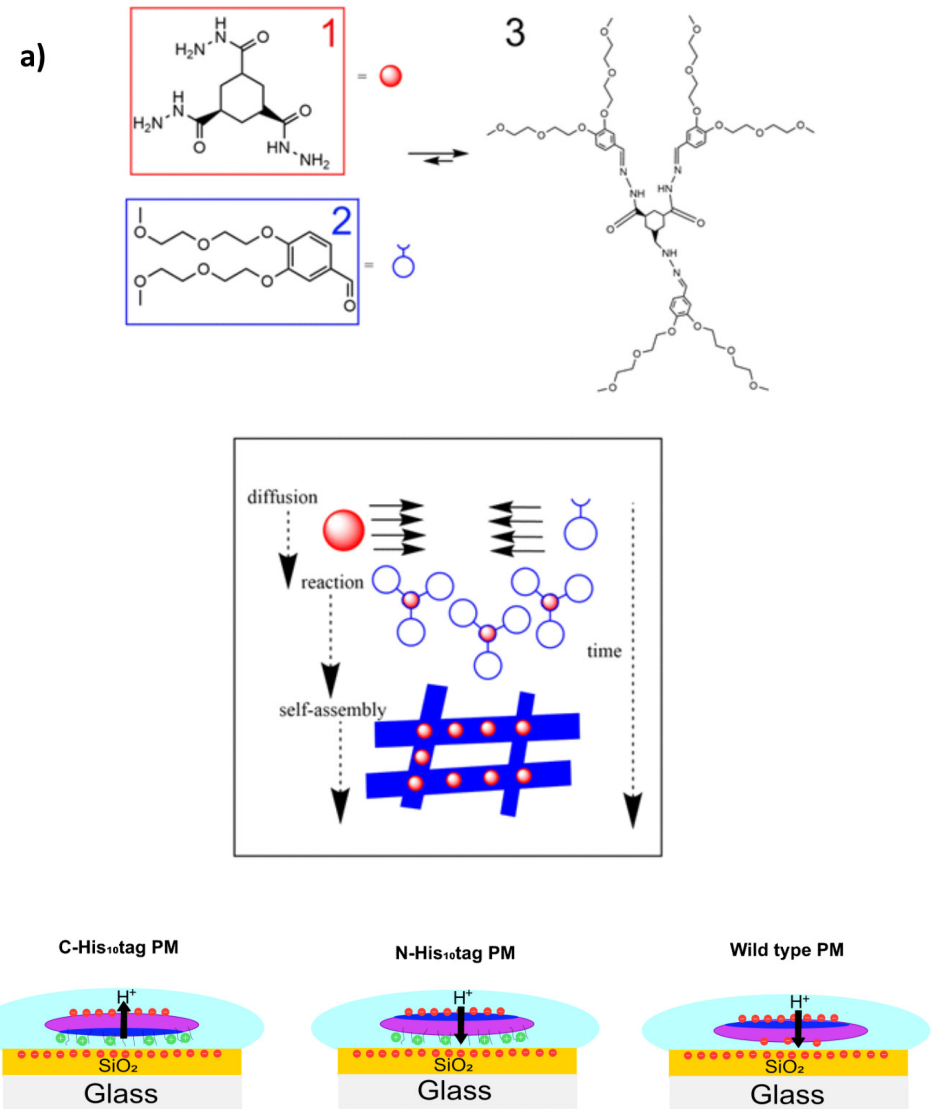

Figure 4.1. a) Catalytic formation of tris hydrazone hydrogelator **3** from soluble building blocks **1** and **2**, leading to fiber formation by self-assembly and, subsequently, to a network of fibers that trapped the surrounding solvent to form a gel network. **b)** Charge distribution between SiO_2 surface and PM in aqueous media for C-His_{10}-tag, N-His_{10}-tag, and wild-type PMs; and respective pump orientation of PMs. The purple, navy blue, light blue, red and green areas represent PMs, cytoplasmatic side of PMs, aqueous media, negative charge, and positive charge, respectively.

4.2.1 Spatiotemporal control of hydrogel formation at microscale via confocal laser scanning microscopy

In a demonstration for in-situ, externally triggered, microlocalized hydrogel formation, we explored whether a PM-coated surface could catalyze the formation of hydrogels confined to a surface. The preparation of the substrate involved covering a PM-coated glass surface with a solution containing hydrogel precursors in a buffered environment at pH 7.0. This minimizes the likelihood of premature gelation in the bulk. [25] A detailed observation of a selected area on the PM-functionalized glass substrate was conducted to examine the aggregate formation resulting from light exposure. In contact with solution, the area was exposed to cycles of monochromatic excitations, alternating between wavelengths of 488 and 543 nm, each for approximately 1 min. The former was used for image acquisition at 517 nm, and the latter was implemented to induce proton pumping. Aiming at scanning the sample prior to expected gelation, the aforementioned light exposure cycle commenced with image acquisition. A blank glass substrate that was not coated with PM served as a control and was subjected to the same experimental procedure, which granted access to a comparative analysis to distinguish the effects and changes attributable to the presence of PMs.

CLSM images in Figure 4.2 present the time progression of gel reactants, where different types of the PMs are present, in comparison to a blank sample in absence of PMs. We noted the onset of a novel phase characterized by globular cluster formation, that further coalesce to form larger domains. This phase does not form in the blank sample. Moreover, the gelation occurs in different timescales depending on the type of PMs; while the gel clusters start appearing for C-His_{10}-tag PM under 7 min and reach a steady state within 44 min they only start forming after 22 min and 55 min for WT PMs and N-His_{10}-tag, respectively. This earlier aggregation likely resulted from the formation of a favorably aligned local pH gradient at the substrate surface due to PM orientation. Previous work [5,25] using turbidity measurements demonstrated that gelation developed much faster in catalyzed samples than in uncatalyzed ones. The acid-catalyzed sample reached maximum absorbance within 60 minutes, while the uncatalyzed sample took approximately nine hours. These findings confirm that gelation is significantly slower in a pH 7.0 buffered medium without a catalyst, consistent with our results.

Interestingly, repeated experiments indicated that gel formation for the C-His_{10}-tag PM coated substrate can occur even prior to exposure to green light (543 nm) intended for pumping. It should be noted, however, that the samples already have been exposed to blue light (488 nm) to acquire the images at t=0 min. This suggests excitation of the PM by 488 nm already leads to proton pumping. Previous work on PMs [28] reported that electrical signals due to PM pumping peak at approximately 560 nm, but still have a significant response at 488 nm, which corroborates this lack of a selective pumping response. It is worth mentioning that the gelation was not observed in samples with N-His_{10}-tag and WT PMs in the initial images, but only at significant later stages.

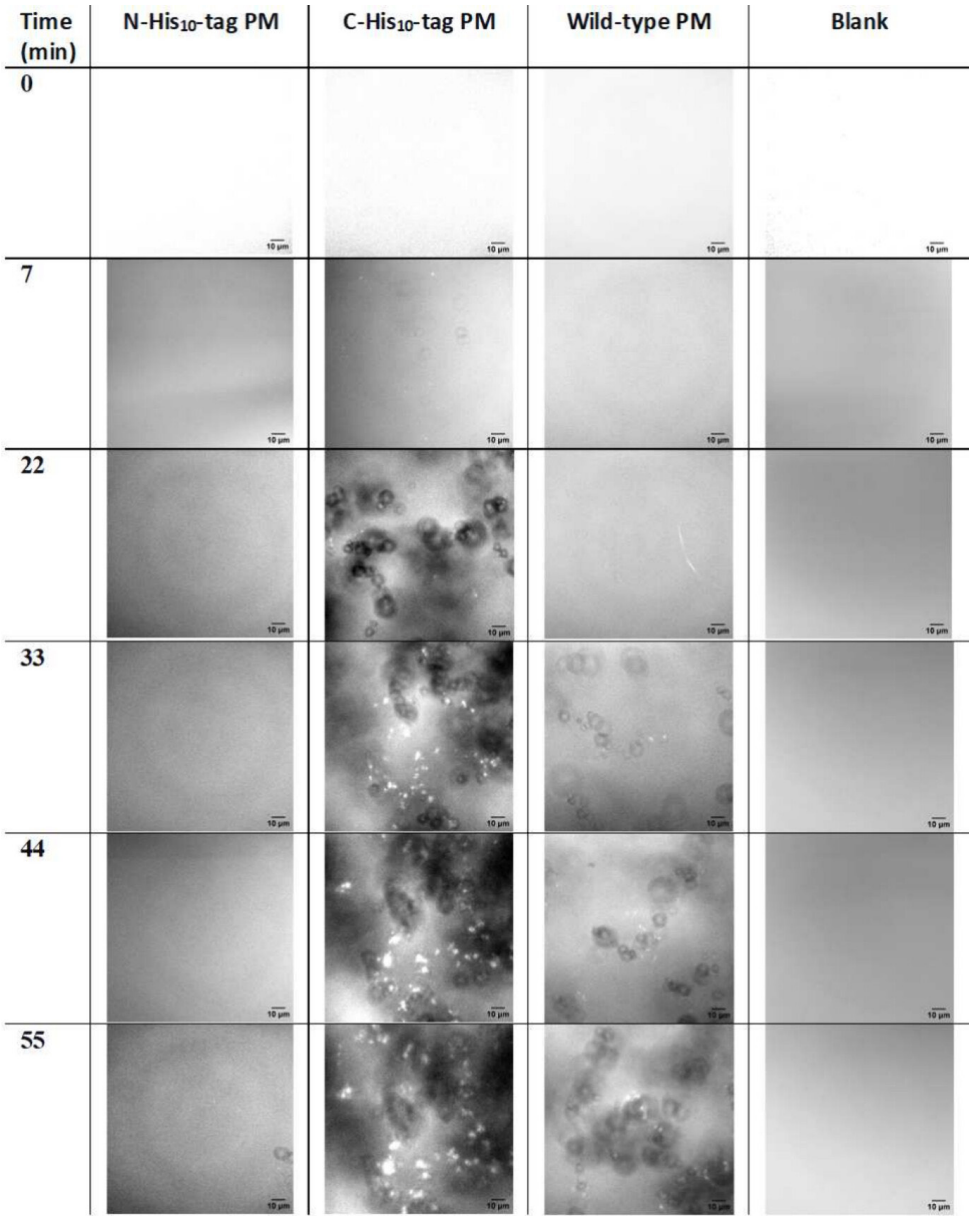

Figure 4.2. Confocal laser scanning microscopic images of the progression of hydrogel formation for different types of PMs and in the absence of PMs (blank). Snapshots were taken at 0, 7, 22, 33, 44, and 55 minutes at 63x magnification.

In summary, the presence and type of PMs significantly influenced the gelation rates. Specifically, C-His_{10}-tag PMs, that are expected to pump protons from the SiO_2 substrate–PM interface to the PM–aqueous interface, promote aggregates directly adjacent to the PM aqueous interface, presumably by creating a favorably aligned pH gradient. In contrast, for WT-PM patches and N-His_{10}-tag PMs, the gel formation is significantly slower. While the supposedly unfavorably aligned pH gradient generated by N-His_{10}-tag PMs exhibits the longest formation time, the unsystematically alignment in WT-PMs yields a much shorter formation time. The most likely explanation is that their relatively reversed orientation does not lead to the same pH decrease near the PM-aqueous interface upon pumping. The C-His_{10}-tag PM-induced pH gradients from the surface toward the bulk solution accelerate formation of the bi-component hydrazone gelator,[25] thereby increasing its local concentration and facilitating the gelation close to the surface. Therefore, the gelation rate is affected by the pH gradient generated by different PM types.

The developed system encouraged further analysis. Although the observations were aligned with our expectations, the limited wavelength selectivity of PM excitation and proton pumping during CLSM measurements asked for additional evidence. Therefore, another set of light-induced gel formation experiments were conducted, where in-situ liquid AFM for image acquisition in the dark in combination with excitation of the PM by an independently operated light source were utilized.

4.2.2 Atomic force microscopy for capturing temporal control over gel formation at nanoscale

Liquid AFM was used to investigate nanoscale hydrogel formation influenced by PM and light near PM-covered SiO_2 surfaces. The conditions for light exposure diverged from those utilized in CLSM as the setup enables image acquisition without irradiation, thereby counteracting the limited wavelength selectivity of CLSM in imaging and pumping. Thus, it was possible to separate pumping and imaging steps, while observing structure formation directly at the PM-aqueous interface for individual PM patches by employing multiple periods of green light exposure (543 nm) interspersed with dark periods.

Figure 4.3 shows the protocol of the AFM and irradiation experiments. Initially, the AFM scan was conducted in the absence of light on a surface coated with PM, which was covered with a buffer at pH 7.0 devoid of any gelator precursor molecules. After two scans, a solution of the gelator precursor molecules was added to the buffer. The final concentrations of gelator precursor reagents were half of those used in CLSM experiments. This reduction was crucial to prevent contamination of the AFM cantilever prior to scanning. Because of the change in liquid refractive index and temperature fluctuations due to addition of reagents, the photodiode signal was unstable for a few minutes (from 4 to 10 min). After the signal stabilized, the image acquisition-irradiation sequence was continued. For all PM types, the scan position remained nearly unchanged, except for C-His_{10}-tag PMs, which shifted to a different area. We scanned two images in the dark, after which we irradiated with green light using a light-emitting diode (LED) localized at

the back of the substrate (Figure S4.1b, SI) for 10 min while scanning. Next, the sample was scanned in the dark for 10 min, and again for another 10 min upon exposure to green light. Finally, the substrate was scanned repeatedly until 1 h after addition of the gelator precursor reagents. Subsequently, a larger scan of 5 x 5 µm² was performed to check for any influence of the tip scan on the structure formation at the surface. For C-His_{10}-tag PMs, this investigation was not possible because the gel had already formed around the entire substrate area before the end of the experiment, contaminating the AFM cantilever with fiber deposits and preventing any further scans.

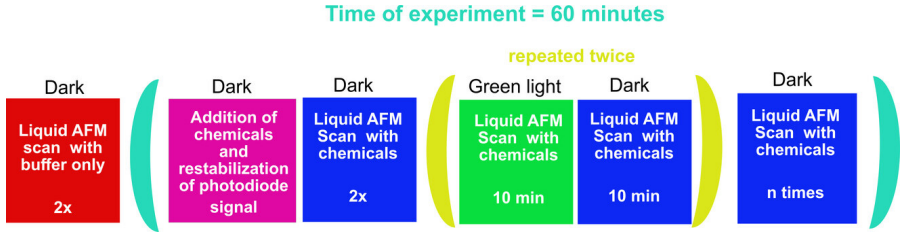

Figure 4.3. Diagram of the protocol of AFM experiments, including irradiation sequences and AFM image acquisition. Red: AFM scan without gel reagents; pink: procedure without scan; blue AFM scan of sample after addition of chemicals in the dark; green: AFM scan of sample after addition of chemicals and under green light.

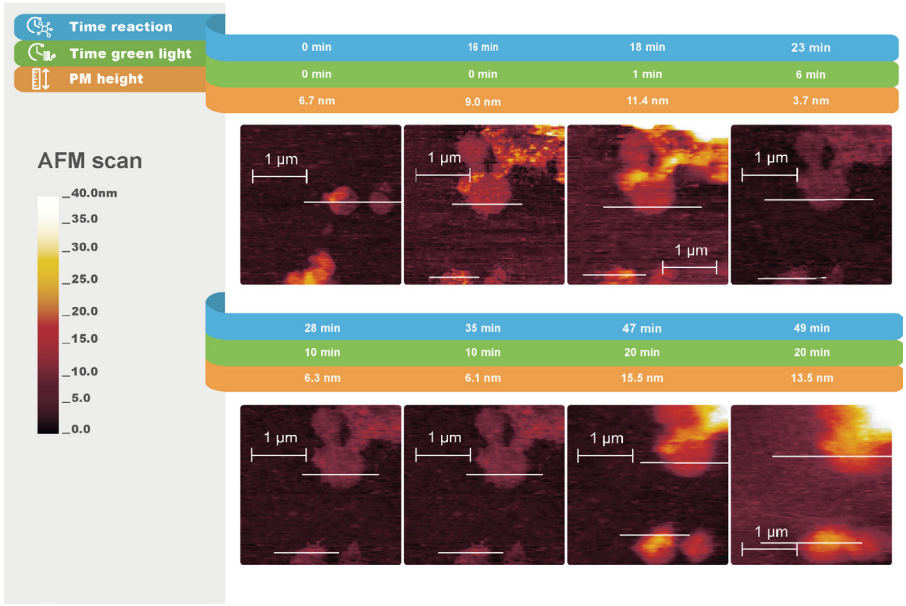

Figure 4.4. In-situ AFM Peakforce Tapping in fluid mode height images of hydrogel formation under the influence of PMs (C-His_{10}-tag PMs) and light at different time points. The lines highlighted in white indicate the cross sections of PMs. The scan direction is from right to left, with a 0◦ scan angle. Cross sectional values for these images are shown in Figure S4.5, SI.

First, a PM-free substrate (Figure S4.3, SI) was subjected to scanning as described in Figure 4.3 as a control experiment. As expected, the AFM scan of the PM-free substrate remained a flat homogeneous surface without any new objects appearing up to 1 h after the addition of gel reagents, even for a large scan area (Figure S4.4, SI). Therefore, we concluded that in the PM-free samples, fibers were not formed on the substrate surface in the dark, nor upon irradiation with green light.

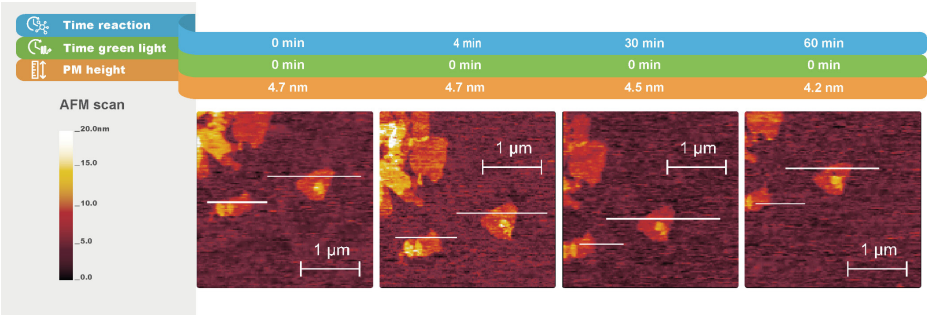

Figure 4.5. In-situ AFM Peakforce Tapping in fluid mode height images of a C-His_{10}-tag PM covered substrate kept in the dark at different time points. The lines highlighted in white indicate the cross sections of PMs. Cross sectional values for these images are shown in Figure S4.6, SI.

In a subsequent series of experiments, we studied the substrates covered with the different types of PM. For all PM types, the AFM scans before the addition of reagents showed ellipsoidal ~500 nm wide homogeneous patches with a height of approximately 5 to 8 nm on an otherwise flat surface (Figure 4.4, Figure 4.5, Figure 4.7 and Figure 4.8, Time reaction = 0 min) that we assigned to PMs adsorbed at the interface. The maximum force at which the AFM tip scanned the membrane was limited to ~ 100 pN to prevent mechanical deformation of bR,[29] and the parameters of the AFM feedback loop were optimized to reduce error signal. [30]

Given the CLSM results, we anticipated a rapid gel formation soon after the green light exposure in the AFM scan of C-His_{10}-tag PM, shown in Figure 4.4. At the onset of the experiment, a patch height difference of 2.3 nm was observed in the dark between AFM scans taken before and after the addition of reactants. This may be associated with variations in patch height. After a 1-minute exposure to green light, the relative height in the PM patches area increased from 9.0 nm to 11.4 nm, along with a general change in the scan image height. Subsequently, while still under light, the relative height in the PM patches area decreased to 3.7 nm. During the time in the dark (reaction times = 28 and 35 minutes), no change in the patch height was observed. From 10 to 20 min of exposure to green light, the height increased again to 15.5 nm. It is hypothesized that fiber networks initially form locally on the patches. The initial increase in the height of the patches of approximately 2.5 nm under illumination is consistent with the height of fibers reported in previous studies. [21]

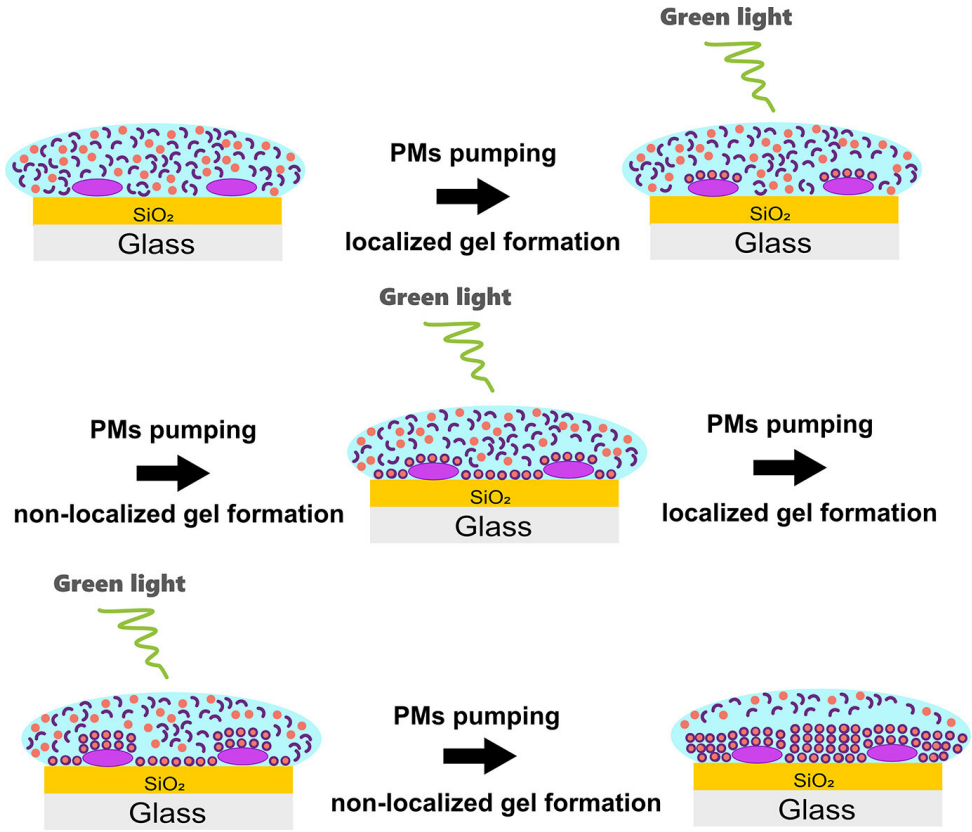

Figure 4.6. Time-lapse illustration of hydrogel formation after contact with C-His_{10}-tag PM and green light observed by liquid AFM. The purple, light blue, dark blue, and red areas represent PMs, aqueous media, hydrazine molecules, and benzaldehyde molecules, respectively. The fiber is formed when three hydrazine molecules react with benzaldehyde.

Subsequently, a reduction in the relative height of the patches is noted. Localized gel formation is observed when the sample is subjected to green light once more, with the patch height increasing from 6.1 nm (Figure 4.4, Time reaction = 35 min) to 15.5 nm (Figure 4.4, Time reaction = 47 min). Ultimately, the hydrogel domains start to coalesce, and fiber formation is observed throughout the scanned area. The results suggest that initially the fibers grew preferentially on the PMs when exposed to light; subsequently, owing to proton diffusion, growth occurred in other areas as well. This indicates the light-triggering influence within the system. To demonstrate this assumption, we compared these results with a C-His_{10}-tag PM-coated substrate scanned by AFM for 1 h in presence of gel reactants in the dark (Figure 4.5). For this sample, the formation of fibrillar structures of gel patches was not observed. Therefore, we concluded that gel fiber formation is driven by the presence of both, C-His_{10}-tag PMs and light.

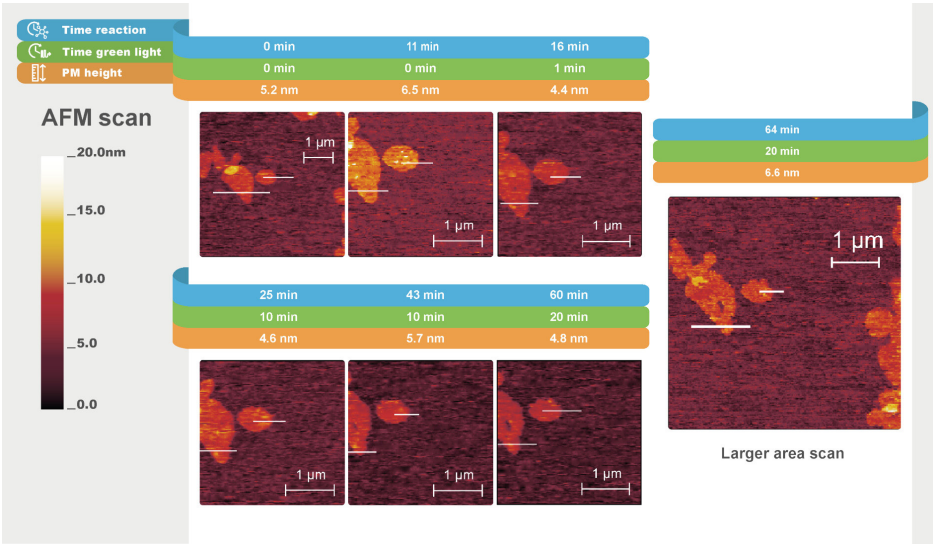

Figure 4.7. In-situ AFM Peakforce Tapping in fluid mode height images of hydrogel formation under the influence of PM (wild-type PM) and light at different time points. The lines highlighted in white indicate the cross sections of PMs. The scan direction is from right to left, with a 0◦ scan angle. Cross sectional values for these images are shown in Figure S4.7, SI.

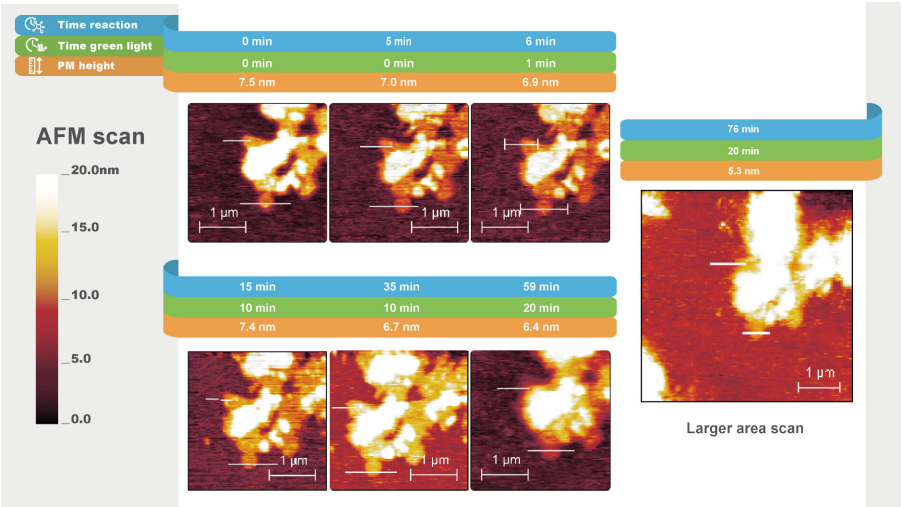

Figure 4.8. In-situ AFM Peakforce Tapping in fluid mode height images of hydrogel formation under the influence of PM (N-His_{10}-tag PM) at different time points. The lines highlighted in white indicate the cross sections of PMs. The scan direction is from right to left, with a 0◦ scan angle. Cross sectional values for these images are shown in Figure S4.8, SI.

Figure 4.6 illustrates the mechanism of gel formation under the influence of PMs and light, specifically observed for C-His_{10}-tag PM. This process initiates with the acid-catalyzed transformation of precursor molecules into the active gelator. Then, when the local concentration of gelator molecules exceeds the critical gelation concentration, gel fibers start to form. During this process, protons diffuse into the bulk, resulting in acidification and the formation of fiber networks across the substrate. This leads to the formation of gelator molecules and eventually to the formation of fibers and gels. However, a localized gel formation then reoccurs. Finally, a fibrous network is observed throughout the substrate owing to the proton diffusion.

Given the behavior of the WT and N-His_{10}-tag PM in comparison to that of C-His_{10}-tag PM in CLSM, the detection of fiber networks near the PM area during the liquid AFM scan was expected to be more challenging. The CLSM results indicate that gel formation rate for the C-His_{10}-tag PM was at least 40 and 80 times faster than that for WT and N-His_{10}-tag PMs, respectively (Figure 4.2). Indeed, the AFM scan of WT PMs (Figure 4.7) after the addition of reagents showed homogeneous PM patches before and after exposure to green light. Changes in relative height were observed over time. The most substantial change occurred when green light was applied to the sample after the addition of chemicals, resulting in a 1.9 nm decrease in patch height. However, over time, no changes in the shape or size of the PM patches were observed, and no new interfacial objects appeared (Figure S4.7, SI). The roughness of the AFM scan was approximately 0.5 nm, and the height difference ranged from approximately 0.2 to 1.1 nm in other cases after the addition of chemicals. The results strongly suggest that fiber growth at or near the WT-PM-aqueous interface did not take place upon exposure to light.

The AFM scan of N-His_{10}-tag PMs (Figure 4.8) showed similar behavior to that of WT PMs. Following the addition of reagents, initially, homogeneous patches approximately 7.0 nm in height were observed before green light exposure. During all irradiation cycles and until the end of the experiment, the relative height of the N-His_{10}-tag PMs did not vary by more than 0.9 nm which we consider insignificant in respect of fiber growth (Figure 4.8). Like with the WT PM, no changes to the shape and size of the PM patches were observed over time and no other interfacial objects appeared (Figure S4.8, SI). Therefore, we concluded that fiber growth near the N-His_{10}-tag PM aqueous interface did not occur upon exposure to light.

4.3 Conclusions

This work demonstrates the possibility of using PM patches to spatiotemporally control the growth pattern of oriented self-assembled gel agglomerates. We expect that the formation of these structures can be used to detect the local formation of pH gradients, which in turn are controlled by the localization and orientation of PM patches and the presence of light. The results show that light-driven catalysts can be confined to produce patterned out-of-equilibrium gel materials. The experiments underscore the feasibility of employing an external stimulus, such as light, to direct self-assembly in synthetic systems through the

spatial confinement of catalytic activity.

The results indicate that the presence and type of PMs significantly influence gelation rates. Depositing PMs on a negatively charged surface, CLSM showed faster in-situ gel formation for C-His_{10}-tag PMs, likely due to a favorably aligned pH gradient. AFM revealed that for C-His_{10}-tag PMs, gels initially formed on PMs, and as protons spread, fibers grew around the PM area. The liquid AFM results were consistent with those obtained from CLSM, and both methodologies provided valuable insights into the effects of PM and light on our system. Specifically, CLSM effectively showed the sensitivity of our system to light, whereas liquid AFM illustrated the process of fiber formation in the vicinity of the PM area. The combination of CLSM and AFM introduced here provides a multifunctional toolbox for the optical imaging and characterization of spatiotemporal control of CRNs, which can be used to examine surface structures of fibers with high-resolution. It may be used to identify and further characterize other CRNs and clarify the manner through which they dynamically assemble into functional domains. However, the identification of different fibers with higher resolution and scan rates remains a challenge. Moreover, for other CRNs, a more complex environment, such as apolar CRN products, can substantially increase the challenges of the experiment.

The strength of the formed hydrogel is a critical factor for its potential applications, particularly in biomaterials science. This study indicates that the components exhibit fast gelation under proton catalysis and stability of the hydrogel under physiological conditions. These properties make this platform highly promising for various biomedical applications, including tissue engineering and drug delivery. Furthermore, the ability to tune the hydrogels strength [31] offers significant potential for biomaterials scientists exploring new materials for these fields. We anticipate that this study can underscore the potential for integrating synthetic self-assembly systems with living metabolic processes, opening avenues for innovative applications to enhance existing biological functions or develop entirely new ones.

Future studies should quantitatively measure the proton gradient based on the amount of light. This would enable the development of intelligent hydrogel networks at the nanoscale for application in sensing pH gradients.

4.4 References

(1) Casey, J. R.; Grinstein, S.; Orlowski, J. Sensors and Regulators of Intracellular pH. *Nat Rev Mol Cell Biol* **2010**, 11 (1), 50–61. https://doi.org/10.1038/nrm2820.

(2) Asokan, A.; Cho, M. J. Exploitation of Intracellular pH Gradients in the Cellular Delivery of Macromolecules. *Journal of pharmaceutical sciences* **2002**, 91 (4), 903–913.

(3) Al-Aribe, K. M.; Knopf, G. K.; Bassi, A. S. Fabrication of an Optically Driven pH Gradient Generator Based on Self-Assembled Proton Pumps. *Microfluidics and nanofluidics* **2012**, 12 (1), 325–335.

(4) Hoffman, A. S. Hydrogels for Biomedical Applications. *Advanced drug delivery reviews* **2012**, 64, 18– 23.

(5) Boekhoven, J.; Poolman, J. M.; Maity, C.; Li, F.; Van Der Mee, L.; Minkenberg, C. B.; Mendes, E.; Van Esch, J. H.; Eelkema, R. Catalytic Control over Supramolecular Gel Formation. *Nature Chem* **2013**, 5 (5), 433–437. https://doi.org/10.1038/nchem.1617.

(6) Aktaş, D. K.; Öztekin, F. pH-Sensitive Poly (Acrylic Acid-Co-Acrylamide) Anionic Hydrogels for Jejunum Targeted Drug Delivery Systems. *Polymer Bulletin* **2023**, 80 (3), 2801–2813.
(7) Syed Azhar, S. N.; Ashari, S. E.; Zainuddin, N.; Hassan, M. Nanostructured Lipid Carriers-Hydrogels System for Drug Delivery: Nanohybrid Technology Perspective. *Molecules* **2022**, 27 (1). https://doi.org/10.3390/molecules27010289.
(8) Zhao, Y.-L.; Stoddart, J. F. Azobenzene-Based Light-Responsive Hydrogel System. *Langmuir* **2009**, 25 (15), 8442–8446.
(9) Gupta, P.; Vermani, K.; Garg, S. Hydrogels: From Controlled Release to pH-Responsive Drug Delivery. *Drug discovery today* **2002**, 7 (10), 569–579.
(10) Ward, J. H.; Bashir, R.; Peppas, N. A. Micropatterning of Biomedical Polymer Surfaces by Novel UV Polymerization Techniques. Journal of Biomedical Materials Research: A*n Official Journal of The Society for Biomaterials, The Japanese Society for Biomaterials, and The Australian Society for Biomaterials and the Korean Society for Biomaterials* **2001**, 56 (3), 351–360.
(11) Ziemecka, I.; Koper, G. J.; Olive, A. G.; van Esch, J. H. Chemical-Gradient Directed Self-Assembly of Hydrogel Fibers. *Soft Matter* **2013**, 9 (5), 1556–1561.
(12) Vigier-Carrière, C.; Boulmedais, F.; Schaaf, P.; Jierry, L. Surface-Assisted Self-Assembly Strategies Leading to Supramolecular Hydrogels. *Angewandte Chemie International Edition* **2018**, 57 (6), 1448–1456.
(13) Stoeckenius, W.; Lozier, R. H.; Bogomolni, R. A. Bacteriorhodopsin and the Purple Membrane of Halobacteria. *Biochimica et Biophysica Acta (BBA) - Reviews on Bioenergetics* **1979**, 505 (3–4), 215–278. https://doi.org/10.1016/0304-4173(79)90006-5.
(14) Oesterhelt, D. Bacteriorhodopsin as an Example of a Light-driven Proton Pump. *Angewandte Chemie International Edition in English* **1976**, 15 (1), 17–24.
(15) Mahyad, B.; Janfaza, S.; Hosseini, E. S. Bio-Nano Hybrid Materials Based on Bacteriorhodopsin: Potential Applications and Future Strategies. *Advances in Colloid and Interface Science* **2015**, 225, 194–202. https://doi.org/10.1016/j.cis.2015.09.006.
(16) Figueiredo Da Silva, J.; Bacheva, V.; Drechsler, U.; Nicollier, P.; Reidt, S.; Fotiadis, D.; Knoll, A.; Wolf, H. Fabrication of a Hybrid Device for the Integration of Light-Triggered Proton Pumps. *Micro and Nano Engineering* **2024**, 23, 100250. https://doi.org/10.1016/j.mne.2024.100250.
(17) Fisher, K.; Yanagimoto, K.; Stoeckenius, W. Oriented Adsorption of Purple Membrane to Cationic Surfaces. *The Journal of cell biology* **1978**, 77 (2), 611–621. https://doi.org/10.1083/jcb.77.2.611.
(18) Stauffer, M.; Hirschi, S.; Ucurum, Z.; Harder, D.; Schlesinger, R.; Fotiadis, D. Engineering and Production of the Light-Driven Proton Pump Bacteriorhodopsin in 2D Crystals for Basic Research and Applied Technologies. *MPs* **2020**, 3 (3), 51. https://doi.org/10.3390/mps3030051.
(19) Ruggeri, F.; Schwemmer, C.; Stauffer, M.; Nicollier, P. M.; Figueiredo da Silva, J.; Bosshart, P. D.; Kochems, K.; Fotiadis, D.; Knoll, A.; Wolf, H. Placement of Biological Membrane Patches in a Nanofluidic Gap With Control Over Position and Orientation. *Advanced materials interfaces* **2022,** 9 (23), 2200941.
(20) Laskowski, P. R.; Pfreundschuh, M.; Stauffer, M.; Ucurum, Z.; Fotiadis, D.; Müller, D. J. High- Resolution Imaging and Multiparametric Characterization of Native Membranes by Combining Confocal Microscopy and an Atomic Force Microscopy-Based Toolbox. *ACS Nano* **2017**, 11 (8), 8292– 8301. https://doi.org/10.1021/acsnano.7b03456.
(21) Olive, A. G.; Abdullah, N. H.; Ziemecka, I.; Mendes, E.; Eelkema, R.; Van Esch, J. H. Spatial and Directional Control over Self-Assembly Using Catalytic Micropatterned Surfaces. *Angewandte Chemie International Edition* **2014**, 53 (16), 4132–4136.
(22) Wang, Y.; Oldenhof, S.; Versluis, F.; Shah, M.; Zhang, K.; Van Steijn, V.; Guo, X.; Eelkema, R.; Van Esch, J. H. Controlled Fabrication of Micropatterned Supramolecular Gels by Directed Self-Assembly of Small Molecular Gelators. *Small* **2019**, 15 (8), 1804154. https://doi.org/10.1002/smll.201804154.
(23) Wang, Y.; Versluis, F.; Oldenhof, S.; Lakshminarayanan, V.; Zhang, K.; Wang, Y.; Wang, J.; Eelkema, R.; Guo, X.; Van Esch, J. H. Directed Nanoscale Self-Assembly of Low Molecular Weight Hydrogelators Using Catalytic Nanoparticles. *Advanced Materials* **2018**, 30 (21), 1707408. https://doi.org/10.1002/adma.201707408.
(24) Maity, C.; Hendriksen, W. E.; van Esch, J. H.; Eelkema, R. Spatial Structuring of a Supramolecular Hydrogel by Using a Visible-light Triggered Catalyst. *Angewandte Chemie International Edition* **2015**, 54 (3), 998–1001.
(25) Poolman, J. M.; Boekhoven, J.; Besselink, A.; Olive, A. G. L.; Van Esch, J. H.; Eelkema, R. Variable Gelation

Time and Stiffness of Low-Molecular-Weight Hydrogels through Catalytic Control over Self- Assembly. *Nat Protoc* **2014**, 9 (4), 977–988. https://doi.org/10.1038/nprot.2014.055.

(26) Boekhoven, J.; Brizard, A. M.; Kowlgi, K. N.; Koper, G. J.; Eelkema, R.; van Esch, J. H. Dissipative Self-assembly of a Molecular Gelator by Using a Chemical Fuel. *Angewandte Chemie* **2010**, 122 (28), 4935–4938.

(27) Carroll, K. M.; Wolf, H.; Knoll, A.; Curtis, J. E.; Zhang, Y.; Marder, S. R.; Riedo, E.; Duerig, U. Understanding How Charged Nanoparticles Electrostatically Assemble and Distribute in 1-D. *Langmuir* **2016**, 32 (51), 13600–13610.

(28) Bamberg, E.; Apell, H.-J.; Dencher, N. A.; Sperling, W.; Stieve, H.; Läuger, P. Photocurrents Generated by Bacteriorhodopsin on Planar Bilayer Membranes. Biophys. *Struct. Mechanism* **1979,** 5 (4), 277–292. https://doi.org/10.1007/BF02426663.

(29) Medalsy, I.; Hensen, U.; Muller, D. J. Imaging and Quantifying Chemical and Physical Properties of Native Proteins at Molecular Resolution by Force–Volume AFM. *Angewandte Chemie International Edition* **2011,** 50 (50), 12103–12108.

(30) Pfreundschuh, M.; Martinez-Martin, D.; Mulvihill, E.; Wegmann, S.; Muller, D. J. Multiparametric High-Resolution Imaging of Native Proteins by Force-Distance Curve–Based AFM. *Nature Protocols* **2014**, 9 (5), 1113–1130. https://doi.org/10.1038/nprot.2014.070.

(31) Abdullah, N. H.; Bakar, W. A. W. A.; Hussain, R.; Bakar, M. B.; van Esch, J. H. Effect of Homogeneous Acidic Catalyst on Mechanical Strength of Trishydrazone Hydrogels: Characterization and Optimization Studies. *Arabian journal of chemistry* **2018**, 11 (5), 635–644.

4.5 Supplementary information

4.5.1 Experimental details

General remarks

All reagents were purchased from commercial sources and were used as provided unless otherwise stated. Tri-acyl hydrazide cyclohexane and benzaldehyde were prepared according to published procedures. Liquid atomic force microscopy (AFM) imaging, data visualization, and data analysis were conducted using Gwyddion. [1] Confocal laser scanning microscopy (CLSM) data were processed using ZEN 2011 (Carl Zeiss) and ImageJ. [2] All imaging was performed at room temperature.

Preparation of glass substrates for spatiotemporal control of gel formation

Before use, glass substrates (24 × 24 mm^2) were treated with acetone and isopropanol, and the samples were cleaned with plasma under a nitrogen stream. The thickness of the glass chips was 170 µm for CLSM and liquid AFM. SiO_2 was deposited (100 nm) on top of the glass chips via plasma-enhanced chemical vapor deposition (PECVD). In the dark, 12.5 µmL of dispersed PM (wild-type (WT), or the genetically modified C-His_{10}-tag or N-His_{10}-tag PMs) was added to the substrates in water at a concentration of 10^{-2} mg·mL^{-1}. The deca-histidine His_{10}-tag attachment to either the cytoplasmatic side (C-His_{10}-tag) or extracellular side (N-His_{10}-tag) of the PM was used to increase a charge asymmetry. [3,4] The engineering of the biological membrane patches is described elsewhere. [3] The samples were dried in the dark under ambient air, rinsed with Milli-Q water, and then dried under a nitrogen stream.

Confocal laser scanning microscopy

In the CLSM experiments, a PM-coated glass was carefully placed on a polydimethylsiloxane (PDMS) cuvette (12 mm x 12 mm x 3 mm) containing gelator precursors in a phosphatebuffered saline (PBS) at pH 7.0. [5] The PMs were facing the solution. The two elements were then flipped and placed on the microscope. A fluorescein-based aldehyde-labeled probe [6] was used at 0.01 molar percentage.

Samples were monitored using a Zeiss LSM 980 equipped with a Zeiss Axio Observer inverted microscope, and Plan-Apochromat 63x oil immersion objective lens (NA 1.4). Incident wavelengths of 488 and 543 nm were used to visualize the gel formation and PM pumping, respectively; and emission at 517 nm was recorded. A z-step size of 48 µm was used to optically section the samples to seven planes. Snapshots of z-stacks were acquired every 67 s using a 488 nm laser, after which the sample was exposed to a 543 nm for PM pumping with the same time exposure. The 8-bit images of the middle plane were used for analysis.

Liquid Atomic force microscopy

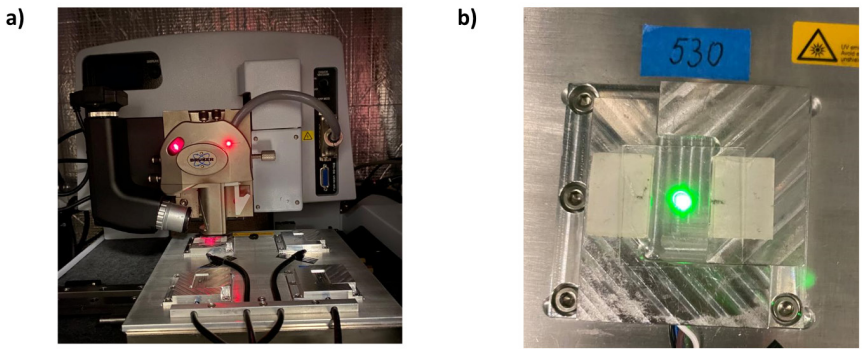

Figure S4.1. a) Liquid AFM setup during a substrate scan. **b)** 24 × 24 mm^2 glass sample exposed to green light by LED.

We operated a commercial Dimension-Icon AFM (Bruker)(Figure S4.1a) equipped with triangular oxide-sharpened silicon nitride (Si_3N_4) cantilevers (length: 70 mm; ScanAssist Fluid$^+$) in PeakAssist Tapping in fluid mode. Images were obtained from cantilevers under 2 kHz oscillation frequency, 3 Hz scanning rate, and 150 nm amplitude. An area of 3 × 3 μm^2 was scanned at 128 × 128 samples/line. After the photodiode signal was stabilized, we began scanning the area again at a rate of 1 scan/min for 1 h. For all samples, we immersed the glass substrate in 140 µl of PBS buffer (100 mM, pH 7.0), and then imaged an area containing at least one PM patch. Subsequently, we injected 140 µl of gelator precursor solution onto the substrate at pH 7.0, at a concentration presented elsewhere. [6] The experiment time is initiated from this point. One hour after the addition of gel chemicals,

an area of 5 × 5 µm² was scanned at 256 × 256 samples/line to check for any tip-induced desorption of gel agglomerates. For illuminating the scanning substrate with green light, we utilized a customized stage comprising a chip holder and a light-emitting diode (LED) green light source (530 nm) with variable intensities positioned beneath the chip holder, as depicted in Figure S4.1b. The intervals and duration of illumination were manually controlled using the T-Cube™ LED Driver (ThorLabs). All experiments were performed with the same light power.

To measure AFM heights, we analysed at least two PM patches and calculated the average intensity within a 10-pixel region around the height line. The average height was then determined from these two areas.

4.5.2 Supplementary results

Air atomic force microscopy

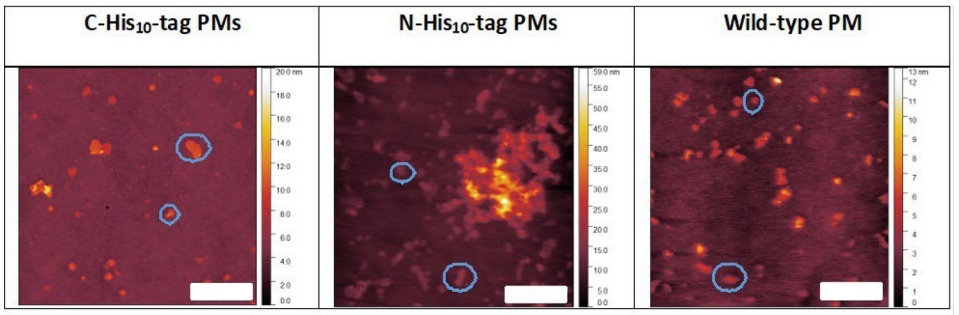

Figure S4.2. Topographical air-AFM image of deposited PMs (wild-type, C-His_{10}-tag, and N-His_{10}- tag PMs on the surface). Blue circles represent examples of single PM patches. Scale bar represents 5 µm.

Figure S4.2 shows a 400 µm² air-AFM scan (Park Systems - NX20, contact mode tetrahedral cantilever) of different PM types. The blue circles indicate an example of single PM patches found under this technique. In air-AFM, a single PM patch presented a height of 5 nm. A height higher than 10 nm indicates a PM agglomeration in the target area. Therefore, the quantitative analysis of Figure S4.2 reveals that N-His_{10}-tag PMs presented the highest density of PM patches, covering 53.5 % of the area scanned. This is followed by WT PMs, with a coverage of 6.4 %, and then C-His_{10}-tag PMs, with a coverage of 4.5%.

Liquid Atomic Force Microscopy

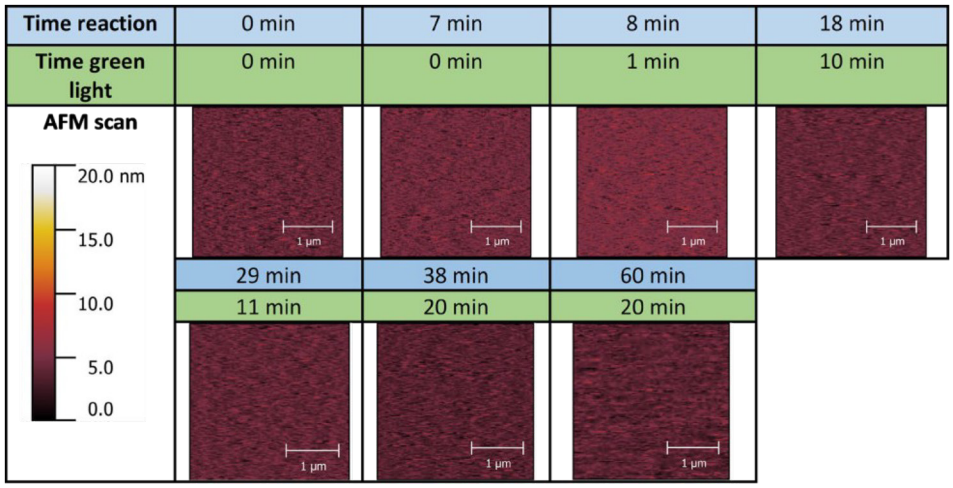

Figure S4.3. In-situ AFM Peakforce Tapping in fluid mode height images of a SiO_2 substrate embedded with hydrogel reagents but without PM patches, under exposure to green light at various time intervals. The scan direction is from right to left, with a 0° scan angle.

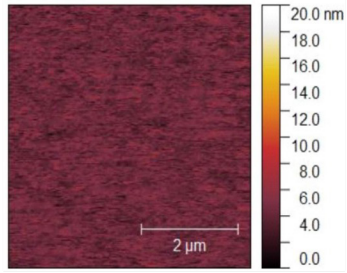

Figure S4.4. In-situ AFM Peakforce Tapping in fluid mode height image of a SiO_2 substrate embedded with hydrogel reagents, but devoid of PM patches, exposed to green light at the conclusion of the experiment. The scan was conducted over a 5 × 5 μm^2 area, with the scanning direction oriented from right to left and at a 0 ° scan angle.

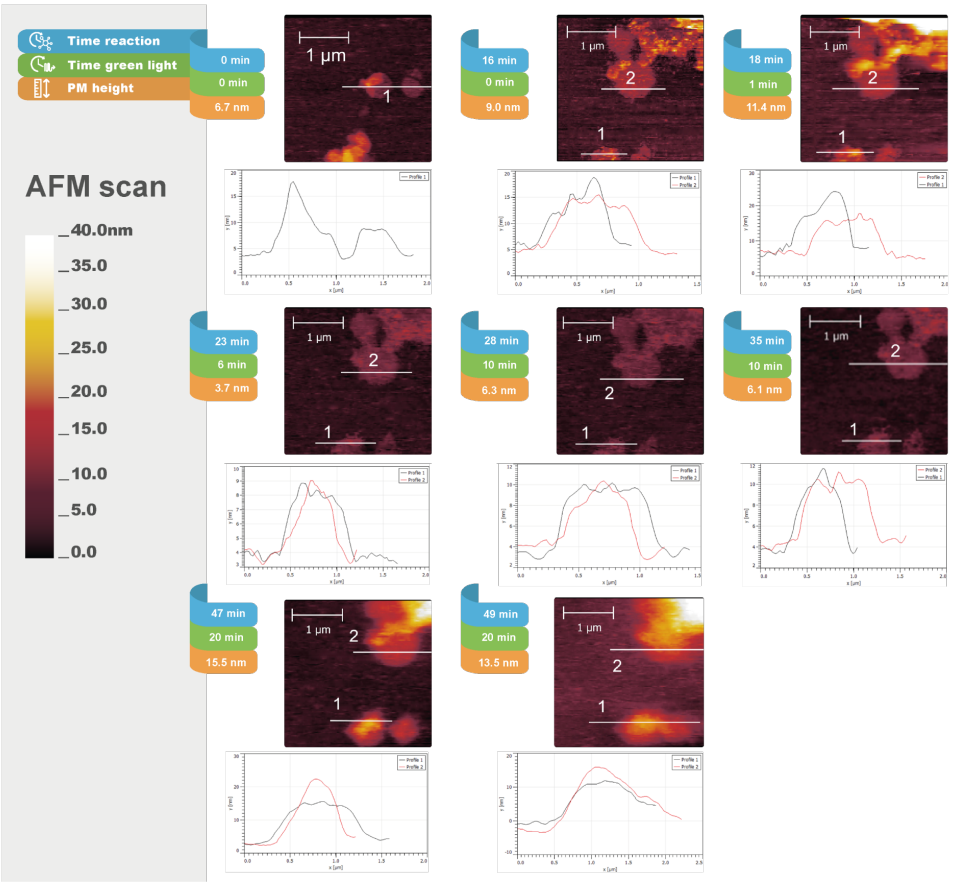

Figure S4.5. In-situ AFM Peakforce Tapping in fluid mode height cross sections of hydrogel formation under the influence of PMs (C-His_{10}-tag PMs) and light at different time points, presented in Figure 4.4 (main text).

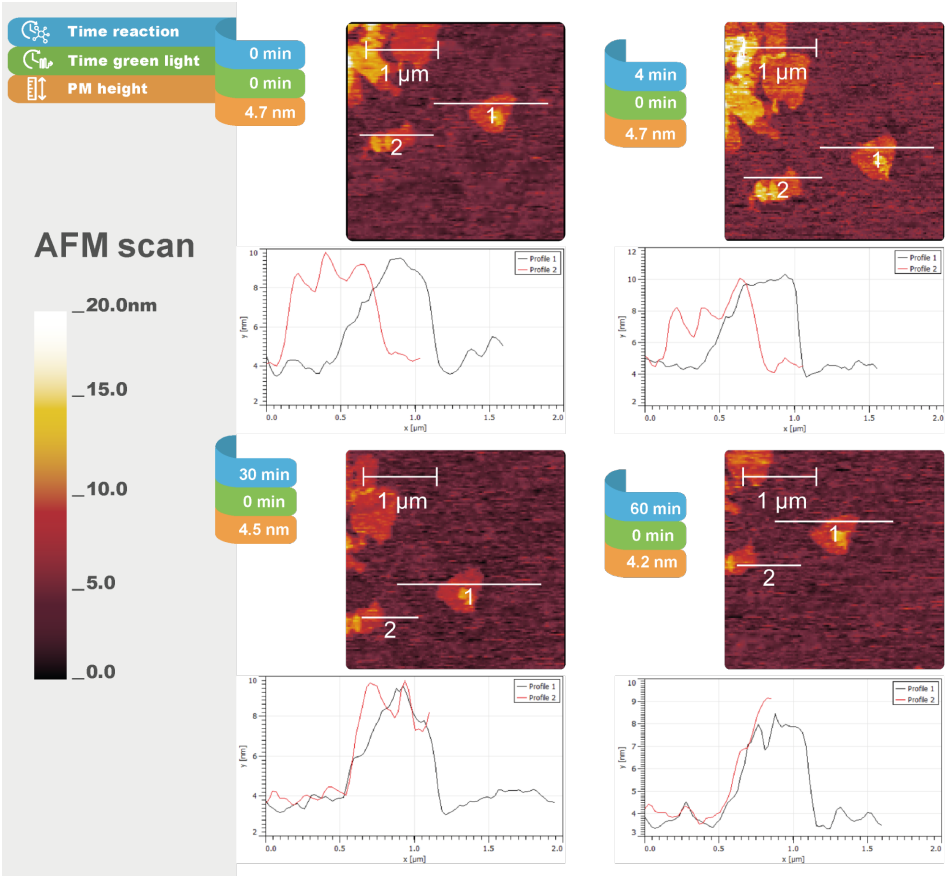

Figure S4.6. In-situ AFM Peakforce Tapping in fluid mode height cross sections of hydrogel formation under the influence of PMs (C-His_{10}-tag PMs) in the dark at different time points, presented in Figure 4.5 (main text).

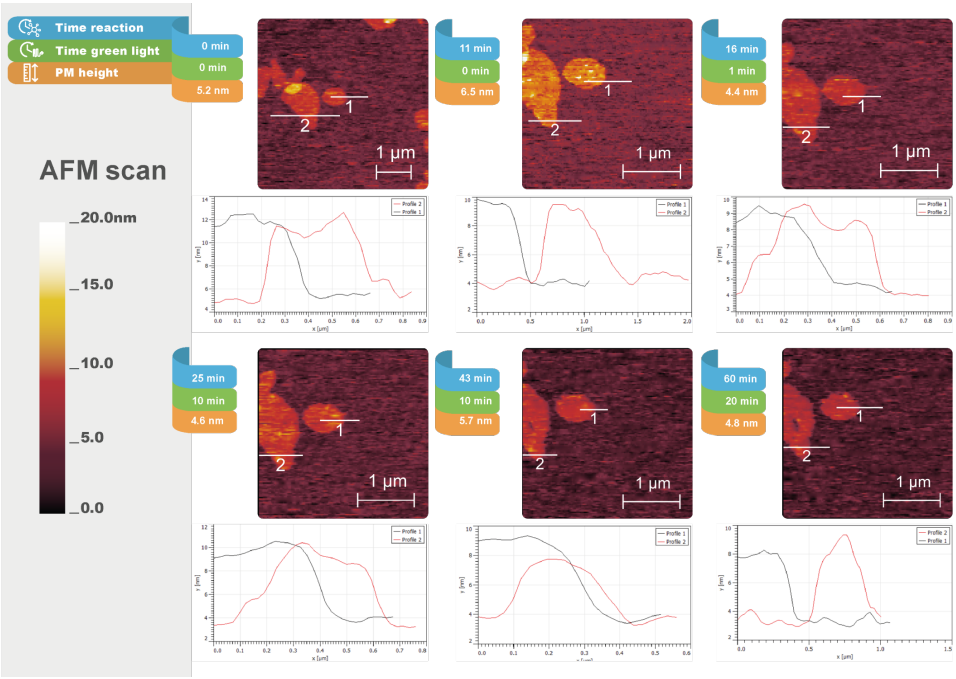

Figure S4.7. In-situ AFM Peakforce Tapping in fluid mode height cross sections of hydrogel formation under the influence of PMs (wild-type PMs) and light at different time points, presented in Figure 4.7 (main text).

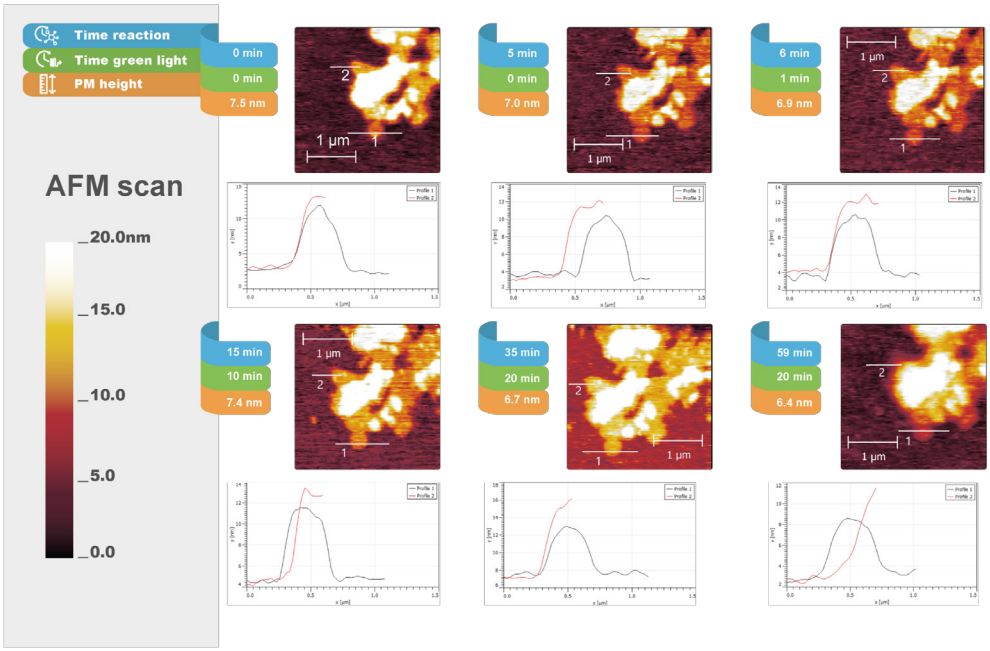

Figure S4.8. In-situ AFM Peakforce Tapping in fluid mode height cross sections of hydrogel formation under the influence of PMs (N-His_{10}-tag PMs) and light at different time points, presented in Figure 4.8 (main text).

4.5.3 References

(1) Nečas, D.; Klapetek, P. Gwyddion: An Open-Source Software for SPM Data Analysis. *Open Phys*. **2012**, 10 (1), 181–188.

(2) Schneider, C. A.; Rasband, W. S.; Eliceiri, K. W. NIH Image to ImageJ: 25 Years of Image Analysis. Nat. *Methods* **2012**, 9 (7), 671–675.

(3) Stauffer, M.; Hirschi, S.; Ucurum, Z.; Harder, D.; Schlesinger, R.; Fotiadis, D. Engineering and Production of the Light-Driven Proton Pump Bacteriorhodopsin in 2D Crystals for Basic Research and Applied Technologies. *Methods Protoc.* **2020**, 3 (3), 51. https://doi.org/10.3390/mps3030051.

(4) Ruggeri, F.; Schwemmer, C.; Stauffer, M.; Nicollier, P. M.; Figueiredo da Silva, J.; Bosshart, P. D.; Kochems, K.; Fotiadis, D.; Knoll, A.; Wolf, H. Placement of Biological Membrane Patches in a Nanofluidic Gap With Control Over Position and Orientation. *Adv. Mater. Interfaces* **2022**, 9 (23), 2200941.

(5) Olive, A. G.; Abdullah, N. H.; Ziemecka, I.; Mendes, E.; Eelkema, R.; Van Esch, J. H. Spatial and Directional Control over Self-Assembly Using Catalytic Micropatterned Surfaces. *Angew. Chem. Int. Ed.* **2014**, 53 (16), 4132–4136.

(6) Boekhoven, J.; Poolman, J. M.; Maity, C.; Li, F.; Van Der Mee, L.; Minkenberg, C. B.; Mendes, E.; Van Esch, J. H.; Eelkema, R. Catalytic Control over Supramolecular Gel Formation. *Nat. Chem.* **2013**, 5 (5), 433–437. https://doi.org/10.1038/nchem.1617.

Chapter 5

Network of light-triggered proton pumps[‡]

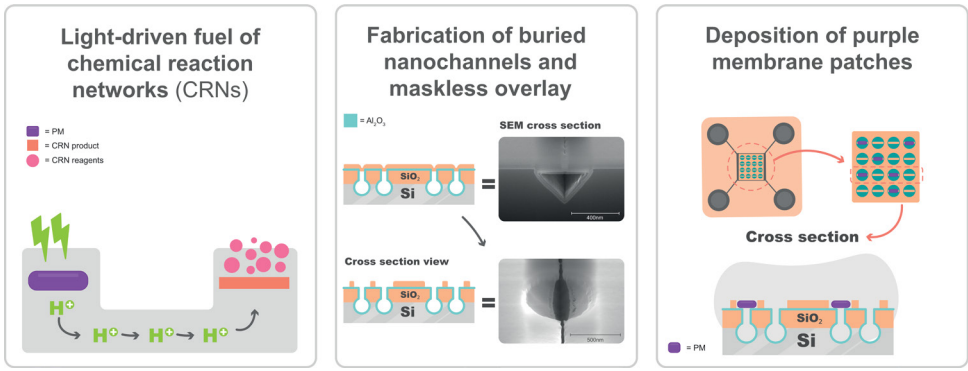

Abstract: Biological ion pumps, such as bacteriorhodopsin (bR), utilize photons to move ions against concentration gradients, offering energy harvesting and spatiotemporal control of chemical gradients. This capability goes far beyond the capabilities of today's synthetic devices, suggesting a hybrid approach to embed bRs in synthetic devices in order to direct the proton flow towards useful system applications. In this study, a hybrid silicon-based nanochannel network with integrated purple membranes (PM) containing bR was fabricated. The fabrication method combines thermal scanning probe lithography, etching techniques, atomic layer deposition, plasma-enhanced chemical vapor deposition, and photolithography to create devices with buried nanochannels on silicon substrates. PM patches were deposited onto specified sites by a tunable nanofluidic confinement apparatus. The resulting device holds the potential for locally controlling directed ion transport in micrometer scale devices, a first step towards applications, such as locally affected proton-catalyzed chemical reaction networks. Furthermore, this fabrication strategy, employing a maskless overlay, is a tool for constructing intricate nanofluidic network designs which are mechanically robust and straightforward to fabricate.

[‡] Part of this chapter has been published: Figueiredo da Silva, J. et al. "Fabrication of a hybrid device for the integration of light-triggered proton pumps." *Micro and Nano Engineering* 23 (2024): 100250.

5.1 Introduction

In biological organisms, efficient energy harvesting systems based on ion transport operate in nanofluidic entities, namely ion pumps and ion channels. [1] The energy conversion and storage systems of these biological networks are based on ion transport and energy storage in molecules. Two ion transport modes, namely passive and active ion transport, are widely used by these organisms. [1,2] An example of an energy harvesting biological ion pump is bacteriorhodopsin (bR), which is the main component of 5-nm thick and ~ 500-nm sized purple membranes (PM) of the archeon Halobacterium salinarum. Upon photon irradiation, bR pumps protons across the membrane, thereby creating an osmotic potential. [3]

Systems based on directed ion transport – also artificial ones – have advantages over electron transport systems, including the robustness against radiation and the inherent supply with energy through delivered ions. [2] However, for practical applications, these energy conversion systems and devices should be further investigated, optimized, and simplified. [4] A recent study reported an artificial proton pump inspired by bR in the development of a photovoltaic device based on a membrane of carbon nitride nanotubes. [5] The device can be reused in photoelectric energy conversion because it remains unchanged before and after illumination. Moreover, different electrolytes, including acid, saline, and alkali solutions, did not modify the energy conversion system. However, sophisticated micro and nanoscale networks cannot be designed in such approach.

Researchers have recently developed “on-chip” pH gradient generators for various applications, primarily for the study of biological phenomena related to pH change. [6] Despite these developments, high intensity illumination and external electric fields can negatively affect biological samples. To address these challenges, in-situ fabrication methods have been developed to create porous structures in microchannels. However, these techniques can leave residues that are toxic to biological processes. While there are improved systems described, [5] the most synthetic pumping systems are less effective in generating gradients from photons than biological ion pumps, [1] which can create membrane potentials even against steep gradients. Earlier work shows that PMs or bR can be positioned over sub-micron holes or nanopores separating aqueous compartments and thus create a proton gradient upon irradiation. [7,8] With a network of nanoscale channels, it will be possible to guide pumped protons towards desired locations by diffusive transport with high efficiency. Such hybrid devices with light- driven ion pumps that can deliver protons to dedicated locations would have many potential applications, e.g., for the local proton-catalyzed synthesis of materials [9] or for the local release of materials trapped in a polymer gel by a pH-driven phase change. [10] Nevertheless, their design remains a challenge. For example, it is crucial to control the orientation of PMs during deposition in hybrid devices [6] to reflect the directionality in bR pumping.

A low power optically driven pH gradient generator can provide an alternative noninvasive mechanism to modify the acidity of a target solution without inducing a strong electric

field near the solution or exposing the solution to high intensity illumination or heat. A previous work [11] showed that bR proton pumps can maintain their primary function when removed from a living organism. In another study, authors used an optically driven pH gradient generator to exploit the photon-activated molecular proton pumps found in PMs. [12] The authors identified several limitations attributed to the random orientation of the proton pumps. Therefore, directional orientation is critical to efficiently use biological materials to pump protons in microfluidic and nanofluidic channels.

The size of PM patches used as building blocks in hybrid devices requires fabrication methods in the size range of single digit micrometers and below. Fabricating fluidic channels traditionally involves standard photolithography followed by wet or dry substrate etching. For dimensions below 2 μm, alternatives such as electron beam lithography and focused ion beam (FIB) lithography are viable options. However, nanochannel fabrication typically demands intricate processes and expensive equipment, making the production of chips inaccessible to many researchers. To address this challenge, there is a need for a simpler fabrication approach that is maskless, highly efficient, and offers precise control of device design. [13]

To optimize the photo efficiency of PM pumps, we formerly developed a strategy to simultaneously control its orientation and position on a device. [14] For localization control, we used a tunable nanofluidic confinement apparatus (TNCA) to accurately deposit bR-containing membrane patches on a patterned substrate. The trapping sites for the membrane interface were prepared by thermal scanning probe lithography (t- SPL).

To fill the gap in the design of light-driven proton transport using PMs, we designed a nanochannel network containing PM patches. We used a combination of fabrication methods to create buried nanochannels [15] with a length of a few ten micrometers between dedicated areas (traps) for the placement and integration of biological building blocks. As a demonstrator of a biological building block, we selected wild-type (WT) PM patches. Furthermore, we initiated the development of a more direct method to identify PM orientation and presence during TNCA deposition. Our objective was to assess the efficiency of PM deposition on the device while maintaining pumping activity. The developed device is expected to provide a nanolocalized proton gradient and to enable the spatiotemporal control of a proton-catalyzed molecular self- assembly, [9] with an optical trigger that can be switched on and off.

5.2 Results and discussion

We used a combination of traditional and unconventional microfabrication methods to prepare the nanofluidic architectures of buried channels and deposition sites for biological membrane patches. As a demonstrator, WT PM patches were deposited at predefined positions of the hybrid device to install light-triggered proton pumps at defined openings of the nanochannels. Finally, we functionalized PM patches with a pH-sensitive dye for use as a pH sensor to identify PM localization and pumping activity in situ.

5.2.1 Device fabrication

In a first step, the pattern of nanochannels was defined by t-SPL. t-SPL is a versatile top-down technique based on heated tips. It can create different nanostructures and write patterns in an organic resist material under atmospheric conditions. Unlike electron beam lithographic tools, the t-SPL instrument is relatively simple and cost- effective. [16] Lines with a width of ~50 nm were patterned by t-SPL on a PPA/thermal oxide/Si substrate (Figure 5.1, step 2; Figure 5.2a). A first anisotropic etch into the SiO_2 was performed to expose the Si in the channels (Figure 5.1, step 3; Figure 5.2b). Subsequently, an isotropic reactive ion etch (RIE) of Si was conducted to form a cavity under the thermal oxide edges (Figure 5.1, step 4). The cavity was substantially wider than the line opened in the thermal oxide layer. As shown in the scanning electron microscope (SEM) images (Figure 5.2c,d), the fabricated channels were successfully patterned by t-SPL and etched via RIE. A cross-sectional SEM image was captured to identify a channel opening of 36 nm in the SiO_2 layer and a triangular-shaped nanochannel of approximately 360 nm × 300 nm (width × height) in the Si layer. Note that the upward bending in Figure 5.2c is likely caused by the stress arising from the Pt deposition. The effect is absent when the channel is closed in Figure 5.2d.

Using a single-layer of PPA patterned to a depth of 50 nm limits lateral resolution in t-SPL to roughly 50 nm due to the conical shape of the tip. Dimensions of <20 nm can be achieved by using a more elaborate three-layer transfer stack in so called high- resolution t-SPL patterning. [16,17] However, in the simple single-layer process used here the wider lines facilitate the isotropic etching of the underlying Si, and the wide opening can still be closed by sufficiently thick atomic layer deposition (ALD) layers. To examine the trench width resulting from our single-layer PPA resist in relation to the targeted line width of the t-SPL layout, we prepared four different trench structures with line widths of 2, 3, 4, and 5 pixels (corresponding to 23, 35, 46, and 58 nm, respectively). The CHF_3 and SF_6/Ar dry etching times were constant (10 and 2 min, respectively) for all samples. The line width in the patterns transferred to the SiO_2 layer varied from 35 to 71 nm (Figure 5.1, step 3). However, the variability of lines of the same pixel width was ±10 nm rather large. In extreme cases, we obtained SiO_2 channels with 117 nm width (Figure S5.1, Supplementary Information (SI)), which could be attributed to instabilities in the SiO_2 dry etching step and/or a blunt tip used for t-SPL patterning. The challenge of achieving exact sub-100 nm line dimensions by t- SPL in a single resist layer is the unknown tip-shape, which may vary due to tip contamination and tip wear. [16] Still, the line dimensions achieved with this standard t- SPL patterning were sufficient for the fabrication of buried nanochannels.

The top of the nanochannels was closed using ALD (Figure 5.1, steps 5,6). ALD is a thin film deposition technique based on the cyclic use of gas phase chemical processes. In each cycle a thin layer (~monolayer) of material is deposited on all accessible surfaces. Therefore, the deposition is very conformal, even in buried holes and channels, as long as there is access to the process gases. First, a 10 nm thin layer of Al_2O_3 was deposited on the substrate which later forms the bottom material for the PM deposition sites and supports the assembly of PMs in the correct orientation. [14] Afterwards, 30 nm of SiO_2 were deposited

by ALD to completely close the nanochannels. ALD has two unique advantages over other methods for nanochannel fabrication. First, the conformal film deposition during ALD allows the self-sealing of nanochannels if the film thickness can cover the entire top trench gap. Second, the nanochannels are also coated with the ALD material, which gives them well-defined surface properties and automatically provides them with a defined diameter once the channel top is sealed, regardless of the deposited ALD film thickness. [15] This self-limiting behavior is promising for the fabrication of highly controllable nanochannels with sublithographic dimensions. After the nanochannels were sealed by ALD, an additional SiO_2 layer of 100 nm was deposited on the substrate by plasma-enhanced chemical vapor deposition (PECVD) (Figure 5.1, step 7).

For the above-mentioned samples of varying line width in the t-SPL patterning step, the dimensions of the cavity in the Si were ranging from 360 to 453 nm in width and 259 to 300 nm in height. After ALD deposition, the buried channel dimensions were ranging from 294 to 362 nm in width and 221 to 290 nm in height (Figure 5.2d). For another set of samples, the duration of the isotropic silicon etch step (Figure 5.1, step 4) was reduced from 2 min to 1 min to achieve smaller channel dimensions. As expected, the channel dimensions were significantly reduced to 235 nm × 132 nm (width × height) before ALD and to 97 nm × 67 nm after ALD (Figure S5.2, SI). Also, we observed a more circular shape of the closed channels as compared to the triangular shape of the larger channels. Thus, sub-100-nm channel dimensions can be achieved by reducing the duration of the silicon etch step.

We performed a maskless t-SPL overlay patterning of 500-nm-diameter circular holes on the buried channels which were intended to act as traps for PM deposition (Figure 5.1, steps 8–10). The main challenges of maskless overlay patterning are the detection of the existing pattern and the accurate placement of the overlay pattern. The maskless process eliminates the need for dedicated alignment marks associated with difficulties in marker degradation and inconsistencies in the positioning of hardware used for reading and writing. [18] The t-SPL instrument can read topography with sub-nanometer sensitivity in the area of interest without causing any resist exposure and pattern nanometer-sized structures into the resist, which provides a unique method for nanometer-precise device fabrication. [17,18] The t-SPL maskless overlay process can be divided into three stages (Figure 5.3). First, the location and orientation of existing patterns were determined by topography measurements (Figure 5.3a). Second, this information was used to calculate the overlay pattern (Figure 5.3b). In this step, cross-correlation between the design file of the nano-channels (cyan lines in Figure 5.3b) and the measured topography is used to find the correct scaling and rotation of the sample and the precise location. Third, the trap pattern (blue in Figure 5.3b) was written on the sample surface aligned with the nanochannel pattern (Figure 5.3c).

Following the overlay process, the PPA underwent complete etching, removing ~70 nm of the >100 nm thick SiO_2 top layer, as illustrated in Figure 5.1, step 11. After completing this step, the nanochannels remained completely sealed, also in the PM trap patterns which formed as cylindrical depressions in the SiO_2 layer. This strategy was implemented

to avoid contamination within the nanochannel structures during subsequent fabrication stages. Subsequently, we utilized photolithography with a positive photoresist to define the microfluidic channels and filling pads, followed by three rounds of etching (SiO_2, Al_2O_3, and Si etch) within the designated photolithographic region (Figure 5.1, steps 12–18).

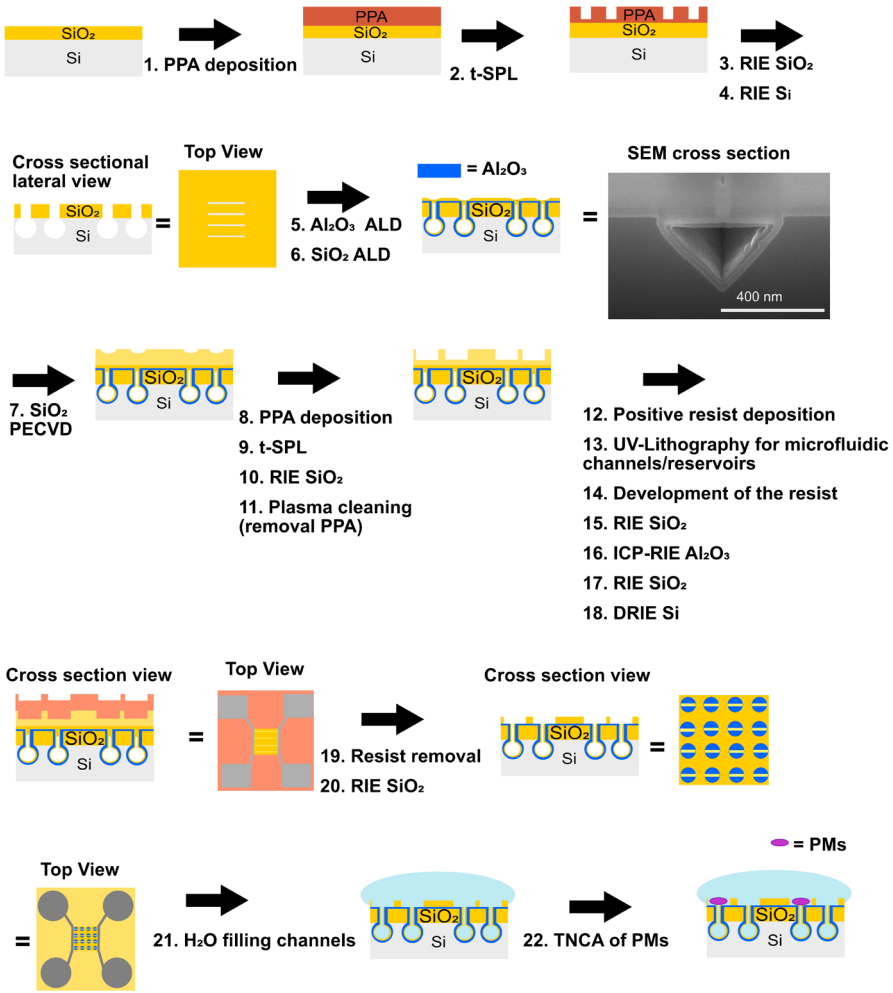

Figure 5.1. Summary of fabrication of bR-nanochannel device. Steps 1 to 4: fabrication of nanochannels by t-SPL. Steps 5 and 6: closure of t-SPL channels by ALD. [15] Steps 7 to 11: design of PM traps by t-SPL. Steps 12 to 18: fabrication of microchannels and macro reservoirs by photolithography. Steps 19 and 20: opening of nanochannels on PM traps. Step 21: filling of channels with water. Step 22: PM deposition. PPA = polyphthalaldehyde; t-SPL = thermal scanning probe lithography; RIE = reactive ion etching; ALD = atomic layer deposition; PECVD = plasma-enhanced chemical vapor deposition; SEM= scanning electron microscope; ICP-RIE = inductively coupled plasma – RIE; TNCA = tunable nanofluidic confinement apparatus; PM = purple membrane.

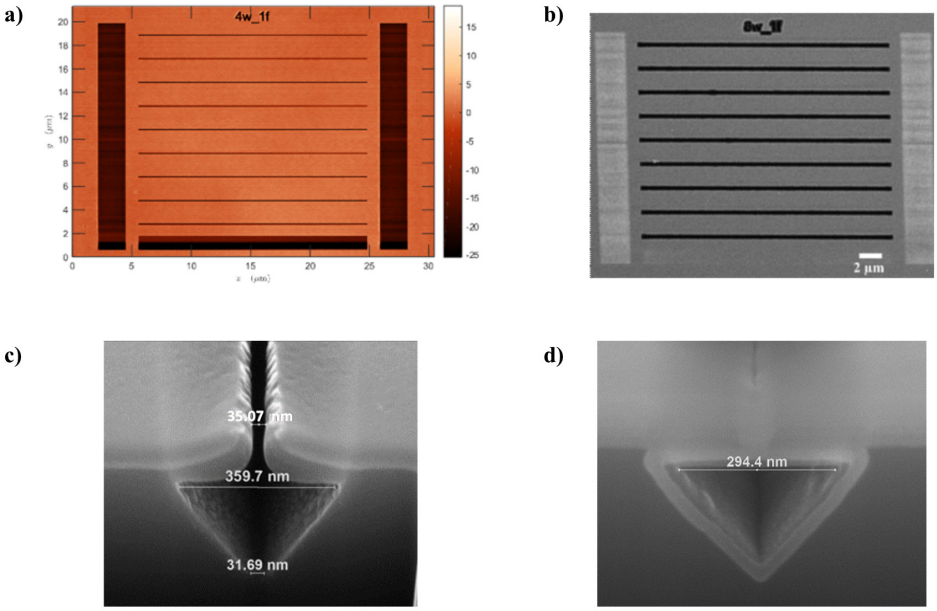

Figure 5.2 a) t-SPL image of 50-nm wide channels after t-SPL patterning in PPA resist (color gradient bar: Z-scale in nanometers). **b)** SEM top view image of channels after RIE, **c)** FIB cross sectional image of nanochannel before and **d)** after ALD.

After removing the photolithographic resist (Figure 5.1, step 19), we subjected the remaining SiO_2 layer to dry etching, as illustrated in Figure 5.1, step 20. This enabled precise control over the opening of nanochannels solely in the trap area. Moreover, it exposed the Al_2O_3 surface at the bottom of the trapping sites and provided finer control over the thickness of the remaining SiO_2 layer, which defines the depth of capture sites for the PMs. It is crucial for the PM layer deposition to achieve a trap depth of 15–20 nm, considering the PM thickness and their optimal deposition conditions. [14]

Figure 5.4 shows the successful photolithographic overlay of the nano and microchannels. Figure 5.4a is a top view of the buried nanochannels with the circular deposition sites for the PMs. On the right and left, the edge towards the much deeper microfluidic channel of the filling structure is visible. Figure 5.4b is a tilted view of the silicon ridge that contains the buried nanochannels which demonstrates the size proportion of the nano and microchannels. Microfluidic channels are approximately 23 µm deep. The horizontal structures on the side of the silicon ridge are due to the Bosch etching process. If needed, the cycle time of the Bosch process can be adjusted: short cycles yield smoother walls, and long cycles yield higher etch rates. [19] Figure 5.4c shows a tilted image of the opening of a buried nanochannel in the upper part of the silicon ridge. The nanochannels were open in the interception of nano and microchannels, which demonstrated the successful

and simple photolithographic overlay of a relatively small structure (20-µm-long channels). Moreover, there was no need for extra etching to open the nanochannel edges to remove dirt, contrary to the procedure reported by Nam et al. [15] The traps' depth, determined to be 20 nm, was measured using atomic force microscopy (AFM). This measurement accurately reflected the remaining SiO_2 layer after the various fabrication steps.

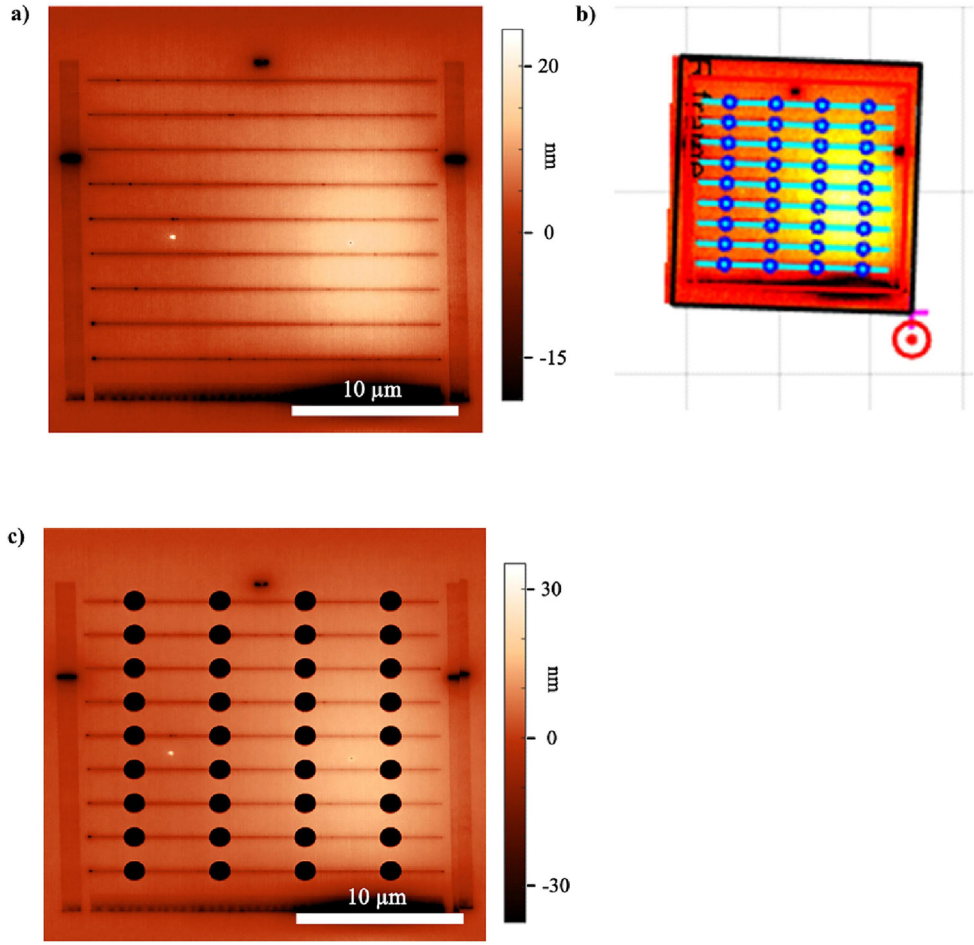

Figure 5.3. Overlay of circular traps on buried nanochannels. **a)** Topography image of buried nanochannels covered by 89 nm PPA resist. **b)** Image from panel a) in real space coordinates (slightly rotated sample). Overlayed are the gds-file layouts of the nanochannels (cyan) and the circular traps (blue). **c)** t-SPL topography image after patterning 1.2 µm diameter traps centered on the nanochannels.

Figure 5.5 presents a successful t-SPL overlay of 500 nm circles on the nanochannels. PECVD of SiO_2 achieved a faster deposition rate than ALD, and the additional material enabled us to design trap patterns on specific areas of the nanochannels, which were locally opened

towards the nanochannels, as shown in Figure 5.5a. The channels elsewhere in the overlay areas remained closed, as shown in Figure 5.5b and Figure 5.5c. The results show that we can locally control the material in a buried structure by combining bottom-up and top-down approaches. This provides us with freedom to design 3D structures for different applications.

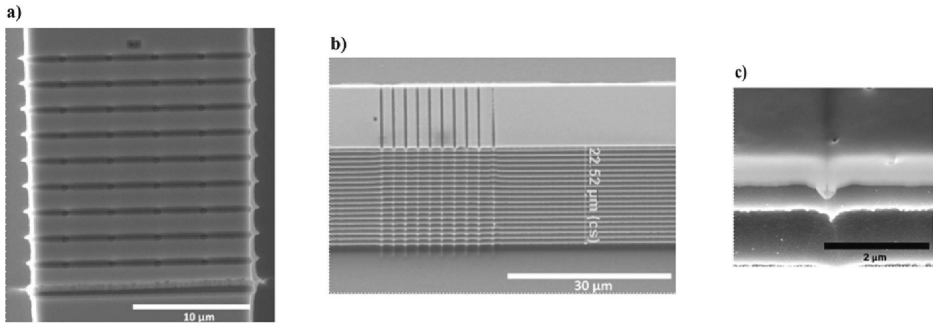

Figure 5.4. **a)** Planar top view and **b)** tilted SEM images of nanochannels and PM traps. **c)** End of open nanochannel after DRIE etch of inlet and outlet microfluidic channels.

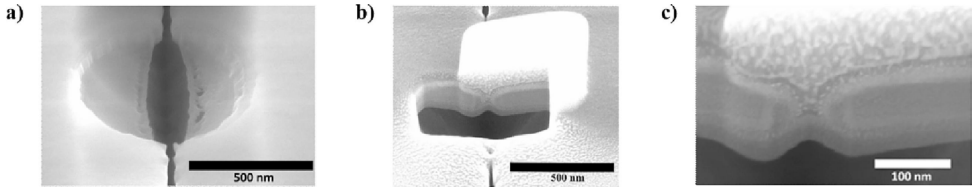

Figure 5.5. SEM-FIB images of **a)** PM trap (titled view); **b)** cross-section of buried part of nanochannel after step 20 (Figure 5.1) followed by platinum deposition, which was used to verify if the channel was open; and **c)** nanochannel closure (zoomed image of b).

5.2.2 PM deposition

The thus fabricated device can receive PM patches with controlled localization and orientation by TNCA. [14] PM deposition and proton pumping must be performed in a liquid environment. Therefore, channels must be prefilled before PM deposition and maintained filled throughout the experiments. Because PMs could only be deposited after the nanochannel filling and the TNCA deposition process requires top access to the PM traps, we could not close the device using a polydimethylsiloxane (PDMS) sheet or via anodic bonding of a cover glass. Thus, filling by pressure was not possible, and we aimed to fill the nanochannels by capillary action. However, surface tension hindered the filling of the device with an aqueous liquid. To decrease the surface tension, we used a 1:3 (V/V) ethanol/Milli-Q water mixture. Filling of nanochannels was observed using a fluorescent dye at micromolar concentrations (Figure S5.3, SI). Because ethanol can interfere with the

bR photocycle, [20] we immersed the substrate in Milli-Q water after filling the nanochannels to dilute the ethanol to negligible levels before the PM deposition. Moreover, TNCA requires reduced ion concentration and a PM density suitable for tracking. [21] Therefore, we did not use any buffered solution for the PM deposition.

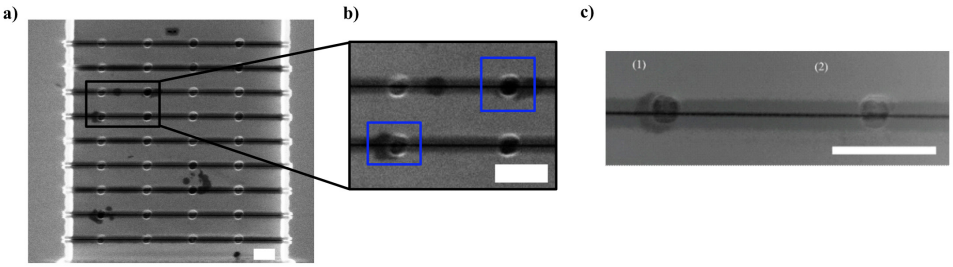

Figure 5.6. SEM images of **a)** device field after deposition of PMs; **b)** 500-nm PM traps, with deposited PMs (dark patches), indicated by blue rectangles; **c)** 500-nm traps from another field **c)-(1)** with deposited PM (dark patch) and **c)-(2)** without deposited PMs. Scale bar: 2 µm.

Finally, we deposited a drop of WT PM at the surface of the chip, and we performed the PM deposition by TNCA. The PM traps of our substrates have a layer of Al_2O_3 at the bottom because it controls the orientation of PM patches with its slightly positive charge in aqueous media. [14] From the SEM image displayed in Figure 5.6a, we identified the presence of darker gray, rounded material on the Al_2O_3 surface of the traps in 5 out of the 36 traps inspected. This observation leads us to infer that certain Al_2O_3 traps were coated with PMs (Figure 5.6b). The visualization of Al_2O_3 material in SEM presents challenges, including surface charging, which can result in distorted or blurry images. Consequently, our ability to visualize PM on such media is compromised. Figure 5.6c) displays two traps in a field following PM deposition: one featuring a PM patch (Figure 5.6c-(1)) and another without any such patch (Figure 5.6c-(2)). This observation highlights the presence of material concentrated in distinct traps. We conclude that we designed a device that can receive PM patches with controlled localization.

5.2.3 Deposition of functionalized PMs with dye (PM-pHrodo)

Our next step is to develop a strategy for measuring PM pumping within our nanochannel network. To achieve this, we aim to integrate a sensor into the system that preserves the integrity of the PMs. This advancement will enable precise control of nanoscale localized proton gradients using our device.

As an initial step in this study, we used fluorescence microscopy (FM) to detect the presence of PM and measure proton pumping in individual PM patches on a flat substrate. To achieve this, PMs were functionalized with pHrodo, a pH-sensitive dye that increases fluorescence intensity as the medium becomes more acidic.

We selected the pHrodo™ iFL STP red ester dye (pHrodo) as a pH-sensitive fluorescent dye for its specificity in detecting pH changes. The pHrodo derivative, containing an amino-reactive group, has a pKa of approximately 6.8. This amino-reactive group enables covalent attachment to surface with amino groups, facilitating stable surface bonding. [22,23] The rationale behind employing amino-reactive dyes lies in their reactivity with the side chains of some of the amino acids in the bR peptide chain. pHrodo has been utilized, for example, in the functionalization of amino-functionalized beads, [24] nanoprobes, [25] and cells [26,27] to facilitate the detection of pH within these environments. The intensity of pHrodo amplifies by 1000% as the pH decreases from 8.0 to 4.0, showcasing its effectiveness in acidic environments. [28,29] The operational characteristics of pHrodo include excitation and emission maxima at approximately 560 nm and 585 nm, respectively, allowing for detection using standard tetramethylrhodamine isothiocyanate (TRITC) filter. Optimal excitation for the pHrodo dye is achieved with green light, which aligns well with the preferred wavelength for PM pumping activity. [30]

The substrates employed in these experiments were prepared as follows: PM patches, dispersed in an aqueous medium, were incubated with the amino-reactive pHrodo derivative. Following incubation, these modified PMs were subsequently coated on an Al_2O_3 surface, as it is for our device traps. To check the functionalization of PMs with pHrodo and evaluate their pumping activity, a drop of Mili-Q water (pH 7.0) or a buffer solution at pH 4.0 (0.10 M acetic acid/0.02 M sodium acetate buffer) was added at the top of the substrates, and fluorescence measurements were undertaken.

Proof-of-concept functionalization of PMs with pHrodo

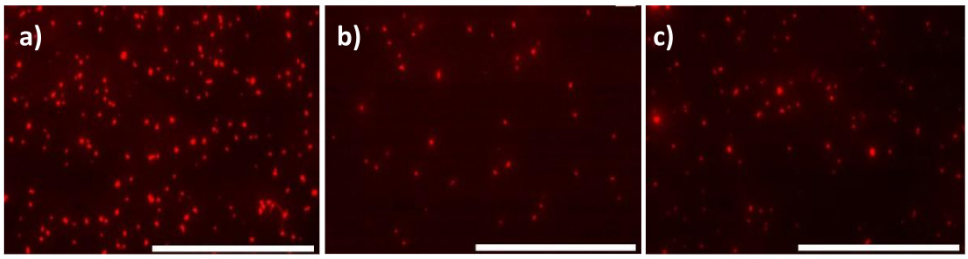

Figure 5.7. Fluorescence images (TRITC filter) of PMs functionalized with pHrodo deposited on an Al_2O_3 substrate with a drop of aqueous buffer at pH 4.0. **a)** Wild-type PM, **b)** C-His_{10}-tag PM, **c)** N-His_{10}-tag PM. Data were obtained from 500 ms exposure time images and 60x objective lens. The scale bar represents 100 µm.

Initially, we confirmed the successful functionalization of PMs with pHrodo, applying this process to WT PM (Figure 5.7a), as well as on two genetically modified variants: C- His_{10}-tag PM (Figure 5.7b) and N-His_{10}-tag PMs (Figure 5.7c). Any native fluorescence of PMs, if present, is not sufficient for imaging with standard fluorescence-based techniques. [3,14] As a result, we anticipate that dye-free PM patches will not exhibit fluorescence. As shown in Fig. 5.7, for all types of PM-pHrodo deposited on surfaces, we observed red

ellipsoids around 1 µm, indicating that these bright objects correspond to individual PMs functionalized with pHrodo. This result proves that all three PM types used in this study could be functionalized with the pHrodo dye.

Measuring PM pumping patch activity using FM

After functionalization, our next step was to determine whether we can study the proton activity of PMs while they are functionalized with pHrodo. For that, we tracked the background-corrected fluorescence intensity (BCFI) variation under different exposure conditions for all PM patch types, as illustrated in Figure 5.8 for neutral non-buffered medium and Figure 5.9 for acidic buffered medium. BCFI variation over time was determined by averaging signals from PM patches and subtracting background fluorescence values. Further details on data processing can be found in the SI.

The substrate underwent exposures to green light, with each exposure lasting 500 ms. The intervals between exposures were varied, set at 30, 20, 10, and 5 seconds. Each interval sequence was maintained for a duration of 10 minutes. We expected that the slope of the fluorescence signal would rise proportionally with shorter intervals between light exposure. This assumption is founded on the reasoning that shorter intervals result in more frequent exposure of the sample to light within a given time.

Measurement of PM patch pumping activity in neutral non-buffered media

The BCFI of all PM patch types in non-buffered neutral medium increased linearly over time, as depicted in Figure 5.8, indicating active pumping detected by the attached dye. Raw fluorescence signals and background details are provided in Figure S5.5, SI. Regression analysis in Table 5.1 examined light exposure intervals, showing increased slopes with shorter intervals from 20 to 5 s. The coefficient of determination (COD) for all PM types and intervals confirms a robust linear relationship between time and BCFI. We conclude that exposing PMs to 500 ms of light at intervals shorter than 20 seconds enhances the proton pumping rate. For the 30-second interval, we observed unstable initial values, and a lower COD compared to the other time intervals.

We aimed to convert fluorescence counts into pH values. Equation (1) was used to translate fluorescence values into pH at different time points

$$(-0.64 \pm 0.03) \times pH_{PMpHrodo} + 5.44 \pm 0.20 = \frac{I_{PMpHrodo}}{I_{pH7}} = \text{BCRFI} \quad (1)$$

where I_{pH7} is the BCFI of a target area at pH 7.0 and time = 0 s; $I_{PMpHrodo}$ is the BCFI intensity at a particular time; and $pH_{PMpHrodo}$ is the pH value at this specific time. The background-corrected ratio FI (BCRFI) is the ratio of $I_{PMpHrodo}$ to I_{pH7}, representing the mathematical relationship between FI and pH: a more pronounced BCRFI indicates a lower pH. The dataset for this Equation was taken from Dolman et al. [29] It assumes that the pHrodo intensity linearly

increased from basic to acidic media. The detailed linear regression used for finding this Equation is described in Figure S5.8, SI.

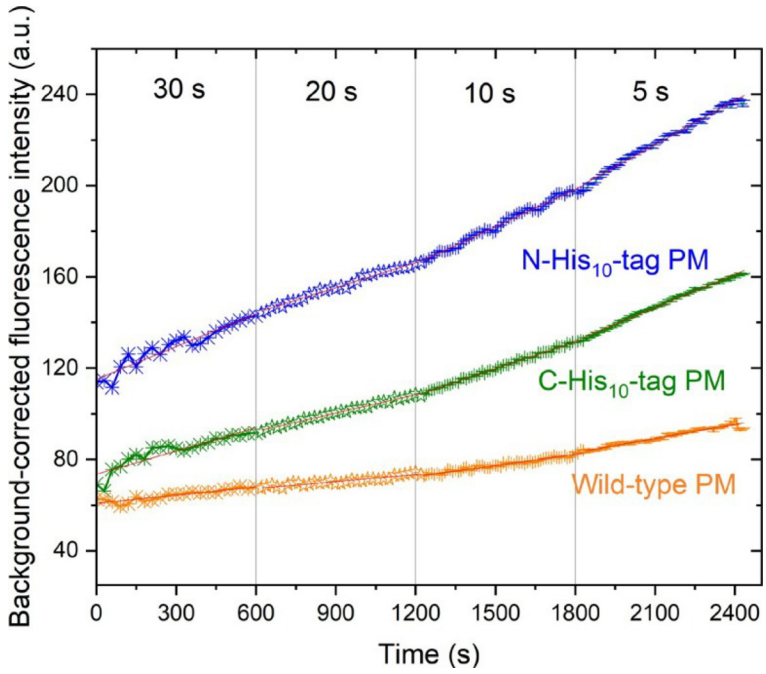

Figure 5.8. Background-corrected ratio fluorescence intensity of PM functionalized with pHrodo over time in Milli-Q water (pH 7.0). Data were obtained with 500 ms exposure time images using a TRITC filter and a 60x objective lens. Orange: wild-type PM. Green: C-His_{10}-tag- PM. Blue: N- His_{10}-tag-PM. The red lines represent linear fit for respective PM data.

Table 5.1. Linear regression of background-corrected fluorescence over time of time-lapse measurement of PM-pHrodo in Milli-Q water. COD = coefficient of determination.

	C-His_{10}-tag PMs		N-His_{10}-tag PMs		Wild-type PMs	
Time interval	**Slope**	**COD**	**Slope**	**COD**	**Slope**	**COD**
30 s	0.034 ± 0.003	0.83	0.048 ± 0.003	0.92	0.012 ± 0.001	0.84
20 s	0.027 ± 0.001	0.99	0.037 ± 0.001	0.99	0.010 ± 0.001	0.88
10 s	0.039 ± 0.000	0.99	0.054 ± 0.001	0.99	0.016 ± 0.000	0.95
5 s	0.048 ± 0.000	0.99	0.064 ± 0.001	0.99	0.020 ± 0.000	0.94

Table 5.2. Background-corrected fluorescence intensity (BCFI), background-corrected ratio fluorescence intensity (BCRFI) and calculated pH from time-lapse measurements of PM-pHrodo patches at MiliQ water (pH 7.0). The pH values were obtained from the fluorescent intensity applied to Equation (1).

	C-His_{10}-tag PMs			N-His_{10}-tag PMs			Wild-type PMs		
Time (s)	**BCFI**	**BCRFI**	**pH**	**BCFI**	**BCRFI**	**pH**	**BCFI**	**BCRFI**	**pH**
0	69.2	1.00	6.94	113.9	1.00	6.94	62.7	1.00	6.94
600	91.6	1.32	6.45	143.0	1.25	6.53	68.1	1.09	6.81
900	100.5	1.45	6.23	154.7	1.36	6.36	69.4	1.11	6.77
1200	108.7	1.57	6.06	165.7	1.46	6.20	74.5	1.19	6.64
1500	119.4	1.72	5.81	180.0	1.58	6.00	77.4	1.24	6.57
1800	131.3	1.89	5.54	197.1	1.73	5.75	83.2	1.33	6.43
2100	146.8	2.12	5.18	217.8	1.91	5.45	88.1	1.41	6.31
2400	159.6	2.30	4.90	237.5	2.09	5.17	98.0	1.56	6.06

Assuming the initial pH of the medium was approximately 7.0, equivalent to that of Mili-Q water, we calculated pH values for pHrodo-functionalized patches over time using Equation (1). The results, presented in Table 5.2, indicate initial differences in BCFI values among various PM types. Despite the initially higher value and more prominent slope of the linear regression of the N-His_{10}-tag PM data, the C-His_{10}-tag PM type presented the highest BCRFI over time (Figure S5.6, SI), corresponding to a greater pH decrease (ΔpH) of approximately 2.1 units. In comparison, the N-His_{10}-tag PM type showed a decrease of 1.8 units, and WT PMs decreased by approximately 0.9 units by the end of the experiments. These calculated pH values align closely with literature-reported values, typically ranging from ΔpH 0.5 to 2.0. [3,31] Furthermore, the findings suggest that attaching pHrodo to the PM surface may minimally affects the pumping behavior of PM patches.

Measurement of PM patch pumping activity in acidic buffered media

As shown in Figure 5.9, the BCFI of all PM patch types increased over time in a buffered acidic medium. Linear regression analysis (Table 5.3) revealed that genetically modified PMs exhibited non-linear pumping behavior, with poor COD for BCFI values, while WT PMs showed a linear BCFI increase across all light intervals. Interestingly, unlike the data in Table 5.1, Table 5.3 indicates that the slope for WT PMs decreases with shorter light exposure intervals, being highest at the 30-second interval and lowest at the 5-second interval. Raw fluorescence signals from the patches and background are shown in Figure S5.7, SI.

Our results indicate that, in an acidic buffer medium, the pumping activity of WT is enhanced compared to that in a non-buffered aqueous medium. This is demonstrated by the higher ΔBCFI = 2.9 (Table S1, SI) between the start and end of the experiment, relative to both other PM types in acidic medium and the ΔBCFI of WT in non-buffered conditions.

Equation (1) could not be used to measure pH over time for the WT PMs due to the lack of an initial pH reference at t=0. Correlating BCFI with actual pH values is of interest but challenging due to limited control experiments and references. A semi-quantitative approach for studying pH changes in an acidic buffered medium is suggested in the SI.

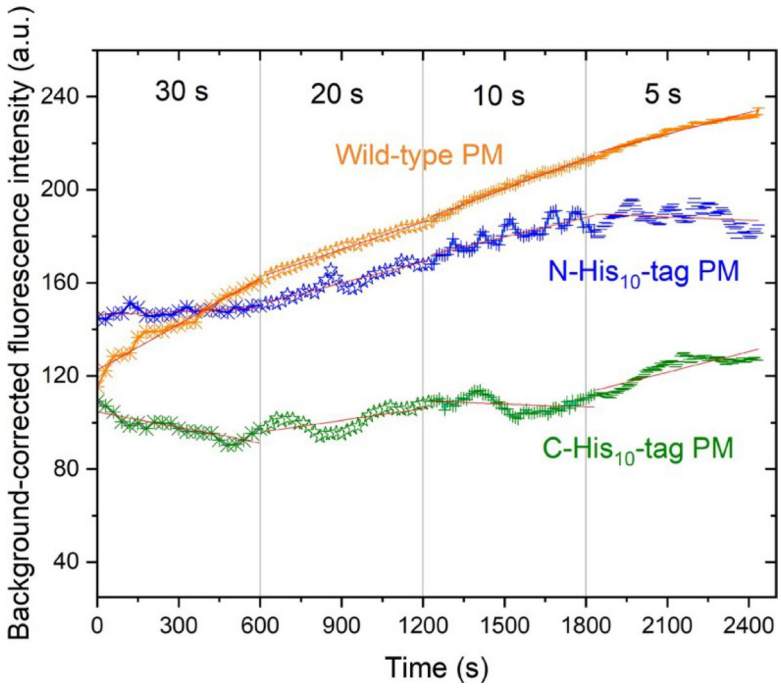

Figure 5.9. Background-corrected ratio fluorescence intensity (BCFI) of PM functionalized with pHrodo over time in buffered acidic medium (pH 4.0). Data were obtained with 500 ms exposure time images using a TRITC filter and a 60x objective lens. Orange: wild-type PM. Green: C-His_{10}- tag-PM. Blue: N-His_{10}-tag-PM. The red lines represent linear fit for respective PM data.

Table 5.3. Linear regression of background-corrected fluorescence intensity (BCFI) over time of time-lapse measurement of PM-pHrodo in buffered acidic media (pH 4). COD = coefficient of determination.

	C-His_{10}-tag PMs		N-His_{10}-tag PMs		Wild-type PMs	
Time interval	**Slope**	**COD**	**Slope**	**COD**	**Slope**	**COD**
30 s	-0.022 ± 0.003	0.72	0.006 ± 0.002	0.32	0.066 ± 0.003	0.96
20 s	0.017 ± 0.003	0.47	0.030 ± 0.002	0.87	0.039 ± 0.001	0.99
10 s	-0.004 ± 0.002	0.06	0.028 ± 0.002	0.71	0.044 ± 0.001	0.98
5 s	0.029 ± 0.002	0.75	-0.005 ± 0.002	0.35	0.030 ± 0.001	0.96

In this study, PM-pHrodo patches coated onto SiO_2 surfaces were excluded from examination due to an adherence failure, which precluded the generation of fluorescent signals from SiO_2-coated PM-pHrodo surfaces. Conversely, it was documented that PMs,

in the absence of pHrodo conjugation, exhibit the capacity to adhere to both SiO_2 and Al_2O_3 surfaces. [14] This observed divergence in adhesion properties between PM-pHrodo and non-functionalized PMs may be ascribed to the augmentation of negative charge on the PM surface following pHrodo conjugation.

Such an increase in surface charge is likely to induce repulsion from SiO_2 surfaces, which are recognized for exhibiting a negative surface charge within aqueous environments. [14] The use of PM-pHrodo in our nanochannel device is advantageous, as we expect PM deposition to occur exclusively in the Al_2O_3 traps, without unintended deposition elsewhere.

Initial Explanations of the results

The differences in pHrodo attachment to the PM surface and the variations in ΔpH across different PM types remain unclear. Additionally, the impact of charge distribution following functionalization with pHrodo has not been fully assessed. We hypothesize that the surface charge of the PMs remains unaffected by pHrodo functionalization, as previous studies suggest that pHrodo attachment does not alter the charge characteristics of amino-silanized surfaces. [24] The nature of the pHrodo functionalization—whether covalent or ionic—has yet to be determined.

Experimental observations revealed the following: (1) pHrodo attachment: pHrodo was detected on all PM types, with the strongest initial BCFI observed in the N-His_{10}-tag PM. The WT and C-His_{10}-tag PMs showed almost identical initial BCFI. (2) Pumping activity: differences in pumping activity between the PM types were minimal, with the C-His_{10}-tag PM exhibiting slightly more activity. The WT PM showed less pronounced pH changes over time compared to the genetically modified PMs. (3) Response in acidic buffer: in an acidic buffer (pH 4.0), genetically modified PMs displayed a non-linear response to green light, while WT PMs showed a significant pH increase under green light exposure.

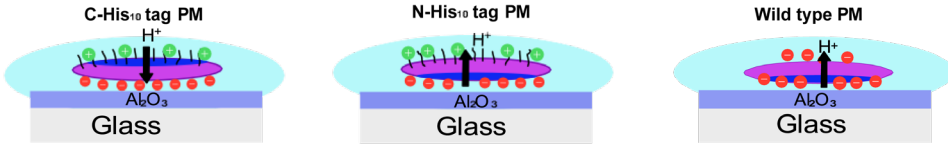

Figure 5.10. Illustration of charge distribution between Al_2O_3 surface and PM in aqueous media for C-His_{10}-tag, N-His_{10}-tag, and wild-type PMs. For each PM type, the pump orientation is demonstrated. Purple, navy blue, and light blue areas represent PMs, cytoplasmatic side of PMs, and aqueous media, respectively.

Before taking initial conclusions, it is important to consider the charge distribution of PM and their pumping orientation. Both are presented in Figure 5.10. Al_2O_3 imparts a mildly positive surface charge in an aqueous environment. [32,33] WT PMs possess fragments with a net negative charge on both sides of the membrane due to the amino acid residues on the bR surface and the PM lipid acidity, while His-tag_{10} peptide sequences confer a positive

charge on the designated side of the PM (C-terminus or N-terminus). [34] C-His_{10}-tag PMs pump protons preferentially from the substrate–PM interfacial layer across the membrane towards the PM-aqueous interfacial layer due to an asymmetric surface charge on the cytoplasmic side, resulting in a substrate- oriented proton gradient. In contrast, N-His_{10}-tag PMs exhibit an extracellular side asymmetric charge, creating a substrate-averse proton gradient. Above pH 5, WT PMs show a more negative surface charge density on the cytoplasmic side, [35] aligning their orientation with N-His_{10}-tag PMs.

The following conclusions can be drawn from these observations. **(1) Extracellular side charge and pHrodo attachment:** the extracellular side charge likely influences pHrodo attachment to the PMs. When the extracellular side charge is more positive, as with the N-His_{10}-tag PM, pHrodo attachment is more substantial. In contrast, both the C-His_{10}-tag and WT PMs exhibit similar fluorescence intensities due to their negatively charged extracellular side surfaces. **(2) Pumping activity and PM orientation:** in the C-His_{10}-tag PM, protons accumulated beneath the PMs, opposite to the orientation observed in the N-His_{10}-tag and WT PMs. This explains the slightly more substantial pumping activity (larger ΔpH) observed for this PM in a neutral pH medium. However, pumping activity was detected in all PM types, suggesting that pHrodo was attached to both sides of the PM, allowing for detection of pumping activity. As PM-pHrodo could not be attached to SiO_2 surfaces, conclusions regarding the efficiency of pumping activity in relation to surface charge and orientation cannot be drawn. **(3) Acidic conditions and histidine ionization:** the variability in pumping activity under acidic conditions can be attributed to the ionization of His_{10}-tag molecules, which is influenced by solution pH and the local pKa of histidine residues. [36] Factors such as burial depth and interactions with neighboring residues contribute to this variability, explaining the inconsistent pumping activity observed in genetically modified PMs under acidic buffered conditions.

In conclusion, the pHrodo sensor effectively detects pumping activity in all PM types, regardless of orientation. However, the relationship between pumping orientation, surface charge, and pumping efficiency remains inconclusive. Despite this limitation, PM-pHrodo represents a promising tool for detecting and studying PM pumping in aqueous, non-buffered media.

5.3 Conclusions

Hybrid devices prepared by micro- and nanofabrication with integrated biological building blocks are promising architectures for energy harvesting, spatiotemporal control of chemical gradients and thus for manipulating chemical reaction networks locally. We use a fabrication method based on a combination of t-SPL, etching methods, ALD and photolithography to prepare devices with buried nanochannels on silicon substrates. The maskless overlay capabilities of t-SPL facilitate the fabrication of deposition sites for functional membrane patches on local nanochannel openings. The combination of etch cycles and ALD offers the opportunity to control the dimensions of the buried nanochannels, whereas the materials used for ALD control the surface chemistry and surface potential of the channels and of

the deposition sites. Inlet and outlet ports integrated with the nanochannels were created using photolithography and DRIE, and the filling of nanochannels was demonstrated by fluorescence detection.

As a demonstrator for the integration of a biological building block, we used WT PM patches as light-triggered proton pumps. The PM patches were deposited onto the selected sites by nanofluidic confinement. The developed device can be potentially used to control the transport of protons and to study their role in nanoscale compartments, as well as in other practical applications that benefit from a mechanically robust and simple fabrication process. The strategies developed in our study represent important tools for fabricating 3D device systems, e. g., the fabrication of connected microreactors with multiple channels crossing in 3D.

Furthermore, we initiated the development of a simplified methodology using pHrodo dyes to quantify proton pumping within our device. Our findings show that PM patches functionalized with pHrodo active ester can carry an internal pH sensor. This sensor works effectively when PMs are in a neutral pH medium. Further progress is needed to refine this approach, including conducting control experiments with PMs and assessing the impact of buffers with varying pH levels on PM-pHrodo-coated substrates. Once these refinements are made, PM pumping can be measured using a straightforward setup and methodology.

Moving forward, the next step involves depositing PM-pHrodo patches using TNCA into our 3D fabricated device. We anticipate several advantages from employing PM-pHrodo patches for orientation-controlled PM deposition. These patches offer a direct means to detect PM presence on traps concurrently with TNCA deposition. Moreover, immediate analysis of proton pumping activity post-deposition allows us to assess deposition efficiency while maintaining functional pumping capability.

5.4 References

(1) Gadsby, D. C. Ion Channels versus Ion Pumps: The Principal Difference, in Principle. *Nature reviews Molecular cell biology* **2009**, 10 (5), 344–352.

(2) Xiao, K.; Schmidt, O. G. Light-Driven Ion Transport in Nanofluidic Devices: Photochemical, Photoelectric, and Photothermal Effects. *CCS Chem* **2022**, 4 (1), 54–65. https://doi.org/10.31635/ccschem.021.202101297.

(3) Stoeckenius, W.; Lozier, R. H.; Bogomolni, R. A. Bacteriorhodopsin and the Purple Membrane of Halobacteria. *Biochimica et Biophysica Acta (BBA) - Reviews on Bioenergetics* **1979**, 505 (3–4), 215–278. https://doi.org/10.1016/0304-4173(79)90006-5.

(4) Feng, Y.; Zhu, W.; Guo, W.; Jiang, L. Bioinspired Energy Conversion in Nanofluidics: A Paradigm of Material Evolution. *Advanced Materials* **2017**, 29 (45), 1702773. https://doi.org/10.1002/adma.201702773.

(5) Xiao, K.; Chen, L.; Chen, R.; Heil, T.; Lemus, S. D. C.; Fan, F.; Wen, L.; Jiang, L.; Antonietti, M. Artificial Light-Driven Ion Pump for Photoelectric Energy Conversion. *Nature communications* **2019**, 10 (1), 74.

(6) Al-Aribe, K. M.; Knopf, G. K.; Bassi, A. S. Fabrication of an Optically Driven pH Gradient Generator Based on Self-Assembled Proton Pumps. *Microfluidics and nanofluidics* **2012**, 12 (1), 325–335.

(7) Gonçalves, R. P.; Agnus, G.; Sens, P.; Houssin, C.; Bartenlian, B.; Scheuring, S. Two-Chamber AFM: Probing Membrane Proteins Separating Two Aqueous Compartments. *Nat Methods* **2006**, 3 (12), 1007–1012.

https://doi.org/10.1038/nmeth965.

(8) Wang, D.; Wang, Y.; Li, H.; Han, Y.; Hu, P.; Ma, K.; Sheves, M.; Jin, Y. Photoactivated Bacteriorhodopsin/SiN x Nanopore-Based Biological Nanofluidic Generator with Single-Protein Sensitivity. *ACS nano***2022**, 16 (1), 1589–1599.

(9) Boekhoven, J.; Poolman, J. M.; Maity, C.; Li, F.; Van Der Mee, L.; Minkenberg, C. B.; Mendes, E.; Van Esch, J. H.; Eelkema, R. Catalytic Control over Supramolecular Gel Formation. *Nature Chem* **2013**, 5 (5),433–437. https://doi.org/10.1038/nchem.1617.

(10) Gupta, P.; Vermani, K.; Garg, S. Hydrogels: From Controlled Release to pH-Responsive Drug Delivery. *Drug discovery today* **2002**, 7 (10), 569–579.

(11) Ort, D. R.; Parson, W. W. Flash-Induced Volume Changes of Bacteriorhodopsin-Containing Membrane Fragments and Their Relationship to Proton Movements and Absorbance Transients. *Journal of Biological Chemistry* **1978**, 253 (17), 6158–6164. https://doi.org/10.1016/S0021-9258(17)34593-3.

(12) Eroğlu, I.; Aydemir, A.; Türker, L.; Yücel, A. M. Photoresponse of Bacteriorhodopsin Immobilized i Polyacrylamide Gel Membranes. *Journal of membrane science* **1994**, 86 (1–2), 171–179.

(13) Wang, H.; Deng, C.; Xiao, C.; Liu, L.; Liu, J.; Peng, Y.; Yu, B.; Qian, L. Fast and Maskless Nanofabrication for High-Quality Nanochannels. *Sensors and Actuators B: Chemical* **2019**, 288, 383–391.

(14) Ruggeri, F.; Schwemmer, C.; Stauffer, M.; Nicollier, P. M.; Figueiredo da Silva, J.; Bosshart, P. D.; Kochems, K.; Fotiadis, D.; Knoll, A.; Wolf, H. Placement of Biological Membrane Patches in a Nanofluidic Gap With Control Over Position and Orientation. *Advanced materials interfaces* **2022**, 9 (23), 2200941.

(15) Nam, S.-W.; Lee, M.-H.; Lee, S.-H.; Lee, D.-J.; Rossnagel, S. M.; Kim, K.-B. Sub-10-Nm Nanochannels by Self-Sealing and Self-Limiting Atomic Layer Deposition. *Nano letters* **2010**, 10 (9), 3324–3329.

(16) Howell, S. T.; Grushina, A.; Holzner, F.; Brugger, J. Thermal Scanning Probe Lithography—A Review. *Microsystems & nanoengineering* **2020**, 6 (1), 1–24.

(17) Ryu Cho, Y. K.; Rawlings, C. D.; Wolf, H.; Spieser, M.; Bisig, S.; Reidt, S.; Sousa, M.; Khanal, S. R.; Jacobs,T. D. B.; Knoll, A. W. Sub-10 Nanometer Feature Size in Silicon Using Thermal Scanning Probe Lithography. *ACS Nano* **2017**, 11 (12), 11890–11897. https://doi.org/10.1021/acsnano.7b06307.

(18) Rawlings, C.; Duerig, U.; Hedrick, J.; Coady, D.; Knoll, A. Nanometer Control of the Markerless Overlay Process Using Thermal Scanning Probe Lithography. In 2014 *IEEE/ASME International Conference on Advanced Intelligent Mechatronics*; IEEE, **2014**; pp 1670–1675.

(19) Laermer, F.; Urban, A. MEMS at Bosch–Si Plasma Etch Success Story, History, Applications, and Products. *Plasma Processes and Polymers* **2019**, 16 (9), 1800207.

(20) Kikukawa, T.; Araiso, T.; Shimozawa, T.; Mukasa, K.; Kamo, N. Restricted Motion of Photoexcited Bacteriorhodopsin in Purple Membrane Containing Ethanol. *Biophysical journal* **1997**, 73 (1), 357–366.

(21) Fringes, S.; Holzner, F.; Knoll, A. W. The Nanofluidic Confinement Apparatus: Studying Confinement Dependent Nanoparticle Behavior and Diffusion. *Beilstein Journal of Nanotechnology* **2018**, 9 (1), 301–310.

(22) HECHT, K.; WiELAND, F.; JAENICKE, R. The Cell Surface Glycoprotein of Halobacterium Halobium. *Physico-Chemical Characterization in the Absence and Presence of Salt*. **1986**.

(23) Fisher, K. A.; Yanagimoto, K.; Stoeckenius, W. Oriented Adsorption of Purple Membrane to Cationic Surfaces. *Journal of Cell Biology*, 1978, 77, 611–621.

(24) Hirose, H.; Maekawa, M.; Ida, H.; Kuriyama, M.; Takahashi, Y.; Futaki, S. A Noncanonical Endocytic Pathway Is Involved in the Internalization of 3 Mm Polystyrene Beads into HeLa Cells. *BiomaterialsScience* **2022**, 10 (24), 7093–7102.

(25) Arppe, R.; Näreoja, T.; Nylund, S.; Mattsson, L.; Koho, S.; Rosenholm, J. M.; Soukka, T.; Schäferling, M.Photon Upconversion Sensitized Nanoprobes for Sensing and Imaging of pH. *Nanoscale* **2014**, 6 (12), 6837–6843.

(26) Lindner, B.; Burkard, T.; Schuler, M. Phagocytosis Assays with Different pH-Sensitive Fluorescent Particles and Various Readouts. *Biotechniques* **2020**, 68 (5), 245–250.

(27) von Kaeppler, E. P.; Wang, Q.; Raghu, H.; Bloom, M. S.; Wong, H.; Robinson, W. H. Interleukin 4Promotes Anti-Inflammatory Macrophages That Clear Cartilage Debris and Inhibits Osteoclast Development to Protect against Osteoarthritis. *Clinical Immunology* **2021**, 229, 108784.

(28) pHrodo™ Dyes for Amine Labeling. https://www.thermofisher.com/order/catalog/product/br/en/P36010 (accessed 2023-01-06).

(29) Dolman, N. J.; Kilgore, J. A.; Davidson, M. W. A Review of Reagents for Fluorescence Microscopy of Cellular Compartments and Structures, Part I: BacMam Labeling and Reagents for Vesicular Structures.

Current protocols in cytometry **2013**, 65 (1), 12.30. 1-12.30. 27.
(30) Schenkl, S.; Zgrablić, G.; Portuondo-Campa, E.; Haacke, S.; Chergui, M. On the Excitation Wavelength Dependence of the Fluorescence of Bacteriorhodopsin. *Chemical Physics Letters* **2007**, 441 (4–6), 322–326. https://doi.org/10.1016/j.cplett.2007.04.086.
(31) Renthal, R.; Lanyi, J. K. Light-Induced Membrane Potential and pH Gradient in Halobacterium Halobium Envelope Vesicles. *Biochemistry* **1976,** 15 (10), 2136–2143.
(32) Hinterdorfer, P.; Dufrêne, Y. F. Detection and Localization of Single Molecular Recognition Events Using Atomic Force Microscopy. *Nature methods* **2006**, 3 (5), 347–355.
(33) Ben Ismail, M.; Carreiras, F.; Agniel, R.; Mili, D.; Sboui, D.; Zanina, N.; Othmane, A. Application of APTES-Anti-E-Cadherin Film for Early Cancer Monitoring. *Colloids and Surfaces B: Biointerfaces* **2016**, 146, 550–557. https://doi.org/10.1016/j.colsurfb.2016.06.048.
(34) Stauffer, M.; Hirschi, S.; Ucurum, Z.; Harder, D.; Schlesinger, R.; Fotiadis, D. Engineering and Production of the Light-Driven Proton Pump Bacteriorhodopsin in 2D Crystals for Basic Research and Applied Technologies. *Methods and protocols* **2020**, 3 (3), 51.
(35) Fisher, K. A.; Yanagimoto, K.; Stoeckenius, W. Oriented Adsorption of Purple Membrane to Cationic Surfaces. *The Journal of cell biology* **1978**, 77 (2), 611–621.
(36) Chaudhury, S.; Ripoll, D. R.; Wallqvist, A. Structure-Based pKa Prediction Provides a Thermodynamic Basis for the Role of Histidines in pH-Induced Conformational Transitions in Dengue Virus. *Biochemistryand biophysics reports* **2015**, 4, 375–385.

5.5 Supplementary information

This section describes the methods used to produce and analyze the device reported in this Chapter. Unless otherwise stated, all chemicals and solvents were purchased from Sigma-Aldrich.

5.5.1 Device fabrication

Thermal scanning probe lithography (t-SPL) and reactive ion etching (RIE)

4-inches silicon wafers with 500 µm thickness were used to fabricate the nanochannels. A 50 nm thick silicon oxide layer was grown by thermal oxidation and characterized using ellipsometry. The wafer was diced into 8 mm × 8 mm-sized chips. For the t-SPL process, 55 nm thick polyphthalaldehyde (PPA) (Allresist) thermal resist was spun onto the chips from 5% anisole solution, and then soft baked at 110°C for 1 min. t-SPL was performed in our homemade system, which is described in detail elsewhere. [1] The t- SPL tool can locally remove the resist (PPA) using a tip that can be heated to several hundred degrees centigrade. The lines were written in the resist to a depth of 45 nm, a nominal width of 58 nm (5 pixels), and length of 20 µm (1700 pixels). No development was needed. The pattern was transferred from PPA into the SiO_2 layer on the substrate using RIE (Oxford Plasmalab 80). As etchant CHF_3 (20 sccm) plasma was used for 10 min, at 15 mTorr and 100 W radio frequency (RF) power. Subsequently, Si was etched isotropically to form the nanochannels. Here, a mixture of SF_6 (80 sccm) + Ar (80 sccm) plasma was used for 2 min, at 100 mTorr and 40 W RF power. Finally, O_2 plasma at 600 W for 7 min was used to remove the remaining PPA resist.

Atomic layer deposition (ALD) and plasma-enhanced chemical vapor deposition (PECVD)

To deposit conformal films of Al_2O_3 and SiO_2, a R-150 ALD (Picosun Sunale, Finland) and a FlexAL ALD (Oxford Instruments, United Kingdom) were used for deposition, respectively. In the Al_2O_3 deposition, we used trimethylaluminum, $Al_2(CH_3)_6$ (TMA), and H_2O as precursors, at a substrate temperature of 250°C. One cycle of Al_2O_3 ALD consisted of precursor pulsing (1 s), vacuum (3 s), Ar purging (3 s), vacuum (3 s), O_2 plasma (RF power 120 W, 7 s), and vacuum (3 s). For the ALD of SiO_2, the substrate temperature was 300°C. We used tris (dimethylamino)silane (3DMAS) and oxygen plasma as SiO_2 precursors. One cycle of SiO_2 ALD consisted of precursor pulsing (1 s), Ar pulsing (5 s), H_2O pulsing (1 s), and Ar purging (5 s). The first Al_2O_3 (10 nm) layer served as a promoting layer of ALD SiO_2 (30 nm). Following the Al_2O_3 deposition (which did not close the nanochannels) and SiO_2 deposition (which closed the nanochannels), we performed PECVD of SiO_2 (100 nm) to completely seal the seam over the nanochannels.

RIE and t-SPL maskless overlay

For the t-SPL maskless overlay, 5% PPA/anisole solution was spun on the substrate to a thickness of 89 nm, and the sample was then soft baked at 110oC for 1 min. The patterns were written into the resist to a depth of 55 nm. RIE was used to remove the PPA and SiO_2 using CHF_3 (12 sccm) + Ar (38 sccm), at 15 mTorr and 100 W RF power for ~6 min.

Photolithography, RIE and deep reactive ion etching (DRIE)

Photolithography was used to create microchannels, which provided a fluidic interface with the nanochannels. One chrome mask was fabricated using a Heidelberg DWL2000 laser writer. The device was first patterned via photolithography (Microchemicals AZ1512 resist and Süss Mask Aligner M6), and a 1.7 μm thick positive photoresist was used to design the inlet and outlet microfluidic channels of the substrate. Only the ends of the nanochannels were exposed to photolithography. After the resist development, multilayer material films under the designed pattern (SiO_2 (130 nm)/Al_2O_3 (10 nm)/SiO_2 (50 nm)/Si (~20 μm)) were etched to connect the microchannels to the end of the embedded nanochannels.

We conducted a four-step RIE process: (1) CHF_3-based RIE for SiO_2 removal using CHF_3 (12 sccm) + Ar (38 sccm), at 15 mTorr and 100 W RF for ~10 min; (2) inductively coupled plasma (ICP)-RIE for Al_2O_3 removal using BCl_3 (40 sccm) + Cl_2 (8 sccm) + Ar (2 sccm), at 6 Pa, 700 W ICP power, and 120 W RF power for ~40 s; (3) RIE using CHF_3 (12 sccm) + Ar (38 sccm), at 15 mTorr and 100 W RF power for ~4 min; and (4) DRIE for Si removal using C_4F_8 (500 sccm) + SF_6 (680 sccm), passivation layer 300 sccm for ~20 min. DRIE was used to fabricate the inlet and outlet ports of these nanochannels. [2]

Subsequently, the substrate was treated with O_2 plasma (600 W, 5 min), followed by acetone and isopropanol sonication, and again with O_2 plasma to remove the photoresist and clean the sample surface. During the device fabrication, the channel entrance was blocked a few times by the redeposition of etching by-products. Therefore, a piranha

solution (H_2SO_3:H_2O_2 3:1, at 25 ◦C) was used to remove by-products. To open the purple membrane (PM) traps, we removed the SiO_2 by CHF_3-based RIE for ~10 min. Finally, the substrate was treated again with O_2 plasma for 5 min.

Nanochannel imaging

The samples for cross sectional- scanning electron microscope (SEM) imaging were prepared on a focused ion beam (FIB)/SEM machine (Helios Nanolab 450S, FEI, Netherlands). We used the standard protocol of a FIB lift-out procedure to prepare the cross-section: the region of interest was locally covered with a protective layer of platinum and then extracted from the bulk using a micromanipulator.

Deposition of PMs

The genetic engineering of biological membrane patches is described elsewhere. [3] For a controlled positioning and deposition of individual PM patches, tunable nanofluidic confinement apparatus (TNCA) was used for the deposition of wild type (WT) PMs on the functionalized substrate. The membrane deposition is described elsewhere. [4]

Functionalization of PMs with pHrodo dye

The PM incubation (C-His_{10}-tag PM, N-His_{10}-tag PM or WT PMs) experiment with pHrodo™ iFL STP red ester dye (pHrodo, Thermo Fisher) was conducted by adding 75 µL of a 0.2 mg.mL^{-1} PM dispersion to a 1.5 mL Eppendorf tube. Subsequently, 167 µL of a 0.3 mM pHrodo solution was added. This solution comprised 5 µL of 10 mM of pHrodo dispersed in dimethyl sulfoxide (DMSO) dissolved in 163 µL of 1 mM of a $NaHCO_3$ buffer at a pH of 8.5. Finally, Milli-Q water was added to achieve a final volume of 300 µL. The material was incubated for 2 h in the dark. After the incubation, the PMs were separated by centrifugation (4000 rpm, 20 min) and washed twice with 0.1 M NaCl solution. Subsequently, PMs were centrifugated and washed ten times with Milli-Q water. The final sample volume was 50 µL, and the supernatant volume was approximately 3000 µL.

PMs were deposited on a 24 × 24 mm^2 diced glass chip with 10 nm of ALD Al_2O_3 on top using 12.5 µL of PM-pHrodo dispersion. Samples were air dried, and the substrates were then rinsed with Milli-Q water and dried with nitrogen gas.

To illustrate the functionalization of PM-pHrodo and its pumping mechanism, a droplet of Milli-Q water or a buffer solution adjusted to pH 4.0 (0.10 M acetic acid/0.02 M sodium acetate buffer) was added to the substrates. Subsequently, fluorescence measurements were conducted. PM patches functionalized with pHrodo were imaged on a Nikon Eclipse Ti inverted bright-field/fluorescence microscope CCD camera (Clara camera, ANDOR technology). TRITC (tetramethylrhodamine) filter images were captured every 30 s for 10 min, then every 20 s for 10 min, every 10 s for 10 min, and finally every 5 s for 10 min. Images were captured with an exposure time of 500 ms. During the remaining time, the chip was

in the dark. All images were taken using a 60x magnification lens. The measurement of fluorescence intensity over time for PM-pHrodo patches was conducted using ImageJ.

5.5.2 Fabrication challenges

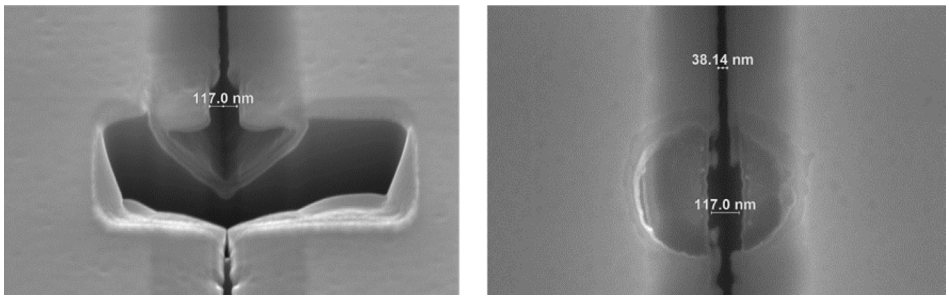

Figure S5.1. Failed sealing of nanochannels by ALD (SiO_2). The SEM tilted view image on the left shows a cross-section of the channel, and the one on the right shows the top view of the channel opening.

In our fabrication, for some devices, control over the t-SPL writing size of 50-nm lines was not always successful (step 2, Figure 5.1). An example is shown in Fig. S5.1. This device was imaged after step 20 (Figure 5.1). We observed the nanochannel being open towards the top both inside and outside the overlay area. Within the trap, the opening has a width of around 117 nm due to the thinner layer of PECVD-SiO_2 present in that area. The size of the nanochannel was self-limited by the Al_2O_3 layer, which does not etch in the presence of CHF_3, used for the SiO_2 etch. Outside the trap, the top opening has a width of around 38 nm.

Nam et al.[5] reported that the shape of channels generated by PECVD was less uniform and circular than those generated by ALD, hindering the production of sub-10-nm dimension nanochannels. When the open channel top was excessively wide after step 3 (Figure 5.1), it could still be sealed by a combination of ALD and PECVD with an adequate thickness. Therefore, the structure of buried nanochannels can be maintained by adopting a thick PECVD layer. Under these conditions, the overlay results were satisfactory.

The variations of the t-SPL writing on PPA can be attributed to the sharpness of t-SPL tips that can vary from one tip to another. Tip deterioration caused by friction and contamination during patterning and imaging depends on the tip and sample materials and affects the heat transfer from the tip to the sample. The attainable resolution generally reduces with tip use. [6]

Influence of duration of silicon etch

The influence of the duration of the silicon etch (Figure 5.1, step 4) was investigated. In Figure S5.2, SEM images showcase nanochannels fabricated with half the silicon etch

time compared to that presented in the main section (1 min etch instead of 2 min). We observed that the nanochannels obtained a circular shape (width: 235.3 nm; height: 132 nm) before ALD, with half the size achieved with a 2 min long etch (Figure 5.2). After ALD, they retained a circular shape (width: 97; height: 67 nm), equivalent to approximately 1/4 of the size achieved with a 2 min long etch (Figure 5.2). A smaller ratio between the SiO_2 opening and Si channel size can provide sub-100 nm buried nanochannels.

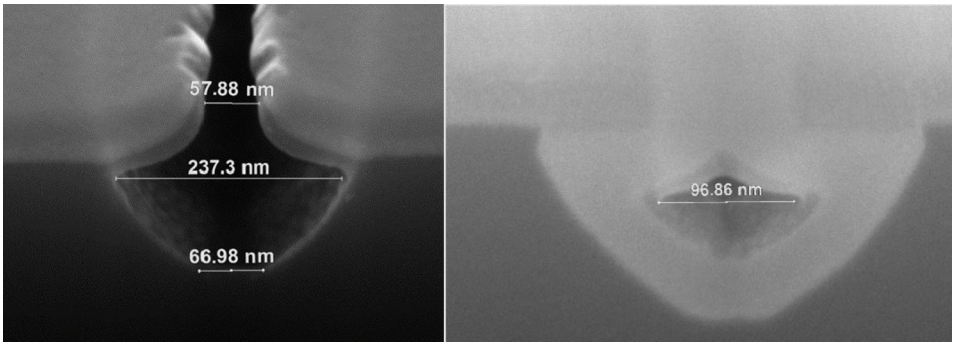

Figure S5.2. Influence of isotropic silicon etch duration on the final size of channels. The SEM image on the left shows the cross-section of the channel for 1 min Si etch time, and the image on the right shows the cross-section of the channel after ALD.

5.5.3 Proof-of-concept: filling of nanochannels

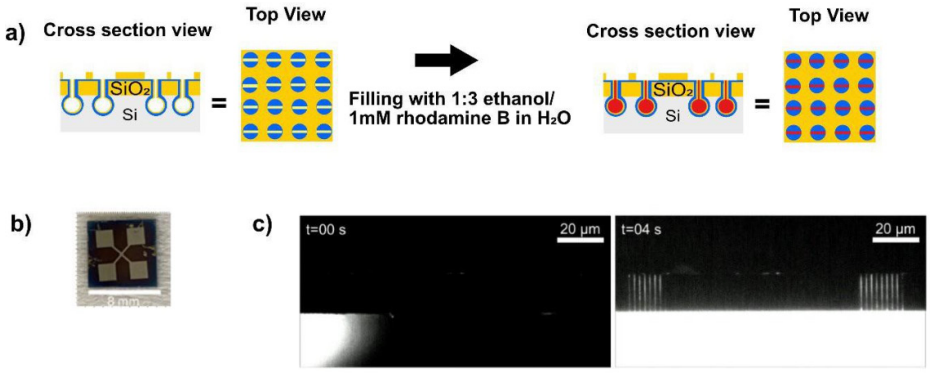

Figure S5.3. a) Scheme of experiment and device design, **b)** photo of device, **c)** fluorescence microscopic images of the device before and after channel filling. Nanochannel length: 20 µm.

We used fluorescence microscopy (FM) to prove the filling of buried nanochannels by capillary action. We observed the nanochannels from the top and filled them through inlet ports from the top to enable the upright microscope to achieve the optimal collection of fluorescent signals. Chips were cleaned by O_2 plasma to render their surface hydrophilic.

We then added a low-surface-tension liquid (ethanol) to a solution containing 1 mM of rhodamine B, a fluorescence dye. After 4.0 s, the nanochannels were filled, as shown by the fluorescence microscopy images in Figure S5.3. A TRITC filter cube was used for imaging, and images were exposed for 20 ms.

5.5.4 Deposition of functionalized PMs with dye (PM-pHrodo)

Data analysis and PM single-patch dye analysis

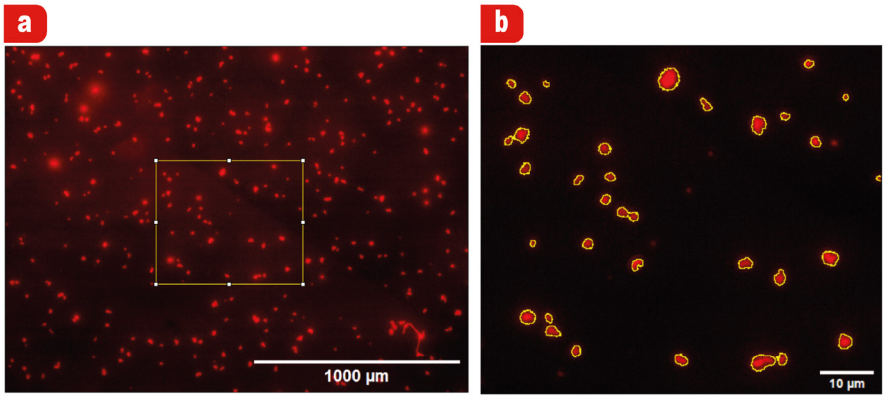

Figure S5.4. Fluorescence images showing **a)** total area of the image with the area of interest (yellow rectangle) and **b)** the cropped area of interest displayed on the right, analyzed using ImageJ.

To investigate the fluorescence intensity (FI) of PM patches functionalized with pHrodo™ iFL STP ester dye (pHrodo), we employed a macro script written in ImageJ for analyzing the FM images. The steps of this process are outlined below:

1. **Region of interest (ROI):** A specific area within an image was selected for analysis. This ROI contained between 20 to 30 PM-pHrodo patches, as exemplified in Figure S5.4.
2. **Threshold method and auto threshold function:** To analyze the images, a threshold method was chosen to distinguish PM-pHrodo patches from the background. The 'Auto Threshold' function was used to automatically set this threshold.
3. **Average signal calculation:** For each PM patch within the ROI, the FI was calculated. This step provided:
   Area count: The area (in arbitrary units (a.u.)) of patches identified.
   Average fluorescence signal (FS): The average brightness of the patches in a.u.
4. **Weighted average intensity (WAFS):** The weighted average FS (WAFS) was calculated by considering the proportion of the area of each patch relative to the total patch area. Larger patches had a greater influence on the average intensity value.
5. **Background subtraction:** To correct any background noise, the background signal was subtracted from the FI values over time.

In summary, the process involved selecting an area of interest in images, applying a

threshold to identify patches, calculating and weighting the fluorescence intensity of those patches, and then correcting the results by subtracting background noise. To calculate the background signal of the stack images, we selected 3 to 4 regions that were free of PMs. We then measured and averaged the intensity of these regions over time.

Figure S5.5 illustrates the variation in FI over time in the neutral non-buffered medium (MiliQ water, pH 7.0). Figure S5.6 represents the background-corrected ratio FI over time in the neutral non-buffered medium. Figure S5.7 illustrates variation in FI over time in the acidic buffered medium (pH 4.0). The shown data at Figure S5.5 and Figure S5.7 incorporates both the weighted average signal from PM patches and the value from areas without PMs (background).

For all PM types in all mediums, we observed lower FI signals from the background compared to the PM. We also observed background values decreased over time, indicating that pHrodo was exclusively attached to the PM surface. Furthermore, an increase in PM FI over time was noted, demonstrating detectable pumping activity under these conditions. Figure S5.6 shows that over time, C-His_{10}-tag PM exhibits the highest BCRFI values, closely followed by N-His_{10}-tag PM. Given the inverse relationship between BCRFI and pH, this suggests that C-His_{10}-tag PM corresponds to lower pH values.

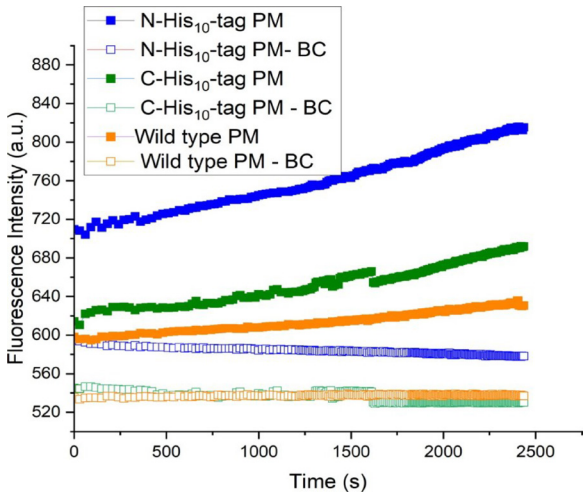

Figure S5.5. FI of PM functionalized with pHrodo over time in Milli-Q water (pH 7.0). Data were obtained with 500 ms exposure time images using a TRITC filter and a 60x objective lens. Orange: wild-type PM. Green: C-His_{10}-tag- PM. Blue: N-His_{10}-tag-PM. Square: FI of PM area. Empty square: background intensity.

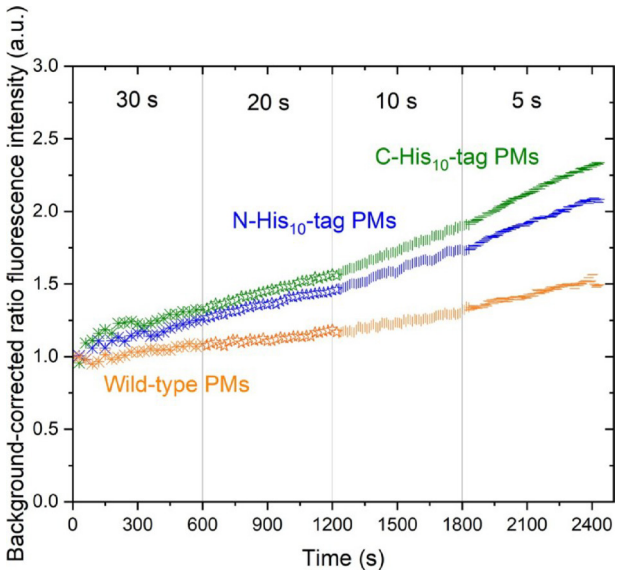

Figure S5.6. Background-corrected ratio Fluorescence intensity (BCRFI) of PM functionalized with pHrodo over time in Milli-Q water (pH 7.0). Data were obtained with 500 ms exposure time images using a TRITC filter and a 60x objective lens. Orange: wild-type PM. Green: C-His_{10}-tag- PM. Blue: N-His_{10}-tag-PM.

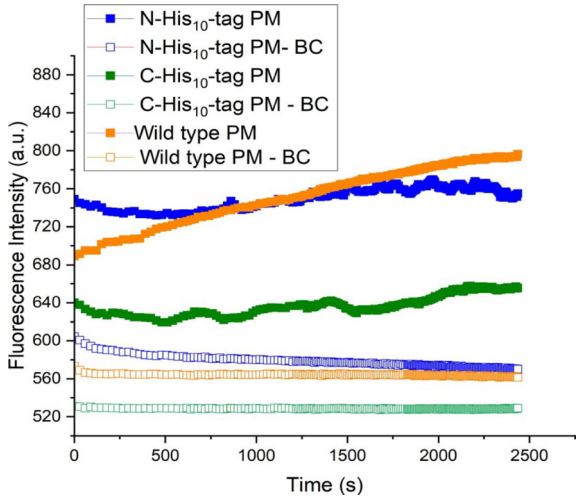

Figure S5.7. FI of PM functionalized with pHrodo over time in a pH 4 buffer. Data were obtained with 500 ms exposure time images using a TRITC filter and 60x objective lens. Orange: wild-type PM. Green: C-His_{10}-tag- PM. Blue: N-His_{10}-tag-PM. Square: FI of PM area. Empty square: background intensity.

pH measurement of PM-pHrodo patches in an acidic buffered medium

The study presented in Table S5.1 aimed to measure pH values for WT PMs in a buffered acidic medium using Equation (1) (main text). The results in Table S5.1 show variations

in background-corrected FI (BCFI) and BCRFI among different PM types and provide pH values. These measurements were based on a reference BCFI ($I_{pHrodo7}$ = 62.7 a.u.) obtained from neutral, non-buffered medium data (Figure 5.8 and Table 5.2). We can rely on this reference value because the PM patches, prior to pHrodo functionalization, were initially stored in non-buffered Milli-Q water, suggesting that the optimal PM-pHrodo reference value was established under these conditions. However, the results are preliminary due to uncertainty about whether the initial pH (t=0) for the buffered acidic medium data (Figure 5.9) was indeed around pH 4.0 or not. In our calculations, we did not account for the initial pH of the PM-pHrodo patches were 4.0.

The C-His_{10}-tag PM type reached a final pH value of approximately 5.6, while the N-His_{10}-tag PM type exhibited a final pH value of 5.8, both lower than those observed in neutral non-buffered medium. However, the final pH for WT PMs decreased by approximately 2.9 units to 2.7, significantly more acidic than at pH 7.0. This indicates that the pumping activity of WT PMs is more pronounced under acidic conditions, likely due to the surplus of protons in the medium.

Table S5.1. Background-corrected fluorescence intensity (BCFI), background-corrected ratio fluorescence intensity (BCRFI) and calculated pH from time-lapse measurements of PM-pHrodo patches at buffered acidic medium (pH 4.0). The pH values were obtained from the fluorescent intensity applied to Equation (1).

	C-His_{10}-tag PMs			N-His_{10}-tag PMs			Wild-type PMs		
Time (s)	**BCFI**	**BCRFI**	**pH**	**BCFI**	**BCRFI**	**pH**	**BCFI**	**BCRFI**	**pH**
0	109.0	1.57	6.06	144.9	1.39	6.32	115.4	1.84	5.63
600	97.3	1.41	6.30	150.3	1.44	6.24	160.8	2.57	4.50
900	95.1	1.37	6.35	158.6	1.52	6.11	175.2	2.80	4.13
1200	108.2	1.56	6.07	167.9	1.61	5.98	185.3	2.96	3.88
1500	105.6	1.53	6.14	184.5	1.77	5.73	201.0	3.2	3.49
1800	110.6	1.60	6.00	184.0	1.77	5.74	212.4	3.38	3.21
2100	126.2	1.82	5.65	192.8	1.86	5.60	225.8	3.60	2.88
2400	126.8	1.83	5.64	180.0	1.73	5.79	232.1	3.70	2.72

Linear regression of pHrodo™ iFL STP ester red dye

To derive a formula correlating pH with the FI from pHrodo, we utilized a dataset reported by Dolman et al. [7] and conducted a linear regression analysis, as depicted in Fig. S5.8. In this dataset, we calculated the relative intensities at each pH (RI_{pHrodo}) and normalized them by dividing them by the relative intensity at pH 7.0, $RI_{pHrodo7}$. The regression achieved a coefficient of determination of 0.99.

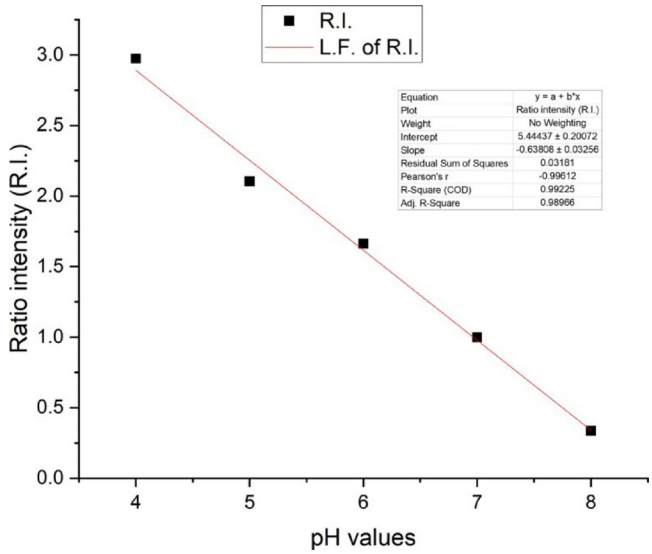

Figure S5.8. Linear regression (L.F.) of pHrodo iFL STP ester red, calculated from data presented at Dolman et al. [7]

5.5.5 Other device applications

We designed another device aiming to fabricate 25 µm deep microreservoir networks below photolithographic magnification with a precise overlay of microreservoirs. The fabrication strategy is shown in Figure S5.9. The length of the microreservoirs varied from 2 to 10 µm, and they were localized on the buried channels. Deep microreservoirs and inlet and outlet channels were etched simultaneously. The maskless overlay was achieved by t-SPL.

As shown in Figure S5.10, the fabrication process for the microreactor network device was inspired by that used for the PM trap device shown in Figure 5.1. In the microreactor network device, the SiO_2 PECVD layer served as a protective coating during the DRIE. The photolithography resist was removed before the DRIE step (step 16, Figure S5.9). Moreover, only ALD SiO_2 was used to close the nanochannels, with the intention of completely exposing the channel in the reactor area during subsequent fabrication stages (step 5, Figure S5.9). A thicker layer of PECVD SiO_2 was deposited on the device (step 6, Figure S5.9), and this layer subsequently functioned as a protective barrier for the buried channels during the DRIE etching. The results indicate that the fabrication approach involving buried nanochannels, elaborately described in Figure 5.1, can be extended to various systems and applications. Following fabrication, we introduced a 500 µm thick glass layer for anodic bonding (step 20, Figure S5.9) to fill the channels using vacuum. The channels were then filled with a 1 mM rhodamine B solution, as evidenced by fluorescence microscopy (Figure S5.11).

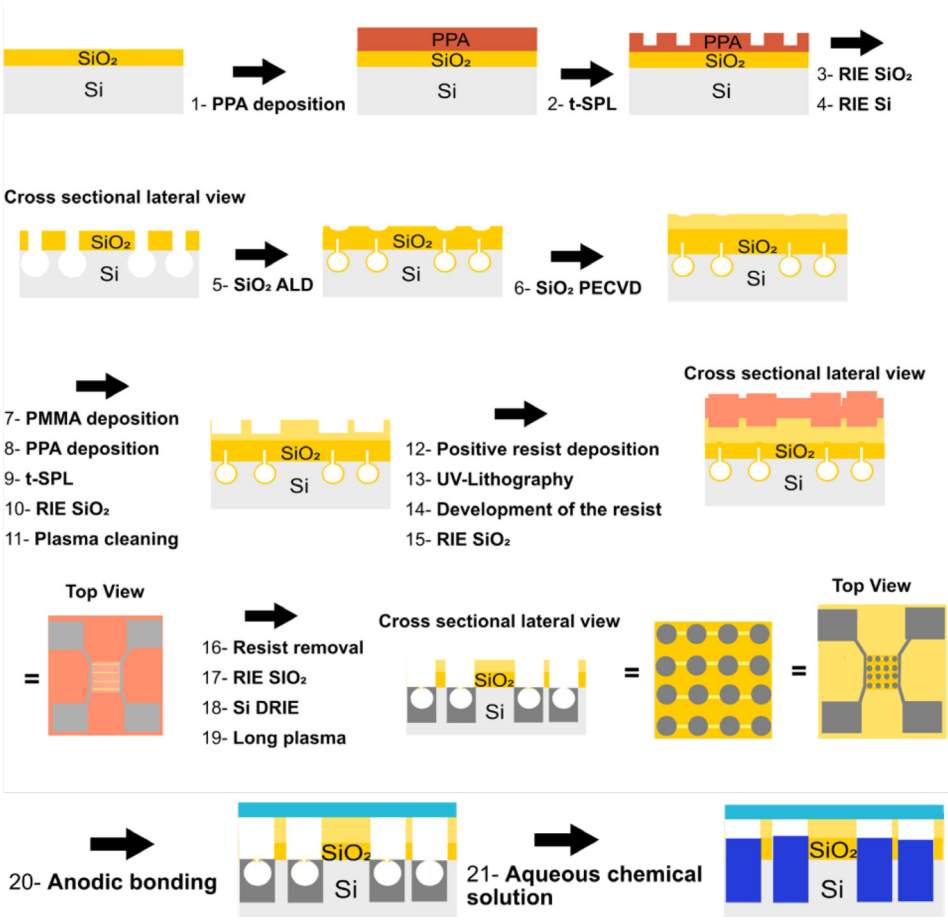

Figure S5.9. Fabrication of microreactor network device. Steps 1 to 4: Fabrication of nanochannels by t-SPL. Step 5: Closure of t-SPL channels by ALD. Steps 6 to 11: Design of microreservoirs by t-SPL. Steps 12 to 15: Fabrication of microchannels and macroreservoirs by photolithography. Steps 16 to 19: Opening of nanochannels on microreservoir area. Steps 20 and 21: Filling of channels with liquid. PPA = Polyphthalaldehyde; t-SPL = thermal scanning probe lithography; RIE = reactive ion etching; ALD = atomic layer deposition; PECVD = plasma- enhanced chemical vapor deposition.

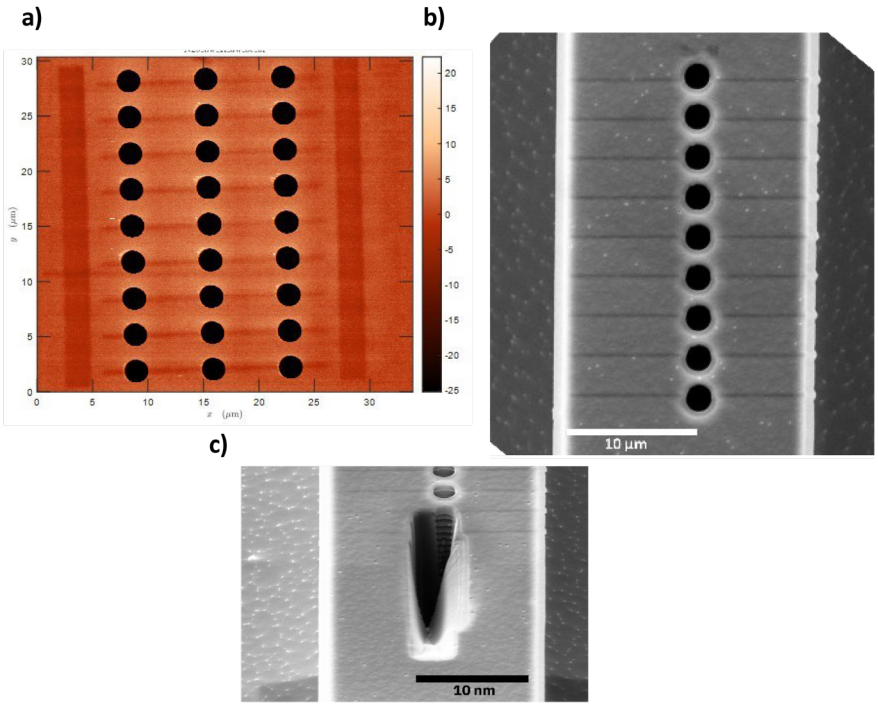

Figure S5.10. a) t-SPL image of maskless overlay pattern. Scale bars indicate writing depth in nanometers. SEM image of **b)** top view of final device, and **c)** FIB cross-section of overlay structure on nanochannels

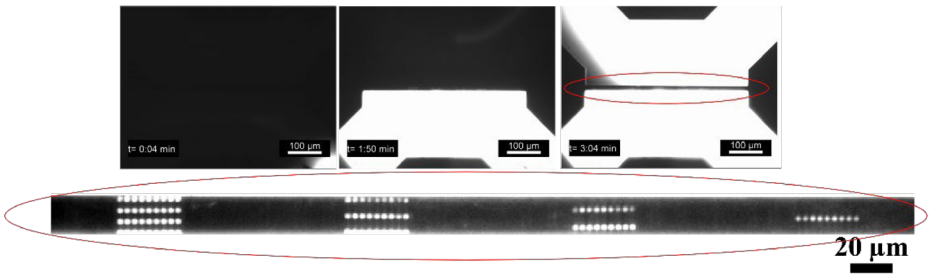

Figure S5.11. Sequence of fluorescence microscopic images of the device before and after channel filling. Nanochannel length: 20 µm. Reservoir depth: 20 µm.

5.5.6 References

(1) Paul, P. C.; Knoll, A. W.; Holzner, F.; Despont, M.; Duerig, U. Rapid Turnaround Scanning Probe Nanolithography. *Nanotechnology* **2011**, 2 2 (27), 275306.

(2) Wu, C.; Jin, Z.; Wang, H.; Ma, H.; Wang, Y. Design and Fabrication of a Nanofluidic Channel by

Selective Thermal Oxidation and Etching Back of Silicon Dioxide Made on a Silicon Substrate. J. *Micromechanics Microengineering* **2007**, 17 (12), 2393.

(3) Stauffer, M.; Hirschi, S.; Ucurum, Z.; Harder, D.; Schlesinger, R.; Fotiadis, D. Engineering and Production of the Light-Driven Proton Pump Bacteriorhodopsin in 2D Crystals for Basic Research and Applied Technologies. *Methods Protoc.* **2020**, 3 (3), 51.

(4) Ruggeri, F.; Schwemmer, C.; Stauffer, M.; Nicollier, P. M.; Figueiredo da Silva, J.; Bosshart, P. D.; Kochems, K.; Fotiadis, D.; Knoll, A.; Wolf, H. Placement of Biological Membrane Patches in a Nanofluidic Gap With Control Over Position and Orientation. Adv. Mater. *Interfaces* **2022**, 9 (23), 2200941.

(5) Nam, S.-W.; Lee, M.-H.; Lee, S.-H.; Lee, D.-J.; Rossnagel, S. M.; Kim, K.-B. Sub-10-Nm Nanochannels by Self-Sealing and Self-Limiting Atomic Layer Deposition. *Nano Lett.* **2010**, 10 (9), 3324–3329.

(6) Howell, S. T.; Grushina, A.; Holzner, F.; Brugger, J. Thermal Scanning Probe Lithography—A Review. Microsyst. *Nanoeng.* **2020**, 6 (1), 1–24.

(7) Dolman, N. J.; Kilgore, J. A.; Davidson, M. W. A Review of Reagents for Fluorescence Microscopy of Cellular Compartments and Structures, Part I: BacMam Labeling and Reagents for Vesicular Structures. *Curr. Protoc. Cytom.* **2013**, 65 (1), 12.30. 1-12.30. 27.

Chapter 6

Networks of microscale chemical oscillators - toward chemical computing

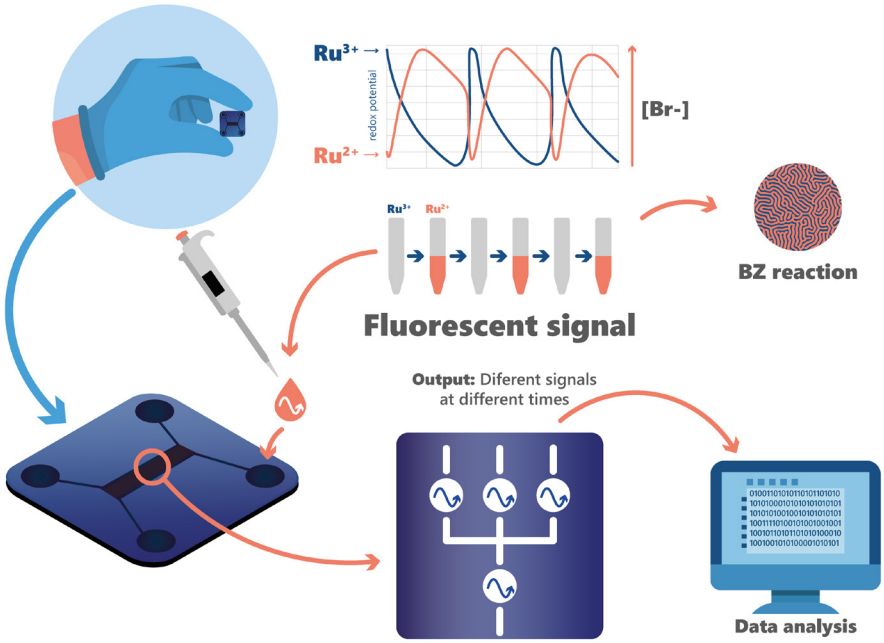

Abstract: This chapter explores the development of chemical computers (CCs) based on information processing by an oscillatory reaction in microscale compartments. We designed and fabricated a diffusion-driven network comprising several sub-100 µm silicon-based microchemical reactors (MCRs) connected by nanofluidic channels. We employed the Belousov–Zhabotinsky (BZ) reaction as oscillatory chemistry in the MCRs. The catalyst of the BZ reaction enabled the visualization of oscillations by fluorescence microscopy. We demonstrated the diffusion-related coupling and synchronization of MCRs. The connecting channels mediated the coupling between compartments, which led to synchronization, an important step in data processing. The results represent an important foundation for the development of scalable chemical computing architectures based on simple molecules.

6.1 Introduction

6.1.1 Unconventional computing

Digital computers execute programmed arithmetic and logical operations and consist of two main components: (1) hardware, the physical elements such as screens, keyboards, and printers that perform tasks as directed by software; and (2) software, the intangible programs and data that provide instructions to the hardware, written in languages like Python or C++ and stored digitally. [1]

As illustrated in Figure 6.1, a computer comprises five primary components: (1) input, where data is received; (2) processing, carried out by the central processing unit (CPU), which includes registers for temporary storage and combinational logic for operations; (3) storage (main memory), used to retain information; (4) the control unit, which manages resources and coordinates hardware and software activities; and (5) output, where results are communicated. These components function through algorithms and binary code (0 and 1), executed via electrical signals within the hardware. [1]

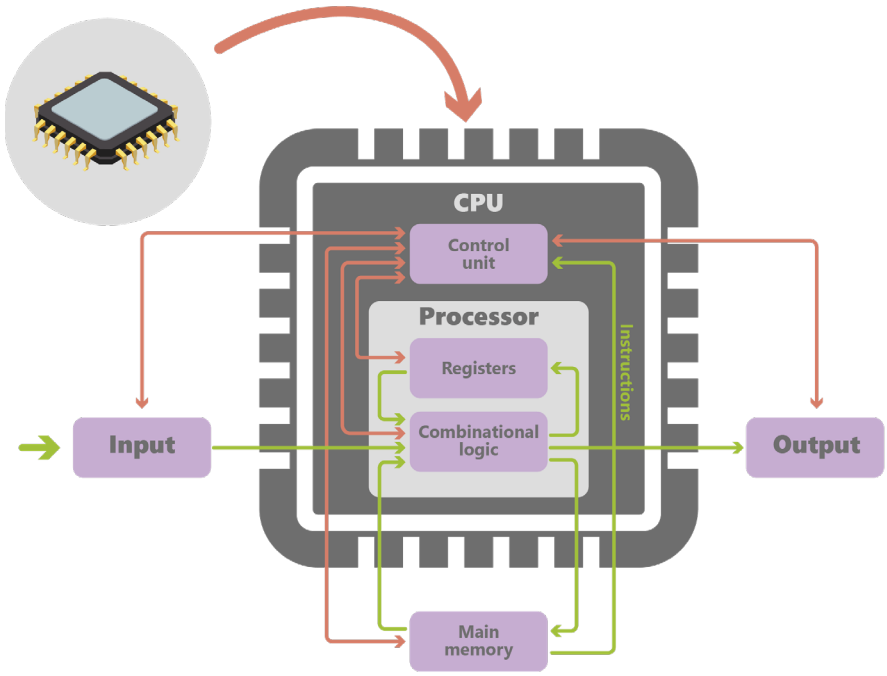

Figure 6.1. Block diagram of a basic computer with a uniprocessor central processing unit (CPU).

Semiconductor technology, primarily based on silicon devices, forms the backbone of modern electronics, including digital computers. [2] Its effectiveness in machine information

processing is primarily attributed to the creation of numerous highly reliable logic gates, which execute logical operations on binary inputs to generate an output. [3] These gates, operated by programmable software, offer extended error-free functionality and can be scaled down to the nanoscale. [2] When integrated into circuits, they enable more complex information processing functions.

Moore's law asserts that the complexity of circuits, and consequently their functionality, doubles in under two years.[2] Undoubtedly, the semiconductor industry has consistently pushed the boundaries to incorporate more transistors onto increasingly compact chips, a trend evident in the evolution of smartphones and microsensors. Additionally, multiprocessor computers have been available for several years, they have reached massive parallelism, which is supposed to solve complex problems. However, the sustained adherence to Moore's Law faces inevitable obstacles. These challenges arise from both physical constraints, such as quantum effects and heat dissipation, and the escalating costs associated with the continuous increase in transistor count on microchips. [2] Furthermore, both data generation and the demand for computing are growing exponentially over time, even more with the development of artificial intelligence (AI). To address the growing demands for computational power, there is a critical need to create new computing primitives, encompassing both hardware and algorithms.

The concept of AI stems from the notion that computers can replicate specific learning abilities akin to those of the human brain. [4] The brain outperforms standard computers in energy efficiency, adaptability, and pattern recognition. It uses minimal power, processes analog signals, [5] and adapts through plasticity. [2] Key features include neurons for signal transmission, synapses for chemical communication, and integrated computation that enables multitasking and collaboration across brain regions. [4] For instance, Microsoft has developed a device that operates according to the principles underlying networks of spiking neurons. The power consumption of this device was roughly four orders of magnitude lower than that of a conventional computer. [6] Therefore, there is high motivation for the development of alternative computing methods that can mimic the brain's functionality. [2]

Unconventional computation (UC) represents a specialized field within interdisciplinary science, and it blends elements of chemistry, physics, mathematics, computer science, nanotechnology, among others. The goal of UC is to reveal and leverage rules and methods that link functional properties with information processing across physical, chemical, and biological systems. This includes designing optimal architectures, developing efficient algorithms, and creating functional prototypes for future-proof computing devices. [7] In a UC, computation occurs when the system is stimulated with input signals, such as oscillations, grounded in coupled oscillator systems across different length scales. UC views the natural progression of time within a spatially distributed environment, the temporal evolution across all regions occurs concurrently, and the algorithms executed are typically characterized by high levels of parallelism. To improve computation through parallelism, a new computing device may incorporate millions or billions of oscillatory units, which must satisfy strict requirements, including low power consumption, high frequency,

programmability, and energy-efficient readout capabilities. Nevertheless, only a limited number of oscillators can meet these specified requirements. [2]

Reaction-diffusion computation based on chemistry-driven devices, also known as chemical computers (CCs), has the potential to fulfill some of these criteria. Chemical computing can be founded on information processing through nonlinear oscillatory chemical reaction networks (CRNs). Chemical substrates have proven effective in implementing computations, [8] making CCs an important category of unconventional computers.

6.1.2 Chemical computing

A chemical computer (CC) is a liquid-based device that executes logical operations through chemical reactions. In a CC, the computation state is defined by the 'collective state' of molecules, determined by their properties and interactions. [9] The key feature of a CC is the spontaneous motion of molecules. In principle, after a CC system is prepared, it does not require external power to operate, except for the thermodynamic necessity of functioning at a finite (room) temperature. This means the system evolves autonomously, without the need for an external influence or explicit wiring. [10]

"CCs" can be observed in nature, such as in the human neural network and in chemical communication, synchronization, and collective behavior among cell colonies. These processes occur through the emission, interdiffusion, and reception of specific messenger molecules, all with minimal energy consumption. [11,12] To emulate nature by developing an 'information processing' system that converts information encoded in reagent concentrations, one approach is to utilize a chemical medium exhibiting highly nonlinear oscillatory behavior, which can integrate incoming signals in a complex way. The next step is to identify non-equilibrium conditions that allow the medium to self-organize into a structure suitable for information processing, such as a product concentration that fluctuates over time. Lastly, factors that alter interactions within the medium, such as introducing additional chemicals or changing reagent concentrations, can be applied to facilitate the learning process, such as the addition of another chemical or the change of concentration of some reagent. In other words, the mechanism which molecular interactions encode and execute algorithms should be clarified. [13] The Belousov–Zhabotinsky (BZ) reaction can be used to match part of these requisites. [14]

6.1.3 Belousov–Zhabotinsky reaction

The BZ reaction is a well-established chemical oscillator, and its mechanism is governed by the interaction between activators and inhibitory feedback loops, and it can generate periodic chemical signals. The BZ reaction is based on the oxidation of an organic compound by bromic acid ($HBrO_3$) [15] mediated by a transition-metal catalyst in an acidic aqueous solution. [16] The BZ reaction consists of two stages: (1) a rapid autocatalytic oxidation of the catalyst by bromate (BrO^-), and (2) a slower reduction of the catalyst by an organic compound, usually malonic acid (MA). During oscillations, the catalyst switches between

two oxidation states that offer several readout possibilities, including color, fluorescence, and redox potential. Moreover, these oscillations can be detected by changes in bromide (Br^-) concentration and/or pH. [15] In the BZ reaction, the intermediate Br^- ion has a crucial function because the system state depends on its concentration. [17] If its concentration surpasses a critical concentration, the catalyst predominantly exists in its reduced state. Conversely, if the Br^- concentration falls below a critical level, an autocatalytic process initiates the production of the activator, $HBrO_2$, and the catalyst switches to its oxidized state. Biochemical oscillators model chemical information [18,19], but are hard to interpret due to complex dynamics. In contrast, the well-understood BZ reaction has documented rate constants.[20] Even though these oscillators have inherent oscillations, external stimuli can modify their phase [11] and amplitude. [21,22]

The oscillation period of a BZ system typically is several tens of seconds (s), [20] which is suboptimal for conventional computation, as the latter operates at significantly higher speeds. Accordingly, researchers have aimed to decrease the BZ oscillation period. A previous study reported that, under specific conditions, changes in temperature and concentration increased the frequency of BZ oscillations by 3–4 orders of magnitude. [23] The BZ reaction exhibited sinusoidal oscillations at elevated temperatures and high concentrations, at frequency of 10 Hz or greater. The study documented the system's complex temporal behavior and proposed pathways for achieving higher frequencies.[23] Another study showed that the frequency cannot increase exponentially, as oscillations eventually cease when the temperature reaches a critical value. [24]

Electrons are faster than ions, and electronic currents outpace chemical diffusion. Electrons are >100,000 times lighter than the atom nucleus, and they travel close to the speed of light. Diffusion is more substantial initially and decays over distance because of its stochastic nature. [25] Then, the potentially high oscillatory speed of BZ reaction is not the central stimulus for creating a BZ driven CC. Instead, the brain's primary functions can be chemically replicated using the BZ reaction with low energy consumption, including (1) nonlinear dynamics and oscillations that forms the basis for simulating processes such as pattern recognition, memory or even decision making; (2) self-organization into evolving dynamic structures or patterns; (3) parallel processing, as the BZ reaction can carry out multiple reactions at once without interference; and (4) information encoding, with the BZ reaction using oscillatory behaviour and chemical interactions to encode information. [26] The interaction between two chemical oscillators can occur through either diffusive coupling or long-range interactions. Long- range interactions, in particular, can be facilitated by mechanisms such as mass exchange regulated by peristaltic pumps, [21] or light pulses. [21,26]

The photosensitive BZ reaction, often catalyzed by $Ru(bpy)_3^{2+}$, is commonly employed to investigate the effects of external perturbations due to its unique photochemical and photophysical properties.[27,28] Variations in both oscillatory period and amplitude have been noted in relation to the applied light intensity. [20] Due to that, light can serve as an attractive alternative input to electricity in our system, as it enables selective and rapid modulation of reaction rates in the BZ reaction. However, an increase in light intensity causes a transition

from large-amplitude periodic oscillations to stable steady states, a phenomenon known as photoinhibition, which limits the use of light for extended durations and high intensities. [20]

Advances have been recently reported towards the use of BZ reaction in information processing [26,29] At the macro scale, researchers have reported a language-recognizing Turing machine based on the addition of aliquots of BZ reagents in a one-pot reactor. [29] Another example features a programmable BZ-based chemical processor in a fluidically-connected reaction array of cells. [30,31] In theoretical study, classification tasks were successfully performed with a reasonable degree of accuracy by training a network of interacting chemical oscillators. [32] However, large reaction volumes require external forces, such as stirring, as diffusion alone cannot ensure uniform molecular distribution. These volumes also demand greater quantities of reactants and result in longer diffusion times, leading to slower computation and reduced energy efficiency, as more chemicals are required per unit of ´processed information´. To address these challenges, the miniaturization of chemical systems has been proposed. [26,33] Microscale systems offer advantages such as faster diffusion, energy efficiency, parallel operations, and enhanced capabilities for complex communication.

6.1.4 Microfluidics for chemical communication

In chemical communication, microfluidic platforms are beneficial for the generation of diffusive-driven reproducible geometrically homogeneous systems and reactors with precisely chemical composition and determined dimensions, all of which can act as microchemical reactors (MCRs). A MCR network comprises microscale reactors (tens to hundreds of microns) housing oscillatory CRNs, such as the BZ reaction. These reactors can communicate by diffusing reaction intermediates, facilitating the spatiotemporal transmission of chemical "information." This process ultimately gives rise to collective behaviors, including coupling and synchronization, which hold potential for advancing complex communication networks. [20]

Studies have demonstrated that networks of chemical micro-oscillators can execute logical operations like AND and OR, [21,34] recognize patterns, make decisions, [35,36] and, in certain cases, exhibit adaptive behavior by responding to external signals. [21,37] Individual compartments can be designed with tailored properties, such as surfactants for emulsions micro-droplets [11] or tailored membranes for liposomes and microspheres. [21,38] However, their multidirectional diffusive interactions and inability to replenish reactants limit functionality. Additionally, in microspheres, ion-exchange resin may degrade under BZ conditions due to oxidation and polymer cross-link rupture.[21]

To enhance the robustness of MCR networks, channels precisely defining diffusive coupling pathways between individual compartments have been used to connect MCRs. Previous study achieved this by arranging MCRs through lithography. [39] Earlier research has demonstrated that wave interactions with complex boundaries support the implementation of path optimization at the microscopic scale. [40] Previous simulation

studies have similarly demonstrated that the geometry of the interconnecting channels between MCRs exerts a greater influence on wave speed and diffusion than the channels' material composition. [41] Further examples of BZ-based chemical micro-oscillators were discussed in a previous review. [21] However, high parallelism and complex synchronization continue to pose limitations. To advance BZ- MCR networks, improvements in the design of the reaction medium are needed. [16] Additionally, the exploration of MCR network architectures with directional diffusive coupling between MCRs is lacking. Difficulties include fabrication strategies, along with the visualization and control of input chemical signals in MCR networks.

To advance the development of a BZ-driven chemical computer, we employed silicon-based chips housing MCR networks with units ranging from tens of microns, containing up to 6000 MCR units. Oscillation visualization was performed with fluorescence microscopy (FM), and wave transmission occurred primarily through diffusion, without the need for electricity or fluidic flow. Our results demonstrate that BZ-MCRs enable high parallelism and complex communication at the microscale, while requiring a minimal amount of reactants. This approach could represent a step toward a BZ-MCR network into a miniature device powered entirely by chemical fuel for chemical computation.

6.2 Results and discussion

Fabricating a chemical medium for thousands of MCRs for long-term operation is complex. Practical CCs require MCR networks with well-defined initial conditions, reliable oscillatory states, and sustained dynamics. The network developed in this study consisted of MCRs connected by nanofluidic channels of varying interconnections and sizes, all containing the same concentration of BZ-CRN reactants. Long-range chemical communication occurred between MCRs over micrometer distances. The study of this phenomenon relies on three main features, namely (1) the use of microfluidics to compartmentalize 'chemical information', (2) stable emission of periodic chemical signals within compartments via the BZ reaction, and (3) appropriate spatiotemporal monitoring of the emitted chemical signals. [38] The input consisted of the initial concentration of BZ reactants and, in certain cases, wave propagation from the microfluidic channels. The output was determined by analyzing the period of oscillations observed in selected MCRs. The transmission of signals through the propagation of waves was propelled by the diffusion of Br_2 and autocatalytic species $HBrO_2$. [20,21] In Section 6.2.1, we discussed the photolithographic fabrication of the BZ-MCR network and how the experiment was executed.

6.2.1 Device fabrication

Silicon, widely used in the semiconductor industry, provides a stable and inert platform for supporting oscillatory BZ reaction. [42] Polydimethylsiloxane (PDMS)-based microfluidic devices, a widely used material in microfluidics, are unsuitable for this study because bromine produced by the BZ reaction is absorbed by PDMS, significantly disrupting oscillatory behavior. [39,41,42] We fabricated miniaturized BZ-MCR networks on silicon using a

two-step photolithography process, as shown in Figure 6.2. The first step was the definition of nanofluidic channels to connect MCRs designed via photolithography (1.5 µm width) and etched (500 nm deep) by inductively coupled plasma– reactive ion etching (ICP–RIE), which provide anisotropic Si etch with smooth walls. [43] The second step was the definition of microfluidic channels (inlet, outlet, and bypass channels) and MCRs (Figure 6.3), which have circular designs with diameters from 5 to 30 µm. MCRs and microfluidic channels were anisotropically etched to a 20 µm depth by deep RIE, which is known as the Bosch process. [44] The bypass channel was designed to extend the duration of oscillations and provide continuous chemical filling in the device. This approach allowed for the precise design of the geometry and size of the MCR networks, the integration of nanofluidic channels with the MCRs, and the creation of distinct feeding channels for fresh reactants and removal of reaction products. To enable the filling of the microfluidic chips by pressure after fabrication on a silicon wafer, we anodically bonded a 500 µm thick glass wafer containing 0.7 mm holes at specific positions. Finally, we diced individual microfluidic chips from the wafer. An image of the chip is shown in Figure 6.3.

The experiment was conducted as follows: first, we pre-filled the microfluidic system with CO_2 at high pressure to prevent air trapping. [45] The microfluidic chip was subsequently installed in the microscope. Following this, all BZ compounds were mixed, and once the first oscillation was observed, the chip was filled with BZ reaction under high pressure. This process enabled the rapid filling of a thousand MCRs and nanochannels, which was monitored in situ via FM. FM measurements were initiated once the filling process was complete. In the experiments conducted, we observed the MCR networks filled with BZ reactants by monitoring the propagation of waves through time-lapse fluorescence images. The process was operated in batch mode, with no continuous or additional input of chemicals after the initial filling of MCRs. For FM measurements, samples were exposed to short light pulses (400 ms) every 1 s. Until the end of this thesis, we could not explore the refilling of our device using bypass channel.

In our experiments, the catalyst of the BZ reaction was a ruthenium bipyridyl complex, $Ru(bpy)_3^{2+}$, which enabled the visualization of oscillations by FM. The Ru complex fluoresces only in the Ru^{2+} state, and it is dark in the Ru^{3+} state. The maximum $Ru(bpy)^{2+}$ absorption occurs at 480 nm. [26] The maximum emission of $Ru(bpy)^{2+}$ occurs at 675 nm. [27] Therefore, the BZ $Ru(bpy)^{2+}$-catalyzed solution periodically fluoresced bright orange when irradiated with blue light, with a high quantum yield and long lifetime. [27] Notably, an intensively illuminated BZ medium typically does not oscillate, as light inhibits oscillations. Under identical initial reagent concentrations, a medium that exhibits oscillatory behavior in darkness transitions to an excitable state under low light intensity and stabilizes into a steady state under strong illumination [27] For this reason, the sample was exposed to light in short pulses during measurement. The light intensity was sufficient to induce fluorescence in the illuminated MCRs while remaining weak enough to preserve periodic oscillations in the MCRs.

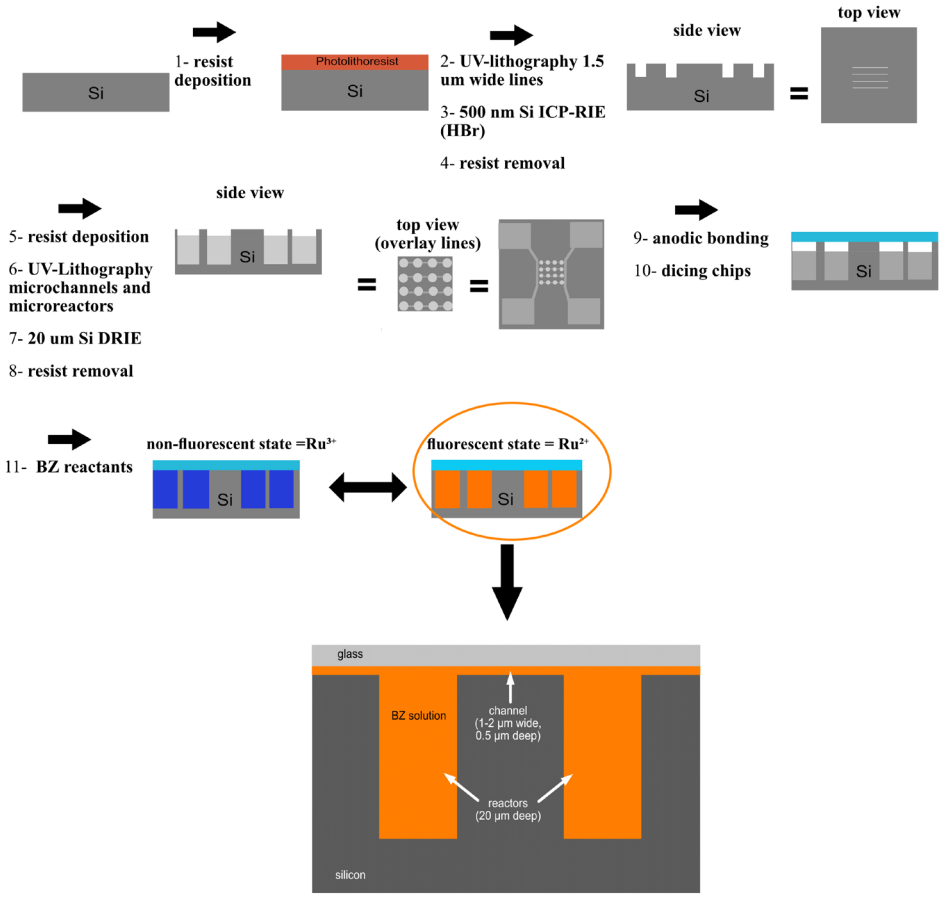

Figure 6.2. Steps for fabrication of BZ-MCR networks. Two photolithographic steps and anodic bonding were conducted at the wafer scale. In the first step, a network of nanochannels was formed. The microreactors, filling, and waste channels were prepared in the second step. RIE = reactive ion etching; ICP–RIE = inductively coupled plasma–RIE; DRIE = deep RIE.

Figure 6.4 illustrates that over 3000 MCRs with diameters ranging from 5 to 15 µm oscillated simultaneously, with the chip housing around 6000 MCRs in total. A mere 3 µL of low-cost reagents sustained the BZ-MCR network, demonstrating the device's reliability, parallelism, and low energy consumption. Fluorescence signals were detected only from MCRs and microfluidic channels, while nanochannels, with a 40-fold shallower depth, exhibited weak fluorescence and were used solely for chemical transport and MCR filling. The discrete nature of the wave's propagation between MCRs and channels was visualized. After the passage of a wavefront, the medium nearly returned to its original state. A trigger wave initiated from the inlet channel led to the formation of a wave along nanochannel-

connected MCRs. Signal offsets in neighboring MCRs reflected variations in oscillator rates and couplings, influenced by distance and size. The amplitude of oscillations slowly decreased over time, ceasing after approximately 50 minutes as the system reached equilibrium. Multiple inputs from waves in the microfluidic channels resulted in outputs—signals in the MCRs— dependent on the geometrical configuration and BZ concentration in each MCR over time. These findings underscore the challenge of optimizing parameters for such "computation" while highlighting the system's robustness in handling multiple wave transmissions simultaneously.

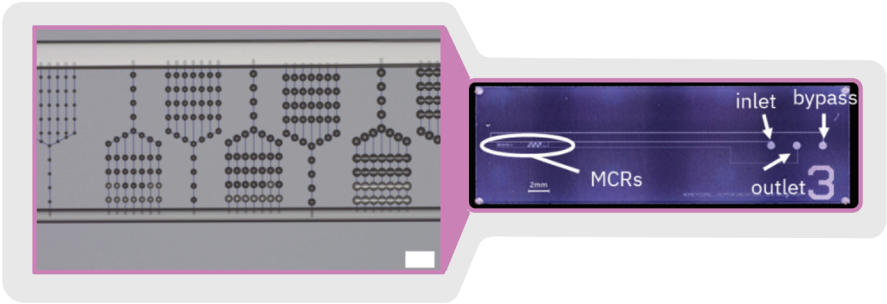

Figure 6.3. The bright-field image on the left shows part of the MCR network during the filling. The scale bar represents 100 µm. The bright-field image on the right shows a 36 × 12 mm chip after step 10 (Figure 6.2). The openings of inlet, outlet, and bypass channels are shown. The scale bar represents 2 mm.

We demonstrated that (1) FM can effectively visualize MCR networks in light-sensitive chemical excitable media; (2) our system enables the design of complex networks of interlinked oscillations with arbitrary arrangements; (3) the CRN operated on chemical waves as a small, chemically driven network without requiring electricity; (4) our BZ- MCR network exhibited significant complexity, enhanced by the increased number of MCRs; (5) the wave transmission time between MCRs on the same line did not affect the wave traveling time between MCRs on other lines, as all operations occurred in parallel. From these statements, we propose that complex information processing can be realized through relatively simple reaction kinetics, provided that the spatial arrangement of reactive regions is carefully designed.[12]

Spatial control over the origin of the wave was lacking in these experiments, with waves randomly initiating simultaneously in multiple MCRs. A more precise data analysis approach is needed to better understand communication between MCRs. For the following discussion, we selected a specific area from time-lapse images containing coupled MCRs with the desired geometry for a detailed study of their oscillatory behavior, although the presented studies remain primarily qualitative. Depending on the amount of air/CO_2 in the inlet and outlet microfluidic channels, it was difficult to control the amount of BZ reactants in these channels. In most situations, the MCRs responded to the trigger signal

when the inlet channel oscillated. When the inlet channel did not oscillate, the triggering of MCRs was determined by their communication with each other. Statistical analysis of the relationship between the size and frequency of MCRs can be done when input is more finely controlled. Moreover, a better time resolution would improve the visualization of oscillations. Regardless, meaningful insights about synchronization, communication, fan-out, and complex communication between MCRs were taken.

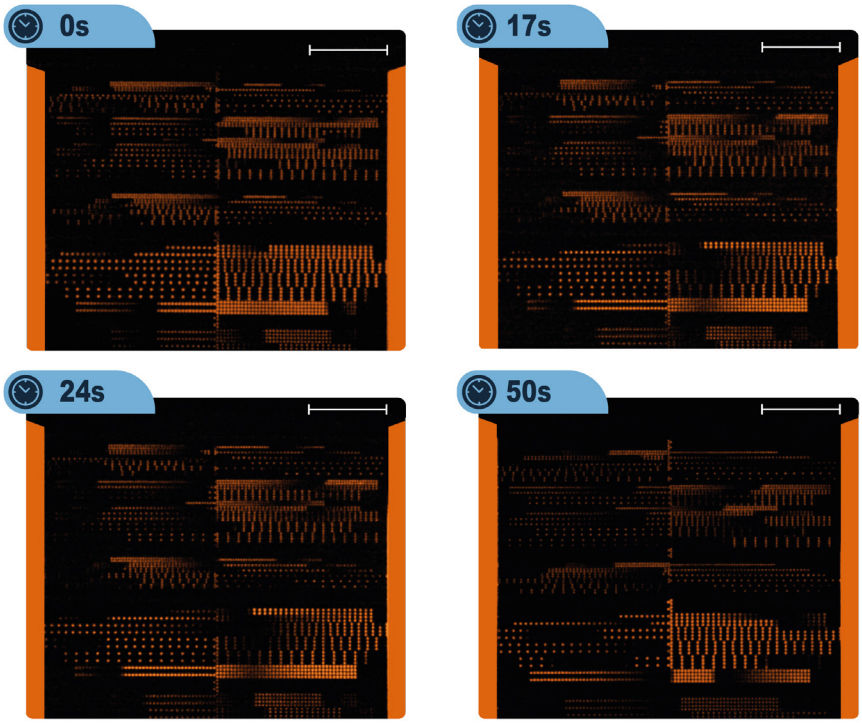

Figure 6.4. Sequence of fluorescence images of MCR networks filled with BZ reactants at different times. Scale bar = 200 µm. Bright orange: low redox potential state of BZ reaction (Ru^{2+}); dark color: high redox potential state of BZ (Ru^{3+}).

6.2.2 Proof-of-concept of MCR communication – MCRs with branching-reactors layout

To employ MCRs in chemical computation, unidirectional diffusive communication between reactors is preferred. Therefore, when analyzing a coupled MCR network, it is crucial to assess how waves are transmitted between MCRs and whether this transmission is influenced by their geometric arrangement. We hypothesized that the wavefront of the BZ reaction propagates between MCRs through diffusion, with the transmission dynamics influenced by their arrangement relative to other MCRs, and the distance from

the wave origin. To validate this, we analyzed the temporal and spatial dynamics of wave propagation within a branched MCR design, where a single nanochannel splits into two, and all channels contain evenly MCRs of identical size (22.5 µm diameter).

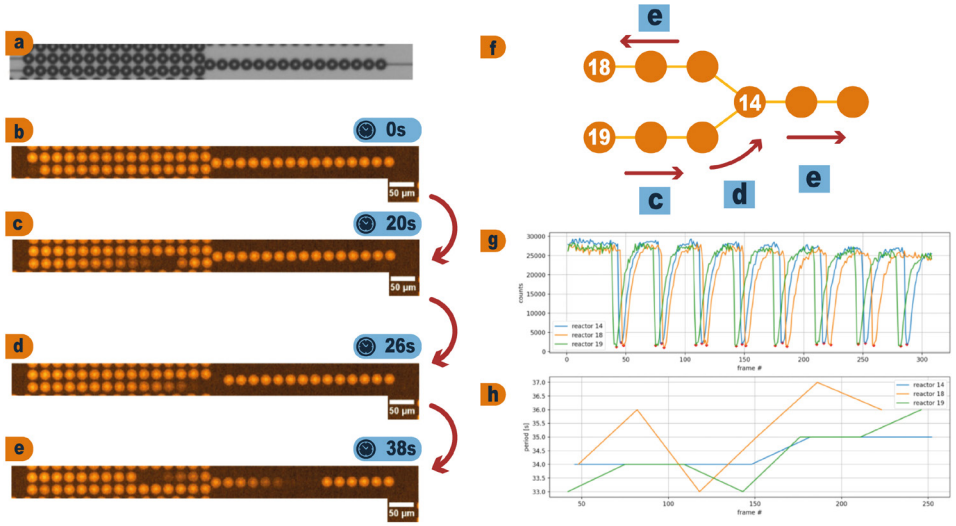

Figure 6.5. Proof-of-concept of communication in an MCR-BZ network. The set of images shows a couple of 22.5 µm diameter MCRs. **a)** Bright-field image of silicon device before filling. **b)** to **e)** Fluorescence images of MCRs at different times. Bright orange: low redox potential state of BZ reaction (Ru^{2+}); dark color: high redox potential state of BZ (Ru^{3+}). **f)** BZ wave direction of images **c)** to **e)**. Graphs illustrate the temporal evolution of **g)** amplitude and **h)** period of MCRs over time. One frame represents 1 s of the experiment.

Figures 6.5b to e show FM images illustrating communication within the MCR network, while Figures 6.5g and h present a semiquantitative study of the oscillatory period and amplitude of selected MCRs. Figure 6.5f illustrates the directionality of the BZ wave as observed in the FM images. As presented in Figure 6.5b, initially, the wave originated in one of the coupled MCR channels. As the wave reached the branching point (Figure 6.5d), it propagated into the two remaining channels (Figure 6.5e). This provided evidence of diffusion-driven wave transmission and directionality between MCRs. Additionally, MCRs '18' and '19' (Figure 6.5f), located at similar distances from the branching MCR (MCR '14'), both exhibited nearly identical oscillation periods of approximately 33-37 s (Figure 6.5h), despite the wave initially propagating through MCR '18'. This observation confirms that oscillation in the MCRs is influenced by their geometric arrangement.

In conclusion, we demonstrate that MCRs communicate via diffusion, with the geometric arrangement playing an important role in the directionality of the diffusion wave from the BZ reaction.

6.2.3 Influence of reactor size – anisometric-reactors layout MCRs

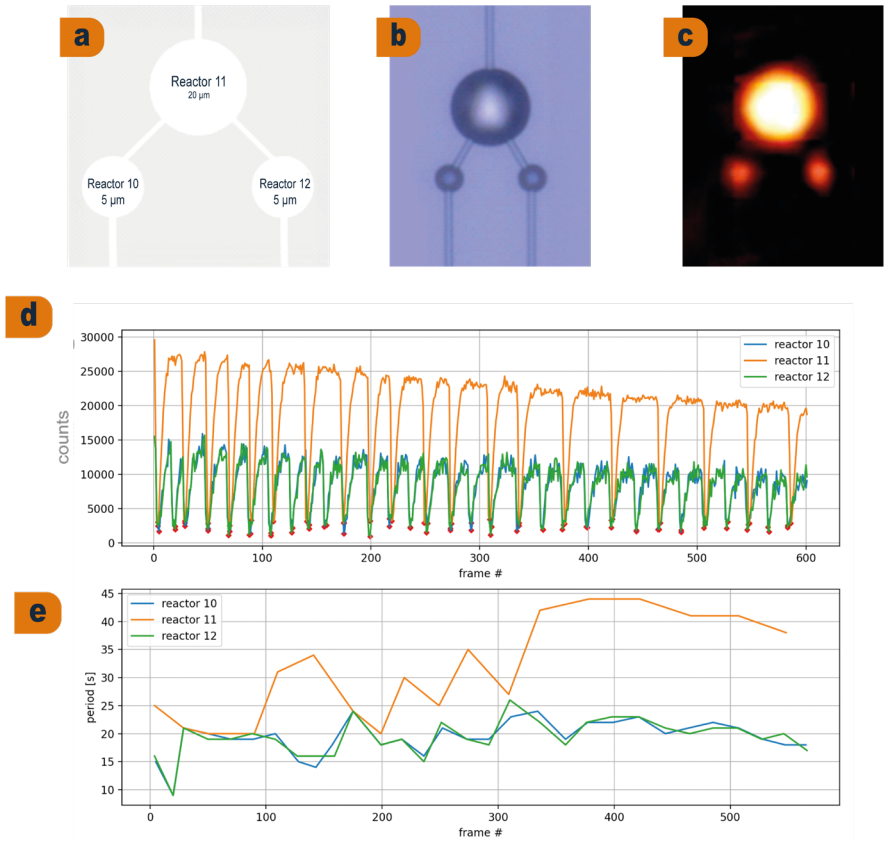

Figure 6.6. Effect of communication among MCRs-BZ network on the oscillation period of different MCR sizes. **a)** MCR design. **b)** Bright-field image of MCR network before channel filling. **c)** Fluorescence image of MCR bright state. Graphs illustrate the temporal evolution of **d)** amplitude and **e)** period of MCRs over time. The scale bar represents 20 µm. One frame represents 1 s of the experiment.

Achieving precise timing and coordination is essential for reliable operation and error correction. We aim to investigate whether synchronization occurs in MCR networks and how it correlates with the size of the MCRs. To this end, we present an anisometric-MCR layout, where a larger MCR is connected to two smaller MCRs. The oscillation period study for MCRs of different sizes is presented in Figure 6.6. We analyzed three MCRs: two with a 5 µm diameter (MCRs '10' and '12') connected to a 20 µm diameter MCR (MCR '11') (Figure 6.6a). Figures 6.6b and c show, respectively, the bright-field and FM images of the MCR network. Figures 6.6d and e present time-lapse data on the amplitude and period of the mentioned MCRs. Period analysis revealed a clear relationship between oscillation period and MCR diameter. After multiple cycles, the larger MCR ('11') oscillated at roughly half the frequency of the smaller MCRs ('10' and '12'). These results show that

the smaller MCRs synchronized to a common frequency, while the larger MCR exhibited a slower final frequency due to its size. This observation, despite identical initial BZ reactant concentrations, can be attributed to the slower diffusion that occurs when the distance over which the molecules must travel is greater, as is the case with larger volumes. Additionally, factors such as light exposure may also play a role, as the BZ reaction with Ruthenium as a catalyst is photoinhibited with increased light exposure. Since larger MCR areas result in greater light exposure per MCR, this may further influence the observed results.

These findings highlight the role of synchronization within the MCR network, which can occur not only among MCRs of the same size but also across MCRs of different sizes. This synchronization was detectable through their intrinsic frequencies, which were related to the diameter of each MCR. It suggests that a system composed of many interconnected units, like MCRs, can reliably synchronize their activities through diffusion. By altering the size and arrangement of the MCRs, their behavior can be controlled to produce specific oscillatory patterns. These oscillations can be influenced by the intrinsic properties of each MCR, such as its volume, as well as the connections between MCRs, including microfluidic channels and neighboring MCRs. Through the manipulation of these factors, the system can recognize or generate distinct patterns of activity within the network.

6.2.4 Parallel transmission of chemical waves - fan-out layout MCRs

Fan-out refers to the capacity of a single logic element to distribute its output signal to multiple subsequent components or devices without compromising functionality or stability. In semiconductor electronics, the number of devices that can be connected to an element is determined by its output current capacity and the input current requirements of the connected components. Each logic gate has a specific capacity for processing input signals and driving output signals. Exceeding this capacity can lead to problems such as signal degradation or improper functionality.

To address the limitations of semiconductor-based computation, which restrict the number of devices that can be connected simultaneously, we investigated a chemically driven fan-out signal by observing the propagation of a chemical wave between channels. We connected one line of MCRs to seven other MCR-containing lines (Figure 6.7a). All MCRs have the same size (25 µm diameter), and the heptafurcation lines contain an equal number of MCRs. Figures 6.7b to d present time-lapse FM images, while Figure 6.7e illustrates the wave propagation, using the FM images as a reference.

We anticipated that wave transmission would be influenced by the geometric arrangement, as well as the number and distance of MCRs from the wave source channel. Fluorescent images in Figures 6.7b to d demonstrate that the network of coupled, synchronizing MCR oscillators can propagate the signal across all seven lines. As expected, the wave propagation along the lines was influenced by the number of MCRs and their distance from the signal source. This is highlighted by the observation that signal from the lines equidistant from the wave source exhibit similar speed (Figure 6.7e). We conclude that the splitting of the

wave in the heptafurcation design of the BZ-MCR network can be successfully achieved, and wave propagation can be controlled by adjusting the distance from the wave source.

These results suggest that wave splitting can be effectively achieved across multiple channels with minimal interference. Therefore, we propose that 3D connectivity could improve the system's fan-out capability, facilitating more complex interconnections between MCRs. This approach allows each MCR to interact with multiple others, improving the network's capacity for complex information processing and synchronization. In Chapter 5 of this thesis, [46] a strategy was introduced for fabricating buried nanofluidic networks. This technique could be extended to the fabrication of 3D BZ-MCR networks. By employing this method, it becomes possible to integrate MCRs at different layers, forming a three-dimensional structure that can increase connectivity and support more complex chemical computation tasks.

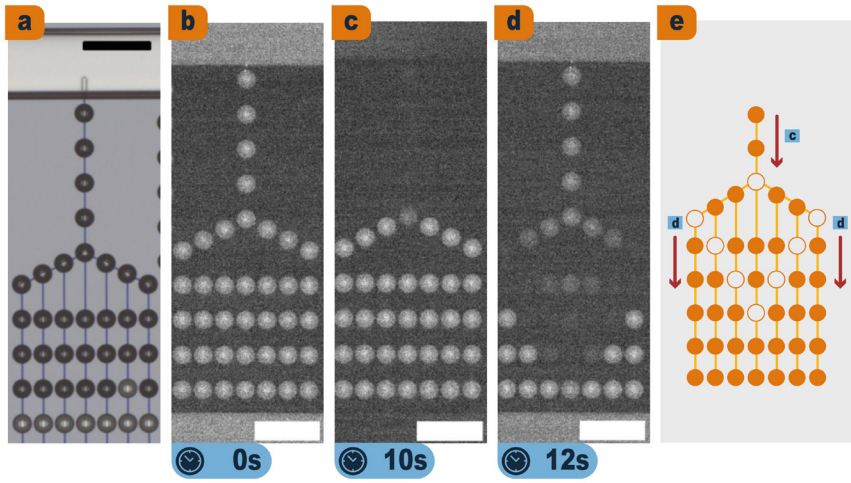

Figure 6.7. Images illustrating the fan-out in an MCR-BZ network with 25 µm diameter MCRs. **a)** Bright-field image of silicon device during filling. **b–d)** Fluorescence images of MCR-network at different times. **e)** Demonstration of BZ wave front of images c and d. Bright color: low redox potential state of BZ reaction (Ru^{2+}); dark areas: high redox potential state of BZ (Ru^{3+}). The scale bar represents 100 µm.

6.2.5 Behavior of complex MCR connections - honeycomb layout MCRs

Essential for applying MCRs to CC is a chemical medium that effectively integrates incoming signals in a non-trivial manner. A method for controlling the coupling strength of MCRs by altering their topographic connections was proposed. Apart from networks of two- and three-coupled active MCRs, the impact on the dynamic modes of a network comprising multiple wave-coupled MCRs in a honeycomb structure was investigated. In this case, the expected outcome remains uncertain; however, we anticipate observing more complex

behavior arising from the intricate geometric arrangements between MCRs.

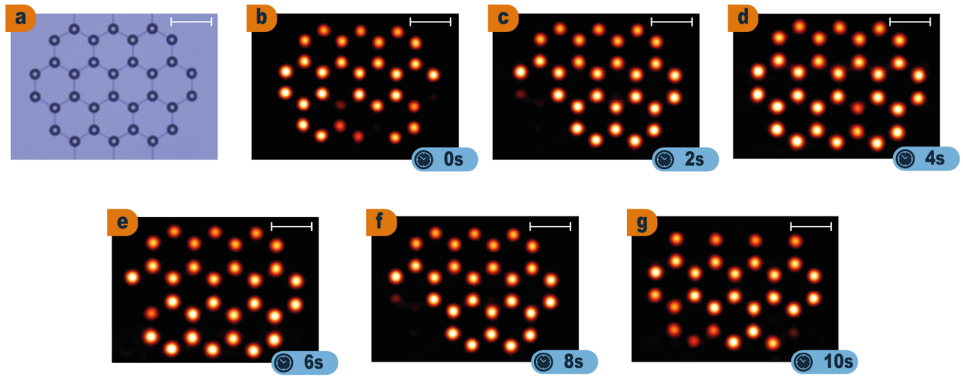

Figure 6.8. Images of a 20 µm honeycomb layout non-triggered MCRs. **a)** Bright-field image of MCRs prior to channel filling. **b)** to **g)** Time-lapse fluorescence images from 0 to 10 seconds. The white scale bar represents 100 µm.

Two types of results were obtained. In the 20 µm coupled MCRs (Figure 6.8), where the inlet channel did not oscillate, the adjustment of coupling strengths led to substantial spontaneous switching among network configurations. FM images in Figure 6.8b to g display six distinct spatial patterns from this design, representing only a subset of the patterns observed in the experiments. Based on this, we suggest that more complex architectures could provide a larger number of states, facilitating the ´processing´ of ´more information`. In the case of honeycomb MCRs triggered by oscillations from the inlet channel, as presented in Figure 6.9b to g, the 20 µm coupled MCRs exhibited uniform wave transmission. Consequently, the oscillations of the MCRs followed the wave originating from the inlet channel, transmitting signals from the MCRs closer to the inlet channels to those farther away. Over time, the MCRs maintained the same sequence of patterns.

Based on these results, we conclude that input signals play a crucial role in determining the oscillatory behavior of complex MCR connections. This highlights a key step toward developing CCs, as the same architecture can produce different outputs depending on the input. When the input is solely from BZ-MCR diffusion among MCRs, the oscillations exhibit a complex pattern, whereas an external diffusive wave source results in a comparatively simpler output.

Building on the outcomes of the previously mentioned studies, we are progressing along a pathway aimed at establishing fundamental and experimentally achievable design principles for the creation of "materials that compute". [47] In our experiments, the main challenges of using such device toward the development of a CC are the prediction and control of their computational behavior. We suggest that the primary challenge in the practical implementation of CC arises from the absence of an efficient signal coding

strategy tailored to this type of chemical network.

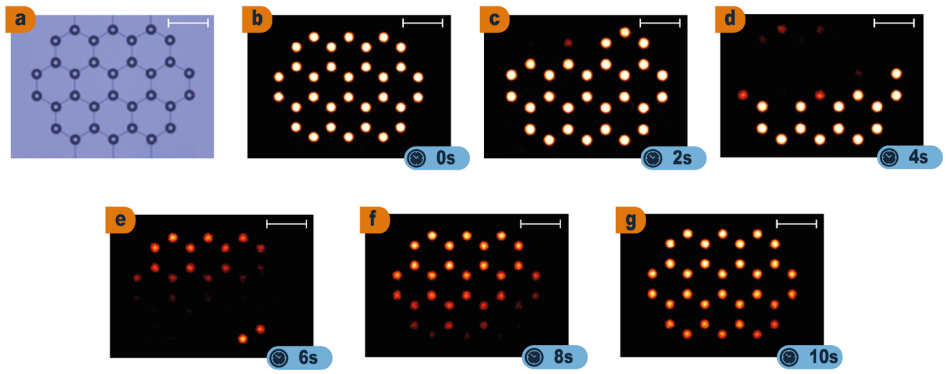

Figure 6.9. Images of a 20 µm honeycomb layout triggered MCRs. **a)** Bright-field image of MCRs prior to channel filling. **b)** to **g)** Time-lapse fluorescence images from 0 to 10 seconds. The white scale bar represents 100 µm.

A widely adopted approach to chemical computing seeks to replicate information processing mechanisms found in semiconductor devices. [29] Another type of readout can be provided by analog computation [48] or cellular automata (CA), which are alternative types of language approaches for computation. CA has been commonly used to investigate explore complex phenomena, such as chemical reaction-diffusion processes and excitation wave dynamics, in various physical, chemical, and biological systems, including models of BZ media. [49–51] Reservoir computation (RC) [52] can also be well applied to CC because due to its versality: only the connections between readout layer and output layer need to be trained. Examples concerning such approach for mimicking neural networks were presented by some groups [5,52–55].

6.2.6 Outlook

We developed a self-sustained device that operates without dependence on an external power supply, enabling sensing, actuation, and communication. Distinct MCR networks, each designed to perform a specific pattern function, were subjected to a series of input patterns. These input patterns corresponded to the initial phase of the oscillations imposed on the respective units. The technique developed in this work used the propagation of waves along defined channels based on the BZ reaction. The results obtained by the fabrication strategy and protocol used to visualize the oscillatory networks indicate that CCs can be successfully created soon. However, despite the observations and advances shown here, improvements are needed to enable the production of reliable CCs. In this regard, the drawbacks, and future perspectives to improving this system are presented.

(1) The time resolution needed for visualizing the oscillations remains limited. To address this issue, modifications to the oscillatory CRN are necessary. A

version of the BZ system that is less sensitive to light but still provides a fluorescence signal indicative of the oscillatory regime would be important. This improvement can also be achieved by employing another oscillatory CRN that enables continuous exposure to light, ensuring an adequate time-lapse signal and short image exposure time. The introduction of light would not interrupt the oscillators and could enhance the signal from the MCRs. Nanoreactors with diameters below 2 µm could be a solution to improve rate of diffusion because of larger surface/ratio area. Chapter 5 of this thesis presents a fabrication strategy using buried nanochannels that can be used to produce chemical networks of nanoreactors.

(2) Control over the input waves is lacking. MCR fabrication allows for the integration of electrical and optical components, such as electrodes. This integration can be achieved through lithographically defined metal patterns, like platinum thin films, which can be utilized for electro-osmotic flow, electrophoresis, and for amperometry and conductometry. [56] Additionally, introducing oxygen into the microfluidic channels to halt oscillations in the main channel can serve as a solution to this issue, as oxygen exerts an inhibitory effect in the BZ reaction. [57]

(3) Insufficient control over light exposure in the chip area is identified as a limitation in the current setup. Presently, a substantial chip area is subjected to blue light, leading to the influence of light on numerous MCRs. To address this, chip design should incorporate sections where microfluidic channels are shielded from light, thereby ensuring a more controllable input. Moreover, laser-based techniques, such as confocal microscopy, should be adopted to enable the exposition of only specific parts of the chip to light. For example, in a medium with a photosensitive BZ reaction, selective illumination of a spatially distributed system can generate excitable channels that facilitate signal propagation. By optimizing the geometric arrangement of excitable and non-excitable regions, excitation dynamics can be precisely controlled, enabling functionalities such as the development of a signal diode. [58] Light can also be used as an input signal for the system. [26] This illustrates that individual optical control of chemical activity in BZ reactors can generate the required input.

(4) Integrating MCRs with a continuous feeding operation in the BZ reaction offers significant potential for improving the stability and control of BZ-MCR systems for CC applications. Unlike batch operation, where the BZ reaction eventually reaches equilibrium and oscillations cease—disrupting radical species dynamics— the continuous inflow of reactants and outflow of products maintains a persistent out- of-equilibrium oscillatory state. This approach ensures well-defined, predictable oscillatory behavior and more consistent radical dynamics. [59]

6.3 Conclusions

In this chapter, we conducted an initial investigation into the behavior of a silicon-based device featuring extensive arrays of MCRs, capable of generating diverse spatiotemporal patterns driven by the BZ reaction. We presented time-lapse FM images of connecting channels mediating the coupling between compartments, which led to communication, synchronization, and fan-out. More complex communication can be developed using more intricate architectures, as demonstrated by the honeycomb MCRs design. These steps are critical first results for the development of scalable chemical computing architectures based on simple molecules.

We believe that the platform and experimental investigation presented in this work can offer a viable new perspective for advancing CC through the utilization of silicon-based devices. Despite their dynamics being constrained in speed by reaction and diffusion rates, silicon-based MCR networks provide opportunities for autonomy, rendering them suitable for targeted functionalities in liquid settings. Additionally, the system described here has the potential to inspire new algorithm designs that uniquely exploit the features of a CC. Such systems could exhibit a vast number of states with low power consumption. Based on our results, we propose that the design of unconventional computing devices should consider silicon-based architecture fabrication and machine-learning algorithms, with implements from by surface chemistry, molecular self-assembly systems, spectroscopic advancements, and new oscillatory artificial CRNs.

As presented by [26,30], we initially considered that chemical computation should be based on the development of experimental hybrid computer architectures, where certain components operate electronically while others function chemically. We then propose that these dependencies be gradually eliminated to facilitate a transition from hybrid CC to a fully autonomous system, in which only inputs and outputs are electronic, mediated by electrochemistry or light-derived mechanisms. We believe that, as a readout of the MCR network, the RC provides an opportunity to explore its maximum performance. We anticipate that, beyond their computational potential, the development of such networks could also provide profound insights into the functioning of the human brain. [21]

6.4 References

(1) Braun, E. L. Digital Computer Design: Logic, Circuitry, and Synthesis; *Academic Press,* **2014**.

(2) Waldrop, M. M. The Chips Are down for Moore's Law. *Nature News* **2016**, 530 (7589), 144.

(3) Moore, G. E. Cramming More Components onto Integrated Circuits. *Proceedings of the IEEE* **1998**, 86 (1), 82–85.

(4) Kendall, J. D.; Kumar, S. The Building Blocks of a Brain-Inspired Computer. *Applied Physics Reviews* **2020**, 7 (1), 011305. https://doi.org/10.1063/1.5129306.

(5) Cucchi, M.; Abreu, S.; Ciccone, G.; Brunner, D.; Kleemann, H. Hands-on Reservoir Computing: A Tutorial for Practical Implementation. *Neuromorphic Computing and Engineering* **2022**, 2 (3), 032002.

(6) Vanag, V. K. Networks of Spike Oscillators and Their Application for Creating Autonomous Intelligent Devices. *Phys. Usp* **2022**, 65, 440–452.

(7) Adamatzky, *A. Advances in Unconventional Computing: Volume 1: Theory*; Springer, **2016**; Vol. 22.

(8) Chatzinikolaou, T. P.; Fyrigos, I.-A.; Ntinas, V.; Kitsios, S.; Tsompanas, M.-A.; Bousoulas, P.; Tsoukalas, D.; Adamatzky, A.; Sirakoulis, G. C. Chemical Wave Computing from Labware to Electrical Systems. *Electronics* **2022**, 11 (11), 1683.

(9) *Advances in Unconventional Computing*; Adamatzky, A., Ed.; Emergence, Complexity and Computation; Springer International Publishing: Cham, **2017**; Vol. 22. https://doi.org/10.1007/978-3- 319-33924-5.

(10) Bergh, E.; Konkoli, Z. On Improving the Expressive Power of Chemical Computation. *Advances in Unconventional Computing: Volume 1*: Theory **2017**, 677–709.

(11) Torbensen, K.; Rossi, F.; Ristori, S.; Abou-Hassan, A. Chemical Communication and Dynamics of Droplet Emulsions in Networks of Belousov–Zhabotinsky Micro-Oscillators Produced by Microfluidics. *Lab ona Chip* **2017**, 17 (7), 1179–1189.

(12) Gorecki, J.; Gizynski, K.; Guzowski, J.; Gorecka, J. N.; Garstecki, P.; Gruenert, G.; Dittrich, P. Chemical Computing with Reaction–Diffusion Processes. *Philosophical Transactions of the Royal Society A: Mathematical, Physical and Engineering Sciences* **2015**, 373 (2046), 20140219.

(13) McAvoy, M. Pulse-Coupled Belousov-Zhabotinsky Oscillators with Activity Dependent Coupling, Brandeis University, Graduate School of Arts and Sciences, 2015.

(14) Kopets, E. E.; Karimov, A. I.; Khafizova, A. M.; Katser, E. A.; Shchetinina, T. G. Simulation of Chemical Oscillator Network. In 2022 *Conference of Russian Young Researchers in Electrical and Electronic Engineering (ElConRus); IEEE,* **2022**; pp 704–707.

(15) Field, R. J.; Koros, E.; Noyes, R. M. Oscillations in Chemical Systems. II. Thorough Analysis of Temporal Oscillation in the Bromate-Cerium-Malonic Acid System. *Journal of the American Chemical Society***1972**, 94 (25), 8649–8664.

(16) Masuda, T.; Akimoto, A. M.; Furusawa, M.; Tamate, R.; Nagase, K.; Okano, T.; Yoshida, R. Aspects of the Belousov–Zhabotinsky Reaction inside a Self-Oscillating Polymer Brush. *Langmuir* **2018**, 34 (4), 1673–1680.

(17) Ruoff, P.; Varga, M.; Koros, E. How Bromate Oscillators Are Controlled. *Accounts of Chemical Research* **1988**, 21 (9), 326–332.

(18) Semenov, S. N.; Wong, A. S.; Van Der Made, R. M.; Postma, S. G.; Groen, J.; Van Roekel, H. W.; De Greef, T. F.; Huck, W. T. Rational Design of Functional and Tunable Oscillating Enzymatic Networks. *Nature chemistry* **2015**, 7 (2), 160–165.

(19) Novák, B.; Tyson, J. J. Design Principles of Biochemical Oscillators. *Nature reviews Molecular cell biology* **2008**, 9 (12), 981–991.

(20) Taylor, A. F. Mechanism and Phenomenology of an Oscillating Chemical Reaction. *Progress in Reaction Kinetics and Mechanism* **2002**, 27 (4), 247–326.

(21) Mallphanov, I. L.; Vanag, V. K. Chemical Micro-Oscillators Based on the Belousov–ZhabotinskyReaction. *Russian Chemical Reviews* **2021**, 90 (10), 1263.

(22) Gáşpár, V.; Bazsa, G.; Beck, M. T. The Influence of Visible Light on the Beloasoy-Zhabotinskii Oscillating Reactions Applying Different Catalysts. *Zeitschrift für Physikalische Chemie* **1983**, 264 (1), 43–48.

(23) Bánsági Jr, T.; Leda, M.; Toiya, M.; Zhabotinsky, A. M.; Epstein, I. R. High-Frequency Oscillations in the Belousov– Zhabotinsky Reaction. *The Journal of Physical Chemistry A* **2009**, 113 (19), 5644–5648.

(24) Misra, G. P. Effect of Temperature and Associated Bifurcation in the Oscillatory Belousov— Zhabotinskii Reaction in a Flow Reactor. *Chemical physics letters* **1992**, 191 (5), 435–440.

(25) Elwood, J. ATOMIC AND NUCLEAR STRUCTURE. *Passing the State Science Proficiency Tests: Essential Content for Elementary and Middle School Teachers* **2013**, 51.

(26) Proskurkin, I. S.; Smelov, P. S.; Vanag, V. K. Experimental Verification of an Opto-Chemical "Neurocomputer." *Physical Chemistry Chemical Physics* **2020**, 22 (34), 19359–19367.

(27) Toth, R.; Taylor, A. F. The Tris (2, 2'-Bipyridyl) Ruthenium-Catalysed Belousov–Zhabotinsky Reaction. *Progress in Reaction Kinetics and Mechanism* **2006**, 31 (2), 59–115.

(28) Jinguji, M.; Ishihara, M.; Nakazawa, T. Primary Process of Illumination Effect on the Tris (Bipyridine) Ruthenium (2+)-Catalyzed Belousov-Zhabotinskii Reaction. *The Journal of Physical Chemistry* **1992**, 96 (11), 4279–4281.

(29) Dueñas-Díez, M.; Pérez-Mercader, J. How Chemistry Computes: Language Recognition by Non-Biochemical Chemical Automata. From Finite Automata to Turing Machines. *Iscience* **2019,** 19, 514–526.

(30) Parrilla-Gutierrez, J. M.; Sharma, A.; Tsuda, S.; Cooper, G. J.; Aragon-Camarasa, G.; Donkers, K.; Cronin, L. A Programmable Chemical Computer with Memory and Pattern Recognition. *Nature communications*

2020, 11 (1), 1442.
(31) Sharma, A.; Ng, M. T.-K.; Parrilla Gutierrez, J. M.; Jiang, Y.; Cronin, L. A Programmable Hybrid Digital Chemical Information Processor Based on the Belousov-Zhabotinsky Reaction. *Nat Commun* **2024**, 15 (1), 1984. https://doi.org/10.1038/s41467-024-45896-7.
(32) Konrad, G.; Jerzy, G. A Chemical System That Recognizes the Shape of a Sphere. *CMST* **2016**, 22 (4),167–177.
(33) Gruenert, G.; Gizynski, K.; Escuela, G.; Ibrahim, B.; Gorecki, J.; Dittrich, P. Understanding Networksof Computing Chemical Droplet Neurons Based on Information Flow. *Int. J. Neur. Syst.* **2015**, 25 (07), 450032. https://doi.org/10.1142/S0129065714500324.
(34) Adamatzky, A.; De Lacy Costello, B.; Dittrich, P.; Gorecki, J.; Zauner, K.-P. On Logical Universality of Belousov-Zhabotinsky Vesicles. *International Journal of General Systems* **2014**, 43 (7), 757–769.
(35) Gizynski, K.; Gorecki, J. Cancer Classification with a Network of Chemical Oscillators. *Phys. Chem.Chem. Phys.* **2017**, 19 (42), 28808–28819. https://doi.org/10.1039/C7CP05655A.
(36) Gizynski, K.; Gorecki, J. Chemical Memory with States Coded in Light Controlled Oscillations of Interacting Belousov–Zhabotinsky Droplets. *Phys. Chem. Chem. Phys.* **2017**, 19 (9), 6519–6531. https://doi.org/10.1039/C6CP07492H.
(37) Vanag, V. K. Plasticity in Networks of Active Chemical Cells with Pulse Coupling. Chaos: *An Interdisciplinary Journal of Nonlinear Science* **2022**, 32 (12).
(38) Tomasi, R.; Noël, J.-M.; Zenati, A.; Ristori, S.; Rossi, F.; Cabuil, V.; Kanoufi, F.; Abou-Hassan, A. Chemical Communication between Liposomes Encapsulating a Chemical Oscillatory Reaction. *Chemical Science* **2014**, 5 (5), 1854–1859.
(39) Sheehy, J.; Hunter, I.; Moustaka, M. E.; Aghvami, S. A.; Fahmy, Y.; Fraden, S. Impact of PDMS-Based Microfluidics on Belousov–Zhabotinsky Chemical Oscillators. *J. Phys. Chem. B* **2020**, 124 (51), 11690–11698. https://doi.org/10.1021/acs.jpcb.0c08422.
(40) Steinbock, O.; Tóth, Á.; Showalter, K. Navigating Complex Labyrinths: Optimal Paths from Chemical Waves. *Science* **1995**, 267 (5199), 868–871.
(41) Litschel, T.; Norton, M. M.; Tserunyan, V.; Fraden, S. Engineering Reaction–Diffusion Networks with Properties of Neural Tissue. *Lab on a Chip* **2018**, 18 (5), 714–722.
(42) Ginn, B. T.; Steinbock, B.; Kahveci, M.; Steinbock, O. Microfluidic Systems for the Belousov−Zhabotinsky Reaction. *The Journal of Physical Chemistry A* **2004**, 108 (8), 1325–1332.
(43) Fouchier, M.; Pargon, E. HBr/O2 Plasma Treatment Followed by a Bake for Photoresist Linewidth Roughness Smoothing. *Journal of Applied Physics* **2014**, 115 (7).
(44) Laermer, F.; Urban, A. MEMS at Bosch–Si Plasma Etch Success Story, History, Applications, and Products. *Plasma Processes and Polymers* **2019**, 16 (9), 1800207.
(45) Tamaki, E.; Hibara, A.; Kim, H.-B.; Tokeshi, M.; Ooi, T.; Nakao, M.; Kitamori, T. Liquid Filling Method for Nanofluidic Channels Utilizing the High Solubility of CO2. *Analytical sciences* **2006**, 22 (4), 529– 532.
(46) Figueiredo Da Silva, J.; Bacheva, V.; Drechsler, U.; Nicollier, P.; Reidt, S.; Fotiadis, D.; Knoll, A.; Wolf, H. Fabrication of a Hybrid Device for the Integration of Light-Triggered Proton Pumps. *Micro and Nano Engineering* **2024**, 23, 100250. https://doi.org/10.1016/j.mne.2024.100250.
(47) Fang, Y.; Yashin, V. V.; Levitan, S. P.; Balazs, A. C. Pattern Recognition with "Materials That Compute." *Science advances* **2016**, 2 (9), e1601114.
(48) MacLennan, B. J. Analog Computation. Encyclopedia of Complexity and Systems Science, 2009, 271–294. https://doi.org/10.1007/978-0-387-30440-3_19.
(49) Adamatzky, A.; Costello, B. D. L.; Asai, T. Reaction-Diffusion Computers; *Elsevier*, **2005**.
(50) Gerhardt, M.; Schuster, H.; Tyson, J. J. A Cellular Automaton Model of Excitable Media Including Curvature and Dispersion. *Science* **1990**, 247 (4950), 1563–1566.
(51) Markus, M.; Hess, B. Isotropic Cellular Automaton for Modelling Excitable Media. *Nature* **1990**, 347 (6288), 56–58.
(52) Baltussen, M. G.; De Jong, T. J.; Duez, Q.; Robinson, W. E.; Huck, W. T. S. Chemical Reservoir Computation in a Self-Organizing Reaction Network. *Nature* **2024**, 631 (8021), 549–555. https://doi.org/10.1038/s41586-024-07567-x.
(53) Pecqueur, S.; Mastropasqua Talamo, M.; Guérin, D.; Blanchard, P.; Roncali, J.; Vuillaume, D.; Alibart, F. Neuromorphic Time-dependent Pattern Classification with Organic Electrochemical Transistor Arrays. *Advanced Electronic Materials* **2018**, 4 (9), 1800166.
(54) Usami, Y.; van de Ven, B.; Mathew, D. G.; Chen, T.; Kotooka, T.; Kawashima, Y.; Tanaka, Y.; Otsuka, Y.;

Ohoyama, H.; Tamukoh, H. In-materio Reservoir Computing in a Sulfonated Polyaniline Network. *Advanced Materials* **2021**, 33 (48), 2102688.

(55) Cucchi, M.; Kleemann, H.; Tseng, H.; Ciccone, G.; Lee, A.; Pohl, D.; Leo, K. Directed Growth of Dendritic Polymer Networks for Organic Electrochemical Transistors and Artificial Synapses. *Advanced Electronic Materials* **2021**, 7 (10), 2100586.

(56) Gardeniers, H. J. Chemistry in Nanochannel Confinement. Analytical and bioanalytical chemistry2009, 394 (2), 385–397.

(57) Luengviriya, J.; Phantu, M.; Müller, S. C.; Luengviriya, C. Inhibitory Effect of Oxygen on Excitation Waves in the Belousov–Zhabotinsky Reaction with Different Excitability. *Chemical Physics Letters***2015**, 618, 6–10.

(58) Agladze, K.; Aliev, R. R.; Yamaguchi, T.; Yoshikawa, K. Chemical Diode. *The Journal of Physical Chemistry* **1996**, 100 (33), 13895–13897.

(59) Hou, L.; Dueñas-Díez, M.; Srivastava, R.; Pérez-Mercader, J. Flow Chemistry Controls Self-Assemblyand Cargo in Belousov-Zhabotinsky Driven Polymerization-Induced Self-Assembly. *Communications Chemistry* **2019**, 2 (1), 139.

6.5 Supplementary information

6.5.1 Materials and methods

6.5.1.1 Chemicals

Commercially available sodium bromate ($NaBrO_3$; Sigma-Aldrich), malonic acid (MA) ($CH_2(COOH)_2$; Sigma-Aldrich), tris(2,2'-bipyridyl) dichlororuthenium (II) hexahydrate ($Ru(bpy)_3Cl_2(6H_2O)$; Sigma-Aldrich), and sulfuric acid solution (H_2SO_4, 5 M; Merck) were used without further purification. Millipore water (18.2 Megaohm) was used to prepare the following stock solutions: 1 M H_2SO_4, 2 M $NaBrO_3$, 3.5 M $CH_2(COOH)_2$, and 0.0125 M $Ru(bpy)_3Cl_2(6H_2O)$.

6.5.1.2 Device fabrication

Silicon wafers with 100 mm diameter and 500 µm thickness were obtained from the University Wafer. Borofloat glass wafers (100 mm) with 500 µm thickness were obtained from PlanOptik AG. Patterns of 0.7 mm holes were drilled through the glass for the fluidic connections. Two chrome masks designed for the device layer structures were fabricated using a Heidelberg DWL2000 laser writer. The silicon wafer was first patterned via photolithography (Microchemicals AZ4533 resist and Süss Mask Aligner M6) and then etched via inductively coupled plasma reactive ion etching (ICP-RIE) using an Oxford Instruments Plasmalab 100. In this fabrication step, the small channels with 1.5 µm width and 500 nm depth were obtained. Subsequently, another photoresist layer (Microchemicals AZ4512) was spin-coated on top of the sample, thereby covering all structures on the device layer. In this step, we patterned the larger microfluidic channels and circular microreactors (diameter: 5 to 30 µm). Their depth of 20 µm was obtained using a deep reactive ion etching (DRIE) tool (Alcatel AMS 200SE I-Speeder). Finally, the channels were sealed by anodic bonding of the drilled cover glass to the wafer at 485 °C and 1.3 kV for ~1 h using a homemade substrate bonder. The glass-covered wafer was diced via ADT ProVectus LA 7100 into twelve 36x12 mm chips. To prevent the channels from being filled with cooling

water during the dicing process, the holes were pre-covered with foil.

Microfluidic setup

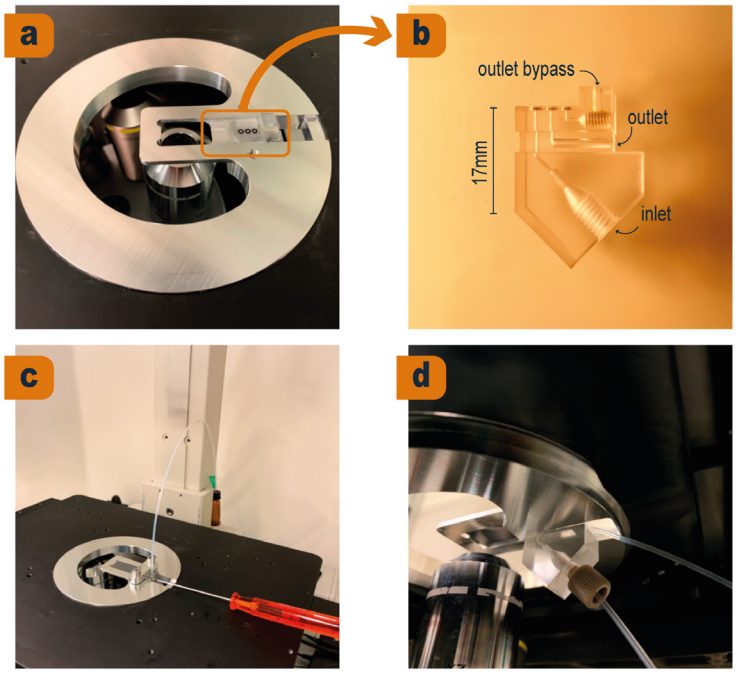

Figure S6.1. Microfluidic design setup used on a Nikon inverted microscope: **a)** chip holder with PMMA fluid interface, **b)** details of fluidic interface, with 0.5 mm O-rings, inlet, outlet, and bypass fluid connections. Setup with the inserted chip: **c)** top view, and **d)** bottom view. The setup was designed by Dr. Robert Lovchik (IBM Research Europe - Zurich, Switzerland).

The microfluidic interface was designed using CATIA V5R20. The aluminum parts of the assembly were machined using a computer numerical control (CNC) tool. The fluidic interface was fabricated by micro milling in poly(methyl methacrylate) (PMMA). The design comprises an inlet, an outlet, and a bypass aperture with a diameter of 0.5 mm. The interface presented ports compatible with 10-32 coned microfluidic fittings (Idex). The fluidic connections to the chips were sealed using Markez FFKM O-rings. The microfluidic setup with the chip was mounted on the stage of an inverted microscope for experiments. Figure S6.1 shows photos of this setup. We used a Nikon Eclipse Ti inverted bright-field/fluorescence microscope with a CCD camera (Clara camera, ANDOR technology) with 10x magnification lens. A customized filter set was used because of the peculiar Ruthenium emissions and excitation wavelengths: excitation filter = FITC filter = 475 nm (blue); emission filter = mCherry filter = 641 nm (orange); dichroic filter = GFP filter = 505–800 nm.

Belousov–Zhabotinsky (BZ) reaction in a microfluidic setup

To fill the nanochannels, we inserted CO_2 gas in the microfluidic tube connected to the inlet channel under pressure for 5 min. During that time, two solutions were prepared in separate Eppendorfs: solution 1 was composed of 1000 µL H_2SO_4 (1 M), 40 µL $Ru(bpy)_3Cl_2(6H_2O)$ (0.0125 M), and 200 µl of $NaBrO_3$ (2 M); whereas solution 2 was composed of 1000 µL H_2SO_4 (1 M), 40 µL Ru(bpy)3Cl2(6H2O) (0.0125 M), and 50 µL MA (3.5 M). Recipe was adapted from [1]. Equal amounts of solutions 1 and 2 were mixed in another Eppendorf. As soon as oscillations could be visually observed, we used a 250 µl syringe to inject the BZ solution under high pressure in the tube connected to the inlet microfluidic channel. The nanochannel filling was observed by fluorescence microscopy. Fluorescence images were obtained at 400 ms exposure time. One picture was taken every second for 10 min.

6.5.2 Data analysis

We employed a macro script scripted in ImageJ to examine the oscillatory signal of MCRs over time and employed a Python script to extract the oscillation periods and generate corresponding plots. Within ImageJ, the initial step included the opening of the image stack from time-lapse experiments. Subsequently, the "Threshold" option was applied to generate an image encapsulating the average signal emanating from the MCRs. This image served as the mask delineating the spatial locations of MCRs. The subsequent operation involved converting the mask into a binary format.

During the "Analyze Particles" step, the "Add to Manager" option was selected. This resulted in the presentation of all positions detected by the binary mask within the region of interest (ROI). The program provided the average intensity of the MCRs area. In the ROI manager, the "measure" option was executed, facilitating the measurement of MCR intensity over time for all components identified by the "analyze particles" function. Consequently, the localized intensity values of MCRs per image were obtained. Each detected area is assigned a numerical identifier.

ImageJ code was as follows:

```
waitForUser("Open", "Welcome to the BZ-micro-reactor analysis. Please choose your BZ-IS image sequence!");
run("Open...");
waitForUser("Z Project", "Please choose the interval of images to be used for averaging!"); run("Z Project...");
waitForUser("Subtract Background", "Please choose the background subtraction parameters for the averaged image!");
run("Subtract Background..."); run("Gaussian Blur...", "sigma=1 stack"); run("Enhance Contrast...", "saturated=0.35");
waitForUser("Threshold", "Please choose the threshold for the averaged image! (Will be used as mask for the location of bz reactors.)");
run("Threshold...");
waitForUser("Click OK when you are done!");
saveAs("tif"); showMessage("Results saved.");
run("Set Measurements...", "mean display redirect=None decimal=3"); run("Analyze Particles...", " show=Outlines display exclude summarize add"); close(); close();
```

```
waitForUser("Subtract Background", "Please choose background subtraction parameters!"); run("Subtract Background...");
// waitForUser("Click OK when you are done!"); run("Gaussian Blur...", "sigma=1 stack");
run("Enhance Contrast...", "saturated=0.35");
run("Set Measurements...", "mean display redirect=None decimal=3"); roiManager("multi-measure measure_all one append");
orgName = getTitle();
output_path = getDirectory("Choose output folder!"); roiManager("save", output_path + orgName + ".zip") showMessage("ROI Extraction saved."); selectWindow("Results");
saveAs("results", output_path + orgName + ".csv"); showMessage("Results saved.");
close();
name = output_path + "AVG_" + orgName open(name);
roiManager("show all with labels"); run("Flatten");
name = getTitle();
name = replace(name, "-1.tif", "_ann.png"); fpath = output_path + name
saveAs("png", fpath); showMessage("Saved annotated image."); roiManager("reset");
close("*");
selectWindow("Results");
run("Close"); selectWindow("Threshold"); run("Close"); selectWindow("Summary"); run("Close"); selectWindow("ROI Manager"); run("Close");
exit;
```

The examination of the oscillations of the MCRs was conducted using a Python script. Upon opening the csv script file that contained the mean intensity of each MCR over time, we identified the MCRs based on their enumeration determined by ImageJ program. Subsequently, the plot of the oscillations and periods over time was generated. The Python script was written by Dr. Heiko Wolf, IBM Research Laboratory – Zurich.

6.5.3 Photolithographic masks in K-layout software design

We employed K-layout software to create photolithographic masks. Figure S6.2a illustrates the mask designed by K-layout for the nanochannels (pink) and another mask designed for the MCRs and microfluidic channels (violet). Figure S6.2b shows the positions of the 0.7 mm holes in the glass with a 100 nm size wafer. The holes precisely corresponded to the features specified in the mask designed by photolithography.

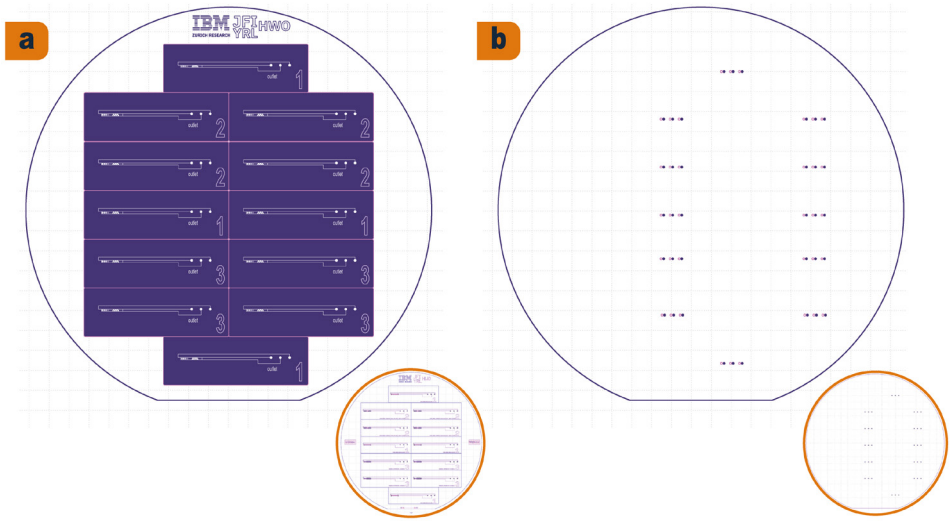

Figure S6.2. K-layout drawings of **a)** photolithographic masks used to fabricate silicon chips (presented in Figure 6.3), and **b)** 0.7 mm holes designed in the glass by drilling, which were anodically bonded to the silicon wafer.

6.5.4 First device generation

In the initial part of this project, we designed a microfluidic device that allowed us to fill the channels at a high pressure (Figure S6.3a). However, we were unable to visualize the in-situ MCR filling using the fluorescent microscope. As shown in Figure S6.3a, the adapter used to connect the tubing to the chips was made from PMMA and aluminum.

Additionally, we used a polydimethylsiloxane (PDMS) gasket to ensure a leak-free connection between the adapter and the chips. This setup was able to withstand the high pressures (> 20 Bar) when we filled the channels (Figure S6.3b). As the sample chips comprised two openings for the inlet, one of them was closed by the PMDS gasket and the side in which the liquid was inserted was held open. The outlet channel was always open.

The chip was fabricated using the procedure described in Chapter 6, except for the absence of a bypass channel and the chip size, which was 12 x 12 mm, as shown in Figure S6.3c. Figure S6.4a shows the K-layout drawing of photolithographic masks of the wafer used to fabricate the chips. Figure S6.4b shows the K-layout drawing for 2 mm holes in the glass.

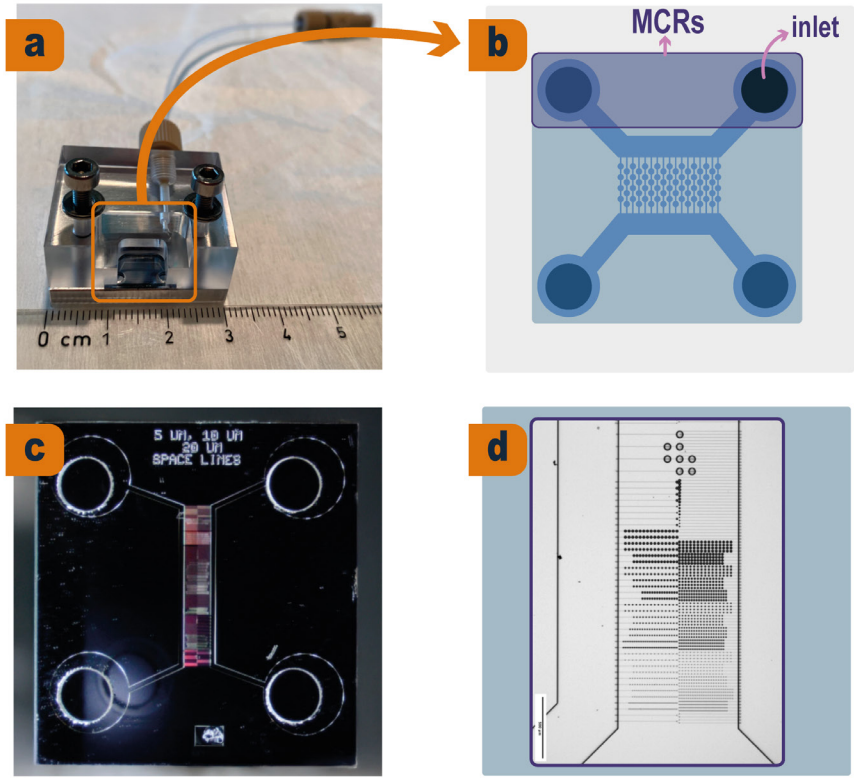

Figure S6.3. Microfluidic design setup using high pressure filling: **a)** chip setup; **b)** PDMS interface, which comprises one hole on one side of the inlet channel; **c)** bright-field image of 12x12 mm chip; **d)** part of MCR network before filling; scale bar = 500 µm.

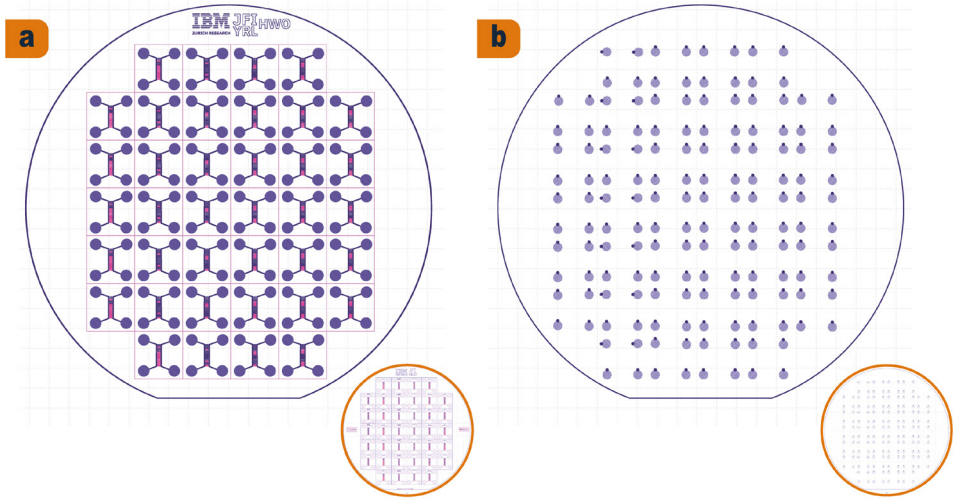

Figure S6.4. K-layout drawings of **a)** photolithographic masks used to fabricate silicon chips (presented in Figure S6.3-c), and **b)** 2 mm holes designed in the glass by sandblasting which were anodically bonded to the silicon wafer.

6.5.5 References

(1) Dueñas-Díez, M.; Pérez-Mercader, J. How Chemistry Computes: Language Recognition by Non-Biochemical Chemical Automata. From Finite Automata to Turing Machines. *Iscience* **2019**, 19, 514–526.

Summary

This PhD thesis, titled **"Reaction Cascades Coupled to Surface-Chemical Nanoscale Patterns,"** aims to develop strategies for spatiotemporal control of chemical reaction networks (CRNs) at the micro- and nanoscale. By controlling the size and shape of nanostructures, the research facilitates the creation of unique material properties and applications. The study integrates micro/nanoscale lithography with two types of CRNs: the first, driven by a synthetic self-assembled system featuring a supramolecular hydrogelator catalyzed by protons, and the second, the Belousov-Zhabotinsky (BZ) reaction, a non-linear chemical oscillatory CRN. Both approaches seek to control local and transient CRNs using micro/nanoscale patterns.

Chapter 1 provides an overview of current methods for spatiotemporal CRN control. **Chapter 2** details the top-down and bottom-up fabrication techniques and outlines the CRN and analytical methods used in the thesis.

Chapter 3, titled **"Quantification of Proton Pumping in Biological Membrane Patches,"** focuses on measuring localized proton gradients from Purple Membranes (PMs), a light-driven proton pump. It describes the design and fabrication of an optically triggered device and uses fluorescence microscopy to document and control proton pumping. Potential applications include managing fuel density and production rates in proton-catalyzed CRNs.

Chapter 4, titled "**Control of a Gel-Forming Chemical Reaction Network Using Light-Triggered Proton Pumps,**" combines an acid catalyst-assisted self-assembly CRN with PMs. It aims to create a localized CRN that can be switched on and off with an optical trigger. The chapter details a system for measuring pH increases through irreversible fiber growth accelerated by protons and demonstrates the influence of PM pumping on microscale hydrogel formation using liquid atomic force microscopy and confocal laser scanning microscopy. The system is designed to develop a pH-responsive hydrogel that responds to external stimuli.

Chapter 5, titled **"Network of Light-Triggered Proton Pumps,"** explores manipulating proton flux for spatiotemporal control of CRNs. It involves fabricating a device that combines nanochannels with locally controlled PM deposition for nanoscale fuel transport. The chapter covers the fabrication of nanochannels on a $Si/SiO_2/Al_2O_3$ substrate using thermal scanning probe lithography (t-SPL), atomic layer deposition, plasma-enhanced chemical vapor deposition, and photolithography. It also discusses localized PM deposition in the Tunable Nanofluidic Confinement Apparatus (TNCA) and the development of a pH sensor using a pH-sensitive dye.

Chapter 6, titled **"Networks of Microscale Chemical Oscillators: Toward Chemical Computing,"** aims to miniaturize and couple microscale chemical reactors (MCRs) to create a network of communicating chemical oscillators. The chapter demonstrates chemical

communication (coupling and synchronization) within complex MCR networks driven by the BZ reaction, aiming to mimic signaling and regulate BZ reactions at specific locations and times. The study proposes new methods for diversifying and optimizing information processing.

Overall, this thesis presents the development and study of CRN-driven devices for spatiotemporal control, advancing applications in sensing, material property studies, and computation. The research is expected to enhance emerging technologies and deepen the understanding of chemistry in relation to biology, materials science, physics, and computing.

Samenvatting

Dit proefschrift, getiteld " **Reaction Cascades Coupled to Surface-Chemical Nanoscale Patterns**," heeft als doel het ontwikkelen van strategieën voor spatiotemporale controle van chemische reactienetwerken (CRN's) op micro- en nanoschaal. Door de grootte en vorm van nanostructuren te beheersen, bevordert dit onderzoek de ontwikkeling van unieke materiaaleigenschappen en toepassingen. De studie integreert micro/nanoschaal lithografie met twee soorten CRN's: de eerste, aangedreven door een synthetisch zelfgeassembleerd systeem met een supramoleculaire hydrogelator die door protonen wordt gecatalyseerd, en de tweede, de Belousov-Zhabotinsky (BZ) reactie, een niet-lineaire chemische oscillatoire CRN. Beide benaderingen beogen het beheersen van lokale en tijdelijke CRN's door middel van micro/nanoschaalpatronen.

Hoofdstuk 1 biedt een overzicht van de huidige methoden voor spatiotemporale controle van CRN's. **Hoofdstuk 2** beschrijft de top-down en bottom-up fabricagetechnieken en schetst de CRN- en analysemethoden die in het proefschrift worden toegepast.

Hoofdstuk 3, getiteld " **Quantification of Proton Pumping in Biological Membrane Patches**," richt zich op het meten van gelokaliseerde protongradiënten van Paarse Membranen (PM's), een lichtgestuurde protonpomp. Dit hoofdstuk beschrijft het ontwerp en de fabricage van een optisch getriggerd apparaat en maakt gebruik van fluorescentiemicroscopie om protonpompen te beschrijven en te controleren. Mogelijke toepassingen omvatten het reguleren van brandstofdichtheid en productiesnelheid in proton-gecatalyseerde CRN's.

Hoofdstuk 4, getiteld " **Control of a Gel-Forming Chemical Reaction Network Using Light-Triggered Proton Pumps**," combineert een door een zuur-catalysator ondersteunde zelfassemblage CRN met PM's. Het doel is het creëren van een gelokaliseerd CRN dat kan worden in- en uitgeschakeld met een optische trigger. Dit hoofdstuk behandelt een systeem voor het meten van pH-verhogingen door middel van onomkeerbare vezelgroei versneld door protonen, en demonstreert de invloed van PM-pompen op de vorming van nanoschaal hydrogel met behulp van liquid atomic force microscopy en confocale laser scanningmicroscopie. Het systeem is ontworpen om een pH-responsieve hydrogel te ontwikkelen reageert op externe stimuli.

Hoofdstuk 5, getiteld " **Network of Light-Triggered Proton Pumps**," onderzoekt de manipulatie van protonflux voor spatiotemporale controle van CRN's. We fabriceren een apparaat dat nanochannels combineert met lokaal gecontroleerde PM-depositie voor nanoschaal brandstoftransport. Dit hoofdstuk behandelt de fabricage van nanochannels op een $Si/SiO_2/Al_2O_3$-substraat met behulp van thermische scanning probe lithografie (t-SPL), atomaire laagafzetting, thermal scanning probe lithography (t-SPL), atomic layer

deposition, plasma-enhanced chemical vapor deposition, en photolithography. Daarnaast wordt lokale PM-depositie in de Tunable Nanofluidic Confinement Apparatus (TNCA) besproken, evenals de ontwikkeling van een pH-sensor met een pH-gevoelige kleurstof.

Hoofdstuk 6, getiteld "**Networks of Microscale Chemical Oscillators: Toward Chemical Computing**," heeft als doel het miniaturiseren en koppelen van microschaal chemische reactors (MCR's) om een netwerk van communicerende chemische oscillatoren te creëren. Dit hoofdstuk demonstreert chemische communicatie (koppeling en synchronisatie) binnen complexe MCR-netwerken die worden aangedreven door de BZ-reactie, met als doel het nabootsen van signalering en het reguleren van BZ- reacties op specifieke locaties en tijdstippen. De studie stelt nieuwe methoden voor om informatieverwerking te diversifiëren en te optimaliseren.

Al met al presenteert dit proefschrift de ontwikkeling en bestudering van CRN- gestuurde apparaten voor spatiotemporale controle, met vooruitgang in toepassingen op het gebied van sensing, materiaaleigenschappen en computationele studies.

Dit onderzoek verbeterd de toepassingen van opkomende technologieën en verdiept de kennis van chemie in relatie tot biologie, materiaalkunde, fysica en computationele wetenschappen.

Acknowledgement

This Ph.D. represents the realization of a long-standing aspiration. Before starting, I was somewhat aware of the challenges involved, but I now fully appreciate how demanding this journey is. Throughout this time, I have grown in many ways, guided by the goal of completing this endeavor to the best of my ability.

Pursuing my Ph.D. at TU Delft, in collaboration with IBM Research – Zurich (IBM ZRL), has been an opportunity beyond my expectations. Living in Switzerland had been a personal goal since my first visit, and beginning my academic work in the Netherlands was an entirely new and rewarding experience. It is an honor to conduct research in both institutions. The combination of academic and industrial environments was essential for broadening my experience. Furthermore, being part of the ITN project was especially valuable, as it enabled me to strengthen both my academic and transferable skills.

I would like to thank my supervisor, **Heiko**, for guiding me throughout my research, supporting the development of my ideas, and providing patient corrections whenever necessary. I also appreciate your collegial support. I thank my promotor, **Jan**, for your constructive and kind feedback on my progress, and for your insights and support in our joint project. I am also grateful to my promotor **Eduardo** for his guidance at the conclusion of this work, and for his motivating and insightful perspectives. I thank **Armin** for his patience, his willingness to share expertise, and his valuable questions and suggestions. **Rolf**, my first manager at IBM ZRL, thank you for your encouragement and supportive leadership, which were vital at an early stage. **Bernd**, my second manager at IBM ZRL, thank you for your support and commitment to the team. I am also grateful to **Heike**, head of the department, for her support.

I thank **Dimitri** (University of Bern) for providing PM patches and for our helpful discussions. I also thank **Juan** (Harvard University) for the opportunity to work in his lab.

This Ph.D. was possible thanks to substantial technical support. I am grateful to the Cleanroom Operations Team at the Binnig and Rohrer Nanotechnology Center (BRNC) and the model shot at IBM-ZRL. In particular, I thank **Ute** for her remarkable teaching and support in the cleanroom, from whom I learned much of what I know about cleanroom facilities. I am also grateful to **Steffen** for his assistance with the FIB-SEM tool at a critical stage of this work, and for his continued support. I also thank **Robi** for his essential contribution to the microfluidics work, and for his clear guidance. At TU Delft, I thank **Marcel** for his exceptional support, patience, and instruction with liquid AFM, from which I learned extensively. From Heidelberg Instruments Nano, I thank **Jana** for her assistance with t-SPL and her collegiality, as well as **Nick**, **Emine**, and **Samuel** for sharing their expertise with the tool and for being excellent officemates.

At IBM, I would like to thank my colleague and friend **Vesna** for her support in the

cleanroom, her scientific contributions, and her friendship. I am also grateful to **Chloe** and **Philippe** for their scientific discussions and contributions, **Silvia** for her assistance with translations and practical matters in Switzerland, **Daniel** for his support and conversations, and **Jilly** for her kind help with technical issues and our discussions.

At TU Delft, I thank **Ardeshir** for his collaboration on one of the projects of this thesis. I also thank **Benni** and **Elmira** for their support, conversations, and moments together. **Suellen**, thank you for your assistance regarding the university and for speaking Portuguese with me in Delft. **Veby**, thank you for your support and kindness.

From ITN CreaNet, I would like to thank all my colleagues, as well as the researchers, for sharing valuable experiences. Although the pandemic limited our interactions, we made every effort to remain connected. From Harvard, I thank **Alberto**, **Jennifer**, and **Chenyu** for their support during my stay, as well as my friend **Jaqueline**, whose companionship was important during the winter in Cambridge. Thanks to **Artur** for his support before and during my stay in USA.

From UniMainz, I thank **Andreas** for the opportunity to work with him and his team. I am grateful to **Olivier** for introducing me to the new world of soft robots, **Piet** for his help in translating my summary into Dutch and for his support, and to colleagues **Koyei**, **Brigitta**, **Yuheng**, and **Diego** for their support and friendship. I also thank **Maria**, **Lorena**, **Soumya**, **Manju**, **Lydia**, **Nikta**, **Ali**, **Miao**, **Doruk**, **Ricarda**, as well as the many other colleagues in the laboratory.

I also wish to thank female colleagues and mentors in science who supported me. My bachelor's supervisor, **Maria Aparecida**, has been an ongoing source of encouragement and guidance, for which I am sincerely grateful. **Camila**, thank you for your kindness and support during my earlier academic years. **Min**, thank you for motivating my frequent visits to Italy and for your example as a researcher and colleague. **Cuifeng**, thank you for your support in pursuing a Ph.D. and for your inspiring example.

For my friends in Mainz, I would like to thank **Yueh-Jen** for making my move to Mainz happier. Also, **Helena** for being a support and grateful company in Germany. **Raimunda** and **Tatá** for making me feel part of your familiar cycle. I also thank my flatmates, **Sara** and **Blerta**, for their support and friendship.

During my years in Zurich, I was fortunate to have friends who provided invaluable companionship: **Antonia** and **Neide**, for being my family in Switzerland; **Patricia**, forcing me to not forget my French and my love for Paris; **Nalva**, for her kindness; **Clara** and **Silvan**, for her presence and art, and for taking the nice profile picture of me presented at this thesis: **Leticia**, for her steadfast friendship; **Lorena**, for her continued company over the phone; **Luci**, for being an inspiration as a strong woman; **Christine** and her family, for supporting me in my move to Switzerland; and **Doris**, for her guidance and support during the process of this thesis.

I also thank my friends in Brasília. **Lais**, for your friendship since the day we met; **Heloísa**, for your integrity, authenticity, and support, as well as for designing the cover and making this thesis book looks so nice; **Aline**, for your strength and inspiration; **Natan**, for your long-standing friendship; **Agni**, for your trust and friendship; **Xani** and **Rodrigo**, for our mutual support and shared experiences; and **Victor**, for being the first friend I made in Brasília and for introducing me to many others. **Jean**, for your companionship; **Manuela**, my partner in crime through long library hours.

From Belém, my hometown, I thank **Andreiza** and **José Adailton** for their long time friendship and their support during my master's and Ph.D. studies with the grammar and illustrations. I also thank **Dilermando** for our reciprocal visits and shared experiences in Europe, **Raimunda** for her understanding and encouragement, **Ana Raquel** for her continuous support, **Matheus** for his life-long friendship, **Laercio** for his inspiring example, **Débora** for her kind messages and sensibility, **Davi** and **Lucas** for staying in touch, **Rodrigo** for his insights about the propositions of this thesis and **Eliana** for her spiritual support.

Finally, I thank my family. My grandmother **Ana**, my godmother that always by my side. My uncles and aunts — especially **Maria do Socorro** — for their care and support during my childhood. My brother **Jhoseffer** for supporting my parents while I have been abroad, and my nephew **Francisco** for the joy he brings. I thank my father **José** for fostering my interest in literature and cinema and for supporting my choices, and my mother **Ana Lúcia** for encouraging my education and respecting my decisions from the beginning.

To anyone not explicitly mentioned but who contributed to this journey, please accept my sincere gratitude.

About the author

Jacqueline Figueiredo da Silva was born on 17 October 1991 in Belém do Pará, in the Amazon region of Brazil. She obtained a bachelor's degree in Chemistry and Industrial Chemistry from the Universidade de Brasília, Brazil, in 2016. As part of her undergraduate studies, she spent one year (2014) as an exchange student at the Université de Savoie, France, supported by *Ciências sem Fronteiras* scholarship, and completed a four-month research internship (2015) at the Université de Montréal, Canada, funded by *ELAP* scholarship.

In 2019, she completed the Erasmus Mundus Joint Master's Degree in Advanced Spectroscopy in Chemistry from the Université de Lille, France, and the Jagiellonian University, Poland, supported by *Erasmus+* scholarship. During her master's studies, she also conducted a summer research internship (2018) at the Adolphe Merkle Institute, Switzerland.

Following the completion of her master's degree, she commenced an industrial doctoral project within the CReaNeT network under an ITN–Marie Skłodowska-Curie Action at IBM Research – Europe, Switzerland, under the supervision of Dr. Heiko Wolf. Her doctoral degree was pursued at TU Delft, the Netherlands, in the Advanced Soft Matter group under the supervision of Prof. Dr. Jan van Esch. In 2023–2024, she also undertook a five-month research internship at Harvard University, United States of America. Her doctoral research focused on the design and fabrication of nanoscale surface-chemical patterns to control the spatial distribution and local concentration of chemical reaction network components, as detailed in this thesis.

Since 2024, she has held a postdoctoral research position at the University of Mainz, Germany, in the laboratory of Prof. Dr. Andreas Walther, where her work is directed toward the development of autonomous soft robotic engines.

List of publications

1. Related to this thesis

- **Publications**

- **Figueiredo da Silva, J.**, Roshanasan, A., Bus, M., Fotiadis, D., Knoll, A. W., van Esch, J. H., & Wolf, H. (2025). Control of a Gel-Forming Chemical Reaction Network Using Light-Triggered Proton Pumps. *Langmuir*, 41(12), 8071-8080.

- **Figueiredo da Silva, J.**, Bacheva, V., Drechsler, U., Nicollier, P., Reidt, S., Fotiadis, D., ... & Wolf, H. (2024). Fabrication of a hybrid device for the integration of light-triggered proton pumps. *Micro and Nano Engineering*, 23, 100250.

- Ruggeri, F., Schwemmer, C., Stauffer, M., Nicollier, P. M., **Figueiredo da Silva, J.**, Bosshart, P. D., ... & Wolf, H. (2022). Placement of Biological Membrane Patches in a Nanofluidic Gap With Control Over Position and Orientation. *Advanced Materials Interfaces*, 9(23), 2200941.

- **Patent**

- Knoll, A., Wolf, H., Nicollier, P. M., Widmer, D., & **da Silva, J. F.** (2024). U.S. Patent Application No. 18/052,989.

2. Not related to the thesis

- **Master thesis**

- **Figueiredo da Silva, J.** (2020). Functionalization of SERS substrates for ex vivo detection of inflammatory state [Master's thesis, Jagiellonian University in Krakow].

- **Publications**

- Skarsetz, O., Swinkels, P. J., **Figueiredo da Silva, J.**, Vozzolo, G., Masukawa, M., Fusi, G., ... & Walther, A. (2025). Soft Robotic Engines with Non-Reciprocal Motion by Physical Intelligence. *Advanced Materials*, e11630.

- De Vreede, L. J., Ying, C., Houghtaling, J., **Da Silva, J. F.**, Hall, A. R., Lovera, A., & Mayer, M. (2019). Wafer-scale fabrication of fused silica chips for low-noise recording of resistive pulses through nanopores. *Nanotechnology*, 30(26), 265301.


TU Delft
Delft
University of
Technology


TU Delft
Delft
University of
Technology